PPG-1021
UCLA-ENG-86-44
FNT-17

Modeling, Analysis and Experiments for Fusion Nuclear Technology

FINESSE Phase I Report

January 1987

Fusion Nuclear Technology
Mechanical, Aerospace and Nuclear Engineering Department
University of California, Los Angeles
Los Angeles, California

DISCLAIMER

This report was prepared as an account of work sponsored by an agency of the United States Government. Neither the United States Government nor any agency thereof, nor any of their employees, makes any warranty, express or implied, or assumes any legal liability or responsibility for the accuracy, completeness, or usefulness of any information, apparatus, product, or process disclosed, or represents that its use would not infringe privately owned rights. Reference herein to any specific commercial product, process, or service by trade name, trademark, manufacturer, or otherwise, does not necessarily constitute or imply its endorsement, recommendation, or favoring by the United States Government or any agency thereof. The views and opinions of authors expressed herein do not necessarily state or reflect those of the United States Government or any agency thereof.

PPG-1021
UCLA-ENG-86-44
FNT-17

Modeling, Analysis and Experiments for Fusion Nuclear Technology

FNT Progress Report: Modeling & FINESSE

January 1987

Work supported by the U.S. Department of Energy under
Grant No. DE-FG03-86ER52123

Modeling, Analysis and Experiments
for Fusion Nuclear Technology

FNT Progress Report: Modeling & FINESSE

M. A. Abdou* (UCLA)
M. S. Tillack* (UCLA)
A. R. Raffray* (UCLA)
A. H. Hadid* (UCLA)
J. R. Bartlit (LASL)
G. E. C. Bell (UCLA)
P. J. Gierszewski* (CFFTP)
J. D. Gordon (TRW)
T. Iizuka (UCLA/JAERI)
C. N. Kim (UCLA)
V. Lankarani-Fard (UCLA)
A. Majid (UCLA)
F. M. Mann (HEDL)
K. A. McCarthy (UCLA)
K. Moshonas (CFFTP)
D. K. Patel (UCLA)
B. F. Picologlou* (ANL)
R. J. Puigh* (HEDL)
M. Song (UCLA)
D. K. Sze* (ANL)
K. Taghavi (U-KY)
S. Tewani (U-KY)
R. H. Whitley* (TRW)

*Lead authors

ACKNOWLEDGEMENTS

The authors wish to acknowledge the technical advice of many members of the fusion community. In particular, we are grateful to Dr. C. Baker (ANL), Prof. N. Ghoniem (UCLA), Prof. M. Hoffman (UC-Davis), Dr. G. Hollenberg (HEDL), Dr. C. Johnson (ANL), Dr. R. Mattas (ANL), Dr. S. Sharafat (UCLA), and Dr. M. Youssef (UCLA) for their review and comments on many parts of the report. Also, the technical assistance of Mr. B. Slatkin (UCLA) is acknowledged.

Many scientists and engineers from outside the U.S. have provided significant contributions to the study, and their efforts are gratefully acknowledged. Special acknowledgement is due to the Canadian Fusion Fuels Technology Project and the Japan Atomic Energy Research Institute.

We also wish to give special recognition to Ms. S. Ehrlich and Ms. M. Pagnusat for their assistance in assembling this report.

TABLE OF CONTENTS

Page

1. Introduction and Summary....1-1
1.1 Introduction....1-1
1.2 Non-Fusion Experiments and Facilities....1-4
1.2.1 Introduction....1-4
1.2.2 Solid Breeder Experiments and Facilities....1-9
1.2.2.1 Solid Breeder Comparison and Testing Priorities....1-9
1.2.2.2 Fission Reactor Evaluation for Advanced Solid Breeder Testing....1-34
1.2.3 Liquid Metal MHD Experimental Facilities....1-43
1.3 Fusion Testing Issues....1-53
1.3.1 Requirements for Nuclear Technology Testing....1-53
1.3.1.1 Heat Source Requirements....1-56
1.3.1.2 Neutron Fluence Requirements....1-60
1.3.1.3 Plasma Burn Time Requirements and Pulsing Effects....1-63
1.3.1.4 Device Geometry and Test Volume Requirements....1-74
1.3.1.5 Magnetic Field Requirements....1-82
1.3.2 Tritium Supply....1-88
1.3.3 Blanket Reliability and Device Availability....1-91
1.4 Theory and Modeling....1-96
1.4.1 Introduction....1-96
1.4.2 Liquid Metal MHD Modeling....1-99
1.4.2.1 Computational Magnetohydrodynamics....1-102
1.4.2.2 Analytical and Approximate Methods....1-113
1.4.3 Modeling of Liquid Metal Mass Transfer (Corrosion/Deposition)....1-117
1.4.4 Heat Transfer in Flows Over a Wedge or a Cylinder With Volumetric Heat Generation....1-119
1.4.5 Tritium Transport Modeling....1-122
1.4.6 Modeling of Plasma-Interactive Components....1-123
1.4.6.1 Design Window for Liquid-Metal-Cooled Limiters....1-123
1.4.6.2 Thermal and Stress Analysis of Limiters....1-125

2. Non-Fusion Experiments and Facilities....2-1
2.1 Introduction....2-1
2.2 Material Properties and Uncertainties....2-6
2.2.1 Thermophysical Properties....2-6
2.2.1.1 Density....2-6
2.2.1.2 Thermal Conductivity....2-7
2.2.1.3 Specific Heat....2-12
2.2.1.4 Breeder Temperature Limits....2-12
2.2.1.5 Other Thermophysical Properties....2-17
2.2.2 Tritium Properties....2-17
2.2.2.1 Diffusion....2-18
2.2.2.2 Solubility....2-22
2.2.2.3 Surface Adsorption....2-28
2.2.2.4 Mechanical Properties....2-31
2.2.2.5 Fabrication....2-40
2.3 Solid Breeder Comparison and Testing Priorities....2-50
2.3.1 Objectives....2-50
2.3.2 Materials and Conditions....2-50
2.3.3 Performance Parameters and Results....2-57
2.3.3.1 Neutronics....2-58
2.3.3.2 Thermomechanics....2-85
2.3.3.3 Tritium....2-100
2.3.3.4 Activation....2-125
2.3.3.5 Economics....2-131
2.3.4 Conclusions and R&D Priorities....2-140
2.4 Fission Reactor Evaluation for Advanced Solid Breeder Testing....2-151
2.4.1 Introduction....2-151
2.4.2 Representative Reactor Conditions....2-154
2.4.3 Evaluation....2-157
2.4.4 Conclusions....2-176
2.5 Liquid Breeder Facilities....2-180
2.5.1 Introduction....2-180
2.5.2 LMF Facility Description....2-186
2.5.2.1 Test Article....2-186
2.5.2.2 Flow Loop....2-188

2.5.2.3 Magnet System....2-192
2.5.2.4 Instrumentation....2-195
2.5.3 Experimental Program....2-198
3. Fusion Testing Issues....3-1
3.1 Introduction....3-1
3.2 Test Requirements....3-3
3.2.1 Summary of Test Requirements....3-3
3.2.2 Analysis of the Effects of Cyclic Operation....3-5
3.2.2.1 Solid Breeder Thermal and Tritium Behavior....3-11
3.2.2.2 Unsteady Liquid Metal Flow Behavior....3-21
3.2.2.3 Unsteady Liquid Metal Blanket Temperature Response....3-35
3.3 External Tritium Supplies....3-42
3.3.1 Natural Tritium....3-42
3.3.2 Bomb Test Tritium....3-42
3.3.3 Fission Reactions....3-42
3.3.4 Heavy Water Absorption....3-43
3.3.5 Lithium Absorption....3-44
3.3.6 Helium-3 Absorption....3-46
3.3.7 Fusion Reactions....3-47
3.3.8 Summary....3-47
3.4 ETR Tritium Breeding Blanket Availability and Testing Requirements....3-48
3.4.1 Introduction....3-48
3.4.2 Blanket MTBF Requirements....3-49
3.4.3 Testing Time and Performance Confidence Levels....3-54
3.4.4 Parallel Testing As a Means of Achieving Performance Confidence....3-58
3.4.5 Conclusion....3-59
4. Theory and Modeling....4-1
4.1 Introduction....4-1
4.2 Computational Methods in Liquid Metal MHD....4-13
4.2.1 Introduction....4-13
4.2.2 Finite Difference Method....4-18
4.2.2.1 Entry Length Effects in MHD Duct Flow....4-22
4.2.2.2 Sensitivity Analysis of MHD Heat Transfer....4-29
4.2.2.3 MHD Flow in a Sudden Duct Enlargement....4-37

4.2.2.4 Concluding Remarks....4-49
4.2.3 Finite Element Method....4-51
4.2.3.1 Introduction....4-51
4.2.3.2 Basic Equations....4-53
4.2.3.3 Illustration of Self-Adaptive Mesh Refinement in the 1-D Hartmann Problem....4-55
4.2.3.4 Two-Dimensional Fully Developed Duct Flow....4-60
4.2.3.5 Extensions and Recommendations....4-87
4.3 Analytic Treatment of MHD Flow in a Curved Pipe....4-88
4.3.1 Introduction....4-88
4.3.2 Analytic Approach....4-90
4.3.3 Results and Discussion....4-94
4.4 MHD Pressure Drop....4-99
4.4.1 Introduction....4-99
4.4.2 Pressure Drop Due to Magnetic Field Entrance or Exit....4-99
4.4.2.1 Background....4-99
4.4.2.2 Description of Methodology....4-101
4.4.2.3 Application to Fusion Reactor....4-116
4.5 Heat Transfer in Flow Over a Wedge or a Cylinder Under the Condition of Heat Generation....4-118
4.5.1 Introduction....4-118
4.5.2 Analysis....4-120
4.5.3 Limiting Cases of $Pr \to 0$ and $Pr \to \infty$....4-125
4.5.4 Analysis for a Cylinder in Cross Flow....4-128
4.5.5 Experimental Apparatus and Procedure....4-130
4.5.5.1 Apparatus....4-130
4.5.5.2 Procedure....4-134
4.5.6 Results and Discussion....4-136
4.5.7 Summary and Conclusions....4-144
4.6 Liquid Metal/Structural Material Interactions Research....4-147
4.6.1 Introduction....4-147
4.6.2 Analytical Approach to Mass Transport....4-148
4.6.3 Liquid Phase Transport Modeling....4-149
4.6.4 Particle Mass Transport Modeling....4-153
4.6.5 Solid Phase Mass Transport Modeling....4-156
4.6.6 Chemical Reactions for Lithium/HT9....4-158

4.6.7 Experimental Investigations of Mass Transport in Lithium/HT9 Systems....4-159
4.6.7.1 Introduction....4-159
4.6.7.2 Thermal Convection Loop Program for Lithium/HT9....4-161
4.6.8 Summary and Future Experimental Work....4-166
4.7 Tritium Transport in Solid Breeders....4-167
4.8 Design Window for a Liquid-Metal-Cooled Limiter....4-170
4.8.1 Introduction....4-170
4.8.2 Design Approach....4-170
4.8.3 Design Constraints....4-171
4.8.4 Choice of Limiting Values and Material Properties....4-172
4.8.5 Geometrical Configuration....4-172
4.8.6 Thermal and Stress Analysis....4-173
4.8.6.1 Analysis of the Flat Face Channel Without Coating....4-174
4.8.6.2 Identifying Maximum Permissible Heat Flux for Flat Face Channel Without Coating....4-177
4.8.6.3 Analysis of the Flat Face Channel with Coating....4-179
4.8.6.4 Defining Maximum Permissible Heat Flux for a Limiter Center Channel with Coating....4-186
4.8.6.5 Analysis of the Channel at the Leading Edge....4-186
4.8.7 Design Window for Limiter Without Coating....4-187
4.9 Thermal and Stress Analysis of Limiters....4-193
4.9.1 Introduction....4-193
4.9.2 Geometric Configuration....4-193
4.9.3 Mathematical Formulation....4-194
4.9.3.1 Thermal Analysis....4-194
4.9.3.2 Stress Analysis....4-196
4.9.3.3 Boundary Conditions....4-202
4.9.4 Results....4-205
4.9.5 Concluding Remarks....4-212

1. INTRODUCTION AND SUMMARY

TABLE OF CONTENTS

Page

1. Introduction and Summary....1-1
   1.1 Introduction....1-1
   1.2 Non-Fusion Experiments and Facilities....1-4
      1.2.1 Introduction....1-4
      1.2.2 Solid Breeder Experiments and Facilities....1-9
         1.2.2.1 Solid Breeder Comparison and Testing Priorities....1-9
         1.2.2.2 Fission Reactor Evaluation for Advanced Solid Breeder Testing....1-34
      1.2.3 Liquid Metal MHD Experimental Facilities....1-43
   1.3 Fusion Testing Issues....1-53
      1.3.1 Requirements for Nuclear Technology Testing....1-53
         1.3.1.1 Heat Source Requirements....1-56
         1.3.1.2 Neutron Fluence Requirements....1-60
         1.3.1.3 Plasma Burn Time Requirements and Pulsing Effects....1-63
         1.3.1.4 Device Geometry and Test Volume Requirements....1-74
         1.3.1.5 Magnetic Field Requirements....1-82
      1.3.2 Tritium Supply....1-88
      1.3.3 Blanket Reliability and Device Availability....1-91
   1.4 Theory and Modeling....1-96
      1.4.1 Introduction....1-96
      1.4.2 Liquid Metal MHD Modeling....1-99
         1.4.2.1 Computational Magnetohydrodynamics....1-102
         1.4.2.2 Analytical and Approximate Methods....1-113
      1.4.3 Modeling of Liquid Metal Mass Transfer (Corrosion/Deposition)....1-117
      1.4.4 Heat Transfer in Flows Over a Wedge or a Cylinder With Volumetric Heat Generation....1-119
      1.4.5 Tritium Transport Modeling....1-122
      1.4.6 Modeling of Plasma-Interactive Components....1-123
         1.4.6.1 Design Window for Liquid-Metal-Cooled Limiters....1-123
         1.4.6.2 Thermal and Stress Analysis of Limiters....1-125

LIST OF FIGURES

		Page
1.2-1	Solid breeder test plan	1-6
1.2-2	Liquid breeder test plan	1-7
1.2-3	Reference blanket design	1-12
1.2-4	Effective tritium breeding ratio as a function of ^{6}Li enrichment for the cases with a separate 12-cm thick Be multiplier region	1-15
1.2-5	Effective tritium breeding ratio for the different cases. For the cases with the solid breeder/beryllium homogeneous mixture, A and B are the lower and upper limits represented by the $LiAlO_2$/Be and Li_2O/Be cases, respectively	1-18
1.2-6	Effective tritium breeding ratio as a function of the first breeder region thickness for two sandwich cases (both with 60% ^{6}Li enrichment)	1-20
1.2-7	Point graph of the effective tritium breeding ratio and of the reciprocal of the total tritium inventory for the different cases	1-30
1.2-8	Point graph of the reciprocal of material cost and of power multiplication for the different cases	1-31
1.2-9	Point graph of the afterheat time to reach the maximum allowable temperature and of the reciprocal of the dose rate after 3-year irradiation and 10-hour cooling for the different cases	1-32
1.2-10	Comparison of neutron flux spectra for the FFTF, NRU, and HFIR reactors normalized to their total flux	1-36
1.2-11	Schematic of one-dimensional model used to calculate tritium production and heat generation rates in fission reactors. The zones in the figure are for an annular test specimen in the FFTF reactor	1-37
1.2-12	Influence of lithium-6 enrichment on temperature profile in Li_2O pellet in the NRU reactor	1-40
1.2-13	Variation of tritium production rates with time in the HFIR reactor	1-41
1.2-14	Schematic of LMF loop	1-47
1.2-15a	Conceptual design of a test section simulating the inlet (or outlet) manifold of the TPSS design. Flows in each of the individual ducts fed from the manifold can be measured with individual EM flow meters	1-49

1.2-15b Conceptual design of a test section simulating the salient features of the BCSS liquid-metal-cooled blanket design.....1-49

1.3-1 Heat source effect on the Li_2O/He/HT-9 first wall temperature profile (reactor at 5 MW/m^2 neutron and 1 MW/m^2 surface heat load; scaled test module at 2.5 and 0.1 MW/m^2).....1-59

1.3-2 Tritium and thermal diffusion time constraints as a function of temperature (γ-$LiAlO_2$).....1-69

1.3-3 $LiAlO_2$ diffusive tritium concentration profiles with 200-s burn, 50-s dwell, and 12-s ramp times (microscopic calculation).....1-71

1.3-4 Transient tritium release rate from 0.2 μm grain $LiAlO_2$ (for 200-s burn, 50-s dwell, and 12-s ramp times).....1-72

1.3-5 Time-dependence of tritium recovery and inventory in $LiAlO_2/H_2O$/Be blanket.....1-73

1.3-6 Transient first wall temperatures of a liquid metal blanket cooling channel at 5 m from the inlet for different velocity profiles.....1-75

1.3-7 Geometrical arrangement for the test module in a fusion test device.....1-79

1.3-8 Variation of the local tritium production rate in the poloidal θ direction for two test module sizes, θ=6° and θ=12°.....1-80

1.3-9 Failure rate over component life.....1-93

1.3-10 The tritium breeding module MTBF (at various values of MTTR) necessary to achieve a blanket availability goal of 0.8 as a function of the number of tritium breeding modules (and tritium breeding ratio).....1-94

1.3-11 Minimum required testing time (at various confidence levels) to achieve a blanket availability of 0.8 as a function of the number of tritium breeding modules and tritium breeding ratio. Also shown is the cost of external tritium supply as a function of the breeding ratio.....1-95

1.4-1 Types and role of experiments and facilities for fusion nuclear technology.....1-97

1.4-2 Liquid metal MHD modeling logic.....1-100

1.4-3 Effect of an axial magnetic field on the development of centerline velocity along the axial distance (x) in a pipe of radius (a).....1-103

1.4-4 Development of the velocity profile along an insulated channel of half-width (a) and axial magnetic field.....1-104

1.4-5 Effect of a perpendicular magnetic field on the velocity profile at the exit of an insulated channel of half-width (a) and insulated walls.....1-105

1.4-6 Effect of a transverse magnetic field on entry length heat transfer in an insulated channel (parabolic inlet profile and constant wall temperature.....1-106

1.4-7 Configuration of pipe expansion and a definition sketch.....1-108

1.4-8 Characteristics of the annular eddy as a function of Reynolds number at different Hartmann numbers (L_1/D_o, relative eddy length; L_2/D_o, relative location of eddy center).....1-109

1.4-9 Effect of axial magnetic field on the development of velocity profile along the pipe.....1-110

1.4-10 Wall pressure distribution along the pipe at different Hartmann numbers.....1-111

1.4-11 Geometry for the fully developed 2-D channel flow problem.....1-114

1.4-12 Comparison of finite element solution with analytic solution.....1-114

1.4-13 Toroidal coordinate system for a coiled pipe in a transverse magnetic field B.....1-115

1.4-14 First perturbed axial velocity profile due to the combined effects of Dean and Hartmann numbers (K=20, Ha=1), together with Poiseuille profile.....1-116

1.4-15 Block diagram of mass transport processes.....1-118

1.4-16 Boundary layer temperature profile for flow over flat plate.....1-120

1.4-17 Design window for lithium-cooled vanadium limiter with insulated conduits at 4 MW/m^2 heat flux.....1-124

1.4-18 Design window for lithium-cooled vanadium limiter with insulated conduits at 5 MW/m^2 heat flux.....1-126

1.4-19 Three-dimensional finite element mesh geometry.....1-127

1.4-20 Temperature distribution in a vanadium limiter. Results are shown for the X-Y plane of Figure 1.4-19.....1-128

1.4-21 Von Mises stress distribution (σ_t) in a lithium-cooled vanadium limiter with 6.0 MW/m^2 heat flux and coolant pressure of 5.5 MPa.....1-129

LIST OF TABLES

		Page
1.2-1	Key Blanket Issues	1-5
1.2-2	Phases of Blanket Testing	1-5
1.2-3	Solid Breeder Materials Considered	1-10
1.2-4	Blanket Concept Parameters	1-11
1.2-5	Performance Parameters	1-13
1.2-6	Blanket Performance Summary	1-14
1.2-7	^{6}Li Enrichment and Atom Density at TBR Saturation (99% of Maximum TBR) for Cases with a Separate Be Multiplier Region	1-16
1.2-8	Classification of the Different Solid Breeder Cases Based on the Effective Tritium Breeding Ratio	1-19
1.2-9	Fission Reactor Capabilities and Characteristics	1-35
1.2-10	Calculational Models for HFIR and NRU and FFTF	1-37
1.2-11	Features and Objectives of Major Liquid Breeder Experiments	1-44
1.2-12	LMF Facility Parameters	1-50
1.3-1	Device Parameters: Reference Conditions and Recommended Values	1-55
1.3-2	General Effects of Fusion Test Device Parameters on Blanket Performance	1-57
1.3-3	Examples of Important Effects as a Function of Exposure	1-62
1.3-4	Reference Burn Cycle Times (in seconds)	1-65
1.3-5	Approximate Characteristic Time Constants in Representative Blankets	1-66
1.3-6	Examples of Number and Size of Test Articles Required for Fusion Nuclear Technology Testing	1-76
1.3-7	Definitions and Evaluation of MHD Parameters	1-84
1.3-8	Potential Tritium Sources	1-89
1.3-9	Representative ETR Parameters Considered in the Reliability Analysis	1-92
1.4-1	Change in Nusselt Number Due to Heat Generation for a Pr=0 Flow Over a Cylinder	1-121

1. INTRODUCTION AND SUMMARY

1.1 Introduction

The importance of moving forward with the development of fusion nuclear technology (FNT) has been clearly recognized by all of the world's major fusion programs. Furthermore, there has been an increased awareness of the complexity of the research and development (R&D) problems of FNT and of the need for careful technical planning of experiments and facilities. FNT is concerned with fuel production and processing, energy extraction and use, and radiation protection of personnel and components. The primary fusion reactor components include the blanket, plasma-interactive components (such as first wall, limiter, and divertor), radiation shield, and tritium system. In 1984-1985, the FINESSE study identified the key technical issues and developed, based on technical evaluations, recommendations on the types, sequences and characteristics of major experiments and facilities in a logically consistent path for FNT development. The results were presented in the two major FINESSE reports,[1,2] with comprehensive summaries in Refs. [3] and [4]. Although technical planning was the driving goal for FINESSE, substantial contributions have also been made to the advancement of the understanding of fusion nuclear components and to the capability of predicting their performance.

Implementation is the logical next step to technical planning. The results from FINESSE showed that the present activities on FNT need substantial enhancement through: a) construction of a number of well defined, small-scale facilities; b) performance of a number of new specific experiments in existing facilities; and c) development of analytical and computational models for predicting the performance of nuclear components.

This document is a progress report on two technical studies carried out during 1986, both of which relate to the implementation phase of FNT. The first, which is a follow-up to FINESSE, focuses on specific key questions for: a) very near-term (0-3 years) non-fusion experiments and facilities, and b) FNT testing in a fusion facility. The second is the initial stage of a detailed effort to develop theory, models and computer codes for predicting the performance of nuclear components.

Chapter 2 addresses a number of selected technical problems for the very near-term experiments of solid and liquid breeders. In previous FINESSE work, a number of advanced solid breeder experiments in fission reactors have been identified. These next-generation experiments are relatively costly and, hence, need to be limited to materials and configurations with the highest potential. An important part of Chapter 2 is an assessment of the relative advantages of the many solid breeders, neutron multipliers and configurations. Recommendations have been developed for reducing the size of the test matrix and for focusing the testing program on important areas of emphasis for the near-term experiments.

The need for a near-term advanced MHD facility, called LMF1, has been identified in FINESSE. This facility is required in addition to existing facilities (e.g., ALEX at Argonne National Laboratory) in order to address critical MHD fluid flow issues. The characteristics and cost of this facility and the experiments which might be performed in it are also discussed in Chapter 2.

Major initiatives are underway to plan and design a fusion engineering test facility (e.g., NET[5] in Europe, FER[6] in Japan, and ETR[7] in the U.S.). The requirements of FNT testing on the major parameters and features of such a facility have been addressed previously in FINESSE. Examination of the impact of these requirements on the design and cost of a fusion engineering facility revealed the need for further examination of a number of issues. A particularly important issue relates to the length of the plasma burn time and to the mode of operation (steady state or pulsed). Another important issue pertains to the need for a tritium-producing blanket and to its impact on the operational availability of the device. These issues are examined in Chapter 3. Because of the renewed strong interest in a fusion engineering facility, a reasonably complete summary of the important FNT testing requirements is also provided in Section 1.3.

Successful development of the predictive capabilities necessary to design, construct and operate fusion nuclear components requires a highly interactive program of theory, modeling and experiments. While Chapters 2 and 3 are concerned with FNT experiments, Chapter 4 reports on the progress of the initial stage of an effort to develop theory and analytical and numerical

models for nuclear components. A major part of the effort to date has focused on modeling of MHD effects for liquid metal blankets. Progress has also been made on modeling tritium transport and inventory in solid breeder blankets and the thermomechanical behavior of liquid-metal-cooled limiters.

The remainder of this chapter is devoted to a summary of Chapters 2 through 4. The summary is relatively detailed for the convenience of readers interested in a comprehensive overview.

1.2 Non-Fusion Experiments and Facilities

1.2.1 Introduction

Experiments in non-fusion facilities can play a key role in the development of fusion nuclear technologies prior to testing in the fusion environment. This was recognized in earlier studies and incorporated as a central element in the FINESSE test plans for blankets and other nuclear components.[2] Recent effort in the Technical Planning Activity[8] (TPA) has confirmed the importance of these experiments.

Non-fusion facilities include non-neutron test stands, fission reactors, and 14 MeV point neutron sources. Each of these provide unique testing capabilities for blanket experiments. The key issues for solid breeder blankets are shown in Table 1.2-1. Because of the dominant role that radiation plays in tritium production, tritium transport, and breeder thermomechanical behavior, fission reactors play a major role in the solid breeder test program. Table 1.2-1 also summarizes the key issues for liquid breeder blankets. Here, the key issues generally involve thermomechanical behavior (including MHD effects), material compatibility, and tritium recovery. Experiments addressing these issues are generally best treated in non-neutron test stands. For all blankets, fuel self-sufficiency is a key issue. 14-MeV neutron sources are needed for experiments on tritium breeding as well as other neutronic and radiation damage issues.

A framework for technical planning of fusion nuclear experiments has been developed earlier in FINESSE.[2] This framework defines four phases that are summarized in Table 1.2-2. During these phases, the emphasis shifts in the level of integration from separate effect, to multiple effect, to partially integrated and, finally, to fully integrated fusion testing. The key elements of the test plans for both solid and liquid breeder blankets are summarized in Figures 1.2-1 and 1.2-2. Both plans culminate in the design of experimental modules for testing in the fusion environment and in an assessment of the feasibility and attractiveness of blanket components and systems. The objectives and milestones for each phase are also shown in Table 1.2-2.

As part of the previous FINESSE effort, many of the technical features of experiments and facilities of the four phases have been defined. The work reported here examines a number of selected technical problems for the near-term experiments of Phase I.

Table 1.2-1 Key Blanket Issues

Solid Breeder
Tritium Self-Sufficiency
Breeder/Multiplier Tritium Recovery and Inventory
Breeder/Multiplier Thermomechanical Behavior
Corrosion and Mass Transfer
Structural Response and Failure Modes
Tritium Permeation and Processing from the Blanket
Liquid Breeder
Tritium Self-Sufficiency
Magnetohydrodynamic Effects
Corrosion and Mass Transfer
Structural Response and Failure Modes
Tritium Permeation and Processing from the Blanket

Table 1.2-2 Phases of Blanket Testing

	Approximate Time Frame	Level of Integration	Primary Objectives	Milestones
Phase I	0-10 yrs	Properties, separate effects	Develop understanding of material behavior and blanket phenomena	Select material combinations[a]
Phase II	5-15 yrs	Multiple effects	Understand phenomena, develop predictive capabilities for complex configurations	Select blanket configurations
Phase III	10-20 yrs	Partially integrated (non-fusion)	Design concept verification in non-fusion environment	Select primary blanket design options for fusion testing
Phase IV	15-25 yrs	Integrated	Design concept verification in fusion facility	Successfully operate test modules

[a]To the extent possible with limited high fluence irradiation data

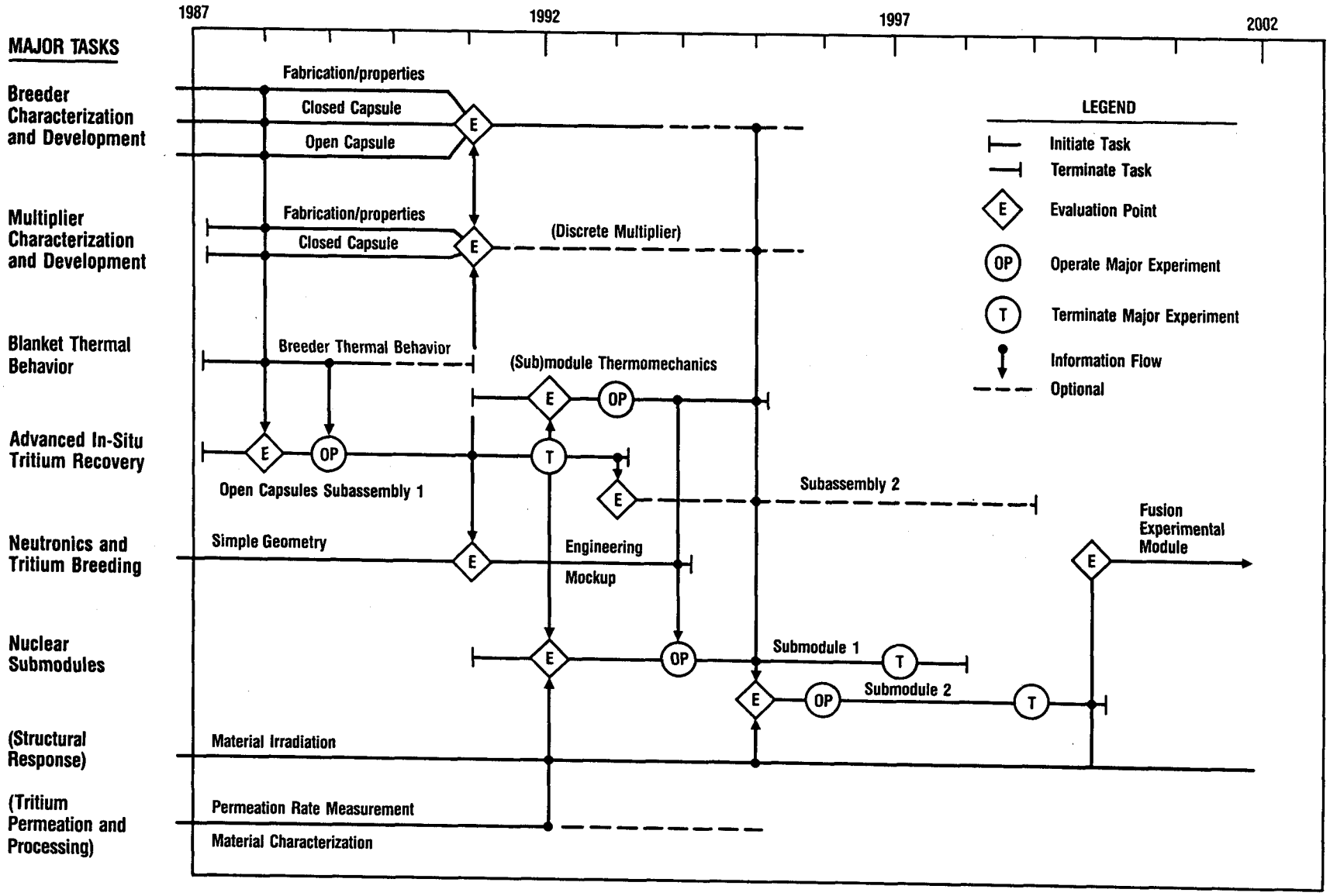


Figure 1.2-1 Solid breeder test plan

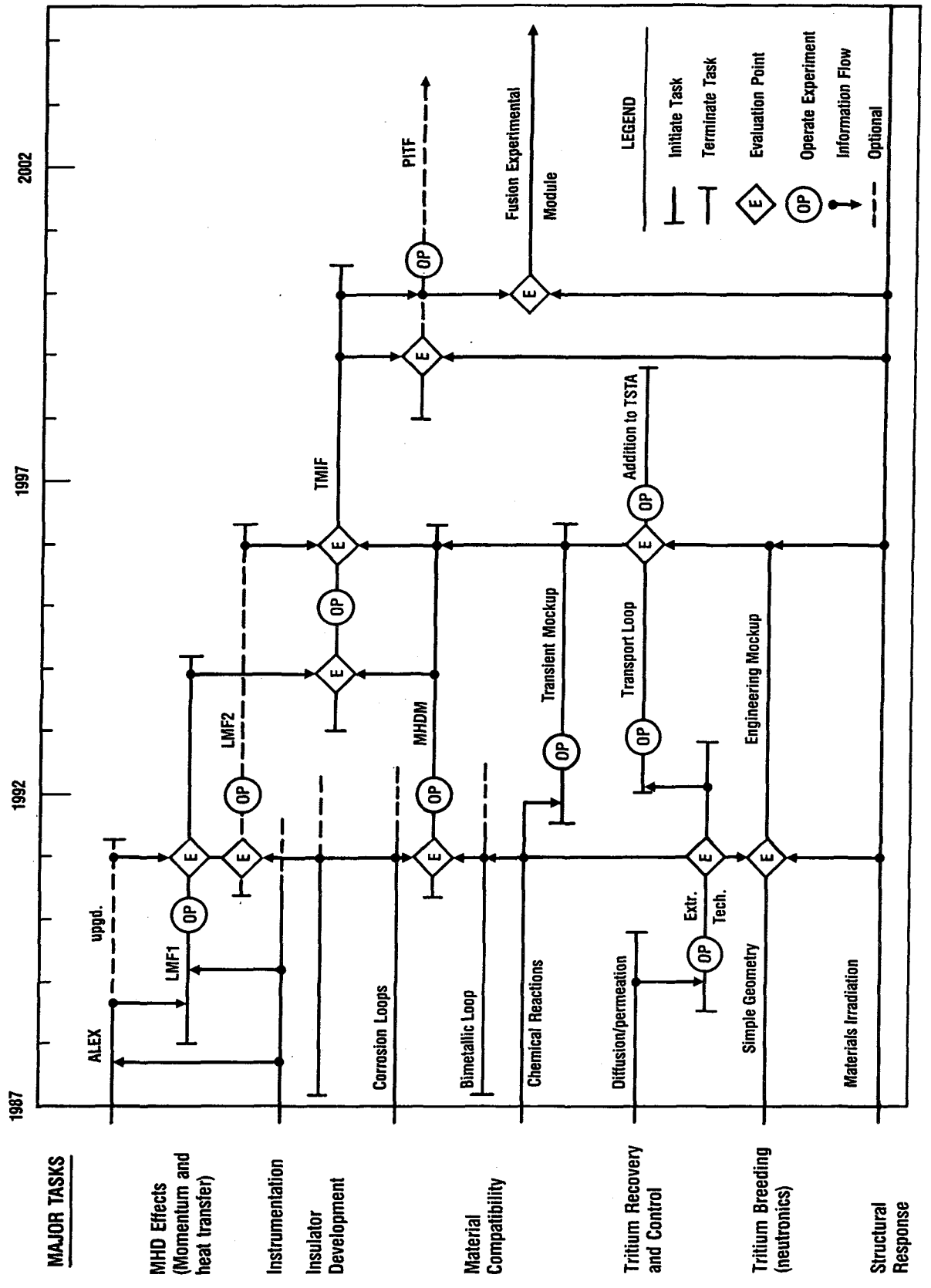


Figure 1.2-2 Liquid breeder test plan

For solid breeder blankets, material selection and characterization are currently at the center of a worldwide effort. On-going and near-term experiments are focused on fabrication, unirradiated properties and in-reactor open and closed capsule tests. At the same time, the world programs include a large number of candidate materials and configurations. This work assesses the relative advantages of the various solid breeders and provides recommendations for reducing the size of the test matrix in upcoming experiments. This is particularly important because of the increased cost of the more complex next-generation experiments.

Section 1.2.2.1 describes the detailed analyses that have been performed to compare different solid breeder materials and configurations. The comparison was based on various performance parameters directly dependent on the solid breeder properties. Prior to the analysis, these properties (and corresponding uncertainty ranges) were assembled from data taken from the literature and past experiments (details can be found in Section 2.2). The calculated performance parameters were then used to identify the more attractive solid breeder candidates and configurations, and recommendations on important areas of emphasis in near-term experiments were derived.

The capabilities of three existing fission reactors with significantly different neutron spectra also have been assessed in order to provide recommendations on the optimum facilities in which to perform future solid breeder experiments. The objective was to explore how well the three fission reactors would match tritium production and temperature profiles in macroscopic test specimens. The results are discussed in Section 1.2.2.2.

For liquid breeder blankets, there is not one central element in the test program. There are many issues, some of which depend strongly on the choice of materials and configuration. For the large and important class of designs, known as self-cooled liquid metal blankets (for which the breeding material also functions as the coolant), MHD effects are the dominant concern. Separate effect tests are currently planned or underway in several countries to address MHD fluid flow and pressure drop issues. An example of a current experiment is ALEX in the U.S.[9] After ALEX and similar experiments, the need for an advanced MHD facility, called LMF1, has been identified (see Figure 1.2-2). The characteristics of this facility and the experiments which might be performed are explored in Section 1.2.3.

1.2.2 Solid Breeder Experiments and Facilities

1.2.2.1 Solid Breeder Comparison and Testing Priorities

Objectives and Calculation Framework

Solid breeder blanket research is in a material development and selection phase which requires the consideration of a large number of potential solid breeder materials, properties, behaviors, and test conditions. A consistent comparison of the effect of solid breeder material choice on blanket attractiveness have been performed to focus the test matrix by reducing the number of solid breeder materials and configurations which need to be tested. The comparison also identifies material tests required to reduce important performance uncertainties.

Table 1.2-3 lists the seventeen solid breeder/multiplier material combinations considered in the context of a representative blanket design and compared on the basis of selected performance parameters. Except for Li_2O and Li_7Pb_2, those solid breeders are ternary ceramics. Beryllium is used as the neutron multiplier in combination with those solid breeders which may require better neutronics performance. Other multipliers (Pb and Zr_5Pb_3) have been proposed[10,11] but are not considered here. Preliminary analysis indicates that they are considerably inferior to beryllium with regard to enhancing tritium production, power multiplication and design simplicity. The low melting point of lead, the relatively poor thermophysical properties of Pb and Zr_5Pb_3, and the high energy threshold of the (n,2n) reaction in Pb and Zr make these neutron multipliers less desirable for reactors with high neutron wall loads (>2 MW/m^2).

Two configurations have been considered for incorporating the beryllium neutron multiplier in the blanket. In the first configuration, the multiplier is placed in a separate region in front of the breeder region. In the second configuration, the solid breeder and multiplier are mixed homogeneously. Analysis for the second configuration was limited to Li_2O and $LiAlO_2$. Since Be will chemically reduce the solid breeder materials (although the rate might be acceptably slow once an initial BeO layer forms), BeO is also included as an alternative for the homogeneous mixture cases.

Table 1.2-3 Solid Breeder Materials Considered

Without a Multiplier	Homogeneous Solid Breeder/Multiplier Mixture	With a Separate Be Multiplier Region
1. Li_2O	6. $LiAlO_2$/Be	10. Li_2O
2. Li_2ZrO_3	7. $LiAlO_2$/BeO	11. $LiAlO_2$
3. Li_8ZrO_6	8. Li_2O/Be	12. Li_5AlO_4
4. $Li_2Be_2O_3$	9. Li_2O/BeO	13. Li_2SiO_3
5. Li_7Pb_2		14. Li_4SiO_4
		15. Li_2ZrO_3
		16. Li_8ZrO_6
		17. Li_2TiO_3

The BCSS[12] $LiAlO_2$/He/FS/Be outboard blanket design is adopted here as a reference blanket configuration. This minimizes unnecessary analysis and provides a consistent blanket framework for the material comparison. However, design parameters that are affected by the choice of solid breeder (such as the plate thickness) are optimized for each particular case. The reference blanket module parameters are listed in Table 1.2-4.

The reference blanket consists of 1125 modules with a 5 MW/m^2 neutron load at the first wall. A typical module is shown in Figure 1.2-3. The solid breeder or homogeneous solid breeder/multiplier mixture is placed in plates with a thin ferritic steel (HT9) cladding on each side. The pressure of the helium purge flow inside the plates is set at 1.0 MPa. The clad plates are wire-wrapped to provide a gap between adjacent plates for the main helium coolant flow which enters through the first wall and exits between the solid breeder plates. For the cases with a separate multiplier region, an array of multiplier rods is placed in front of the breeder plates. The thickness of the breeder plates is determined so that the maximum breeder temperature does not exceed the design limit. Since the volume fractions (and, hence, the plate thicknesses) are required for the neutronics calculations, a few

Table 1.2-4 Blanket Concept Parameters

Parameter	Comment
Solid breeder material	As shown in Table 1.2-3
Multiplier	None or beryllium
Structural material	HT9
Coolant and purge gas	Helium
Width	0.3 m
Length	2.0 m
Blanket depth	0.7 m to coolant plenum
Coolant plenum depth	0.2 m
Shield depth	0.3 m Fe1422
Breeder plate geometry	Wire-wrap clad plates Radial depth = 0.32 m for cases for separate multiplier cases = 0.57 m for cases without a multiplier and for homogeneous SB/M cases Plate thickness is SB-specific
Clad geometry	0.5 mm thick plate ≈ 10 cm wire-wrap spacing, with 1 mm OD wires Accommodation of swelling/thermal expansion unspecified, possibly as in BCSS
Multiplier geometry	Unclad axial pins Multiplier region radial depth is SB-specific
Coolant channel geometry	1 mm channel between solid breeder plates Coolant flows through module perimeter and first wall, and then enters multiplier/breeder region
First wall geometry	Lobed first wall with surface grooving and internal cooled channels: Total thickness = 9 mm; first wall thickness = 1.5 mm; second wall thickness = 0.5 mm; groove dimension = 7 x 1 mm^2; channel dimension = 7 x 1 mm^2
Coolant thermal-hydraulics	5.1 MPa and 275°C inlet conditions to first wall 5.1 MPa and 332°C at entrance to multiplier or breeder zone from first wall Exit conditions are SB-specific Coolant flow rate 1.12 m^3/sec per module (275°C)
Breeder/multiplier thermal-hydraulics	Minimum and maximum temperature are material-specific
Neutronics	Multiplier region thickness is SB-specific ^6Li enrichment is SB-specific Tritium breeding, energy multiplication rate, activation and heating profile are SB-specific
Tritium recovery	Purge flow pressure = 1 MPa Purge flow rate = 0.01 m^3/sec per module (300°C) Composition: He with 1% added H_2 Tritium inventory is SB-specific Tritium permeation rate is SB-specific
Blanket lifetime	15 MW-yr/m^2, or 4 years at 75% availability

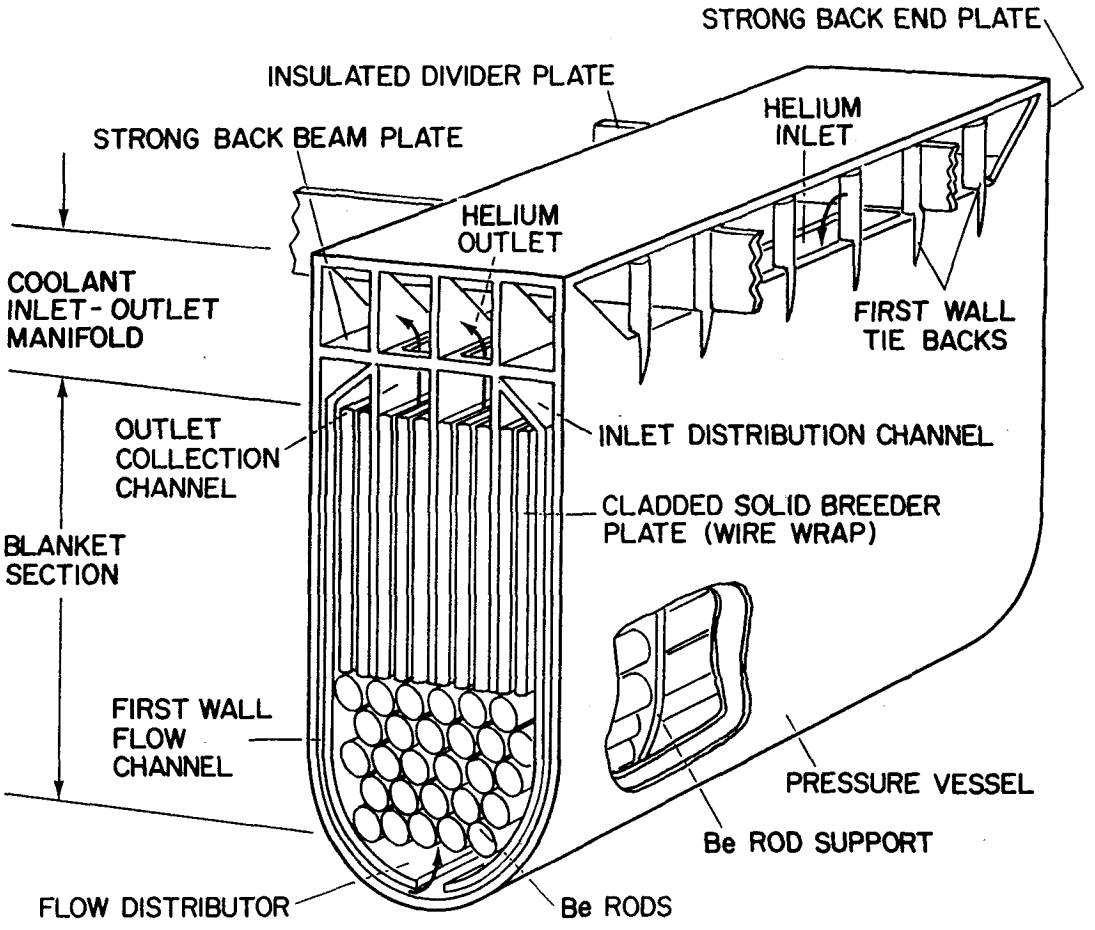


Figure 1.2-3 Reference blanket design

iterations between the temperature and neutronics calculations are needed in each case. The ^{6}Li enrichment, the multiplier region radial thickness (for the cases with a separate multiplier region), and the ratio of solid breeder to multiplier volume fraction (for the homogeneous mixture cases), are chosen based on optimizing the tritium breeding ratio.

Blanket performance parameters were selected as a basis for the solid breeder comparison. They fall in the five general categories of neutronics, thermo-mechanics, tritium, activation, and economics, and are listed in Table 1.2-5. The calculations performed for the different parameters are described in detail in Section 2.3.

Table 1.2-5 Performance Parameters

Neutronics:
Tritium Breeding Ratio
Power Multiplication (power generated in first wall and blanket, divided by the 14-MeV-neutron power)
Maximum Li Burnup at 15 MW•yr/m^2 [3 Full Power Years (FPY)]
Thermo-Mechanics:
Clad Stress and Deflection
Thermal Stress in Breeder
Tritium:
Tritium Inventory
Tritium Permeation
Activation:
Waste Disposal Rating (relative to Class C limits at 3 FPY)
Biological Hazard Potential (relative to maximum permissible concentration at 3 FPY)
Recycling Hazard
Afterheat
Economics:
Material Cost (including Be)
Net Thermal Efficiency (including pressure drop in blanket)
Power Leakage from Blanket to Shield

The results for each of these categories are summarized in Table 1.2-6 and discussed below. Because of the particular importance of the tritium breeding ratio (for tritium self-sufficiency) and of the blanket tritium inventory (for safety), the results for these two parameters are discussed in more details.

Results

Tritium Breeding Ratio

The tritium breeding ratio (TBR) was calculated from a one-dimensional (1-D) neutronics computer code. These 1-D neutronics calculations typically over-estimate the actual TBR by about 15-20% because of the assumptions of full coverage, fully homogeneous regions, and equal inboard and outboard blanket thickness.[13] For that reason, effective TBR values (which are assumed to be 15% lower than the 1-D TBR values) are considered in this section.

Table 1.2-6 Blanket Performance Summary

Solid Breeder	Effective TBR[a]	Power Mult.	$\dot{q}^3$ (W/cm^3)[b]	Peak Li Burnup (at.%)	Gross η_{th} (%)	Power Leakage (MW)	Blanket SB & M Cost ($M)	Breeder Total T Inventory (g)	Breeder Permeation Rate (g T/d)	Pumping Power Ratio (%)	Dose Rate at 1 m[c] (REM/hr-g)	Afterheat Time to Reach T_{max} (hr)
Cases Without a Multiplier												
Li_2O	1.08 (nat)	1.22	41.8	2.9	39.4	5.6	28	5.6	1.4	5.4	0.0029	183
Li_2ZrO_3	0.93 (29)	1.02	35.5	6.1	37.8	4.1	90	85.8	1.8	6.0	24.1	0.048
Li_8ZrO_6	0.98 (nat)	1.12	41.4	3.7	38.6	4.2	54	85.2	2.0	5.3	24.1	0.047
$Li_2Be_2O_3$	1.09 (nat)	1.31	47.6	5.4	39.7	3.4	135	552,000	2.4	4.1	0.031	56
Li_7Pb_2	1.22 (29)	1.18	33.7	5.0	39.1	14.9	110	1,590	2.9	5.6	2.64	0.024
Cases With a Homogeneous SB/M Mixture												
$LiAlO_2$/Be	1.51 (36)	1.51	43.9	46.8	41.4	7.1	104	230	2.2	3.1	1.86	5.4
$LiAlO_2$/BeO	1.09 (40)	1.36	43.5	35.3	40.3	6.1	96	76.5	1.3	3.6	1.27	20
Li_2O/Be	1.57 (nat)	1.52	45.9	19.5	41.2	4.7	73	8.1	2.3	3.1	0.0033	420
Li_2O/BeO	1.14 (14)	1.36	43.7	14.3	40.3	3.8	81	9.5	1.6	3.7	0.027	940
Cases With a Separate Be Multiplier Region												
Li_2O	1.24 (20)	1.42	81.6	15.8	40.7	1.2	68	43.9	1.2	3.5	0.0029	130
$LiAlO_2$	1.09 (62)	1.39	64.9	37.8	40.4	2.5	75	36.4	1.1	3.6	7.1	2.6
Li_5AlO_4	1.17 (30)	1.40	72.6	23.2	40.6	2.5	68	23	1.9	3.3	7.1	0.51
Li_2SiO_3	1.10 (50)	1.37	68.5	31.2	40.4	2.6	78	9.6	1.7	3.4	0.14	21
Li_4SiO_4	1.14 (33)	1.38	70.0	24.9	40.5	2.5	71	9.2	1.5	3.5	0.14	2.5
Li_2ZrO_3	1.17 (58)	1.27	67.1	31.8	39.7	2.4	97	47	1.3	3.9	24.1	0.041
Li_8ZrO_6	1.22 (26)	1.34	74.6	21.2	40.3	2.1	91	45.4	1.6	3.5	24.1	0.036
Li_2TiO_3	1.12 (51)	1.39	65.5	32.9	40.6	3.2	77	4.1	1.1	3.6	5.6	5

[a] % ^{6}Li enrichment corresponding to optimum TBR is shown in parentheses; (nat) is for natural lithium (7.25% ^{6}Li).
[b] At 0.5 cm from tip of breeder plate.
[c] After 3-year irradiation and 10-hour cooling.
For the separate multiplier cases, the dose rate for Be is 0.0034 REM/hr-g and is due entirely to impurities.
For the homogeneous SB/M mixture cases, the dose rate for the multiplier (0.0034 REM/hr-g for Be and ≃ 0.03 REM/hr-g for BeO) have been included in these figures.

The TBR was first calculated for different values of the neutron multiplier thickness and a 60% ^{6}Li enrichment (as an initial estimate) for the separate Be multiplier cases. The general trend is that the TBR increases as the neutron multiplier thickness is increased, until saturation is reached. Consideration of the TBR incremental rate of change with increased Be thickness led to the selection of a 12-cm multiplier zone thickness (with a 0.54 volume fraction of Be at 80% theoretical density) as a reference thickness. This choice provided an optimized TBR for all the cases. For this multiplier thickness, the TBR was then calculated for different values of ^{6}Li enrichment and the results are shown in Figure 1.2-4. The TBR increases as the ^{6}Li enrichment is increased and reaches saturation at different ^{6}Li enrichment depending on the solid breeder.

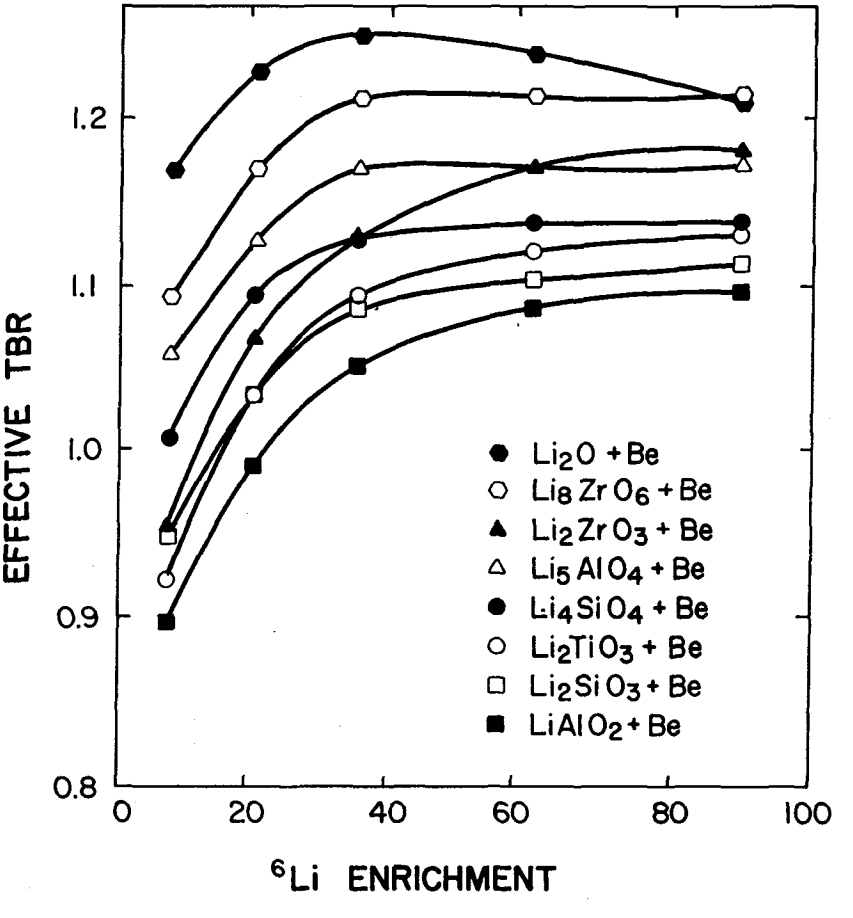


Figure 1.2-4 Effective tritium breeding ratio as a function of ^{6}Li enrichment for the cases with a separate 12-cm thick Be multiplier region

Table 1.2-7 shows the ^{6}Li enrichment and the Li atom density at saturation (assumed here to correspond to 99% of the maximum TBR) for the different breeder materials. Saturation tends to occur at lower ^{6}Li enrichment as the lithium atom density of the material increases. The ^{6}Li atom densities at saturation is very close to $1.0 \times 10^{22}/cm^3$ for all the materials considered. Note that although the ^{6}Li atom density is about the same at saturation for the different cases, the TBR is different, tending to vary directly with the total Li atom density. This is mainly due to the difference in the tritium production from ^{7}Li between the different cases, and to the differences in the neutronics characteristics (e.g. slowing-down power, absorption) of non-lithium atoms present (e.g. O, Zr, Si).

The TBR of Li_2ZrO_3 peaks later than the other materials when varying with ^{6}Li enrichment (and earlier than the other cases when varying with Be thickness). This is due to the high physical density ($4.15\ g/cm^3$) of Li_2ZrO_3, and hence, to its relatively high Zr atom density which acts as an additional neutron multiplier.

Table 1.2-7 ^{6}Li Enrichment and Atom Density at TBR Saturation (99% of Maximum TBR) for Cases with a Separate Be Multiplier Region

	Li Atom Density at 100% T.D. ($10^{22}/cm^3$)	Optimum ^{6}Li Enrichment (%)	^{6}Li Atom Density at Optimum Enrichment ($10^{22}/cm^3$)[a]
Li_2O	8.07	20	1.02
Li_8ZrO_6	5.87	26	0.93
Li_5AlO_4	5.30	30	0.94
Li_4SiO_4	4.56	33	0.90
Li_2ZrO_3	3.25	58	1.17
Li_2SiO_3	3.36	50	1.00
Li_2TiO_3	2.84	51	0.92
$LiAlO_2$	2.33	62	0.90

[a]Based on the corresponding breeder volume fraction and 80% breeder theoretical density

For the cases without a multiplier, the neutron spectrum has more high energy neutrons than for the cases with a multiplier. The $^{7}Li(n,n'\alpha)t$ reaction is significant at high neutron energy. Therefore, as the ^{6}Li enrichment is increased, the tritium production by ^{7}Li is decreased, which tends to have a stronger reducing effect on the total tritium production than the corresponding increase in tritium production through ^{6}Li.

For the four homogeneous breeder/multiplier mixture cases, increasing the breeder volume fraction in the mixture beyond 20% decreases the TBR. This indicates that only a small amount of breeder is required to achieve maximum tritium production. Furthermore, only a slight increase in TBR is observed when the ^{6}Li enrichment is increased, with saturation occurring fairly rapidly at about a 30% ^{6}Li enrichment. The Li_2O cases (Li_2O/Be and Li_2O/BeO) have a higher tritium production than the $LiAlO_2$ cases because the lithium atom density of Li_2O is larger than that of $LiAlO_2$. Also, the Be mixtures (Li_2O/Be and $LiAlO_2$/Be) show much larger values of TBR than the BeO mixtures (Li_2O/BeO and $LiAlO_2$/BeO) because the atom density of beryllium is 1.7 times larger than that of beryllium oxide. The 20% breeder and 80% multiplier mixture case was selected as reference because the TBR values were already high enough in all cases. Notice, however, that the high multiplier proportion in the mixture is only needed in the blanket region closest to the first wall; at deeper regions, it can be substantially reduced without significantly affecting the TBR.

The TBR results are summarized in Figure 1.2-5, which shows the optimum effective TBR for each case. To satisfy the tritium self-sufficiency criterion within the given uncertainties, the effective TBR can be ranked in different categories. Table 1.2-8 shows the risk associated with each TBR category and classifies the different solid breeder cases based on their effective TBR. Note that since the homogeneous $LiAlO_2$/Be case is in the low risk category, it is anticipated that all homogeneous mixtures of ternary ceramics (which usually have higher Li atom densities than $LiAlO_2$) with beryllium would be in the same category.

The general conclusions that can be made from the TBR results are that:

1) all solid breeders require a separate neutron multiplier except for Li_7Pb_2 and possibly Li_2O and $Li_2Be_2O_3$;

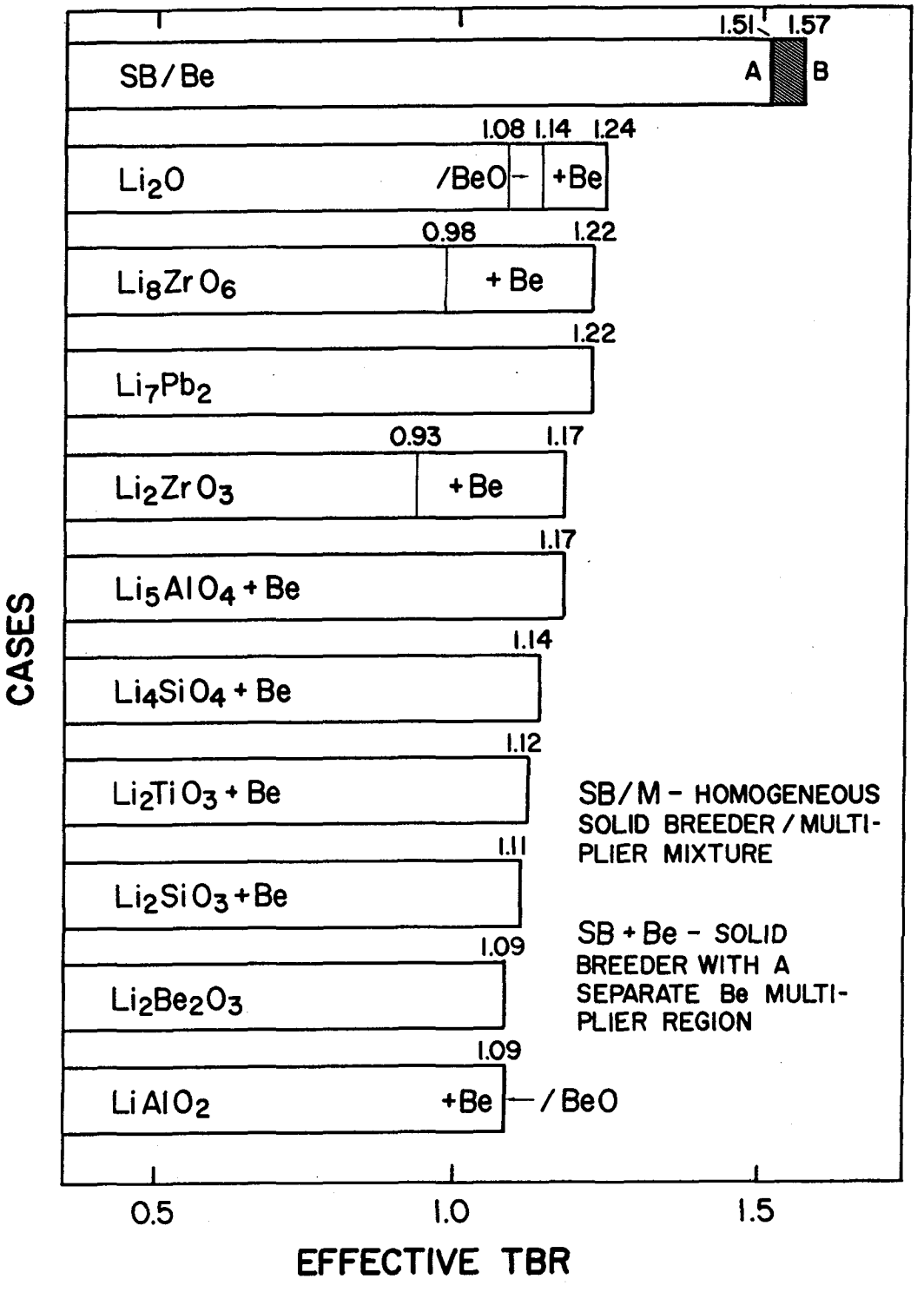


Figure 1.2-5 Effective tritium breeding ratio for the different cases. For the cases with the solid breeder/beryllium homogeneous mixture, A and B are the lower and upper limits represented by the $LiAlO_2$/Be and Li_2O/Be cases, respectively.

Table 1.2-8 Classification of the Different Solid Breeder Cases Based on the Effective Tritium Breeding Ratio

Effective TBR Range	Risk Category	Cases
<1.05	Unacceptable	Li_2ZrO_3, Li_8ZrO_6, all ternary ceramics without a multiplier element
1.05 - 1.10	High risk	Li_2O, $Li_2Be_2O_3$, $LiAlO_2$+Be, $LiAlO_2$/BeO
1.10 - 1.20	Medium risk	Li_7Pb_2, Li_2SiO_3+Be, Li_2TiO_3+Be, Li_4SiO_4+Be, Li_5AlO_4+Be, Li_2ZrO_3+Be, Li_2O/BeO
>1.20	Low risk	Li_8ZrO_6+Be, Li_2O+Be, all Solid Breeder/Be homogeneous mixtures

2) the homogeneous SB/Be cases show exceptional neutronics performance;
3) Be exhibits a much superior performance than BeO as a neutron multiplier; and
4) Li_2O is the most attractive solid breeder candidate, showing the highest TBR for the unmultiplied, separate multiplier and homogeneous SB/M cases.

These particular results are based on one assumed blanket configuration, but it is not expected that different designs (e.g., solid breeder pins rather than plates or breeder out of tube) would significantly affect the relative solid breeder TBR performance. Similarly, the choice of coolant is not expected to affect the relative rankings. One particular configuration, however, might be an exception. It involves placement of a thin layer of breeder in front of the multiplier to absorb back-scattered neutrons in ^6Li (and also reduce first wall activation). Calculations were done for two cases, one exhibiting a high TBR (Li_8ZrO_6) and the other a low TBR ($LiAlO_2$), to determine if the neutronics results were design-dependent, favoring a particular solid breeder material over another. The TBR was calculated for different values of the front breeder region thickness, ranging from 0.2 cm to 4 cm (with a 0.54 volume fraction of 80% dense solid breeder). The back

breeder region thickness was adjusted to keep the total breeder thickness the same as before and the ^{6}Li enrichment was set at 60%.

As shown in Figure 1.2-6, adding a thin breeder zone in front of the multiplier zone increases the tritium breeding in a similar way up to a certain thickness for both $LiAlO_2$ and Li_8ZrO_6. Qualitatively, too little front breeder does not capture the reflected neutrons, while too much scatters the incident neutrons and reduces the Be (n,2n) reaction rate, which explains the shape of the TBR curve in the figure. The maximum increase in TBR is about 0.05, corresponding to an equivalent 100% dense breeder region thickness of 0.13 to 0.2 cm. However, the corresponding peak heating rate in the breeder front region is very high--of the order of 150 MW/m^3. The other solid breeder materials are expected to show similar behavior and, thus, this choice of configuration does not affect the relative TBR solid breeder rankings.

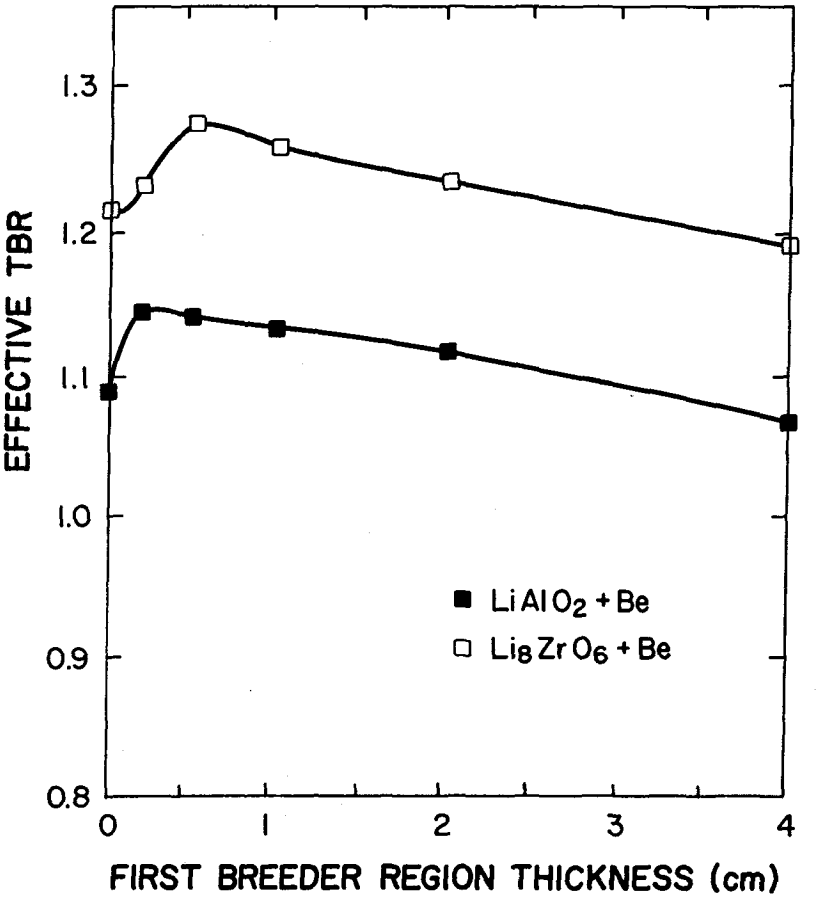


Figure 1.2-6 Effective tritium breeding ratio as a function of the first breeder region thickness for two sandwich cases (both with 60% ^{6}Li enrichment)

Power Multiplication

The power multiplication, M, corresponding to the each optimum TBR case, is shown in Table 1.2-6. The M results tend to vary in accordance with the TBR results and thus reinforce the TBR-based conclusions. The only notable exception is the case of Li_7Pb_2, which, although showing a high effective TBR of 1.22, exhibits a rather low M of 1.18. This is due to the higher (n,2n) threshold energy in Pb compared to Be.

Note that the TBR and M results are rather insensitive to small changes in the volume fractions. For example, changing the breeder volume fraction from 0.70 to 0.75 in the case of Li_4SiO_4+Be does not change the power multiplication (1.37) and only decreases the 1-D TBR from 1.35 to 1.34. Again, this indicates that the relative solid breeder behavior is fairly independent of the specific design configuration.

Peak Heating

Table 1.2-6 shows that the separate-multiplier cases have higher peak heating values ($\dot{q}$) than the other cases. For example, Li_2O with a separate multiplier has a 81.6 W/cm^3 peak heating value, while Li_2O/Be in the homogeneous mixture case and unmultiplied Li_2O only show 45.9 and 41.9 W/cm^3 values, respectively. It is interesting to note that the peak heating rate tends to increase with the Li atom density, as is indicated in particular in the cases with a separate multiplier. These peak heating rates constrain the size of the breeder plates, and hence the breeder volume fraction. However, as noted earlier, the TBR and M results are not strongly affected by small changes in the breeder volume fraction. Consequently, the heating rates are not expected to strongly affect the solid breeder comparison.

Peak Lithium Burnup

The peak lithium burnup due to tritium-producing reactions (which constitute 99% or more of lithium burnup), was calculated at 0.5 cm from the tip of the solid breeder plate and is shown in Table 1.2-6 for each case. The peak burnup is high for the three cases involving $LiAlO_2$ with a multiplier, with the homogeneous $LiAlO_2$/Be case exhibiting the highest burnup (46.8 at.%). This is due to the high volume fraction of Be needed at the front of the SB/M region, which means that the amount of Li is small and the burnup fraction is high.

The cases without a multiplier have lower values of burnup, with Li_2O showing the lowest value (2.9 at.%). This difference is due to the lower-energy secondary neutrons produced by the multiplier which react with ^6Li in the front section of the breeder to produce high burnups. It can also be observed that the burnup fraction is generally higher for the cases with lower lithium atom density. Consequently, a breeder material ranking based on the least burnup tends to be the same as the ranking based on the highest TBR, since both are directly dependent on the Li atom density. Although concern exists about the possibility of high burnups affecting the material chemical composition and compatibility at the tip of the breeder section, it is not clear yet how important this is as a criterion for comparing solid breeder materials. In general, it seems reasonable to assume that lower values of peak burnup are more attractive than higher values. The average burnup, which has not been calculated for this study, could also be an important factor, particularly in connection with its effect on tritium inventory.

Clad Stress and Deflection

As part of the thermo-mechanics calculations, the stresses in the clad and the clad deflection caused by the breeder total volumetric expansion (thermal expansion + swelling) were estimated for four cases for which swelling data after fast irradiation to 10^{27} captures/m^3 were available: Li_2O, $LiAlO_2$, Li_2ZrO_3 and Li_4SiO_4 The expansion was assumed to be fully relieved by deflection of the clad side walls. This may be most applicable to the sphere-pac form. It was found that the stresses in the clad were well within the clad maximum allowable stress. However, the clad deflection tended to be large relative to the 1 mm thickness of the gap (coolant channel) between adjacent solid breeder plates. For example, for the Li_2O case which exhibits the largest total volume expansion (about 13%), the clad deflection is on the order of 1.5 mm for each plate. In this respect, Li_2O is unattractive, Li_4SiO_4 (6.7% total volumetric expansion) is marginal, and $LiAlO_2$ and Li_2ZrO_3 (3.6% and 2.6% total volumetric expansion, respectively) are acceptable. However, if a means for expansion is provided, such as a bellow-type arrangement at the plate ends or extra porosity, then the importance of this expansion for differentiating between the different solid breeder materials will be diminished.

Note that the corresponding stresses on the solid breeder sphere-pac material were also calculated and found to be significantly lower than the solid breeder fracture stress.

Breeder Thermal Stress

The thermal stresses for the solid breeder in sintered block form were also estimated. The plate temperature distribution was first calculated by solving the 2-D heat conduction equation (with the neutron heat generation as source term) by means of a finite difference technique. The stresses were found to be several times higher than the allowable fracture strength (which is on the order of 50 MPa and 70 MPa for Li_2O and $LiAlO_2$, respectively). In order for the thermal stress not to exceed the fracture stress, 2-D calculations show that the maximum plate thickness needs to be less than 0.5 mm for $LiAlO_2$ and Li_2O. This shows the disadvantage of using the sintered block form, as extensive stress-induced cracking will occur affecting the temperature distribution and the tritium inventory. Consequently, the test program should investigate conditions with substantial temperature gradients to reproduce this cracking, and/or consider sphere-pac material.

Tritium Inventory

The tritium inventory in the solid breeder and multiplier was calculated as the sum of diffusion, solubility and surface adsorption components. Details about the property data (which have uncertainties ranging from a factor of 2 to a factor of 100) and about the calculations can be found in Sections 2.2 and 2.3 respectively. In general, swamping the purge flow with hydrogen will drastically reduce the adsorped and dissolved tritium.[14] Here, it is assumed that the tritium solubility and surface adsorption inventories are reduced to 1% of the possible inventory due to the inclusion of hydrogen in the purge flow at a ratio of 100:1 relative to the tritium.

The three components of the tritium inventory are strongly dependent on temperature. Consequently, the tritium diffusive, solubility and surface adsorption inventories were determined based on numerically integrating the inventories over the 2-D temperature and tritium generation rate profiles in the plate. The total inventory for each material is shown in Table 1.2-6 (based on average property values).

The tritium inventory results should be interpreted carefully because of the huge ranges of uncertainty, which clearly points to the need for obtaining more precise experimental property data. $Li_2Be_2O_3$, with an average diffusive inventory of 550 kg per blanket, is evidently unattractive, assuming the BeO-like tritium diffusion used in the absence of any data is correct. Li_7Pb_2 also has a high inventory (due to tritium solubility) and so does $LiAlO_2$/Be (due to diffusion). Apart from these, it is hard to differentiate between the other cases within the uncertainty range. Except for the $LiAlO_2$ cases, where the diffusive inventory is significant, and for the Li_7Pb_2 and Li_2O cases, where the solubility inventory is dominant, the total inventory for all the other cases consists mainly of the surface adsorption component. By further increasing the isotope swamping of the purge flow, these surface adsorption inventories could be further reduced beyond the 0.01 factor already used. This indicates the need for further experimental data related to the adsorption mechanism and to the effect of isotope swamping. The effect of large protium additions on tritium permeation and tritium recovery must also be considered in a blanket design context.

There are many uncertainties in the properties and design that can affect the tritium inventory indirectly. Analyses were performed to determine the effect on the tritium inventory of: 1) using a temperature dependent instead of constant thermal conductivity; 2) including the size variation of the breeder grains; and 3) inserting a helium-filled gap near the tip of the plate, assuming a sintered block form. It was found that the tritium inventory was increased in the three cases (by up to about 25%, 12% and 50%, respectively), but the magnitude of the increase is small compared to the uncertainties in the solid breeder tritium-related property data.

The diffusive inventory in the multiplier was also estimated. For Be, the inventory is very low both for the separate region case and for the homogeneous case (about 10^{-8} g per blanket). For BeO, however, the inventory is high (about 8 kg per blanket) and does not reach equilibrium during the blanket life.

Tritium Permeation

The permeation rate of tritium from the solid breeder to the coolant is a function of the tritium form and partial pressure, and the cladding area,

thickness and temperature. Furthermore, H_2 addition to the purge effectively forces the released tritium into the HT form, and the addition of H_2 at 100:1 (H:T) is assumed here for the reference blanket. The permeability estimated for HT9 clad material and an oxide barrier factor of 100 (see Section 2.3) is uncertain by about an order of magnitude, primarily because of the uncertainty in the surface conditions and associated barrier factor.

From Table 1.2-6, the resulting permeation rates from the solid breeder into the helium coolant are about 1-3 g/d for a 1.6 GWe reactor, similar to the 2 g/d estimated for the BCSS $LiAlO_2$/He/Be blanket.[10] Thus, the effect of solid breeder choice is roughly a factor of three (due to differences in the breeder temperature limits and thermal conductivity) which, given the uncertainties in the permeation coefficient and barrier factor (a factor of ten), is probably not significant. Tritium is also produced in the multiplier at about 1% of its production rate in the solid breeder, or 7.5 g T/d in a 5.4 GWth reactor. For mixed breeder/multiplier materials, the additional tritium would not affect the tritium permeation. If the multiplier is separate and unclad, however, this tritium will eventually permeate into the coolant and would dominate over any tritium permeating through the breeder cladding, regardless of the solid breeder material. Such a permeation rate into the coolant may be unacceptably large, and require cladding on the multiplier.

Activation

The activation of different solid breeder materials (including presumed impurities) was calculated for two different spectra, one with a beryllium multiplier and one without. Also calculated for the former case was the activation of the beryllium multiplier. The fluxes used in the calculation correspond to the front of the breeder region (near the first wall). It was found that the results were approximately similar for both spectra.

The results include the dose rate (which gives an indication of the recycling hazard) and the Biological Hazard Potential (as a measure of accidental release hazard) after 3-year irradiation and 10-hour cooling and the Class C waste disposal limit after 3-year irradiation and 10-year cooling (as an indication of waste disposal hazard). The dose rate is chosen to represent activation because it is least dependent on impurities, and impurities can, in principle, be removed (at a cost). The dose rates for the different solid

breeder cases are shown in Table 1.2-6. The zirconates and Li_7Pb_2 are the least attractive based on this criterion, the aluminates are marginal, while the oxide, beryllate and silicates (to a lesser extent) are attractive.

Afterheat

Decay heat values, one hour after shutdown, were calculated by assuming that the only contributions were from products of the primary elements. Contributions from products of impurity elements were ignored. They were then used in combination with the average steady-state temperature at the tip of the solid breeder plate, the maximum allowable temperature (usually based on the sintering limit) of the solid breeder and the solid breeder heat capacity to obtain the time to reach the maximum temperature after shutdown under adiabatic conditions.

The results, shown in Table 1.2-6, indicate that Li_2O and $Li_2Be_2O_3$ are very attractive (with times of 7.6 and 2.3 days, respectively) and, to a lesser extent, so are the silicates (with times of the order of 1 day). Li_2TiO_3, $LiAlO_2$, and possibly Li_5AlO_4 are adequate (with times of 5, 2.5 and 0.5 hours, respectively). However, the two zirconates and Li_7Pb_2 show times of about 1.5-3 minutes to reach the maximum temperature. If a loss of coolant accident occurs, this leaves very little time for corrective action before the solid breeder is irreversibly damaged. Again, these results are based on activation of the primary constituents, and are not determined by assumed impurities. The time parameter considered here is important in developing inherently safe blankets, particularly as it relates to protection of investment.

Material Costs

Material unit costs were estimated (see Section 2.2) to compare the fabrication costs for blankets containing the various breeder and multiplier materials. The highest unit costs are for beryllium and for ^6Li enrichment at \$400/kg Be and \$1500/kg ^6Li. Table 1.2-6 lists the cost per blanket (1125 modules) for each case.

For the four homogeneous (20/80) breeder/multiplier mixture cases, the homogeneous mixture is assumed to be contained in the first 20 cm of breeder region, with breeder only in a second 37 cm breeder region. This reduces the

amount of expensive beryllium while the decrease in TBR is acceptable (the effective tritium breeding ratio is reduced from 1.59 to 1.49 for the Li_2O/Be case and from 1.53 to 1.35 for $LiAlO_2$/Be).

The highest costs are for $Li_2Be_2O_3$ and Li_7Pb_2, with most of the other cases showing multiplier and breeder material costs between about \$67.5 million to \$107 million for the blanket module. The cost for the unmultiplied Li_2O case, however, is appreciably lower than those of all the other cases (\$28 million for the blanket), making unmultiplied Li_2O quite attractive on this basis. Note, however, that the solid breeder and multiplier costs are typically only about < 5% of the total commercial reactor cost.

Thermal Efficiency and Pumping Power

The thermal efficiency, η_{th}, of the steam cycle was calculated from the helium main flow bulk temperature at the exit of the blanket (obtained from the mass flow rate, fusion power and multiplication factor). The steam cycle was based on the one described in Ref. [15] with a condenser temperature of 311 K in the condenser. For this cycle, η_{th} was found to be 68% of the ideal Carnot efficiency.

For the pumping power calculations, both the pressure drop across the multiplier region (if applicable) and the pressure drop across the breeder plates were considered. Estimates for the pressure drop in the helium circuit outside the breeder were obtained from Ref. [16]. The other components include the inlet manifold, distribution channel, the side flow path, the grooved first wall, the collection channel, and the outlet manifold, with a combined 48 kPa pressure drop.

The pressure drop across the breeder region and multiplier regions were calculated from expressions for the relevant geometry and flow rates given in Ref. [13]. The pressure drop calculations were made under the assumption of constant mass flow rate for all the different solid breeder cases. This maintained the same first wall conditions for this particular blanket design. However, one should be cautious not to generalize these results to other designs.

The cycle thermal efficiency and pressure drop results are summarized in Table 1.2-6. The total pressure drop has been converted to a pumping power

ratio (PPR), which is equivalent to the pumping power required divided by the electric power generated by the heat transported out of the blanket by the helium. The gross thermal efficiency can be seen to vary from 37.8% for the unmultiplied Li_2ZrO_3 case to 41.3% for the $LiAlO_2$ homogeneous mixture case. Apart from the unmultiplied Li_2ZrO_3 case, all the cases have thermal efficiencies within 3 percentage points. The main coolant pumping power ratio tends to vary inversely to the thermal efficiency, and shows a maximum of 6% for the unmultiplied Li_2ZrO_3 case and a minimum of 3.1% for the $LiAlO_2$ homogeneous case. However, the variation is mostly due to the number of plates in the design; the fewer the plates, the fewer the channels and the larger the pumping power for a given mass flow rate. The mass flow rate here is fixed by the first wall design. For blankets where the coolant does not initally flow through the first wall, the PPR could be changed. Also, since the neutronics are rather insensitive to small changes in the breeder volume fraction, it is conceivable that a fixed number of plates of the same size be used for all the cases, which will then have essentially the same pumping power requirements.

Power Leakage

From the neutron flux spectrum and the neutron energy at the back of the 30-cm reflector, the power leakage was calculated. This criterion can be important for space-limited reactors since higher power leakage implies the need for additional shielding, leading to larger reactor size and cost. A factor of 2 to 3 increase in power leakage typically requires about an additional 5 cm shield thickness. However, the importance of the power leakage can be minimized in a tokamak-type reactor by limiting this additional shield increase to the outboard region where space is less restricted. On the inboard region, where space is critical, the blanket thickness can be reduced by a few centimeters without a serious reduction in the tritium breeding ratio. From the results shown in Table 1.2-6, Li_7Pb_2, with the highest leakage power (about 14.9 MW for the whole blanket), is certainly less attractive than the other solid breeders. The values for the other cases all fall within the range 1.2 to 7.1 MW for the whole blanket, with Li_2O showing the lowest value.

Conclusions and R&D Priorities

The performance parameters considered are not of equal importance. TBR

is the most important parameter since tritium self-sufficiency is a requirement. Safety concerns dictate that the tritium inventory is also of high importance. However, the magnitude of the uncertainties in the tritium-related property data tends to make a comparison between the different cases difficult. Other important parameters include activation, afterheat, power multiplication and material cost. The dose rate after 3-year irradiation and 10-hour cooling, which gives an indication of the recycling hazard, is the activation parameter considered here. The time to reach the maximum allowable temperature after shutdown with no coolant flow (calculated from the decay heat) is also an important parameter. It indicates how much time is available to restart the cooling system in case of accidental shutdown, without damaging and having to replace the solid breeder and/or multiplier. Power multiplication and material cost are included here as the key power and economic parameters. Note that the relative (and even absolute in some cases) values of these parameters for the different solid breeder materials tend to be independent of the geometric details of the design. An important performance parameter not considered here is the compatibility of the breeder with the structure.

These six major parameters of importance can be classified in pairs based on the indications that they give about tritium (TBR and tritium inventory), economics (power multiplication and material cost), and safety (dose rate and afterheat time to reach the maximum allowable breeder temperature). Graphical representations of the comparison of the various cases based on these three pairs of major parameters are illustrated in the point graphs shown in Figures 1.2-7 (effective TBR and reciprocal of the tritium inventory), 1.2-8 (reciprocal of material cost and power multiplication), and 1.2-9 (afterheat time to attain the maximum allowable material temperature and reciprocal of dose rate). The choice of variables is such that the more attractive cases will appear in the top right hand corner of each figure.

Based on the study and, in particular, on the results illustrated in Figures 1.2-7 to 1.2-9, the following general conclusions can be made:

(1) A neutron multiplier is needed for all solid breeders, except possibly for Li_2O, which has a marginal chance of satisfying the tritium self-sufficiency criterion without a multiplier. (Note that Li_7Pb_2 and $Li_2Be_2O_3$ are considered as multiplied here because of their neutron multiplier components, lead and beryllium, respectively).

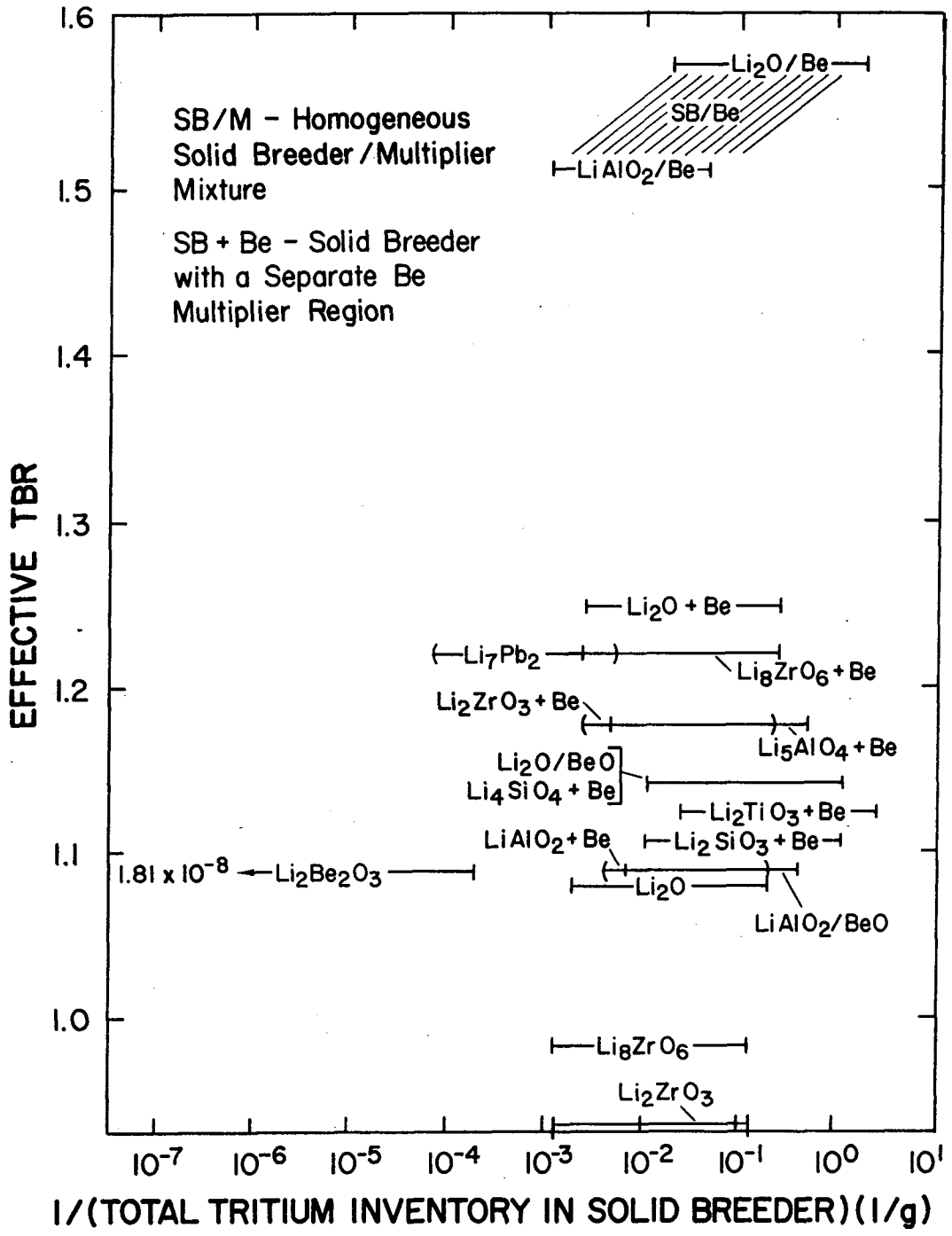


Figure 1.2-7 Point graph of the effective tritium breeding ratio and of the reciprocal of the total tritium inventory for the different cases

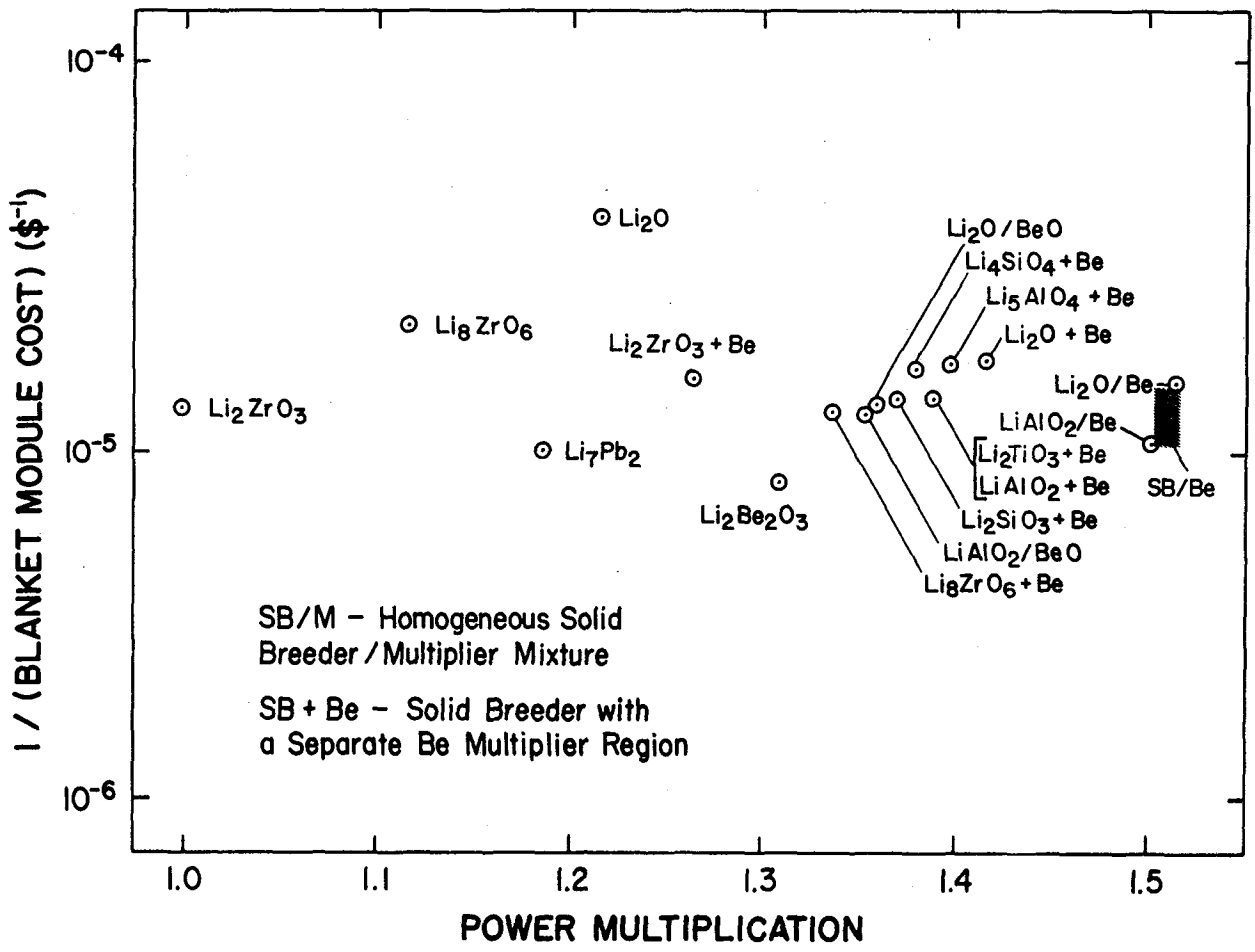


Figure 1.2-8 Point graph of the reciprocal of material cost and of power multiplication for the different cases

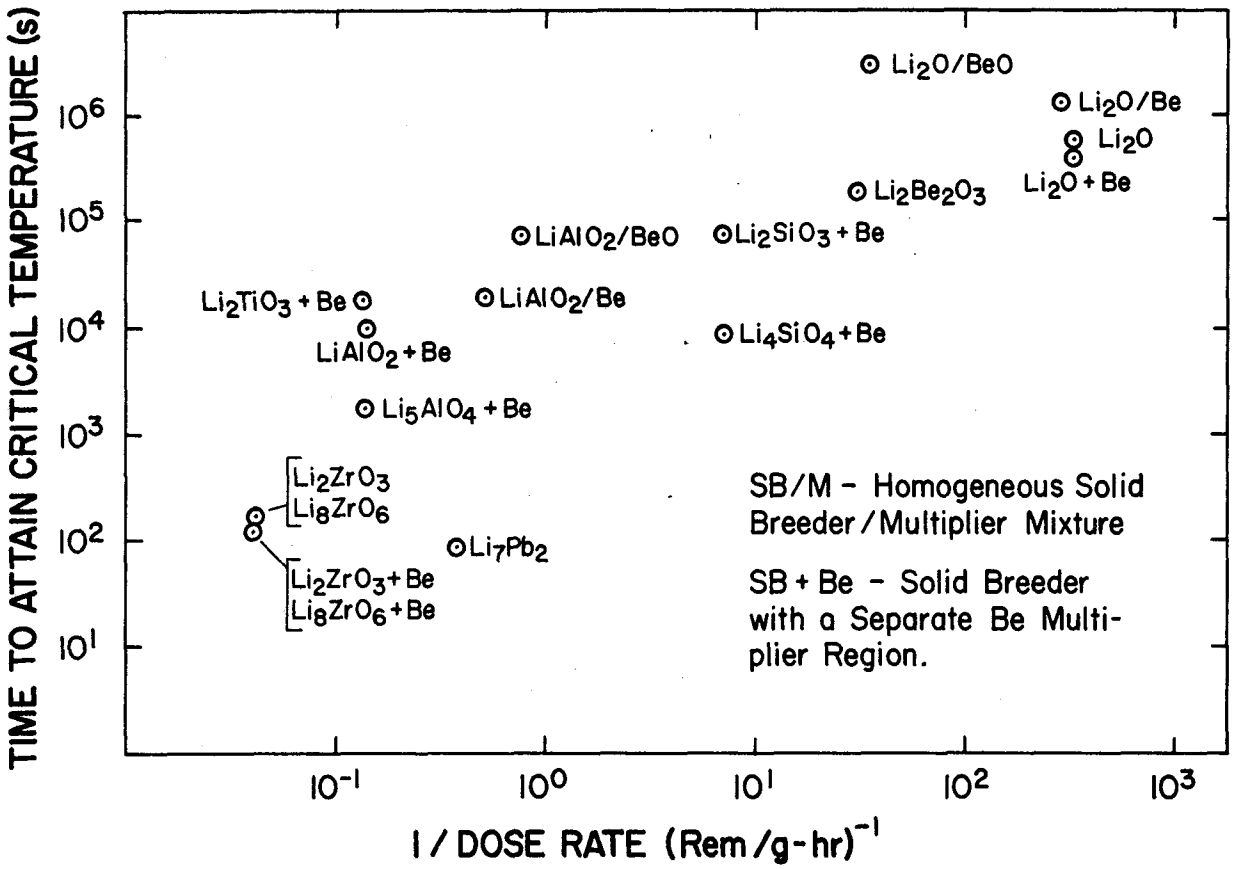


Figure 1.2-9 Point graph of the afterheat time to reach the maximum allowable temperature and of the reciprocal of the dose rate after 3-year irradiation and 10-hour cooling for the different cases

(2) Based on optimized neutronics performance, a homogeneous mixture of beryllium and solid breeder is superior to separate beryllium and solid breeder regions.

(3) Beryllium is superior to BeO in terms of improvement of tritium breeding and energy production. BeO is also unattractive based on its high tritium diffusive inventory.

(4) Even if Li_2O requires the use of a multiplier, the Li_2O and beryllium combination remains more attractive than all ternary ceramic and beryllium combinations in terms of achievable tritium breeding ratio and power multiplication.

(5) Among the ternary ceramics, the Li_4SiO_4 and Li_2SiO_3 (to a lesser extent) appear to be the most attractive. They result in the least activation and their tritium breeding ratio and energy multiplication are virtually as good or better than other ternary ceramics.

(6) $Li_2Be_2O_3$ does not appear attractive because of its relatively high tritium diffusive inventory (assuming BeO-like tritium diffusion) and its marginal tritium breeding ratio. While Li_7Pb_2 shows reasonable tritium breeding, it results in lower energy multiplication and higher tritium inventory, which, combined with its limited operating temperature range, does not make it particularly attractive.

With regard to the near-term experimental program for solid breeders, it is recommended that the following be emphasized:

(1) Materials: Li_2O without a neutron multiplier, and Li_2O, Li_4SiO_4, and Li_2SiO_3 with beryllium.

(2) Configurations: Both homogeneous mixtures of beryllium and solid breeder, and sphere-pac solid breeder are seen as attractive. Since the homogeneous mixture is attractive from many aspects, problems related to such a configuration, e.g., chemical stability and tritium release, should be experimentally investigated. In addition, neutronics integral experiments should include homogeneous configurations.

(3) Properties: The uncertainties in tritium-related properties are particularly large and important for designs as well as breeder comparisons.

(4) Test Conditions: A better understanding of lithium burnup is needed to clarify its importance and to accurately define the maximum allowable burnup limits. Tests should also include temperature gradients to determine the importance of cracking and/or breeder mass transfer.

1.2.2.2 Fission Reactor Evaluation for Advanced Solid Breeder Testing

Objectives

The major advantage of fission reactor testing is the ability to provide a neutron flux over a moderately large test volume prior to the availability of a high power DT fusion device. In earlier work, specific requirements were identified for fission reactor facilities used for advanced solid breeder testing: sufficient flux, suitable spectrum, on-line instrumentation capability, and adequate test volume.[17,18]

The ability of fission reactor testing to match anticipated fusion-relevant conditions has been evaluated, based on a comparison of tritium production and heat generation rates from microscopic calculations.[2,19] Here, the objective is to explore and compare the testing capability of various fission reactors to match these tritium production and temperature profiles which are anticipated in test elements with sufficient size to address advanced solid breeder performance issues. These issues include cracking under thermal stress, differential swelling, global tritium transport, internal mass transfer, purge flow distribution and temperature predictability. To accomplish this, representative reactors with significantly different neutron spectra were considered. Selected solid breeder cylindrical geometries and sizes were considered, as were various ^{6}Li enrichments. Results were calculated for Li_2O, but could be extrapolated to other breeder materials. Tritium production and neutron heating rate profiles, temperature gradients, and time-dependent tritium production rate distributions were calculated.

Representative Reactor Conditions

Three test fission reactors were chosen for investigation: The Fast Flux Test Facility (FFTF) at Hanford, the High Flux Isotope Reactor (HFIR) at Oak Ridge, and the National Reactor Universal (NRU) at Chalk River, Canada. These

reactors have different neutron spectra, as shown in Table 1.2-9 and Figure 1.2-10 (where the relative neutron energy spectra are normalized by the total neutron flux).

The FFTF reactor is a fast neutron spectrum source. Other reactors in this class include: EBR-II (U.S.), JOYO (Japan), Phenix/SuperPhenix (France), and KNK (Germany). The FFTF was designed for testing and has in-core instrumentation capabilities. It runs with typical cycle lengths of 60-150 days. The largest available position for instrumented testing is a hexagonal position measuring 12 cm flat-to-flat. The axial length of the core region is 91.4 cm. The space above the core region could also be utilized for testing if desired. The flux and energy spectrum chosen are for a row four position at the core midplane.

HFIR is a water-cooled reactor which has a softer neutron energy spectrum when compared to the liquid metal reactors. It is presently having its instrumentation capabilities increased through refitting. The HFIR runs with typical cycle lengths of 21-23 days. The largest available position for instrumented testing at present is a circular position measuring 3.7 cm in diameter. The axial length of the core region is 51 cm.

The NRU reactor is a water-cooled thermal reactor with a relatively modest non-thermal component of its neutron flux. Other reactors of this class include: ATR (U.S.), JMTR (Japan), and SILOE (France). The NRU reactor can accommodate instrumented in-core tests. It runs with typical cycle lengths of 14-30 days. The largest available position for instrumented testing would be a cylindrical position with a diameter of 10 cm. The axial

Table 1.2-9 Fission Reactor Capabilities and Characteristics

Reactor	Reactor Power (MWth)	Flux ($\times 10^{15}$ n/cm^2-s)		Core Materials Structure/Fuel/Coolant
		Thermal	Fast	
FFTF	300-400	small	4.3	316-SS/UO_2/Na
HFIR	100	2.3	1.5	SS/UO_2/H_2O
NRU	125	0.24	0.04	Zr/UO_2/D_2O

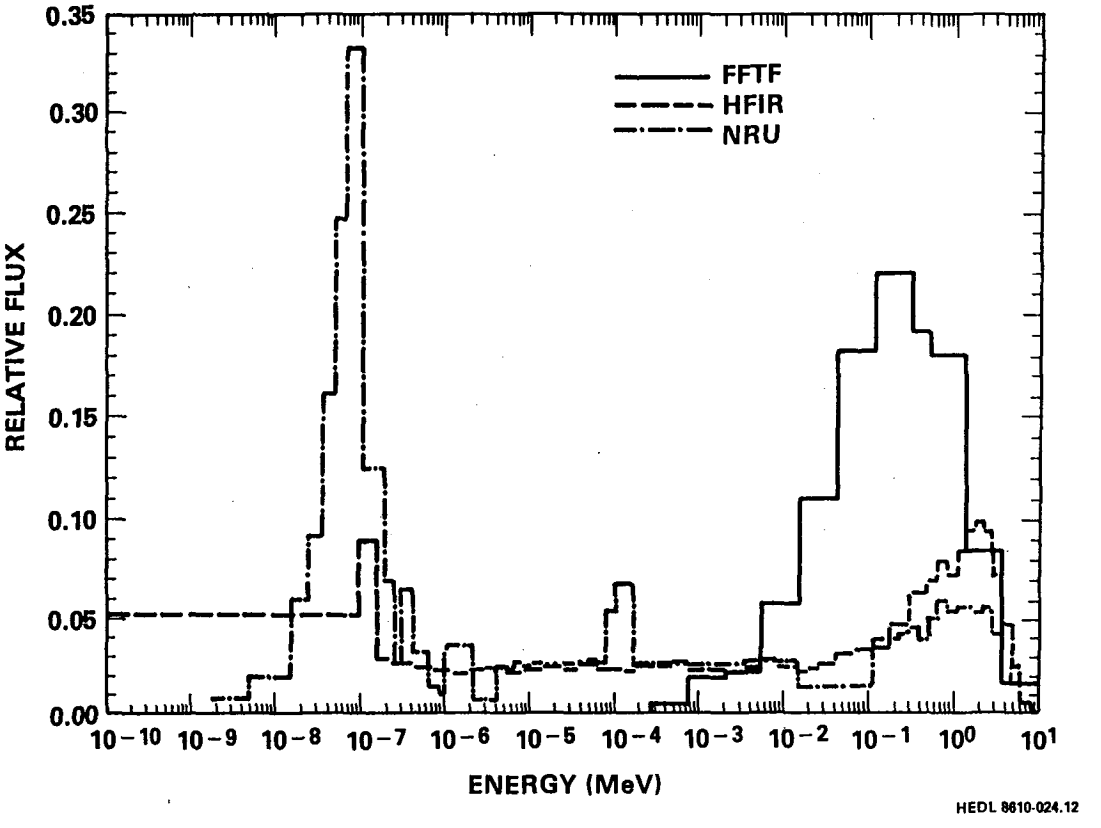


Figure 1.2-10 Comparison of neutron flux spectra for the FFTF, NRU and HFIR reactors normalized to their total flux

length of the core is 300 cm. The selected flux and energy spectra are for a spectrally tailored position within the core chosen to optimize the relative fast component of the neutron energy spectrum from NRU.

Calculations and Results

Details of the cylindrical test assembly model are shown in Figure 1.2-11. Specifically, each cylindrical test specimen consists of a solid or annular pellet which is surrounded by a stainless steel jacket. A gas gap (for temperature control) is included between this first stainless steel jacket and the second jacket which serves as a boundary between the reactor environment and the test configuration. The calculational models for FFTF, HFIR and NRU are described in Table 1.2-10. The Li_2O regions were divided into five equal volume zones to enable spatial distributions through the pins to be computed using the MCNP Monte Carlo program. The calculations were done for a neutron source applied at the outer boundary of each model.

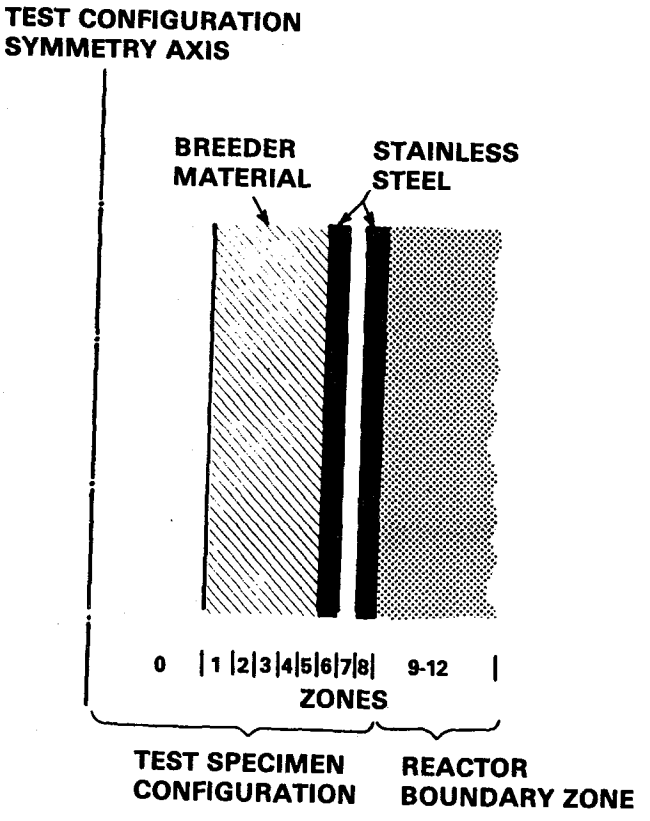


Figure 1.2-11 Schematic of one-dimensional model used to calculate calculate tritium production and heat generation rates in fission reactors. The zones in the figure are for an annular test specimen in the FFTF reactor.

Table 1.2-10 Calculational Models for HFIR and NRU and FFTF

Zone	Outer Radius (cm)	FFTF	HFIR	NRU
0-8	1.487	Li_2O Test Specimen		
9	2.120	36% SS/64% Na	H_2O	H_2O
10	2.730	36% SS/64% Na	H_2O	Zr
11	3.240	36% SS/64% Na	H_2O	H_2O
12	6.335	36% SS/64% Na		

The model has several limitations. The calculations do not consider the incident photon flux. Therefore, the total heating rates in the test specimen will be somewhat higher (by about 10%) than reported here, and the spatial distribution of this component will be different from the neutron heating profile. The model assumes that the incident flux and spectrum at the boundary of the test specimen are not perturbed by the presence of the solid breeder material. Thus, the comparison of the absolute values for the calculated parameters between the different reactor types should be viewed as approximate. Finally, the model cannot address the impact of the solid breeder test upon the reactivity of the reactor. This could limit the quantity of ^{6}Li in a given test reactor. The effect on reactor reactivity was considered in earlier FINESSE effort.(1)

Results for the FFTF reactor show that the total flux decreases by ~ 15% at the center of the test specimen configuration when the ^{6}Li-enrichment is increased from 7.5% to 80%. The integrated neutron heating rate within the Li_2O increases from 158 to 891 W/cm of axial length. Also, the integral tritium production rate increases from 13 to 105 x 10^{13} T/s/cm of axial length. Note that the tritium production rate increases when the ^{6}Li-enrichment is increased from 7.5% to 80% but the increase is 27% lower than anticipated by linearly interpolating from the 7.5% ^{6}Li-enrichment value. This result suggests that while the total neutron flux suppression was only ~ 15%, the larger suppression in the tritium production rate is due to the preferential absorption of the lower energy neutrons (self shielding) at the outer region of the highly enriched Li_2O. The radial gradients for both the tritium production and heating rates within the solid breeder material were very modest, even for the one-inch diameter pellet for FFTF testing.

The HFIR results indicate that the neutron heating and tritium production rates are almost an order of magnitude higher than FFTF for a given enrichment although the absolute incident flux at the specimen boundary (source) is comparable to the FFTF case, as shown in Table 1.2-9. The NRU results, however, show rates comparable to FFTF although, from Table 1.2-9, the NRU absolute flux is an order of magnitude lower than that of FFTF. Apart from this, the HFIR and NRU results show similar behavior. In both cases, neither the neutron heating nor the tritium production rates increase linearly with ^{6}Li-enrichment. This is due to the self-shielding occurring in test specimens of

this size. The ratio of the neutron heating to the tritium production rates are fairly constant in both cases, which implies that the neutron heating contribution from elastic and inelastic scattering is relatively small. Also, the radial gradients for both heating and tritium production rates become quite large for ^{6}Li-enrichments greater than 0.5%. The same behavior is found for the annular pellet test geometry, with the integrated neutron heating and tritium production rates being only slightly smaller than for the solid pellet.

The neutron heating rates were transformed into temperature gradients based on the following test assumptions. (1) The temperature of the outer radius of the Li_2O pellet was maintained at 400°C; (2) the center temperature for the pellet, or inner radius temperature, reached steady state; (3) all heat transfer occurred radially; and (4) the heat transfer coefficient was independent of temperature. The temperature profiles were then calculated using curves interpolated through the calculated heat generation rates for each of the five zones in the solid pellet cases. The results show that both the NRU and FFTF have an acceptable peak temperature for a one inch diameter pellet, with maximum temperatures of about 550°C and 700°C, respectively. However, testing of such a pellet size in the HFIR reactor would lead to unacceptable temperatures (above 2500°C) in the center of the pellet. The impact of lithium enrichment on the temperature profile achieved in a one inch diameter pellet is summarized in Figure 1.2-12 for the NRU reactor. The center-line temperature decreases with increasing ^{6}Li enrichment due to the significant self-shielding which occurs when testing in this reactor. Similar results were obtained for HFIR.

Finally, the impact of testing time and the associated lithium burnup are considered. For FFTF, the ^{6}Li absorption rate is fairly independent of radius, even at 80% ^{6}Li-enrichment. Therefore, the lithium burnup profile remains fairly uniform with time within the entire volume of the breeder material. However, for HFIR and NRU, the large ^{6}Li absorption rate leads to changes in the radial tritium production rate profiles with time. The time-dependent tritium production profiles in HFIR, shown in Figure 1.2-13, were estimated by assuming that the structural integrity of the pellet remains the same as ^{6}Li burnup occurs and the self-shielding does not change with time.

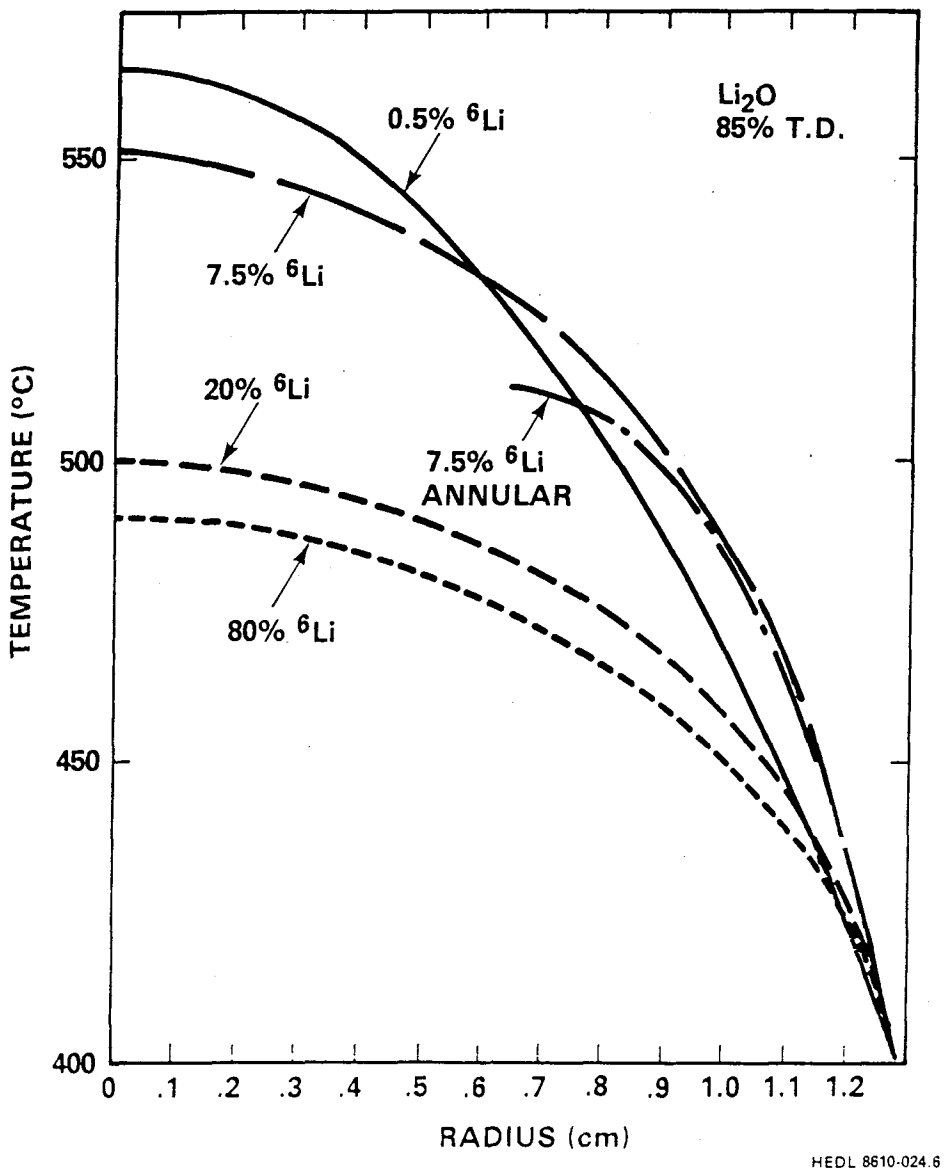


Figure 1.2-12 Influence of lithium-6 enrichment on temperature profile in Li_2O pellet in the NRU reactor

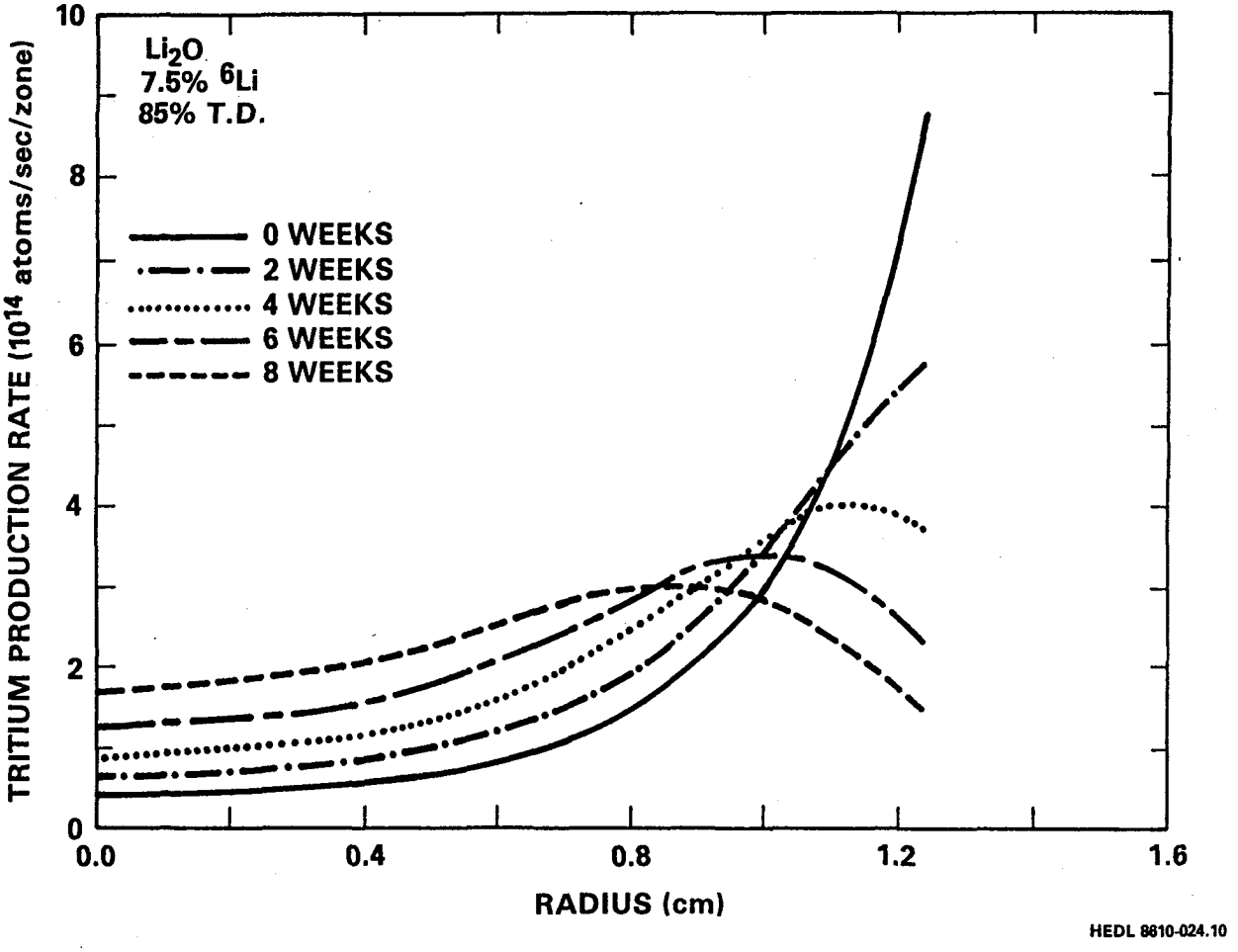


Figure 1.2-13 Variation of tritium production rates with time in the HFIR reactor

As anticipated, the region of peak tritium production moves radially inward as a function of test time. The calculations for the HFIR reactor for this ^{6}Li-enrichment extend only to eight weeks, since at that point the total tritium production within the sample has dropped by ~ 15%. A similar behavior is observed in the NRU testing of a similar test specimen configuration and ^{6}Li-enrichment over a much longer period of three years (because of the lower neutron flux in the NRU reactor).

Conclusions

The spatial gradients for both the heat generation and tritium production rates are more favorable in a fast flux spectrum (FFTF) when compared to the steeper gradients obtained in the thermal or modified thermal spectra such as those for HFIR and NRU. Although the spectra for the HFIR and NRU reactors are different, the calculated heat generation and tritium production rates are quite similar if the differences in flux between the two reactors are used to normalize the results. This is not surprising since these rates depend predominately upon the thermal portion of the spectrum. The temperature differences across the breeder pellet for either a 2.5 cm diameter cylindrical or 1.2 cm thick annulus become too large, even in the FFTF, if the enrichment is much higher than 20% ^{6}Li. For both the NRU and HFIR reactor, these temperature differences are prohibitively high unless the lithium enrichment is kept below 1-2% and the specimen width is small.

The peak tritium production rates in both HFIR and NRU move radially inward with test time due to lithium burnup in the outer zones for ^{6}Li-enrichments greater than ~ 7%. For FFTF the tritium production rate is relatively insensitive to enrichment up to 80% and, therefore, the burnup is apparently uniform with test time.

The analysis suggests the following general conclusions regarding the different capabilities offered by the spectra of existing fission reactors for solid breeder testing. For basic material property testing, fission reactors with either predominantly fast or mixed energy neutron spectra can be utilized. Care must be taken to choose the appropriate ^{6}Li enrichment and specimen size to achieve the desired test environment in a given test reactor. For "prototypic" solid breeder testing with relevant temperature and tritium production gradients, the choice of an appropriate reactor for testing becomes

more difficult. Fission reactors with significant thermal neutron flux are limited to small test specimen dimensions or low reaction rates primarily due to self-shielding effects. Reasonable gradients for the initial tritium production and temperature within the test specimens can be obtained only for small test specimens with ^{6}Li enrichments of less than 2-3%. Also, the selective ^{6}Li burnup within the sample is quite severe and leads to a change in the tritium production gradient within the specimen as a function of the test time. Fission reactors with fast neutron spectra are less susceptible to self-shielding issues and, therefore, larger specimen sizes and higher burnup rates can be explored. High tritium production rates and acceptable temperature gradients within the test specimens can be obtained for larger diameter specimens ($\geq$2.5 cm in diameter) and higher ^{6}Li enrichments (up to 20%) with minimal change in the tritium production gradients with test time. The major limitation of fast neutron reactors is that the lowest achievable test temperature in the specimen is ~ 360°C. Lower temperatures (~ 260°C) are possible only at significantly higher cost.

1.2.3 Liquid Metal MHD Experimental Facilities

For the large and important class of designs known as self-cooled liquid metal blankets, MHD effects are a dominant concern. The strong magnetic field in a fusion reactor causes a body force which substantially increases the pressure needed to drive the coolant through the blanket. It also indirectly affects the heat and mass transfer by suppressing turbulence and altering, in some cases dramatically, the flow distribution within the blanket. Understanding the nature and the consequences of the interaction of liquid metal flows with strong magnetic fields, and development of an appropriate experimental data base and predictive tools are necessary before detailed designs of liquid metal-cooled blankets can be developed. Table 1.2-11 summarizes the features and objectives of the major non-neutron experiments for liquid metal blanket testing. The experimental program, prior to integrated fusion testing, can be divided into three phases of increasing level of integration.

The first phase involves analytical, experimental, and numerical investigations of the structure of flow in typical components of flow networks (ducts, manifolds, expansions, contractions, etc.). Heat transfer experiments

Table 1.2-11 Features and Objectives of Major Liquid Breeder Experiments

ALEX[a]/ALEX Upgrade	LMF[b]	MHDM[c]	TMIF[d]	PITF[e]
• Testing of flow network components	• Testing of segments of blanket modules	• Basic elements of relevant geometry	• Actual materials and geometry	• Prototypic blanket module
• Working fluid: NaK	• Working fluid: NaK	• Relevant materials combination		
• Loop structural material: austenitic stainless steel	• Loop structural material: austenitic stainless steel	• Transport loop	• Transport loop	• Transport loop
• Magnetic flux density: 2-2.5 T	• Magnetic flux density: 4-6 T	• Relevant T, ΔT, impurities, V	• Relevant environmental and operating conditions	• Prototypic environmental and operating conditions
• Available dimension in B-field direction: 15-30 cm	• Available dimension in B-field direction: 120 cm	• Long operating time per experiment		
• Measurement of velocity, pressure, temperature, and electric potential distributions	• Measurement of velocity, pressure, temperature, and electric potential distributions	• Measurement of dissolution and deposition rates	• Measurement of integral quantities (ΔP, T, corrosion, and deposition rates)	• Measurement of integral quantities
• Develop and test instrumentation for local measurements in NaK environment	• Develop and test instrumentation in NaK environment	• Develop and test instrumentation in relevant environments	• Design data for blanket test module	• Engineering design data
• Validate MHD flow, pressure, and heat transfer predictive capability for individual flow network components	• Validate MHD flow, pressure, and heat transfer predictive capability for segments of blanket modules	• Design data on MHD heat and mass transfer	• Confirm and refine configurations	• Reliability data in non-fusion environment
• Obtain design data for flow network components	• Obtain design data for segments of blanket modules	• Verify techniques to reduce corrosion and corrosion effects		
	• Explore techniques to reduce pressure drop and enhance heat transfer			

[a]Exists (ANL)
[b]Liquid Metal Flow Facility
[c]MHD Mass Transfer Facility
[d]ThermoMechanical Integration Facility
[e]Partially Integrated Test Facility (may be upgrade of TMIF)

are expected to be of a confirmatory nature in this phase, since temperature profiles should be fairly straightforward to calculate once the velocity profiles are known. The effect of MHD flow distribution on mass transfer may be much more difficult to assess due to the importance of loop chemistry. For this reason, in this experimental phase, experimental investigation of MHD effects on corrosion should be preceded by thorough testing in ordinary forced convection loops (with no magnetic field) with controlled impurity levels. The ALEX facility in the U.S.,[9] and similar facilities worldwide,[20,21] are already contributing information on MHD fluid flow for Phase I. In addition, several small thermal and forced convection loops exist in various locations for exploring material interactions without magnetic fields.[7,22] Much more data is needed in both of these areas.

The second phase of MHD experiments will be carried out in test modules simulating more complex features of leading blanket designs. Because of the electrical coupling between individual ducts in the blanket, the use of test modules of representative size and complexity is necessary. More powerful magnets with increased magnetic field volume will be needed to achieve test parameters approaching those in a reactor blanket. Data obtained during this second phase will be used to validate predictive capability for pressure drop and heat transfer, and to obtain design data for blanket configuration screening and further development. The experiments will include exploration of techniques for MHD pressure drop reduction and/or heat transfer enhancement at parameter ranges close to those of the blanket environment. The second phase also includes MHD mass transfer (corrosion and deposition) testing. Corrosion tests, which involve measurement of dissolution and deposition rates, require long operating times per experiment in loops of prototypic temperatures, temperature differences, structural and coolant materials, and impurity levels. A separate facility called MHDM (MHD Mass Transfer Facility) has been identified because of the unique features of the facility and the experimental program.

The third phase involves experiments on modules with actual materials and geometry and with operating conditions as close to prototypic as possible. Engineering design data of the overall thermomechanical performance of the blanket modules and their corrosion characteristics will be obtained as well

as information pertaining to design reliability in a non-neutron environment. Additional details on elements of the liquid breeder test program can be found in Ref. [1].

A facility called LMF (Liquid Metal Flow Facility) has been identified as a critical near-term experiment which provides a bridge between the first and second phases of testing. The characteristics of LMF have been explored in detail, including both the physical aspects of the facility and the experimental program. Chapter 2 contains a more detailed description of LMF.

The purpose of LMF is to carry out both isothermal and heat transfer tests on elements of future blanket designs for which there are unresolved MHD-related issues. The quantities to be measured include velocities, pressures, and voltages at selected locations. During heat transfer tests, temperature distributions will also be obtained. Heat transfer measurements fall into two categories. In the first category, heat transfer is used as a diagnostic tool for the study of flow distribution for those cases in which direct measurement of flow structure is not practical or requires confirmation. In the second category, heat transfer parameters at or near prototypic conditions are obtained for direct validation of predictive calculational tools and/or for the creation of an empirical data base.

The major components of LMF are shown schematically in Figure 1.2-14. They include: a) the test article, b) the flow loop, c) the magnet system, and d) the instrumentation and data acquisition system.

a. Test Article

The test articles largely determine the design and functional requirements of the facility. Blanket simulation submodules must have sufficiently large dimensions to achieve prototypical thermal and flow behavior. Long development lengths parallel to the magnetic field impose the most difficult requirements on test volume. This necessitates magnets with considerably larger pole face separation than ALEX or ALEX Upgrade. For a dipole-type magnet, the required pole face separation is about 1 m.

The facility also should be able to accommodate a variety of other test articles, each of which is designed to address a particular design issue related to MHD. Such testing may be necessary if there is reason to believe

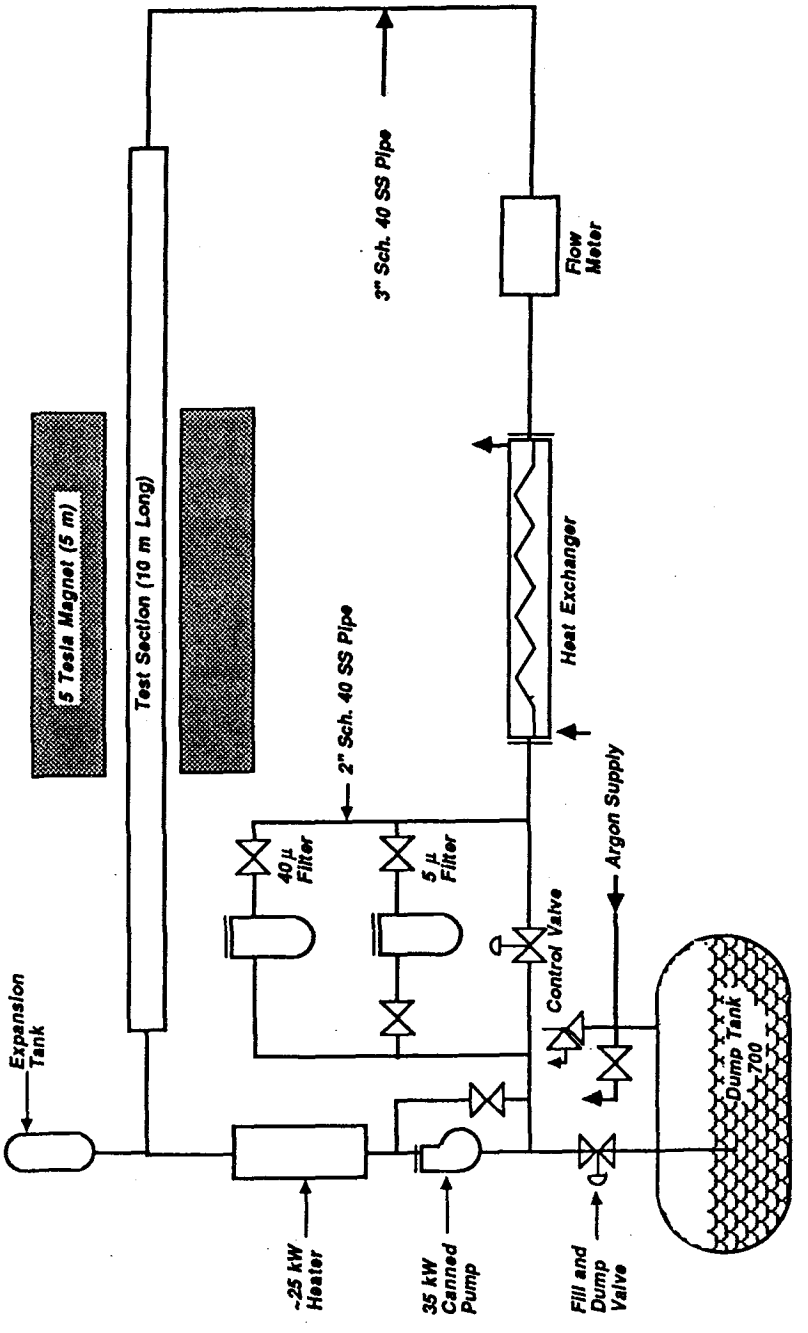


Figure 1.2-14 Schematic of LMF loop

that the higher values of Hartmann number (M) and interaction parameter (N) in LMF will reveal additional information of engineering relevance. It is desirable that the facility be able to accept the identical test articles previously tested at lower M and N. Test articles, incorporating the most important geometric features of the BCSS and TPSS blankets, are shown in Figure 1.2-15a and b.

b. Flow Loop

The recommended flow loop for testing lithium blanket designs uses NaK in stainless steel at low temperature. Low temperature operation with NaK simplifies the loop design and greatly facilitates operations. (LiPb eutectic has significantly different MHD properties as compared with elemental lithium; therefore, testing of a LiPb blanket might be better achieved using a fluid with more similar properties, such as mercury or Wood's metal).

The possible negative effects of low temperature operation in NaK have been determined to be acceptable. Corrosion obviously requires high temperature and correct materials, but the LMF facility is not intended for corrosion studies. Heat transfer depends primarily on temperature differences, rather than absolute temperature, except for a secondary effect on material properties. The only remaining advantage of lithium over NaK for heat transfer/fluid flow experiments is that, at identical test conditions, the Hartmann number with lithium is 50% higher than that of NaK, and the interaction parameter is 100% higher (although this can be compensated by reducing the bulk flow rate). The disadvantage in Hartmann number is not high enough to balance the expected reduction in the quality and variety of test data brought about by high temperature operation in lithium.

The size of the loop can be much smaller than a reactor primary cooling system and still maintain prototypical values of M and N. Some estimated loop parameters are shown in Table 1.2-12. Loops operating at high temperature or loops made of different materials for corrosion studies will be considerably more expensive. This estimate includes all loop hardware and engineering, excluding the magnet. It is assumed that the loop will be sited in an existing building with existing cranes and other support hardware, utility hookups, exhaust stacks, etc.

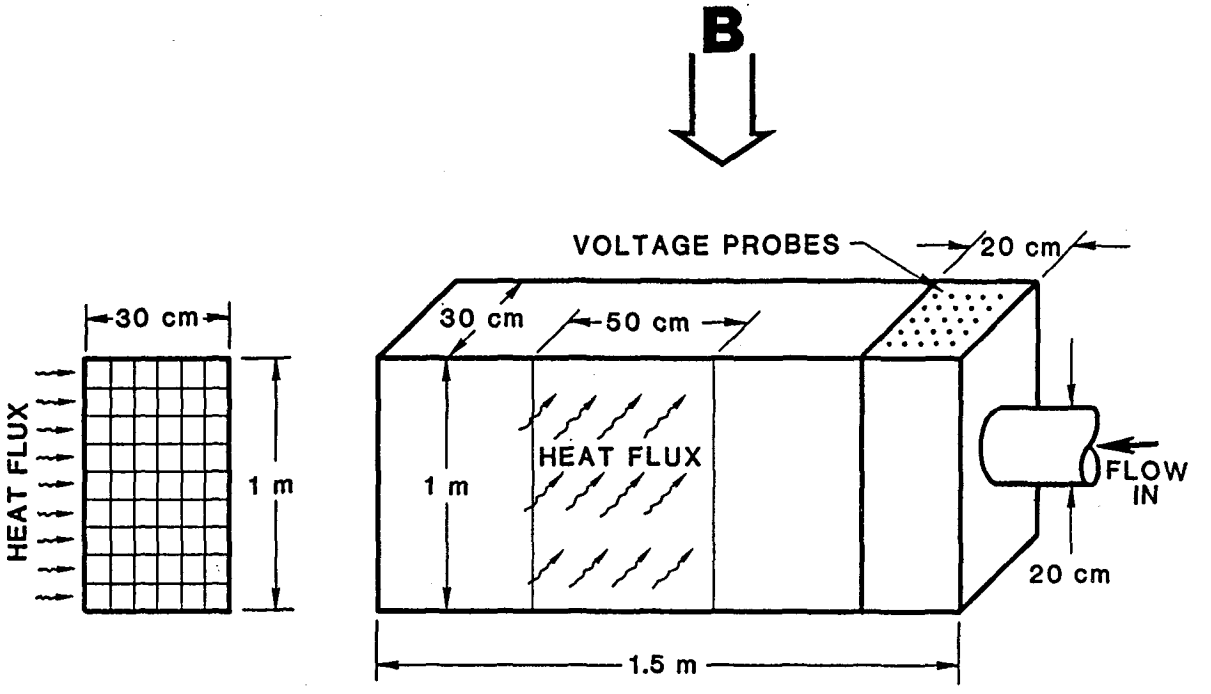


Figure 1.2-15a Conceptual design of a test section simulating the inlet (or outlet) manifold of the TPSS design. Flows in each of the individual ducts fed from the manifold can be measured with individual EM flow meters.

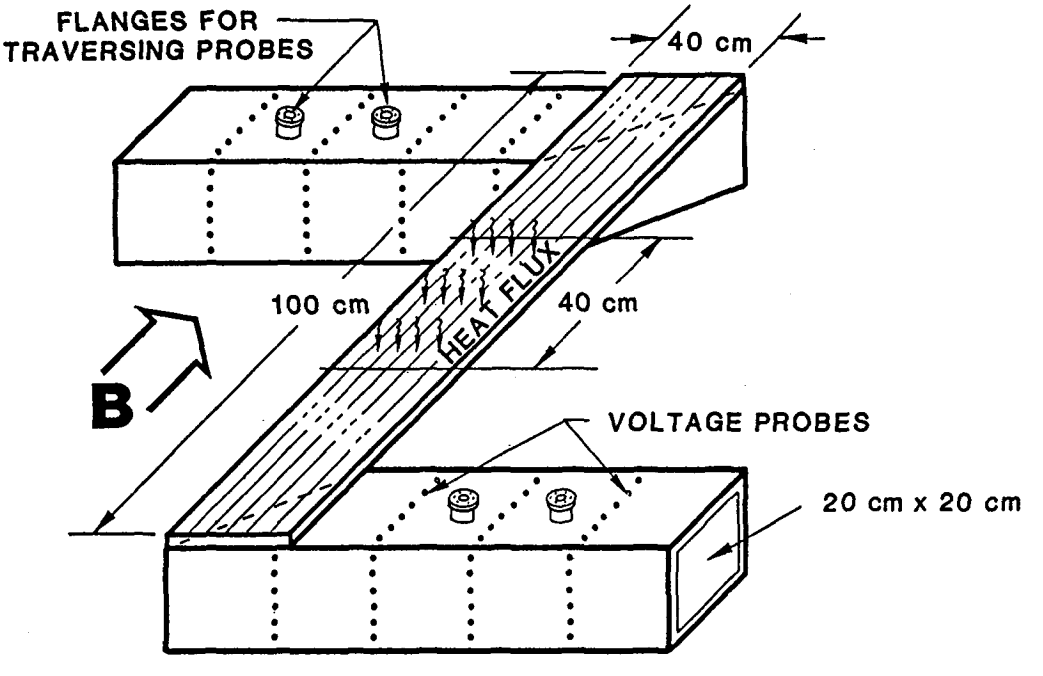


Figure 1.2-15b Conceptual design of a test section simulating the salient features of the BCSS liquid-metal-cooled blanket design

Table 1.2-12 LMF Facility Parameters

Loop Parameters	
Working Fluid	NaK Eutectic
Inventory of Working Fluid	700 liters
Loop Materials	Predominantly 300 Series S/S
Volumetric Flow Rate Through Test Articles	1-25 liters/s
Pump Outlet Pressure	1 MPa
Pump Outlet Temperature	$\leq$100°C
Test Article Conditioning Temperature (at Low Pressure and Flow Rate)	300°C
Overall Length of Test Article (Between Flanges for Test Section Replacement)	~10 m
Cost (excluding cost of test articles)	$1M
Magnet Parameters	
Peak Field	5 T
Warm Bore	1.2 m
Uniform Field Volume	1 m x 0.3 m x 3 m
Field Uniformity	± 5%
Dipole Magnet Cost	$12M
Solenoid Magnet Cost	$15M

c. Magnet System

The magnet system for LMF is the largest and most expensive element of the facility. The characteristics of the magnet will control to a large extent the scale and cost of the entire facility. Two major options exist for the magnet system: iron core versus superconducting, and dipole versus solenoid.

Although design and fabrication of a superconducting magnet such as the one envisioned for the LMF facility is a challenging task, the required technology and expertise exist and have been demonstrated. A superconducting magnet has advantages in power consumption, but requires a higher level of supervision and frequent helium replenishment. A conventional iron core

electromagnet, as opposed to a superconducting magnet, requires less maintenance and supervision between tests, can be energized in a much shorter time, and its design, operation, modification, or repair is much more straightforward. On the other hand, the power supply and cooling water requirements are so demanding that, for the size and magnetic flux density magnitude envisioned for the LMF, the use of conventional iron core magnets is all but precluded.

Solenoid magnets are generally less costly than dipoles; however, a larger solenoid volume is required for the same testing capability as in a dipole magnet. Costs have been estimated for dipole and solenoid magnets and are given in Table 1.2-12 together with the major parameters. The dimension of 1 m is in the direction parallel to the field. For the same type of magnet, the cost scales roughly with the magnetic flux density and the magnet volume.

Although a solenoid magnet may, at first, appear to be preferable because it simulates geometrically a segment of a tokamak torus, the solenoid magnet has severe test volume access limitations for testing in predominantly transverse fields. Radial access to the test volume can only be allowed at a very limited number of windows. This limits the type and variety of test articles that can be tested. Although additional attention must be paid to this question, as well as to the final cost differential between the two magnet types, it appears that a dipole magnet is preferable.

d. Instrumentation

Measurements of direct engineering importance are those of velocity, pressure, and temperature distributions. Although of limited engineering importance by themselves, voltage distributions can, under certain conditions, be directly related to the velocity profiles.

Measurements of the pressure drop and heat transfer coefficient are fairly straightforward, as these are integral parameters. Relatively standard pressure transducers can be used to measure pressure drop. Heat transfer coefficients can be obtained by measuring temperatures with standard thermocouples. Electric potential measurements are also relatively simple, since they can be accomplished by attaching wires directly to the channel walls.

The measurement of velocity distributions, on the other hand, is much more complicated, but is also very important. Common instruments for measuring velocities are Pitot probes and hot film anemometers. The former are of very limited use for the low velocities relevant to MHD testing. Hot film anemometry has been used successfully in the past for liquid metal MHD studies. However, calibration shift due to sensor contamination and reduced sensitivity due to reduced heat transfer in the magnetic field make such measurements extremely tedious. The shortcoming of reduced sensitivity is experienced by all heat transfer-based measuring instruments.

For flow conditions in which the product of the current density and the electrical conductivity is much smaller than the voltage gradient, a very attractive measuring instrument is the LEVI probe (Liquid Metal Electromagnetic Velocimeter Instrument). LEVI measures the emf generated locally in the flow, analogous to an electromagnetic flow meter which measures the global voltage drop across a channel. This technique has been shown to give excellent sensitivity and temporal response without the need for calibration.[9] The primary limitation of LEVI relates to its dependence on the local magnetic field. It can only be used in the presence of a transverse magnetic field and its sensitivity decreases as the magnetic field strength decreases. In addition, its accuracy diminishes as the wall conductance ratio approaches unity.

There would undoubtedly be cases where, because of the small sizes of the ducts, reliable detailed velocity profiles would be exceedingly difficult to obtain. In such cases, the flow structure can be deduced indirectly by carefully designed heat transfer experiments. In such experiments, information about the flow distribution can be obtained by measuring the temperature distribution with thermocouples strategically placed on the surface of the test article and within the flow ducts. In fact, heat transfer experiments should be viewed as much as a means for obtaining information about the flow structure and distribution as for measuring overall heat transfer parameters.

Because of the complexities of the velocity distribution measurements, it is unrealistic to expect that the flow field within a complex test article would be completely mapped. It is important, therefore, to apply pre-experimental analysis to the maximum extent possible to carefully select the locations for velocity profile measurements that provide the most important information.

1.3 Fusion Testing Issues

Integrated testing is essential for concept verification and demonstration of fusion nuclear components. It has been shown previously in the FINESSE study that only a fusion facility can provide the proper combination of environmental conditions for integrated testing.[1]

Major initiatives are already underway in Europe (NET),[5] Japan (FER),[6] the U.S. (TIBER/ETR),[8,23] the U.S.S.R. (OTR),[7] and internationally (INTOR)[24] to plan and design a fusion engineering test facility. These programs vary in the degree to which nuclear technologies are emphasized, but a primary objective for all of them is testing of fusion nuclear components.

A fusion engineering test facility will be a central and relatively expensive step in the fusion program. Fusion nuclear technology issues must be weighed together with other issues in the fusion program, including physics, engineering, and system integration concerns, in order to define the optimum design and operating characteristics of the facility.

Earlier effort in FINESSE[1] has addressed many of the fusion nuclear technology testing requirements on the major parameters and features of a fusion test facility. Issues related to tritium supply and the reliability of a tritium-producing blanket also have been addressed. Subsequent examination of the impact of the FINESSE results on the cost and design of a fusion test facility have identified a number of critical issues that require further attention. An example is the requirements on the plasma burn time and the need for steady-state operation. These issues are examined in this section. Because of the renewed strong interest in a fusion engineering testing facility, this section also reviews the influence of fusion nuclear technology objectives on the fusion test facility characteristics and design, and on fusion testing in general. The section is organized into three topics: 1) Requirements for Nuclear Technology Testing, 2) Tritium Supply, and 3) Blanket Reliability and Device Availability.

1.3.1 Requirements for Nuclear Technology Testing

Successful testing requires that the physical and operating characteristics of the test facility meet certain conditions. Previous analyses in the

FINESSE study have been performed to quantify the test requirements and provide guidelines for the fusion engineering test device characteristics.[1,25] The test program also impacts the facility design and operation outside the reactor core. For example, large and complicated ancillary equipment, such as heat transport and rejection, tritium extraction, chemistry control, and instrumentation systems, often accompanies component testing. The safety impact of the test program is another important consideration. For example, in NET, a tritium-producing blanket with liquid lithium has been ruled out for safety reasons.[5] Protection of the facility against mechanical failures and radiation hazards (including accidental tritium releases) must also be considered.

The most important test requirements are those related to the major parameters of the test facility. These are summarized in Table 1.3-1. These requirements on the test facility parameters are related to the assumed reference conditions for a commercial reactor. The table also provides a set of reference conditions based on a survey of recent tokamak reactor and reactor blanket design studies.[11,12,26,27] Two categories of parameter values are given: minimum and recommended. The minimum values are based primarily on detailed analysis of the important blanket phenomena under altered test conditions. One can show that test device parameters below the minimum value in any category will seriously limit the usefulness of nuclear testing for at least one identifiable phenomenon. There is a high probability that results could not be extrapolated to reactor conditions under these circumstances. Future analysis of additional phenomena may result in more stringent minimum test requirements, due to an increased understanding of the complexities of blanket behavior. It is likely that the minimum parameter values will be reduced only if the reference device parameters are reduced.

While the minimum parameter estimates provide values <u>below</u> which there is confidence that results <u>cannot</u> be extrapolated to reactor conditions, the recommended parameter ranges provide values <u>above</u> which there is confidence that results <u>could be</u> extrapolated to reactor conditions. The recommended values are determined partly from analysis and partly from engineering judgment. While testing at prototypical values is clearly most beneficial, the large majority of nuclear issues can still be adequately addressed if the recommended parameters are achieved in the fusion test device. However, since

Table 1.3-1 Device Parameters: Reference Conditions and Recommended Values

Parameter	Test Facility		Reference Reactor
	Minimum	Recommended	
Neutron Wall Load (MW/m^2)	1	2-3	5
Surface Heat Load on First Wall (MW/m^2)	0.2	0.2-0.5	1
Fluence at Test Module[a] ($MW-yr/m^2$)	2	3-6	15-20[b]
Plasma Burn Time (s)	500	>1000[c]	steady state
Plasma Dwell Time (s)	<100	<50	--
Continuous Operating Time	days	weeks	months
Availability (%)	20	30-50	70
Test Port Size (m^2 x m)	0.5x0.3	1x0.5	--
Total Test Surface Area (m^2)	5	10-20	--
Magnetic Field Strength (T)	3	5	7

[a]Fluence at test module. Required test device lifetime is greater (by about a factor of two).
[b]Blanket lifetime.
[c]Steady state is preferred.

we do not fully understand engineering phenomena under fusion reactor conditions, a judgement is required based on typical experience in scaling from other technologies in addition to the analysis of known behavior. Note that operating at the recommended set of parameters gives no guarantee that the results will be fully valid at full reactor parameters.

For both the minimum and recommended values, future analysis will likely result in further refinement of the estimates in Table 1.3-1. Precise specification of the requirements on test device parameters is difficult. In general, the physical behavior in nuclear components varies gradually with the device parameters, showing threshold effects only in a limited number of cases (such as the transition from laminar to turbulent flow and the transition from elastic to plastic strains). The determination of test requirements must be constructed from analyses of the many phenomena which are affected by varying device parameters, and from an informed engineering judgement on how far the conditions can be extrapolated in order to confidently predict behaviors under full reactor conditions.

Exact simulation of all the conditions in the blanket (including temperature profiles, tritium concentration profiles, geometric boundary conditions, etc.), is not possible with device parameters that are scaled down from the reference reactor conditions. Therefore, it is important to define the degree to which imperfect simulation of the reactor conditions can be tolerated, based on whether or not the needed data can still be obtained. In addition, modifications to the test modules themselves can be partially successful in recovering reactor relevant behavior under scaled conditions. The process of altering test module characteristics to enhance the value of testing is called Engineering Scaling.

Table 1.3-2 shows the relationships between the parameters of the fusion test device and the main categories of blanket performance. The test parameters from Table 1.3-1 are grouped into four areas: 1) neutron wall loading, which is the primary device parameter in determining the heat sources (surface and bulk heating), nuclear reaction rates, and accumulated fluence; 2) plasma burn time and pulsing, which represents effects related to non-steady-state operation; 3) device geometry and test volume; and 4) magnetic field strength and geometry. Relationships also exist among the performance categories; for example, the thermal condition of the blanket strongly impacts structural, corrosion, and tritium behaviors. These indirect relationships are not explicitly defined in Table 1.3-2.

In the remainder of this subsection, the device parameter areas are examined individually to define more clearly the important nuclear phenomena which contribute to the definition of test requirements for the blanket.

1.3.1.1 Heat Source Requirements

Heat sources provide the energy input which controls blanket temperatures, and thereby all processes and interactions activated by temperature levels and gradients. The two principal heat sources for the blanket/first wall are surface heating, caused by particle and radiation loads to the first wall, and bulk heating resulting from neutron and secondary gamma-ray radiation. For given materials and geometry, the bulk heating is linearly proportional to the neutron wall load. The surface heating on the first wall depends on the partitioning of energy loss from the plasma between radiation

Table 1.3-2 General Effects of Fusion Test Device Parameters on Blanket Performance

	Neutronics	Thermal	Structural	Flow/Corrosion	Tritium
Neutron Wall Load:					
Heat Source (Surface and Bulk Heating)	nuclide density and geometric changes due to thermal expansion and cracking	temperature profiles, heat transfer coefficient, thermophysical properties	thermal stresses, material properties, thermal creep, temperature-dependent radiation damage profiles	mass transport/ corrosion rates and profiles, coolant properties, wall electrical conductivity (LM)	diffusion and other transport processes, solubility and surface adsorption, mass transfer, grain growth, porosity changes (sintering)
Reaction Rates	R.R.	R.R.	R.R.	R.R.	tritium production rate
Fluence	transmutations, activation	thermophysical properties, gap conductance	material properties, swelling, ductility, creep	degradation of MHD insulators, radiation-enhanced corrosion	tritium generation, trapping, burn-up related thermochemistry changes (SB), effect on permeation barriers
Plasma Burn Time and Pulsing	--	transient temperature profiles	fatigue, crack growth, ratchetting, creep/fatigue	corrosion equilibrium	inventory and recovery equilibrium; permeation rate and barrier characteristics
Device Geometry and Test Volume	neutronic boundary conditions, extrapolation to full blanket coverage, deep penetrations	thermal boundary conditions, MHD heat transfer, thermal entrance effects	component sizes (especially aspect ratios)	MHD velocity profiles and pressure drop entrance effects, MHD mass transfer, spatial profiles of corrosion	tritium breeding and inventory
Magnetic Field (Strength and Geometry)	--	MHD heat transfer	steady and transient forces, MHD pressure stresses	MHD fluid flow and corrosion	--

and particles, but the maximum (for an ignited plasma) is limited to 25% of the neutron wall load.

Nearly every important phenomenon in the blanket is in some way affected by temperature, from basic properties to complex thermomechanical and chemical interactions. Examples of the most important temperature-dependent thermophysical, thermochemical, and thermomechanical properties include thermal conductivity, chemical solubility and diffusivity, yield strength, creep rate, and radiation swelling rate. Simple processes, such as thermal expansion and heat conduction are dominated by temperature profiles. More complex interactions, such as mass transport/redeposition and tritium transport, are strongly dependent on temperature, sometimes in ways which are not fully understood. These more complex interactions provide the greatest uncertainties in our ability to perform testing under scaled conditions.

In general, both the absolute level of temperature as well as temperature profiles are important to maintain. Control over the average temperature in a component is usually easy to obtain by allowing the coolant temperature to rise. On the other hand, temperature gradients are proportional to the local heat flux. Changes in the heat flux will result in unavoidable changes in the temperature gradients. Temperature differences across an element can be adjusted by geometrical changes, but local temperature gradients can not be adjusted independent of the heat source. Therefore, even with careful test module design, there are limits on how far the heating rates can be lowered. Limits have been studied for: 1) total amount of heat input, 2) relative contributions of surface versus bulk heating, and 3) geometric constraints on the heat source.

A reduction in the heat source results in lower spatial temperature gradients. A common engineering scaling technique to enhance temperature differences across blanket elements is to increase their thicknesses. For structural similarity, aspect ratios should normally be maintained, although there are some structural effects which are not linear in the dimensions (like fracture mechanics). Hard limits on the reduction in heat input come when space limitations prohibit increasing dimensions or when the dimensions are so altered from the reference case that new effects may occur, such as crack growth, axial conduction, and altered neutronics. These limits occur at roughly a factor of 3-5 reduction in the heat source.

A thermal analysis was performed on a plate-type, helium-cooled, solid breeder blanket module to demonstrate the extent to which temperature profiles can be affected by a reduction in wall loading. Reactor conditions were assumed to be 5 MW/m^2 wall load with 1 MW/m^2 surface heat flux, and the test device was assumed to provide only 2.5 MW/m^2 wall load with 0.1 MW/m^2 surface heat flux. The blanket module design uses a lobed first wall, with coolant entering through first wall cooling channels at the rear of the module, passing toward the front ($\theta=\pi/2$), where an orifice redirects the flow through the interior of the blanket. Scaling was applied to both the module dimensions and the coolant flow rate to maintain the bulk temperature rise in the coolant and the temerature drop across the first wall. Figure 1.3-1 shows the results, which indicate that with a reduction in the wall load the temperatures can be matched only partially, even with careful engineering scaling.

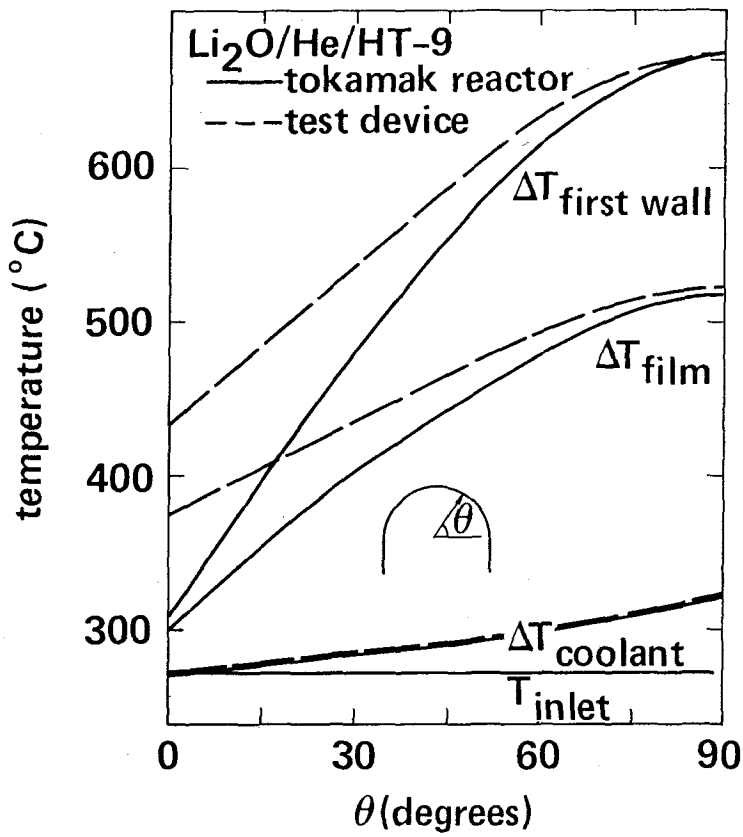


Figure 1.3-1 Heat source effect on the $Li_2O/He/HT-9$ first wall temperature profile (reactor at 5 MW/m^2 neutron and 1 MW/m^2 surface heat load; scaled test module at 2.5 and 0.1 MW/m^2)

As mentioned above, incorrect temperature profiles in the first wall will affect many important phenomena activated by temperature.

The possiblity for enhancing nuclear and surface heating by external means (e.g., resistive heaters or fissile materials) have been explored, but the methods proposed to date are awkward and/or add new uncertainties to data interpretation. For solid breeders, addition of uranium has been considered, but tritium and chemical behavior will almost certainly be affected.

The ratio of surface to bulk heating is important because the temperature profiles and heat transfer coefficients are affected. For example, it is well known that the temperature variation in a plate resulting from a surface heat flux is linear, as opposed to the parabolic distribution resulting from uniform bulk heating. Thermal stresses in first-wall and front-of-blanket elements are especially sensitive to these profile variations.

Liquid metal blankets have special difficulties with reduced heat sources because the magnetic field tends to couple the geometric features of the blanket with the heat transfer. Engineering scaling for the heat source must also account for the resulting effects on MHD phenomena, including entrance-region velocity and temperature profile development. Temperature profile development lengths can be much longer than the channel length, which means that the entire blanket is in the thermal entry region, in which heat transfer strongly depends on location. As discussed in Section 1.4, the heat sources, velocity profiles, and geometry play a highly coupled role in determining the temperatures in liquid metal blankets. Geometric effects are treated in more detail below.

1.3.1.2 Neutron Fluence Requirements

A number of specific reactions result from neutron radiation, including tritium and helium production, atomic displacements, and transmutations. As a result of some of these reactions, neutrons are responsible for numerous changes in material properties and behavior. Material damage due to neutrons is an important factor in determining design limits for the blanket, including the anticipated lifetime. Many of the anticipated blanket failure modes are intimately related to neutron damage. Some of the effects include changes in thermophysical and thermomechanical properties, radiation swelling, embrittlement, creep, and solid breeder sintering.

In a test reactor with DT neutrons, these effects will depend primarily on the accumulated dose. They are not readily scaled to lower fluences. Test requirements can be identified based on achieving fluences at which significant changes in behavior occur or saturate. However, changes in behavior often result from interactions of different effects rather than single effects, for example, creep/swelling interactions and solid breeder/clad interactions. Therefore, a knowledge of material property changes alone is not sufficient to determine test requirements.

Table 1.3-3 shows some of the important phenomena which occur in fusion nuclear components as a function of neutron fluence. Engineering effects are emphasized in addition to basic property changes. These include interactive effects (such as breeder/clad mechanical interaction or radiation-enhanced corrosion) and behaviors which are not strictly related to material damage (such as tritium production and afterheat).

Radiation effects are extremely sensitive to material choices and operating conditions (primarily temperature). In addition, the lack of data results in large uncertainties. Therefore, the entries in Table 1.3-3 are only approximate estimates. They represent the most important anticipated effects for the primary candidate materials and designs as they are currently understood. Exceptions to these guidelines will undoubtedly occur for particular materials or designs.

From these estimates of fluence effects, some general conclusions can be drawn. Radiation effects can be classified into roughly four categories (depending on many factors, including the specific material and design): beginning-of-life effects, occurring between 0-0.2 MW-yr/m^2; early-life effects, occuring between 0.2-2 MW-yr/m^2; middle-of-life effects, occurring between 2-10 MW-yr/m^2; and lifetime effects, occurring between 10-20 MW-yr/m^2. A minimum requirement has been defined based on matching the exposure required to activate or saturate early-life engineering phenomena. It is very desirable to activate the middle-of-life effects. There are a very large number of phenomena which can be explored without pushing to end-of-life fluences. Clearly higher levels of exposure are better if they can be attained at reasonable cost. It is desirable to test components to their full lifetime values or beyond in order to anticipate lifetime and long-exposure failure

Table 1.3-3 Examples of Important Effects as a Function of Exposure

Exposure MW-yr/m^2	Phenomena/Effects
0-0.2	Thermophysical Property Changes (e.g., Thermal Conductivity) Solid Breeder Cracking Liquid Metal Embrittlement of Structure Onset of Li_2O and Multiplier Swelling Insulator Embrittlement and Conductivity Changes First Wall Erosion Initial Operational Stress Effects Tritium Permeation through First Wall and Clad Hydride Formation and Hydrogen Embrittlement in Structure Porosity in Breeder May Close Off Radiation-Induced Sintering and Grain Growth
0.2-1	Li_2O Swelling Dominates Breeder/Clad Mechanical Interaction Ductility Changes (HT-9, 316 SS) Initiation of Fatigue and Creep/Fatigue First Wall Erosion/Redeposition and Surface Cracking Relaxation of Thermal Stress Radiation-Induced Trapping in Structure (Defect Saturation) Reduction in Fracture Toughness (Structure) Early Transmutation Effects (e.g., Drop in Conductivity of Copper Due to Ni Production) Measurable Radioisotope Concentration
1-3	Changes in Ductility Start to Saturate (HT-9, 316) Fracture Toughness, Δ-DBTT Saturates Thermal Stress Relaxation Complete Burnup Effects on Chemistry, Compatibility, Breeding Breeder/Clad Corrosion Irradiation Hardening (<450°C)/Softening (>450°C) Saturates
3-5	Possible Fatigue Crack Propagation Onset of Irradiation Creep/Swelling Interaction of Austenitic Alloy Clad Swelling (316) Dominates Breeder/Clad Interaction Possible Fracture Toughness Degradation (HT-9)
5-10	Potential Onset of Irradiation Creep/Swelling Interaction of HT-9 Possible Fatigue Failure Change in Fracture Mode Changes in Toughness/Strength/Ductility and Tearing Modulus
10-20	End-of-Life Phenomena: Operational Stress Effects - First Wall Thinning - Unstable Deformation - Fatigue, Creep Fatigue - Unstable Cracking Unforseen High-Fluence Material Behavior (e.g., Solid Transmutations)

modes; however, in the first fusion facility, cost considerations may preclude any testing beyond the middle-of-life effects.

It is extremely important to distinguish between the fluence attained at the test module and the test facility lifetime. The fluence values discussed above and in Tables 1.3-1 and 1.3-3 are those that need to be achieved at the test module. The test facility lifetime should be longer for at least two key reasons. First, most of the important test modules are not exposed directly to the plasma, and the highest neutron flux at the module is generally a factor of two or more lower than that at the first wall. Second, it is inconceivable for the first fusion test facility that a useful module can be irradiated for the entire life of the facility. Early modules are expected to fail, and knowledge will be incorporated for testing better modules during the life of the facility.

1.3.1.3 Plasma Burn Time Requirements and Pulsing Effects

Steady-state plasma operation is a generally accepted goal for the development of competitive commercial fusion reactors.[11,26,27,28] Given this, a key question now is whether the design basis for the first fusion engineering test reactor (ETR) should be steady state or pulsed and, if it is pulsed, how long of a burn time is needed.

Key reasons in favor of steady state (or, at least, long plasma burn time) as the design basis for ETR include:

1. Demonstration of steady-state plasma operation is a necessary element in exploring the long-term reactor potential of the confinement concept.[8,27,28]

2. Steady-state operation should reduce the failure rate and improve the reliability of many of the basic ETR components. Reduced cycling will extend the achievable lifetime and fluence in the test facility.

3. Steady-state operation will improve substantially the usefulness of nuclear technology testing in ETR.

This last item concerning the benefits of steady-state operation to nuclear technology testing is amply supported in previous work[1-4] and is the subject of further analysis in this subsection. Before summarizing this analysis, some general observations are worth noting. Adopting steady-state operation as the basis for ETR will require further development in plasma physics.[8] However, regardless of ETR needs, such development is required to demonstrate a key aspect of the long-term reactor potential of selected confinement concepts. Accelerating the current drive development for ETR operation is well justified in terms of the benefits of improved reliability and usefulness to nuclear technology testing. The use of some non-inductive current drive may not increase the cost of ETR; it may actually reduce the cost.[23] Key components such as the impurity control and exhaust system will not require any additional design features or increments in cost to achieve steady state beyond those required for burn times longer than hundreds of seconds. Many components, such as magnets, first wall and limiter/divertor, will have better reliability and probably lower cost in an experimental device if they are designed for steady state [the INTOR[24] design has identified many problems associated with the short plasma burn time]. It is suggested that ETR studies carefully evaluate the impact of using non-inductive current drive on the cost of development, construction, and operation of ETR.

Steady-state operation is extremely important for successful nuclear technology testing. Plasma cycling means time-dependent changes in the major environmental conditions for nuclear testing: 1) nuclear (volumetric) heating, 2) surface heating, 3) poloidal magnetic field, and 4) tritium production rate. These time-dependent changes in the "source conditions" will result in time-dependent changes in the "response" of test elements such as blanket modules, heat and tritium transport loops, and sections of limiter/divertor plates. These time-dependent changes in the responses will introduce new effects and phenomena that: 1) can be, in some cases, more dominant than the steady-state effects for which testing is desired, or 2) will, in many cases, complicate the tests and make the results difficult to model, interpret and understand.

The rest of this subsection is concerned with analysis of the effects of burn time on the usefulness of some key nuclear technology tests. Table 1.3-4 indicates a range of burn cycle times that may exist in an ETR. The burn

Table 1.3-4 Reference Burn Cycle Times (in seconds)

Burn Time	
<200	Short Burn
>5,000	Long Burn
>10,000	Quasi-steady State
Plasma Startup/Shutdown	
15	
Dwell Time	
20	Minimum Time to Evacuate
100	Relaxed Requirements on Vacuum Pumps, Ducts, Etc.

cycle consists of periods of time for plasma start-up, burn, shutdown, and a dwell (or rejuvenation) time. Operating time requirements are based on analysis of the time dependent responses of all the important blanket phenomena. These include thermal, fluid flow, corrosion, structural, tritium, and neutronic performance.

The unsteady behavior of the blanket is generally very complex, but often the evaluation of burn cycle requirements can be related to relatively simple time constants for the processes involved. Many engineering processes can be described approximately with an exponential dependence on time, such as:

$$f = f_o\left(1 - e^{-t/\tau}\right)$$

where τ is a fundamental time constant. Time constants for more complex processes can be expressed in terms of the percentage achievement of the equilibrium value (for example, the time to reach 99% of the equilibrium value).

A partial list of estimated basic time constants is given in Table 1.3-5. These time constants were evaluated using blanket characteristics from the reference designs described in Ref. [1]. Three major classes of time constants which recur frequently are:

1. Diffusive processes governed by a diffusivity and scale length, $\tau_c = L^2/D$. This includes primarily thermal and mass diffusion.

Table 1.3-5 Approximate Characteristic Time Constants in Representative Blankets

Flow	
Solid Breeder Purge Residence	6 s
Liquid Breeder Coolant Residence	30 s
Liquid Breeder Cooling Circuit Transit	60 s
Thermal	
Structure Conduction	4 s
Structure Bulk Temperature Rise	20 s
Liquid Breeder Conduction (Li)	30 s
Solid Breeder Conduction ($\frac{1}{2}$ -cm plate)	50-100 s
(1-cm plate)	200-400 s
Coolant Bulk Temperature Rise (200 K at 4000 MW_t)	
Li	100 s
LiPb	1500 s
Solid Breeder Bulk Temperature Rise ($LiAlO_2$, 300-1000°C)	
Front (Near Plasma)	120 s
Back (Away from Plasma)	1800 s
Material Interactions	
Dissolution of Fe in Li (500°C)	40 days
Tritium	
Diffusion Through Solid Breeder ($LiAlO_2$, 0.2 μm grains)	
1250 K	8-200 s
750 K	13-300 hours
Surface Adsorption ($LiAlO_2$)	3-10 hours
Diffusion Through SS316	
800 K	10 days
600 K	150 days
Inventory in Solid Breeder (Water-Cooled $LiAlO_2$, 0.2 μm grains)	
67% of equilibrium	6 months
99% of equilibrium	4 years
Inventory in Liquid Breeder	
LiPb	30 minutes
Li	30 days

2. Convective processes governed by a velocity and scale length, $\tau_c = L/v$. This applies primarily to various residence times.

3. Changes in bulk quantities, such as tritium inventory or blanket bulk temperatures.

The time constants follow some general trends: flow processes are usually very fast, material interaction and tritium processes are usually very slow, and thermal processes are in between--of the order of minutes. To understand the relationship between unsteady responses and the test requirements, it is helpful to consider three possible situations for the time constant of a given process relative to the burn time:

1. Time constant much shorter than the burn time. A good example of this is MHD velocity profiles, which have a time constant of the order of 1 s or less. In this case, the process reaches a true equilibrium within a single burn time. If the duty cycle (burn time divided by total time) of the machine is high, then the conditions in the blanket are prototypical most of the time.

2. Time constant much longer than the burn time plus dwell time. A good example of this is corrosion, which normally takes weeks to months to become developed. In this case, the process eventually reaches a quasi-equilibrium after many cycles, with conditions changing very little during a single burn cycle. The higher the duty factor, the closer the quasi-equilibrium will be to the true equilibrium condition.

3. Time constant roughly equal to the burn or dwell time. A good example of this might be temperature responses, particularly in solid breeder blankets (which possess relatively low thermal conductivities). This condition is the most problematic, and requires detailed analysis to determine the nature of the responses that depend on temperature.

There are two situations which cannot be accommodated by this simplified classification: threshold effects and interrelated processes of different time constants. Structural responses provide good examples of important threshold effects. For example, irradiation of ferritic steels generally increases the ductile-to-brittle transition temperature (DBTT). If the blanket temperature falls below the DBTT due to plasma cycling, then the structural response could

be dominated by low temperature effects rather than the reference conditions. Another example is high cycle fatigue, which is a structural response that would not properly represent the conditions in a continuous burn reactor. Some of the known time-dependent threshold effects include, for example, temperature-dependent chemical reactions; high cycle fatigue and fracture mechanics; DBTT - low temperature embrittlement; solid breeder thermal fracture; and plastic deformations, especially ratchetting. In addition, Table 1.3-3 contains a large number of fluence-related threshold effects.

Interrelated time constants also complicate the definition of test requirements. For example, even though corrosion is dominated by long time constant processes, it is also strongly affected by blanket temperatures, which have relatively short time constants. The cyclic effects on temperature could result in significantly different corrosion behavior, such as temperature-sensitive chemical reactions and redeposition. It is difficult to predict all of the effects of cycling because of the large number of important interrelationships between phenomena which exist in a blanket. These factors strongly support steady operation to match the conditions in the reference reactor.

Some of the time constants are strong functions of temperature and can vary over many orders of magnitude. Figure 1.3-2 shows the large variation in tritium diffusivity for $LiAlO_2$ over the temperature range between 650°C and 1250°C for a grain radius of 0.1 μm. There is a fairly large band of uncertainty indicated in the figure. For comparison, the thermal diffusion time constant for 0.5 cm of $LiAlO_2$ is also shown.

While the time constants provide a good general understanding of the time dependent behavior of the blanket, it is necessary in many cases to perform more detailed calculations. This is especially true when several processes are operating simultaneously, and possibly nonlinearly.

A calculation was performed to determine the transient tritium release rate from $LiAlO_2$ plates under pulsed conditions. Because of the large temperature-dependence of the tritium properties, a 2-D time-dependent temperature calculation was performed first to determine the breeder plate temperature. The tritium calculation included intragranular diffusion, grain boundary diffusion, pore diffusion, surface adsorption, and solubility.

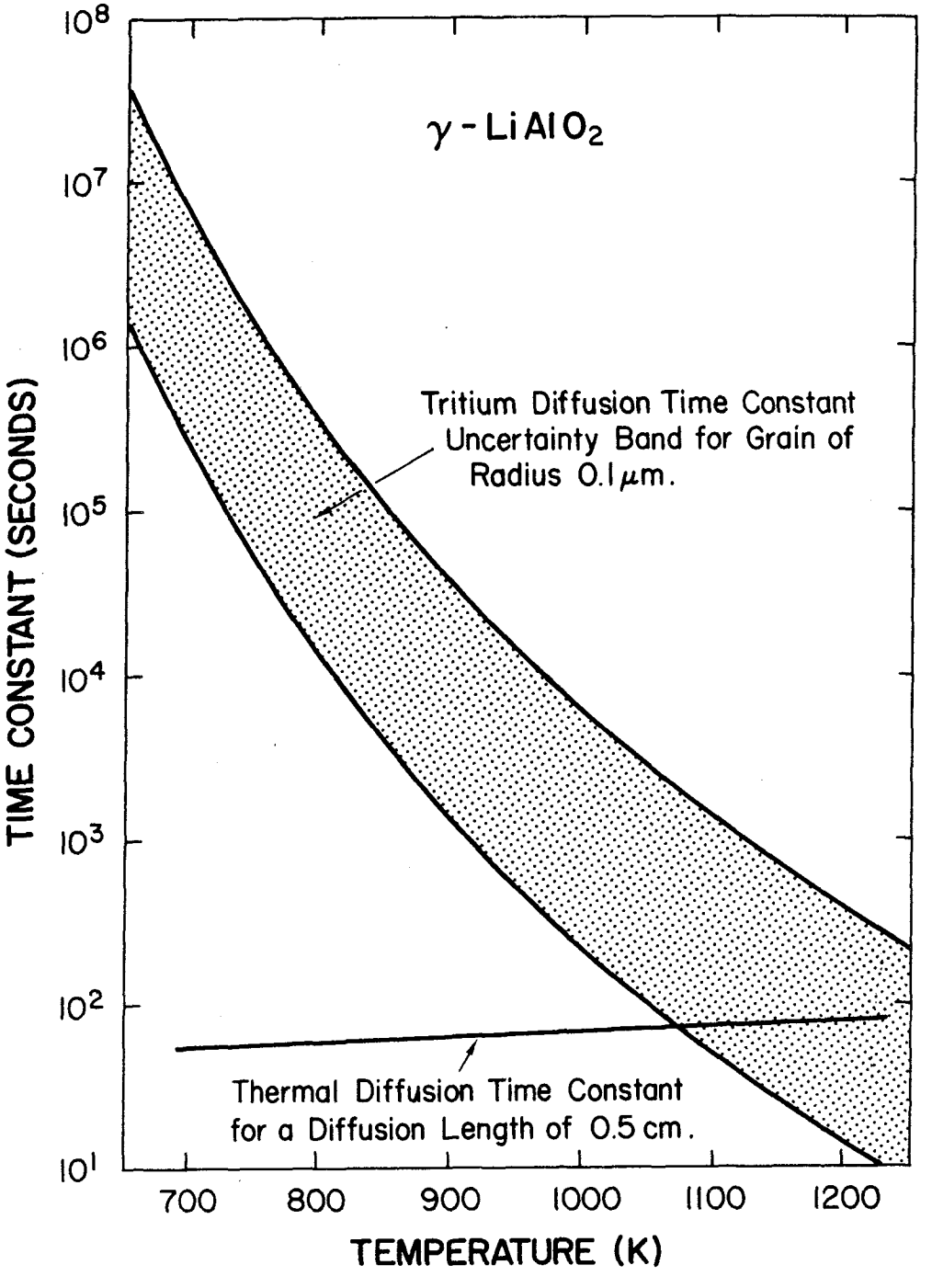


Figure 1.3-2 Tritium and thermal diffusion time constants as a function of temperature (γ-$LiAlO_2$)

The tritium model is one-dimensional in the tritium transport pathway. Three separate zones are included: the grain interior, the grain boundary, and the interconnected porosity. Distance from the grain center is measured in non-dimensional units, where 0-1 is the grain, 1-2 is the grain boundary, and 2-3 is the interconnected porosity. Figure 1.3-3 shows the diffusive tritium concentration as a function of time in the three zones. The tritium generation rate is pulsed in accordance with the plasma burn scenario, with 200-second burn time, 50-second dwell time, and 12-second ramp times (during which the generation rate is assumed to increase or decrease linearly). The sharp increase of diffusive inventory during the initial part of the burn is due to the tritium production suddenly increasing while the temperature and, hence, the tritium diffusivity and solubility, remain relatively low. After the breeder heats up, the diffusive inventory quickly drops back down.

Figure 1.3-4 shows the tritium release rate from one grain to the purge flow (at an effective non-dimensional radius of 3.0) as a function of time from a location at the center of the breeder plate in the radial position nearest the plasma. The release rate is proportional to the gradient of the concentration (Figure 1.3-3) at the purge stream boundary. The tritium generation rate in the grain is also shown in the figure and illustrates the burn, dwell and ramp times considered for each cycle. The release rate takes about three cycles to reach its short-term maximum value. The tritium release rate per cycle is not equal to the tritium generation rate in the grain per cycle for the time period shown because of the long surface adsorption response time. It is likely that at times of the order of the surface adsorption response time (1-10 hours), the surface adsorption process will reach some type of quasi-steady state. The tritium released per cycle will then approach the tritium generated per cycle.

The release rate shows two peaks per cycle. This is an interesting behavior observed for the 100-second solubility time assumed in the calculations. The release rate increases initially as the generation rate increases, then the release rate begins to decrease due to dissolution. When the dissolution mechanism saturates, the release rate starts to increase again. Finally, during the ramp down and dwell times, the release rate decreases.

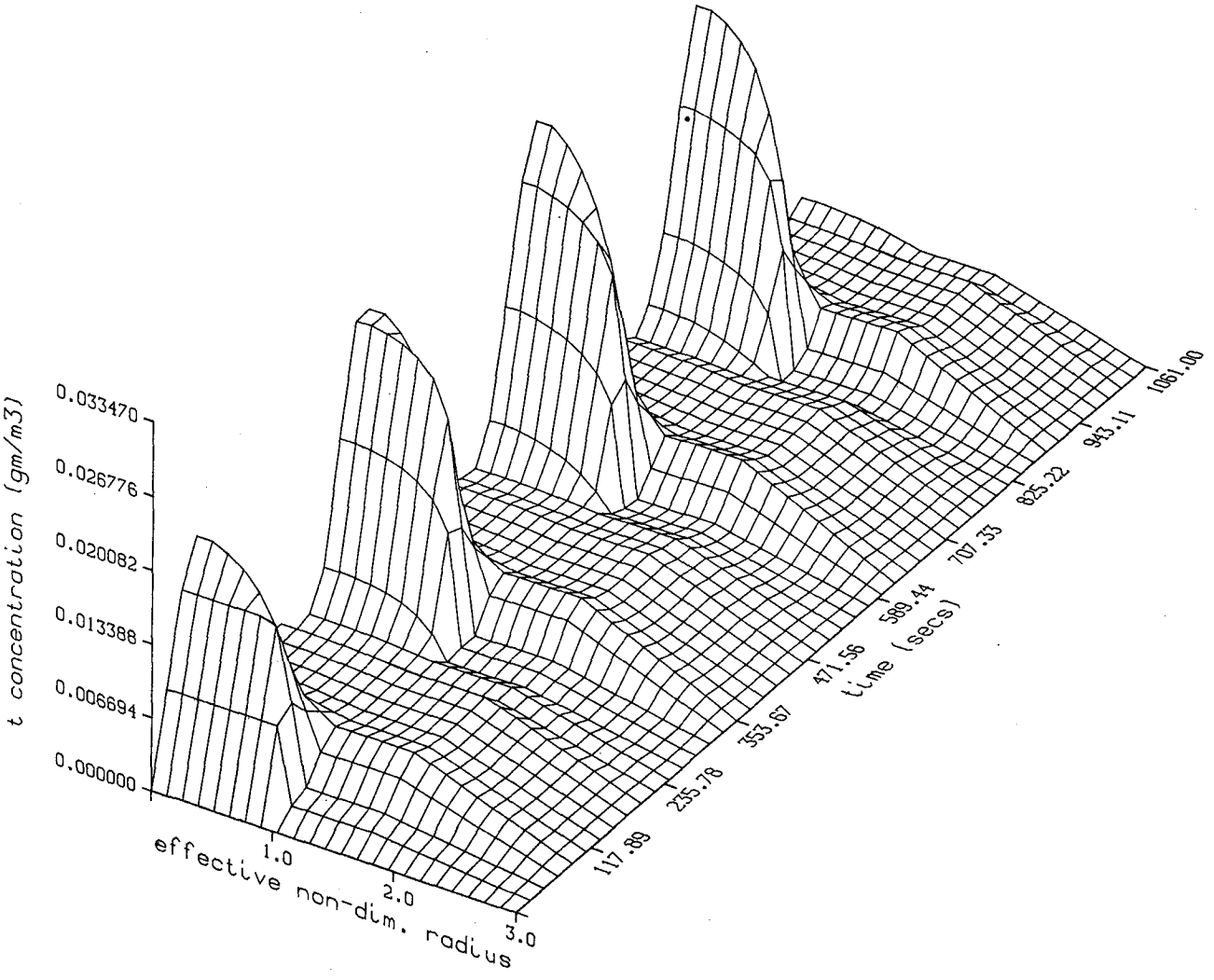


Figure 1.3-3 $LiAlO_2$ diffusive tritium concentration profiles with 200-s burn, 50-s dwell, and 12-s ramp times (microscopic calculation)

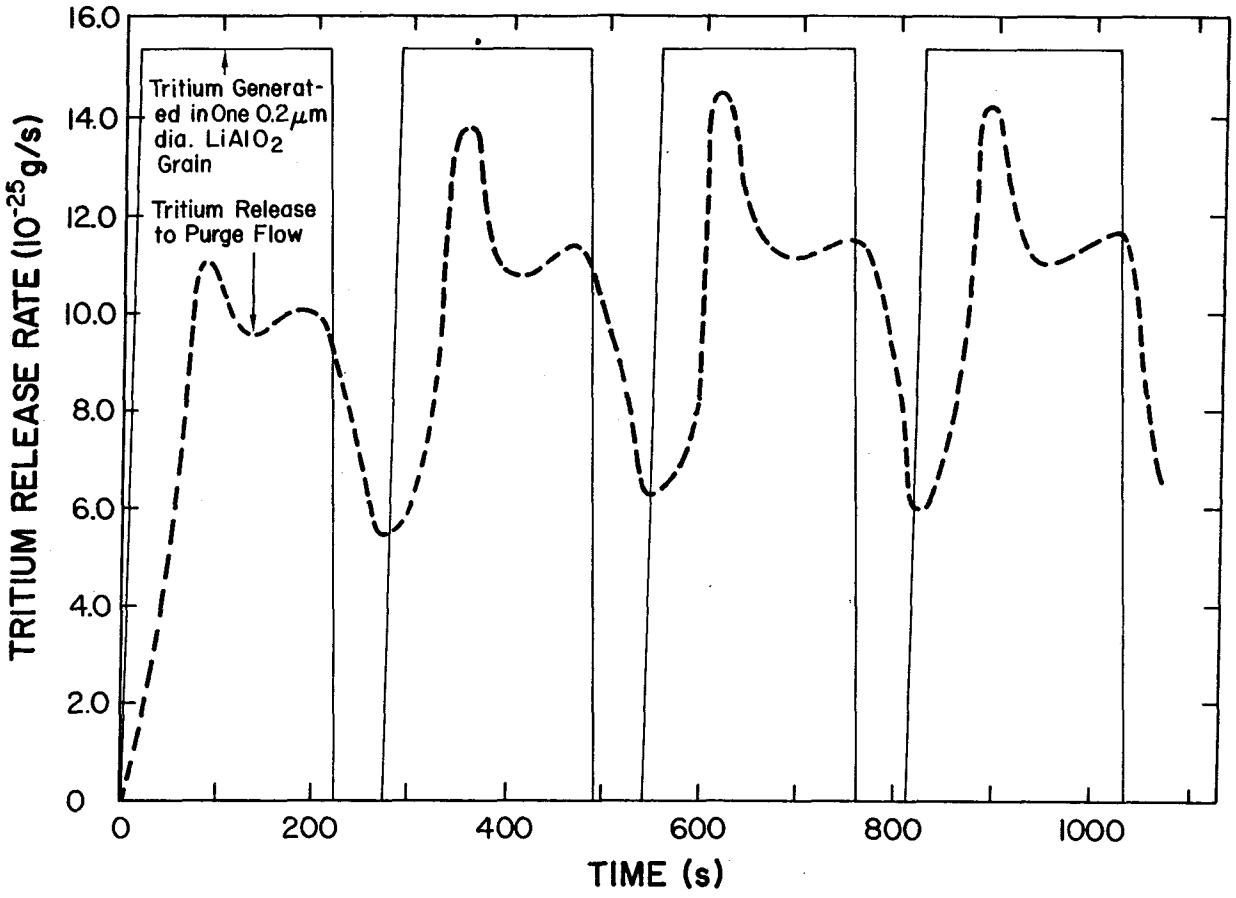


Figure 1.3-4 Transient tritium release rate from 0.2 μm grain $LiAlO_2$ (for 200 s burn, 50 s dwell, and 12 s ramp times)

Figures 1.3-3 and 1.3-4 show the large effect that pulsing has on tritium concentration profiles and release rates. This behavior is markedly different from that for steady-state operation. Experimental results with such short pulses may be difficult to interpret and extrapolate to reactor conditions.

The calculation above was performed at the front of the blanket where temperatures are the highest and diffusion is the fastest. The lower temperatures at the rear of the blanket lead to substantially longer time constants, which provide requirements on the total operating time as long as days, or even months. For example, Figure 1.3-5 shows the results of a calculation of the total, integrated blanket tritium release rate and inventory based on diffusion in a $LiAlO_2$ water-cooled blanket. The release rate is relatively fast, provided the level of approximation to the equilibibrium rate is not

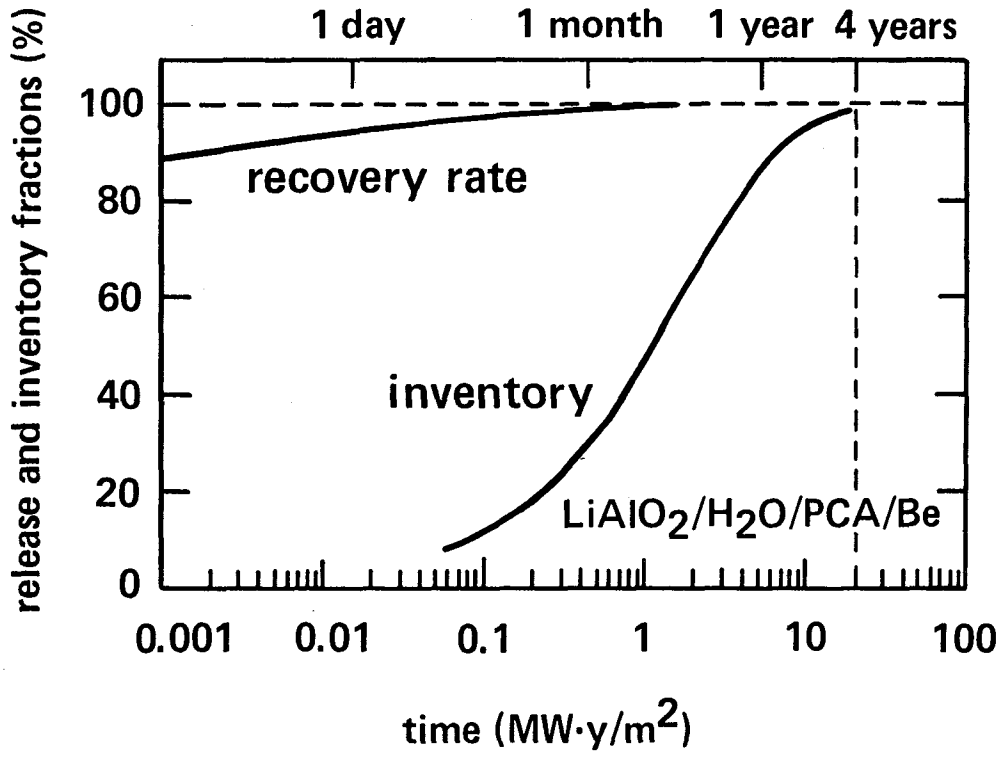


Figure 1.3-5 Time-dependence of tritium recovery and inventory in $LiAlO_2/H_2O/Be$ blanket [reprinted from FINESSE Interim Report[1]]

required to be too high. On the other hand, primarily due to the colder rear part of the blanket, the total inventory can take many months to reach an equilibrium. Important safety and fuel self-sufficiency issues will be difficult to assess without long total test times.

Analysis of the time-dependent thermal behavior of liquid breeder blankets was also performed. The importance of the velocity profiles in determining the magnitude of the steady state heat transfer coefficient has been clearly demonstrated in previous studies.[1,29] Here we have observed that the velocity profiles also play a major role in determining the time constant for temperature responses. Figure 1.3-6 shows the wall temperature in a cooling channel several meters from the entrance. The first wall is subjected to a constant uniform heat flux of 0.5 MW/m^2 and no volumetric heating. Slug, parabolic, and skewed velocity profiles were assumed. The shape of the skewed profile is also shown in Figure 1.3-6. While the time to reach equilibrium for slug and parabolic profiles is roughly 10-20 seconds, the time for a skewed profile can be 100 s or longer.

1.3.1.4 Device Geometry and Test Volume Requirements

Testing of blanket components is assumed to occur at various test locations in the test device. Since the fusion engineering test facility will be the first accurate simulation of all reactor environmental conditions, a wide array of test types will be desired. Some of these tests will be oriented towards verification of overall component behavior, and some will focus on specific issues or elements of the design which can provide substantial information on the effects of the fusion environment. A proposed matrix of tests is provided in Table 1.3-6, including five categories of increasing size and complexity: specimen, element, submodule, module and sector. The table characterizes the types of tests which are considered in each category and the approximate space requirements. Overall space requirements can be computed from this table if the use of parallel and sequential testing is properly considered. The total test surface area given earlier in Table 1.3-1 does not include the "sector" testing indicated in Table 1.3-6. Cost/benefit analysis needs to be performed prior to a decision on "sector" testing.

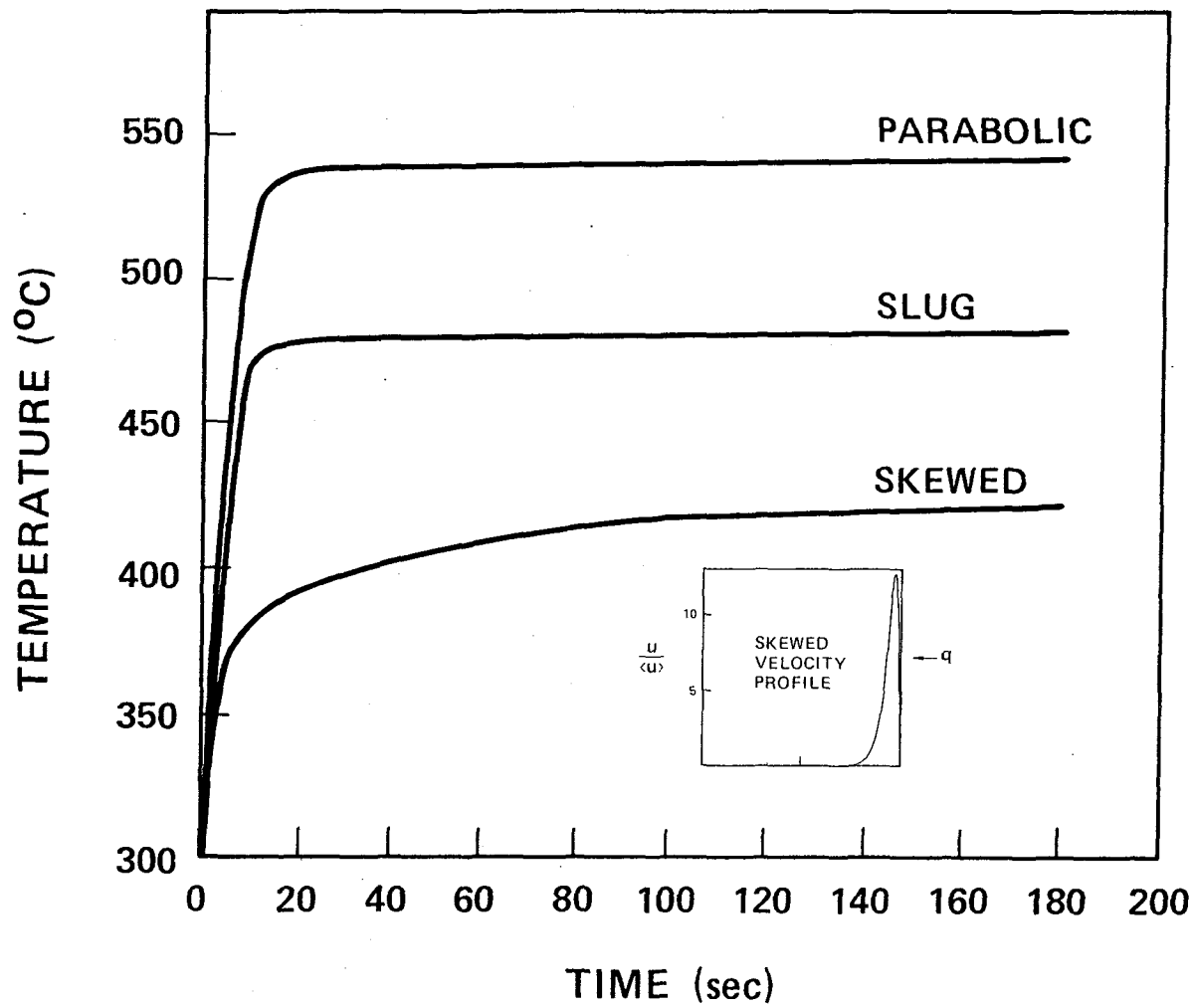


Figure 1.3-6 Transient first wall temperatures of a liquid metal blanket cooling channel at 5 m from the inlet for different velocity profiles

Table 1.3-6 Examples of Number and Size of Test Articles Required for Fusion Nuclear Technology Testing

Tests	Typical Test Article Size (cm x cm x cm)	Number of Test Articles[a]
Specimen		
Structural material irradiated properties	1 x 1 x 2	30,000
Solid breeder and multiplier irradiated properties	1 x 1 x 2	1,200
Plasma interactive materials irradiated properties	1 x 1 x 5	900
Radiation damage indicator cross-sections	1 x 1 x 0.5	500
Long-lived isotope activation cross-sections	1 x 1 x 0.1	200
Element		
Structure thermomechanical response	10 x 10 x 10	50
Effects of bulk heating on heat transfer	10 x 10 x 100	5
Various element tests for solid breeder blankets	10 x 10 x 5	50
Weld behavior	10 x 10 x 5	50
Optical component radiation effects	2 x 2 x 2	20
Instrumentation transducer lifetime	1 x 1 x 2	70
Insulator/substrate seal integrity	1 x 1 x 2	20
Submodule		
Unit cell thermal and corrosion behavior	LB[b]: 100 x 50 x 30 SB[b]: 10 x 50 x 30	5 5
Submodule mechanical responses Tritium behavior (e.g., permeation in coolant, response to thermal and flow transients)	10 x 50 x 10	3
Module		
Verification of neutronic predictions - Tritium breeding, nuclear heating during operation, and induced activation	50 x 50 x 100	4
Full module verification - Thermal and corrosion - Module thermomechanical lifetime - Tritium recovery	LB[c]: 100 x 100 x 50 SB: 100 x 100 x 50	5 5
Shield effectiveness in complex geometries	50 x 50 x 100	50
Biological dose rate profile verification	DT device	1
Afterheat profile verification	DT device	1
Sector		
Blanket performance and lifetime verification	LB: 900 x 300 x 80 SB: 300 x 100 x 80	3 3
Radiation effects on electronic components	1 x 1 x 1	20
Instrumentation performance and lifetime	5 x 5 x 5	100

[a]Test article defined as one physical entity tested at one set of conditions. Duplication of tests for statistical purposes, off-normal conditions, data at several time intervals, for high fluence tests, etc., are not included in the number of test articles.

[b]LB = liquid breeder blankets, SB = solid breeder blankets.

[c]Some designs require larger test volume.

Besides space requirements, geometry can significantly impact the conditions in the test module. Important characteristics of the test locations and their relationship to the device include:

1. the shape, volume, and surface area exposed to the plasma;
2. the position of test parts relative to the device (e.g., inboard vs. outboard, proximity of other components); and
3. the overall geometry of the device, including the plasma, magnetic field, and structure geometry.

These factors are grouped into the category of geometric test requirements.

In addition to determining test requirements, changes in the test module geometry can be intentionally utilized as a primary factor in engineering scaling. Engineering scaling in the test module can allow certain phenomena to be recovered if reduction in one of the device parameters results in an unacceptable loss of information.

Geometry influences most phenomena to some extent, but is a primary factor for neutronic, structural, and liquid metal MHD issues.

Geometric Effects on Neutronics Responses

In a test device, it is desirable to maintain similar profiles of nuclear heating, tritium production, and radiation damage parameters in order to test the thermal and mechanical performance. The extent to which the profiles match the reference reactor defines the quality of the simulation. Tests to verify neutronics behavior are a special class, since the accuracy required in the measurements is much greater. Tritium production provides the most stringent requirements, because the required accuracy in predicting tritium self-sufficiency has been shown to be very high.[13]

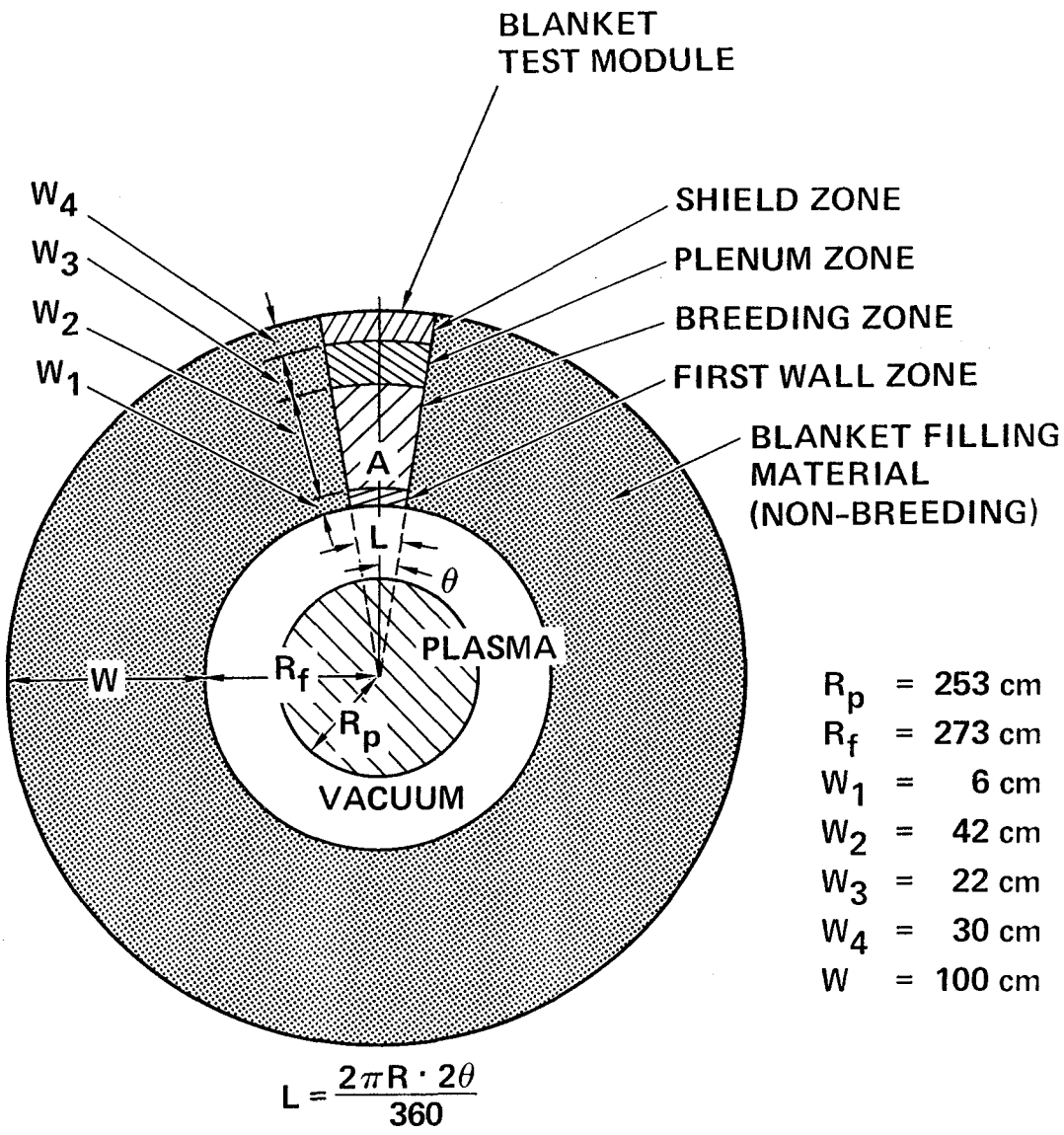
Extensive calculations were performed in previous FINESSE studies[1] to determine the effects of test module size, device size, plasma distribution, and test port geometry on the neutronics behavior of the blanket. The calculations were based on analysis of the helium-cooled Li_2O/HT9 plate-type breeder and the self-cooled lithium/vanadium-alloy designs; however, the results are expected to be generally applicable to other designs. The presence of a neutron multiplier or ^6Li enrichment will cause the most significant differences, since the contribution of low energy neutrons is greater in these cases.

Some of the largest effects occur due to altered boundary conditions, which result from factors such as partial coverage or non-prototypical reflector conditions. Changes in the volumetric tritium production rate due to partial coverage were explored using a two-dimensional neutron transport calculation.[30] Figure 1.3-7 shows the geometrical arrangement assumed for the test module. The reference reactor case has full coverage in the poloidal angle, whereas the test module occupies an angle of 2θ. The remainder is filled with a reflective filling material (stainless steel). Figure 1.3-8 indicates that both the absolute values and the spatial profiles of tritium production are strongly influenced. The relative contributions of ^{6}Li and ^{7}Li are also affected.

Altering the absolute value of the tritium production rate adds significant uncertainty to the demonstration of tritium self-sufficiency. Altering the spatial gradients adds to this uncertainty, and also restricts the ability to perform accurate neutronic measurements.

Calculations of the effect of varying the device size and test module dimensions (including width, radial depth, and first wall thickness) indicate that the neutronic parameters in the test module usually can be maintained within 20-30% of reactor values, provided the boundary conditions are suitably maintained. The impact of scaling can be roughly judged from a knowledge of the neutron mean free paths in the blanket materials. The mean free path is roughly 5 cm in structural materials, 7.5 cm in solid breeder materials, and 15 cm in liquid lithium. If the first wall thickness is increased beyond 2-3 cm or the blanket radial depth is decreased to less than about 20 cm, then the neutronics profiles will be affected significantly (by 25% or more). These conclusions are supported by more detailed calculations.

In conclusion, adequate simulation of neutronics parameters in the test module should be feasible for testing most non-neutronics issues (e.g., thermomechanics and tritium recovery), provided the dimensions are not changed by more than a factor of 2-3 away from the reference reactor values. However, measurements of tritium breeding ratio and some other neutronics parameters require much higher accuracy, and may not be practical without full-size "look-alike" test modules (or full sectors). If modules are used, the surface area at the first wall should be no less than 1 m x 1 m. Further details on neutronics test requirements can be found in Ref. [31].



FIRST WALL ZONE:	PCA, 6.6% DENSE, BALANCE HELIUM
BREEDING ZONE:	6% PCA, 85% Li_2O (DENSITY FACTOR 0.8) BALANCE HELIUM
PLENUM ZONE:	PCA, 10% DENSE, BALANCE HELIUM
SHIELD ZONE:	100% STAINLESS STEEL

Figure 1.3-7 Geometrical arrangement for the test module in a fusion test device (Ref. 30)

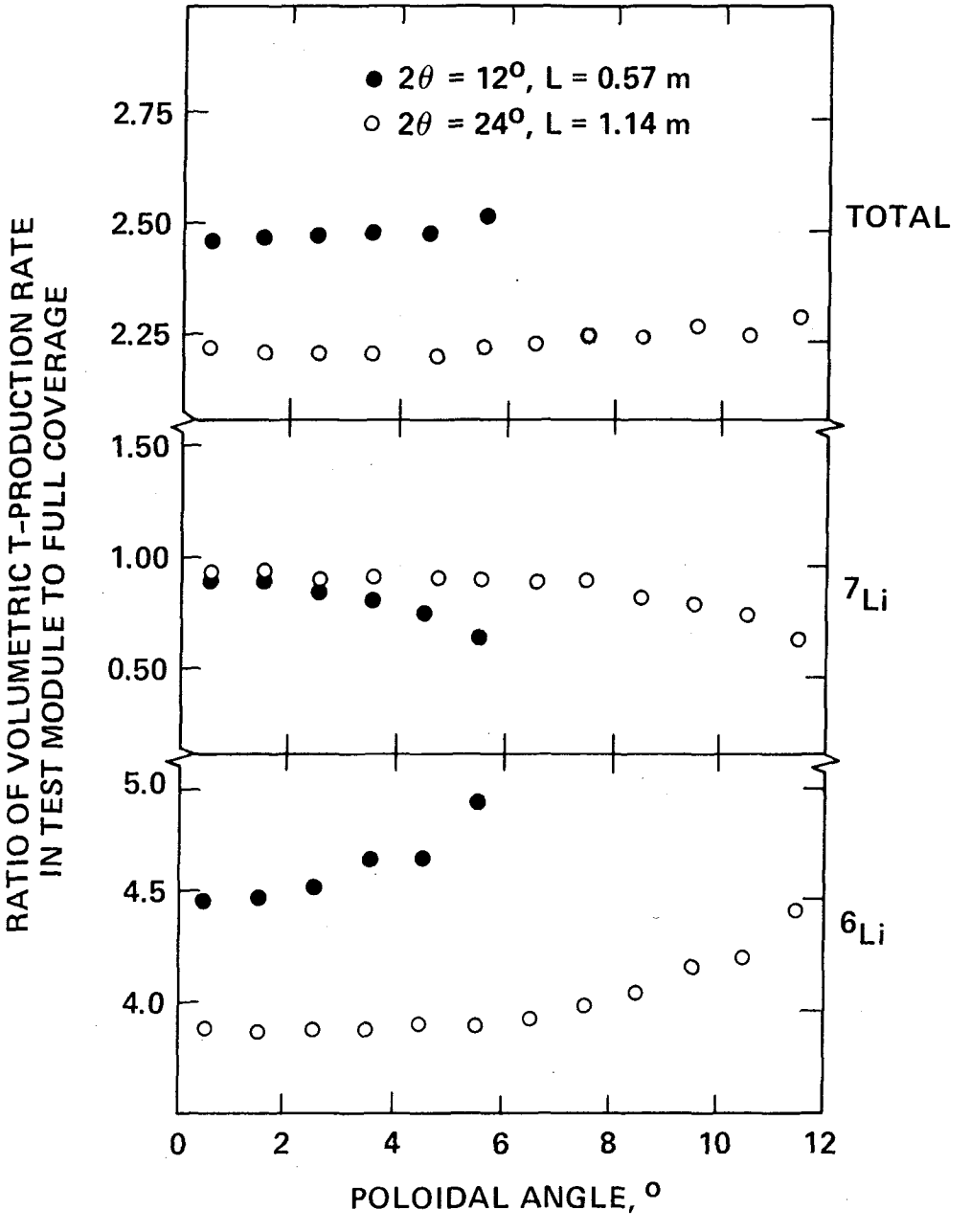


Figure 1.3-8 Variation of the local tritium production rate in the poloidal θ direction for two test module sizes, θ=6° and θ=12° (Ref. 30)

Geometric Effects on Structural Responses

Elastic stresses and strains can usually be preserved even if the test volume is limited, provided aspect ratios are maintained. The same is not true for inelastic strains. For example, structural effects due to radiation damage are difficult to scale because the damage profiles depend primarily on neutron reaction cross sections and kinematics, which are relatively independent of geometry. The impact of altered damage profiles can be very large.

Structural response is so dependent on the loading conditions, that a more important issue is how geometry affects thermal stresses, pressure stresses, and so on.

Aspect ratio scaling is an important option in test module design, but great care must be maintained in order to avoid altering the other phenomena in the test. For example, as discussed below, heat transfer in liquid metal blankets depends more on the channel length than the length-to-diameter ratio.

Geometric Effects on MHD-Related Responses

The uncertainties in liquid metal MHD-related phenomena (discussed in more detail in the next subsection) arise almost entirely due to the complex influence of geometry. The velocity profiles not only depend on the channel dimensions and shape, but also on the wall thickness and the blanket configuration outside the channel. They are also strongly influenced by the details of the magnetic geometry. Because of these dependencies and because it is precisely these interactions which provide the largest uncertainties in blanket behavior, very careful attention must be given to geometric similarity for testing liquid metal blankets.

The test requirements on space can be very severe. The two primary reasons for this are the possibility of long entry lengths for the development of velocity, temperature, and mass concentration profiles, and the possibility of global (interchannel) eddy currents.

One possible method of scaling to allow testing in smaller modules involves the concept of residence time. For diffusive processes, including heat and mass transfer in laminar flow, profile development depends primarily on the amount of time the fluid is in the channel. Reducing the flow velocity

in proportion to the reduction in channel length will result in approximately the same level of profile development. This is especially important because the heat and mass transfer coefficients are very strong functions of distance along the channel in the entrance region.

Another phenomenon which would require larger test modules is global eddy currents. Global eddy currents can arise when geometric perturbations cause voltage differences between channels. If the structure is electrically continuous (i.e., the channel walls are not insulated), interchannel currents can have a large influence on both velocity profiles and pressure drop. This occurs because the MHD-induced currents are no longer constrained to return through thin channel walls. If aspect ratios are maintained, then global eddy currents may be reproduced in smaller test modules; however, the smaller test modules must contain the relevant geometric details of the larger reference blanket.

Because of the large negative impact of global eddy currents, they should be eliminated in reactor designs. However, testing must confirm this. Even a small amount of interchannel current could have a significant effect.

1.3.1.5 Magnetic Field Requirements

Except for ferromagnetic forces (in ferretic steels) and transient magnetic field effects, the influence of the magnetic field is limited primarily to liquid metal blankets. Many liquid metal blanket phenomena are influenced by the magnetic field through its effects on the fluid dynamics. The interaction of magnetic fields with flowing liquid metals is generally referred to as liquid metal magnetohydrodynamics, or MHD. The most important effects are an increase in the pressure drop across the blanket, leading to high internal pressures and higher pumping power, and changes in heat and mass transfer resulting from fluid mechanics which bears little resemblance to that of ordinary fluid flow.

Both self-cooled and separately cooled liquid metal blankets can be strongly affected by the magnetic field. The liquid metal flow rate in separately-cooled designs is determined primarily by tritium extraction requirements. In LiPb systems, with its extremely low tritium solubility, the required flow rate could be nearly as high as the coolant flow rate in order

to keep tritium permeation within acceptable limits. Even if separately-cooled blankets require very small flow rates, the magnetic field will still significantly alter pumping requirements, material interactions, and heat transfer (especially natural convection).

A small number of nondimensional parameters (defined in Table 1.3-7) are typically used to describe the MHD flow regimes. These include the Hartmann number (Ha), which represents the ratio of magnetic forces to viscous forces; the interaction parameter (N), which represents the ratio of magnetic forces to inertial forces; the magnetic Reynolds number (Re_m), which is the ratio of induced field strength to the applied field strength; and the wall conductance ratio (C), which determines the level of control that the walls exert over the flow conditions. Table 1.3-7 summarizes the important dimensionless parameters and evaluates them for representative reactor conditions using properties for both Li and 17Li-83Pb. In most fusion applications, the Hartmann number and interaction parameter are extremely large (order of 10^3-10^5), indicating that the magnetic field totally dominates the fluid flow characteristics (there are exceptions, such as reversed-field pinches, in which Ha and N are much lower). The magnetic Reynolds number is very small, which means that induced magnetic fields can be neglected, leading to substantial simplifications in modeling. And finally, the wall conductance ratio is small but finite.

Achieving values of these parameters in an experiment identical to those in the reference blanket ensures the experiment will be fully prototypical in MHD flow. Most test reactor designs provide magnetic field strengths very close to the value prescribed in the reference reactor. However, regions of high magnetic field in a fusion test facility, such as the tokamak inboard region, are generally not considered for test modules because of space, cost, and accessibility. Furthermore, the closely related parameters of magnetic field geometry and test module size are of equal or greater importance in determining the fluid flow characteristics, as discussed earlier in the subsection on geometry.

MHD effects are treated here in three parts: MHD velocity profile and pressure drop requirements, MHD heat transfer requirements, and MHD mass transfer requirements.

Table 1.3-7 Definitions and Evaluation of MHD Parameters

Parameter	Definition	Typical Reactor Values	
		Li	17Li-83Pb
Hartmann Number	$Ha = aB\sqrt{\frac{\sigma}{\mu}}$	6.3×10^4	1.6×10^4
Reynolds Number	$Re = av\frac{\rho}{\mu}$	6.6×10^4	3.1×10^5
Interaction Parameter	$N = \frac{aB^2}{v}\frac{\sigma}{\rho}$	6.0×10^4	825
Magnetic Reynolds Number	$Re_m = av\ \mu_o\sigma$	0.19	0.052
Wall Conductance Ratio	$C = \frac{\sigma_w t}{\sigma a}$	0.025	0.090
Property Values: (all units mks)		$\sigma = 3 \times 10^6$ $\mu = 0.38 \times 10^{-3}$ $\rho = 495$	0.83×10^6 1.5×10^{-3} 9200
Reactor Conditions Assumed: (all units mks)	$a = 0.1$ $B = 7$ (at inboard) $v = 0.5$	$\sigma_w = 1.5 \times 10^6$ $t = 0.005$ $\mu_o = 4\pi \times 10^{-7}$	

MHD Velocity Profile and Pressure Drop Requirements

While preserving the exact values of the nondimensional parameters ensures prototypical operation, it may be possible to reduce the device parameters and still adequately test blanket components. The most difficult parameter to maintain is the Hartmann number, which is proportional to both the magnetic field strength and the test module dimension along the field line. While the magnetic field in the test reactor will probably be nearly the same as the reference conditions, the region available for testing on the outboard of a tokamak will most likely have a much lower field than the inboard region (typically a factor of 2). Furthermore, in these testing regions space is likely to be limited. The interaction parameter can be adjusted by varying the bulk flow rate, but this technique is risky, because other phenomena (heat transfer in particular) may be strongly affected.

Operating at reduced parameters may be acceptable if the most important phenomena are adequately simulated. For the pressure drop and velocity profiles (ignoring the secondary effects on heat and mass transfer), the most important requirement is to maintain similar fluid flow characteristics. In this case, the data should be easily extrapolated.

One important regime to maintain is suppression of turbulence. This is discussed below as part of the heat transfer requirements. In addition, different flow regimes can result when the balance of forces changes. For example, it is known that the characteristics of flow around bends turning parallel to the magnetic field depends on the competition of inertial and viscous effects. The requirement to maintain reactor prototypical regimes for this type of geometry is $Re \gg Ha^{1/2}$. More details on MHD flow regimes can be found in Refs. [1] and [2].

A complication arises because the scaling of pressure drop and velocity profile as a function of the nondimensional parameters depends on geometric factors. Geometries have been identified in which fractional powers of the wall conductance or Hartmann number are involved. For example, boundary layers near magnetic field entrance regions might scale like $C^{1/6}$.(32) Inertial terms which are normally neglected can become important if $C < N^{-3/5}$, which is a regime that is entirely possible in future blanket designs.

At the present time, there are many uncertainties in liquid metal MHD. The correct scaling of MHD fluid flow is known only for a small number of simple geometries. In this atmosphere of uncertainty, conservatism is necessary in establishing the test requirements. A magnetic field greater than 1-2 T is clearly needed. However, operation above 5 T in the region where the test modules are located would remove many uncertainties.

MHD Heat Transfer Requirements

Because of its influence on the velocity profiles and suppression of turbulence, the magnetic field is also a dominant factor in determining the thermal and structural characteristics of liquid metal blankets. A determination of the minimum required magnetic field must take account of these effects as well as the basic fluid mechanics.

The fact that the flow is laminarized in a strong magnetic field has a huge effect on heat transfer, leading to a large reduction in the heat transfer coefficient and great increases in the thermal entry length. The transition from turbulent to laminar flow occurs at Hartmann numbers lower than those expected in any test reactor [Ha>Re/500 for magnetic field perpendicular to the flow and Ha>Re/60 for magnetic field parallel to the flow[33]]. Magnetic field strengths greater than about 1 T are required.

Probably more constraining are restrictions due to the changes in heat transfer coefficient that accompany changes in the spatial variation of the velocity profiles. The velocity profiles in MHD flow can usually be separated into the core region and boundary regions for the purpose of analysis and discussion. The flow quantity in the boundary layers (such as Hartmann layers) is negligible in many cases of interest. If the hydrodynamic boundary layer is much thinner than the thermal boundary layer, then the hydrodynamic boundary layer is nearly transparent to heat transfer. The thermal boundary layer thickness depends on location in the blanket. At channel inlet regions, it can be extremely small; at the exit of a channel of length 1-10 m, it may be of the order of centimeters. Velocity boundary layer thicknesses tend to be inversely related to the nondimensional parameters described above. Although the Hartmann number and interaction parameter are usually very large, the layer thickness can be related to a fractional power of the nondimensional parameters. The requirements would then be much more stringent.

In some cases, the flow quantity in the layer is finite. For this type of flow, the effect on heat transfer can be very strong, and better simulation of the nondimensional parameters is required.

It is known that the heat transfer coefficient is altered by bulk heating when the velocity profiles are strongly nonuniform. As above, the requirement on magnetic field depends on the nature of the boundary layers.

In conclusion, the effect of the magnetic field on heat transfer is not simple to describe, but rather depends on the details of the geometry and wall conductivity. In many cases of interest, if the Hartmann number and interaction parameter are larger than 10^3, then the heat transfer coefficient should not be greatly affected by further increases. Cases in which higher field would probably be required include:

1. nonconducting duct,
2. geometric perturbations which lead to fractional scaling in B, and
3. boundary layers with finite flow quantity.

More quantitative definition of the minimum field for heat transfer simulation will require further analysis.

MHD Mass Transfer Requirements

Mass transfer is also affected by the magnetic field through the MHD velocity profiles. In this case, the thickness of mass diffusion boundary layers is much thinner than thermal boundary layers. Therefore, the core flow is relatively unimportant.

The details of the thin MHD velocity layers can affect mass transfer if they are not much thinner than the mass diffusion layer thickness and if mass transfer is determined primarily by convection in the liquid phase. Past studies have shown that for liquid-phase dominated mass transfer there can be an increase of as much as a factor of 5 in corrosion rate if the Hartmann number is increased from about 100 to about 10,000.[1] For Ha>10,000, the effect is largely saturated because the Hartmann layer thickness is smaller than the mass diffusion boundary layer thickness. The corresponding magnetic

field strength depends on the channel dimensions; for a 10-cm channel, this corresponds to a field strength of about 1 T.

This estimate is very preliminary, since data about material interactions is limited, even outside the magnetic field. It is not at all clear that solid phase diffusion and interface reactions can be ignored in determining the corrosion rate. More analysis is clearly needed to determine test requirements due to liquid metal material interactions.

1.3.2 Tritium Supply

Ensuring adequate supply of fuel is an absolute requirement for successful operation of a DT fusion test facility. The amount of tritium needed for the test facility is uncertain because the characteristics of the reactor and its operating scenario are not firmly fixed at this time. The amount of tritium available from external sources is limited. If the requirements for tritium cannot be economically met from external sources, then internal tritium production must be provided by tritium-producing blankets.

Table 1.3-8 summarizes the potential external sources of tritium.[34-37] The most significant civilian source is existing fission reactors. CANDU reactors produce larger amounts of tritium than standard LWR's due to neutron absorption in deuterium in the heavy water moderator and coolant. Present CANDU reactors produce about 0.23 kg/yr of tritium per GWe. Both light-water and heavy-water fission reactors could be modified to produce more tritium by replacing fuel or absorber material with lithium. In CANDU reactors, this enhanced capacity has been estimated at 500 g/yr per GWe (for no change in power production).

Overall, there is a reasonably assured steady supply of 2-2.5 kg/yr from CANDU reactors, and there is a potential for an additional 1 kg/yr from modified power reactors and fuel reprocessing. The availability of tritium from military production reactors is very uncertain.

It is likely that an engineering test facility would operate in separate phases of increasing availability and, therefore, of increasing tritium consumption. During the initial phases of commissioning, plasma optimization, and short-duration engineering performance testing, the total tritium consumed

Table 1.3-8 Potential Tritium Sources[34-37]

Source	Supply Rate (kg/yr)	Inventory (kg 1986)
Atmosphere/oceans		
Cosmic rays	0.2	4
Atmospheric bomb tests	0	145
Unmodified power reactors		
PWR/BWR (1 GWe)	0.002	0.006
CANDU (12 GWe)	2.5	8
Modified power reactors		
PWR/BWR (1 GWe)	0.1	0
CANDU (1 GWe)	0.5	0
Fuel reprocessing plant		
1000 Mg U/yr capacity	0.05-0.1	--
Military production reactors		
US/USSR/UK/France/China	30-40(?)	--

would be small. A calculation for NET estimated 4 kg of tritium total needed to operate during these phases.[38] This amount is probably available from existing sources such as CANDU reactors.

During the high-availability testing phase, the tritium consumption rate at 50% availability and 600 MW fusion power will be 16.8 kg/yr (56 g/MW-yr is the conversion constant). From the evaluation of possible external supplies given above, tritium to sustain a device with such power over long periods of time will be difficult to obtain. There are great incentives to design a test facility with lower fusion power to reduce capital costs, tritium and other operating costs. Fusion nuclear technology testing requires only about 20 MW of fusion power, but plasma physics and engineering considerations for tokamaks require fusion power greater than ~300 MW at reasonable wall loading.

of fusion power, but plasma physics and engineering considerations for tokamaks require fusion power greater than ~300 MW at reasonable wall loading.

Even if tritium could be made available from external sources, the financial burden might be prohibitively high. Using an estimated present cost of tritium of $10,000/g, a consumption rate of 16.8 kg/yr translates into an annual operating cost of $168 million for tritium alone. Producing tritium within the test facility may be a financial necessity.

The operation of tritium-producing blankets as a part of the test facility has been considered in several previous studies.[5,24] There are a number of possible options for "internal" tritium production. For example, the NET team is considering water-cooled LiPb, water-cooled solid breeder, He-cooled solid breeder, and self-cooled liquid breeder blanket options.[38] The INTOR group, in its Phase II report chose water-cooled Li_2O as the primary option.[24] Water-cooled Li_2SiO_3 with Pb multiplier and water-cooled $Li_{17}Pb_{83}$ were chosen as alternates. A recent study explored the use of aqueous lithium salt blankets.[39]

Risk is an important concern in making a decision to implement a tritium-producing blanket in a test facility, and also in the choice of a specific blanket option. If a tritium-producing blanket must be implemented, several measures can be taken to reduce the risk. First, one can select the design which appears most feasible using existing technology to the maximum extent possible, and operate with temperatures and pressures as low as practical. It should be noted, however, that the fusion environment will be "new" to any type of blanket selected. Provisions must be made to cope with unanticipated problems or changes in behavior. In addition, a key problem with this type of blanket is that the information obtained through its operation will probably not provide the maximum benefit for extrapolation to commercial reactor blanket designs. Second, an aggressive pre-fusion test program must be implemented to eliminate as many potential failure modes as possible. Without fusion testing, it is difficult, if not impossible, to fully qualify a tritium-producing blanket of any design.

In this study, a clear distinction is made between the functions of a test blanket (or "blanket test module") and a tritium-producing blanket. The two functions may be performed in a single component; however, the objectives of maximizing device availability and maximizing testing benefit may dictate

separate components. In general, it is clear that many design options exist and there are no clearly superior choices. Much more effort and analysis are required in this area.

1.3.3 Blanket Reliability and Device Availability

If tritium-producing blankets are used in ETR, then blanket components will require a program of pre-operational testing and development. Depending on the desired tritium breeding ratio, and hence the total number of breeding modules employed, the test time needed to confidently provide an acceptable impact on overall device availability may be very long (>10 years).

The required pre-operational testing of blanket modules has been evaluated by performing parametric studies in three areas:

1. Calculation of the minimum mean time between failure (MTBF) required to achieve a given availability goal for the blanket system.
2. Calculation of the amount of pre-operational testing required to provide a given amount of confidence in meeting the MTBF requirement.
3. Determination of the effect of parallel testing on the time required to reach a given level of confidence in the MTBF.

There is a trade-off between the amount of pre-testing of tritium breeding blanket modules (required to achieve some overall blanket availability goal) and the need for externally supplied tritium. If a smaller tritium breeding ratio is acceptable (and, therefore, a smaller number of breeding modules are employed), then the testing needed to obtain a given level of confidence in the overall blanket availability is reduced. At the same time, the presence of fewer breeding modules results in a greater need for externally-supplied tritium. Analysis is provided to compare the on-site tritium breeding cost savings and the blanket module testing time requirements.

For the purposes of this study, it is assumed that the ETR operational goal is an availability of 50% and that this requires a tritium breeding blanket availability goal of at least 80%. These and other assumptions are summarized in Table 1.3-9. Operation with fewer than the full number of breeding modules is assumed to reduce the tritium breeding capability of the machine linearly.

Figure 1.3-9 shows the three standard periods during component life. "Burn-in" and "wear-out" failures are not considered here. It has been assumed that pre-operational testing has been successful in eliminating design and fabrication problems which can result in early failures. The analytic model used in this analysis pertains to the useful life period and assumes that module failure occurs due to the randomly-occurring event, a process which can be described by an exponential distribution of failure times.

If the availability for an individual blanket module is given by a_m and there are n identical blanket modules, then the overall blanket system availability is:

$$A_b = a_m^n$$

where a_m is the "availability" per module and is a function of the MTBF and the mean time to repair (MTTR):

$$a_m = MTBF/(MTBF+MTTR)$$

Table 1.3-9 Representative ETR Parameters Considered in the Reliability Analysis

Fusion Power	300 MW
ETR Availability Goal	0.5
Blanket Availability Goal	0.8
Number of Blanket Sectors	12
Number of Modules per Sector	5
Total Number of Modules	60
Number of Test Modules	2 minimum[a]
Full Coverage TBR	1.05
Tritium Consumption Rate	8.4 kg/FPY
Tritium Cost	$84 M/FPY

[a]Two test modules are provided even for the "full coverage" case, resulting in a TBR of 1.05 with 58 tritium breeding modules. The number of test modules can be increased for lower coverage cases.

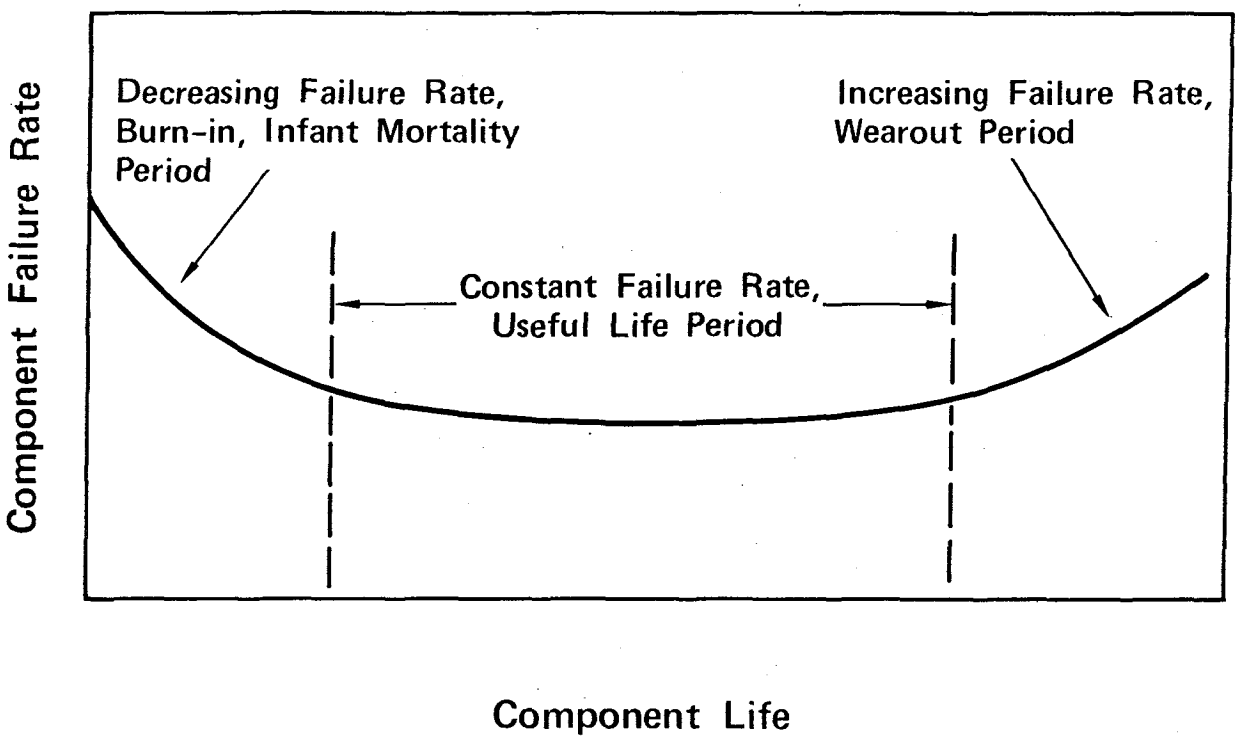


Figure 1.3-9 Failure rate over component life

If the MTTR, A_b, and n are specified, then the MTBF for a blanket module can be calculated directly. Figure 1.3-10 shows the MTBF for tritium breeding modules (at various values of MTTR) required to achieve an overall blanket availability of 0.8 as a function of the number of breeding modules and the breeding ratio.

If blanket module testing is viewed as a series of time-terminated trials, then the occurence of module failures can be described as a Poisson process. A detailed derivation of the failure rate confidence level versus the expected failure rate, total testing time, and test failure occurences is given in Chapter 3. Using Poisson statistics, Figure 1.3-11 shows the minimum test time to achieve a given confidence level in the availability goal. This test time increases with the number of tritium-breeding modules because the required MTBF per module increases. For all these cases, the MTTR was fixed at 336 hours and the number of test failures was assumed to be zero. The confidence in a given MTBF is actually degraded by test failures, making this a best-case estimate.

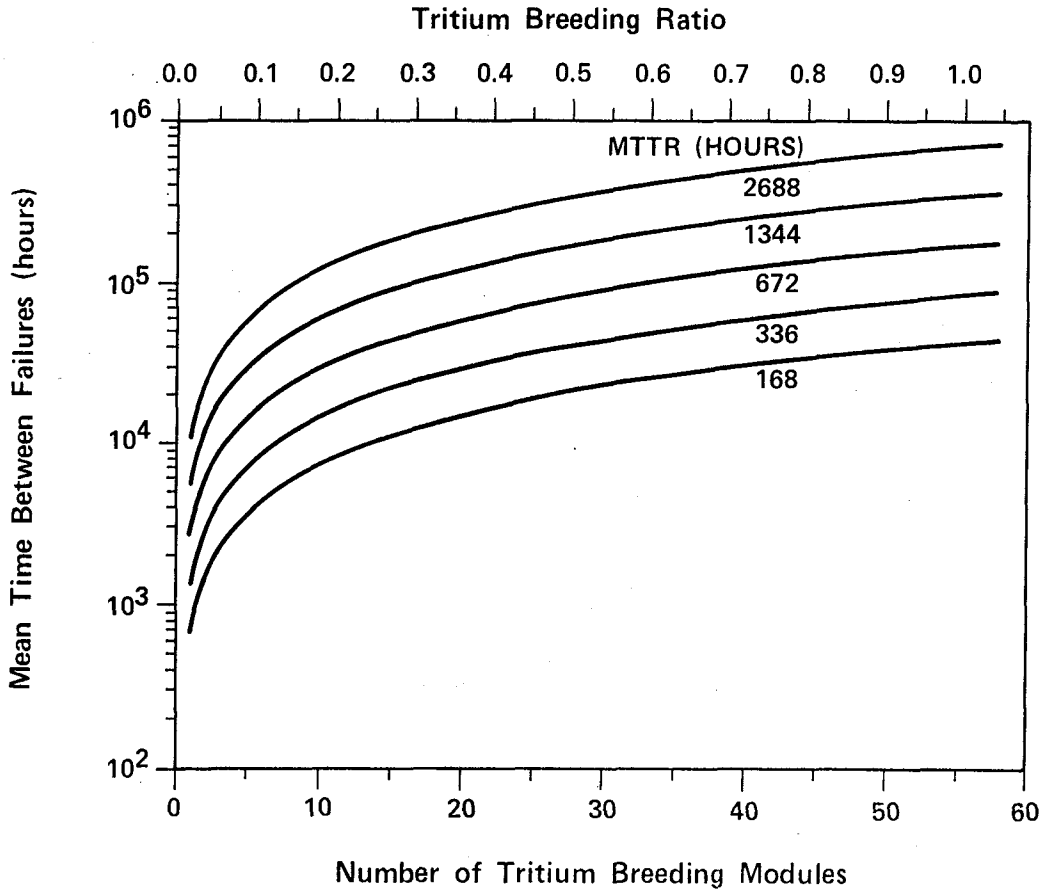


Figure 1.3-10 The tritium breeding module MTBF (at various values of MTTR) necessary to achieve a blanket availability goal of 0.8 as a function of the number of tritium breeding modules (and tritium breeding ratio)

Also shown in Figure 1.3-11 is the cost of tritium required from external sources if the number of breeding modules is less than 58. (A full-coverage TBR of 1.05 is achieved with two test modules and 58 tritium breeding modules.) As stated above, the amount of make-up tritium is assumed to be linearly related to the number of breeding modules.

In conclusion, for a facility with 300 MW of fusion power and an availability goal of 50% (a tritium-producing blanket availability goal of 80%), the required MTBF may be 90,000 hours or more, depending on the module replacement time. High confidence (90%) in this level of performance will require testing times of at least several times the MTBF. Parallel testing can significantly reduce the actual calandar time for testing, although more elaborate testing programs will be more expensive.

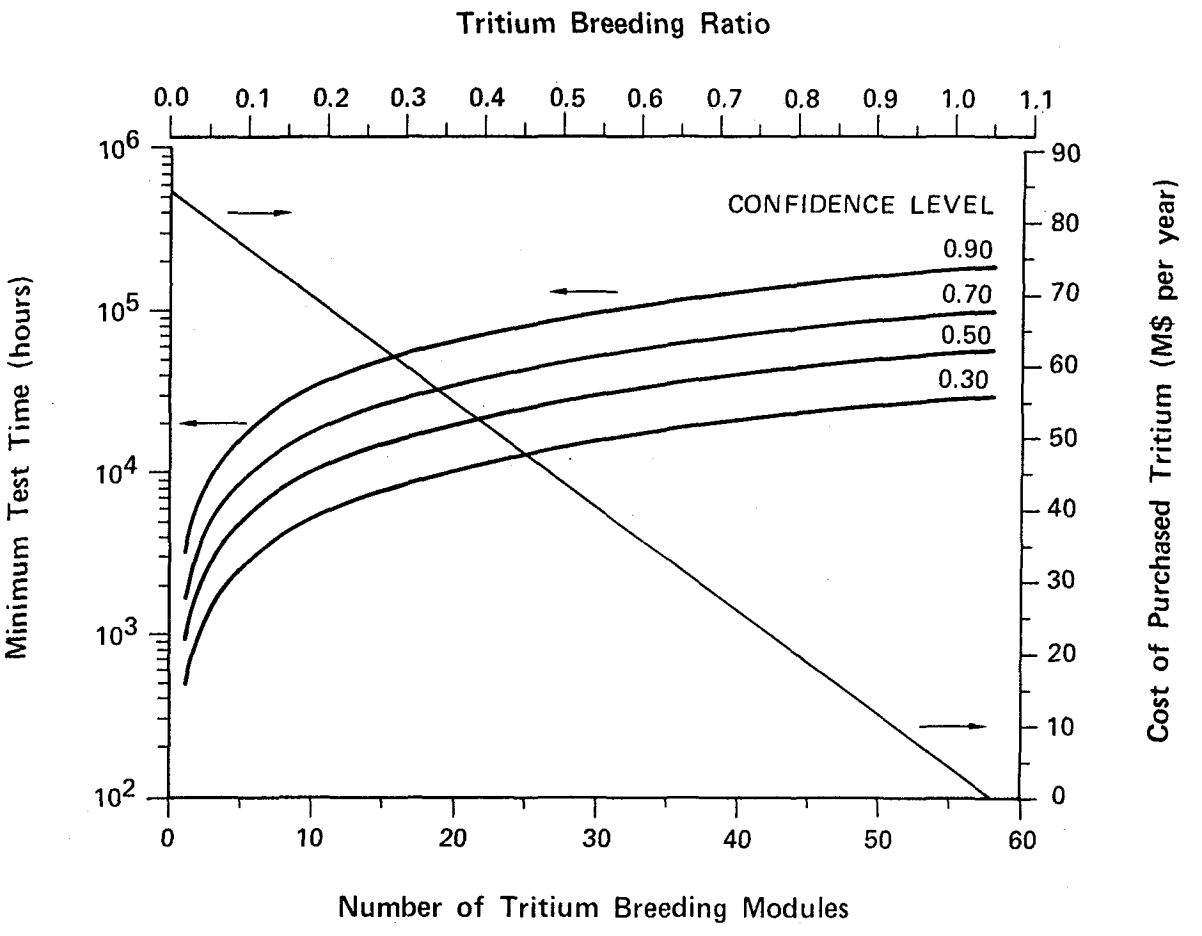


Figure 1.3-11 Minimum required testing time (at various confidence levels) to achieve a blanket availability of 0.8 as a function of the number of tritium breeding modules and tritium breeding ratio. Also shown is the cost of external tritium supply as a function of the breeding ratio.

It is quite likely that such lengthy testing times will not be achieved prior to fusion testing. If significant tritium breeding is attempted in ETR without adequate testing, then confidence in the breeding modules, in a statistical sense, will be low. This means high risks for the fusion test facility. Such risks should be reduced by an aggressive development program prior to fusion testing. However, tradeoffs among increased costs and risks for the fusion facility must be carefully weighed in plans for a fusion engineering test facility.

1.4 Theory and Modeling

1.4.1 Introduction

A fundamental objective of the R&D plan for fusion nuclear technology is the development of predictive capabilities, which are necessary to design, construct, and operate fusion nuclear components. This requires a highly interactive program of theory, modeling, and experiments. In the early stages of R&D, theory and models are used to anticipate scientific and engineering phenomena, to define performance parameter ranges of interest, and to characterize uncertainties. Thus, theory and modeling are necessary in planning and designing experiments to maximize their benefits. Results from experiments are then used to verify analytical and numerical models.

The coupling between experiments and modeling efforts in fusion nuclear technology is shown more clearly in Figure 1.4-1, developed previously in FINESSE. Whereas the ultimate goal of the experimental program is fusion integrated testing, the ultimate goal of the modeling program is an integrated set of design codes for overall predictions of the performance of fusion nuclear components. This design code may consist of a combination of analytical, numerical, and empirical parts.

The major components of interest in fusion nuclear technology are the blanket, tritium and vacuum systems, plasma-interactive components, and radiation shielding. The present level of understanding and available methods to model each of these components vary considerably. In the liquid metal blanket, for example, the interaction between the magnetic field (necessary for plasma confinement) and the flow of the liquid metal coolant can be represented by Navier-Stokes and Maxwell's equations. Although these equations are well defined, they are extremely difficult to solve fully because of the nonlinearity and the three-dimensional nature of the problem. Modeling of tritium transport systems in solid breeder blankets, on the other hand, is complicated due to the lack of understanding of the microscopic transport processes in the fusion environment.

The blanket has received the largest amount of attention, particularly liquid metal blankets. The emphasis on modeling liquid metal blankets has been motivated by two reasons: 1) the present ability to predict blanket thermomechanics, particularly MHD effects, is very limited; and 2) the

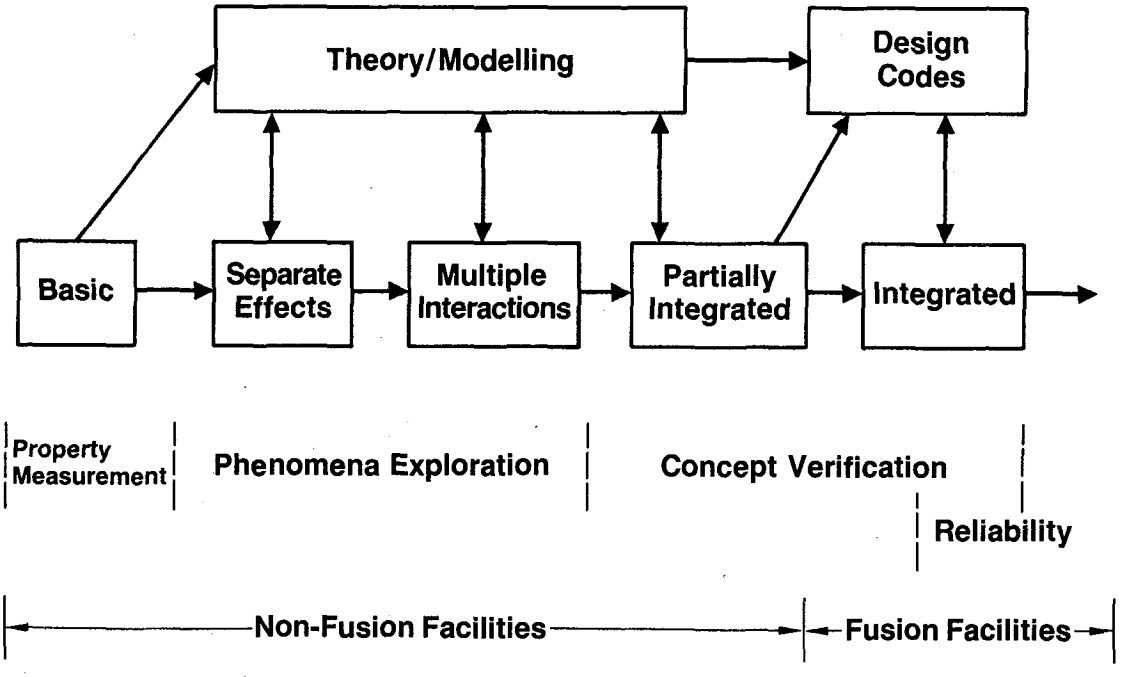


Figure 1.4-1 Types and role of experiments and facilities for fusion nuclear technology [reprint from Phase I FINESSE report(2)]

potential for advancement in predictive capabilities and the planning of effective experiments through theory and model development is great.

Three areas of MHD modeling have been studied in this work. First, an analytical method using a perturbation technique is used for developed MHD flows in simple geometries. Second, numerical analysis for a variety of simple MHD fluid flow and heat transfer problems in two-dimensional geometries is described. Both the finite element method for fully developed MHD flows and the finite difference method for developing MHD flows are considered. Third, approximate solutions to the MHD pressure drop is studied at the entrance and exit regions of a magnetic field.

Studies of heat and mass transfer in liquid metal blankets were performed. Both theoretical and experimental work was carried out to explore the effects of bulk heating on heat transfer in liquid metal blankets and to define the validity of probe measurements under the conditions of bulk heating. Initial efforts are underway to develop models to predict corrosion and mass

transport in a lithium-HT9 system. Data is being taken in two thermal convection loops to provide empirical data and to test the models.

Work on areas other than liquid metal blankets has also been performed. The development of a preliminary model for predicting tritium transport and inventory in solid breeders is described. Thermomechanical modeling of liquid metal cooling of limiters is discussed, in which thermal hydraulic and structural analysis are included.

1.4.2 Liquid Metal MHD Modeling

Figure 1.4-2 shows a logic diagram for MHD model development that traces the primary elements in the modeling program and their relationships. Three primary modeling tasks are shown: theory and analytical method development, numerical methods, and analysis. The intimate ties with the experiments and the interaction with conceptual design studies are illustrated in the figure. The ultimate aim of the MHD modeling effort is a design code for liquid metal blankets. However, to achieve that goal, different stages of development will be encountered where modeling of simpler geometries will be performed in the early stages to validate and guide the improvement of the models.

Modeling of any physical phenomenon starts with a set of equations which describe the physics of the process. In MHD flows, the equations which describe the interaction of a flowing conducting fluid with the magnetic field are Navier-Stokes and Maxwell's equations. To make the problem amenable to analysis, a set of simplifying assumptions, an efficient method of solution, and a set of initial and boundary conditions are needed.

Various solution methods exist, depending on the complexity of the problem. Analytical methods seek a closed form solution, in which approximations and simplifications (in both geometry and physical conditions) are needed to make the solution tractable. Analytic solutions are restricted to relatively simple, idealized geometries, and the results may not be fully applicable in realistic situations. MHD problems in actual blanket geometries are usually too complex for analytic treatment. Therefore, while the physical laws which govern the MHD process are known, it is impossible, by relying solely on classical mathematics, to provide predictions of its behavior which have general engineering merit.

Approximate analytical solutions to simplified sets of the MHD equations for flows at high Hartmann numbers and interaction parameters can be found in the work of Hunt,[40] Walker, et al.,[41] Walker and Ludford,[42] Petrykowski and Walker,[43] and many others. Asymptotic techniques to analyze large interaction parameter flows are employed. A separate solution is obtained for the inviscid core region, which is matched to the boundary layer solution. These methods, however, are approximate and have serious limitations. In real reactor blankets, pipings and ducts may have complicated geometry which can

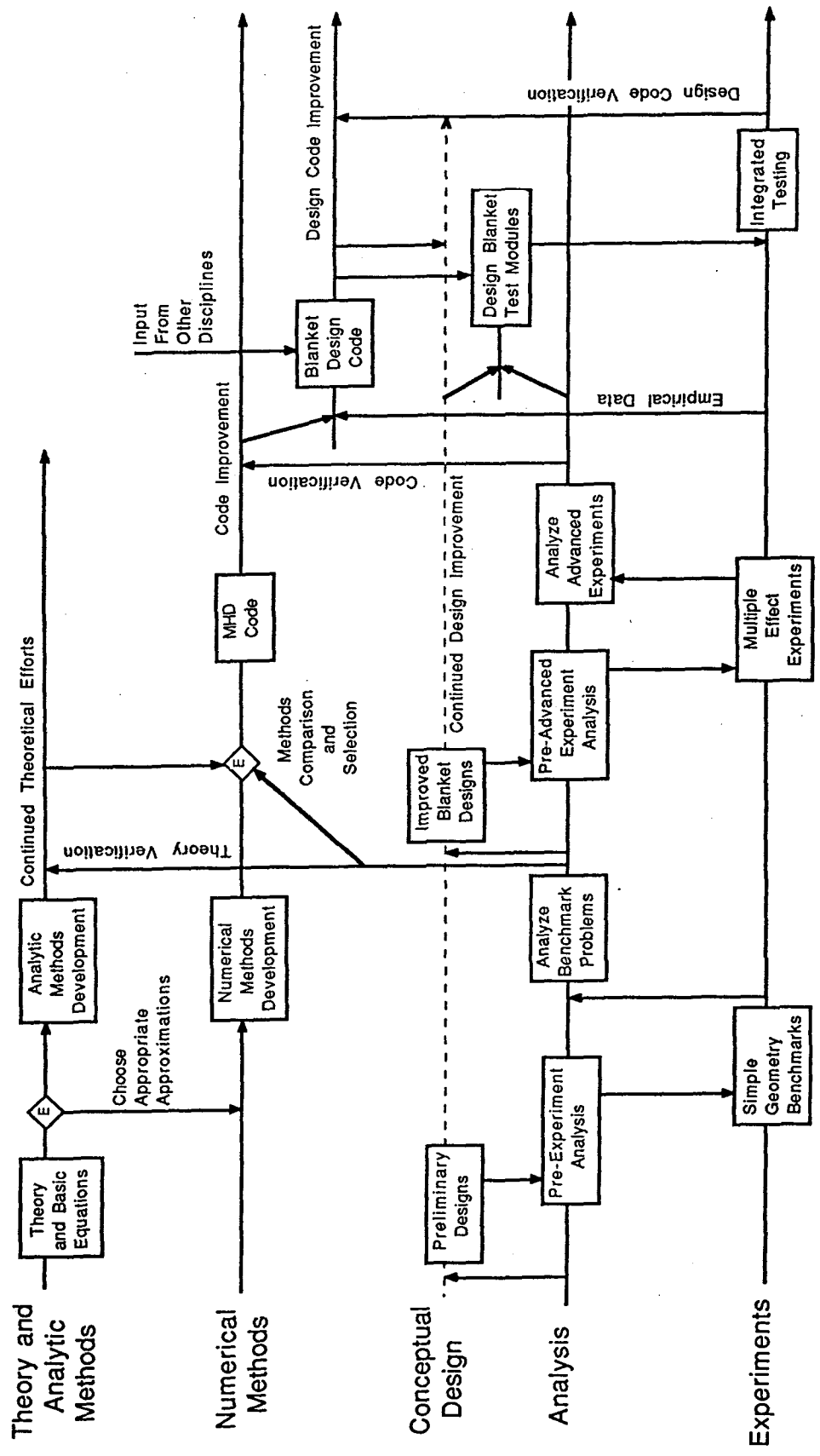


Figure 1.4-2 Liquid metal MHD modeling logic

give rise to large velocity gradients where inertial forces can be large and comparable with the electromagnetic ones. While viscous boundary layers are usually small, geometric effects can increase their size and importance. The flow is then developing and it is important to be able to analyze these effects.

By using and modifying existing methods in computational fluid dynamics (CFD) to account for the magnetic forces, solutions to practical MHD problems may be obtained. These and other numerical techniques based on infinite Hartmann numbers and interaction parameters (which render the flow inertialess and inviscid) offer the potential to solve problems in geometries and parameter ranges for which purely analytical solutions are intractable.

MHD problems solved numerically in this work utilized the SIMPLE[44] method to predict the flow development of a conducting fluid in simple two-dimensional geometries in the presence of a magnetic field. The finite element method was also used to solve the fully developed flow in rectangular ducts with a perpendicular field, where a mesh refinement technique was emphasized in the solution procedure to resolve the thin Hartmann layer near the walls.

Numerical problems arise in dealing with high magnetic field flows. These stem from the diminishing effect of inertia and viscosity, and the disparate scale lengths in the core region and boundary layers. For very high magnetic field, magnetic forces are larger than inertial and viscous forces that are used for correcting the pressure in CFD. Modifications to the pressure correction procedure are necessary to account for the electromagnetic forces, and future plans will be aimed in that direction, which might be termed as computational magnetohydrodynamics (CMHD). Improvements in the use of mesh refinement will also contribute to the accuracy of the solution.

These first attempts at numerical solutions to the MHD flow equations were performed primarily to develop and test certain solution techniques. The ultimate development of an MHD code for fusion applications will require years of concentrated effort and much work remains to be done.

1.4.2.1 Computational Magnetohydrodynamics

The calculational procedure solves the equations of motion (Navier-Stokes equation), which describe the flow of a conducting fluid in the presence of a magnetic field. The flow is assumed steady, incompressible and laminar, and two-dimensional duct geometries are considered. The assumption of small magnetic Reynolds number decouples Maxwell's equations from the hydrodynamic ones. In this case, the induced magnetic field is neglected and the magnetic body force is linearly related to the velocity field through Ohm's Law.

The finite difference solution algorithm is based on the SIMPLE (Semi-Implicit Method of Pressure Linked Equations) method,[44] where an iterative process of pressure and velocity guess and correct operation is utilized to drive the residual mass errors to zero or small values. Because the magnetic Reynolds number is small, the magnetic body forces in the hydrodynamic equations can be linearly related to the velocity field through Ohm's Law. The electromagnetic body force thus appears as a source term in the momentum equations. When the electromagnetic forces are very large compared to the viscous or inertial forces, divergence may result.

The general discretized equation of the differential equations can be written as:

$$A_P\phi_P = A_N\phi_N + A_S\phi_S + A_E\phi_E + A_W\phi_W + S_\phi \qquad (1)$$

where ϕ stands for the dependent variable being solved, and A_P, A_N, A_S, A_E and A_W are the coefficients at nodes P, N, S, E and W, which characterize a control volume, and S_ϕ is the source term of the variable ϕ, which can represent external body forces, such as electromagnetic ones.

The problems analyzed numerically include developing flow in ducts with the magnetic field in the plane of the flow aligned with the main flow direction or perpendicular to it. The development of two-dimensional velocity and temperature profiles are explored for a conducting fluid in the entrance region of straight ducts in the presence of a magnetic field. The main effect of a magnetic field aligned with the flow direction is to delay flow development.

In a pipe flow, for example, the development of the centerline velocity along the pipe can be seen in Figure 1.4-3 for a range of values of N/Re, where N is the interaction parameter and Re in the Reynolds number. The centerline velocity (u_c) is normalized with respect to the average velocity across the pipe. The results compare favorably with the analytic solution of D'Arcy and Schmidt.[45] The electrical conductivity of the pipe walls remains arbitrary and has no effect on the dynamics of the flow. As can be seen from the figure, for N/Re=30, the entry length is about 3.5 times that of the non-magnetic case.

In a channel flow, the delay in flow development due to a parallel field can be clearly seen in Figure 1.4-4. The velocity at the entrance is either a slug or a skewed profile and the channel walls are assumed insulated. The channel half-width is (a). The figure shows the development of the velocity

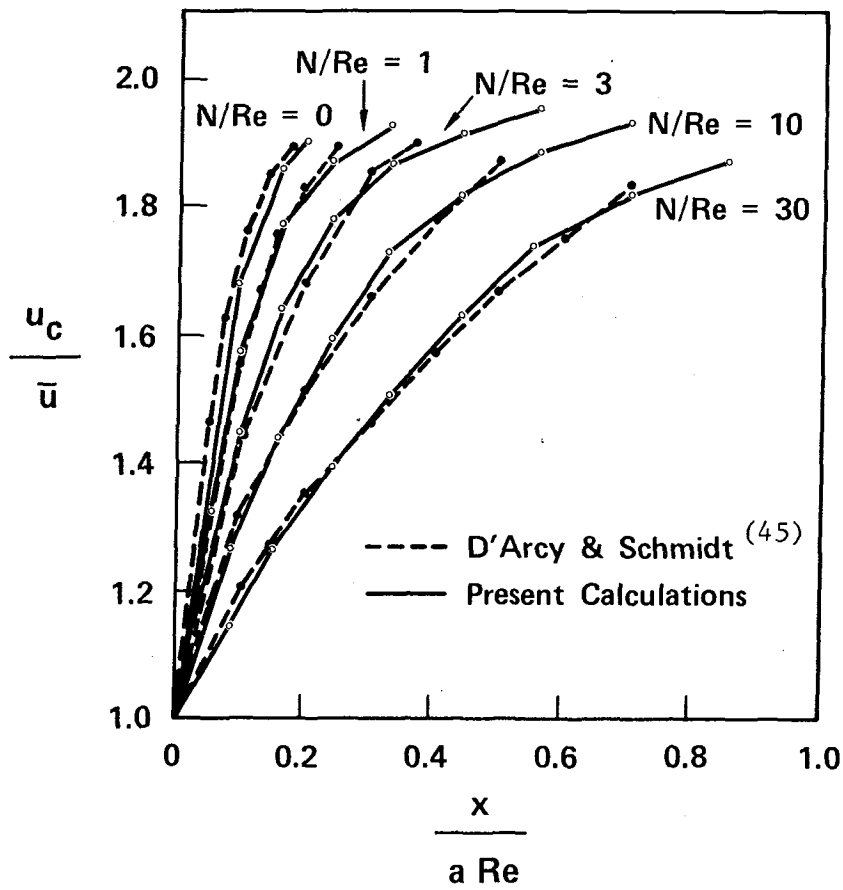


Figure 1.4-3 Effect of an axial magnetic field on the development of centerline velocity along the axial distance (x) in a pipe of radius (a).

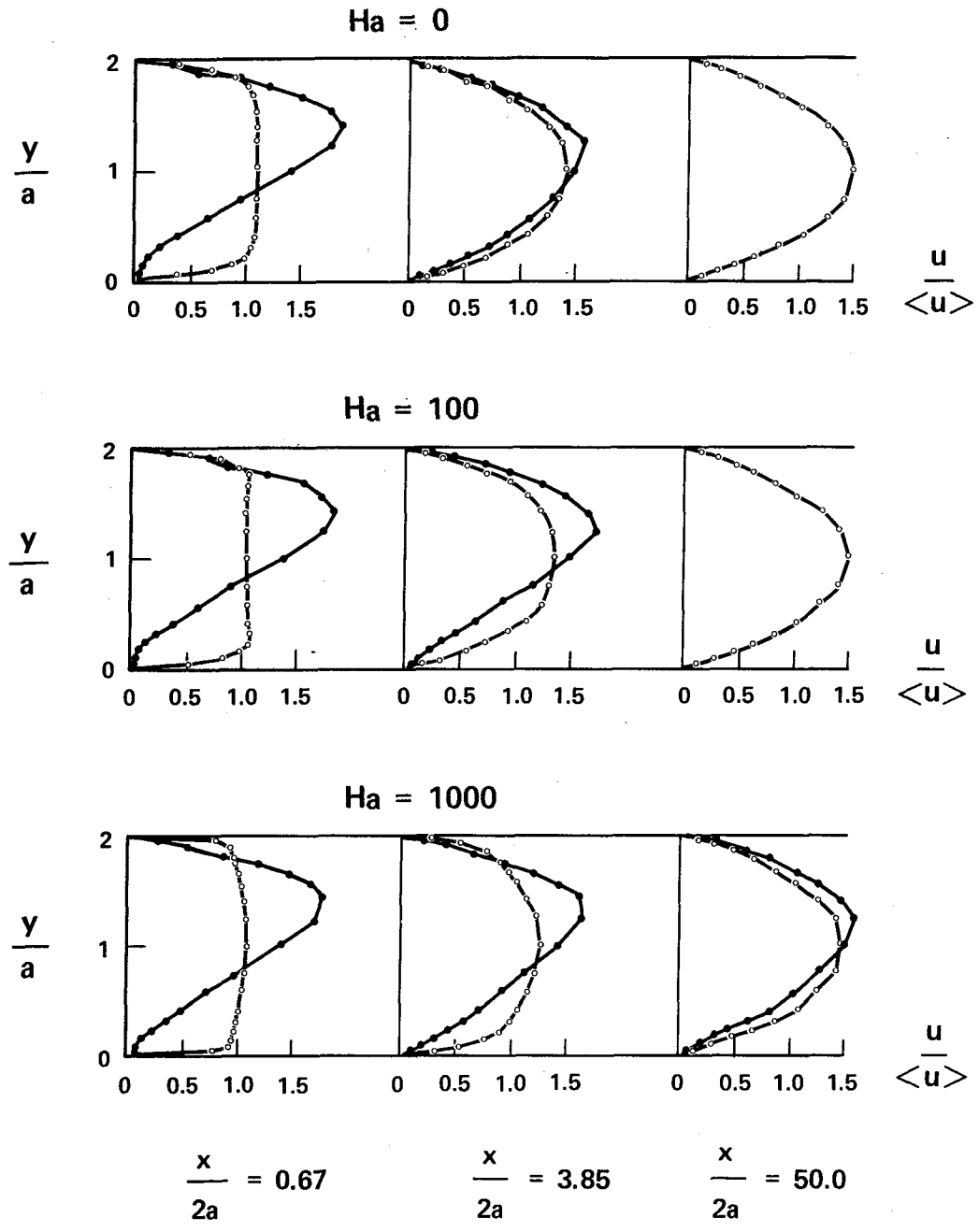


Figure 1.4-4 Development of the velocity profile along an insulated channel of half-width (a) and axial magnetic field

profile along the channel for different values of Hartmann number (Ha). For Ha=0 and Ha=100, the velocity is fully developed at a distance of 50 channel widths for both the slug and the skewed inlet profiles, while at Ha=1000 the velocity profile is still developing. At higher Ha, the development of the velocity will be delayed further. This means that liquid metal coolants in a reactor blanket that flow parallel to a strong magnetic field will not reach full development in this configuration.

For a magnetic field applied perpendicular to the mean flow direction, the flow develops quickly in a few channel diameters to a flat Hartmann profile. Figure 1.4-5 shows normalized velocity profiles at the channel exit across the channel, which is assumed fully insulated. For Ha=100 and Re=200, the velocity profile is fully developed Hartmann profile at the channel exit, which is at (3.3a) from the inlet.

These effects of the magnetic field on the flow of liquid metal coolants in reactor blankets can influence the heat transfer from the first wall. Since there is no interaction between a parallel field and a fully developed

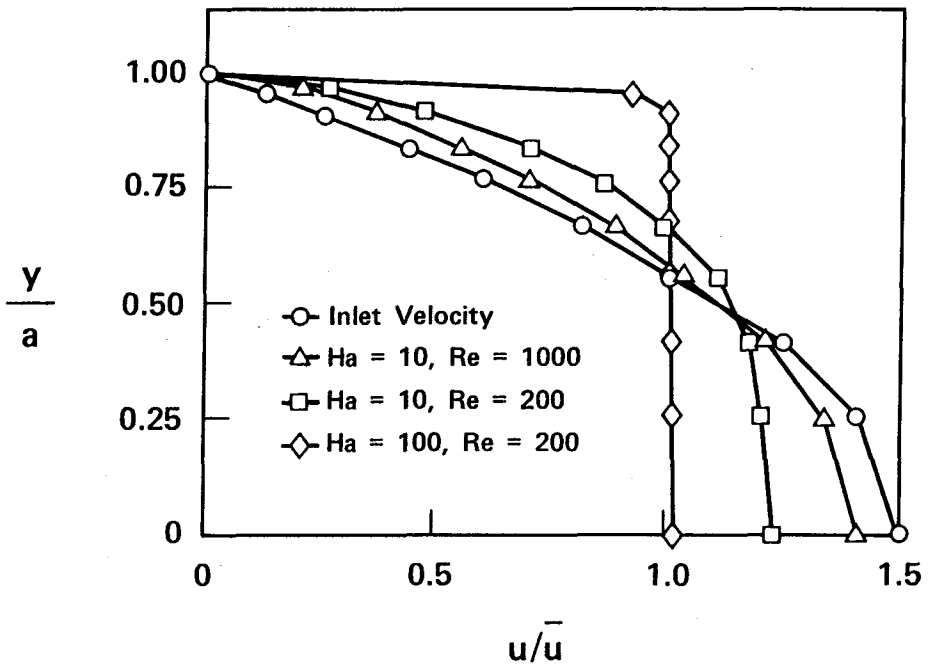


Figure 1.4-5 Effect of a perpendicular magnetic field on the velocity profile at the exit of an insulated channel of half width (a) and insulated walls

laminar velocity field, no change in heat transfer is expected. However, for a developing laminar flow the interaction with a parallel field can enhance heat transfer slightly due to the suppression of velocity profile development.

In laminar flow perpendicular to the magnetic field, higher fields enhance heat transfer by increasing the flow rate near the wall. Figure 1.4-6 shows how Nusselt number (Nu) changes along the channel with increasing Hartmann numbers.

In a real reactor blanket, liquid metal coolant flows through regions of varying geometry and/or varying magnetic field. Large velocity gradients can exist when the coolant flows through ducts of varying geometries, such as flow

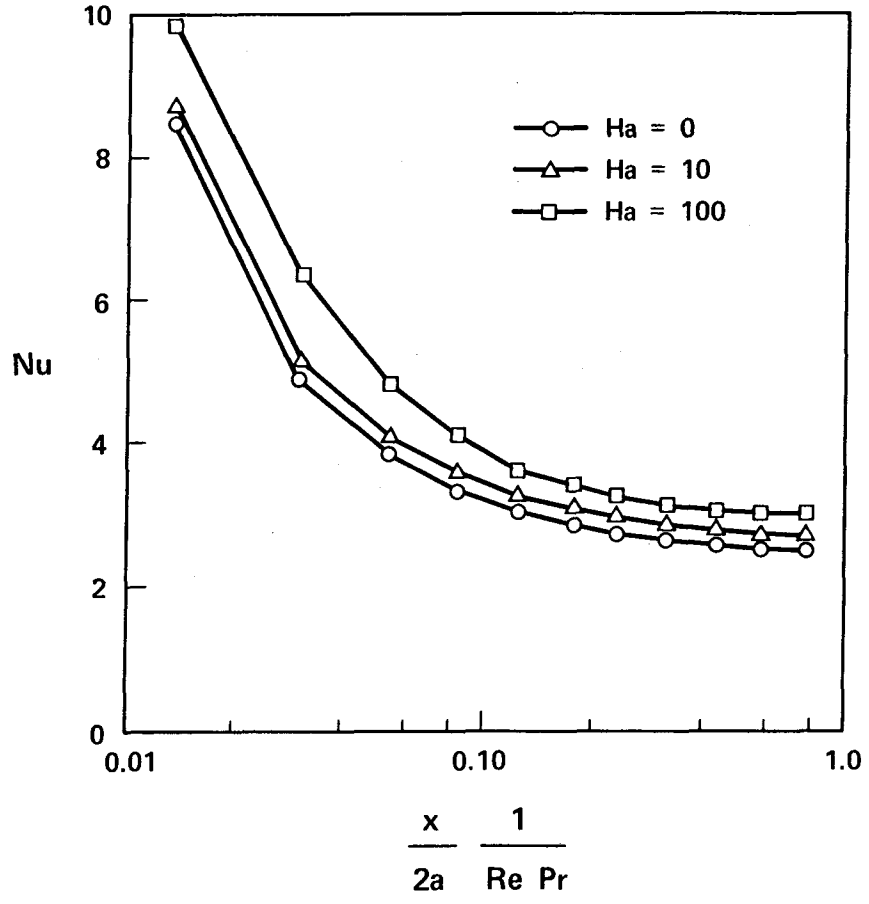


Figure 1.4-6 Effect of a transverse magnetic field on entry length heat transfer in an insulated channel (parabolic inlet profile and constant wall temperature

behind a sudden enlargement. Peculiar M-shaped profiles may exist when the coolant flows through a fringing magnetic field. All these variations can have a significant effect on the ability of the coolant to transfer heat from the first wall and, therefore, detailed analysis of the flow behavior is needed.

Numerical calculations of MHD laminar, viscous flow through an abrupt expansion of a circular channel clearly show the flow behavior when a magnetic field is applied in the direction of the main flow. The effects of this interaction on the recirculating eddy of a conducting fluid behind an orifice show that the body forces act in an opposite direction to the vortex eddy. This tends to weaken it, creating an almost stagnant region behind the orifice.

Macagno and Hung[46] studied the behavior of a captive eddy in a non-conducting flow both experimentally and numerically. They showed that at relatively small Reynold's numbers the re-attachment location moves downstream with increasing Reynolds number. McMichael and Deutsch[47] obtained an analytical solution using asymptotic expansion techniques for a conducting flow in slowly varying tubes in the presence of an axial magnetic field. They showed the appearance of flow separation along the wall in both converging and diverging regions of the tube. Their results, however, are limited to slowly varying tube radius.

Figure 1.4-7 shows the arrangement of the problem considered. The flow pattern can be described as a main stream that has generated an annular eddy between itself and the walls. Figure 1.4-8 shows the relative location of the re-attachment region and the eddy center as a function of Reynolds and Hartmann numbers. When the applied magnetic field is zero, the results show good agreement with the experiments of Macagno and Hung.[46] When a horizontal magnetic field is applied, the re-attachment point moves downstream. Figure 1.4-9 shows the effect of an axial magnetic field on the development of the velocity profile along the pipe. It can be seen from the figure that as Hartmann number increases, the length of the recirculating zone increases and the intensity of the eddy decreases. This creates an almost stagnant region behind the enlargement, which can have a great effect on heat transfer from

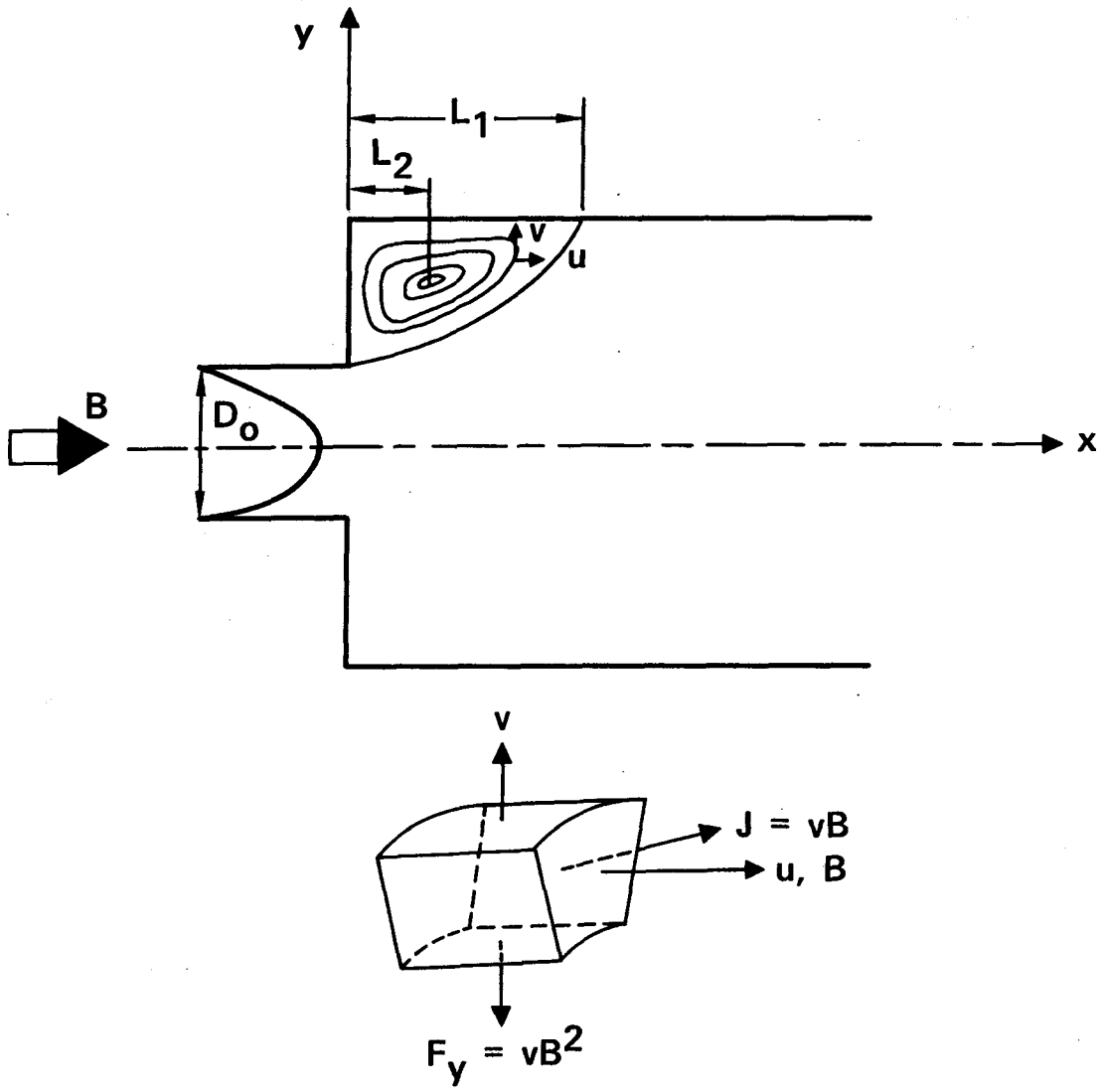


Figure 1.4-7 Configuration of pipe expansion and a definition sketch

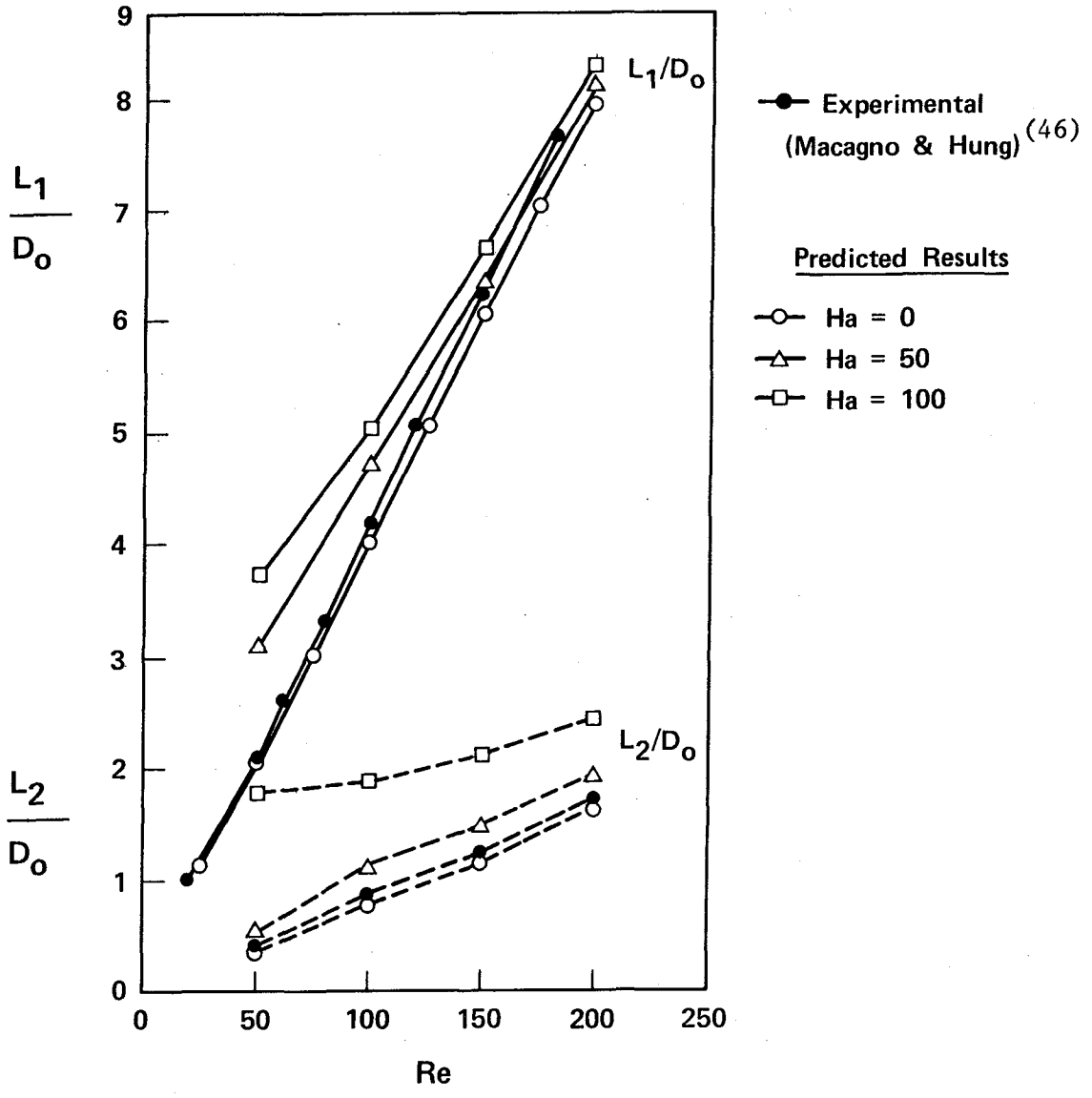


Figure 1.4-8 Characteristics of the annular eddy as a function of Reynolds number at different Hartmann numbers (L_1/D_o, relative eddy length; L_2/D_o, relative location of eddy center)

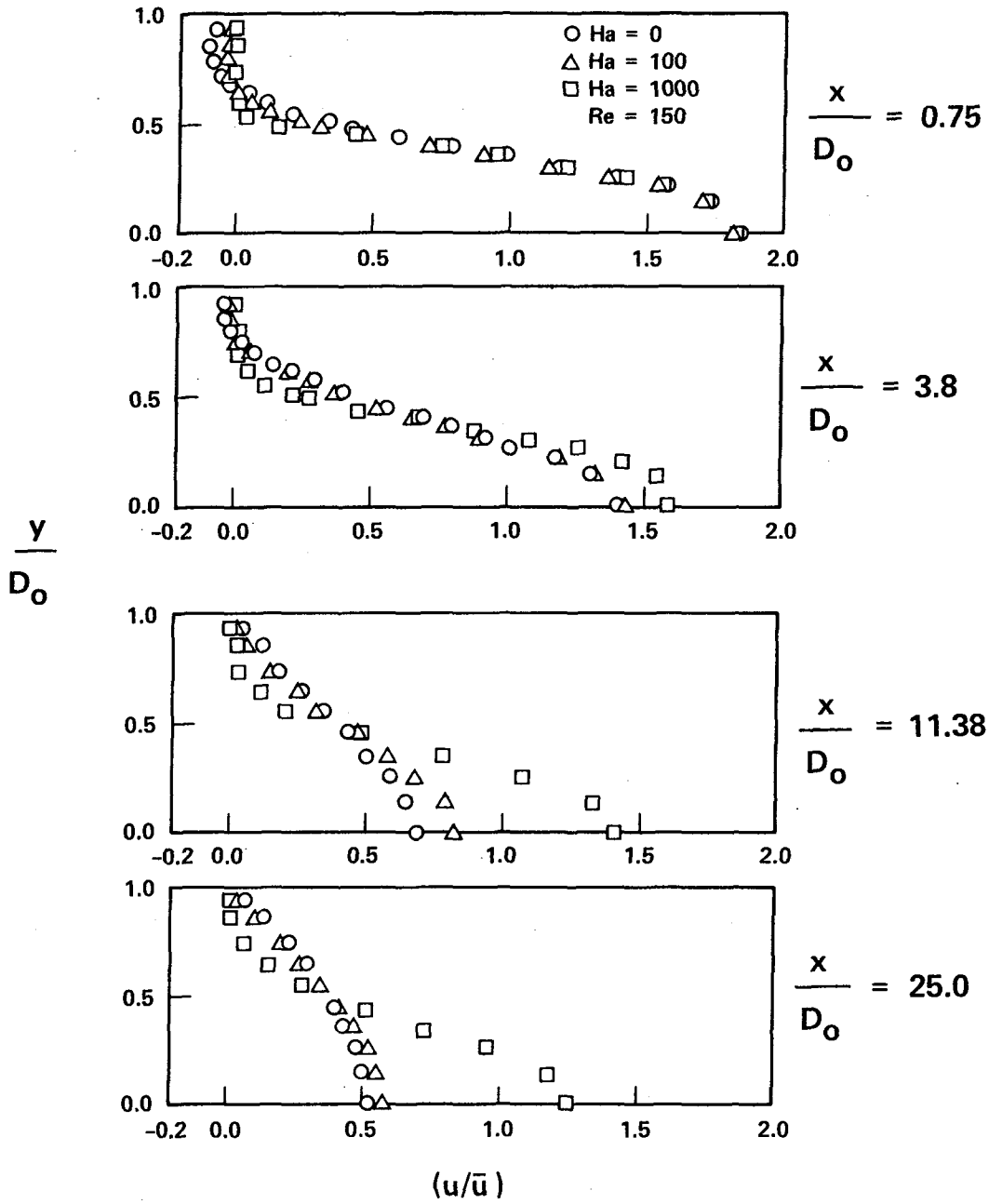


Figure 1.4-9 Effect of axial magnetic field on the development of velocity profile along the pipe

the first wall in the presence of obstacles in liquid metal coolant ducts. Figure 1.4-10 shows the wall pressure distribution along the pipe at different Hartmann numbers. In the non-magnetic case, large adverse pressure gradients develop downstream of the enlargement. Magnetic forces, however, tend to decrease the maximum pressure gradients behind the enlargement and shift the maximum further downstream.

Convergence of Eq. (1) may be impaired if the variation between the coefficients and the source term is large. One possible remedy to this problem is to vary the variable ϕ slowly between iterations, i.e., use an under-relaxation method. If the variable ϕ, which was computed in the (k-1)th iteration, is denoted by $\phi^{(k-1)}$ and the value which would be computed in the normal way in the k^{th} iteration is denoted by ϕ^{k}, then the value which would be actually used in iteration K is:

$$\phi = \alpha\, \phi^{k} + (1-\alpha)\phi^{k-1} \qquad (2)$$

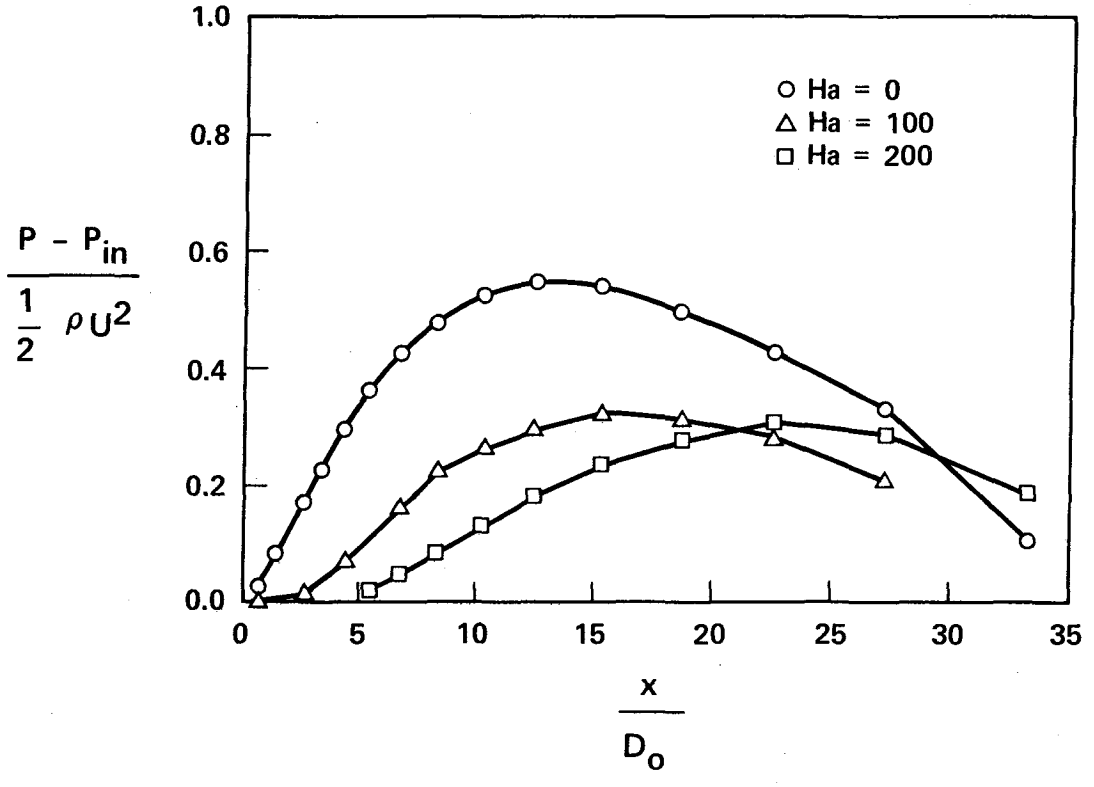


Figure 1.4-10 Wall pressure distribution along the pipe at different Hartmann numbers

where α is the under-relaxation parameter ($0 < \alpha < 1$). In the present calculations, α was varied between 0.5 and 0.1 depending on the problem being considered. Another possible remedy which was not tried is to reduce variations in the source term S_ϕ at each iteration.

To procure convergence at high Hartmann number flows, the electromagnetic forces must be included in the pressure and velocity iterative correction process. Consider the combined Navier-Stokes and Maxwell's equations. The coupled non-linear partial differential equations which govern the flow of a steady, constant property conducting fluid in a magnetic field can be written as:

$$\rho \frac{\partial}{\partial x_j}(u_i u_j) - \frac{1}{\mu_0}\frac{\partial}{\partial x_j}(b_i b_j) = -\frac{\partial}{\partial x_i}\left(P + \frac{|\vec{b}|^2}{2\mu_0}\right) + \mu \frac{\partial^2 u_i}{\partial x_j \partial x_j} \qquad (3)$$

where u_i and b_i are the velocity and magnetic field components in the x_i-space ($i = 1,2,3$). P, ρ, μ and μ_o are the fluid pressure, density, viscosity and magnetic permeability. The equation which governs the magnetic field can be written as:

$$\frac{\partial}{\partial x_j}(u_j b_i) - \frac{\partial}{\partial x_j}(u_i b_j) = \frac{1}{\mu_0 \sigma}\frac{\partial^2 b_i}{\partial x_j \partial x_j} \qquad (4)$$

where σ is the electrical conductivity of the fluid. The velocity and magnetic field must satisfy

$$\frac{\partial u_i}{\partial x_i} = 0 \quad \text{and} \quad \frac{\partial b_i}{\partial x_i} = 0 \qquad (5)$$

As can be seen from Eq. (3), the term $(|\vec{b}|^2/2\mu_0)$ is added to the pressure. This must be included in any pressure correction scheme. A solution method would iterate between Eqs. (3) and (4) to calculate intermediate values of u_i and b_i. Then, using the continuity equations (5), a pressure correction equation can be constructed which can correct the velocities and, hence, the induced magnetic field. The process is repeated until the residual errors in Eq. (5) are made very small. This seems a preferred method of solving MHD flows and further work is being pursued in this direction.

Another important fact of high Hartmann number flows is the narrow boundary and free shear layers which have to be resolved accurately by increasing

the number of grid nodes. This, however, will increase the number of iterations required for convergence. In the present calculations, variable grid spacing was used to improve spatial resolution in regions of high velocity gradients.

Mesh refinement can be an efficient method to improve the accuracy of MHD calculations while minimizing the amount of computational effort (storage spaces as well as time). However, it is not possible, in general, to predict the size and location of areas which require a refined mesh. One way to improve the mesh is by using the errors calculated from an initial coarse-grid calculation to indicate regions which require a finer mesh. Increasingly finer meshes can be iteratively determined until the desired level of accuracy is obtained.

To test the effectiveness of this technique, a finite element solution for 2-D fully developed duct flow is under development. Initial results have been obtained with pre-defined meshes of various sizes, and residual errors have been calculated. While self-adaptive solutions have been obtained successfully in 1-D problems, results are not yet available for the 2-D duct geometry.

Figure 1.4-11 shows the geometry of the duct in the x-y plane with a fully developed velocity in the z-direction. A uniform magnetic field is applied in the y-direction perpendicular to perfectly conducting walls and parallel to the non-conducting walls. Figure 1.4-12 shows the finite element solutions of the velocity using 5x5, 10x10, and 20x20 meshes, as compared to Hunt's[40] analytical solution for the velocity along the axis y=0. The velocity in the figure is normalized with respect to the channel average velocity. Increasingly finer meshes show the trend towards approaching the analytic solution.

1.4.2.2 Analytical and Approximate Methods

Theoretical analysis using the perturbation technique was used in an attempt to examine the fully developed flow of a conducting liquid in highly conducting, loosely coiled pipe in a magnetic field perpendicular to the plane of the pipe. Figure 1.4-13 shows a circular pipe of cross-sectional area (a) coiled in a circle of radius (R). The toroidal coordinate system (r', α, θ)

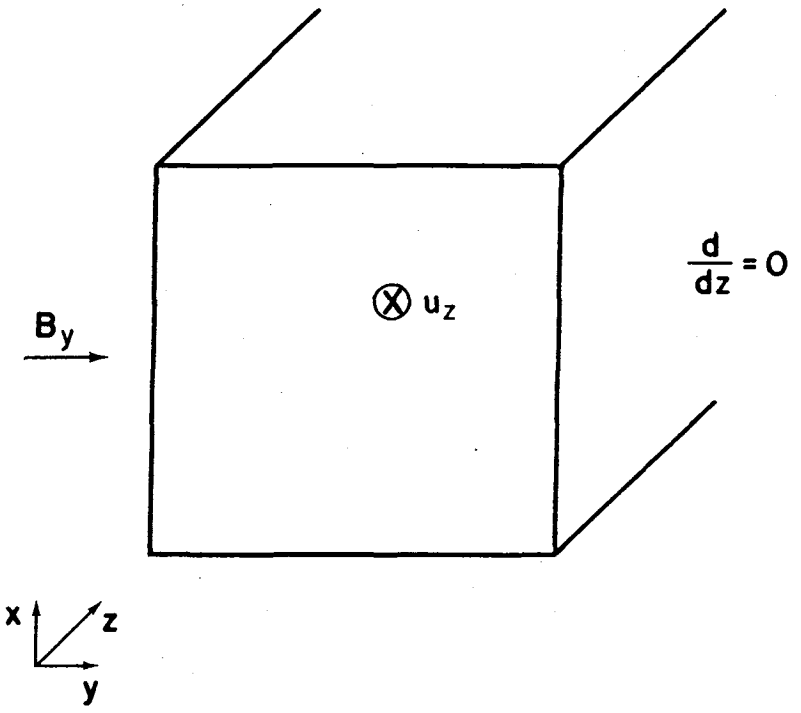


Figure 1.4-11 Geometry for the fully developed 2-D channel flow problem

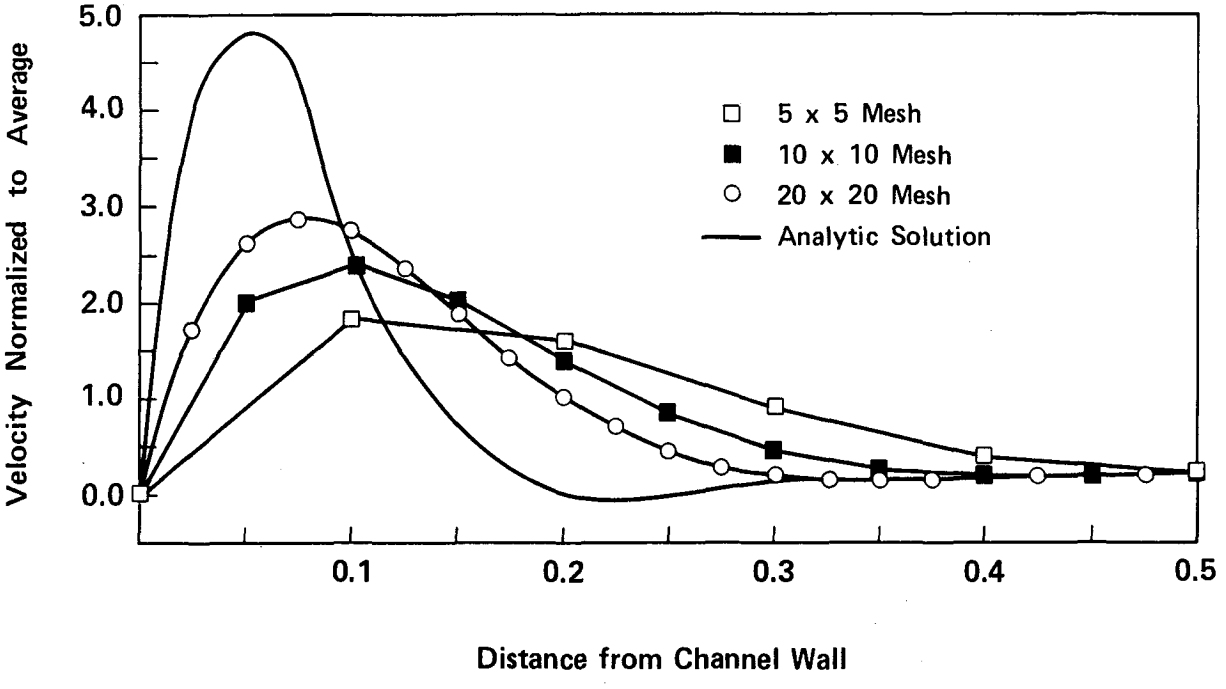


Figure 1.4-12 Comparison of finite element solution with analytic solution

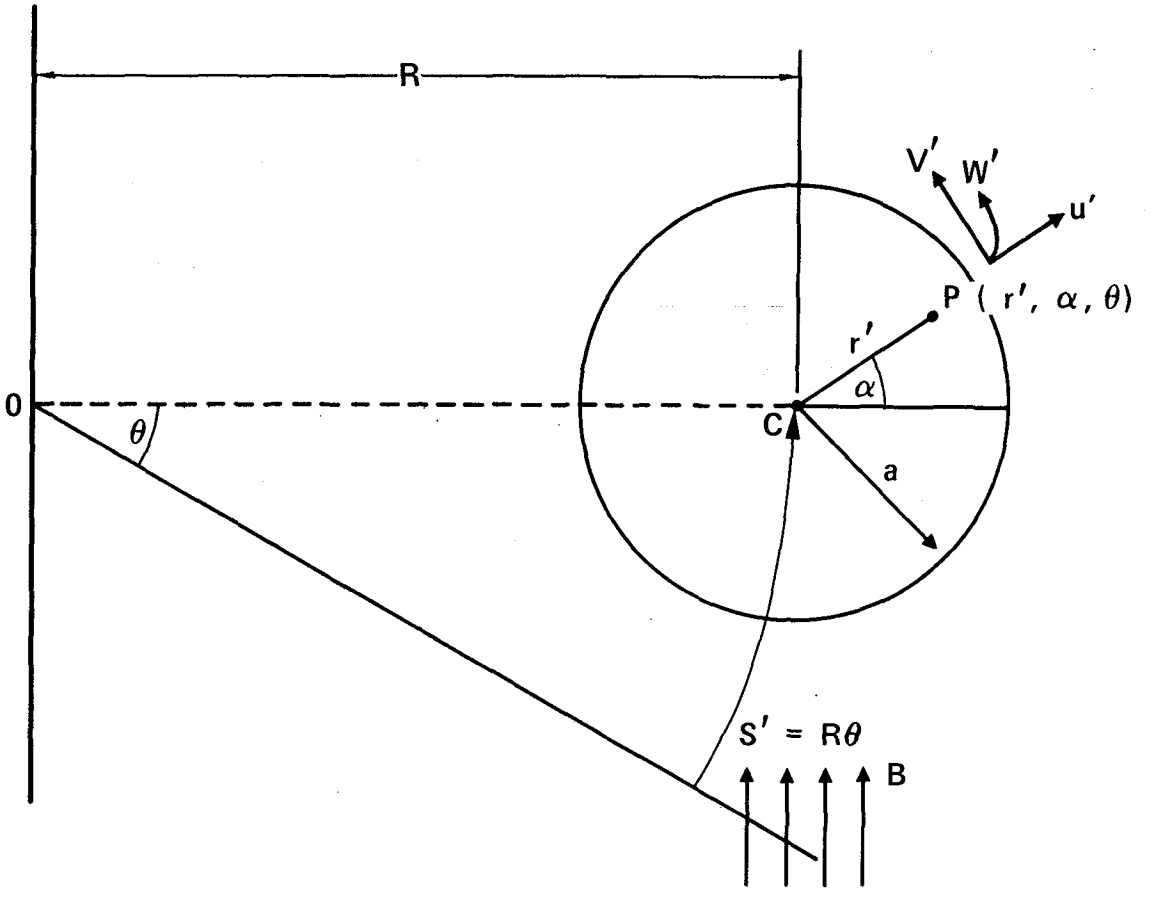


Figure 1.4-13 Toroidal coordinate system for a coiled pipe in a transverse magnetic field B

represents radial, azimuthal and axial directions, respectively, with corresponding velocities (u,v,w). The MHD flow field is analyzed as a deviation from Poiseuille flow for small values of Dean and Hartmann numbers. The series solution is obtained by expanding the axial velocity (w) along the pipe axis (z) and the stream function (ψ) in a series in powers of Dean (k) and Hartmann numbers (Ha):

$$w = \sum_{n=0}^{\infty} \sum_{m=0}^{\infty} k^{2n} \, Ha^{2m} \, w_{n,m}(r,\alpha), \quad \psi = \sum_{n=0}^{\infty} \sum_{m=0}^{\infty} k^{2n+1} \, Ha^{2m} \, w_{n,m}(r,\alpha)$$

where r and α are the radial and azimuthal coordinates. The following solutions are obtained for w and ψ.

$$w(r,\alpha) = (1 - r^2)\left(-\frac{\partial \overline{P}_o}{\partial z}\right) + \frac{k^2}{138240}(3r^9 - 30r^7 + 90r^5 - 120r^3 + 57r)$$

$$\left(-\frac{\partial \overline{P}_o}{\partial z}\right)^3 \cos\alpha + \frac{Ha^2}{16}(-r^4 + 4r^2 - 3)\left(-\frac{\partial \overline{P}_o}{\partial z}\right) + \ldots \qquad (6)$$

$$\psi(r,\alpha) = \frac{k}{576}(-r^7 + 6r^5 - 9r^3 + 4r)\sin\alpha +$$

$$+ \frac{k^3}{1327104}(0.001714r^{14} - .05143r^{12} + .375r^{10} - 1.6r^8$$

$$+ 4.05r^6 + 19.74r^4 - 22.52r^2)\sin 2\alpha + \ldots \qquad (7)$$

Figure 1.4-14 shows the axial velocity, w, across the pipe where the point of maximum velocity is shifted outside due to the centrifugal forces and the effect of the magnetic field is to retard the flow. Further study is being carried out to obtain series solutions for high Hartmann numbers.

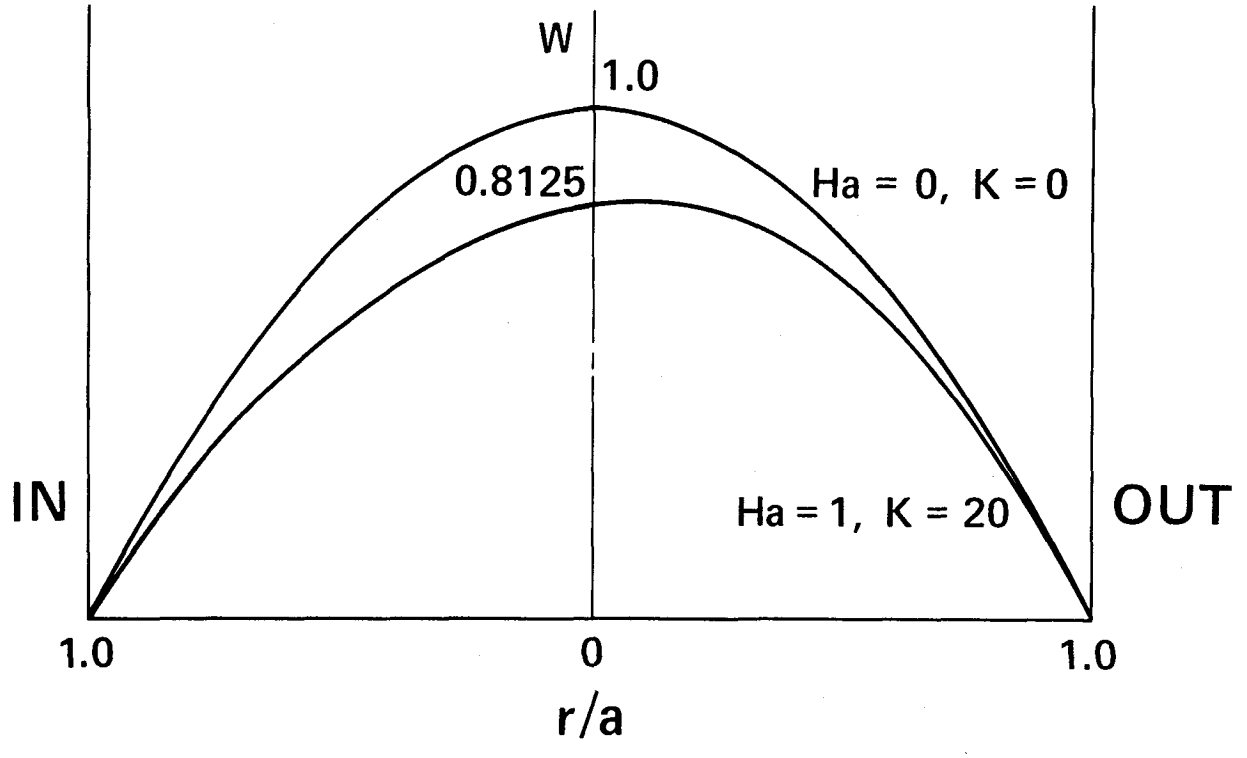


Figure 1.4-14 First perturbed axial velocity profile due to the combined effects of Dean and Hartmann numbers (K=20, Ha=1), together with Poiseuille profile

1.4.3 Modeling of Liquid Metal Mass Transfer (Corrosion/Deposition)

The objective of liquid metal mass transport modeling being carried out in this study is to characterize the mass transport of a ferritic steel alloy (HT9) in lithium. The modeling effort is being carried out along with an experimental program to reach a better understanding of the processes which govern the mass transport and deposition in lithium/HT9 systems.

Figure 1.4-15 shows a block diagram representing the chemical and transport processes for a liquid metal system with both mass removal and deposition. There are three distinct physical regions which must be modeled: the solid phase, the liquid phase, and the interface between the solid and liquid phases.

The research presently underway aims at modeling the mass removal (corrosion) and deposition in the experimental loop and comparing the predicted mass transport with the experimentally measured coupon weight loss and surface chemistry. The mass transport model is currently under development, and will include:

1. one-dimensional solid state diffusion of iron and chromium;
2. chemical reactions of iron and chromium with lithium nitride in solution with lithium and at the solid/liquid interface;
3. convection and bulk transport of products and reactants;
4. particle growth and dissolution; and
5. particle and molecular deposition in the loop.

The experimental research activity aims at determining the mass transport and deposition behavior of a structurally homogeneous lithium/HT9 system. Two thermal convection loops will operate in chemically similar lithium between 350 and 650°C for up to 3000 hours of integrated exposure. The experimental loops have been designed such that some of the uncertainties associated with modeling mass transfer experiments have been eliminated. Preliminary runs and measurements are expected in the near future from a joint cooperation program between UCLA and Oak Ridge National Laboratory. Detailed design of the experimental apparatus is given in Section 4.6-7 of Chapter 4.

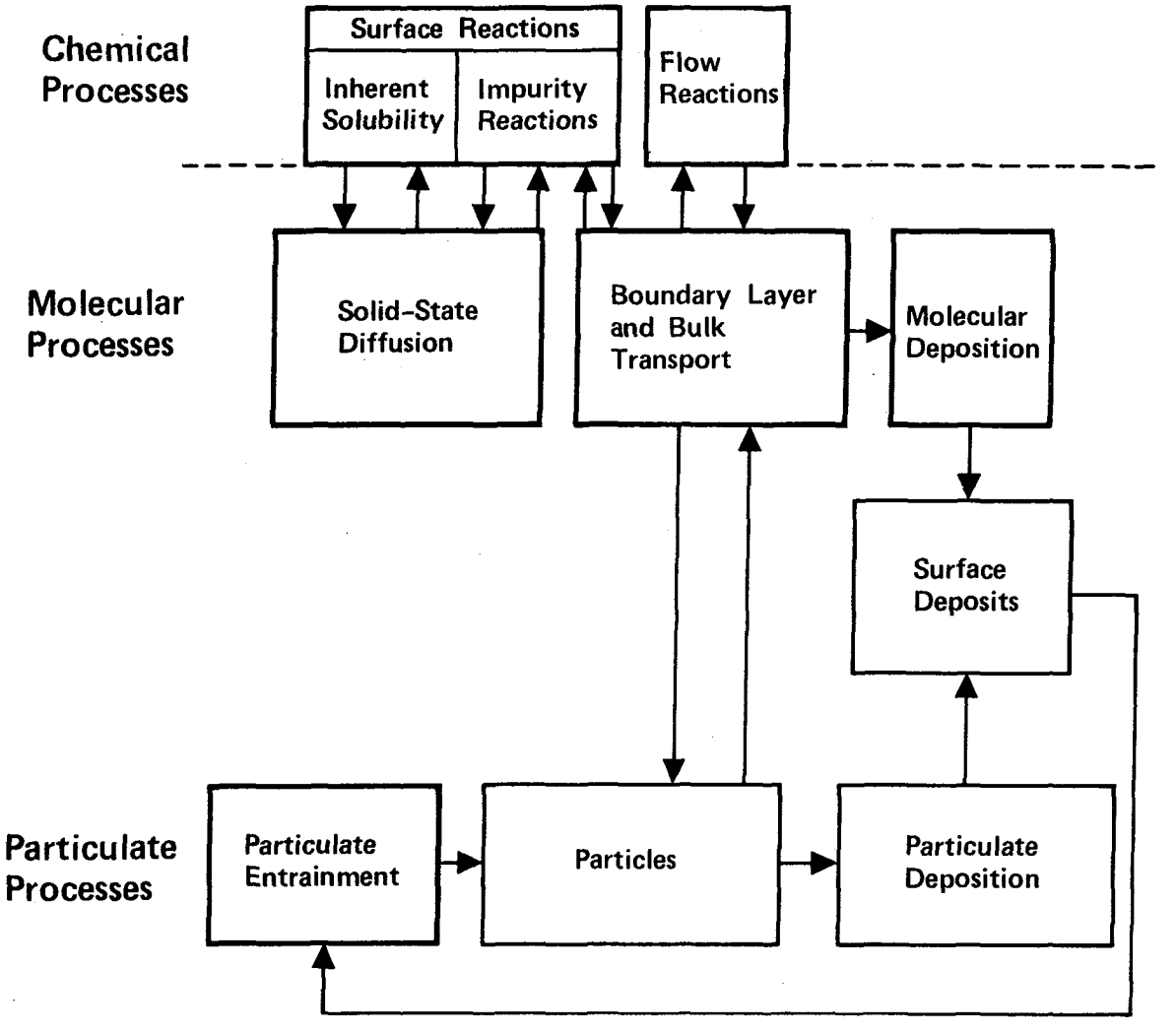


Figure 1.4-15 Block diagram of mass transport processes

1.4.4 Heat Transfer in Flows Over a Wedge or a Cylinder With Volumetric Heat Generation

The importance of volumetric heat generation in liquid metals presents a unique and interesting heat transfer problem: in addition to causing the bulk temperature of the coolant to rise, it can alter the temperature profile and, hence, the heat transfer coefficient. It has been found[29] that volumetric heat generation can decrease the heat transfer coefficient and, as a result, cause an increase in the wall temperature. One of the primary purposes of this work was to determine the effects of heat generation in the coolant on hot film probes used to measure velocity profiles in the liquid metal. However, it also has general relevance to flows over plates and wedges. Both analytical and experimental work have been performed.

The analytical work utilized a similarity transformation similar to Chambre[48] to convert the partial differential equations governing the velocity and temperature into ordinary differential equations. The equations are then solved numerically. The analysis considers flows over wedges and over circular cylinders. For flow over a flat plate (wedge angle equals zero), an abnormal temperature overshoot in the temperature profiles is observed. Figure 1.4-16 shows the boundary layer temperature profiles for flow over a flat plate at different Prandtl numbers. The figure indicates that the temperature of the flow near the wall is greater than the wall and free stream temperatures. For liquid metal coolants ($Pr \sim 0.01$), no temperature overshoot is expected. However, it is more pronounced for high Prandtl number flows.

The analysis has also been extended to flows over a circular cylinder, where an equivalent wedge method is used for performing the analysis. The average change of Nusselt number for the unseparated flow region of the cylinder due to heat generation for $Pr \to 0$ is:

$$\Delta\overline{Nu}_d = 1.23\ \lambda_d\ Re_d^{-1/2}\ Pr^{-1/2} \qquad (8)$$

where λ_d is a heat generation parameter based on the hot film diameter (d) defined as:

$$\lambda_d = Q_v d^2/K(T_s - T_{in})$$

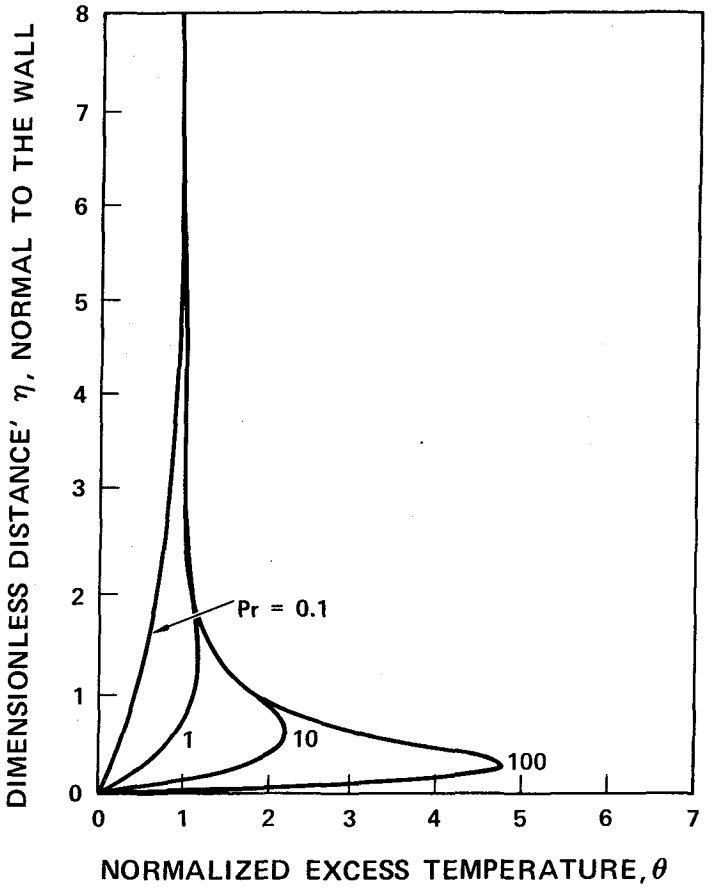


Figure 1.4-16 Boundary layer temperature profile for flow over flat plate

where Q_v is the volumetric heat generation, T_{in} is the inlet flow temperature, and T_s is the surface temperature.

To obtain the actual Nusselt number for flows over a cylinder, first the average Nusselt number without heat generation, $\overline{Nu}_0$, should be obtained from literature. Then the change $(\overline{\Delta Nu})$ is obtained from Eq. (8), and the actual Nusselt number $(\overline{Nu})$ is obtained from $\overline{Nu} = \overline{Nu^0} - \overline{\Delta Nu}$.

To obtain an approximate estimate of the effect of heat generation on the heat transfer coefficient for flow over a hot film anemometer, the change in Nusselt number relative to the Nusselt number for the case of no heat generation can be written as:

$$\frac{\Delta Nu_x}{Nu^0_x} = \frac{2\,\lambda_x}{Re_x\,Pr} \qquad Pr \to 0 \tag{9}$$

where x is for a flat plate when $x = \frac{\pi d}{4}$. This value of x corresponds to the top location of the cylinder if the cylinder is cut open and transformed to a flat plate.

Equation (9) indicates that the change is proportional to the heat generation parameter (λ_x), and inversely proportional to the Reynolds and Prandtl numbers. Therefore, the change is largest for higher heat generation, lower velocity, and low Prandtl number fluids. Table 1.4-1 shows the result of the comparison for various Reynolds numbers and heat generation parameters. For small hot film diameters, the effect of heat generation on the Nusselt number is negligible. However, the effect is large for larger cylinders.

For a hot film anemometer placed in a liquid metal flow with volumetric heat generation, no appreciable change in Nusselt number is expected due to the small diameters of the hot film. This conclusion was verified in this study using a small scale experiment where a liquid metal loop was built and the few experiments performed confirm the prediction that the change in Nusselt number is small.

Table 1.4-1 Change in Nusselt Number Due to Heat Generation for a Pr = 0 Flow Over a Cylinder[a]

Diameter d (m)	Heat Generation Rate Q_v (W/m^3)	Velocity V (m/s)	$\Delta Nu_x/Nu_x^0$ (%)
152×10^{-6}	33×10^5	0.14	0.04
10×10^{-3}	33×10^5	0.14	0.3
5×10^{-2}	33×10^5	0.14	13
152×10^{-6}	50×10^6	1	0.08
10×10^{-3}	50×10^6	1	0.5
5×10^{-2}	50×10^6	1	26

[a]The cylinder is approximated by a flat plate with the length of $x = \pi d/4$.

1.4.5 Tritium Transport Modeling

The feasibility of a fusion reactor depends on the development of economical and safe methods to extract tritium from the blanket breeding material at a rate equal to the breeding rate. It is important, therefore, to predict the tritium inventory and to understand quantitatively the movement of tritium in the blanket and tritium processing systems. A comprehensive model of the total tritium systems is needed to provide this understanding.

The effort in this area has been directed mainly toward modeling the tritium transport in solid breeder blankets. The model focuses on the different transport mechanisms of the tritium generated in the solid breeder grain to the purge flow, which is subsequently carried out of the blanket for removal and measurement. The model considers different mechanisms which bring the tritium from the grain to the purge flow. These include diffusion through the grain boundary and open porosity. Solubility and surface adsorption are also included as effective source terms in the grain and grain boundary diffusion equations, respectively. All these processes are temperature dependent, so the temperature distribution must also be calculated. This is done by solving the heat conduction equation in two-dimensional geometry. The tritium generation rate in the breeder grain is obtained from neutronics calculations. The numerical formulation of the tritium transport equations is in its final stages.

1.4.6 Modeling of Plasma-Interactive Components

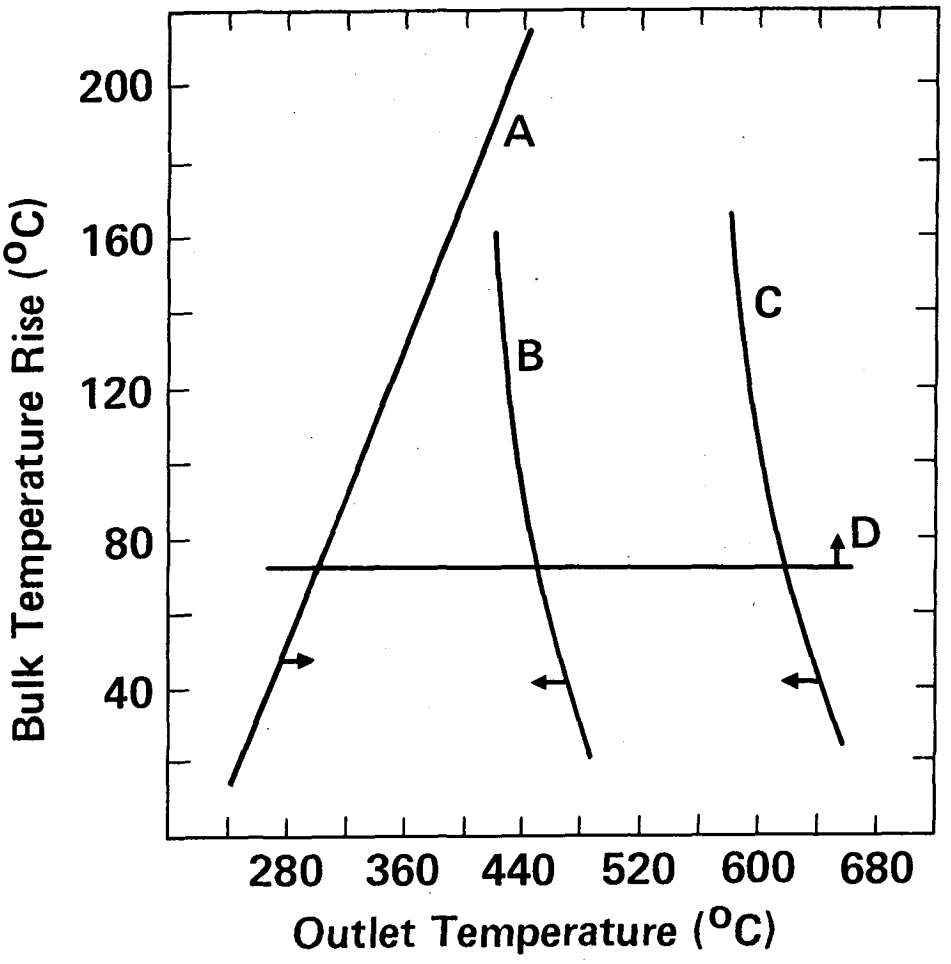
Successful operation of the impurity control system depends on the thermomechanical behavior of its components. If liquid metal blankets are used, safety considerations dictate the use of coolants other than water in the in-vessel components. The present research considers the viability of using liquid metal as a coolant for in-vessel components such as limiters and diverter plates. Detailed thermal and mechanical stress analysis of the limiter is also considered, and a three-dimensional finite element code was developed for stress analysis.

1.4.6.1 Design Window for Liquid-Metal-Cooled Limiters

The purpose of this work is to investigate the feasibility and attractiveness of liquid metals as coolants for in-vessel components. In detailed calculations, a pumped limiter in a tokamak reactor was used as an example. A technique used extensively in this work is that of defining the possibility of a design using a design window. A design window can be explained as a permissible region of operation defined by various limits.

Considerable effort has been devoted to developing a geometrical configuration for the limiter that minimizes the problems associated with liquid metal coolants. Key factors are: a) minimizing the coolant flow path length inside the limiter in order to reduce the required flow speed for a given temperature and surface heat flux; b) optimizing flow direction relative to the magnetic field; and c) flow mixing and other techniques to enhance heat transfer inside coolant channels. The purpose of the first two items is to reduce MHD pressure drop. Enhancing heat transfer reduces the temperature at the coolant/structure interface and reduces the maximum temperature in the structure.

An example of the results is found in Figure 1.4-17, which shows the "design window" under some of the most favorable conditions for a lithium-cooled limiter with insulated feed pipes. The limiter is double-edged and is shaped to make the incident heat flux uniform. The flow in the inlet and outlet manifolds is perpendicular to the toroidal field, while it is parallel to the field inside the small cooling channels within the limiter. The poloidal width of the limiter is 2.1 m and the cooling channel length is 30 cm in



A - Minimum inlet temperature limit

B - Maximum structure temperature limit

C - Maximum interface temperature limit

D - Maximum primary stress limit

Figure 1.4-17 Design window for lithium-cooled vanadium limiter with insulated conduits at 4 MW/m^2 heat flux

the toroidal direction. The lithium inlet temperature is 230°C. The maximum thickness of the vanadium wall is 1.5 mm. The maximum temperature for the structure is about 700°C. The results in Figure 1.4-17 show that a design window exists at a heat flux of 4 MW/m^2, but the window is not sufficiently wide to compensate for the many present uncertainties.

Figure 1.4-18 is similar to Figure 1.4-17, except that the surface heat flux is increased to 5 MW/m^2. The use of insulated walls is necessary in this case. The results are also found to be sensitive to the fluid velocity profile (slug flow was assumed in Figures 1.4-17 and 1.4-18).

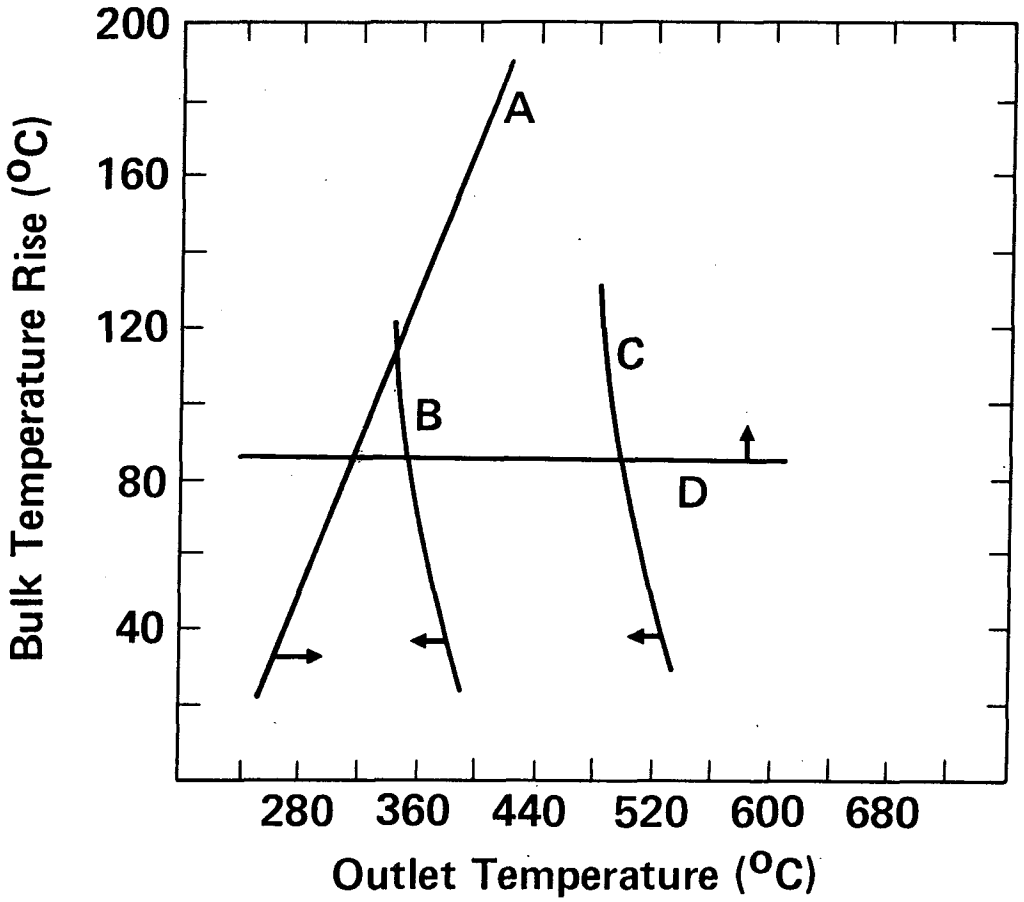
These calculations were performed for an uncoated limiter with vanadium as the structural material. The use of beryllium as a coating, which may be required from a plasma contamination and/or erosion lifetime standpoint, imposes additional thermal stresses on the vanadium structure and narrows the design window further.

1.4.6.2 Thermal and Stress Analysis of Limiters

Detailed thermal and primary stress analysis for double-edged limiters was carried out. The thermal analysis considers the temperature distribution in an elemental section of the limiter for a given wall heat flux. A three-dimensional stress analysis code was developed to calculate both thermal stresses caused by wall heat flux, and primary stresses caused by the coolant pressure. Copper limiters with water coolants, and vanadium alloy limiters with lithium coolant were considered.

Assuming a uniform heat flux on the surface of the limiter, the temperature distribution was calculated by solving the energy equation. These temperatures are then used to calculate the stress intensity in the limiter. Figure 1.4-19 shows the geometry of the limiter specimen and the rectangular finite element mesh. The plane EFE'F' faces the plasma. The results obtained consider only the central portion of the limiter where the heat flux is assumed uniform. However, plans to model the curved leading edge of the limiter are under consideration.

Figure 1.4-20 shows the temperature distribution in x-y plane for a vanadium limiter with a wall heat flux of 6 MW/m^2 and a coolant Nusselt number of 7.0.



A - Minimum inlet temperature limit

B - Maximum structure temperature limit

C - Maximum interface temperature limit

D - Maximum primary stress limit

Figure 1.4-18 Design window for lithium-cooled vanadium limiter with insulated conduits at 5 MW/m^2 heat flux

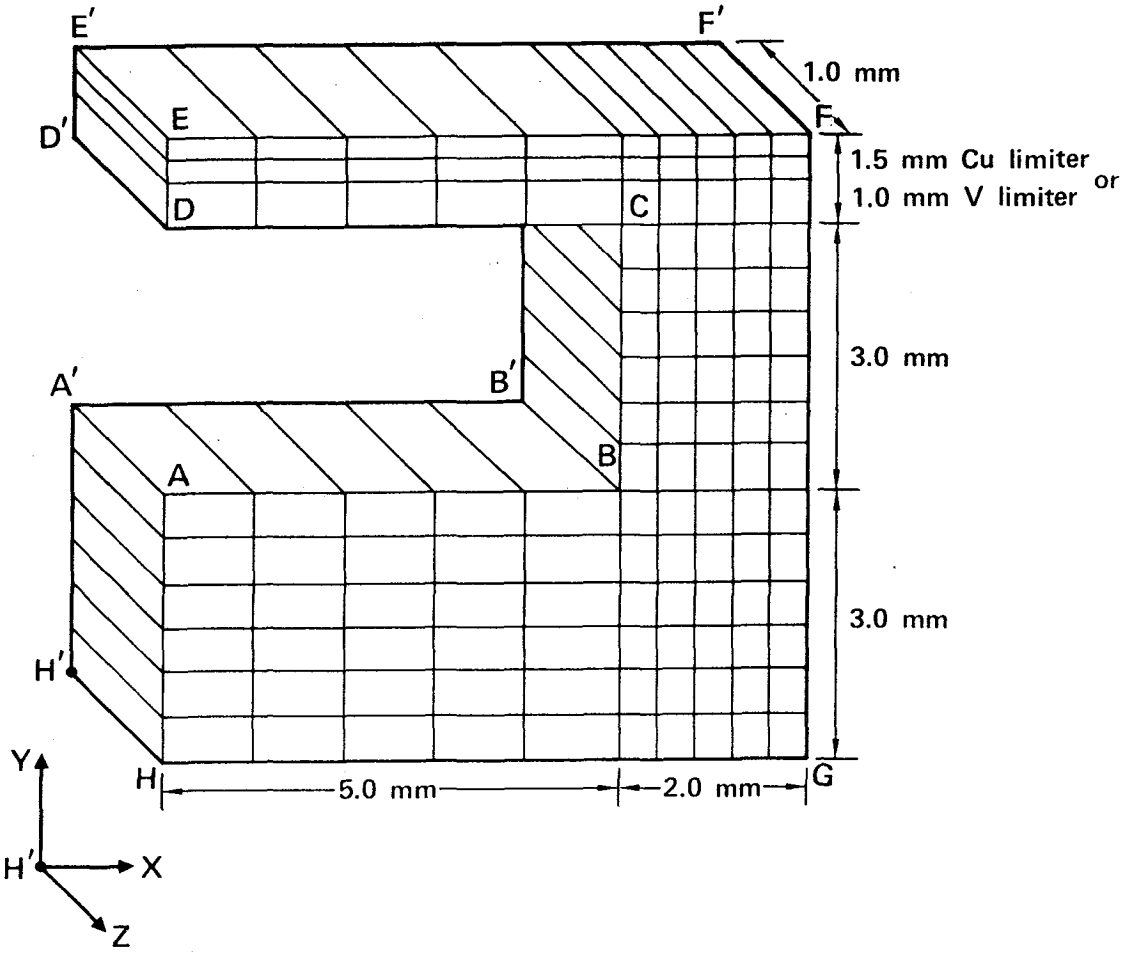
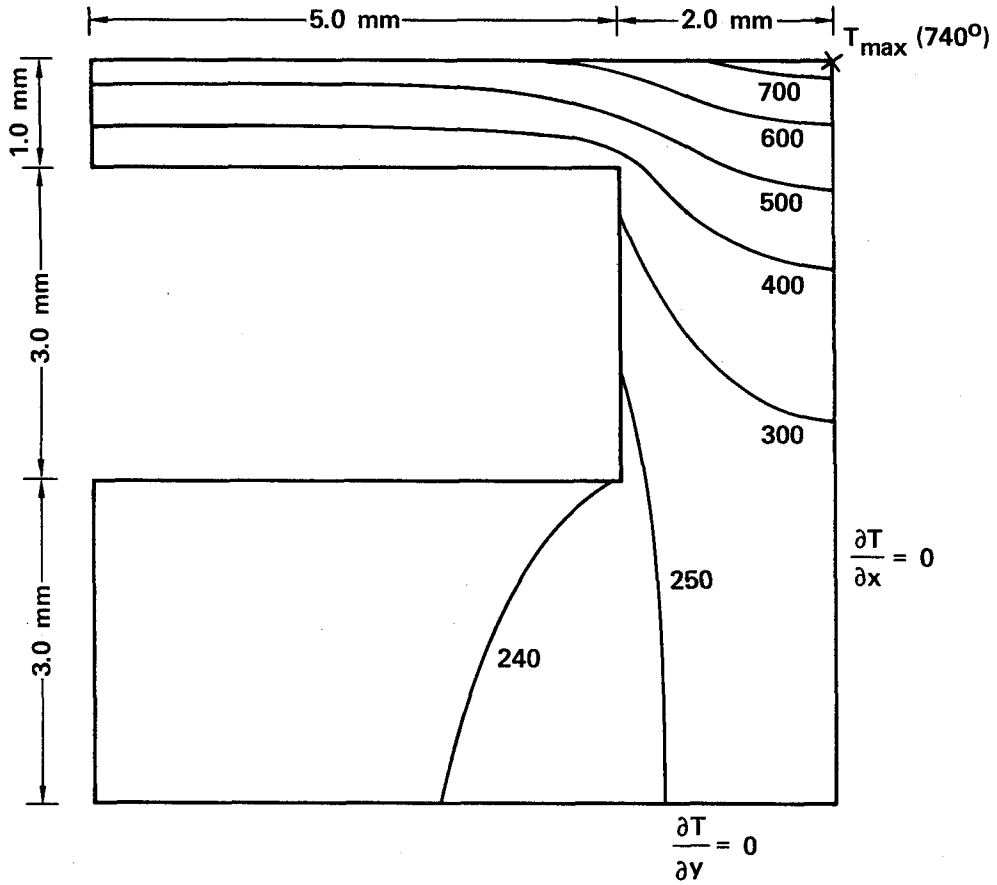


Figure 1.4-19 Three-dimensional finite element mesh geometry



VANADIUM
HEAT FLUX = 6.0 MW/m^2

HEAT TRANSFER COEFF. =
7.5×10^4 W/m^2K

BULK TEMP. = 230° C

COOLANT PRESSURE = 5.5 MPa

Figure 1.4-20 Temperature distribution in a vanadium limiter. Results are shown for the X-Y plane of Figure 1.4-19.

The results show that for water-cooled copper limiters (with 1.5 mm wall thickness without coating), the maximum heat flux allowable is about 5.2 MW/m^2. A maximum coolant pressure of about 3.7 MPa is allowed based on the ASME code of stress limits for the structural material. On the other hand, lithium-cooled vanadium alloy limiters (with 1 mm wall thickness and no coating) have higher limits of 6.0 MW/m^2 heat flux and 8.0 MPa coolant pressure.

Figure 1.4-21 shows an example of the Von Mises stress distribution (σ_t) in a cross-section of a lithium cooled vanadium limiter under a 6.0 MW/m^2 heat flux and coolant pressure of 5.5 MPa.

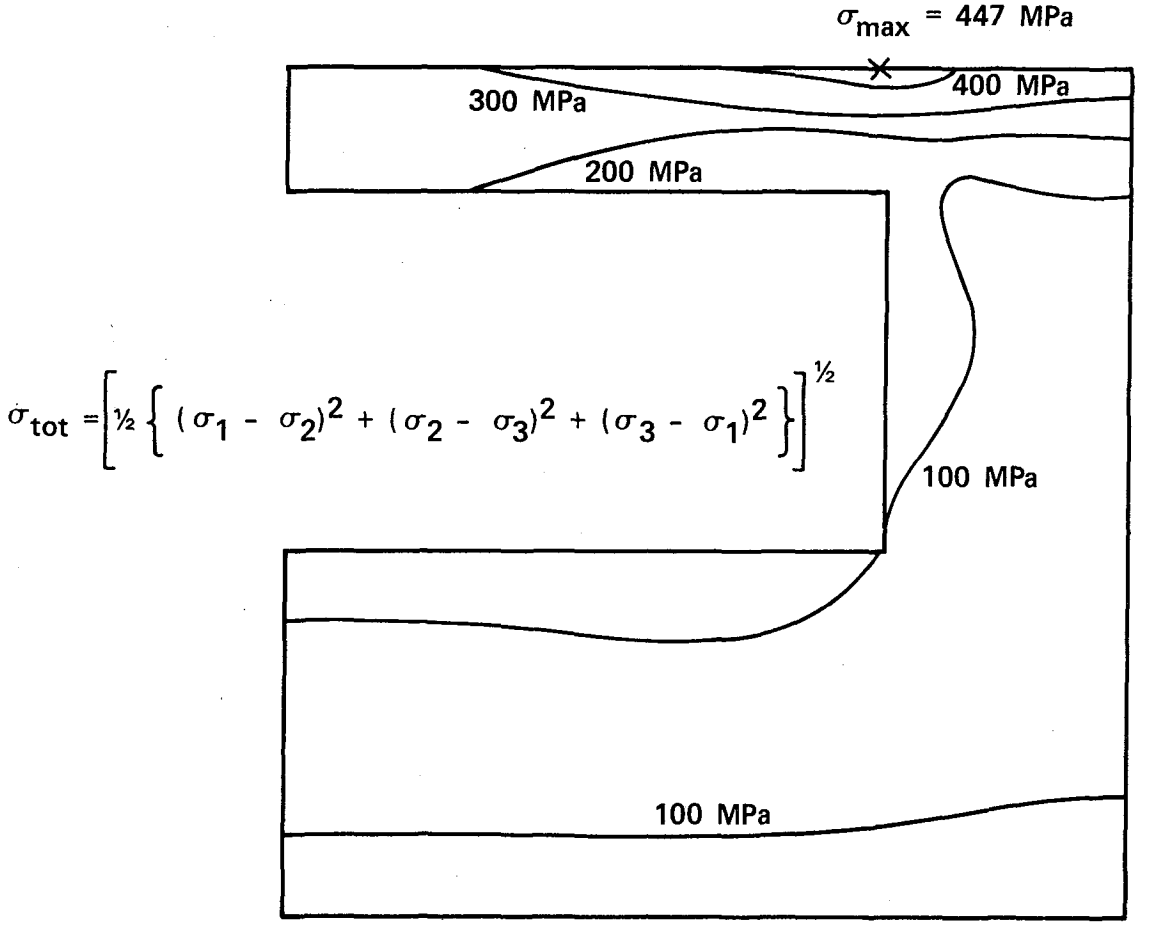


Figure 1.4-21 Von Mises stress distribution (σ_t) in a lithium-cooled vanadium limiter with 6.0 MW/m^2 heat flux and coolant pressure of 5.5 MPa

References for Chapter 1

1. M.A. Abdou, et al., "FINESSE: A Study of the Issues, Experiments, and Facilities for Fusion Nuclear Technology Research and Development (Interim Report)," PPG-821, UCLA-ENG-84-30, University of California, Los Angeles (1984).

2. M.A. Abdou, et al., "Technical Issues and Requirements of Experiments and Facilities for Fusion Nuclear Technology (FINESSE Phase I Report)," PPG-909, UCLA-ENG-85-39, University of California, Los Angeles (1985).

3. M.A. Abdou, et al., "A Study of the Issues and Experiments for Fusion Nuclear Technology," Fusion Tech., 8, 2595-2645 (1985).

4. M.A. Abdou, et al., "Technical Issues and Requirements of Experiments and Facilities for Fusion Nuclear Technology," accepted for publication in Nucl. Fusion.

5. The NET Team, "NET Status Report," NET Report 51 (1985).

6. T. Tone, et al., Nucl. Tech./Fusion, 4, 573 (1983).

7. M.A. Abdou, et al., "Fusion Reactor Design IV: Report on the IAEA Technical Committee Meeting and Workshop, Yalta, USSR, 26 May - 6 June 1986," Nucl. Fusion, 26, 1377-1428 (1986).

8. "Technical Planning Activity Final Report," ANL/FPP-87-1, Argonne National Laboratory (1987).

9. B.F. Picologlou, C.B. Reed, P.V. Dauzvardis and J.S. Walker, "Experimental and Analytical Investigations of Magnetohydrodynamic Flows Near the Entrance to a Strong Magnetic Field," Fusion Tech., 10, 860-865 (1986).

10. W.M. Stacey, Jr., et al., "The U.S. Contribution to the International Tokamak Reactor Phase 1 Workshop," USA-INTOR/81-1 (June 1981).

11. C.C. Baker, et al., "STARFIRE - A Commercial Fusion Tokamak Power Plant Study," ANL/FPP-80-1, Argonne National Laboratory (1980).

12. "Blanket Comparison and Selection Study - Final Report," ANL/FPP-84-1, Argonne National Laboratory (1984). See also, "Blanket Comparison and Selection Study - Interim Report," ANL/FPP-83-1, Argonne National Laboratory (1983).

13. M.A. Abdou, et al., "Deuterium-Tritium Fuel Self-Sufficiency in Fusion Reactors," Fusion Tech., 9, 250-285 (1986).

14. M.C. Billone, "The Influence of Surface Desorption on Tritium Recovery and Inventory in Fusion Solid Breeders," J. Nucl. Mat., 141-143, 316-320 (1986).

15. R.F. Bourgue, Note for BCSS Progress Meeting, Argonne National Laboratory (May 1984).

16. F. Kreith, Principles of Heat Transfer, Third Edition, Harper & Row, New York (1973).

17. P.J. Gierszewski and R.J. Puigh, "Testing Needed Experiments for Solid Breeder Blankets," J. Nucl. Mat., 141-143, 311-315 (1986).

18. G.A. Deis, L.G. Miller and M. Youssef, "Utilization of Fission Reactors for Fusion Engineering Testing," Fusion Tech., 8, 1115-1123 (1985).

19. P.J. Gierszewski, M.A. Abdou and R.J. Puigh, "Fission Reactor Experiments for Solid Breeder Blankets," Fusion Tech., 10, 1097-1101 (1986).

20. Ja. Dekeyser and J.L. Walnier, "Characteristics of Experimental Facilities for Fusion Research and Development in Lithium and Lithium-Lead Technology," CEN/SCK, FT/MOL/B4-7/T82-002 (1985).

21. A. Inoue, H. Madarame and T. Tone, "Outline of Heat-Removal Studies in Japan," J. Fusion Energy, 3, 425-428 (1983).

22. D.R. Harries, "The European Community Fusion Materials Program," EUR-FU/XII-80/86/65 (Oct. 1986).

23. C. Henning and B.G. Logan, "TIBER-II: Tokamak Ignition/Burn Experimental Reactor - 1986 Status Report," UCID-20863, Lawrence Livermore National Laboratory (1986).

24. "International Tokamak Reactor, Phase Two A, Part I," STI/PUB/638, IAEA, Vienna (1983). See also, "International Tokamak Reactor, Phase Two A, Part II," STI/PUB/714, IAEA, Vienna (1986).

25. P.J. Gierszewski, et al., "Engineering Scaling and Quantification of the Test Requirements for Fusion Nuclear Technology," Fusion Tech., 8, 1100-1108 (1985).

26. C.C. Baker, et al., "Tokamak Power Systems Studies - FY 1985," ANL/FPP-85-2, Argonne National Laboratory (1985).

27. M.A. Abdou, et al., "A Demonstration Tokamak Power Plant Study (DEMO)," ANL/FPP-82-1, Argonne National Laboratory (1982).

28. M.A. Abdou, et al., "Recent Progress in Design Studies for Tokamak Demonstration and Commercial Power Plants," Fusion Reactor Design and Technology, IAEA-TC-392/15, pp. 231-272 (1983).

29. K. Taghavi, M.S. Tillack and H. Madarame, "Special Features of First Wall Heat Transfer in Liquid Metal Fusion Reactor Blankets," to be published in Fusion Tech. (March 1987).

30. M.Z. Youssef and M.A. Abdou, "Neutronic Testing Requirements in Fusion Devices," Trans. Am. Nuc. Soc., 46, 234-235 (1984).

31. Y. Oyama, M.Z. Youssef and M.A. Abdou, "Operating and Geometrical Arrangement Requirements for Fusion Neutronics Testing," Fusion Tech., 8, 1484-1490 (1985).

32. J.S. Walker, "Liquid-Metal Flow in a Thin Conducting Pipe Near the End of a Region of Uniform Magnetic Field," ANL/FPP/TM-205, Argonne Natioanl Laboratory (1986).

33. M.A. Hoffman, "Magnetic Field Effects on the Heat Transfer of Potential Fusion Reactor Coolants," UCRL-73993, Lawrence Livermore National Laboratory (1972).

34. B. Brown, "Tritium in the Environment," CRNL-2739-4, Chalk River Nuclear Laboratories (1986).

35. A. Bleier, R. Kroebel, K.H. Neeb and E. Schneider, "Tritium Inventories and Behavior in Zircaloy Cladding of Spent Light Water Reactor Fuel Rods," Proc. Fuel Reprocessing and Waste Management Conf., Vol. 1, pp. 238-248 (1984).

36. K.Y. Wong, et al., "Canadian Tritium Experience," Ontario Hydro (1984).

37. J. Couture, "Status of the French Reprocessing Industry," Proc. Fuel Reprocessing and Waste Management Conf., Vol. 1, pp. 33-45 (1984).

38. M. Chazalon and B. Libin, "Strategy of Breeding Blanket Introduction in Net and Test Requirements," 14th Symposium on Fusion Technology (SOFT), Avignon, France (Sept. 1986).

39. P.J. Gierszewski, et al., "A Low-Risk Aqueous Lithium Salt Blanket for Engineering Test Reactors," 14th Symposium on Fusion Technology (SOFT), Avignon, France (Sept. 1986).

40. J.C. Hunt, "Magnetohydrodynamic Flow in Rectangular Ducts," J. Fluid Mech., 21, Part 4, 577-590 (1965).

41. J.S. Walker, G.S. Ludford and J.C. Hunt, "Three-dimensional MHD Duct Flows with Strong Transverse Magnetic Fields, Part 2: Variable-Area Rectangular Ducts with Conducting Sides," J. Fluid Mech., 46, 657-684 (1971).

42. J.S. Walker and G.S. Ludford, "Three-Dimensional MHD Duct Flows with Strong Transverse Magnetic Fields, Part 4: Fully Insulated, Variable-Area Rectangular Ducts with Small Divergences," J. Fluid Mech., 56, 481-496 (1972).

43. J.C. Petrykowski and J.S. Walker, "Liquid-Metal Flow in a Rectangular Duct with a Strong, Non-uniform Magnetic Field," J. Fluid Mech., 139, 309-324 (1984).

44. S.V. Patankar, Numerical Heat Transfer and Fluid Flow, McGraw-Hill, New York, 1980.

45. G.P. D'Arcy and P.S. Schmidt, "Entry Region Effects on Lithium Flow and Pressure Drop in Fusion-Reactor Blankets," Proc. Symp. Technology of Controlled Thermonuclear Fusion Experiments and the Engineering Aspects of Fusion Reactors, Univ. of Texas, Austin (1972).

46. E.O. Macagno and T.K. Hung, "Computational and Experimental Study of a Captive Annular Eddy," J. Fluid Mech., 28, 43-64 (1967).

47. J.M. McMichael and S. Deutsch, "Magnetohydrodynamics of Laminar Flow in Slowly Varying Tubes in an Axial Magnetic Field," Phys. Fluids, 27, 110-118 (1984).

48. P.L. Chambre, "The Laminar Boundary Layer with Distributed Heat Sources or Sinks," Applied Scientific Research, Section A, 6, 393-401 (1957).

2. NON-FUSION EXPERIMENTS AND FACILITIES

TABLE OF CONTENTS

Page

2. Non-Fusion Experiments and Facilities....2-1
2.1 Introduction....2-1
2.2 Material Properties and Uncertainties....2-6
2.2.1 Thermophysical Properties....2-6
2.2.1.1 Density....2-6
2.2.1.2 Thermal Conductivity....2-7
2.2.1.3 Specific Heat....2-12
2.2.1.4 Breeder Temperature Limits....2-12
2.2.1.5 Other Thermophysical Properties....2-17
2.2.2 Tritium Properties....2-17
2.2.2.1 Diffusion....2-18
2.2.2.2 Solubility....2-22
2.2.2.3 Surface Adsorption....2-28
2.2.2.4 Mechanical Properties....2-31
2.2.2.5 Fabrication....2-40
2.3 Solid Breeder Comparison and Testing Priorities....2-50
2.3.1 Objectives....2-50
2.3.2 Materials and Conditions....2-50
2.3.3 Performance Parameters and Results....2-57
2.3.3.1 Neutronics....2-58
2.3.3.2 Thermomechanics....2-85
2.3.3.3 Tritium....2-100
2.3.3.4 Activation....2-125
2.3.3.5 Economics....2-131
2.3.4 Conclusions and R&D Priorities....2-140
2.4 Fission Reactor Evaluation for Advanced Solid Breeder Testing....2-151
2.4.1 Introduction....2-151
2.4.2 Representative Reactor Conditions....2-154
2.4.3 Evaluation....2-157
2.4.4 Conclusions....2-176
2.5 Liquid Breeder Facilities....2-180
2.5.1 Introduction....2-180

2.5.2 LMF Facility Description.....2-186
2.5.2.1 Test Article.....2-186
2.5.2.2 Flow Loop.....2-188
2.5.2.3 Magnet System.....2-192
2.5.2.4 Instrumentation.....2-195
2.5.3 Experimental Program.....2-198

LIST OF FIGURES

Page

2.1-1 Test sequence for major solid breeder blanket tasks.....2-3

2.1-2 Test sequence for major liquid breeder blanket tasks.....2-4

2.2-1 Specific heat for various solid breeder and multiplier materials.....2-13

2.2-2 Hydrogen isotope diffusion in $LiAlO_2$.....2-19

2.2-3 Hydrogen isotope diffusion in Li_2SiO_3 and Li_4SiO_4.....2-21

2.2-4 Tritium diffusion coefficient in candidate breeder materials.....2-23

2.2-5 Hydrogen isotope solubility in various breeder materials, expressed in the form of the Sievert's law constant.....2-26

2.2-6 Tritium inventory adsorbed onto material surfaces.....2-29

2.2-7 Elastic modulus [GPa] at 25°C for various breeder materials as a function of density. Solid lines indicate experimental basis, dashed lines indicate estimated.....2-32

2.3-1 Reference blanket design.....2-52

2.3-2 One-dimensional model for the cases without a multiplier and for the homogeneous SB/M mixture cases.....2-59

2.3-3 One-dimensional model for the cases with a separate Be multiplier region.....2-60

2.3-4 Tritium breeding ratio as a function of Be region thickness for the cases with a separate Be multiplier region.....2-64

2.3-5 Tritium breeding ratio as a function of ^6Li enrichment for the cases with a separate Be multiplier region.....2-65

2.3-6 Tritium breeding ratio as a function of the solid breeder material ^6Li number density for the cases with a separate Be multiplier region (all cases have 60% ^6Li enrichment).....2-66

2.3-7 TBR as a function of ^6Li enrichment for the cases without a multiplier.....2-68

2.3-8 T_6 (TBR due to $^6Li(n,\alpha)t$) as a function of ^6Li enrichment for the cases without a multiplier.....2-69

2.3-9 T_7 (TBR due to $^6Li(n,n'\alpha)t$) as a function of ^6Li enrichment for the cases without a multiplier.....2-69

2.3-10 TBR as a function of breeder volume fraction for the homogeneous SB/M mixture cases (60% ^{6}Li).....2-70

2.3-11 TBR as a function of ^{6}Li enrichment for the homogeneous SB/M mixture cases (20/80%).....2-71

2.3-12 TBR as a function of the first breeder region thickness for the $LiAlO_2$ and Li_8ZrO_6 sandwich cases (both cases have 60% ^{6}Li enrichment).....2-73

2.3-13 Power multiplication as a function of ^{6}Li enrichment for the cases without a multiplier.....2-74

2.3-14 Power multiplication as a function of ^{6}Li enrichment for for the cases with a separate Be multiplier region.....2-74

2.3-15 Power multiplication as a function of Be region thickness for the cases with a separate Be multiplier region.....2-75

2.3-16 Power multiplication as a function of breeder volume fraction for the homogeneous SB/M mixture cases.....2-76

2.3-17 Power multiplication as a function of ^{6}Li enrichment for the homogeneous SB/M mixture cases (20/80).....2-76

2.3-18 Power multiplication as a function of the first breeder region thickness for the sandwich case.....2-77

2.3-19 Li burnup at 0.5 cm from the tip of the breeder plate after 3 full power years for the different cases (all cases have 60% ^{6}Li enrichment, except for the unmultiplied Li_2O case which has 7.5% ^{6}Li enrichment.....2-82

2.3-20 Effective tritium breeding ratio for the different cases.....2-84

2.3-21 Power multiplication for the different cases.....2-86

2.3-22 Plate configuration for 2-D temperature calculations.....2-87

2.3-23 Breeder plate configuration for stress calculations.....2-92

2.3-24 (a) Beam model for calculating stresses in clad;
(b) membrane model for calculating stresses in clad.....2-93

2.3-25 Stresses in the clad calculated from the beam model as a function of wire separation for four different solid breeders.....2-97

2.3-26 Compressive stress (σ_{comp}) on sphere pac Li_2O as a function of wire separation (δ_s).....2-98

2.3-27 Plate temperature distribution for the $LiAlO_2$+Be case.....2-103

2.3-28 Plate diffusive tritium inventory distribution for the $LiAlO_2$+Be case.....2-104

2.3-29 Plate surface adsorption tritium inventory distribution for the $LiAlO_2$+Be case.....2-105

2.3-30 Plate solubility tritium inventory distribution for the $LiAlO_2$+Be case.....2-106

2.3-31 Plate total tritium inventory distribution for the $LiAlO_2$ case.....2-107

2.3-32 Upper and lower limits of calculated tritium inventory for the cases without a multiplier and for the homogeneous SB/M mixture cases.....2-109

2.3-33 Upper and lower limits of calculated tritium inventory for cases with a separate Be multiplier region.....2-110

2.3-34 Plate temperature distribution for $LiAlO_2$+Be case with a 0.076 cm thick crack at x = 0.95 cm and y = 0 to 3.9 cm; k_{crack} = 0.43 W/m-K.....2-113

2.3-35 Plate diffusive tritium inventory distribution for $LiAlO_2$+Be case with a 0.076 cm thick crack at x = 0.95 cm and y = 0 to 3.9 cm; k_{crack} = 0.43 W/m-K.....2-114

2.3-36 Plate surface adsorption tritium inventory distribution for $LiAlO_2$+Be case with a 0.076 cm thick crack at x = 0.95 cm and y = 0 to 3.9 cm; k_{crack} = 0.43 W/m-K.....2-115

2.3-37 Plate solubility tritium inventory distribution for $LiAlO_2$+Be case with a 0.076 cm thick crack at x = 0.95 cm and y = 0 to 3.9 cm; k_{crack} = 0.43 W/m-K.....2-116

2.3-38 Plate total tritium inventory distribution for $LiAlO_2$+Be case with a 0.076 cm thick crack at x = 0.95 cm and y = 0 to 3.9 cm; k_{crack} = 0.43 W/m-K.....2-117

2.3-39 Diffusive inventory in multiplier region as a function of the diffusion coefficient.....2-119

2.3-40 Cost per module for the different solid breeder cases (the chosen ^6Li enrichment for each case is shown in between parentheses).....2-133

2.3-41 Thermal efficiency for the different cases (The PPR for each case is also shown in brackets).....2-136

2.3-42 Pumping power required for the purge flow as a function of plate thickness for different purge flow total volume flow rates.....2-139

2.3-43 Point graph of the effective tritium breeding ratio and of the reciprocal of the total tritium inventory in the solid breeder for the different cases.....2-145

2.3-44 Point graph of the reciprocal of material cost for a blanket module and of the power multiplication for the different cases.....2-148

2.3-45 Point graph of the afterheat time to reach the maximum allowable temperature and of the reciprocal of the dose rate after 3-year irradiation and 10-hour cooling for the different cases.....2-149

2.4-1 Microscopic neutronics calculations for representative Light Water Reactor (LWR) and Fast Test Reactors (FTR) compared to anticipated tritium production and heat generation rates for the Li_2O/He/HT9 blanket concept.....2-152

2.4-2 Microscopic neutronics calculations for representative Light Water Reactor (LWR) and Fast Test Reactors (FTR) compared to anticipated tritium production and heat generation rates for the $LiAlO_2/H_2O$/HT9 blanket concept.....2-153

2.4-3 Comparison of neutron spectra for the FFTF, NRU, and HFIR reactors normalized to their total flux.....2-156

2.4-4 Schematic of one-dimensional model used to calculate tritium production and heat generation rates.....2-158

2.4-5 Total neutron heating rate as a function of ^6Li enrichment for the representative reactors.....2-170

2.4-6 Total tritium production rates as a function of ^6Li enrichment for the representative reactors.....2-170

2.4-7 Anticipated temperature profiles in FFTF, HFIR, and NRU reactors.....2-174

2.4-8 Influence of ^6Li enrichment on temperature profile in the NRU reactor.....2-175

2.4-9 Time evaluation of tritium production rates in the HFIR reactor.....2-177

2.4-10 Decrease in total tritium production as a function of test time in the HFIR reactor.....2-177

2.4-11 Time evaluation of tritium production rates in the NRU reactor.....2-178

2.5-1 Hartmann number, M, and interaction parameter, N, ranges for the blanket, in general, and the first wall coolant channels, in particular. The portion of the parameter space which can be covered by testing at ALEX, ALEX Upgrade, and LMF (with a 5 T magnet) is also shown.....2-184

2.5-2 Conceptual design of a test section simulating the salient features of the BCSS liquid metal-cooled blanket design.....2-187

2.5-3 Conceptual design of a test section simulating the inlet (or outlet) manifold of the TPSS design. Flows in each of the individual ducts fed from the manifold can be measured with individual EM flow meters.....2-188

2.5-4 Schematic of LMF loop.....2-189

2.5-5 An example of a superconducting dipole magnet of the scale required for LMF. The magnet shown was built for DOE's Plasma MHD Energy Conversion Program and has a tapered field with a peak value of 6 T, a tapered warm bore with a maximum diameter of 109 cm and minimum diameter of 80 cm, and a warm bore length of 640 cm. It weighs 172 metric tons.....2-193

2.5-6 Solenoid magnet for LMF (all dimensions in centimeters).....2-194

LIST OF TABLES

Page

2.1-1 Key Blanket Issues....2-2

2.1-2 Phases of Blanket Testing....2-2

2.2-1 Solid Breeder/Multiplier Materials and Properties Considered....2-6

2.2-2 Density Of Candidate Solid Breeder and Multiplier Materials....2-7

2.2-3 Representative Reported Thermal Conductivities for Candidate Breeder and Multiplier Materials at Various Conditions....2-8

2.2-4 Effect of Several Material Variables on the Thermal Conductivity of $LiAlO_2$ and Li_2O....2-9

2.2-5 Reference Thermal Conductivity for Candidate Solid Breeder and Multiplier Materials....2-12

2.2-6 Upper Temperature Limits for Candidate Solid Breeder and Multiplier Materials (°C)....2-15

2.2-7 Estimated Tritium Diffusion Coefficients for Candidate Solid Breeder and Multiplier Materials....2-24

2.2-8 Hydrogen Diffusion Coefficient in Metal Oxides....2-24

2.2-9 Hydrogen Isotope Solubility in Various Materials....2-27

2.2-10 Suggested Values for Unirradiated Elastic Modulus for Candidate Solid Breeder and Multiplier Materials and for Metal Oxides....2-33

2.2-11 Linear Thermal Expansion Coefficient (α) Data for Various Materials....2-36

2.2-12 Summary of Mechanical Properties at 300 K for Candidate Solid Breeder and Multiplier Materials....2-37

2.2-13 Poisson's Ratio Data for Various Materials....2-38

2.2-14 Fracture Strength Data for Various Materials....2-39

2.2-15 Candidate Solid Breeder and Multiplier Fabricated Grain Size (μm)....2-41

2.2-16 Material Costs and Estimates from Previous Studies....2-42

2.2-17 Unit Cost Estimates for Breeder Materials....2-44

2.2-18 Typical Impurity Levels in Primary Feed Materials (wppm)....2-46

2.2-19 Reported Impurity Levels In Breeder Materials (wppm).....2-48

2.2-20 Reference Impurity Levels for Candidate Breeder and Multiplier Materials (wppm).....2-49

2.3-1 Solid Breeder Materials Considered.....2-51

2.3-2 Blanket Concept Parameters (SB = Solid Breeder; M = Multiplier).....2-54

2.3-3 Performance Parameters.....2-57

2.3-4 Volume Fractions for the Cases Without a Multiplier and for the Homogeneous SB/M Mixture Cases.....2-61

2.3-5 Volume Fractions for the Cases With a Separate Be Multiplier Region.....2-62

2.3-6 Lithium Atom Density for the Different Solid Breeder Cases.....2-63

2.3-7 ^{6}Li Enrichment and Atom Density at TBR Saturation (99% of Maximum TBR) for Cases With a Separate Be Multiplier Region.....2-67

2.3-8 Maximum Heating, TBR and M for the Different Cases.....2-78

2.3-9 Tritium Production Rate at 0.5 cm from Tip of Plate, TPR (All Cases Have 60% ^{6}Li Enrichment Except for Unmultiplied Li_2O Which has Natural Li).....2-80

2.3-10 Plate Thickness and Volume Fractions for the Different Cases (With 60% ^{6}Li Enrichment Except for the Unmultiplied Li_2O Case).....2-90

2.3-11 Breeder Volume Fractions Calculated Assuming Constant Thermal Conductivity (k) and Temperature Dependent Thermal Conductivity (k(t)).....2-91

2.3-12 Volumetric Swelling, Thermal Expansion, and Resulting Maximum Clad Deflections for Four Different Solid Breeder Cases.....2-96

2.3-13 Thermal Stresses in Sintered Block Solid Breeder Materials.....2-99

2.3-14 Tritium Inventory Results for the Different Cases.....2-108

2.3-15 Effect of a Crack With Low Thermal Conductivity on the Plate Maximum Temperature and Tritium Inventory (Crack Location Is At x = 0.95 cm, y = 0 to 3.9 cm).....2-118

2.3-16 Tritium Diffusive Inventory in the Multiplier for the Four Homogeneous Breeder/Multiplier Mixture Cases.....2-122

2.3-17 Tritium Permeation for Solid Breeder Blankets.....2-124

2.3-18 Activation After Three Year Irradiation at 5 MW/m^2 for Reference Design at Front of Breeder Region.....2-127

2.3-19 Elements Providing Greatest Contribution to Activation After 3 Year Irradiation, 10 h Cooling for Reference Design at Front of Breeder Region.....2-127

2.3-20 Elements Providing Greatest Contribution to Activation After 3 Year Irradiation, 10 y Cooling for Reference Design at Front of Breeder Region.....2-128

2.3-21 Time After Shutdown to Reach the Solid Breeder Maximum Allowable Temperature.....2-130

2.3-22 Blanket Material and Fabrication Costs.....2-132

2.3-23 Total Power Leakage at the Back of the 30 cm Partial Shield for the Different Cases.....2-141

2.3-24 Summary of the Performance Results for All Cases.....2-142

2.4-1 Fission Reactor Capabilities Reactor Characteristics.....2-155

2.4-2 Calculational Models for HFIR and NRU and FFTF.....2-159

2.4-3 Calculational Model of Lithium Oxide Fusion Blanket Test Pin Geometries.....2-159

2.4-4 Material Atom Densities.....2-160

2.4-5 Spectrum of FFTF Boundary Source.....2-161

2.4-6 Spectrum of HFIR Boundary Source.....2-162

2.4-7 Spectrum of NRU Boundary Source.....2-164

2.4-8 Neutronics Results for Solid Li_2O Test Pin Geometry in FFTF.....2-167

2.4-9 Neutronics Results for Solid Li_2O Test Pin Geometry in HFIR.....2-168

2.4-10 Neutronics Results for Annular Li_2O Test Pin Geometry in HFIR.....2-169

2.4-11 Neutronics Results for Solid Li_2O Test Pin Geometry in NRU.....2-172

2.4-12 Neutronics Results for Annular Li_2O Test Pin Geometry in NRU.....2-173

2.5-1 Features and Objectives of Major Liquid Breeder Experiments.....2-183

2.5-2 LMF Loop Parameters.....2-191

2. NON-FUSION EXPERIMENTS AND FACILITIES

2.1 Introduction

Non-fusion experiments can play a key role in the development of fusion nuclear technologies. This was recognized in earlier studies and incorporated as a central element in the FINESSE test plans for blankets and other nuclear components.[1] Recent effort in the Technical Planning Activity[2] (TPA) has confirmed the importance of these experiments. This chapter focuses on the near-term non-fusion experiments for blankets, with emphasis on solid breeders. Analysis is performed for important aspects concerning the technical planning, selection and design of these near-term experiments.

Non-fusion facilities include non-neutron test stands, fission reactors, and point neutron sources. Each of these provide unique testing capabilities for blanket experiments. The key issues for solid breeder blankets are shown in Table 2.1-1. Because of the dominant role that radiation plays in tritium production, tritium transport, and breeder thermomechanical behavior, fission reactors are essential to the solid breeder test program. Table 2.1-1 also summarizes the key issues for liquid breeder blankets. These issues generally involve thermomechanical behavior (including MHD effects), material compatibility, and tritium recovery. Experiments addressing these issues are generally best treated in non-neutron test stands. For all blankets, fuel self-sufficiency is a key issue. 14-MeV neutron sources are an important resource for experiments on tritium breeding as well as other neutronic issues.

A framework for planning fusion nuclear experiments has been developed in our earlier effort.[1] This framework defines four phases during which the emphasis shifts in the level of integration from separate effects, to multiple effects, to partially integrated fusion testing, and finally to fully integrated fusion testing. The detailed test plans for both solid and liquid breeder blankets are shown in Figures 2.1-1 and 2.1-2. Both plans culminate in the design of experimental modules for testing in the fusion environment and in an assessment of the feasibility and attractiveness of blanket components and systems. Intermediate objectives and milestones are shown in Table 2.1-2.

In this chapter, an emphasis has been placed on critical near-term experiments (Phase I in Table 2.1-2). For solid breeder blankets, material selec-

Table 2.1-1 Key Blanket Issues

Solid Breeder
tritium self-sufficiency
breeder/multiplier tritium inventory and recovery
breeder/multiplier thermomechanical behavior
corrosion and mass transfer
structural response and failure modes
tritium permeation and processing from the blanket
Liquid Breeder
tritium self-sufficiency
magnetohydrodynamic effects
material interactions
structural response and failure modes
tritium recovery and control

Table 2.1-2 Phases of Blanket Testing

	Approximate Time Frame	Level of Integration	Primary Objectives	Milestones
Phase I	0-10 yrs	properties, separate effects	develop understanding of material behavior and blanket phenomena	select material combinations[a]
Phase II	5-15 yrs	multiple effects	understand phenomena, develop predictive capabilities for complex configurations	select blanket configurations
Phase III	10-20 yrs	partially integrated (non-fusion)	design concept verification in non-fusion environment	select primary blanket design options for fusion testing
Phase IV	15-25 yrs	integrated	design concept verification in fusion facility	successfully operate test modules

[a]To the extent possible with limited high fluence irradiation data

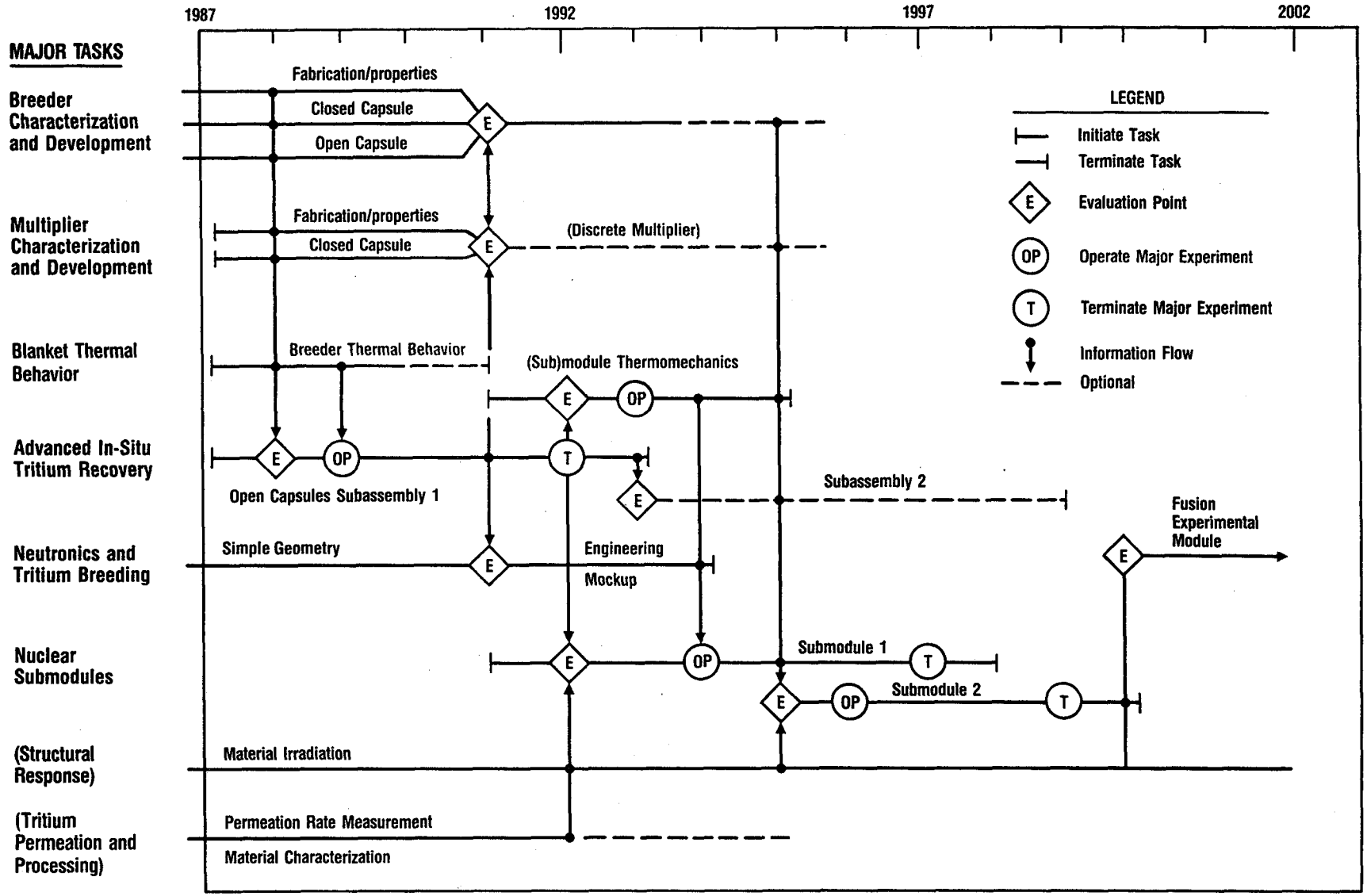


Figure 2.1-1 Test sequence for major solid breeder blanket tasks

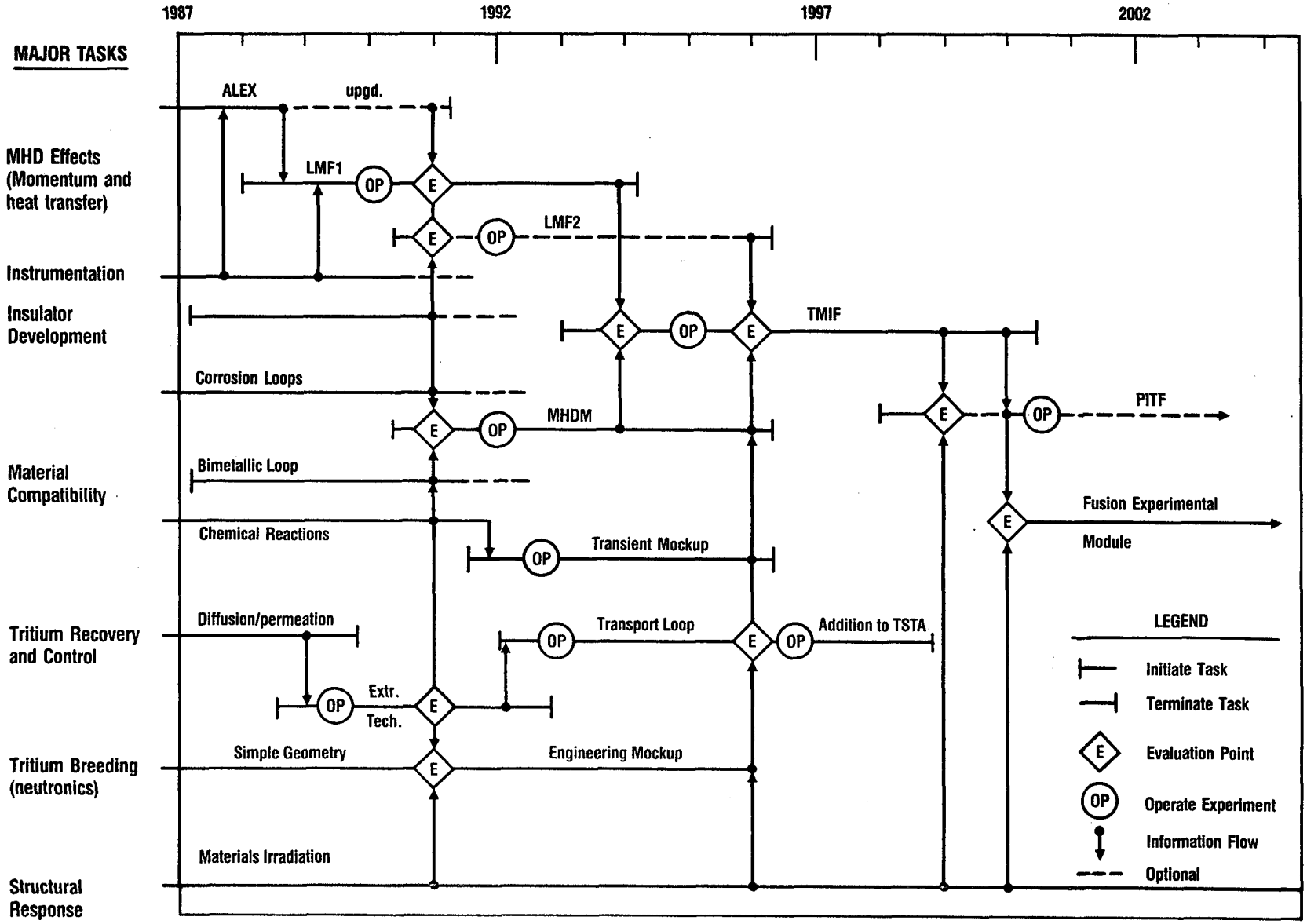


Figure 2.1-2 Test sequence for major liquid breeder blanket tasks

tion and characterization are currently at the center of worldwide attention. On-going and near-term experiments are focused on open and closed capsule assemblies for characterizing breeder/multiplier characteristics, including in-situ tritium recovery. At the same time, the international programs currently encompass a large number of candidate materials and configurations. It would be useful to assess the relative advantages of the various solid breeder materials and develop recommendations for the test matrix in upcoming experiments. This is particularly important because of the increased cost of the more complex next-generation experiments. In light of this, detailed analyses have been performed to compare different solid breeder materials and configurations. They are described in Section 2.3. The comparison was based on different performance parameters directly dependent on the solid breeder properties. Prior to the calculations, these properties were carefully assembled from data taken from the literature and past experiments, and a confidence range was included wherever appropriate, as described in Section 2.2. The performance parameter results were then used to evaluate the different solid breeder cases so as to focus the experimental program on the more attractive solid breeder candidates and the more important property uncertainties. In addition, the capabilities of existing fission reactors have been assessed in order to provide recommendations on the facilities in which future solid breeder experiments can be performed. The results are discussed in Section 2.4.

For liquid breeder blankets, the test program is not dominated by a single central element since the nature of the most critical issues depends strongly on the choice of liquid breeder and blanket type. For the large and important class of designs known as self-cooled liquid metal blankets, MHD effects are a dominant concern. Separate effects tests are currently planned or underway in several countries to address MHD fluid flow and pressure drop issues. The ALEX facility in the U.S. is currently the most advanced facility for exploring MHD issues. After ALEX and similar experiments, the need for an advanced MHD facility, called LMF1, has been identified (see Figure 2.1-2) The characteristics of this facility and the experiments which might be performed are explored in Section 2.5.

2.2. Material Properties and Uncertainties

The feasibility and attractiveness of a solid breeder blanket is driven to a large extent by the properties of the solid breeder and multiplier materials. However, the uncertainties in the properties of present candidate materials are quite large since there are often limited or non-existent data. Furthermore, these materials and their engineered properties are still evolving. In this section, the available data are summarized and consistent estimates provided for the major engineering properties (and their uncertainty) for several candidate solid breeder and multiplier materials (Table 2.2-1).

Table 2.2-1 Solid Breeder/Multiplier Materials and Properties Considered

Materials		Properties
Li_2O		Density
$LiAlO_2$		Thermal conductivity
Li_5AlO_4		Specific heat
Li_2SiO_3		Temperature limits
Li_4SiO_4		Tritium diffusivity
Li_2ZrO_3		Tritium solubility
Li_8ZrO_6		Tritium surface adsorption
Li_2TiO_3		Elastic modulus
$Li_2Be_2O_3$		Thermal expansion
Li_7Pb_2		Poisson's ratio
Be		Fracture strength
BeO		Material cost
		Grain size
		Impurities

2.2.1 Thermophysical Properties

2.2.1.1 Density

The densities for the various solid breeders are generally available at room temperature, and are summarized in Table 2.2-2. The density depends on the particular ceramic phase, which is also indicated. Reported densities for

Table 2.2-2 Density of Candidate Solid Breeder and Multiplier Materials

Material	Phase	Temperature (°C)	Density Total	$(g/cm^3)^a$ Lithium	References
Li_2O	-	25	2.01	0.94	3-5
$LiAlO_2$	γ	25	2.55	0.27	3-5
Li_5AlO_4	β	25	2.22	0.61	3-5
Li_2SiO_3	-	25	2.52	0.39	3-5
Li_4SiO_4	α	25	2.39	0.55	4
	γ	665	2.21	0.51	4
Li_2ZrO_3	mono	25	4.15	0.38	3-5
Li_8ZrO_6	-	25	3.01	0.69	4,5
Li_2TiO_3	β	25	3.43	0.43	4
	γ	1150	2.57	0.32	4
$Li_2Be_2O_3$	-	25	2.54	0.43	6
Li_7Pb_2	-	25	4.59	0.48	3
BeO	-	25	3.0	0	7
Be	-	25	1.85	0	8
Zr_5Pb_3	-	25	9.69	0	9

[a]100% theoretical density

γ-$LiAlO_2$ vary from about 2.55[4,5] to 2.61 g/cm^3,[10] possibly depending on the amount of α (3.40 g/cm^3) or β (2.68 g/cm^3) phase present. For Li_4SiO_4, there are two stable phases which change at 665°C.[4] Refs. [2,5] give densities of 2.28 g/cm^3 for Li_4SiO_4 without specifying the temperature. The monoclinic Li_2ZrO_3 is stable up to 1100°C, where it then changes to tetragonal form. For Li_2TiO_3, the β-phase density is listed, but it transforms to the γ-phase with a density of 2.57 g/cm^3 above 1150°C.[4] Refs. [3,5] list the γ-phase density for Li_2TiO_3, although the β-phase would be more appropriate over most of the blanket.

2.2.1.2 Thermal Conductivity

Table 2.2-3 summarizes reported thermal conductivities for candidate breeder and multiplier materials. The effects of porosity, temperature, irradiation or sphere-pac form can be seen, but are illustrated more clearly for $LiAlO_2$ in Table 2.2-4, based largely on theoretical calculations.[5,11-13]

Table 2.2-3 Representative Reported Thermal Conductivities For Candidate Breeder and Multiplier Materials at Various Conditions

Material	Thermal Conductivity (W/m-K)	Form	Density (% TD)	Temperature (K)	Reference
Li_2O	4.8	Sintered/He	85	800	4
	4.5	Sintered	85	800	12
	2.5	Sint/Irrad	85	1000	5
	1.3	Sphere/Irrad	87	1000	5
$LiAlO_2$	2.3	Sintered	85	800	12
	2.3	Sintered	85	800	4
	2.0	Sintered	78	800	10
	2.5	Sintered	85	1000	14
	1.6	Sint/Irrad	85	1000	5
	1.1	Sphere/Irrad	87	1000	5
	7.3	Sintered	90	400	14
	4.4	Sintered	90	800	14
Li_5AlO_4	2.3	Sintered	85	1000	5
Li_2SiO_3	2.0	Sintered	80	873	15
	1.5	Sintered	85	1000	5
Li_4SiO_4	2.3	Sintered/He	85	800	4
	1.5	Sintered	85	1000	5
Li_2ZrO_3	2.2	Sintered	85	800	4
	1.3	Sintered	85	1000	5
Li_8ZrO_6	2.8	Sintered	100	800	16
	1.8	Sintered	85	1000	5
Li_2TiO_3	1.8	Sintered/vac	81	800	4
	2.0	Sintered	85	1000	5
Li_7Pb_2	17	-	-	-	13
Be	190	-	-	300	17
	96	Sintered	100	870	18
	103	-/Unirrad	-	800	19
	103	-/Irrad	-	800	19
BeO	51	Polycrystal	100	810	20
	66	-/Unirrad	-	800	19
	36	-/Irrad	-	800	19
Zr_5Pb_3	7.5	-	-	293	9
Pb	33	-	100	293	9
Li	44	-	100	450	17
$Li_{17}Pb_{83}$	16	-	100	-	3
ZrO_2	2.0	Polycrystal	100	810	20
TiO_2	3.9	Polycrystal	100	810	20
SiO_2	1.5	Glass	100	370	7

Table 2.2-4 Effect of Several Material Variables on the Thermal Conductivity of $LiAlO_2$ and Li_2O

Density (% TD)	Temperature (°C)	Form	Fluence (n/m^2)	Helium (MPa)	Thermal Conductivity[a]	
					Li_2O (W/m-K)	$LiAlO_2$ (W/m-K)
100	700	Sintered	0	-	4.8	2.6
85	700	Sintered	0	-	3.8	2-2.5
85	400	Sintered	0	-	5.2	2.5
85	700	Sintered	10^{18}	-	2.5	1.6
87	700	Sphere-pac	0	0.1	1.4	1.2
87	700	Sphere-pac	0	0.6	2.2	1.7
87	700	Sphere-pac	10^{18}	0.1	1.2	1.1
87	727	Sphere/80% Be	10^{18}	0.1	-	1.6
87	727	Sphere/80% Be	10^{18}	0.6	-	3.0

[a]Underlined values have been measured, the rest are extrapolated.

The effect of temperature (T) and porosity (ε) can usually be described by a relation of the form:[10,12,21]

$$k = k_0\ (T)\ \frac{1 - \varepsilon}{1 + C\ \varepsilon}$$

Ref. (21) suggests the following expressions:

$k_0 = 100/(1.40 + 0.01828\ T)$ Li_2O

$k_0 = 1.47 + 943/T$ $LiAlO_2$

$k_0 = 1.98 + 850/T$ Li_4SiO_4

$k_0 = 1.174 + 1260/T$ Li_8ZrO_6

$k_0 = 1.02 + 668/T$ Li_2ZrO_3

and $C = 1.95 - 0.0008\ T$

where k_0 is in W/m-K, ε is fractional porosity, and T is in K. There are data for $LiAlO_2$ which show that the thermal conductivity is constant at about 2.4 W/m-K for temperatures from 800 to 1400 K, much higher than expected from lower temperature extrapolations.[11,14]

The available data for Li_5AlO_4 and Li_4SiO_3 are similar enough to $LiAlO_2$ and Li_4SiO_4 that the latter expressions may be used as a first approximation. The only reported data for Li_2TiO_3 show less than 10% temperature dependence over 100-1000°C.[4] For 100% dense BeO and Be, the temperature dependence can be described by:[18,20]

Be: $k = 182 - 0.1\ T$

BeO: $k = -40 + 73860/T$

There are no data on thermal conductivity for the lithium beryllates. Two analogies might be drawn in order to make an estimate. First, the lithium metal oxides are similar to those of the corresponding single metal oxides, which would imply a very good thermal conductivity for the beryllate based on BeO (possibly 10 W/m-K). Alternately, the various ternary ceramics for which there are data have similar thermal conductivities, which would imply a low thermal conductivity for the beryllate (around 2 W/m-K).

Factors in sphere-pac thermal conductivity include solid- and gas-phase conduction, temperature jumps at the solid/gas interface and contact resistance at the solid/solid interface.[12,13] The thermal conductivity is affected by the sphere size distribution (which also defines the porosity), and by the fill gas. From fission reactor experience, a sphere-pac bed with 87% theoretical density can be achieved with a mix of 1200-, 300- and 30-micrometer spheres.[12] For the same density, the sphere-pac thermal conductivity is reduced from the sintered material value due to the additional interface effects. Factors of three reduction are reported for UO_2.[12]

The importance of the fill gas depends on the thermal conductivity in the solid phase. For ceramic solid breeders, the solid thermal conductivity is sufficiently low that the sphere-pac bed heat transport is affected by the gas, and particularly by its pressure. Although the thermal conductivity of a gas is not generally a function of pressure at the 0.1-1 MPa conditions of interest here, the temperature jump effect at the gas/solid interface represents an inefficiency in heat transfer that decreases with increasing pressure. UO_2 data[12] and models[13] indicate that this pressure effect saturates above 0.6 MPa helium gas in ceramic breeder blankets. For 85% dense material, increasing the helium gas from 0.1 to 0.6 MPa increases the thermal

conductivity by about 1 W/m-K for UO_2 and Li_2O, and 0.5 W/m-K for $LiAlO_2$[12] over the range of temperature (and possibly irradiation) of interest.

In some breeder concepts, multiplier and breeder materials are mixed together. Since beryllium has a high thermal conductivity, the average effective thermal conductivity can be improved over the breeder material alone. Factors of 2-3 improvement are expected for sphere-pac $LiAlO_2$ mixed with Be spheres as the beryllium content changes from 0 to 100%.[5]

Irradiation reduces the solid thermal conductivity through displacements and cascade damage, possibly improves the contact conductance by promoting sintering, and has no effect on the gas-phase transport. Irradiation has been observed to have a 50% effect on UO_2, and 10-75% effects on Al_2O_3, Y_2O_3-1% ZrO_2, $MgAl_2O_4$ and MgO for sintered material at conditions of interest. There were indications of saturation around a neutron fluence equivalent to 1 MW-yr/m^2. Based on an analysis of this data, irradiation is expected to reduce the solid phase thermal conduction by 50% for Li_2O and 25% for $LiAlO_2$. Data in Ref. [19] show no significant irradiation effect in Be at high fluence, but a 50% reduction for BeO to about 40 W/m-K at 800 K. For sphere-pac material, the overall effect is reduced because the heat transport is generally limited by processes other than the solid phase conduction.

In Table 2.2-5, thermal conductivities are suggested for the candidate materials at the same conditions - 85% dense sintered material at 1000 K after about 1 MW-yr/m^2 irradiation. Radiation effects are extended by analogy to all the materials. In particular, it is assumed that the ternary ceramics with similar thermal conductivity before irradiation will have similar thermal conductivity after irradiation, and that the effects of irradiation on metallic compounds is small.

The variation of thermal conductivity with temperature, form, porosity and irradiation can be quite large and is generally unmeasured, and even the existing data shows considerable variation between different investigators at apparently similar conditions. For example, the thermal conductivities recently measured in $LiAlO_2$ at high temperature[14] were about 30% higher than expected. Overall, thermal conductivities appear uncertain by about 30%.

Table 2.2-5 Reference Thermal Conductivity for Candidate Solid Breeder and Multiplier Materials[a]

Material	Thermal Conductivity		
	Unirradiated 800 K (W/m-K)	Unirradiated 1000 K (W/m-K)	Irradiated 1000 K (W/m-K)
Li_2O	4.5	3.8	2.5
$LiAlO_2$	2.9	2.5	2.0
Li_5AlO_4	2.7	2.3	1.8
Li_2SiO_3	2.4	2.0	1.5
Li_4SiO_4	2.4	2.0	1.5
Li_2ZrO_3	1.8	1.8	1.3
Li_8ZrO_6	2.4	2.0	1.5
Li_2TiO_3	1.9	1.9	1.5
$Li_2Be_2O_3$	2.4	2.0	1.5
Li_7Pb_2	17	17	17
Be	100	72	72
BeO	60	40	25
$LiAlO_2$/Be	3.0	2.7	2.5 (20/80)

[a]Suggested values for 85% dense sintered material at ~ 1 MW-yr/m^2 irradiation.

2.2.1.3 Specific Heat

The results of a literature survey on specific heats have been plotted on Figure 2.2-1. The curves have been estimated using data from the following references: Li_2O;[22-24] Li_2TiO_3;[23] $LiAlO_2$;[7,10,23,25] $Li_2Be_2O_3$;[17] $LiAl_5O_8$;[23] BeO;[20,22,24] Li_2SiO_3;[23] Be;[7,17,22] Li_4SiO_4;[23] LiAl;[23] Li_2ZrO_3;[4,23] Pb;[7] and Li_8ZrO_6.[16,26] The Li_7Pb_2 specific heat was estimated from Li and Pb specific heat using the Dulong-Petit Rule.[7] The data were consistent within 0.1 kJ/kg-K or less up to 1000 K. Above this, there was much less data and the curves in Figure 2.2-1 can be considered uncertain by 0.2 kJ/kg-K.

2.2.1.4 Breeder Temperature Limits

The breeder and multiplier materials have temperature limits which define a range of temperature conditions acceptable for fusion blanket designs.

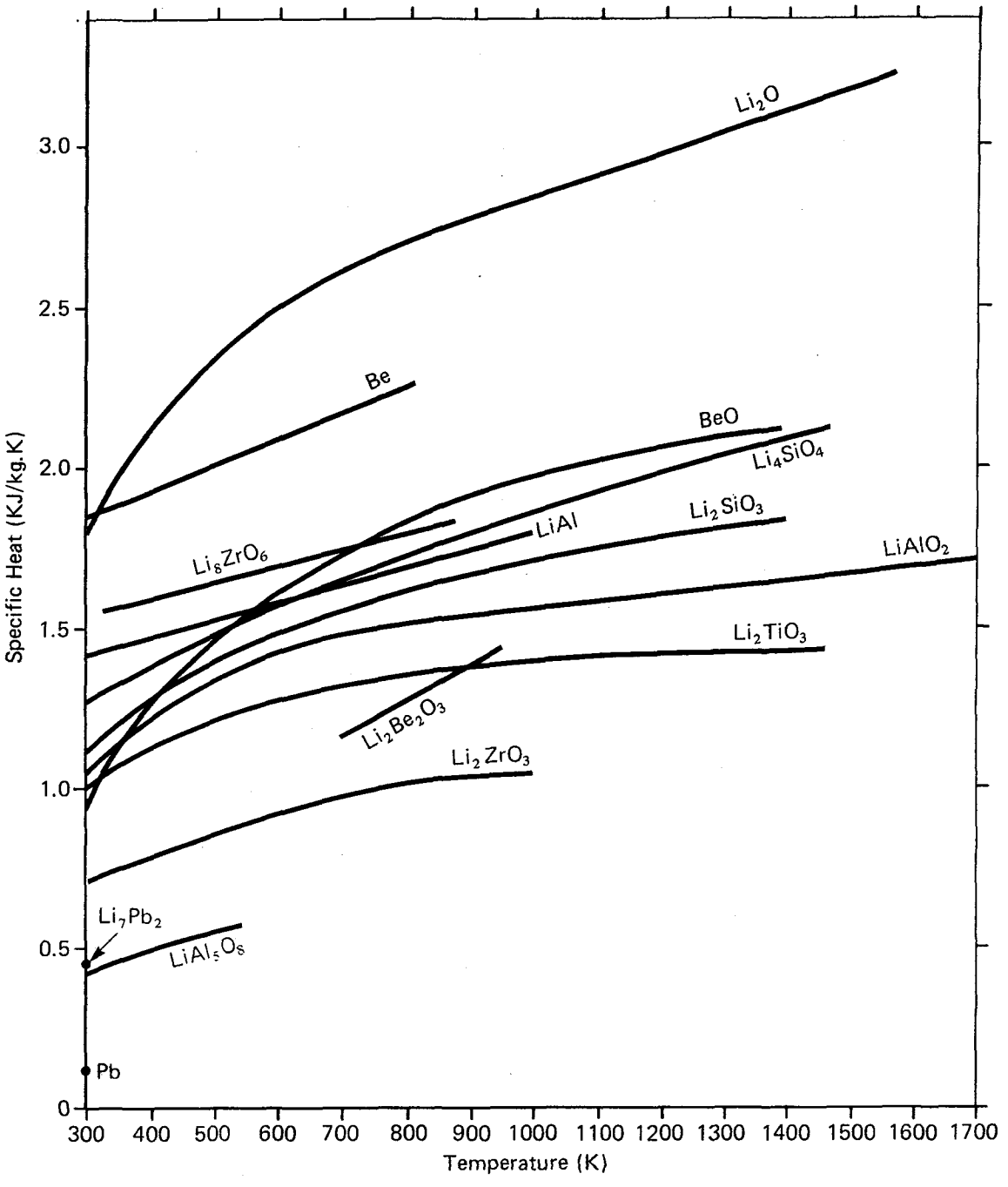


Figure 2.2-1 Specific heat for various solid breeder and multiplier materials

In most materials, a lower temperature limit does not reflect a change in behavior, but rather the decreasing mobility of tritium at lower temperatures. To the extent that the tritium transport characteristics (e.g., diffusivity, solubility, surface adsorption) are known at lower temperatures, the tritium inventory can be calculated. Since the temperature profile is blanket specific but defines the total blanket inventory, the lower temperature limit is dependent on the blanket design. For example, in a blanket with hot reactor-relevant helium coolant, the breeder material would probably be hot enough for diffusion to be reasonably fast, but the same breeder material with cold water coolant in an Engineering Test Reactor may have unacceptable tritium retention. In this sense, a low temperature limit cannot be defined as a material-specific parameter. Rather, there is simply a need to make sure that tritium properties are available over the full range of temperatures.

In Li_2O at temperatures below about 410°C, LiOH becomes a stable phase at high hydrogen concentrations.[5] Of more concern at reactor conditions is an apparent decrease in the diffusion rate due possibly to the formation of a tritium/vacancy complex. Also, in BeO, microcracking may also set a minimum temperature limit depending on the irradiation exposure and the extent to which its mechanical integrity is important.[1]

The upper temperature is set by breeder material changes that lead to loss of integrity or reduced ability to purge the tritium from the blanket. There may be additional blanket design constraints due to cladding temperature limits, but these are not breeder-specific. Table 2.2-6 lists various breeder-specific factors that influence the upper temperature limit.

The melting temperatures for the breeder materials are listed in Table 2.2-6. In practice, the important breeder microstructure and porosity would be changed well before the melting point was reached, leading to irreversible changes in the ability to recover the bred tritium.

Fission reactor data indicate that significant vapor phase mass transport occurs at around 0.1 Pa vapor pressure in a static environment. In a fusion breeder, this mass transport could lead to closure of pores and possibly mass loss. The lithium species vapor pressure in a breeder material can be a significant function of oxygen activity as well as temperature.[27] Table 2.2-6 indicates the vapor pressure limit based on the highest lithium species vapor pressure over, if specified, an oxygen activity range of 10^{-20} to 10^{-10}.

Table 2.2-6 Upper Temperature Limits for Candidate Solid Breeder and Multiplier Materials (°C)

Material	Melting	Vapor Pressure[a]	Sinter[b]	Other	Limit[c]	Range[d]
Li_2O	1433	800,[27] 1200,[3] 1100[4,28]	850 800[29]	500 creep	800	500- 900
$LiAlO_2$	1610	1100,[27] 1300,[28] 1400[3,4]	970 > 1000[29]	-	970	850-1200
Li_5AlO_4	1047	1000,[3] 1100,[28] 1200[4]	600	-	600	520- 800
LiAl	717	560[3]	380	-	380	320- 520
$LiAl_5O_8$	1950	1400-1700[3]	1190	-	1190	1060-1500
Li_2SiO_3	1200	1300[4,28]	700	1150 at 30% BU	700	610- 900
Li_4SiO_4	1250	900,[27] 1200[3,28]	730 950[29]	665 phase chnge 1250 at 30% BU	730	640- 950
Li_2TiO_3	1540	-	920	1430 at 30% BU	920	820-1200
Li_2ZrO_3	1610	1300[4,28]	970	-	970	860-1200
Li_8ZrO_6	1295	1200[4,28]	760	660 phase chnge	760	670- 980
Li_7Pb_2	726	-	390 > 600[29]	600-1000 swell. 570 at 30% BU	420	330- 530
$Li_2Be_2O_3$	1150	-	670	-	670	580- 870
Be	1285	1100[7]	750	500-600 swell. 700 helium comp	650	500- 970
BeO	2540	-	1580	-	1580	1400-2000
Li_2O/Be	(Be)	-	-	Compatibility	(Be)	
Li_2O/BeO	(Li_2O)	-	-	Compatibility	(Li_2O)	
$LiAlO_2$/Be	(Be)	-	-	Compatibility	(Be)	
$LiAlO_2$/BeO	($LiAlO_2$)	-	-	Compatibility	($LiAlO_2$)	

[a]Significant vapor pressure (0.1 Pa total Li-bearing vapor for oxygen activity of 10^{-20}, 10^{-10}, 10^{-10})

[b]0.66 T_{melt} for onset of radiation-induced sintering

[c]Suggested upper temperature limit set by sintering, except for Li_2O and Be where vapor pressure and swelling influence limit

[d]Lowest temperature limit or 0.6 T_{melt}, to 0.8 T_{melt}

In some cases, the different values are based on different vapor species. For the breeder ceramics, the Li and LiOH vapor pressures set the mass transport temperature limit.

Also, from fission reactor data, thermal sintering is generally observed at about 0.8 T_{melt}, while radiation-induced sintering can occur at 0.6-0.66 T_{melt}. The sintering temperatures listed in Table 2.2-6 reflect the 0.66 T_{melt} radiation-induced limit. This approximation was arbitrarily extended to the metallic compounds. Ref. [29] provides sintering limits for some materials without significant irradiation and is more consistent with the 0.8 T_{melt} approximation. There are recent indications that tritium transport is quite fast in very low porosity materials, at least for Li_2O, Li_4SiO_4, and perhaps $LiAlO_2$. If true, then sintering need not be as much a limit as has been assumed.

Swelling is a complex function of temperature and fluence, and is also susceptible to design solution (e.g., perhaps by starting with higher porosity), so it does not clearly provide an absolute temperature limit. Swelling temperature limits are provided where there is a temperature at which a significant amount of swelling (e.g., 10 vol. %) occurs at a fluence roughly equivalent to 10 MW-yr/m^2. For beryllium, this occurs at 500-600° C.[8] The corresponding upper temperature limit was chosen to limit, but not necessarily prevent, swelling. Swelling was also identified as a concern for Li_7Pb_2 at possibly 1 MW-yr/m^2.[3]

In some blanket concepts, mixed breeder/multiplier materials may be used.[5] Chemical reactions, particularly between beryllium and oxide ceramics, could alter the chemical properties of the breeder and affect tritium transport. However, the temperature dependence and kinetics of the reactions are not known (e.g., will a BeO layer form on Be that retards further reactions?) and so are not included here. Also, some breeder materials are fairly soft and may creep at high temperatures leading to loss of open porosity. For Li_2O, this has been identified as a potential concern at as low as 500°C. It is probably not a concern for the ternary oxides, but might be for Li_7Pb_2.

As the breeder is irradiated, the burnup of lithium will change the stoichiometry. The effect of more than a few percent burnup has not been experimentally established. However, some detrimental effects on the melting temperature are noted in Table 2.2-6, based on the phase diagrams and assuming

30% burnup.[4,28] $LiAl_5O_8$, formed from $LiAlO_2$ burnup, has a higher melting temperature and vapor pressure limit than $LiAlO_2$.

The phase transformations observed in Li_4SiO_4[4] and Li_8ZrO_6[16] are observed to be more displacive than destructive. However, the effect on the breeder after many thermal cycles is not clear. It is not assumed significant in the upper temperature limits suggested here, but does influence the uncertainty in these limits.

In Table 2.2-6, a range or uncertainty estimate for the upper temperature limit is provided. The lower range of the temperature limit is set from the lowest identified temperature limit, or 0.6 T_{melt} (the lowest predictive onset of radiation-induced sintering). The upper range is set at 0.8 T_{melt}, assuming that sintering and vapor phase transport are not necessarily a problem in the hot breeder regions if the tritium diffusion rate also improves.

2.2.1.5 Other Thermophysical Properties

Other thermophysical properties are described in various references. Phase diagrams and crystalline properties, for example, are in Ref. [4]. The electrical conductivities of the various materials are in Ref. [30].

2.2.2 Tritium Properties

Although a clear picture of the mechanisms for tritium transport and retention in solid breeders is far from accepted, tritium behavior is generally interpreted with respect to three processes - diffusion, solubility, and surface adsorption/desorption. Irradiation trapping may be important, particularly at high burnup, but is not considered here. Also, both pore (gas phase) and grain boundary diffusion are considered to be fast enough that they can be neglected as a significant contributor to tritium retention. Data on tritium transport and retention that can be interpreted with respect to these basic material properties are summarized here.

The available experimental data is not sufficient to quantify the tritium retention mechanisms with good accuracy. Even where there is a reasonable amount of data, particularly for Li_2O and $LiAlO_2$, there are large discrepancies. Where necessary, analogies have been drawn to corresponding metal oxide data. It is emphasized that the numerical estimates are often based on very limited or inconsistent data, and must be viewed as preliminary.

2.2.2.1 Diffusion

Reported diffusion coefficients reflect different interpretations of the data. Some analysts use the grain radius as the characteristic radius of diffusion, while others prefer an effective diffusion based on the pellet radius. Both approaches have advantages. The grain-size approach supports mechanistic model development and extrapolation to other microstructures, but assumes that the tritium retention and release mechanisms are understood sufficiently well to resolve particular processes. The grain radius interpretation is used here.

Even with a consistent interpretation, significant differences (orders of magnitude) in apparent diffusivity are observed between large grain samples and small grain samples.[31,32] This is not understood. Explanations range from experimental method, to inadequate characterization of the microstructure, to the relative importance of bulk versus surface behavior.[10,31] Although this difference has not been resolved, fusion applications will use small-grained materials. Consequently, diffusivities suggested here are based on the apparent diffusivities measured in small-grain samples.

Li_2O: Data have been provided by Guggi, and Ihle & Wu.[5,28] The FUBR-1A data[33] with up to 3% burnup was roughly consistent with diffusion, but modified by some other process such as irradiation trapping.

$LiAlO_2$: Diffusion coefficients reported by different investigators appear to be inconsistent by several orders of magnitude.[10] Ihle and Wu[28] used 3 mm solidified melt specimens, suggesting 100% dense and single crystal behavior, and found 2×10^{-11} m^2/s at 1000 K. Recently, Botter, et al.,[32] reported 2×10^{-13} m^2/s for 4 mm single-crystal samples at 923 K. These can be compared with the diffusivities reported from various small-grained specimens, including purged capsule tests, which are shown in Figure 2.2-2 and average about 10^{-17} m^2/s at 1000 K.[34-36] Since fusion blankets will use small-grain materials, the suggested diffusivity is drawn from the data in Figure 2.2-2, and the uncertainty band includes only this data spread.

Li_5AlO_4: Ihle & Wu found the diffusivity of Li_5AlO_4 to be somewhat higher than that for $LiAlO_2$, and consistent with the generally high diffusion rates measured in their solidified melt specimens. For a small-grained polycrystalline specimen, the diffusion for Li_5AlO_4 is assumed to have the same relationship as the small-grain $LiAlO_2$ data.

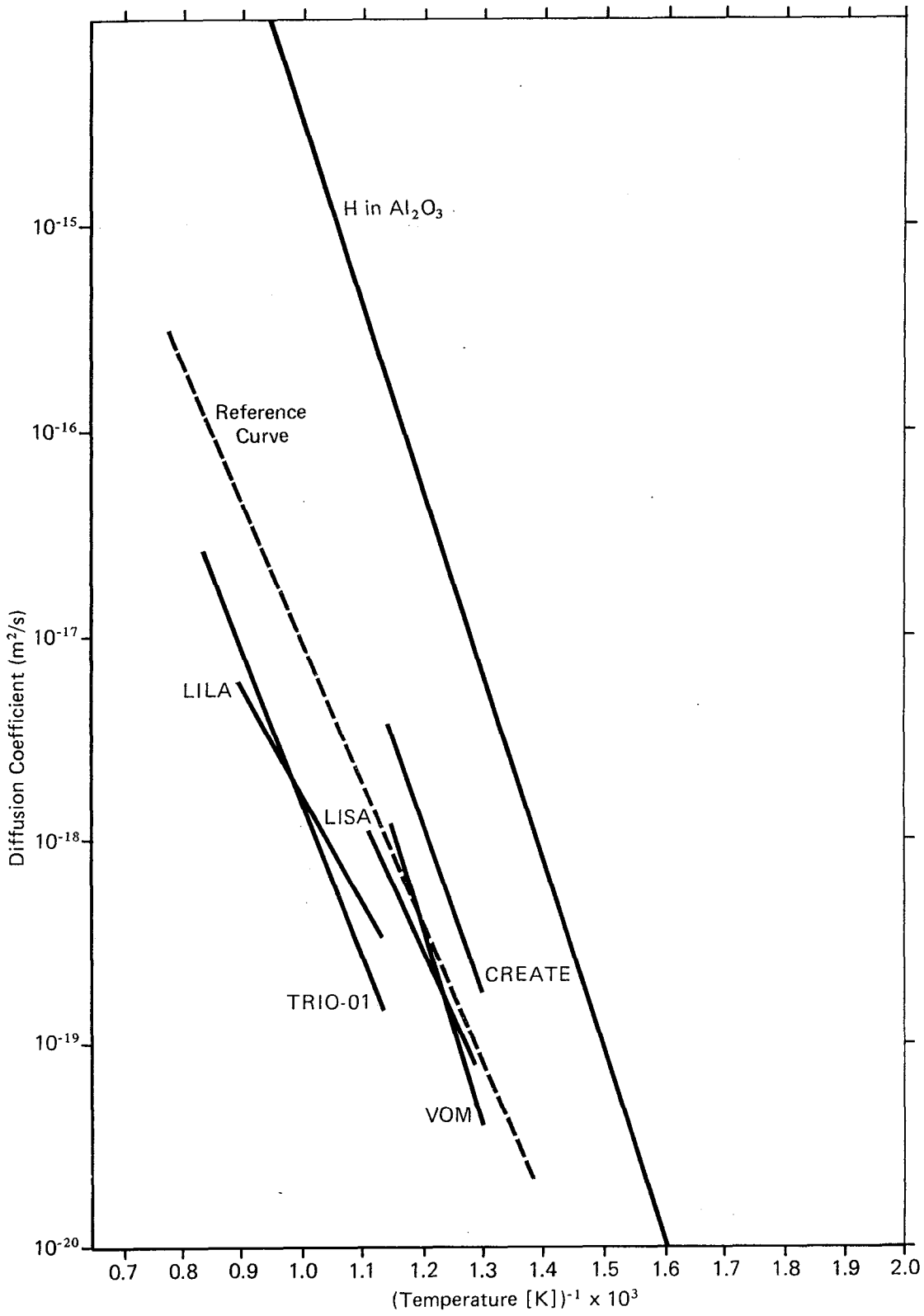


Figure 2.2-2 Hydrogen isotope diffusion in $LiAlO_2$

$LiAl_5O_8$ and $LiAlO_2$ + 1% MgO: Ref. [32] reports that tritium diffusion in $LiAl_5O_8$, a possible burnup product of $LiAlO_2$, shows much slower tritium diffusion, while the addition of a small amount of MgO substantially improves tritium diffusion.

LiAl: Ref. [10] gives diffusion coefficients ranging from 10^{-10} to 10^{-13} m^2/s at 450°C.

Li_2SiO_3 and Li_4SiO_4: The diffusivity data is shown in Figure 2.2-3.[3,10,28,34,37] Again, the 3 mm solidified melt Li_4SiO_4 specimens of Ihle & Wu gave much higher diffusivities than the small-grain polycrystalline material in the LISA experiments, although the activation energies are similar. The suggested diffusivities follow the LISA and Vasilyev data for the ortho- and meta-silicate, respectively. The FUBR-1A data[33] was not used due to uncertainties in determining which mechanisms were dominant.

Li_2ZrO_3 and Li_8ZrO_6: The only tritium transport data for these materials is for the metazirconate from the FUBR-1A experiment.[33] Quantitative diffusion coefficients cannot be easily drawn from this data since there is no discrimination between mechanisms, although it was observed that the metazirconate had the lowest tritium retention of the materials tested. In order to estimate a diffusivity for the lithium zirconates, an analogy with hydrogen diffusivity in ZrO_2[37] is made based on similarities of behavior between other lithium and single metal oxides (alumina and lithium aluminate, silica and lithium silicate). In particular, the same activation energy is assumed as for hydrogen diffusion in ZrO_2, and the pre-exponential is set at 1000 times less than the ZrO_2 data. This results in lithium zirconate diffusivities of the same order as those for the silicates, zirconates and titanates, as is true for hydrogen diffusion in silica, zirconia and titania.

Li_7Pb_2: Data for Li_7Pb_2 from Wiswall, reported in Ref. [10], is based on crushed and sieved solidified melt. Vasilyev[38] reported tritium release from irradiated Li_7Pb_2 as characterized by an activation energy of 100 kJ/mol over 350-425°C, but only 30 kJ/mol at 150-300°C.

Li_2TiO_3: The diffusion coefficient was estimated from hydrogen diffusion data in titania[37], based on the metal oxide analogy discussed earlier.

BeO and $Li_2Be_2O_3$: The diffusion coefficient for BeO has been estimated

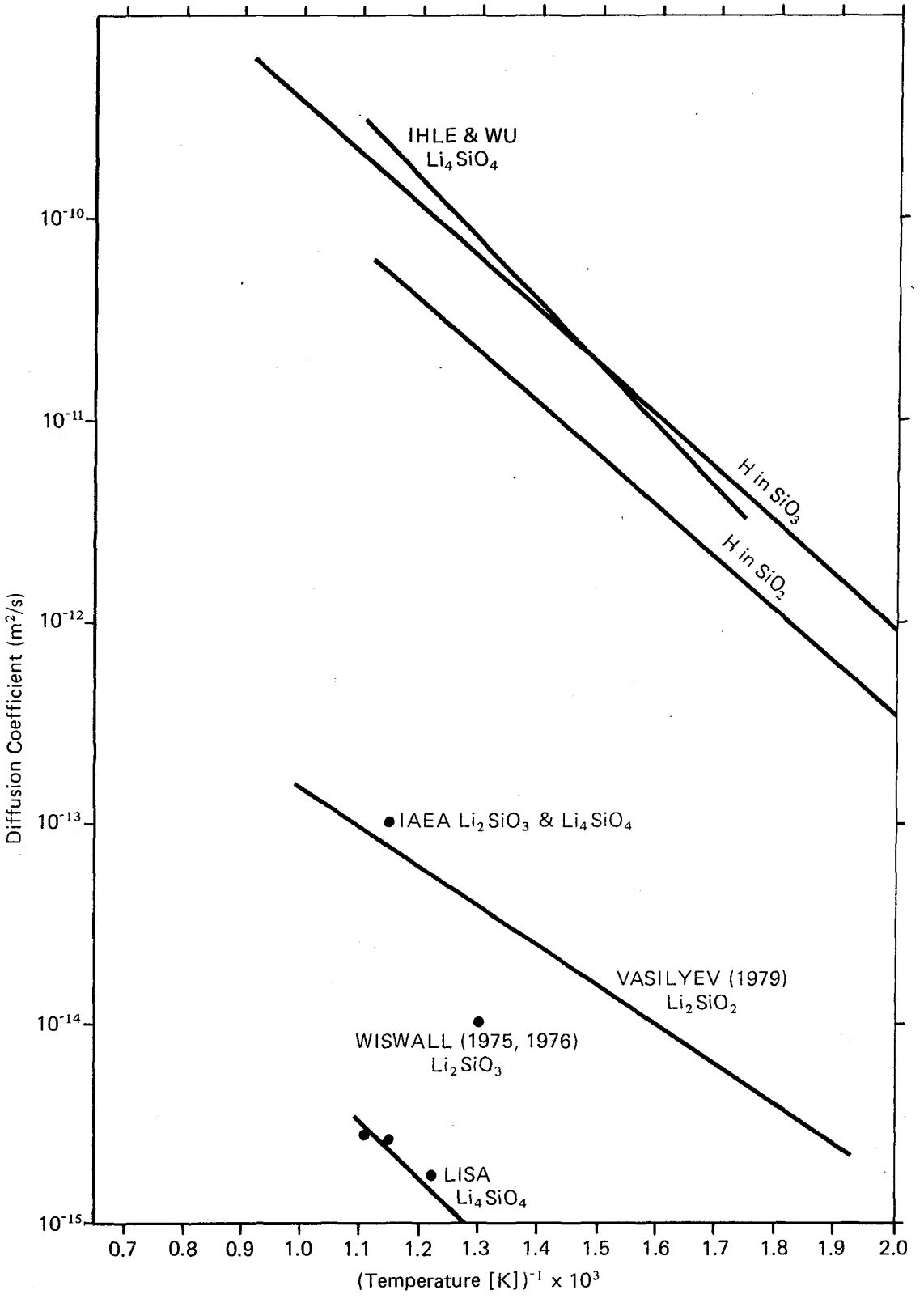


Figure 2.2-3 Hydrogen isotope diffusion in Li_2SiO_3 and Li_4SiO_4

from data for tritium in single crystal and sintered BeO and for H in BeO.[37,38] These data have a spread of over three orders of magnitude, although the activation energies are very close (203-219 kJ/mole). Tritium diffusion data in BeO reported in Ref. [40], however, show an activation energy of 101 kJ/mole and the diffusion coefficient is about a factor of 100 lower than shown by the previous data at 1000 K. The suggested tritium diffusivity here is based on the middle of the higher diffusion data. The diffusion coefficient for $Li_2Be_2O_3$ is estimated to be similar to BeO, given the data uncertainty and the already low value for BeO.

Be: Beryllium metal has a relatively high tritium diffusion coefficient and a low activation energy.[41]

Figure 2.2-4 and Table 2.2-7 summarize the suggested diffusion coefficients and uncertainties for the candidate materials. Diffusion in BeO and, by assumption, in lithium beryllate is expected to be among the slowest, while diffusion in Li_2O and in Li_7Pb_2 are anticipated to be the fastest. Diffusion can be described by $D = D_0 e^{-E/RT}$, where E and D_0 are given in Table 2.2-7. Estimates for the uncertainty (at least relative uncertainty) are given as multiplicative factors. The activation energies are generally fairly close among the different experiments, although the actual diffusion rates vary considerably. Note that the activation energy uncertainty factor is included in the uncertainty factor for the overall diffusion rate given.

Diffusion coefficients for several metal oxides are given for comparison in Table 2.2-8.

2.2.2.2 Solubility

Figure 2.2-5 summarizes the reported solubility data in the form of Sievert's law constant, $K_s = C/p^{0.5}$, where C is the dissolved concentration, K_s is Sievert's constant, and p is the vapor pressure of the hydrogen-bearing species.

Li_2O: The solubility of hydrogen in Li_2O has been experimentally measured by Tetenbaum,[42] and Norman and Hightower.[43] These results have provided a good data base to determine the thermodynamic non-idealities of this system. It is clear that these non-idealities can be large, and that the oxygen activity (effectively the oxygen partial pressure over the breeder) has

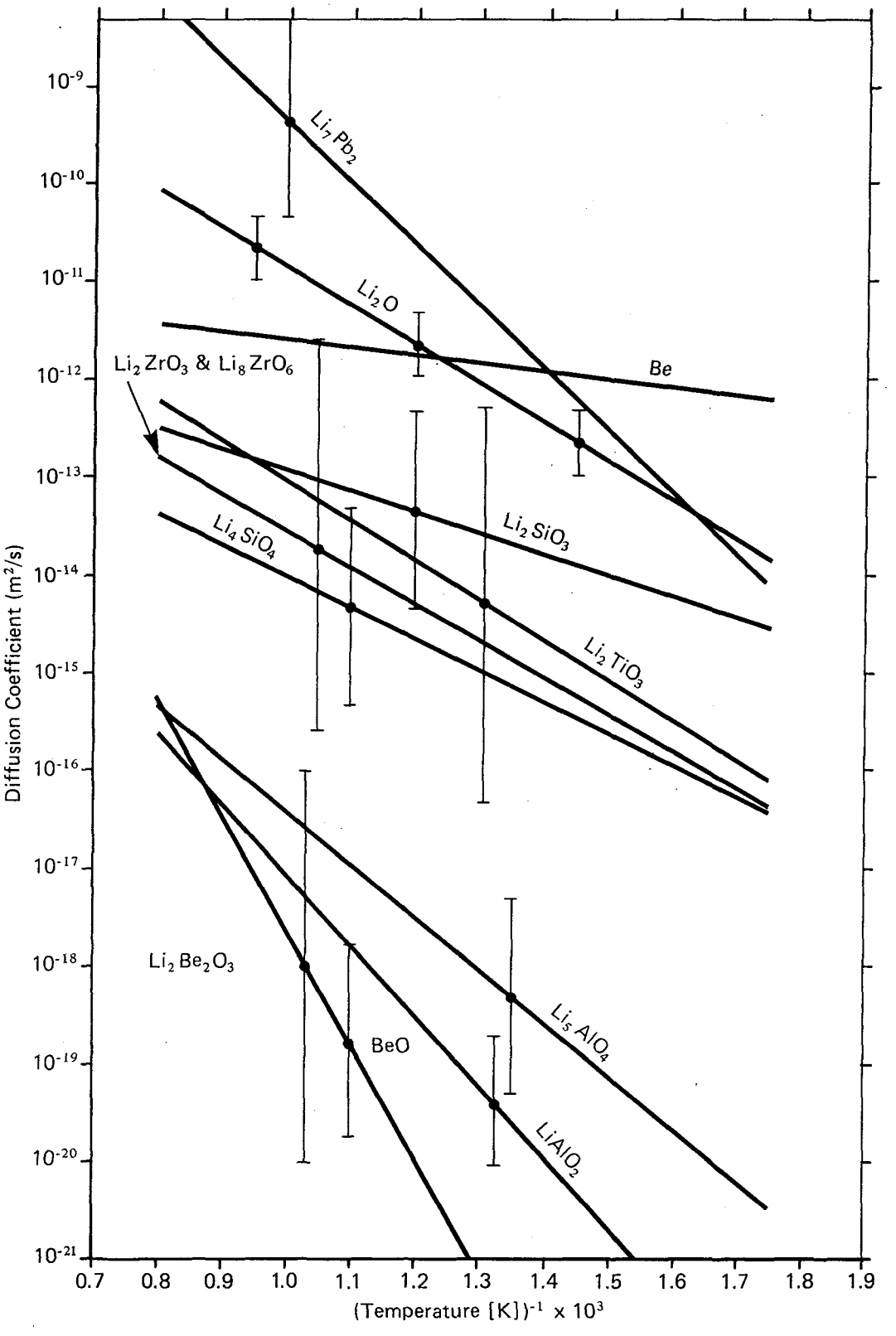


Figure 2.2-4 Tritium diffusion coefficient in candidate breeder materials

Table 2.2-7 Estimated Tritium Diffusion Coefficients for Candidate Solid Breeder and Multiplier Materials[a]

Material	Activation Energy E [kJ/mol]	Uncertainty Factor for Activation	Pre-exponential D_0 [m^2/s]	Uncertainty Factor for Diffusion
Li_2O	76	1.10	1.17×10^{-7}	2
$LiAlO_2$	135	1.30	1.1×10^{-10}	5
Li_5AlO_4	105	1.30	$1. \times 10^{-11}$	10
Li_4SiO_4	64	1.20	2.1×10^{-11}	10
Li_2SiO_3	38	1.30	1.4×10^{-11}	10
Li_2ZrO_3	68	1.50	8.9×10^{-8}	100
Li_8ZrO_6	68	1.50	8.9×10^{-8}	100
Li_7Pb_2	119	1.30	8.6×10^{-4}	10
Li_2TiO_3	84	1.50	3.8×10^{-9}	100
$Li_2Be_2O_3$	220	1.50	$1. \times 10^{-6}$	100
BeO	220	1.20	$1. \times 10^{-6}$	10
Be	18	1.30	3.1×10^{-11}	10

[a] $D = D_0 \exp(-E/RT)$

Table 2.2-8 Hydrogen Diffusion Coefficient in Metal Oxides

Material	Activation Energy E [kJ/mol]	Pre-exponential D_0 [m^2/s]
Al_2O_3	179	8.7×10^{-6}
SiO_2	50	4.7×10^{-8}
SiO_3	49	1.5×10^{-7}
ZrO_2	68	8.9×10^{-8}
TiO_2	84	3.8×10^{-6}

a significant effect on the solubility. Tetenbaum's data shown in Figure 2.2-5 applies to fairly high oxygen activities, greater than about 10^{-15}.[27]

Li_7Pb_2 and $Li_{17}Pb_{83}$: Hydrogen solubility has been measured in the lithium-lead system (Fig. 2.2-5).[28,39] Although hydrogen solubility is low and fairly independent of temperature in $Li_{17}Pb_{83}$,[28] the hydrogen interacts more strongly with the lithium at higher lithium contents, such as in Li_7Pb_2, leading to substantial dissolution.

$LiAlO_2$ and Li_5AlO_4: Hydrogen isotopes are not very soluble in metal oxides such as alumina and silica, and are not generally believed to be very soluble in ternary ceramics such as lithium aluminate. Vasilyev[44] measured the equilibrium water vapor pressure in the system $LiAlO_2$-H_2O with varying initial water content. This data, if interpreted as dissolved hydrogen, implies significant solubility - about 3000 appm/atm 0.5 over 500-1000 K. In a related experiment,[44] the release of tritium oxide from neutron irradiated $LiAlO_2$ was found to have an activation energy of 12-50 kJ/mol, much less than observed in the $LiAlO_2$ diffusivity data discussed in the previous section, but possibly more consistent with the activation energies for solubility. However, the amount of retained tritium indicated in Vasilyev's data is also possibly consistent with surface adsorption.

The most direct estimate of hydrogen solubility in lithium aluminate is that of Johnson & Fischer.[27] They assumed ideal thermodynamic behavior for the aluminate system and calculated the expected tritium in condensed and gas phases as a function of oxygen activity. Within a range of oxygen activity (10^{-20} to 10^{-10}), the dissolved tritium, expressed relative to gaseous tritium through Sievert's law, was on the order of 100 appm/atm$^{0.5}$ for 900-1300 K. This is similar to some of the deuterium/alumina solubility data.

Li_2SiO_3 and Li_4SiO_4: No data was found for hydrogen isotope solubility in lithium silicates. Data for hydrogen in silica indicates a low solubility.[37] Within the uncertainties, the same general solubility as for the aluminates might be a reasonable estimate. However, the ideal thermodynamic calculations of Johnson & Fischer[27] were also extended to Li_4SiO_4. In contrast to the $LiAlO_2$ results, the orthosilicate was found to have a small tritiated vapor phase pressure (mostly T_2 or T_2O, depending on oxygen activity) for a given amount in the condensed phase as LiOT. This implies a fairly

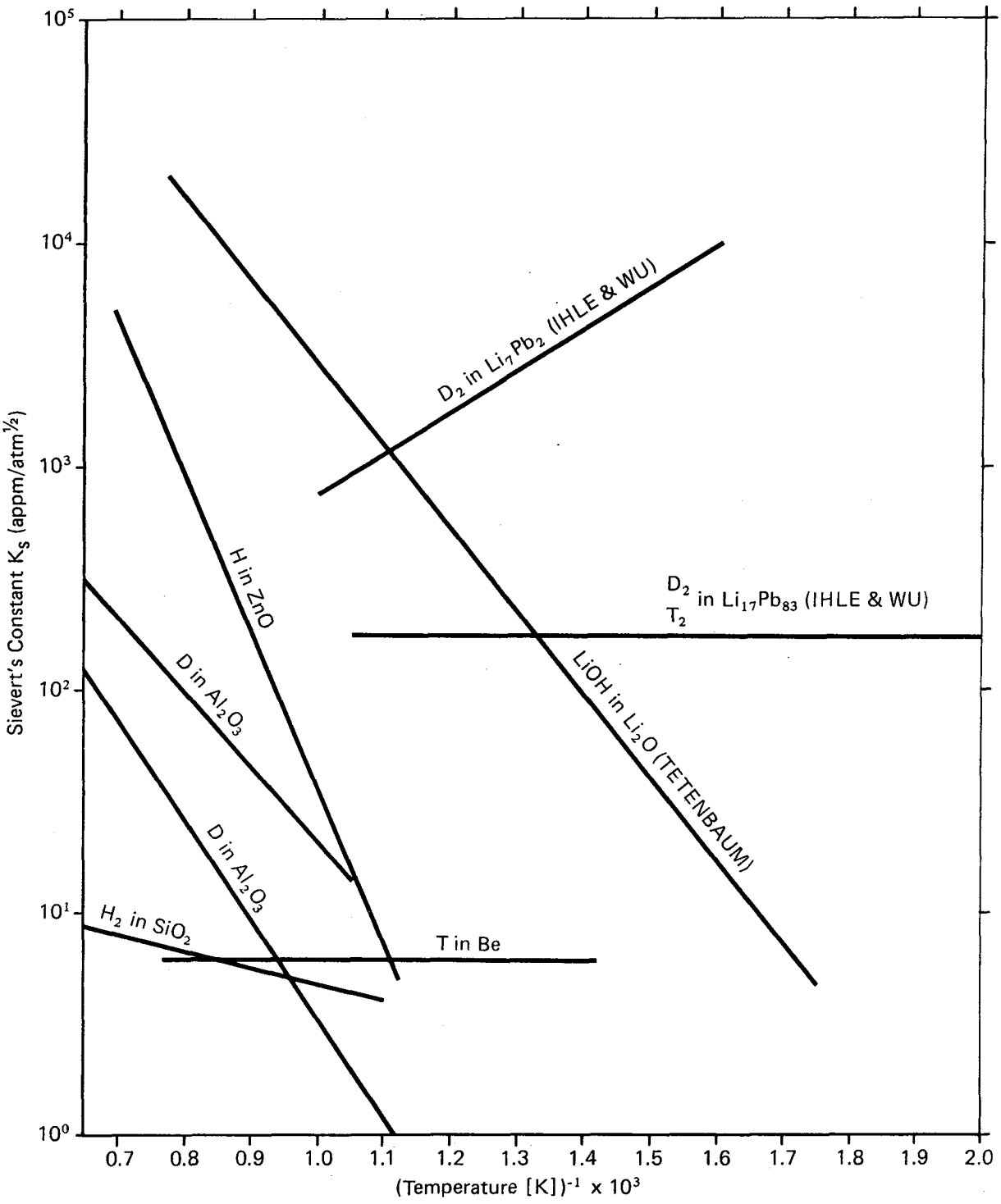


Figure 2.2-5 Hydrogen isotope solubility in various breeder materials, expressed in the form of the Sievert's law constant

high solubility - on the order of 10^3 to 10^5 appm/atm$^{0.5}$ around 1000 K, with the higher values for oxygen activities of 10^{-20} or more.

Li_2ZrO_3, Li_8ZrO_6, Li_2TiO_3, $Li_2Be_2O_3$ and BeO: No solubility data or calculations were found. In the absence of any reason to assume high solubility, a solubility similar to the aluminates is suggested as an interim estimate.

Be: The tritium solubility in beryllium is reported as 6.1 appm/atm$^{0.5}$ over roughly 700-1200 K.[41,45] Hydrogen solubility in metals can have a strong positive or negative dependance on temperature.[37] In beryllium, which is not a hydride former[45], a strong positive temperature dependence would not be expected.

Table 2.2-9 summarizes the expressions for solubility in Sievert's constant form. These data should be considered order-of-magnitude only, given the limited data, and the known importance of parameters such as oxygen activity. The latter, for example, makes it necessary to consider more advanced expressions than the simple Sievert's constant given in the table, even for Li_2O, unless the oxygen activity is above about 10^{-15}. It may also be noted that for fine-grained moderate-porosity breeder materials, the surface adsorption tritium inventory may be of the same order as these solubility estimates.

Table 2.2-9 Hydrogen Isotope Solubility in Various Materials

Material	Isotope	Sievert's Constant (K_s [appm/atm$^{0.5}$])	Temperature range (K)
Al_2O_3	D	1.1×10^5 exp(-64[kJ/mol]/RT)	800-1300
Li_2O	T	1.73×10^7 exp(-72[kJ/mol]/RT)	500-1300
Li_7Pb_2	T	0.20 exp(68[kJ/mol]/RT)	500-1100
$Li_{17}Pb_{83}$	T	170	500-1000
Be	T	6.1	700-1200

2.2.2.3 Surface Adsorption

Figure 2.2-6 summarizes the reported surface adsorption data. In general, there are on the order of a few times 10^{19} potential surface adsorption sites per m^2 of surface area based on typical atomic spacings. The data are roughly consistent with this limit.

Surface adsorption depends on many factors, such as material, impurity content, vapor pressure and temperature. The fairly wide scatter of the data does not suggest any particular simple correlation. In the absence of better data, 4 x 10^{18} H atoms per m^2 is suggested for estimating surface adsorption inventory, within an uncertainty of a factor of 10, for all solid breeder/multiplier materials over the conditions of interest to fusion blankets.

Li_2O: Based on the FUBR-1A tritium inventories, and subtracting the estimated diffusive and soluble inventories (assuming 40 mm grain size, 0.085 m^2/g surface area and 30 Pa T_2 vapor pressure) yields the surface adsorption inventory shown in Fig. 2.2-6. This is somewhat higher than the estimated number of sites available, the difference perhaps due to the assumed gas conditions in the closed capsule experiment. For Li_2O, tritium is believed to be adsorbed onto surfaces as LiOT, which then dissolves into the breeder bulk. Consequently, the distinction between solubility and surface adsorption is particularly unclear for Li_2O.

$LiAlO_2$ and Li_5AlO_4: Some data is available with respect to surface adsorption of hydrogen in aluminates (Fig. 2.2-6), and further experiments are planned at Argonne National Laboratory. The data for Al_2O_3 indicate saturation of the surface sites at lower temperatures, at roughly 10^{19} maximum available surface sites per m^2. A discussion of surface desorption behavior and regimes is provided in Ref. [46]. Recent data from specific measurements of surface adsorption in $LiAlO_2$ are also shown.[47] These measurements are being extended. TRIO and LISA data for $LiAlO_2$[34,46] from in-situ tritium recovery experiments may be very indicative of the surface inventory under fusion blanket conditions, but are also harder to interpret. The TRIO values are based on the difference in total tritium released before and after H_2 addition to the purge stream. Only results from early runs are shown since the interpretation of later runs could be complicated by remaining effects from earlier runs, particularly those with O_2 addition. The LISA estimates were similarly obtained by integrating the decrease in tritium release after

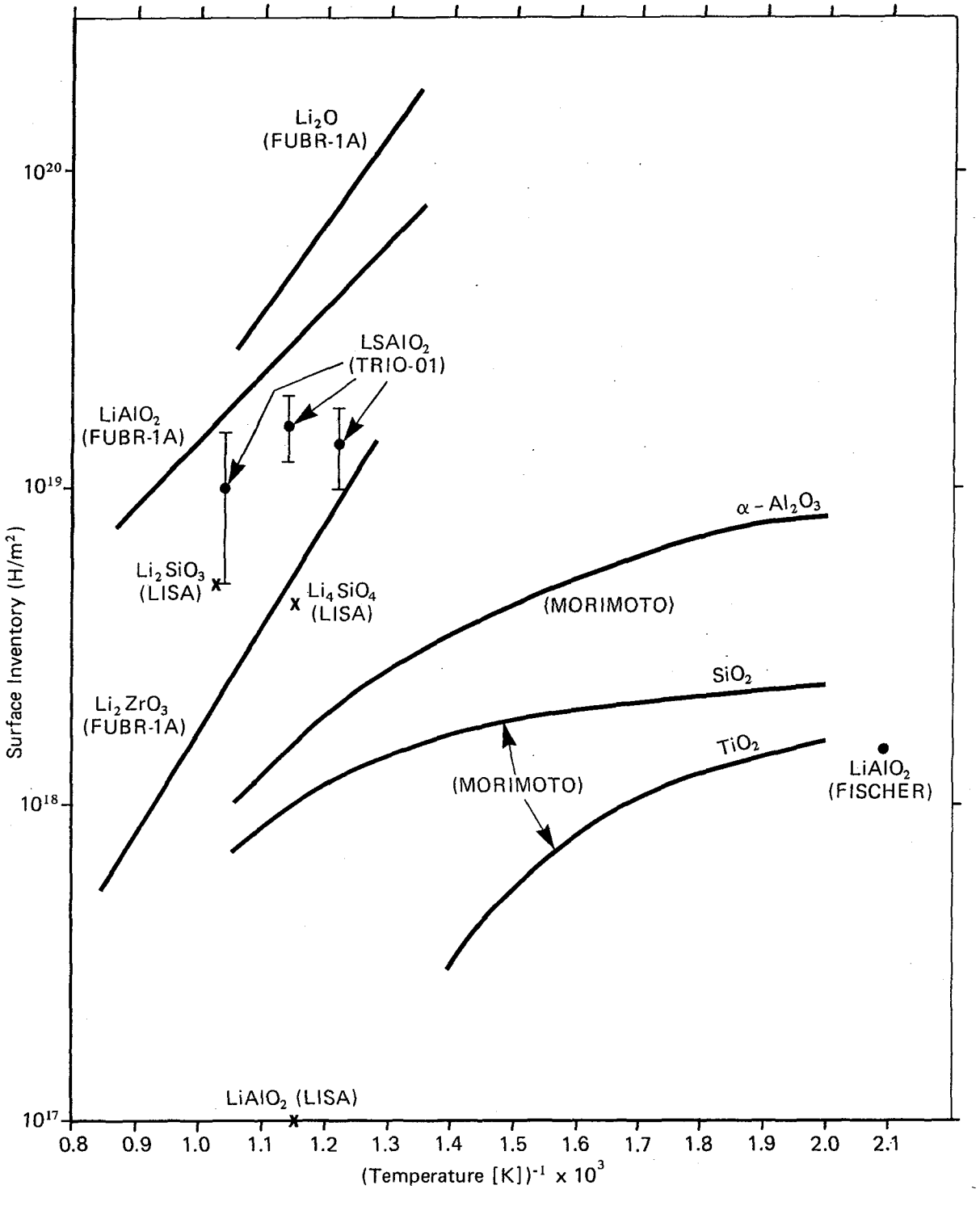


Figure 2.2-6 Tritium inventory adsorbed onto material surfaces

hydrogen was removed from the purge stream in Runs 10-12. The reported grain size for LISA of 0.38 mm was estimated to imply a surface area of 4.07 m^2/g. Vasilyev's data are not shown, but assuming his 9 x 10^{18} $H/m^{2(44)}$ value to be primarily due to surface adsorption, it is consistent with the maximum anticipated inventory of 10^{19} H/m^2. Subtracting estimated diffusion and solubility inventory, the FUBR-1A closed capsule data indicate a major tritium contribution from surface adsorption, as may be expected, although the particular magnitude seems too high. Overall, given the large variability in data and the complex functional dependency of surface adsorption, it is suggested that surface adsorption be assumed as 4 x 10^{18} H/m^2 within a factor of 10.

Li_2SiO_3 and Li_4SiO_4: In estimating surface adsorption, two points have been analyzed from LISA data (Fig. 2.2-6), with surface areas assumed at 0.021 m^2/g (metasilicate), and 0.054 m^2/g (orthosilicate). These calculations represent the integrated difference in tritium release rate after stopping the addition of 0.1% H_2 to the purge stream (Runs 10 & 11, cycle C, Ref. [34]) and neglecting dissolved tritium. The two data points are somewhat higher than the SiO_2 data, but are consistent with the TRIO and LISA data for $LiAlO_2$. They fall within the error bars of the of 4 x 10^{18} % factor of 10 H/m^2 general estimate.

Li_2ZrO_3 and Li_8ZrO_6: Subtracting the estimate for diffusion from the total FUBR-1A inventory, the resulting inventory is attributed to surface adsorption if solubility is negligible. This results in a surface adsorption inventory comparable to that from other estimates for other ternary ceramics (Fig. 2.2-6). This general agreement in surface adsorption also supports the estimate for diffusion in lithium zirconates.

Li_7Pb_2 and $Li_{17}Pb_{83}$: No lithium lead surface adsorption data was found. Therefore, the inventory is estimated at 4 x 10^{18} tritium atoms per m^2, as for other solid breeder materials.

Li_2TiO_3: No data was found for surface adsorption on lithium titanate, although data was obtained[46] for adsorption of OH^- on TiO_2. It predicts a lower inventory than other materials, but is consistent within the data scatter. Hence, the general estimate (4 x 10^{18} T atoms per m^2) is applicable.

$Li_2Be_2O_3$, BeO and Be metal: No data was found for these materials, hence surface adsorption is estimated as 4 x 10^{18} H/m^2.

2.2.2.4 Mechanical Properties

Elastic Modulus

Measurements of the elastic modulus (E) have been reported for the sintered product form of Li_2O[48], $LiAlO_2$[10,25,49], Li_2SiO_3[15,25,50] and BeO.[19,20,48]

Data is available for alumina[7,48], silica[7,51], beryllia[20,48], zirconia[20] and titania.[20] Except for silica, the metal oxide values cluster together. With the addition of lithium, the modulus decreases strongly for $LiAlO_2$ with respect to Al_2O_3, but the elastic modulus for SiO_2 and Li_2SiO_3 are similar. As a rough estimate for solid breeder materials where there is no data available, the elastic modulus for 100% dense material at room temperature is assumed here to be a factor of 1.5 less than the corresponding single oxide. This is intermediate between the aluminate (factor of 2) and the silicate (factor of 1.1). For the breeder/multiplier mixtures, an effective elastic modulus can be assumed based on the relative volumes: $E = E_1 V_1 + E_2 V_2$, where V is the relative volume of each material.[20]

Data for the metal Be is available.[7,19,20] No Li_7Pb_2 or Li data was found, but values for Pb are suggested for Li_7Pb_2 (Pb provides 80% of the compound mass), although the exact values are sensitive to the particular compounds mixed with the lead.

The elastic modulus is a strong function of the amount of porosity, and also a function of other variables such as temperature, microstructure and irradiation. Table 2.2-10 and Figure 2.2-7 summarize the suggested values for the elastic modulus as a function of porosity, and the effect of the different variables is discussed below. Table 2.2-10 also indicates the uncertainty in these estimates.

Porosity: The elastic modulus decreases strongly with porosity. This relationship has typically been expressed as:

$$E = E_0 \exp(-B\,\varepsilon) \qquad \text{or} \qquad E = E_0\,(1-\varepsilon)/(1+A\,\varepsilon) \tag{2-1}$$

where E_0 is at 100% theoretical density, and ε is the fractional porosity. Denouziere & Roux[10] report fitting aluminate data as:

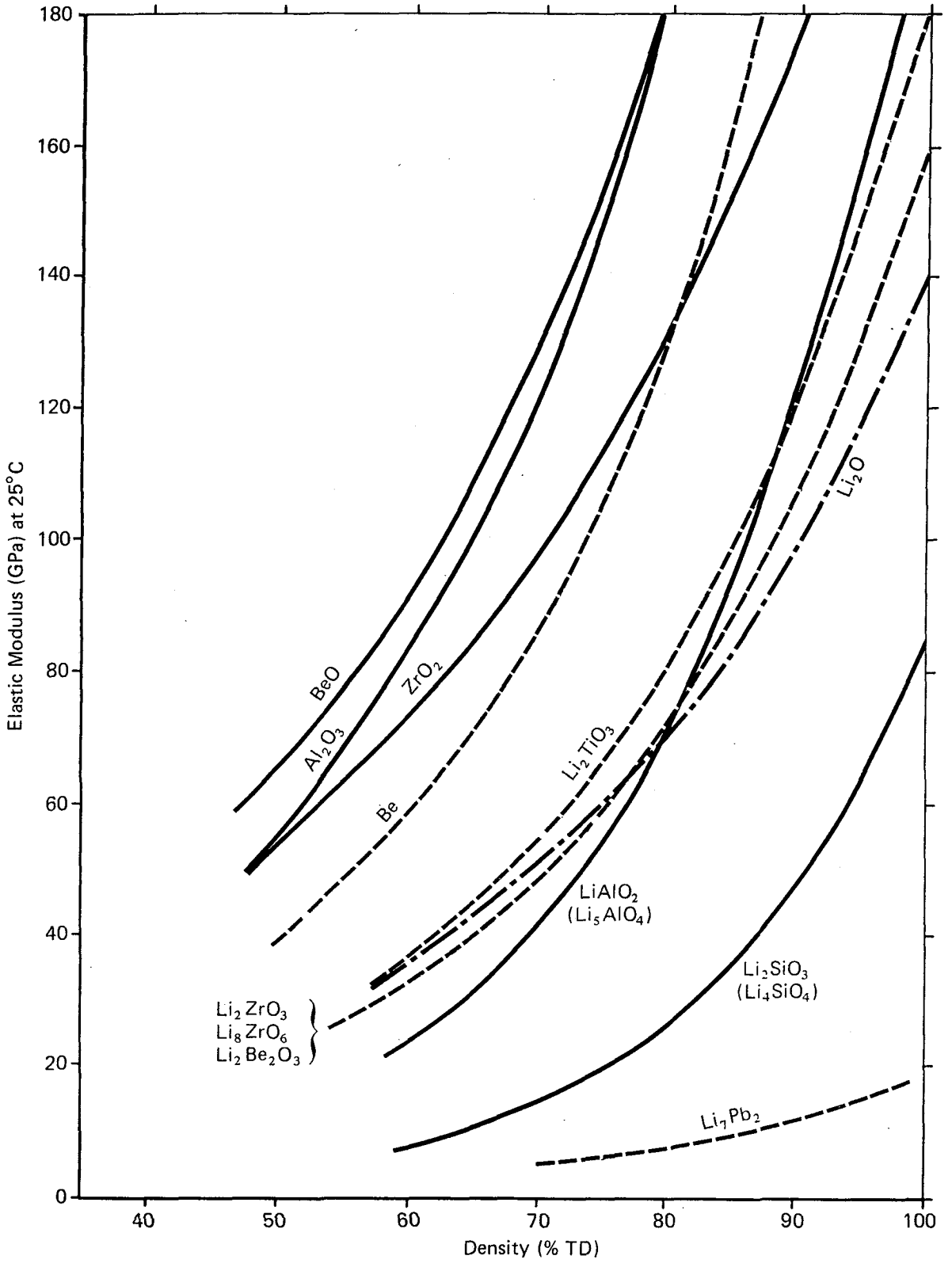


Figure 2.2-7 Elastic modulus [GPa] at 25°C for various breeder materials as a function of density. Solid lines indicate experimental basis, dashed lines indicate estimated.

Table 2.2-10 Suggested Values For Unirradiated Elastic Modulus for Candidate Solid Breeder and Multiplier Materials and for Metal Oxides[a]

Material	E_0 (GPa)	B	Uncertainty in E
Li_2O	141	3.4	20%
$LiAlO_2$	210	5.4	20%
Li_5AlO_4	210	5.4	50%
Li_2SiO_3	85	5.8	30%
Li_4SiO_4	85	5.8	50%
Li_2ZrO_3	160	4.0	Factor of 2
Li_8ZrO_6	160	4.0	Factor of 2
Li_2TiO_3	180	4.0	Factor of 2
$Li_2Be_2O_3$	180	4.0	Factor of 2
Li_7Pb_2	20	4.0	Factor of 3
BeO	360	3.4	20%
Be	290	4.0	50%
Al_2O_3	407	4.0	-
ZrO_2	241	3-4	-
SiO_2	70	-	-
TiO_2	283	-	-

[a] $E = E_0 \exp(-B\varepsilon)$, where E_0 is elastic modulus at room temperature (25°C) and 100% dense material, and ε is fractional porosity.

$$E = C\,\rho_{100}\,(1-\varepsilon)(0.7-\varepsilon)^2 \qquad (2\text{-}2)$$

where ρ_{100} is the theoretical density. The first is more commonly used, but implies that E does not go to zero as the porosity approaches 100%. Over the range of interest to solid breeder blankets (0-30% porosity) this should not be significant. The second expression has difficulty in matching $E(\varepsilon)$ over a wide range of porosity, at least for the aluminate.

For present purposes, the first expression will be used. Reported values for the porosity-related parameter B are: 3.4 for BeO,[48] 1.8 for UO_2,[48] 4.0 for Al_2O_3,[48] 4.7 for MgO,[48] 3.01 at 27°C and 4.08 at 1000°C for ZrO_2.[20] The aluminate and silicate data imply a B value of about 5.5. Where data is lacking, B = 4 is suggested.

Temperature: The elastic properties of ceramics are not strong functions of temperature (T), at least until very near the melting point (T_m). A proposed temperature dependence for Li_2O is:

$$E = E_0 \left(1 - (T/T_m) \exp(1-T_m/T) \right) \tag{2-3}$$

which reduces to zero at the melting point. However, over a fairly wide range of temperature, data for the various lithium ceramics and related single oxide ceramics show a linear dependence of about 0.02%/K.[20] For example, data for alumina have been given by

$$E = 407 \ (1 - 0.00018 \ T) \ GPa \tag{2-4}$$

and Ref. [50] reported 5-10% decreases for $LiAlO_2$ from room temperature (RT) to 400-600°C. Consequently, a linear temperature dependence is proposed for relevant temperatures (e.g., below melting) of:

$$E = E_0 \left(1 - 0.00018 \ (T-T_0)\right) \tag{2-5}$$

where T is in K, and T_0 is room temperature.

Grain Size: Grain size is not observed to have a strong effect on Young's modulus in ceramics.[20] Data for lithium aluminate from Ref. [49] indicate little effect over grain sizes from 0.35 to 13 mm.

Cracks: Cracking is a possibility in sintered product ceramics due to their brittle nature and the potentially large operational stresses. The sphere-pac form can be considered a pre-cracked material form. Cracking reduces the effective elastic modulus of the material. Ref. [52] suggests that, based on UO_2 data:

$$E = E_0 \ \sigma/\sigma_0 \qquad \sigma < \sigma_0$$

$$E_0 \qquad \sigma > \sigma_0$$

where σ is the compressive stress on the material, and σ_0 is a stress at which the cracks are sufficiently compressed that the material behaves as if the cracks were not present. Based on the UO_2 data, σ_0 is about 100 MPa.

Irradiation: Data on the irradiation effects on lithium aluminate is provided in Ref. [49]. Various specimens were irradiated to up to 1.1% lithium atom burnup (4.7×10^{20} n/cm^2 fast and 1.5×10^{20} n/cm^2 thermal). There appears to be no observable effect of radiation (up to 1% burnup) at temperatures < 400°C, but a 10% reduction in E is observed at 500°C and 1% burnup. For solid breeder and multiplier materials in blankets, the burnup can exceed 10%. For blanket design, it is suggested that a uniform reduction of 10% for radiation effects be included.

Thermal Expansion

Thermal expansion coefficient data for the various breeder and multiplier materials are listed in Table 2.2-11. In several cases, the values for α represent average values over a range of temperatures. The rate of expansion tends to increase with temperature, as much as 100%, as illustrated in Table 2.2-11. Table 2.2-12 summarizes the suggested values for thermal expansion at room temperature in 100% dense material. At these conditions, the thermal expansion values in Table 2.2-12 are uncertain by about 10%.

Poisson's Ratio

Values for Poisson's ratio are summarized in Table 2.2-12 at 300 K and 100% theoretical density, with a summary of the available data given in Table 2.2-13. Poisson's ratio may have a small dependence on porosity as well as temperature. However, this is well within the uncertainty in the present data. The uncertainty in the values suggested in Table 2.2-12 for the breeder materials is estimated at only 20%, in spite of the lack of data, due to the relatively small variability of Poisson's ratio among a wide variety of materials.

Fracture Strength

Fracture strength is affected by porosity, grain diameter, temperature, impurities or additives, stress direction, and possibly irradiation. Much of the data does not adequately specify these parameters, which makes it difficult to correlate the data. Nonetheless, Table 2.2-14 includes suggested values for fracture strength for the breeder and multiplier materials at 300 K and 100% density. Table 2.2-14 summarizes the actual fracture strength data.

Table 2.2-11 Linear Thermal Expansion Coefficient (α) Data for Various Materials

Material	Temp Range (K)	α (10^{-6}/K)	Reference
Li_2O	-	33.6	26
	373	22.5[a]	22
	1073	34.5[a]	22
	< 550	19.3	4
$LiAlO_2$	273-973	11.8	53
	< 1273	12.4	26
	< 1273	12	5
	< 600	10.4	4
	300	12.6	25
$LiAl_5O_8$	< 900	7.7	4
	-	8.2	26
Li_2SiO_3	298-973	18.1	15
	373-973	11.3	4
	300	13.4	25
Li_4SiO_4	300-1300	20.4	4
	300-700	18.8	4
	-	23.8	26
SiO_2 (fused)	300-600	0.5	7
Li_2ZrO_3	< 1200	10	4
Li_8ZrO_6	273-1273	20	16
ZrO_2	300-700	7.5	20
(stabilized)	700-1033	12	20
	1033-1590	15	20
	1590-2480	16	20
Li_2TiO_3	< 500	16	4
TiO_2	300-1770	8.8	20
Be	300-800	15.9	19
	298-1273	18.4	17
	298	12	7
BeO	294-700	7.4	20
	700-1480	10.3	20
	1480-2370	13.5	20
	300-800	8.20	19
Li	293	56	17
Pb	290-373	29.3	17

[a] α [10^{-6}/K] = 0.01714 T[K] + 16.1

Table 2.2-12 Summary of Mechanical Properties at 300 K for Candidate Solid Breeder and Multiplier Materials

Material	Thermal Expansion α (10^{-6}/K)	Poisson's Ratio ν	Fracture Strength[b] σ_c/σ_t (MPa)
Li_2O	23	0.19	(250)/50
Al_2O_3	-	0.13-0.32	1200/100
$LiAlO_2$	12	(0.23)	400/(80)
$LiAl_5O_8$	8	(0.25)	(400/80)
SiO_2	-	0.16	(200/50)
Li_2SiO_3	13	(0.23)	300/60
Li_4SiO_4	22	(0.20)	(300/60)
ZrO_2	8	0.26-0.29	1000/100
Li_2ZrO_3	10	(0.25)	(200/50)
Li_8ZrO_6	20	(0.25)	(200/50)
TiO_2	9	-	300/30
Li_2TiO_3	16	(0.25)	(300/30)
Be	16	(0.1)	300/300
BeO	8	0.34	400/50
$Li_2Be_2O_3$	(20)	(0.2)	(400/50)
Li_7Pb_2	(30)	(0.4)	(10/10)
Pb	30	0.44	10/10

[a]Values in parentheses are suggested in the absence of data. At the given conditions, these results are uncertain by about 10% for thermal expansion, 20% for Poisson's ratio, and a factor of 3 for fracture strength.
[b]Grain diameter on the order of 0.5-2 μm; 85% dense sintered material

Table 2.2-13 Poisson's Ratio Data for Various Materials

Material	Density (% TD)	Temperature (K)	Poisson's Ratio ν	Reference
Li_2O	91.9	298	0.18	48
	92.4	298	0.20	48
	92.9	298	0.19	48
$LiAlO_2$	90.0	300	0.23	25
Al_2O_3	100	298	0.13-0.32	48
ZrO_2	100	300	0.255-0.29[a]	20
	100	300	0.324[b]	20
Li_2SiO_3	90.0	300	0.23	25
SiO fused	100	300	0.16	7
Be	100	300	0.02-0.075	17
BeO	100	298	0.34	48
Pb	-	293	0.44	54
	100	300	0.4-0.45	17

[a]with 4% CaO
[b]with 10% CaO

The dependence of fracture strength (σ_f) on porosity (ε) and grain diameter (d) is often expressed in the form:

$$\sigma_f = \frac{A \exp(-B\varepsilon)}{d^n}$$

where A, B and n depend on the material. Typical values for n include 0.5 (Be,[8] $LiAlO_2$[10]) to 0.64 (SiO_2 fibers[55]). Typical values for B include 10 ($LiAlO_2$[10]) and 8 (BeO[55], ZrO_2 + 4% MgO[55]). Alternate forms include $(A + B/d^n)$ for the grain size dependence, and $(1-\varepsilon)/(1+A\,\varepsilon)$ for the porosity dependence.[20]

There is no good general rule for the temperature dependence, other than that strength decreases with increasing temperature. Ref. [10] gives:

$$\sigma_{comp} = \ln \frac{2200}{T} \frac{\exp(-10\varepsilon)}{d^{0.5}} \text{ GPa} \qquad (2\text{-}6)$$

for $LiAlO_2$ where T is in K, and d is in μm.

Table 2.2-14 Fracture Strength Data for Various Materials

Material	Grain Diameter [μm]	Porosity ε	Temperature [K]	Fracture Strength σ_c [MPa]	Fracture Strength σ_t [MPa]	Reference
Li_2O	-	0.25-0.1	973-1073	-	>20	48
$LiAlO_2$	0.42	0.25	300	270	-	10
	0.42	0.25	770	150	-	
	0.42	0.25	970	120	-	
	0.42	0.25	1370	83	-	
	-	0.137	298	136	-	Gurwell
	-	0.139	298	102	-	in 10
	-	0.16	298	119	-	
	-	0.174	298	77	-	
	-	0.187	298	46	-	
	-	0.2	298	60	-	
	-	0.261	298	13	-	
	-	0.267	298	9.4	-	
	-	0.268	298	11	-	
	-	0.269	298	11	-	
	-	0.282	298	13	-	
	-	0.1	300	550	110	25
Al_2O_3	-	-	293	2940	259	55
	-	0.	1700	100	30	
Li_2SiO_3	-	0.2	298	230	-	15
	-	-	298	-	53	53
	-	0.1	300	420	84	25
SiO_2	-	-	293-1573	176-970[a]	-	55
	1.5	0 fiber	293	-	9000	
	2.0	0 fiber	293	-	8000	
	4.0	0 fiber	293	-	5500	
	7.0	0 fiber	293	-	3900	
	10.0	0 fiber	293	-	3000	
	15.0	0 fiber	293	-	2300	
	20.0	0 fiber	293	-	1700	
	-	0 fused	300	48	>1100	7
Be	Unirrad.		800	90	90	19
	Irrad.		800	110	110	
	10	0	600	200-220[a]	200-220[a]	8
	10	0	400		230-260[a]	
	10	0	900		110	
	1.5	0	400		680	
BeO	-	0.03-0.07	293-1273	-	137-69[a]	55
	-	0.11	293-1473	-	103-27[a]	
	-	0.06	773-1873	490-49[a]	-	
	-	0.4	293	48	-	
	-	0.33	293	89	-	
	-	0.26	293	137	-	
	-	0.19	293	206	-	
	-	0.13	293	412	-	
	-	0.06	293	755,784	-	
	-	0.03	293	1176	-	
	-	0.01	293	1372	-	
	-	-	800	-	76	19
	-	0.02	300	1840	-	20
	-	0.02	600	950	-	
	-	0.02	1000	510	-	
	-	0.02	1500	240	-	
	-	0.05	300	780	-	20
	-	0.05	600	590	-	
	-	0.05	1000	370	-	
	-	0.05	1500	200	-	
	-	0.3	300	140	-	20
	-	0.3	1000	82	-	
TiO_2	-	0.26	293	245	-	55
	-	0.03-0.07	293-1273	-	55-41[a]	
	-	0.05	298	-	51	20
ZrO_2	-	0	300	680-1650[a]	-	20
(4.2% MgO	-	0.01	1773	20	-	55
stabilized)	-	0.05	293	2058	-	
	-	0.09	293	1960	-	
	-	0.16	293	980	-	
	-	0.26	293	490	-	
	-	0.48	293	98	-	
	-	0.62	293	39	-	
	-	0.01-0.04	293-1573	-	137-70[a]	
Pb	-	-	300		12-14[a]	17

[a]Refers to temperature range.

For brittle materials such as ceramics, the compressive strength is usually substantially larger than the tensile strength. As an approximate rule, the compressive strength of ceramics is about eight times their tensile strength (within a factor of two). For metals, the yield in compression is usually very close to that in tension.

Impurities and additives strongly affect the fracture strength. The effect of removing small impurities to produce high-grade beryllium block increased the yield strength by up to 25%.[8] The moisture content is known to affect the softness of Li_2O.[48] Adding MgO to ZrO_2 'stabilizes' it and gives it strength.

For several low Z materials at approximately 800 K, irradiation either increased yield strength or had no effect (Be, C, SiC).[19] For other materials (e.g., Graph-N3M high-strength graphite[19]), high fluence irradiation reduced the tensile strength by 50%. Some irradiation results for solid breeder materials are reported in Refs. [5,10,29,33]. These extend up to about 3% burnup in the FUBR-1A tests. Swelling and/or grain growth was reported in some samples, as well as a decrease in mechanical strength.

2.2.2.5 Fabrication

Grain Size

The grain size of the breeder material influences its tritium recovery and, to some extent, its mechanical properties. It is generally desirable to reduce the grain size in order to reduce the tritium diffusion path length. However, this must be balanced with the potential for increased surface area, and thus surface adsorption of tritium, and the cost of producing small-grain material. Also, under reactor conditions of time, temperature and irradiation, initially small grains might grow larger anyway.

Table 2.2-15 summarizes the average grain sizes reported by various groups. These are used to identify the smallest grain size for each material that can be fabricated with existing processes.

Table 2.2-15 Candidate Solid Breeder and Multiplier Fabricated Grain Size (μm)

Material	Data	Assumed Minimum
Li_2O	8,[21] < 10,[4] 3,[5] 5-10,[56] 4-10 FUBR-1A, VOM-15H; 50 TULIP	3
$LiAlO_2$	0.2,[5] 0.2 TRIO,[36] < 1 FUBR-1A, 0.4,[34] 0.2-0.5,[57] 1[56]	0.2
Li_5AlO_4	--	2
Li_2SiO_3	2-10,[4] 30,[34] 0.2-0.5[56,58]	0.2
Li_4SiO_4	5,[4] 2[5]	2
Li_2ZrO_3	5,[4] 2[5]	2
Li_8ZrO_6	2[5]	2
Li_2TiO_3	--	2
Li_7Pb_2	--	2
$Li_2Be_2O_3$	--	2
Be	25 typical, 2 high purity ingot[8]	2
BeO	25[20]	2

Unit Costs

The cost of solid breeder material includes costs for raw material, fabrication into the desired form, ^6Li enrichment, and multiplier costs. Factors to be considered include the difficulty in handling the raw materials, the complexity of the fabrication process, and the required product purity. For example, a very fine-grained material may be more costly to fabricate due to the increased processing of the initial powder. At present, solid breeder materials are not available in reactor-relevant quality and quantity so there is no direct cost data. However, several observations can be made to estimate the cost, particularly the relative cost of the different material options.

Pure Li_2O has been fabricated in reasonably large quantities (600 kg) for neutronics experiments (TFTR Lithium Blanket Module Experiment and JAERI/US Fusion Neutronics Source experiments). The cost was ~ 300 $/kg for the Li_2O powder and 300 $/kg for final form fabrication.[1] Methods to reduce the cost for Li_2O were suggested as part of the TFTR LBM effort.[59] $LiAlO_2$ and LiAl have been produced in large quantities for military programs. Quantitative information on the quantity and material cost is, however, not available.

Other solid breeder materials have only been fabricated in small amounts (typically 100 g batches) for experimental purposes. Due to the experimental nature of the work, fabrication costs are not available or meaningful for reactor-quantity materials.

Beryllium is presently available in rods and other standard forms in reasonably large amounts. However, it is a relatively rare material only available in quantity from one source in the western world, is used in other technologies in significant amounts, and is chemically toxic in fine powder form.[8] Therefore, it is a fairly expensive material at ~ 400 $/kg raw material. Prices of 2000 $/kg have been quoted for a 2 cm drawn rod. Recent fabrication cost estimates for fusion-relevant material forms and quantities are ~ 100 $/kg based on advanced powder metallurgy fabrication techniques.[8]

^6Li is presently available in quantity (up to 1 kg) from military stockpiles in the U.S., and possibly France. It is no longer being produced in the U.S. Lithium itself is widely available, but contains about 7.5% ^6Li. The isotope enrichment process leads to a relatively expensive product. Recent U.S. prices[60] for fully enriched Li_2CO_3 were about $1000/kg carbonate, or $3000/kg ^6Li. These costs would likely be reduced in commercial production.

The costs for breeder materials in large quantities were estimated in the U.S. Blanket Comparison and Selection Study,[5] and are given in Table 2.2-16. The costs for sphere-pac and sintered product material were considered to

Table 2.2-16 Material Costs and Estimates from Previous Studies

Material	Actual costs ($/kg 1984)		Estimated reactor costs ($/kg 1984)	
	LBM/FNS[1]	BCSS[5]	BCSS[5]	NET[60]
Natural Li_2O	300/300 a	-	40	-
Natural $LiAlO_2$	-	-	53	-
Natural Li_8SiO_3	-	-	-	7/108[a]
^6Li	-	-	1500	1970
Natural LiPb	-	-	4/-[a]	6.6
Be	-	400/-[a]	350/90[a]	460
Pb	-	-	-	6.6
Steel	-	-	50	62

[a]Raw material/fabrication costs, single value is total cost

be within about 10% of each other. A recent revision of the cost model for NET also estimated material costs as given in Table 2.2-16. Since the costs for natural lithium and lead are comparable to about 7 $/kg raw material[61], the raw material costs for the solid Li_7Pb_2 material are assumed to be similar to those for the liquid $Li_{17}Pb_{83}$ material quoted in Refs. [5,61].

From present fabrication experience,[60] it has been estimated that the ternary ceramics are similar in fabrication effort, and thus costs. They have no particularly expensive base materials (other than ^6Li), and are not notably reactive or hygroscopic. Li_2O, however, is significantly hygroscopic so it must be handled more carefully, preferably with inert atmosphere. This might be anticipated to increase Li_2O fabrication costs by a factor of 2-3 relative to the ternary ceramics. Materials containing beryllium involve chemical toxicity hazards that require control of the atmosphere in the fabrication area. These materials might consequently be roughly a factor of 3-4 more expensive to fabricate than ternary ceramics. Solid lithium-lead involves no particular materials or hazards, so it is expected to be similar in fabrication costs to the ternary ceramics.

Table 2.2-17 summarizes the recommended breeder material costs, combining materials costs and fabrication costs. The raw material costs for Be and ^6Li are significantly higher than the others - none of the other metals used in the base materials are particularly expensive. The lithium beryllate and BeO costs are assumed to be a factor of two less than for Be, reflecting the smaller amount of Be per unit mass of material, along with the generally more difficult fabrication effort with beryllium. Li_2O has the advantage of being a simpler chemical system, but needs more care in fabrication. There is already considerable experience with this material, and the net material cost is suggested here to be comparable to that for the ternary ceramics. At present, it is believed that reasonably conventional fabrication methods can be identified to produce either sphere-pac or sintered pellets with desirable microstructure for the candidate breeder materials. Once the base material costs have been established with natural enrichment lithium (7.5% ^6Li), the costs for enriched material can be directly computed based on the assumed 1500 $/kg cost of ^6Li.

These cost estimates are driven by the costs for beryllium and ^6Li, and consequently, the uncertainties in these costs. In BCSS Ref. [5], the beryl-

Table 2.2-17 Unit Cost Estimates for Breeder Materials[a,b]

Material	Density[c] (gSB/cm^3)	(gLi/cm^3)	Natural	30% ^6Li	60% ^6Li	90% ^6Li
Li_2O	2.01	0.93	50	210	410	620
$LiAlO_2$	2.56	0.27	50	90	130	180
Li_5AlO_4	2.22	0.61	50	140	270	390
Li_2SiO_3	2.52	0.39	50	110	170	240
Li_4SiO_4	2.28	0.53	50	130	230	340
Li_2ZrO_3	4.15	0.38	50	80	120	160
Li_8ZrO_6	4.0	0.91	50	130	230	330
Li_2TiO_3	2.6	0.33	50	90	150	210
$Li_2Be_2O_3$	2.5	0.43	200	260	340	410
Li_7Pb_2	4.59	0.48	50	85	130	180
BeO	3.01	-	200	-	-	-
Be	1.8	-	400	-	-	-

[a]No major cost difference between sphere-pac and pellet forms

[b]1500 \$/kg ^6Li

[c]100% theoretical density

lium cost was estimated to be as low as 150 \$/kg for sphere-pac material, and as high as 1000 \$/kg for rod and ball material. The cost of the solid breeder material was considered uncertain within 30 \$/kg based on the cost of the natural lithium itself. Uncertainties in ^6Li were not considered. Here, it is recommended that all material costs be considered uncertain within a factor of two, based on the present lack of definition of reactor-grade material characteristics and the associated fabrication processes, as well as uncertainties in the supply of the raw materials.

Impurity Levels

Significant differences among the breeder materials in activation are expected. The activation levels are functions of the base material and the impurity content.

It might be expected that impurities that are chemically similar to the primary materials will be present. Thus, for example, the lithium zirconates would have more heavy metal impurities than the lithium silicates. However, the actual impurity levels are strong functions of the feed material, the manufacturing process, and the care taken to reduce specific contaminants. Consequently, it is not presently possible to identify the impurity levels in reactor-grade material. For example, impurity control is not a major factor in current fabrication efforts, so specific impurities can be reduced with deliberate effort. However, this may be offset by difficulties in controlling purity in a large-scale commercial production environment.

In order to estimate the relative activation of the materials, a range of impurity levels can be considered based on: 1) pure material (no impurities, representing the ideal limit); and 2) present experience (current feedstock purity and fabrication methods).

Feedstock Impurities: Data for some feedstock materials are summarized in Table 2.2-18. Where a range was given, the maximum value is listed in the table. Li_2CO_3 is often used as the initial lithium-bearing material, and the ternary ceramics can be formed by solid state reactions between the single metal oxide and lithium carbonate (e.g., Ref. [4]). Single oxide impurities are indicated in the table for two grades of commercial purity. These impurities are representative of the impurities associated with the primary metal, even though other feed materials might be used in specific fabrication processes. Single oxide ceramics such as alumina, silica and zirconia have been produced to electronic quality with less than 1-10 ppm of almost all elements.

Fabrication Impurities: Impurities associated with fabrication are particular to the process. For example, ball milling of ternary ceramics to reduce the powder size was observed to add about 100 ppm Al if Al_2O_3 balls were used.[4] Others have noted small amounts (10-30 ppm) of Fe and related alloying elements in materials processed in steel containers. Reactions in platinum crucibles with various ternary ceramics led to mixed results in terms of contamination by Pt.[4] Use of crucibles formerly used for grinding other materials (e.g., U), have been noted to lead to those impurities in the first batch of lithium ceramics, even after cleaning. With the zirconates, it was reported that the feedstock can be varied to minimize Cl contamination such as through the use of $ZrO(NO_3)_2 \cdot nH_2O$ rather than $ZrOCl_2 \cdot 8H_2O$.[4]

Table 2.2-18 Typical Impurity Levels in Primary Feed Materials (wppm)[a]

	Li_2CO_3 99.9%/ACS	Al_2O_3 99.8/99%	SiO_2 99.9/99.5%	ZrO_2 99.9/99%	Be 99/98%/BCSS
Li	x				3/5/3
Be					x
B		15		0.6	2/5/2
C	x				1200/1500/1000
N	5/5				-/-/300
O	x	x	x	x	-/-/7000
F					
Na	10/1000	400	75		
Mg		5	25/100	10/100	600/800/800/80(7)
Al		x	250/400	25/800	900/1500/900/90(7)
Si		200/500	x	85/1500	800/800/600/60(7)
P					
S	5/2000	/50		300	
Cl	/50				
K	10/100				
Ca	50/100	100	/60	10/20	200/200/200
Ti		40	100/200	25/700	
V				5	
Cr				10	200/400/100
Mn				5	200/400/150
Fe	1/20	50/50	200/100	10/200	1400/1800/600/100(7)
Co				5	5/10/5
Ni				10	300/400/300
Cu		1	/15	10	150/200/100
Zn				50	/10/200
As					
Sr					
Zr				x	
Hf				26	
Nb				50	/ /5
Mo				5	20/20/20
Ag					10/10/-/0.5(7)
Cd				0.2	2/5/2
Sn				10	
Sb			/1200		
Ba					
Ta				100	
W				10	
Pb	20/20	/10		5	20/20/20
Bi			/1200		
U				2	
Th				100	

[a] 'x' indicates that the element is a major constituent, not an impurity.

Breeder and Multiplier Typical Impurity Levels: Table 2.2-19 summarizes the impurity levels reported for some particular fabricated breeder materials. When particular impurities are reported, it is not generally stated whether other impurities are specifically not present. Considerably more detail in the impurities has been reported for Li_2O, $LiAlO_2$ and $Li_{17}Pb_{83}$ from the Blanket Comparison and Selection Study.[5] Typical N, F and Cl levels are indicated based on half of the FUBR-1B maximum level specifications for these impurities.[21] Additional impurity levels were identified in Ref. [62] for Li_2O, and Ref. [53] for $LiAlO_2$.

Table 2.2-20 summarizes the 'typical' impurity levels suggested here for comparison purposes. These represent an average value from among those reported. It is assumed that the fabrication process and impurities are similar enough within each material class (i.e., aluminates, silicates, titanates, zirconates, beryllates, lithium-lead alloys, and Be/BeO) as compared to the uncertainties in the impurity differences between material classes. It is emphasized that these results are approximate.

In general, the impurity levels in Table 2.2-20 were estimated by first combining the reported impurities for the feedstock materials as a reference case (assuming roughly a factor of two reduction in wppm based on the general stoichiometry of the lithium breeder). The higher purity materials were assumed, except for beryllium where the low values for Mg, Al and Si reported in Ref. [8] are about an order of magnitude lower than in Refs. [5,63,64]. These reference values were then adjusted according to the available data for actual fabricated material. Where the impurity appeared to be due primarily to common materials or fabrication processes (e.g., K from the lithium feedstock, Fe from the fabrication container), impurity levels were held to similar levels at least among the ternary ceramics. The very high Zn, As and Sr contents reported in Ref. [5] for $LiAlO_2$ and $Li_{17}Pb_{83}$ were not observed in any other reports or materials. This may be due to the particular materials considered in that study, or to the lack of impurity detail available for the other materials. The high levels were reduced to more typical impurity levels of 200 wppm in order not to overly penalize these materials.

Table 2.2-19 Reported Impurity Levels in Breeder Materials (wppm)[a]

	Li_2O	$LiAlO_2$	Li_4SiO_4	Li_2SiO_3	Li_2ZrO_3	Li_8ZrO_6	$Li_{17}Pb_{83}$	Li_2TiO_3
Li	x	x	x	x	x	x	x	x
Be		10					10	
B		10					10	
C	150							
N		500	500	500	500	500	10	
O	x	x	x	x	x	x	260	x
F	80	80	80	80	80	80		
Na	50,20	50	500				100	
Mg								
Al	20	x	100		100		50	
Si	10		x	x			10	300
P		500					500	
S							300	
Cl	100,80	100,80	80	80	80	80	20	
K	370	500					300	
Ca	210	30					100	
Ti		30					30	x
V		30					30	
Cr		30,30	250				20	
Mn	20,4	10					10	
Fe	100	30,200	500				100	
Co		30,0.2					30	
Ni	20	20	200				10	300
Cu	6	10					10	
Zn		500,50					500	
Pt								300
As		500,3					300	
Ga		2						
Sr		1000					1000	
Zr		100			x	x	300	
Nb								
Mo		30,10					30	
Ag		10					10	
Cd		100					50	
Sn		300					10	
Sb		100,0.2					30	
Ba		100,40					100	
La		2						
Pb	80	10					x	
Bi		10					100	
U		3						

[a] 'x' indicates that the element is a major constituent, not an impurity

Table 2.2-20 Reference Impurity Levels for Candidate Breeder and Multiplier Materials (wppm)[a]

	Li_2O	$LiAlO_2$ Li_5AlO_4	Li_4SiO_4 Li_2SiO_3	Li_2TiO_3	Li_2ZrO_3 Li_8ZrO_6	$Li_2Be_2O_3$	Li_7Pb_2	Be/BeO
Li	x	x	x	x	x	x	x	3
Be	-	10	-	-	-	x	10	x
B	-	10	-	-	-	2	10	2
C	-	-	-	-	-	-	-	1000
N	-	-	-	-	-	100	10	300
O	x	x	x	x	x	x	300	7000/x
F	-	-	-	80	-	-	-	-
Na	50	50	50	50	50	50	100	-
Mg	-	2	10	10	10	200	10	800
Al	20	x	200	20	20	200	50	900
Si	10	200	x	200	80	200	10	600
P	-	500	-	-	-	-	500	-
S	5	5	5	5	100	-	300	-
Cl	80	80	80	80	80	80	20	-
K	400	500	400	400	400	400	300	-
Ca	200	30	30	30	10	100	100	200
Ti	-	30	-	x	-	-	30	-
V	-	30	-	-	2	-	30	-
Cr	-	30	100	-	-	50	20	100
Mn	20	10	-	-	2	70	10	150
Fe	100	30	50	50	50	50	100	100
Co	-	30	-	-	2	2	30	5
Ni	20	20	50	50	50	100	10	300
Cu	6	10	10	10	10	50	10	100
Zn	-	200	-	-	20	100	200	200
As	-	200	-	-	-	-	200	-
Sr	-	200	-	-	-	-	200	-
Zr	-	100	-	-	x	-	300	-
Nb	-	-	-	-	20	2	-	5
Mo	-	30	-	-	2	10	30	20
Ag	-	10	-	-	-	-	10	1
Cd	-	100	-	-	-	1	50	2
Sn	-	30	-	-	5	-	10	-
Sb	-	100	100	-	-	-	30	-
Ba	-	100	-	-	-	-	100	-
Ta	-	-	-	-	50	-	-	-
W	-	-	-	-	5	-	-	-
Pb	20	10	10	10	10	20	x	20
Bi	-	10	100	-	-	-	100	-
U	-	1	-	-	1	-	-	-

[a] 'x' indicates that the element is a major constituent, not an impurity

2.3 Solid Breeder Comparison and Testing Priorities

2.3.1 Objectives

Solid breeder blanket research is in a material development and selection phase which requires the consideration of a large number of candidate materials with respect to their properties and relative behavior under test conditions. A consistent and detailed comparison of the effect of solid breeder material choice on blanket attractiveness could focus the test matrix by reducing the number of solid breeder materials which need to be tested. This comparison could also identify material tests required to reduce important performance uncertainties. The Blanket Comparison and Selection Study[5] (BCSS) provided a fairly detailed assessment of various blanket concepts, but did not attempt a specific and consistent comparison among the solid breeder materials in a blanket design context. BCSS chose $LiAlO_2$ and Li_2O as representative and attractive solid breeders based on a review of the available solid breeder data in 1983. In fact, there is a large number of potential solid breeder/multiplier materials with particular features and issues but it would be very expensive to consider all the options in experimental detail. The present study considers seventeen solid breeder/multiplier material combinations in a blanket design context and compares them on the basis of selected performance parameters. The objectives of this study are to: 1) provide a consistent comparison of the effect of solid breeder material choice on blanket attractiveness using the most recent data available; 2) evaluate the impact of uncertainties about breeder material properties and behavior on blanket feasibility and attractiveness; and 3) provide guidance to the test program on the choice of experimental parameters and solid breeders.

2.3.2 Materials and Conditions

The different materials considered in this study are listed in Table 2.3-1. The list includes all solid breeder materials currently seen as potentially attractive candidates. Except for Li_2O and Li_7Pb_2, all other solid breeders are ternary ceramics. Beryllium is used as the neutron multiplier in combination with these solid breeders which may require better neutronics performance. Other multipliers (Pb and Zr_5Pb_3) have been proposed, but are not considered here. Their primary advantage (cost) is offset by a combination of

Table 2.3-1 Solid Breeder Materials Considered

Without a Multiplier	Homogeneous Solid Breeder/Multiplier Mixture	With a Separate Be Multiplier Region
1. Li_2O	6. $LiAlO_2$/Be	10. Li_2O
2. Li_2ZrO_3	7. $LiAlO_2$/BeO	11. $LiAlO_2$
3. Li_8ZrO_6	8. Li_2O/Be	12. Li_5AlO_4
4. $Li_2Be_2O_3$	9. Li_2O/BeO	13. Li_2SiO_3
5. Li_7Pb_2		14. Li_4SiO_4
		15. Li_2ZrO_3
		16. Li_8ZrO_6
		17. Li_2TiO_3

inferior neutronics and thermophysical properties. For most cases considered here, the multiplier is separate and in front of the breeder. However, for Li_2O and $LiAlO_2$, a homogeneous mixture of solid breeder and multiplier is also considered to examine the features of this approach. Since Be will chemically reduce the solid breeder material (although the rate might be acceptably slow once an initial BeO layer forms), BeO is also included as an alternative for the homogeneous mixture cases.

The material combination, SB/He/Be/FS, where SB denotes solid breeder and FS denotes ferritic steel, was generically identified as attractive in the BCSS and other studies.[5] The BCSS $LiAlO_2$/He/FS/Be outboard blanket design (ranked R=1 in BCSS) is adopted here as a reference blanket configuration to the extent that the design details are independent of the solid breeder. This choice minimizes unnecessary analysis and provides a consistent blanket framework for the material comparison. However, it is important to make sure that the fixed assumptions do not arbitrarily affect one material more than the others, and where required, sensitivity calculations have been done to evaluate the effect of design changes on the performance of the solid breeders.

The reference blanket design consists of 1125 modules; the neutron load at the first wall is 5 MW/m^2. A typical module is shown in Figure 2.3-1. The

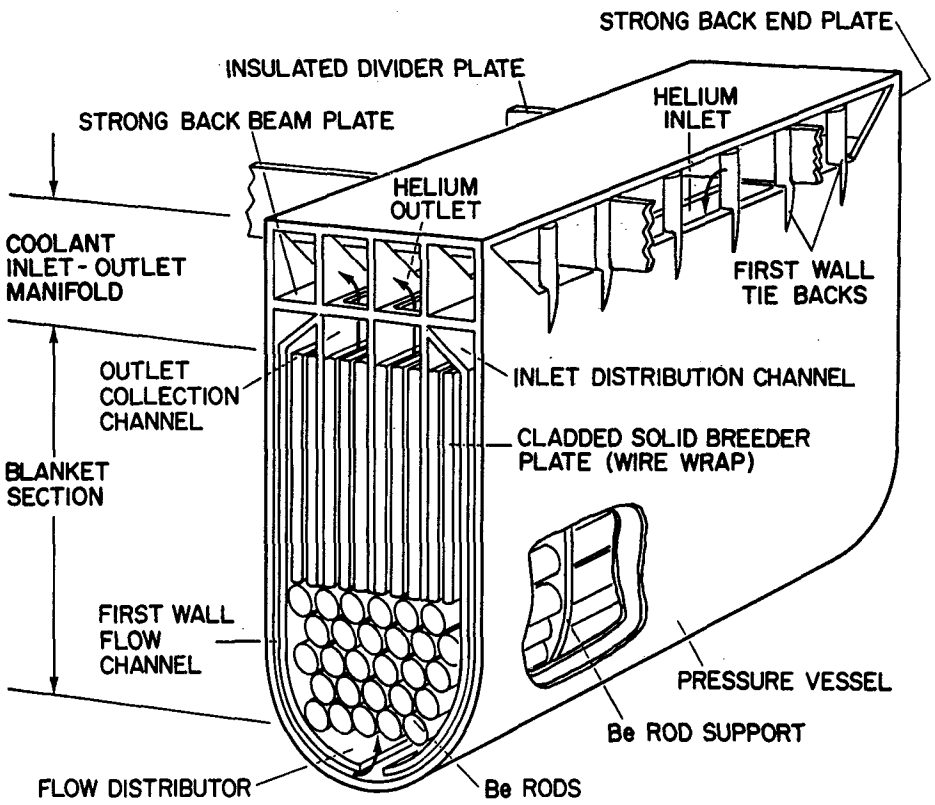


Figure 2.3-1 Reference blanket design

solid breeder or homogeneous solid breeder/multiplier mixture is in the form of flat plates with a thin HT9 cladding on each side. The plates are wire-wrapped to provide a gap between adjacent plates for the main helium flow which enters through the first wall and exits radially through the multiplier and breeder regions. For cases with a separate multiplier region, an array of multiplier rods is placed in front of the breeder plates. The thickness of the breeder plates is calculated from the nuclear heating rate, the thermal conductivity and the maximum allowable temperature for the material. Since the volume fractions (and, hence, the plate thickness) are required for the nuclear heating rate calculation, a few iterations between the temperature and neutronics calculations are required in each case. The ^{6}Li enrichment, the multiplier region radial thickness for the cases with a separate multiplier

region, and the ratio of solid breeder to multiplier volume fraction for the homogeneous mixture cases, are chosen based on optimization of the tritium breeding ratio.

The reference blanket module parameters are listed in Table 2.3-2. It is emphasized that the solid breeder comparison would be largely unaffected if the values of many of these particular blanket design parameters were altered. Some important design issues which must be treated consistently are discussed below.

1. Purge Flow Pressure

The helium purge flow pressure may range from 0.1 MPa to 10 MPa. The advantages of low purge flow pressure are that: 1) the breeder clad will not rupture if the first wall is ruptured and the blanket module depressurized; and 2) the clad is pressed firmly into contact with the breeder by the coolant pressure (for sufficiently thin clad) which improves the breeder/clad interface heat transfer and its predictability. The advantages of high purge pressures are that: 1) for a sphere-pac configuration, the effective thermal conductivity of the breeder can be improved; and 2) purge pressure control allows blanket operation with the reactor at fractional power. The selected approach is to adopt an intermediate pressure of 1.0 MPa with enough cladding thickness to withstand coolant depressurization.

2. Solid Breeder Form

The different breeder forms (sintered block or sphere-pac) raise different issues (e.g., assembly, cracking and gap conductance for the sintered block form, lower thermal conductivity for the sphere-pac form) that are more dependent on the form than on the breeder material. The advantages of sphere-pac form were generally recognized in previous studies but it was not clear whether sphere-pac could be produced for the candidate breeder materials (Li_2O in particular). On the other hand, there has been very limited effort to produce this form, and no fundamental technical limitations have been identified. $LiAlO_2$ has been fabricated in sphere-pac, and some ideas have been explored for Li_2O.

Table 2.3-2 Blanket Concept Parameters
(SB = Solid Breeder; M = Multiplier)

PARAMETER	COMMENT
Solid breeder material	As shown in Table 2.3-1
Multiplier	Beryllium
Structural material	HT9
Coolant and purge gas	Helium
Module width	0.3 m
Module length	2.0 m
Blanket depth	0.7 m to coolant plenum
Coolant plenum depth	0.2 m
Shield depth	0.6 m Fe1422 (0.3 m used to establish neutronics albedo)
Breeder geometry	Wire-wrap clad plates Radial depth = 0.32 m for cases with a separate multiplier = 0.57 m for cases without a multiplier and for homogeneous SB/M cases Plate thickness is SB-specific
Clad geometry	0.5 mm thick, wrapped around breeder plate ≈ 10 cm wire-wrap spacing, with 1 mm OD wires Accommodation of swelling/thermal expansion unspecified
Multiplier geometry	Unclad axial pins Multiplier region radial depth SB-specific
Coolant geometry	1 mm channel between solid breeder plates Coolant flows through module perimeter and first wall, and then enters multiplier/breeder region
First wall geometry	Lobed first wall with surface grooving & internal cooled channels: Total thickness = 9 mm; first wall thickness = 1.5 mm; second wall thickness = 0.5 mm; groove dimension = 7 x 1 mm^2 channel dimension = 7 x 1 mm^2
Coolant thermal-hydraulics	5.1 MPa and 275 °C inlet conditions to blanket 5.1 MPa and 332 °C at entrance to multiplier or breeder zone from first wall Exit condition is SB-specific Coolant flow rate 1.12 m^3/s per module
Breeder/Multiplier thermal-hydraulics	Min and max temperature are material-specific
Neutronics	Multiplier region thickness is SB-specific ^6Li enrichment is SB-specific Tritium breeding, energy multiplication rate, activation, and heating profile are SB-specific
Tritium recovery	Purge flow pressure = 1 MPa Purge flow rate = 0.01 m^3/s per module Composition: He with 1% added H_2 Tritium inventory is SB-specific Tritium permeation rate is SB-specific
Blanket lifetime	15 MW-yr/m2, or 4 years at 75% availability

For this study, sintered block is adopted as the standard solid breeder form. Although the temperature (i.e. thermal conductivity-related) calculations are specific to sintered-block material, much of the relative results apply also to the sphere-pac form. The effect of cracking on sintered material performance is considered.

3. Beryllium Configuration

The BCSS design adopted unclad beryllium pins positioned axially behind the first wall. These pins were structurally self-supporting over the blanket life, and the lack of cladding aided the tritium breeding. However, problems that were identified include: the removal of tritium generated in the multiplier; the physical separation of the multiplier from the breeder (a tritium breeding penalty and an additional configuration complexity); the lack of a thin layer of solid breeder in front of the multiplier (another tritium breeding penalty); and the possibility of too much beryllium swelling for structural integrity. In addition to the BCSS configuration, there are three basic alternatives:

1. A clad multiplier in axial pins would add a tritium breeding penalty, but could resolve structural and tritium recovery concerns since, for example, the multiplier could be made porous reducing the impact of swelling, and the helium purge stream could also be directed to the multiplier (although this then raises chemical compatibility concerns).
2. Mixing the multiplier with breeder material would improve breeding and thermal conductivity, reduce configuration complexity and remove multiplier tritium recovery and structural integrity concerns. Furthermore, the multiplier-breeder mixture ratio could be varied to optimize tritium breeding. However, Be will chemically reduce any candidate ceramic breeder material, although the rate might be acceptably slow once an initial BeO layer forms. BeO multiplier, with reduced tritium breeding, is an alternative.
3. A third option is to incorporate a clad multiplier into the breeder plates. This would allow a breeder zone just behind the first wall. The multiplier cladding could be thin enough to allow tritium permeation into the breeder purge stream, and the multiplier could be of high porosity for swelling resistance. This configuration complicates the breeder plate design, but simplifies the blanket module design.

At this point, all alternatives should be considered for blanket designs. For this study, however, the approach is to use the unclad axial pin design for the separate multiplier cases. The effect of the mixed SB/Be and SB/BeO configuration will be assessed through the four homogeneous mixture cases. A sensitivity analysis will be done for the cases with a separate multiplier to evaluate the increase in tritium breeding when using a thin layer of solid breeder in front of the multiplier, and the corresponding effect, if any, on the solid breeder comparison.

4. Lithium Enrichment

The breeder ^{6}Li content can be varied to maximize the tritium breeding. However, it is not optimum to make the enrichment uniform or maximized throughout the breeder. For example, for some solid breeder materials, concerns over phase change as a function of burnup suggest that a minimum ^{7}Li content be maintained in order to limit the degree of compositional change during burnup. Also, since high ^{6}Li levels just behind the multiplier can lead to local power peaking, locally reducing the ^{6}Li enrichment might lead to an overall design improvement. On the other hand, if the lithium enrichment level is assumed to be fully variable within the blanket, then the neutronics optimization task becomes a major effort if more than one solid breeder material is to be considered.

The approach here is to assume a uniform ^{6}Li content within the blanket for the multiplied cases and to determine the uniform ^{6}Li enrichment which maximizes the tritium breeding ratio. The burnup and peak heating rates will be checked in each case.

5. Clad Integrity

The breeder/multiplier cladding must accommodate differential thermal expansion, breeder/multiplier swelling, and clad/breeder/multiplier creep. The plate geometry is difficult to analyze due to the complex temperature and swelling profiles, and the soft or brittle nature of the breeder material. Bellows and crushable insulation were assumed in the BCSS Li_2O designs, but were not analyzed. Since this is an area where solid breeders may differ (some swell much more than others, for example), some comparative analysis of the mechanical conditions in the clad and breeder is needed. However, it is

not clear what would be a useful clad geometry at the front of the breeder plate (e.g., bellows, or a flexible half cylinder), and what useful analysis can be provided. In this analysis, it is assumed that breeder thermal expansion and radiation swelling can be accommodated. However, the clad deflection and stresses will be estimated for the extreme case where no expansion allowance is provided in order to assess how severe a penalty could be imposed by swelling and thermal expansion.

2.3.3 Performance Parameters and Results

Table 2.3-3 lists the blanket performance parameters selected as a basis for the solid breeder comparison. The parameters fall in five general categories: neutronics, thermo-mechanics, tritium, activation, and economics.

Table 2.3-3 Performance Parameters

Neutronics:
Tritium Breeding Ratio
Energy Multiplication
Breeder Lifetime (maximum Li burnup at 3 Full Power Years (FPY))
Thermo-Mechanics:
Clad Stress and Deflection
Thermal Stress in Breeder
Tritium:
Tritium Inventory
Tritium Permeation
Activation:
Waste Disposal Rating (relative to Class C limits at 3 FPY)
Biological Hazard Potential (relative to Maximum Permissible Concentration (MPC) at 3 FPY)
Recycling Hazard
Afterheat
Economics:
Material Cost (including Be)
Net Thermal Efficiency (including pressure drop in blanket)
Power Leakage from Blanket

2.3.3.1 Neutronics

Method of Analysis

A one-dimensional cylindrical model is used for this analysis. The neutronics calculations were performed by the one-dimensional S_n code, ANISN, using a 46 group (25n-21γ) cross-section library. The library data were retrieved from the Vitamin-C/DLC-41B library, which was derived from the ENDF/B-IV nuclear data library. Data from the ENDF/B-IV library result in about 15% lower tritium production in ^{7}Li. However, the relative rankings of the tritium breeding ratio reported here for various materials do not change. S_8P_3, with 8 discrete directions and third-order Legendre expansions in the poloidal cylindrical geometry were used in the ANISN calculation. All results were normalized to a 5 MW/m^2 wall loading.

The material arrangements for the cases without a multiplier and for cases with the homogeneous SB/M (solid breeder/multiplier) mixture are shown in Figure 2.3-2. Breeder regions I and II have the same materials but those material volume fractions are different because of the inclusion of the structural elements holding the end walls in region II. For the homogeneous SB/M mixture cases, the breeder regions I and II include the SB/M mixture. The breeder and multiplier are at 80% theoretical density. HT9 is used for the shield material and no coolant is included in the shield.

The corresponding material configuration for the cases with a separate multiplier region is shown in Figure 2.3-3. The neutron multiplier zone contains a 54% volume fraction[5] of beryllium at 80% theoretical density (TD). The breeder materials are assumed to also have an 80% theoretical density. The detailed volume fractions for the three sets of cases are given in Tables 2.3-4 and 2.3-5. The volume fractions were obtained after two iterations between the neutronics calculations (which use the volume fractions to compute the heat generation per unit volume in the breeder plate), and the temperature calculations, described in Section 2.3.3.2 (which use the heat generation values to calculate the plate thickness). The corresponding lithium atom densities for the three sets of cases are shown in Table 2.3-6.

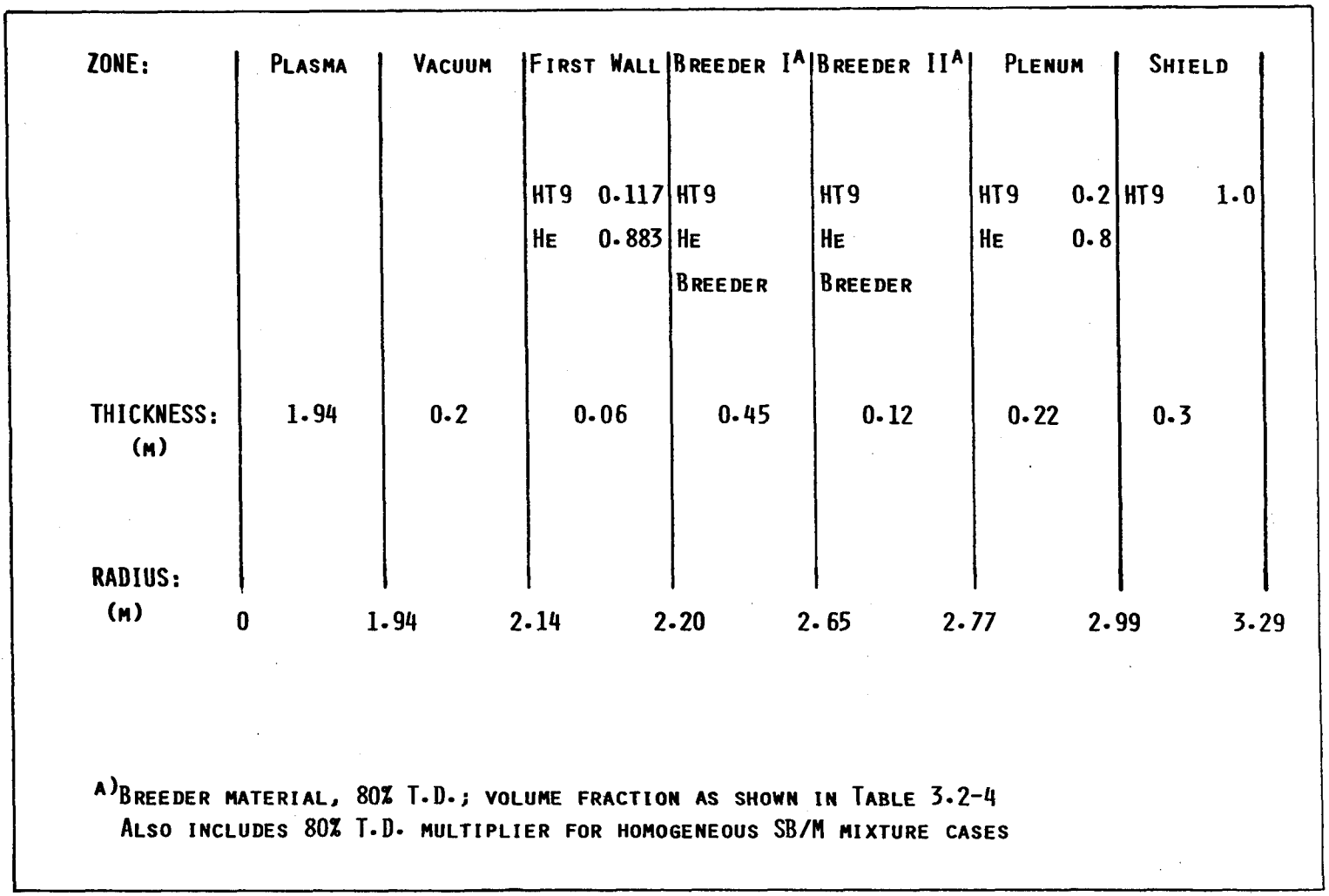


Figure 2.3-2 One-dimensional model for the cases without a multiplier and for the homogeneous SB/M mixture cases

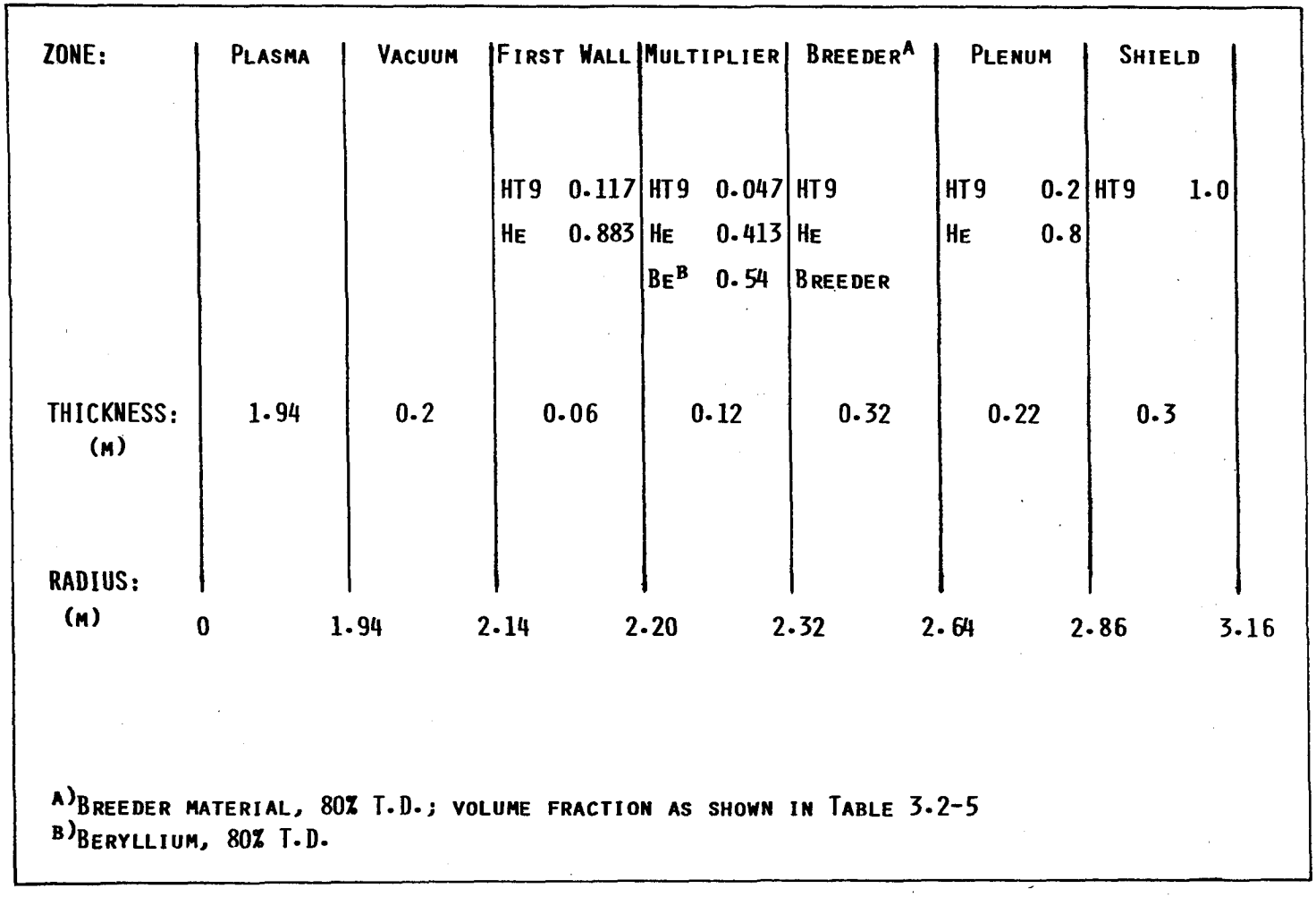


Figure 2.3-3 One-dimensional model for the cases with a separate Be multiplier region

Table 2.3-4 Volume Fractions for the Cases Without a Multiplier and for the Homogeneous SB/M Mixture Cases[a]

	FIRST WALL		BLANKET I			BLANKET II			PLENUM		SHIELD
	HT9	Helium	HT9	Helium	Breeder[b]	HT9	Helium	Breeder[b]	HT9	Helium	HT9
Cases Without a Multiplier											
Li_7Pb_2	11.7%	88.3%	6.07%	7.43%	86.5%	26.7%	4.9%	68.4%	20%	80%	100%
Li_2O	11.7	88.3	7.0	9.3	83.7	14.2	6.28	79.5	20	80	100
Li_8ZrO_6	11.7	88.3	7.6	10.8	81.6	28.2	8.0	63.5	20	80	100
$Li_2Be_2O_3$	11.7	88.3	7.9	11.6	80.5	28.6	9.0	62.4	20	80	100
Li_2ZrO_3	11.7	88.3	7.3	10.2	82.5	27.9	7.7	64.4	20	80	100
Cases With a Homogeneous SB/M Mixture					SB/M			SB/M			
Li_2O/Be	11.7	88.3	8.2	12.3	79.5	28.9	9.7	61.4	20	80	100
$LiAlO_2$/Be	11.7	88.3	8.3	11.8	79.9	29.0	9.2	61.8	20	80	100
Li_2O/BeO	11.7	88.3	8.1	11.9	80.0	28.7	9.0	62.3	20	80	100
$LiAlO_2$/BeO	11.7	88.3	7.9	11.5	80.6	28.6	8.9	62.5	20	80	100

[a] outboard case
[b] 80% dense

Table 2.3-5 Volume Fractions for the Cases With a Separate Be Multiplier Region[a]

	FIRST WALL		MULTIPLIER			BLANKET			PLENUM		SHIELD
	HT9	Helium	HT9	Helium	Be[b]	HT9	Helium	Breeder[c]	HT9	Helium	HT9
Li_2O	11.7%	88.3%	4.7%	41.3%	54%	14.4%	6.5%	79.1%	20%	80%	100%
Li_8ZrO_6	11.7	88.3	4.7	41.3	54	15.2	8.3	76.5	20	80	100
Li_5AlO_4	11.7	88.3	4.7	41.3	54	16.2	10.3	73.5	20	80	100
Li_2ZrO_3	11.7	88.3	4.7	41.3	54	14.7	7.3	78.0	20	80	100
Li_4SiO_4	11.7	88.3	4.7	41.3	54	15.7	9.3	75.0	20	80	100
Li_2TiO_3	11.7	88.3	4.7	41.3	54	14.2	6.3	79.5	20	80	100
Li_2SiO_3	11.7	88.3	4.7	41.3	54	15.9	9.6	74.5	20	80	100
$LiAlO_2$	11.7	88.3	4.7	41.3	54	14.7	7.3	78.0	20	80	100

[a] outboard cases

[b] Be-thickness, 12 cm, 80% dense

[c] 80% dense

Table 2.3-6 Lithium Atom Density for the Different Solid Breeder Cases[a]

Breeder Material	Breeder 100% Theoretical Density (g/cm^3)	100% Theoretical Li Atom Density ($10^{22}/cm^3$)	Lithium Atom Density ($10^{22}/cm^3$)[b]	
			^7Li	^6Li
Cases Without a Multiplier:				
Li_2O[c]	2.01	8.07	5.05	0.41
Li_8ZrO_6	2.97	5.87	1.64	2.46
Li_7Pb_2	4.59	4.22	1.01	1.52
Li_2ZrO_3	4.15	3.25	0.88	1.31
$Li_2Be_2O_3$	2.50	3.76	0.97	1.45
Cases With a Homogeneous SB/M Mixture (20/80)				
$LiAlO_2$/BeO	2.93	0.47	0.12	0.18
$LiAlO_2$/Be	1.96	0.47	0.12	0.18
Li_2O/BeO	2.81	1.61	0.41	0.60
Li_2O/Be	1.84	1.61	0.42	0.61
Cases With a Separate Be Multiplier Region				
Li_2O	2.01	8.07	0.90	1.35
Li_8ZrO_6	2.97	5.87	1.44	2.15
Li_5AlO_4	2.22	5.30	1.25	1.87
Li_4SiO_4	2.28	4.56	1.09	1.64
Li_2ZrO_3	4.15	3.25	0.81	1.21
Li_2SiO_3	2.52	3.36	0.80	1.20
Li_2TiO_3	2.60[d]	2.84	0.72	1.08
$LiAlO_2$	2.56	2.33	0.58	0.87

[a] 60% Li-6 enrichment for all cases except Li_2O without a multiplier

[b] For 80% theoretical density and the volume fractions listed in Tables 2.3-4 and 2.3-5

[c] Natural lithium

[d] This is the density for the γ phase. In practice, the β phase would be more appropriate at likely blanket conditions with a density of 3.43 g/cm^3 at 100% T.D.

Tritium Breeding Ratio (TBR)

In order to optimize the tritium breeding ratio (TBR), TBR values were calculated for each case for ^{6}Li enrichment varying from 7.5% to 90%. In addition, the thickness of the multiplier region was varied from 6 cm to 15 cm for the cases with a separate multiplier, and the volume fraction of breeder in the mixture was varied from 20% to 80% for homogeneous SB/M mixture cases.

For the separate multiplier cases, the TBR was calculated for different thicknesses of the neutron multiplier and a 60% breeder-material ^{6}Li enrichment. As shown in Figure 2.3-4, the general trend is that the TBR increases as the neutron multiplier thickness is increased, until saturation is reached.

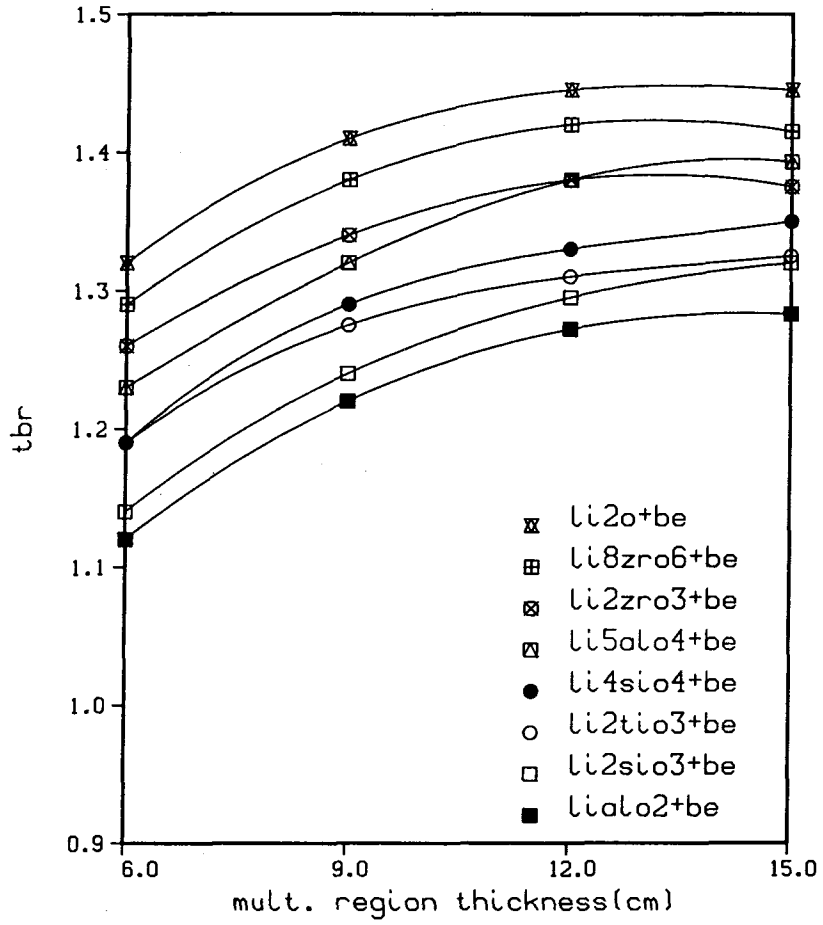


Figure 2.3-4 Tritium breeding ratio as a function of Be region thickness for the cases with a separate Be multiplier region

Note, however, that the thickness of the multiplier region could not extend beyond 12-15 cm due to consideration of maximum allowable temperature for the multiplier. It should be emphasized that the beryllium effective density in the multiplier region corresponds to (0.8 x 0.54) 43.2% of the theoretical density. Optimization of the TBR incremental rate of change with increased Be thickness led to the selection of a 12 cm multiplier zone as a reference thickness for the TBR for all the cases. For a constant 12 cm neutron multiplier, the TBR was then calculated for different values of ^{6}Li enrichment and the results are shown in Figure 2.3-5. It is interesting to note that the "TBR vs. Be thickness" and the "TBR vs. ^{6}Li enrichment" sets of curves tend to follow the same pattern and that the material ranking is almost the same in

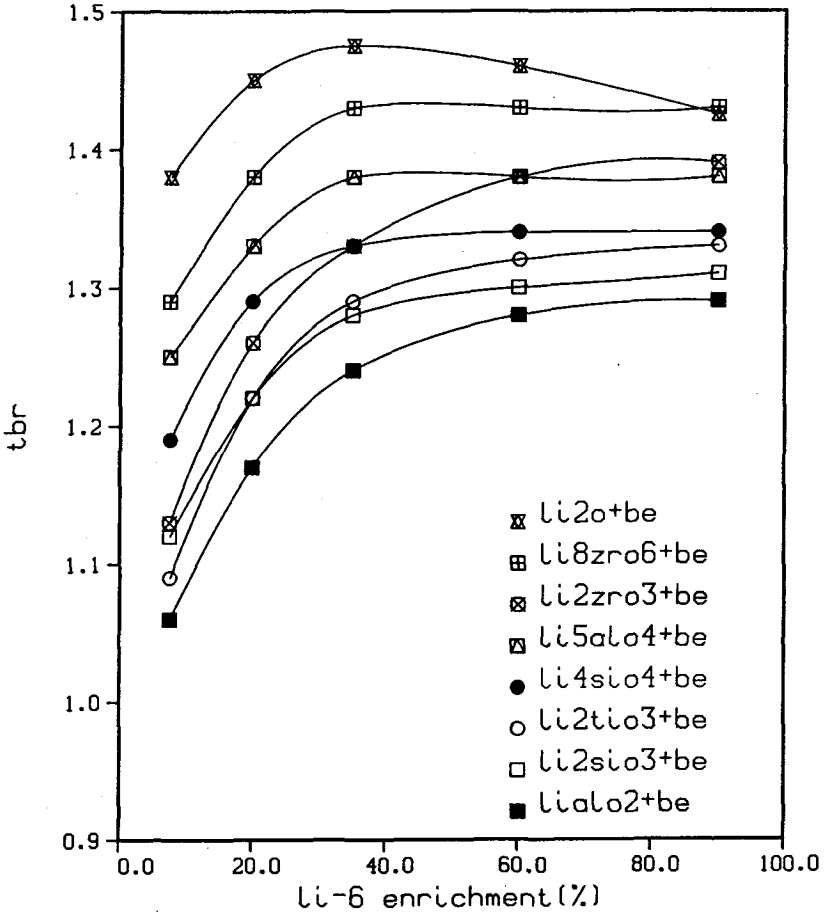


Figure 2.3-5 Tritium breeding ratio as a function of ^{6}Li enrichment for the cases with a separate Be multiplier region

both cases for all ^6Li enrichments and Be thicknesses (except for Li_2ZrO_3, whose particular behavior will be explained later), with Li_2O exhibiting the highest TBR and $LiAlO_2$ the lowest. The ranking of the solid breeders in terms of achievable TBR can be explained by their respective Li atom density, as illustrated by the "maximum TBR vs. ^6Li atom density" point curve, shown in Figure 2.3-6. In general, for cases with a multiplier, the achievable TBR increases as the ^6Li density increases.

It can be observed from Fig. 2.3-5 that the saturation point, assumed here to correspond to 99% of the maximum TBR in each case, tends to occur at lower ^6Li enrichment as the lithium atom density of the material increases. Table 2.3-7 shows the ^6Li enrichment and the Li atom density at saturation for the different cases. The ^6Li atom densities at saturation fall between the narrow range of 9×10^{21} cm^3 to $10 \times 10^{21}/cm^3$, except for the Li_2ZrO_3 case which saturates at a higher ^6Li atom density due to its high density. The material with the highest total lithium atom density considered in this study is Li_2O, which shows saturation in TBR at about 20% ^6Li enrichment. If the

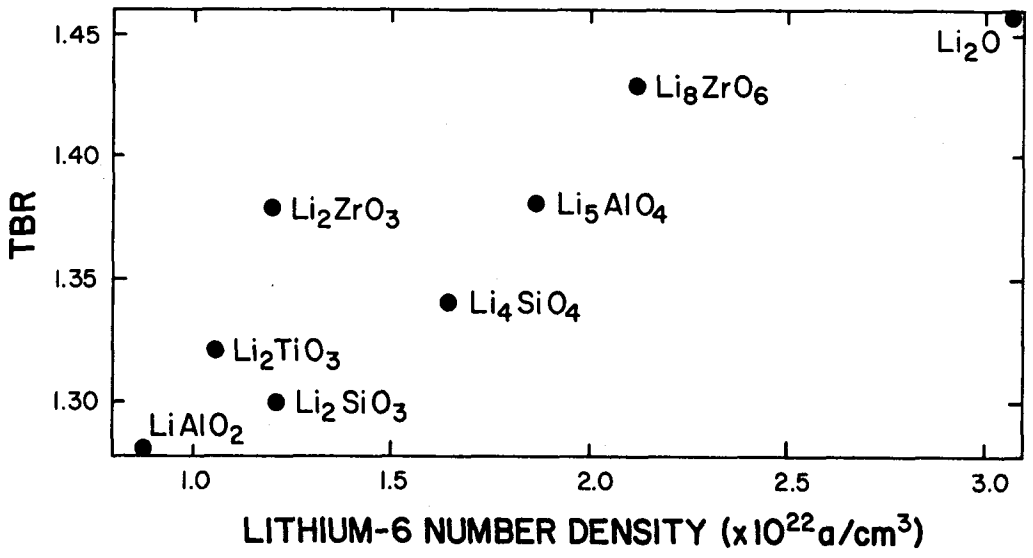


Figure 2.3-6 Tritium breeding ratio as a function of the solid breeder material ^6Li number density for the cases with a separate Be multiplier region (all cases have 60% ^6Li enrichment)

Table 2.3-7 ^{6}Li Enrichment and Atom Density at TBR Saturation (99% of Maximum TBR) for Cases with a Separate Be Multiplier Region

	^{6}Li Enrichment (%)	^{6}Li Atom Density ($10^{22}/cm^{3}$)
Li_2O	20	1.02
Li_8ZrO_6	26	0.93
Li_5AlO_4	30	0.94
Li_4SiO_4	33	0.90
Li_2ZrO_3	58	1.17
Li_2SiO_3	50	1.00
Li_2TiO_3	51	0.92
$LiAlO_2$	62	0.90

argument about saturation occurring at a ^{6}Li atom density of about 9.5 x $10^{21}/cm^{3}$ is extended, then for a 80% dense solid breeder with a 0.78 volume fraction to show saturation at a natural ^{6}Li enrichment (7.25%), it needs to have a 100% theoretical lithium atom density of about 2.1 x $10^{23}/cm^{3}$ (obtained from 9.5 x 10^{21}/(0.0725 x 0.8 x 0.78)).

Note that although the ^{6}Li atom density is about the same at saturation for the different cases, the TBR is different. This is mainly due to the differences in ^{7}Li tritium production between the different cases and to the differences in the neutronics characteristics of non-lithium atoms present (e.g., O, Zr, Si).

Another interesting point noted in Figs. 2.3-4 and 2.3-5 is the behavior of Li_2ZrO_3, whose TBR tends to peak earlier than the other cases when varying the Be thickness and later than the other cases when varying the ^{6}Li enrichment. This is due to the high mass density of Li_2ZrO_3, 4.15 g/cm^{3}, and hence, to its relatively high Zr atom density. For the neutron spectra investigated, Zr has a large cross section for (n,2n) reactions and, in effect, acts as an additional neutron multiplier, causing the TBR curve to saturate earlier with increasing Be thickness and later with increasing ^{6}Li enrichment.

For the cases without a multiplier, the neutron spectrum has a greater fraction of high energy neutrons than for the cases with a separate multiplier.

The $^{7}Li(n,n'\alpha)t$ reaction is significant at high neutron energy. Therefore, as the ^{6}Li enrichment is increased, the tritium production from ^{7}Li is decreased, which tends to have a stronger negative effect on the total tritium production than the corresponding increase in tritium production from ^{6}Li, (see Figs. 2.3-7 to 2.3-9). Note that the higher the initial T_7 (the part of the tritium breeding ratio due to tritium production in ^{7}Li), the sharper the decrease in T_7 as the ^{6}Li enrichment is increased (Fig. 2.3-9). Figure 2.3-7 shows that Li_2O exhibits the sharpest decline in TBR with increasing ^{6}Li enrichment because it does not have a neutron multiplier that will produce secondary neutrons to increase the T_6 production. Li_7Pb_2 and Li_2ZrO_3, however, exhibit an increase in TBR first and then a gradual decrease as ^{6}Li enrichment is increased. This is due to the higher atom density of Pb and Zr (both showing (n,2n) reactions) in those breeder materials.

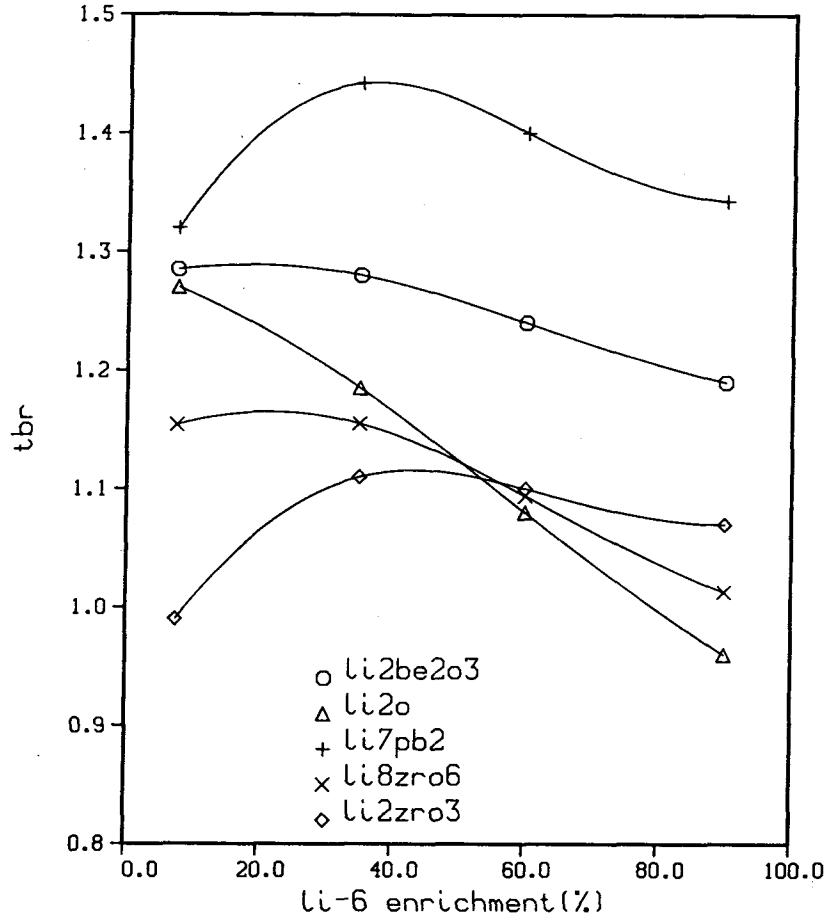


Figure 2.3-7 TBR as a function of ^{6}Li enrichment for the cases without a multiplier

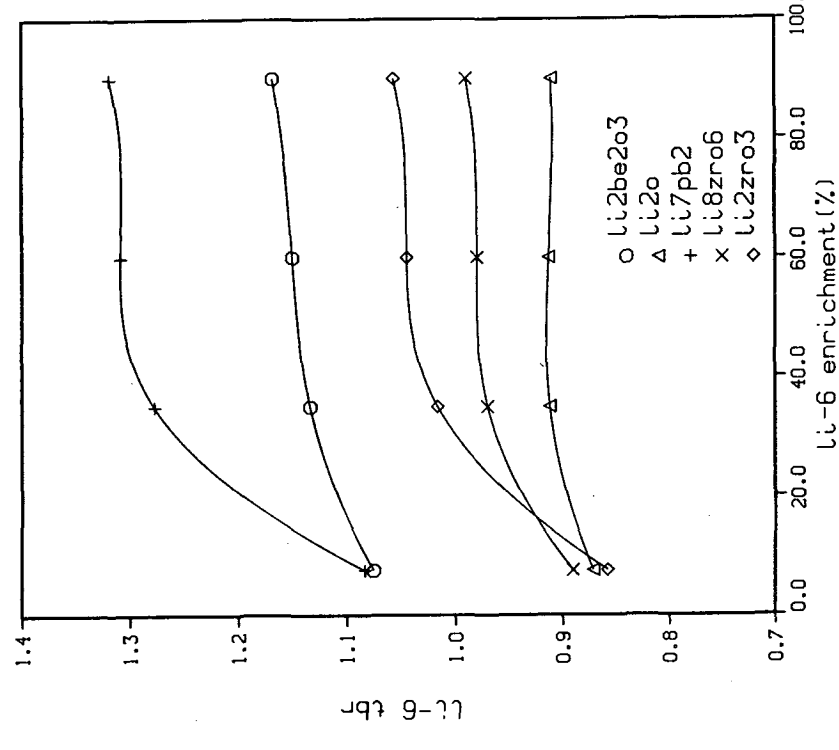


Figure 2.3-8 T_6 (TBR due to $^6Li(n,\alpha)t$) as a function of ^6Li enrichment for the cases without a multiplier

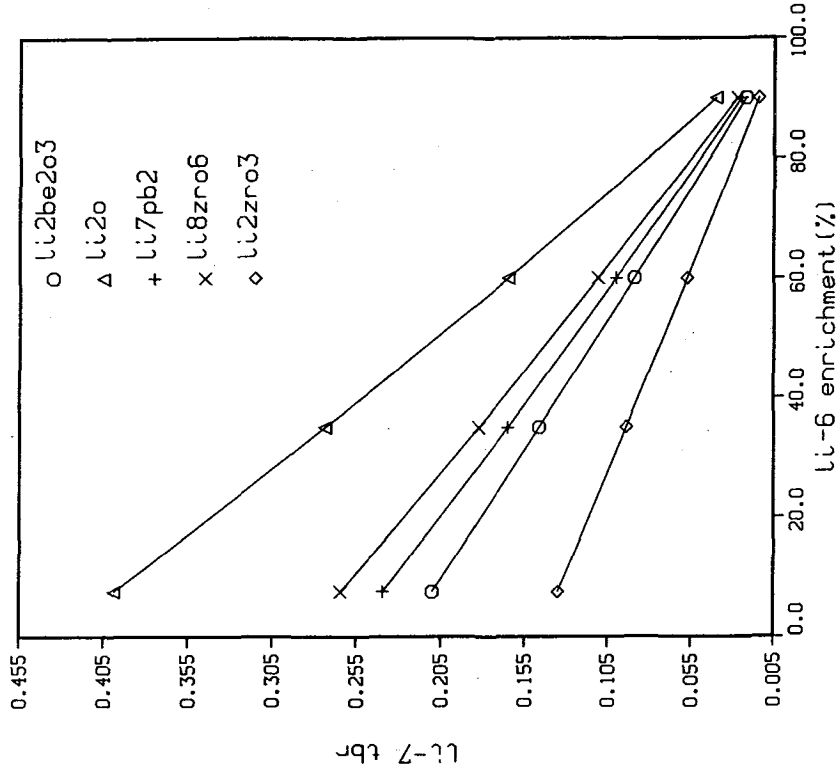


Figure 2.3-9 T_7 (TBR due to $^6Li(n,n'\alpha)t$) as a function of ^6Li enrichment for the cases without a multiplier

Four cases (Li_2O/Be, Li_2O/BeO, $LiAlO_2$/Be, and $LiAlO_2$/BeO) are considered as homogeneous mixtures of multiplier and breeder materials. Increasing the breeder volume fraction beyond 20% decreases the TBR in all four cases. As illustrated in Figure 2.3-10, this indicates that only a small amount of breeder material enriched to 60% ^6Li is required to achieve maximum tritium production. The Li_2O cases (Li_2O/Be and Li_2O/BeO) have a higher tritium production than the $LiAlO_2$ cases because the lithium atom density of Li_2O is larger than that of $LiAlO_2$. Also, the Be mixtures (Li_2O/Be and $LiAlO_2$/Be) show larger values of TBR than the BeO mixtures (Li_2O/BeO and $LiAlO_2$/BeO) because the atom density of beryllium is 1.7 times larger than that of beryllium oxide. The case with 20% breeder and 80% multiplier was selected as

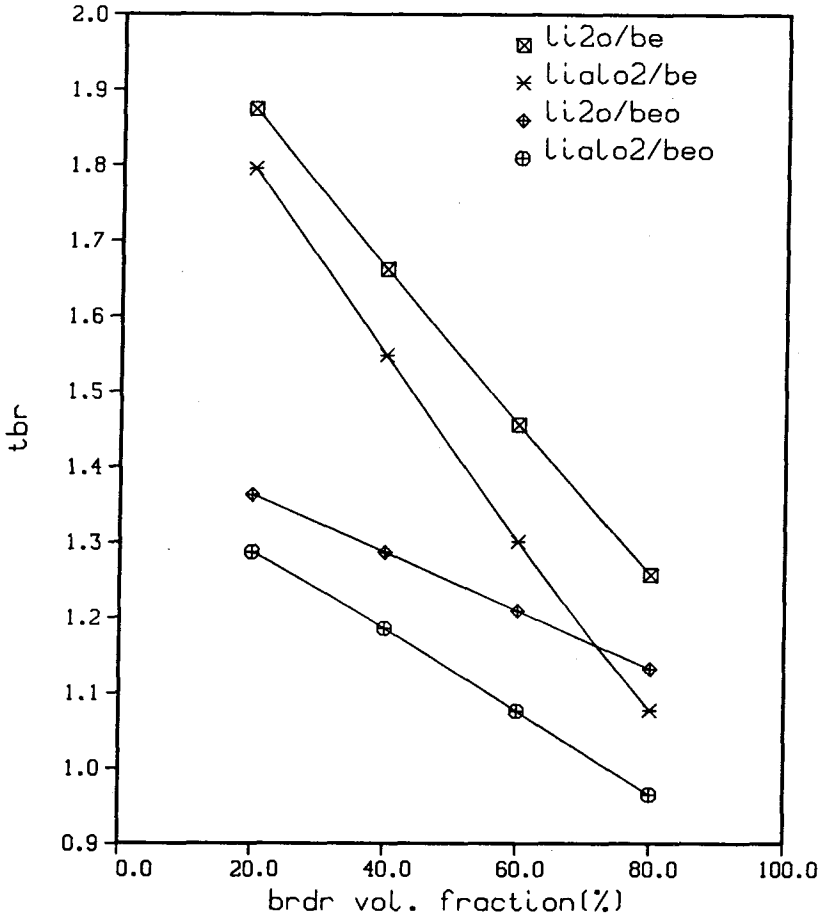


Figure 2.3-10 TBR as a function of breeder volume fraction for the homogeneous SB/M mixture cases (60% ^6Li)

reference for all cases because the TBR values were already high enough in all cases. Notice, however, that the higher volume fraction of multiplier is needed only in the first blanket region closest to the first wall; at deeper regions, the multiplier volume fraction can be substantially reduced without significantly affecting the TBR.

Figure 2.3-11 shows the variation of TBR with ^{6}Li enrichment for the four homogeneous mixture cases. Only a slight increase in TBR is observed when the ^{6}Li enrichment is increased, with saturation occurring fairly rapidly. It should be noted that the maximum TBR values for the homogeneous 20/80 mixtures of Li_2O/Be (1.87) and $LiAlO_2$/Be (1.80) are much higher than for the corresponding breeder and separate multiplier cases (1.47 for Li_2O + Be and 1.28 for $LiAlO_2$ + Be from Fig. 2.3-5).

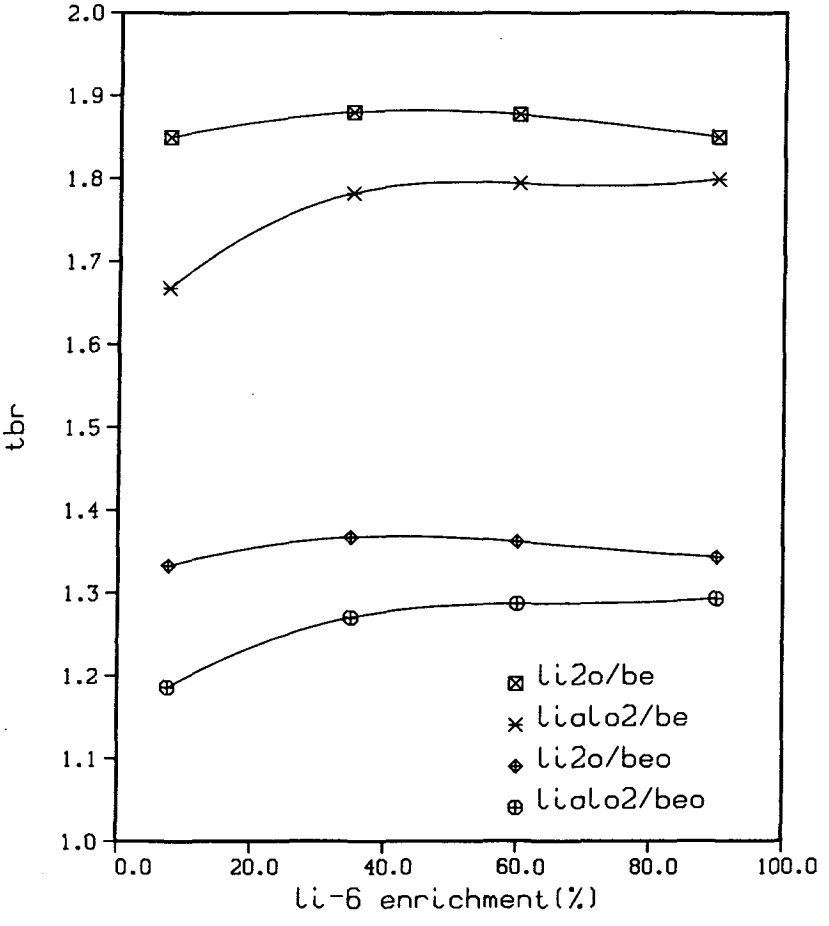


Figure 2.3-11 TBR as a function of ^{6}Li enrichment for the homogeneous SB/M mixture cases (20/80%)

As a sensitivity analysis for the cases with a separate multiplier, a sandwich-type geometry was considered, in which another breeder zone which is highly enriched in ^6Li is placed in front of the neutron multiplier zone. This geometry provides better TBR performance since the low energy neutrons scattered back from the multiplier region to the first wall are absorbed in the ^6Li in the front breeder zone. It is also probable that this will reduce the (n,γ) reaction (caused by low energy neutrons) in the first wall, which is a strong source of activation, thereby reducing the first wall activation. Neutronics calculations were done for this sandwich-type geometry to verify if the neutronics results were design-dependent and would favor a particular solid breeder material over another. Two cases were considered, one exhibiting a high TBR (Li_8ZrO_6) and the other a low TBR ($LiAlO_2$). The TBR was calculated for different values of the front breeder region thickness, ranging from 0.2 cm to 4 cm (with a 0.54 volume fraction of 80% dense solid breeder). The back breeder region thickness was adjusted to keep the total breeder thickness the same as before.

As shown in Figure 2.3-12, the effect on the TBR of adding a thin breeder zone in front of the multiplier region is similar for both the $LiAlO_2$ and Li_8ZrO_6 cases. This tends to indicate that such a change of geometry will similarly increase the TBR for all the candidate materials. To maximize the TBR, the thickness of the first region should not exceed the mean free path of the high energy neutrons that contribute to the (n,2n) reaction in the multiplier zone. Therefore, beyond a certain thickness of the first breeder region, the TBR starts to decrease, as illustrated in Figure 2.3-12. The figure shows that for both cases the maximum increase in TBR is about 0.06, which corresponds to a 0.3 to 0.5 cm first breeder region thickness (equivalent to a 100% dense thickness of 0.13 to 0.2 cm). However, the corresponding peak heating rate is very high -- of the order of 150 MW/m^3.

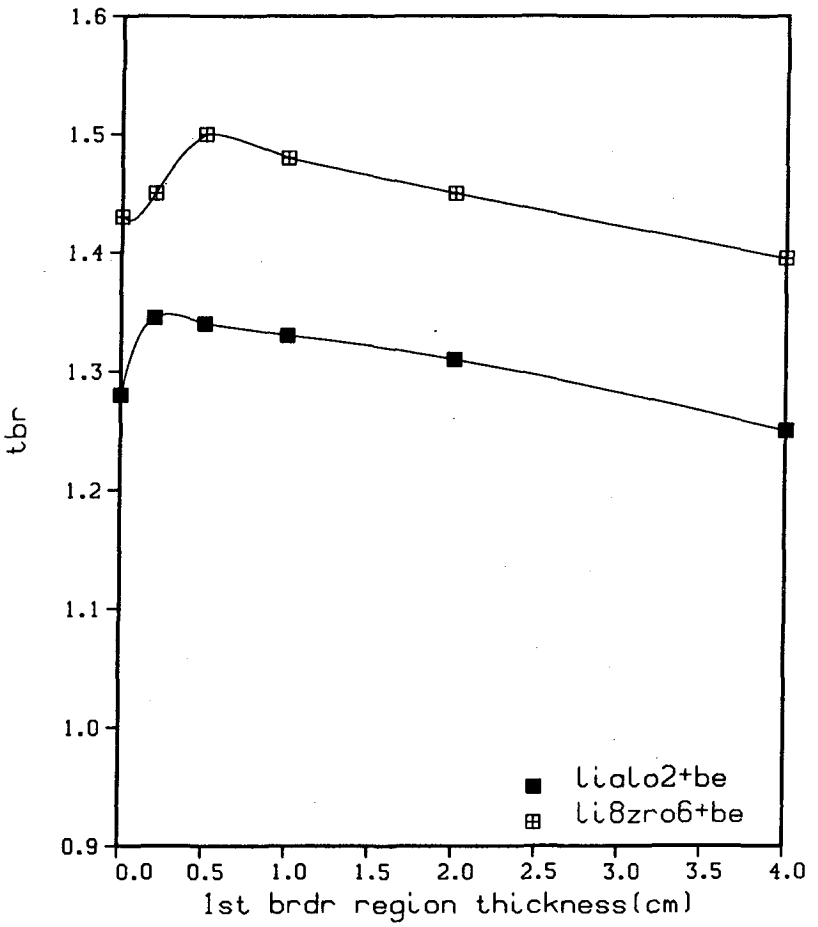


Figure 2.3-12 TBR as a function of the first breeder region thickness for the $LiAlO_2$ and Li_8ZrO_6 sandwich cases (both cases have 60% ^6Li enrichment)

Power Multiplication and Heat Generation

Figures 2.3-13 and 2.3-14 show the variation of power multiplication (M) with ^6Li enrichment for the cases without a multiplier and with a separate multiplier region, respectively. Changes in the ^6Li enrichment only slightly affect M in all cases. When the ^6Li enrichment is increased, M in the breeder region increases due to the exothermic $^6Li(n,\alpha)$ reaction. However, the radiative capture reaction rate in the structure, which has a larger Q value than that of $^6Li(n,\alpha)$, decreases. Therefore, the overall M is actually slightly

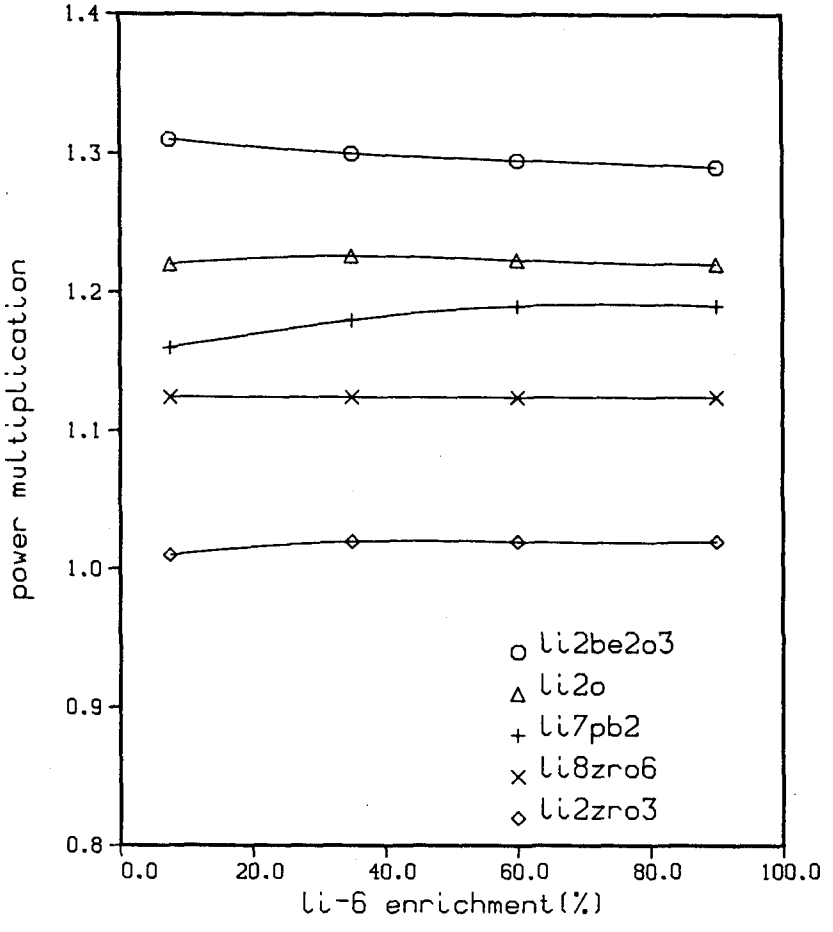


Figure 2.3-13 Power multiplication as a function of ^{6}Li enrichment for the cases without a multiplier

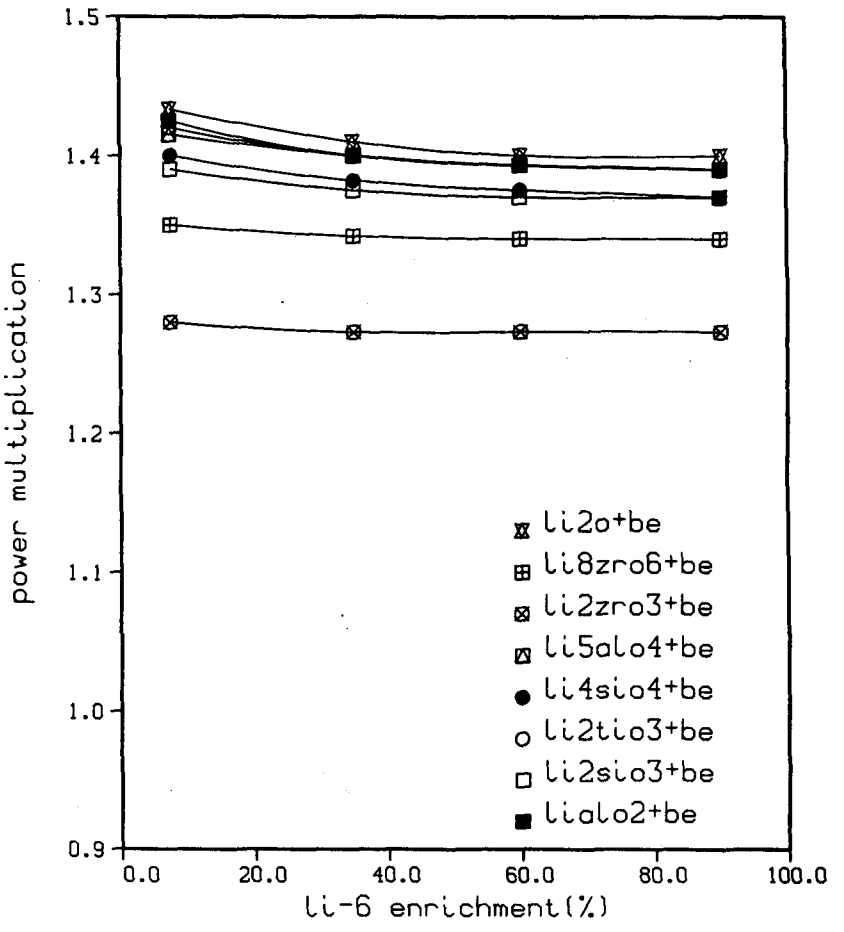


Figure 2.3-14 Power multiplication as a function of ^{6}Li enrichment for the cases with a separate Be multiplier region

decreased. For the cases with a separate multiplier region, M increases as the Be region thickness is increased due to the increase in secondary neutron production, as shown in Figure 2.3-15. In agreement with these results, M for the homogeneous breeder/multiplier mixture cases decreases markedly with increasing breeder volume fraction and shows a slight decrease with increasing ^6Li enrichment, as shown in Figures 2.3-16 and 2.3-17. Finally, for the $LiAlO_2$ and Li_8ZrO_6 sandwich cases, as illustrated in Figure 2.3-18, M decreases with an increase in the front breeder region thickness as the number of fast neutrons reaching the multiplier is reduced. Note that for all the cases, the relative M rankings tend to remain the same for all values of ^6Li enrichment and of Be volume fraction.

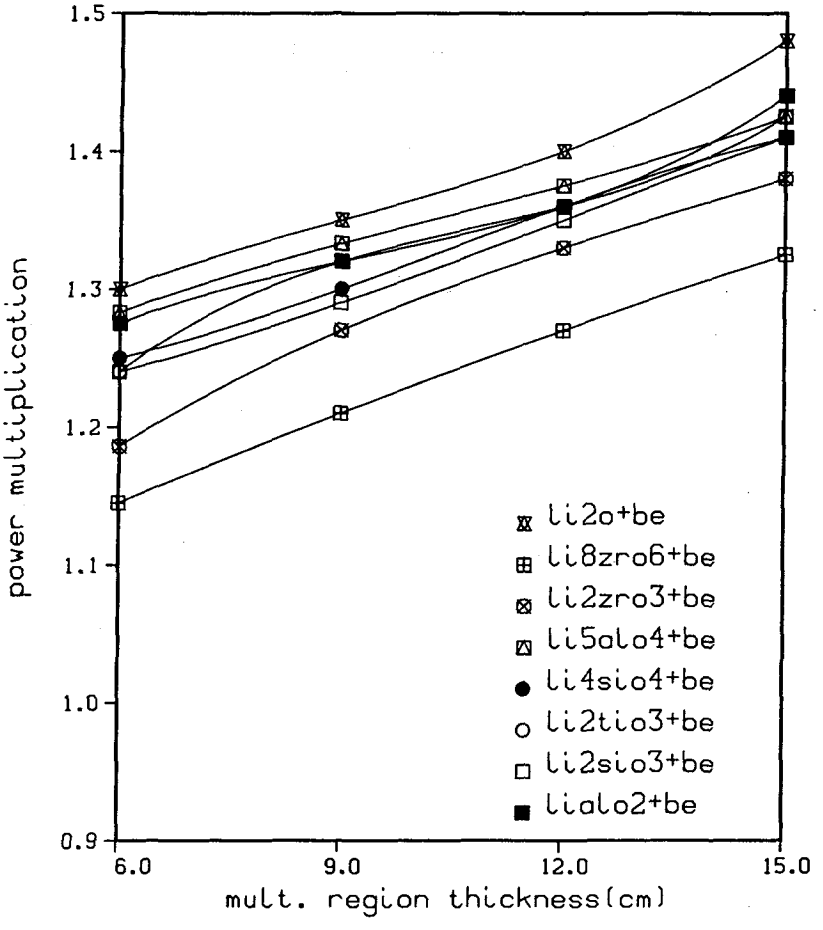


Figure 2.3-15 Power multiplication as a function of Be region thickness for the cases with a separate Be multiplier region

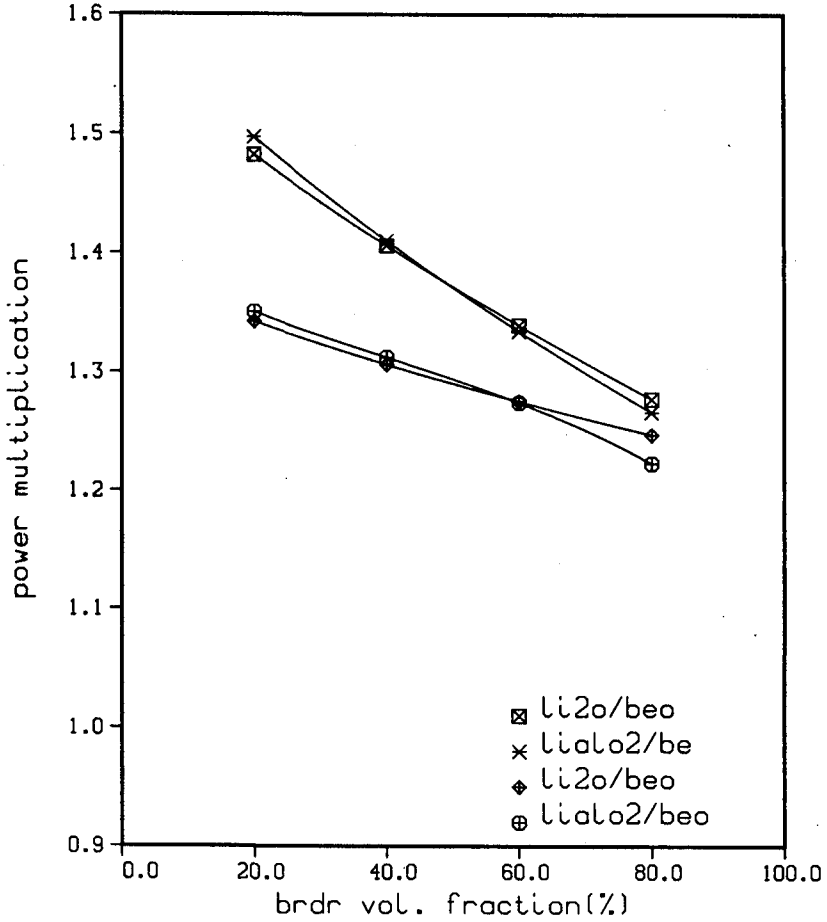


Figure 2.3-16 Power multiplication as a function of breeder volume fraction for the homogeneous SB/M mixture cases

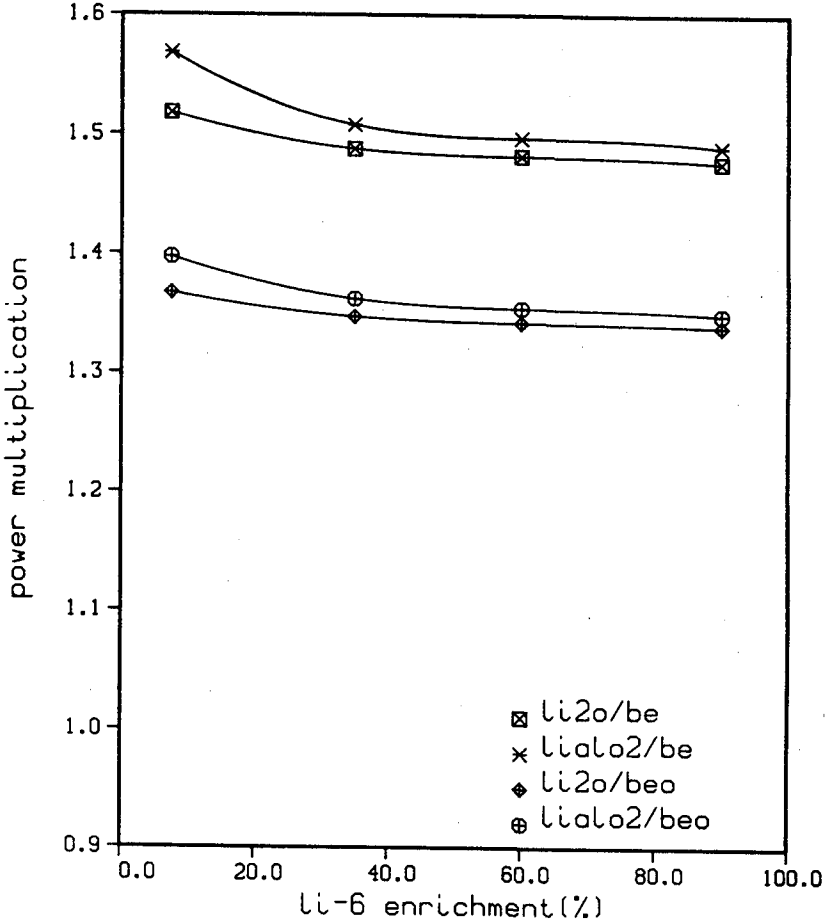


Figure 2.3-17 Power multiplication as a function of ^{6}Li enrichment for the homogeneous SB/M mixture cases (20/80)

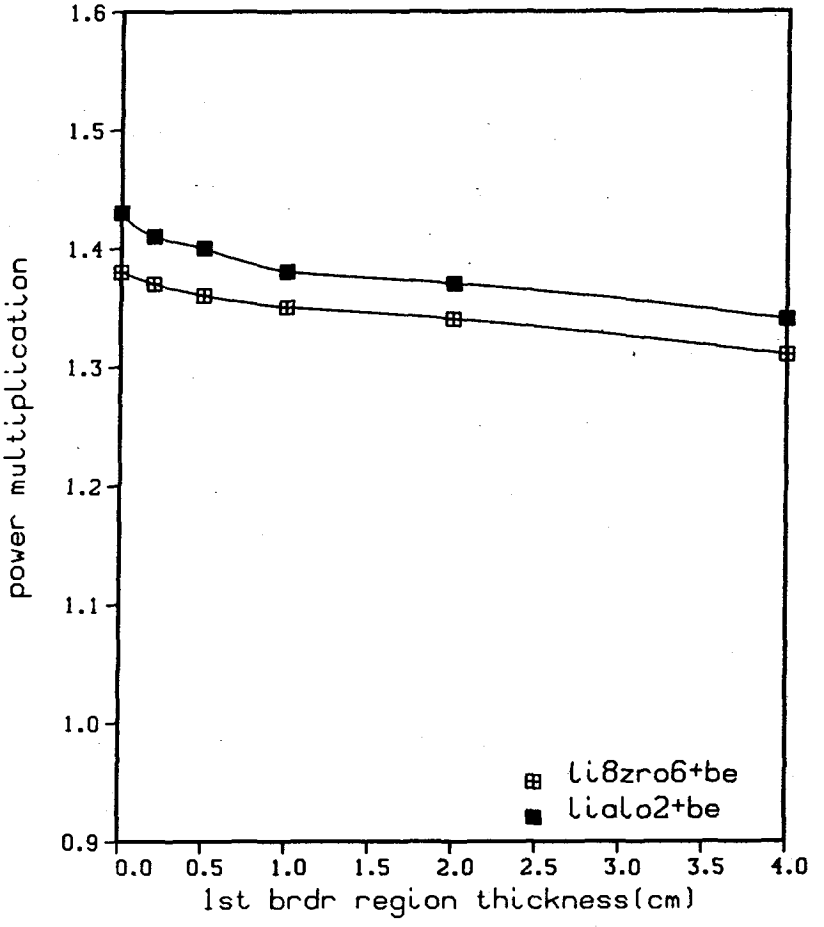


Figure 2.3-18 Power multiplication as a function of the first breeder region thickness for the sandwich case

The peak heating rates for the 17 cases considered are shown in Table 2.3-8 along with the corresponding values of TBR and M. Except for Li_2O which has natural lithium, all the other cases have 60% ^6Li enrichment. The TBR and M results can be seen to be rather insensitive to a small change in material volume fraction. For example, changing the breeder volume fraction from 0.70 to 0.75 in the case of Li_4SiO_4 + Be does not change the power multiplication (1.37) and only incrementally changes the TBR from 1.35 to 1.34. Table 2.3-8 also shows that the separate multiplier cases have higher peak heating rates than the other cases. For example, Li_2O with a separate multiplier has a 81.6 W/cc peak heating rate, as compared with the Li_2O/Be homogeneous mixture case

Table 2.3-8 Maximum Heating, TBR and M for the Different Cases[a]

		$\dot{q}$ (W/cm^3)[b]	TBR	M	Breeder Volume Fraction
Cases Without a Multiplier	Li_2O[c]	41.8	1.27 (1.27)	1.22 (1.23)	0.837 (0.86)
	Li_2ZrO_3	35.5	1.11	1.02	0.825
	Li_8ZrO_6	41.4	1.10	1.12	0.816
	$Li_2Be_2O_3$	44.9	1.25	1.31	0.805
	Li_7Pb_2	33.7	1.40 (1.34)[d]	1.19 (1.19)	0.865 (0.76)
Cases With a Homogeneous SB/M Mixture[f]	$LiAlO_2$/Be	43.9	1.80	1.50	0.799[e]
	$LiAlO_2$/BeO	43.5	1.29	1.35	0.806[e]
	Li_2O/Be	45.9	1.87	1.46	0.795[e]
	Li_2O/BeO	43.7	1.36	1.34	0.802[e]
Cases With a Separate Be Multiplier Region	Li_2O	81.6	1.46	1.40	0.790
	$LiAlO_2$	64.9	1.28 (1.27)	1.38 (1.39)	0.780 (0.75)
	Li_5AlO_4	72.6	1.38 (1.39)	1.38 (1.38)	0.735 (0.68)
	Li_2SiO_3	68.5	1.30 (1.31)	1.36 (1.36)	0.745 (0.69)
	Li_4SiO_4	70.0	1.34 (1.35)	1.37 (1.37)	0.750 (0.70)
	Li_2ZrO_3	67.1	1.38 (1.38)	1.27 (1.28)	0.780 (0.73)
	Li_8ZrO_6	74.6	1.43 (1.44)	1.34 (1.34)	0.765 (0.72)
	Li_2TiO_3	65.5	1.32 (1.33)	1.38 (1.38)	0.795 (0.75)

[a] 60% ^{6}Li enrichment, except for the Li_2O case without a multiplier
[b] At 0.5 cm from tip of breeder plate
[c] Natural lithium
[d] All TBR and M values in brackets are based on corresponding volume fractions in brackets
[e] Solid breeder/multiplier mixture volume fraction
[f] 20/80 solid breeder/multiplier homogeneous mixture

and the unmultiplied Li_2O which show only peak heating rates of 45.9 and 41.9 W/cc, respectively. It is interesting to note that the peak heating rate tends to increase with the Li atom density. This effect is most pronounced in the cases with a separate multiplier.

Lithium Burnup

The lithium burnup at 0.5 cm from the tip of the breeder plate after 3 full power years was calculated for each case. All the solid breeders are considered to have 60% ^6Li enrichment, except for unmultiplied Li_2O and Li_8ZrO_6, which contain 7.5% ^6Li enrichment. The burnup rate is proportional to the Li number density:

$$\frac{dN_{Li}}{dt} = -\alpha N_{Li} \tag{2-7}$$

which leads to an exponential time distribution:

$$N_{Li}(t) = N_{Li}(0)\, e^{-\alpha t} \tag{2-8}$$

where α is the burnup constant and $N_{Li}(t)$ the number of lithium atoms at time t.

Then the burnup fraction after time t is:

$$\frac{N_{Li}(0) - N_{Li}(t)}{N_{Li}(0)} = 1 - e^{-\alpha t} \tag{2-9}$$

The burnup constant, α, is equal to the sum of the rates of "destructive" reactions per lithium atom. Tritium-producing reactions are dominant in lithium and other destructive reactions (e.g. (n,γ), (n,d), (n,2n)) can be ignored since they contribute much less than 1% to lithium burnup. Therefore, α can be approximated by:

$$\alpha(1/\text{sec}) = \left(\frac{TPR}{(n_{Li}^6 + n_{Li}^7)\, A_m}\right) \tag{2-10}$$

where

TPR = Tritium Production Rate (kg/cm^3-sec) (determined from

neutronics results and shown in Table 2.3-9 for all the cases)

A_m = Atomic mass of tritium = 5.006×10^{-27} kg/atom

n_{Li}^6, n_{Li}^7 = atom density of ^6Li and ^7Li (at.ms/cm^3) (shown in Table 2.3-6)

Table 2.3-9 Tritium Production Rate at 0.5 cm from Tip of Plate, TPR
(All cases have 60% ^6Li enrichment except for unmultiplied Li_2O which has natural Li)

Material	TPR (kg/cm^3-sec) x 10^{-14}
Cases Without a Multiplier:	
$Li_2Be_2O_3$	8.27
Li_2O	8.53
Li_7Pb_2	6.93
Li_8ZrO_6	7.91
Li_2ZrO_3	7.24
Cases With a Homogeneous SB/M Mixture (20/80):	
$LiAlO_2$/BeO	6.91
$LiAlO_2$/Be	9.96
Li_2O/Be	11.8
Li_2O/BeO	8.32
Cases With a Separate Be Multiplier:	
$LiAlO_2$	36.5
Li_5AlO_4	43.6
Li_2SiO_3	39.6
Li_4SiO_4	41.4
Li_2TiO_3	38.1
Li_8ZrO_6	45.4
Li_2ZrO_3	41.0
Li_2O	46.3

Figure 2.3-19 shows the results for all the cases. The peak burnup is high for the three cases involving $LiAlO_2$ with a multiplier, with the homogeneous $LiAlO_2$/Be case exhibiting the highest burnup (46.8 at.% Li). This is an interesting result since it was believed that the use of a homogeneous SB/M mixture instead of a separate multiplier would reduce both the peak heating rate and burnup. Table 2.3-8 shows that the peak heating rate is indeed reduced, as discussed in the previous section, but the burnup fraction is increased. This is due to the high volume fraction of Be needed at the front of the SB/M region, which means that the amount of Li is small and the burnup fraction is high. Note that, for the purpose of the 1-D neutronics calculations, the homogeneous SB/M cases are assumed to have the same SB/M proportion (20/80) over the whole breeder region. For a design, the 20/80 proportion would only be used for the front section, the multiplier proportion decreasing in the region away from the plasma. However, the above results for the front of the breeder region will not be affected.

The cases without Be multiplier tend to have lower values of burnup, with Li_2O showing the lowest value (2.9 at.% Li). The difference in the burnup values between the unmultiplied and multiplied cases can be attributed to the lower-energy secondary neutrons produced by the multiplier which react with ^6Li in the front section of the breeder to produce high burnups. It can also be observed that the burnup fraction is generally higher for the cases with lower lithium atom density. This explains why the ranking based on the lowest burnup tends to be the same as the ranking based on the highest TBR, which is also directly dependent on the Li atom density. In that sense, the burnup results tend to reinforce the relative ranking of the cases based on the TBR results. Although concern exists about the possibility of high burnups affecting the material chemical composition and compatibility at the tip of the breeder section, it is not clear yet how important this is as a criterion for comparing solid breeder materials. In general, it seems reasonable to assume that lower values of peak burnup are more attractive than higher values. It should be noted that the average burnup, which has not been calculated for this study, could also be an important factor, particularly in connection with its effect on tritium inventory.

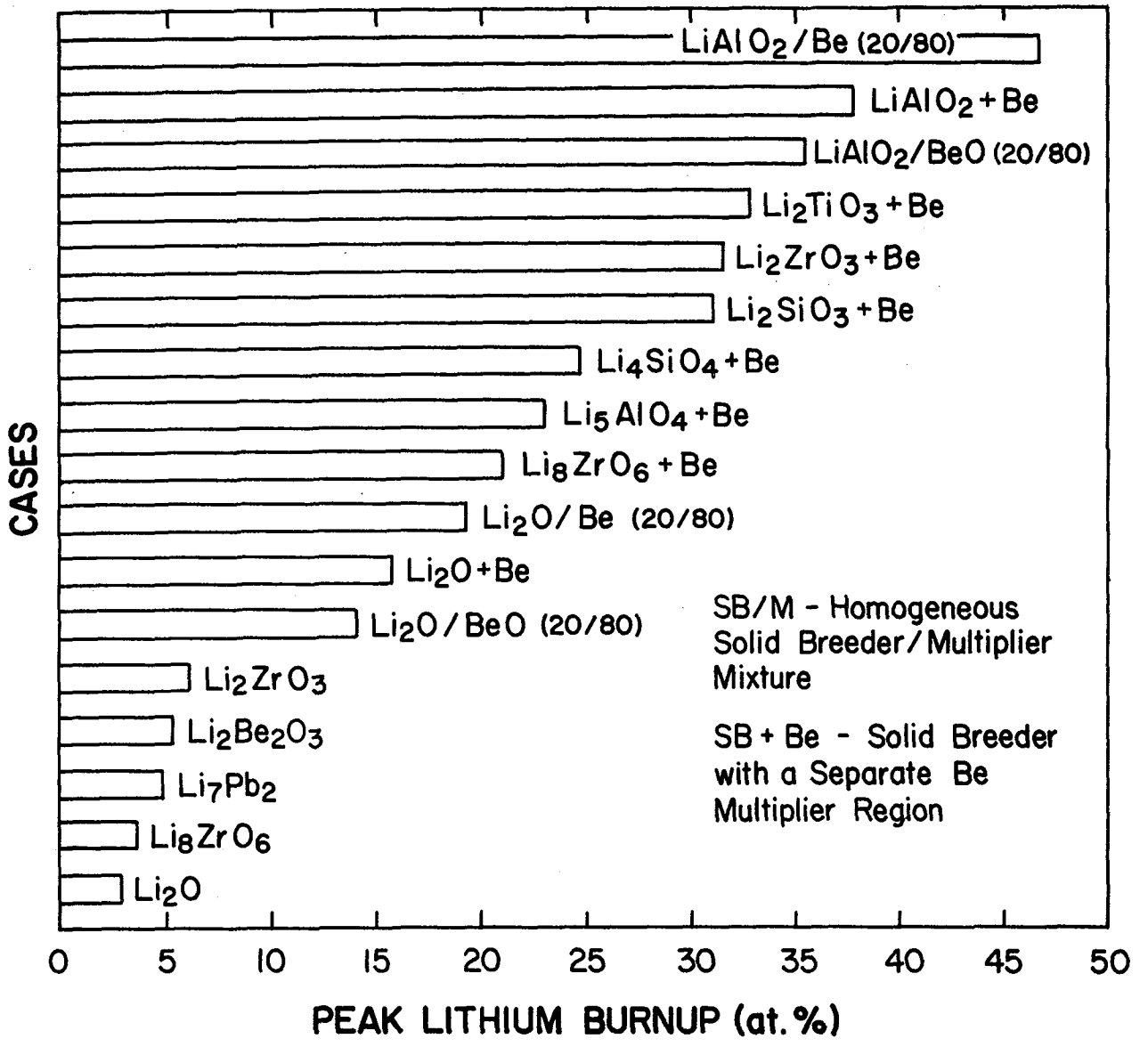


Figure 2.3-19 Li burnup at 0.5 cm from the tip of the breeder plate after 3 full power years for the different cases (all cases have 60% ^{6}Li enrichment, except for the unmultiplied Li_2O case which has 7.5% ^{6}Li enrichment.

Summary

Because of the importance of achieving tritium self-sufficiency, the TBR is the major neutronics criterion followed by power multiplication, which is the basic power parameter. For this study, the peak heating rate is of less importance since its major effect is to reduce the solid breeder plate thickness (and hence, volume fraction) so that the maximum allowable solid breeder temperature is not exceeded; previously, it was shown that the neutronics calculations are rather insensitive to small changes in solid breeder volume fractions.

It is important to stress the difference between the 1-D neutronics calculations performed in this study and more accurate 3-D neutronics calculations. The 1-D calculations typically over-estimate the actual TBR by about 15%-20% because of the assumptions of full coverage, fully homogeneous regions, and equal inboard and outboard blanket thickness. Consequently, the 1-D results were reduced by 15% to obtain effective TBR values. Figure 2.3-20 shows a bar chart of the optimum effective TBR (assumed to be 99% of the maximum effective TBR value) for the different solid breeder cases. To satisfy the tritium self-sufficiency criterion within the given uncertainties, the effective TBR can be ranked in the following categories:

< 1.05	rejected
1.05 - 1.10	high risk
1.10 - 1.20	medium risk
> 1.20	low risk

From Figure 2.3-20, and based on the above criterion, the unmultiplied Li_2ZrO_3 and Li_8ZrO_6 cases are rejected. The unmultiplied Li_2O and $Li_2Be_2O_3$ cases, the separate multiplier cases with $LiAlO_2$, and the homogeneous $LiAlO_2$/BeO mixture case are in the high risk category. The separate multiplier cases with Li_2SiO_3, Li_2TiO_3, Li_4SiO_4, Li_5AlO_4, Li_2ZrO_3, and the homogeneous Li_2O/BeO mixture case are in the medium risk category. Finally, the Li_7Pb_2 case without a multiplier, the separate multiplier cases with Li_8ZrO_6 and Li_2O, and the homogeneous $LiAlO_2$/Be and Li_2O/Be cases are in the low risk category. Since the homogeneous $LiAlO_2$/Be case is acceptable, it is anticipated that all homogeneous mixtures of ternary ceramics (which usually have higher Li atom densities than $LiAlO_2$) with beryllium would be acceptable from a TBR consideration.

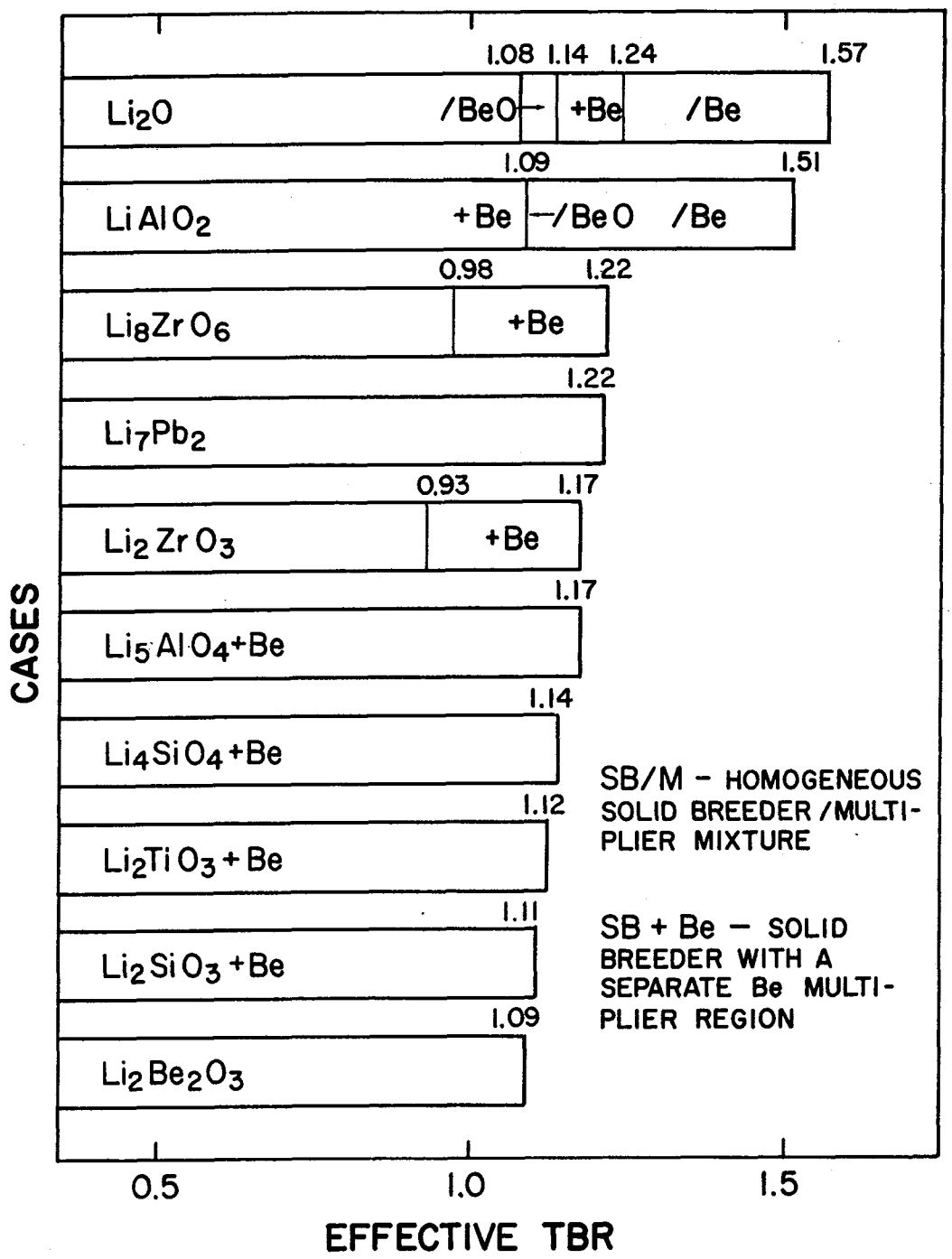


Figure 2.3-20 Effective tritium breeding ratio for the different cases

The general conclusions which can be made from the TBR results are that: 1) Be exhibits a much superior performance than BeO as a multiplier; 2) Li_2O is the most attractive solid breeder candidate, showing the highest TBR for the unmultiplied, separate multiplier and homogeneous SB/M cases, 3) Li_2O is the only solid breeder with a plausible chance of performing satisfactorily without a multiplier; and 4) the homogeneous SB/Be cases show exceptional TBR performance and should be considered in the test program.

The power multiplication results, shown in Figure 2.3-21, tend to vary in accordance with the TBR results and thus reinforce the above conclusions. The only notable exception is the case of Li_7Pb_2, which, although showing a high effective TBR of 1.22, exhibits a rather low M of 1.18. This is due to the higher (n,2n) threshold energy in Pb compared to Be.

2.3.3.2 Thermo-Mechanics

The steady-state temperature distribution in the solid breeder plate was first calculated to determine the maximum dimensions of the plate, the anticipated tritium inventory, and the thermal stresses in the breeder.

The two-dimensional heat conduction equation with temperature-dependent solid breeder thermal conductivity, k(T), was used in conjunction with the plate geometry shown in Figure 2.3-22.

$$\frac{\partial}{\partial x}\left(k(T)\frac{\partial T}{\partial x}\right) + \frac{\partial}{\partial y}\left(k(T)\frac{\partial T}{\partial y}\right) = \dot{q}(y) \qquad (2\text{-}11)$$

where T is the temperature varying in the x- and y-directions, and $\dot{q}$ is the heat generated per unit volume varying in the y-direction. This equation is solved using an explicit finite difference technique to obtain the temperature distribution in the plate. Heat transfer at the plate ends is assumed negligible due to coolant flow stagnation at the front end and separation at the back end:

$$\frac{\partial T}{\partial y} = 0 \text{ at } y = 0 \text{ and } y = R_{br} \qquad (2\text{-}12)$$

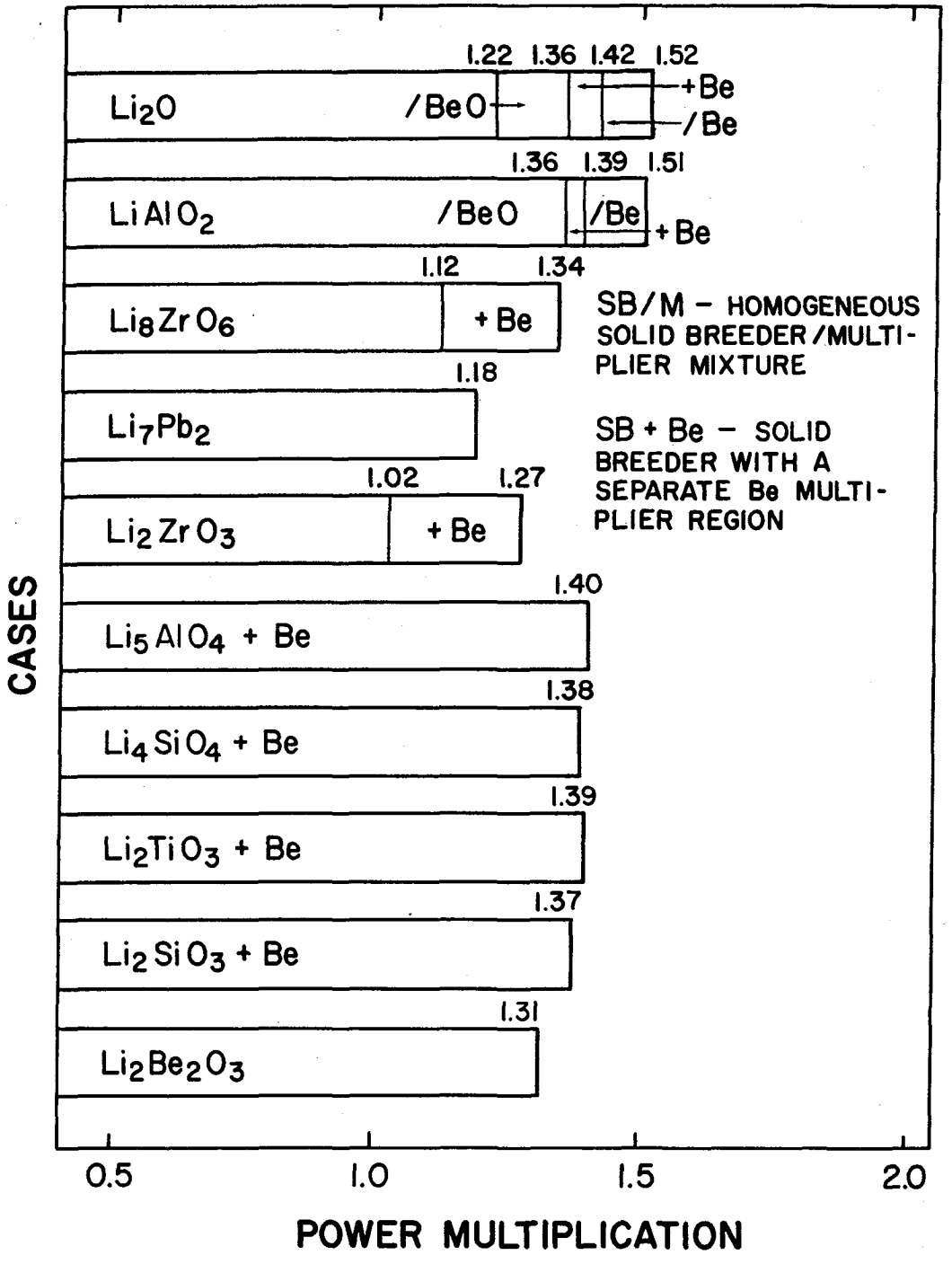
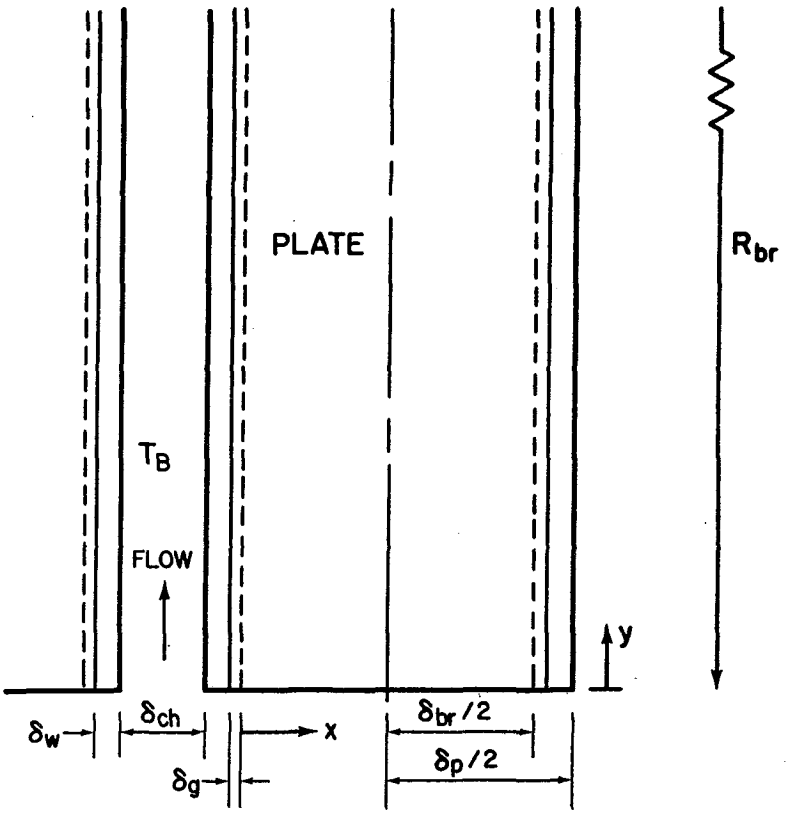


Figure 2.3-21 Power multiplication for the different cases



δ_{ch} = Channel Thickness
δ_p = Plate Thickness
δ_{br} = Solid Breeder Thickness
δ_w = Wall or Clad Thickness
δ_g = Interface Effective Gap Thickness
T_B = Bulk Temperature of Main Helium Flow

Figure 2.3-22 Plate configuration for 2-D temperature calculations

The solid breeder surface temperature, T(0,y), is the sum of the helium bulk temperature and of the film, wall and gap temperature rises. The helium bulk temperature at each increment along the gap is deduced from the heat transfer from the plate. T(0,y), can then be obtained from Eqs. (2-13) to (2-18). The possibility of including a crack in the solid breeder, with a different thermal conductivity, is provided by the code, but the bulk temperature

of the He flow on each side of the plate is assumed to be equal. Thus, if a crack exists, there is an asymmetric temperature profile with more heat flowing to one side of the plate than to the other. The heat transfer from each adjacent plate is supposed to adjust itself accordingly and compensate for the unequal heat transfer from the plate considered so that the bulk temperatures on each side of this plate tend to be the same.

At the breeder surface (x = 0):

$$T(0,y) = T_B(y) + \Delta T_f(y) + \Delta T_w(y) + \Delta T_g(y) \qquad (2\text{-}13)$$

$$q''(0,y) = -k_{br} \frac{\partial T}{\partial x}(0,y) \qquad (2\text{-}14)$$

$$\Delta T_f(y) = (q''(0,y) + \dot{q}(y)\, \delta_w)/h \qquad (2\text{-}15)$$

$$\Delta T_w(y) = (q''(0,y) + \dot{q}(y)\, \delta_w)\, \delta_w/k_w \qquad (2\text{-}16)$$

$$\Delta T_g(y) = q''(0,y)\, /h_g \qquad (2\text{-}17)$$

$$T_B(y) = T_B(y-\Delta y) + q''(0,y) + q''(\delta_{br},y) + 2\, \dot{q}(y)\, \delta_w)\, \Delta y\, /\, (\dot{m}'\, C_p) \qquad (2\text{-}18)$$

where

$T_B(y)$ = helium flow bulk temperature at location y

$\Delta T_f(y)$ = film temperature drop at location y

$\Delta T_w(y)$ = wall temperature drop at location y

$\Delta T_g(y)$ = gap temperature drop at location y

k_{br} = breeder thermal conductivity

$\dot{q}(y)$ = rate of heat generated per unit volume at location y

$q''(x,y)$ = heat flow rate per unit area at location (x,y)

h = convective heat transfer coefficient

k_w = wall (clad) thermal conductivity

h_g = interface gap effective heat transfer coefficient

Δy = y increment

$\dot{m}'$ = mass flow rate of helium in channel per unit axial length of breeder

C_p = specific heat of helium

For each increment in y, the temperature at the x = 0 boundary is obtained from Eqs. (2-13 through 2-18). A similar set of equations is used to obtain the temperature at the $x = \delta_{br}$ boundary. The bulk temperature of the helium is then calculated from Eq. (2-18) using the latest values for the temperature gradient at the boundaries to calculate $q''(0,y)$ and $q''(\delta_{br},y)$.

This heat transfer model was used in conjunction with the neutronics calculations to obtain the plate thickness, δ_p, for each solid breeder case based on the maximum allowable temperature for the solid breeder material. Iterating twice between the neutronics and temperature calculations yielded the plate thicknesses shown for all the cases in Table 2.3-10. The structural volume fractions were based on the BCSS volume fractions for the similar blanket configuration.[5]

It was observed that about 15% of the heat at the tip of the plate flowed radially along the plate (in the y-direction), while 85% of the heat flowed along the thickness of the plate to the coolant. This means that, for the same maximum allowable temperature, plate thicknesses determined from the 2-D calculations were higher than the original 1-D results. From a neutronics perspective, however, small changes in volume fraction do not strongly affect optimized TBR/M (see Table 2.3-8). The volume fractions are also slightly affected when the more accurate temperature-dependent thermal conductivities are used, as can be seen in Table 2.3-11. But, again, this will have little effect on the neutronics results.

Breeder/Clad Mechanical Interaction

The structural behavior of the breeder and its interaction with the cladding are of concern for a number of reasons. The stress in the breeder material could cause cracking which would affect the temperature profile across the breeder and the tritium inventory. The crack conductivity could be

Table 2.3-10 Plate Thickness and Volume Fractions for the Different Cases (with 60% ^6Li enrichment except for the unmultiplied Li_2O case)

	k (W/m-k)	T_{max} (K)	$\dot{q}$ at 0.5 cm (W/cm^3)	δ_p (cm)	Volume Fractions			
					Region 1		Region 2	
					Breeder	Struc.	Breeder	Struc.
Cases Without a Multiplier								
Li_2O[a]	~ 2.5[b]	1073	41.8	1.58	0.84	0.07	0.66	0.27
Li_2ZrO_3	~ 1.3[b]	1273	35.5	1.30	0.82	0.07	0.64	0.28
Li_8ZrO_6	~ 1.8[b]	1033	41.4	1.11	0.81	0.08	0.63	0.29
$Li_2Be_2O_3$	2.0	943	44.9	0.91	0.79	0.09	0.61	0.29
Li_7Pb_2	17.0	693	33.7	0.71	0.75	0.10	0.57	0.30
Cases with a Homogeneous SB/M Mixture								
$LiAlO_2$/Be	2.5	923	43.9	1.01	0.80	0.08	0.61	0.29
$LiAlO_2$/BeO	3.0	1273	43.5	1.77	0.85	0.07	0.67	0.27
Li_2O/Be	2.5	923	45.9	0.98	0.79	0.08	0.61	0.29
Li_2O/BeO	3.0	1073	43.7	1.42	0.83	0.07	0.65	0.28
Cases With a Separate Be Multiplier Region								
Li_2O	~ 2.5[b]	1073	81.6	1.05	--	--	0.77	0.15
$LiAlO_2$	~ 2.5[b]	1273	64.9	1.11	--	--	0.78	0.15
Li_5AlO_4	2.3	873	72.6	0.60	--	--	0.69	0.18
Li_2SiO_3	1.5	973	68.5	0.69	--	--	0.72	0.17
Li_4SiO_4	1.5	1003	70.0	0.80	--	--	0.74	0.16
Li_2ZrO_3	~ 1.3[b]	1273	67.1	0.93	--	--	0.76	0.16
Li_8ZrO_6	~ 1.8[b]	1033	74.6	0.77	--	--	0.73	0.16
Li_2TiO_3	2.0	1203	65.5	1.16	--	--	0.78	0.15

[a] Natural lithium
[b] Temperature-dependent thermal conductivity used (see Section 2.2)

Table 2.3-11 Breeder Volume Fractions Calculated Assuming Constant Thermal Conductivity (k) and Temperature Dependent Thermal Conductivity (k(t)[a])

Solid Breeder	Breeder Conductivity	Breeder Volume Fraction	Structure Volume Fraction
$LiAlO_2$	k = 2.5 W/m-K	0.780	0.147
	k = k(t)	0.780	0.147
Li_4SiO_4	k = 1.5 W/m-K	0.747	0.159
	k = k(t)	0.769	0.152
Li_8ZrO_6	k = 1.8 W/m-K	0.757	0.155
	k = k(t)	0.760	0.154
Li_2ZrO_3	k = 1.3 W/m-K	0.778	0.149
	k = k(t)	0.770	0.150
Li_2O w/o Be	k = 2.5 W/m-K	0.834 0.653	0.0707 0.277
	k = k(t)	0.853 0.672	0.0640 0.271

[a]From Section 2.2

low enough to cause the material to reach its sintering temperature, which would cause the closing of open porosity, and an increase of the tritium inventory. Expansion of the solid breeder could increase stresses on the clad, possibly resulting in clad rupture. Excessive thermal stresses could result if the sintered block form is used (as will be shown in the next section).

Two simple models, a beam model and a membrane model, were used as limiting cases to estimate the stresses and deflection in the cladding under unrestrained breeder expansion. As a limiting case, the breeder is assumed to 'flow' under thermal expansion and swelling, causing the cladding to deflect under the application of a constant pressure per unit length, q.

Figure 2.3-23 shows the breeder plate configuration and Figure 2.3-24 illustrates the beam and membrane models. For the beam model, the cladding is assumed to behave as a beam of length δ, and cross-section ($R_{br} \times \delta_w$), rigidly supported at both ends. In other words, the cladding is assumed to be able to withstand bending moments at the location of the wires. The equation describing this deflection, y, is:[65]

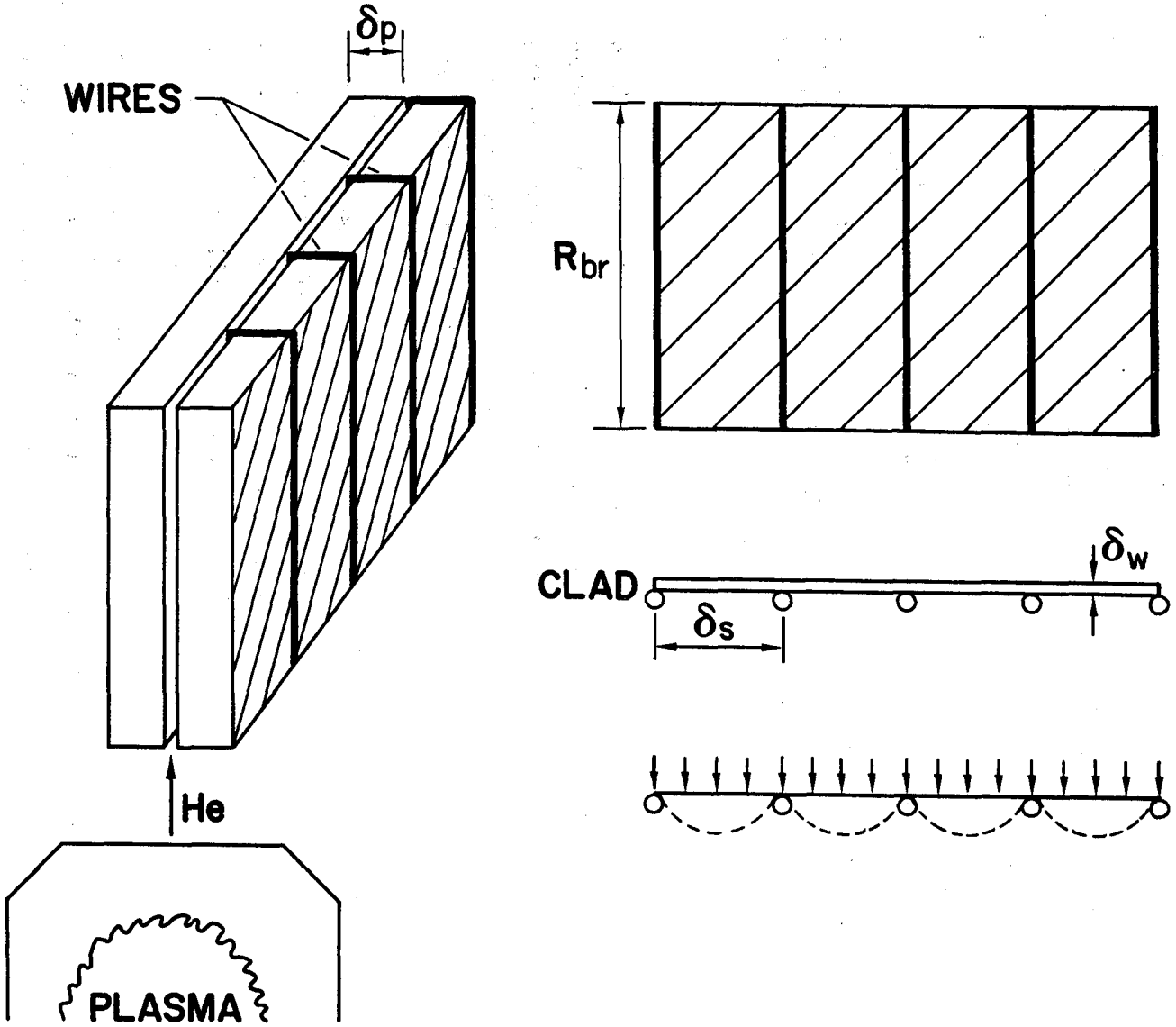


Figure 2.3-23 Breeder plate configuration for stress calculations

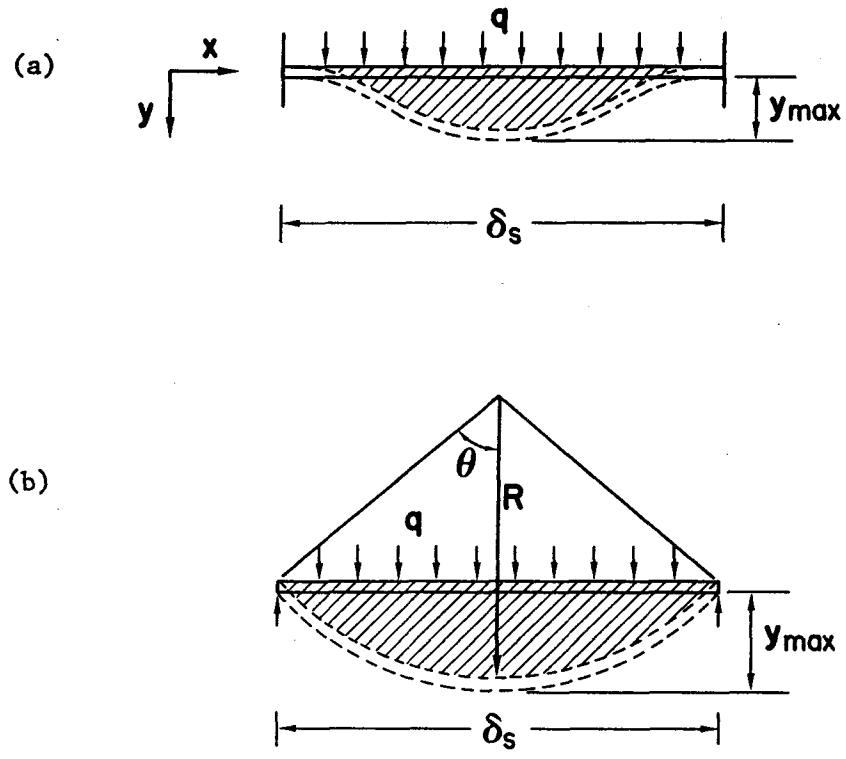


Figure 2.3-24 (a) Beam model for calculating stresses in clad; (b) membrane model for calculating stresses in clad

$$y = \frac{q}{12EI} [0.5\ x^4 - \delta_s x^3 + 0.5\ \delta_s^2\ x^2] \qquad (2\text{-}19)$$

where

E = elastic modulus

I = second moment of area

The clad deflection volume per unit length, V_{cl} (shaded area in Fig. 2.2-23(a)) can be equated to the volume increase of the breeder material as follows:

$$V_{cl} = \int_0^{\delta_s} y\ dx = \frac{q\ \delta_s^5}{720EI} = \left(\frac{\Delta V}{V}\right)_{TOT} \delta_s\ \delta_p/2 \qquad (2\text{-}20)$$

where $(\frac{\Delta V}{V})_{TOT}$ = total volumetric strain due to swelling and thermal expansion. The force on the cladding is then proportional to the volumetric expansion since

$$q = 360\ \delta_p\ EI\ (\frac{\Delta V}{V})_{TOT}\ /\delta_s^{\ 4} \tag{2-21}$$

and the maximum clad deflection is

$$y_{max} = \frac{q\ \delta_s^{\ 4}}{384EI} = 0.9375\ \delta_p\ (\frac{\Delta V}{V})_{TOT} \tag{2-22}$$

It is interesting to note that y_{max} is independent of δ_s (the wire-wrap spacing) based on this model. The maximum stress, σ_{max}, is obtained from the maximum bending moment $(q\ \delta_s^{\ 2}/12)$,[65] the distance from the edge to the neutral axis $(\delta_w/2)$, and the second moment of area $(I = R_{br}\ \delta_w^{\ 3}/12)$.

$$\sigma_{max} = \frac{(\frac{q\ \delta_s^{\ 2}}{12})\ (\frac{\delta_w}{2})}{(R_{br}\ \delta_w^{\ 3}/12)} = \frac{15\ \delta_p\ \delta_w\ E}{\delta_s^{\ 2}}\ (\frac{\Delta V}{V})_{TOT} \tag{2-23}$$

where Eq. (2-21) has been used to substitute for q.

The membrane model assumes that the cladding is too thin to withstand bending moments and instead it acts as a thin flexible membrane (see Fig. 2.3-24(b)). The clad deflection volume per unit length, V_{cl}, can be equated to the total volume expansion per unit length, as follows:

$$V_{cl} = [\frac{\delta_s^{\ 2}\ \theta}{4\ \sin^2\theta} - \frac{\delta_s^{\ 2}}{4\ \tan\theta}] = (\frac{\Delta V}{V})_{TOT}\ \delta_s\quad \delta_p/2 \tag{2-24}$$

Equation (2-24) can be solved for θ and then y_{max} and the stress in the clad, σ_{max}, (based on the strain) can be calculated from the following expressions.

$$y_{max} = \delta_p\ (\frac{\Delta V}{V})_{TOT} - \frac{\delta_s}{2}\ [\frac{\theta}{\sin^2\theta} - \frac{1}{\sin\theta}] \tag{2-25}$$

$$\sigma_{max} = \frac{E}{(1 - \nu)}\ \cdot\ [\frac{2r\theta}{\delta_s} - 1] \tag{2-26}$$

where ν is the Poisson's ratio of the material (assumed here to be 0.25 for all cases). Note that for small θ, y_{max} is independent of δ_s.

$$y_{max} = \delta_p \left(\frac{\Delta V}{V}\right) \tag{2-27}$$

The results obtained from the two models are summarized in Table 2.3-12. Of the four materials for which swelling data were available after fast irradiation to 10^{27} captures/m^3 (Li_2O, $LiAlO_2$, Li_2ZrO_3, and Li_4SiO_4), Li_2O had the highest volume expansion of 12.8% (including thermal expansion). Swelling could be a severe problem unless allowance is made for expansion. The cladding deflection in the case of Li_2O is on the order of 1.5 mm for each plate, as compared to a gap thickness between two plates of 1 mm. In this respect, Li_2O is unattractive, Li_4SiO_4 is marginal, and $LiAlO_2$ and Li_2ZrO_3 are acceptable. However, if a means for expansion is provided, such as a bellows-type arrangement at the plate ends or extra porosity, then the importance of this criterion for differentiating between the different solid breeder cases will be diminished.

Figures 2.3-25 shows the stress in the clad as a function of the wire separation for the beam model. The calculated stress is within the allowable clad stress for wire separations of about 9 cm or more for all four solid breeders.

The compressive stress on the spheres in the sphere-pac configuration was also calculated to verify if the fracture stress of the solid breeder materials would not be exceeded. Under stress, the spheres will tend to move to relieve the pressure. The highest possible compressive stress on any sphere, σ_{comp}, will be equal to the pressure exerted by the clad under tension, plus the resultant pressure of the inside purge flow and outside main flow, as shown below:

$$\sigma_{comp} = \frac{q}{R_{br}} + P_p \tag{2-28}$$

where q and R_{br} are described in Figs. 2.3-23 and 2.3-24, and P_p is the resultant pressure of the coolant flow (5 MPa) and purge flow (1 MPa). q is obtained from Eq. (2-21) and σ_{comp} can then be calculated as a function of the

Table 2.3-12 Volumetric Swelling, Thermal Expansion, and Resulting Maximum Clad Deflections for Four Different Solid Breeder Cases

	T(°C)	$(\frac{\Delta V}{V})$ Swelling	$(\frac{\Delta V}{V})$ Thermal	$(\frac{\Delta V}{V})$ Total	Plate Thickness (cm)	y_{max} Beam Model (mm)	y_{max} Membrane Model (mm)
Li_2O	800	5.25×10^{-2}	7.50×10^{-2}	1.28×10^{-1}	1.25	1.49	1.19
$LiAlO_2$	1000	3.0×10^{-3}	3.30×10^{-2}	3.60×10^{-2}	1.03	0.35	0.27
Li_2ZrO_3	970	3.0×10^{-3}	2.25×10^{-2}	2.55×10^{-2}	0.89	0.22	0.18
Li_4SiO_4	730	8.4×10^{-3}	5.85×10^{-2}	6.69×10^{-2}	0.71	0.45	0.36

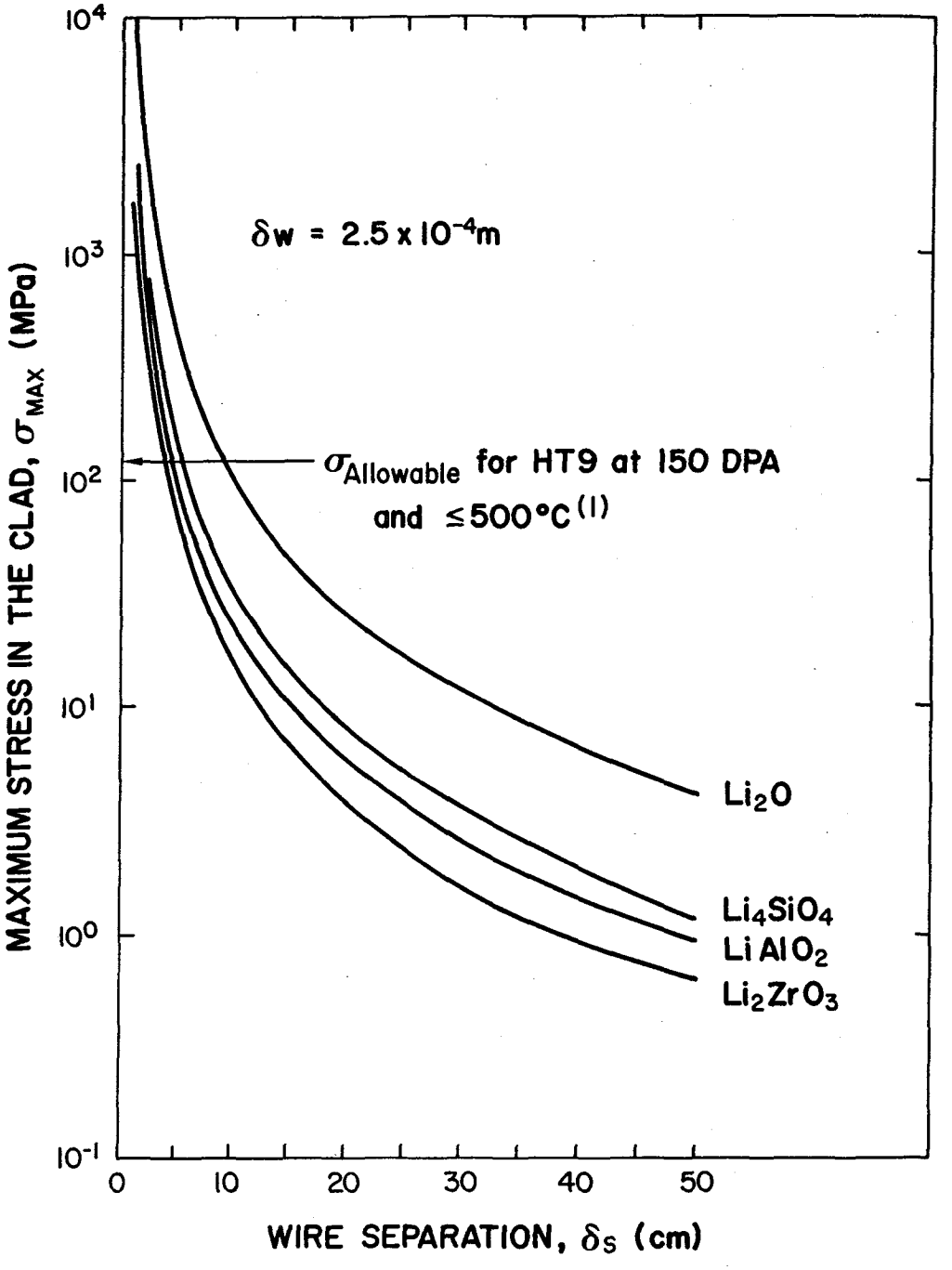


Figure 2.3-25 Stresses in the clad calculated from the beam model as a function of wire separation for four different solid breeders

wire separation. The results for Li_2O (which has the highest associated volume expansion) are shown in Figure 2.3-26. The stress on the sphere-pac material is within the fracture stress for wire separations greater than about 8 mm. Since the wire separation for a 2 m long plate is at least about 10 or 15 cm, the stress calculations for the cladding and sphere-pac material indicate that all solid breeders will be within the maximum allowable stress for the cladding and breeder materials.

For lack of data, creep was not considered in the calculations. Creep will tend to relieve the stresses in the solid breeder and cladding.

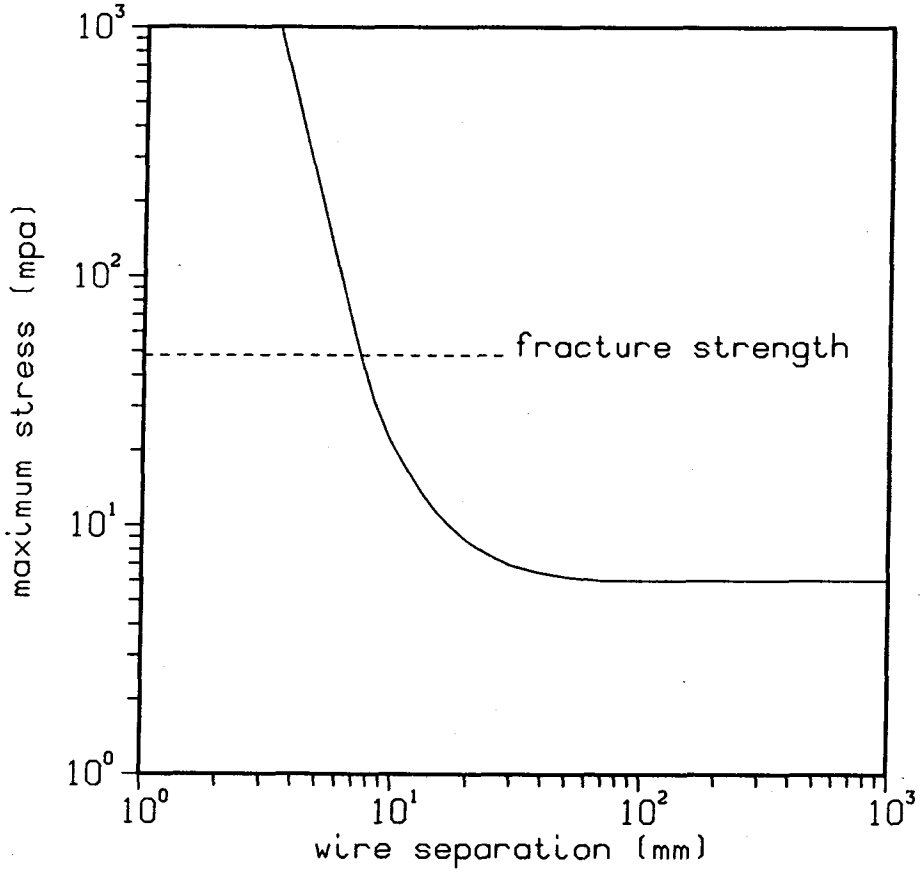


Figure 2.3-26 Compressive stress (σ_{comp}) on sphere pac Li_2O as a function of wire separation (δ_s)

For the solid breeder in sintered block form, the thermal stress in the solid breeder due to the temperature difference can be simply estimated by:

$$\sigma_{th} = \frac{E\ \alpha\ \Delta T}{(1 - \nu)} \qquad (2\text{-}29)$$

where

σ_{th} = thermal stress

E = elastic modulus

α = thermal expansion coefficient

ΔT = average temperature difference across the breeder

ν = Poisson's ratio (assumed here to be 0.25 for all cases)

The values of the above variables and the resulting stresses are shown in Table 2.3-13 (see Section 2.2 for the property data). ΔT is estimated as half the maximum temperature difference.

It is clear that in all cases the thermal stresses in the sintered block material are several times higher than the fracture strength of the candidate materials (which is on the order of 50 MPa and 70 MPa for Li_2O and $LiAlO_2$, respectively). In order for the thermal stress not to exceed the fracture stress, 2-D calculations show that the maximum plate thickness needs to be less than 0.5 mm for $LiAlO_2$ and Li_2O. This requirement shows the disadvantage of using the sintered block form, as extensive stress-induced cracking will occur affecting the temperature distribution (and the tritium inventory).

Table 2.3-13 Thermal Stresses in Sintered Block Solid Breeder Materials

Material	E (GPa)	α (x 10^{-5}/K)	T_{max} (K)	T_{min} (K)	σ_{th} (MPa)
Li_2ZrO_3	72	1.2	1240	756	597
Li_2SiO_3	27	1.5	973	742	131
Li_4SiO_4	27	2.5	1000	722	264
Li_8ZrO_6	72	1.9	1030	744	559
$LiAlO_2$	71	1.2	1270	767	614
Li_2O	71	3.0	1070	736	1021

2.3.3.3 Tritium

Tritium Inventory in Solid Breeder

The tritium inventory in a solid breeder and multiplier is modeled as the sum of diffusion, solubility, and surface adsorption components.

The diffusive inventory, I_{d_g}, in the grain, calculated from the mass transport continuity equation,[66] is given by:[5]

$$I_{d_g} = \int_0^{r_g} C_d \, 4\pi \, r^2 dr = \frac{G \, r_g^2 \, V_g}{15D} \tag{2-30}$$

where V_g is the volume of the solid breeder, C_d is the diffusive concentration of tritium per unit volume of solid breeder, G is the rate of generation of tritium per unit volume of solid breeder, r_g is the solid breeder grain radius, and D is the diffusion coefficient of tritium in the solid breeder.

The diffusion coefficient, D, is a function of temperature, T

$$D = D_o \exp\left(-E_{A_d}/RT\right) \tag{2-31}$$

where

D_o = diffusion constant

E_{A_d} = activation energy

R = universal gas constant

The solubility inventory is calculated from a form of Sievert's law:

$$C_s = \frac{P_{HT}}{\sqrt{P_{H_2}} \, k_s} \tag{2-32}$$

where

C_s = tritium solubility concentration

k_s = Sievert's constant

Like the diffusivity, the solubility is a function of temperature and k_s can be expressed in an Arrhenius form.

$$k_s = k_o \exp\left(-E_{AS}/RT\right) \tag{2-33}$$

The hydrogen partial pressure, P_{H2}, in the purge stream is set at 36 Pa to provide roughly a 200:1 H:T ratio. The HT partial pressure, P_{HT}, is about 0.36 Pa based on the tritium production and purge flow rates.

The surface adsorption inventory is calculated according to the method described by Billone[46], using the chemisorption data from Morimoto, et al.[67] Curve fitting the data gives the following expressions for the number of hydrogen (H or T) atoms, N_a, adsorped per m^2 of surface area for the oxides α-Al_2O_3, TiO_2 and SiO_3. These expressions are assumed to provide a reasonable indication of the tritium surface adsorption for the two lithium aluminates ($LiAlO_2$ and $LiAl_5O_4$), the titanate (Li_2TiO_3), and the two silicates (Li_2SiO_3 and Li_4SiO_4).

For α-Al_2O_3:

$$N_a = 7.1 \times 10^{18} (1064/T - 1) \text{ H/m}^2 \text{ for } T < 1000 \text{ K} \quad (2\text{-}34)$$
$$N_a = 1.52 \times 10^{15} (1300-T) \text{ H/m}^2 \text{ for } 1000 \text{ K} < T < 1300 \text{ K}$$
$$N_a = 0 \text{ for } T > 1300 \text{ K}$$

For TiO_2: $$N_a = 3800 (T-273)^{-1.41} \text{ H/m}^2 \quad (2\text{-}35)$$

For SiO_3: $$N_a = -3.5 \times 10^{-3} (T-273) + 3.2 \text{ H/m}^2 \quad (2\text{-}36)$$

For all the other solid breeder cases, as discussed in Section 2.2, N_a, is assumed to be 4.0×10^{18} H/m^2. To convert to wppm of tritium in the breeder, N_a is multiplied by A_s (the specific pore-solid surface area in m^2/g) times 10^6 divided by Avogadro's number. In general, swamping the purge flow with hydrogen will drastically reduce the surface adsorption inventory of tritium,[46] and for this study it is assumed that the actual surface adsorption inventory is only 1% of the calculated values due to the inclusion of about 1% of hydrogen in the purge flow.

The three components of the tritium inventory are dependent on temperature. Consequently, the tritium diffusive, solubility, and surface adsorption inventories were determined based on numerically integrating the inventories over the 2-D temperature and tritium generation rate profiles in the plate. The diffusivity and solubility data are discussed in Section 2.2. The uncertainty in the data ranges up to orders of magnitude.

Typical temperature and tritium inventory distributions over a solid breeder plate are shown in Figures 2.3-27 to 2.3-31 for the $LiAlO_2$+Be case. The numerical treatment of the zero temperature gradient boundary condition at the plate tip (y=0) leads to an artificial first node behavior. Figure 2.3-27 illustrates the sharp temperature gradient in the y-direction at the front of the plate (due to the exponential decrease in the heat generation values) which transfers 10-15% of the peak heat generation radially into the plate.

The diffusive inventory, shown in Figure 2.3-28, behaves in an opposite manner from the temperature distribution, due to the inverse dependence of diffusion on temperature.

The surface adsorption inventory, shown in Figure 2.3-29, illustrates the strong inverse dependency of surface adsorption on temperature, and Figure 2.3-30 illustrates the strong direct dependency of the solubility on temperature. Note that the transition between the two expressions used to calculate the surface adsorption inventory at 1000 K (see Eq. (2-34)) can be observed on the curve along the center of the plate at a distance of about 4 cm from the tip. Finally, Figure 2.3-31 shows the total combined inventory distribution for the plate, which, for the case of $LiAlO_2$+Be, is dominated by the surface adsorption and diffusive components.

Table 2.3-14 summarizes the tritium inventory results. The contribution of each inventory mechanism is shown, along with the total reactor blanket inventory. The effect of the uncertainties in the tritium data (see Section 2.2) is reflected in the average, upper, and lower values of total inventory for all the cases considered. The total inventory for the whole blanket was calculated by multiplying the gram inventory of the plate by the number of plates in a module, times the number of modules in the whole blanket (1125). A graphic representation of the lower and upper limits of the total inventory based on the property data uncertainties is shown in Figure 2.3-32 for the cases without a multiplier and for the homogeneous SB/M mixture cases, and in Figure 2.3-33 for the cases with a separate multiplier region.

The huge range between the lower and upper limits of the inventory clearly points to the need for obtaining more precise experimental property data for the tritium behavior in solid breeders. $Li_2Be_2O_3$, with a diffusive inventory between 12 wppm (6 kg per blanket) and 1.2×10^5 wppm (6×10^4 kg per blanket), is evidently unattractive if the low diffusivity value used (based

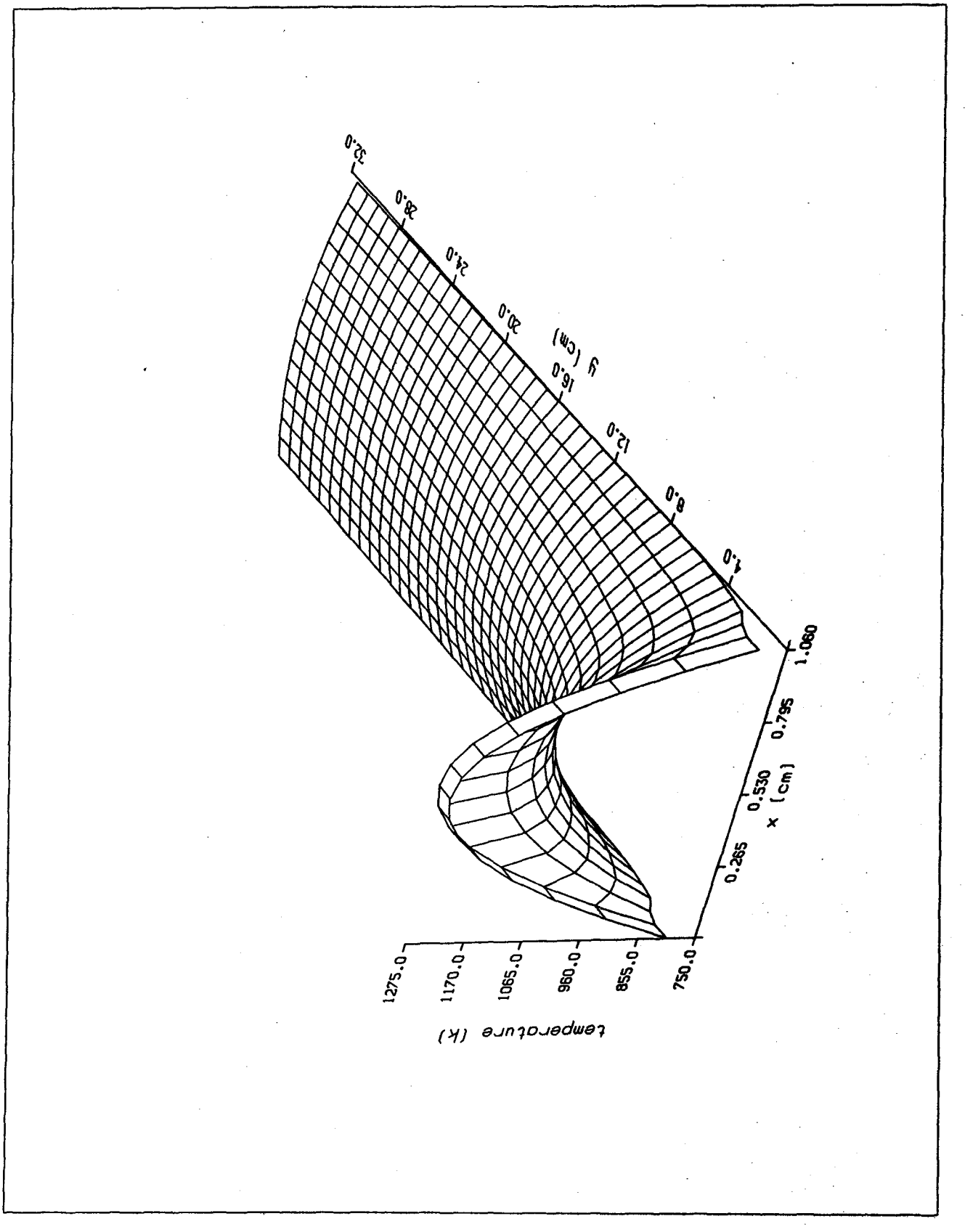


Figure 2.3-27 Plate temperature distribution for the $LiAlO_2$+Be case

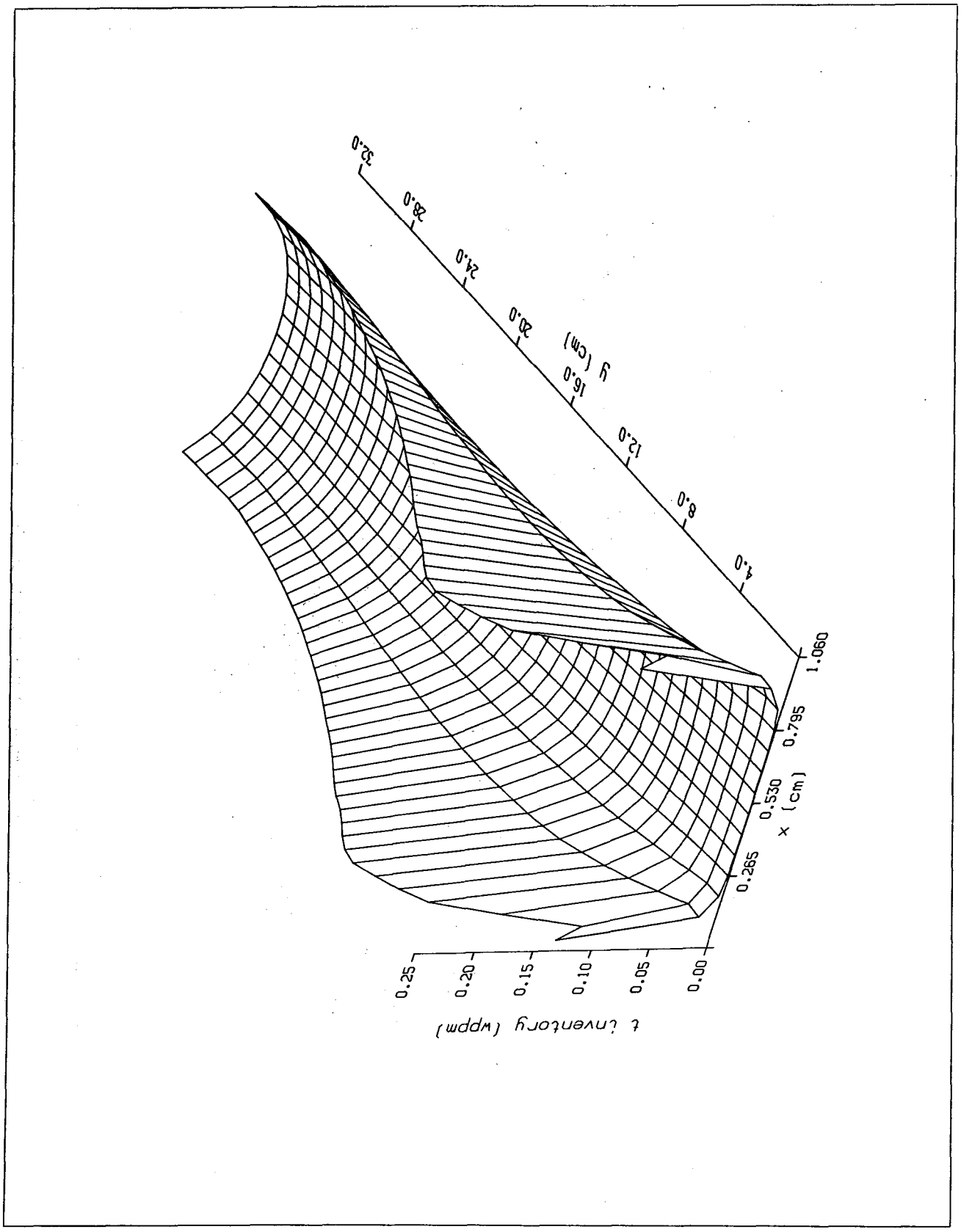


Figure 2.3-28 Plate diffusive tritium inventory distribution for the $LiAlO_2$+Be case

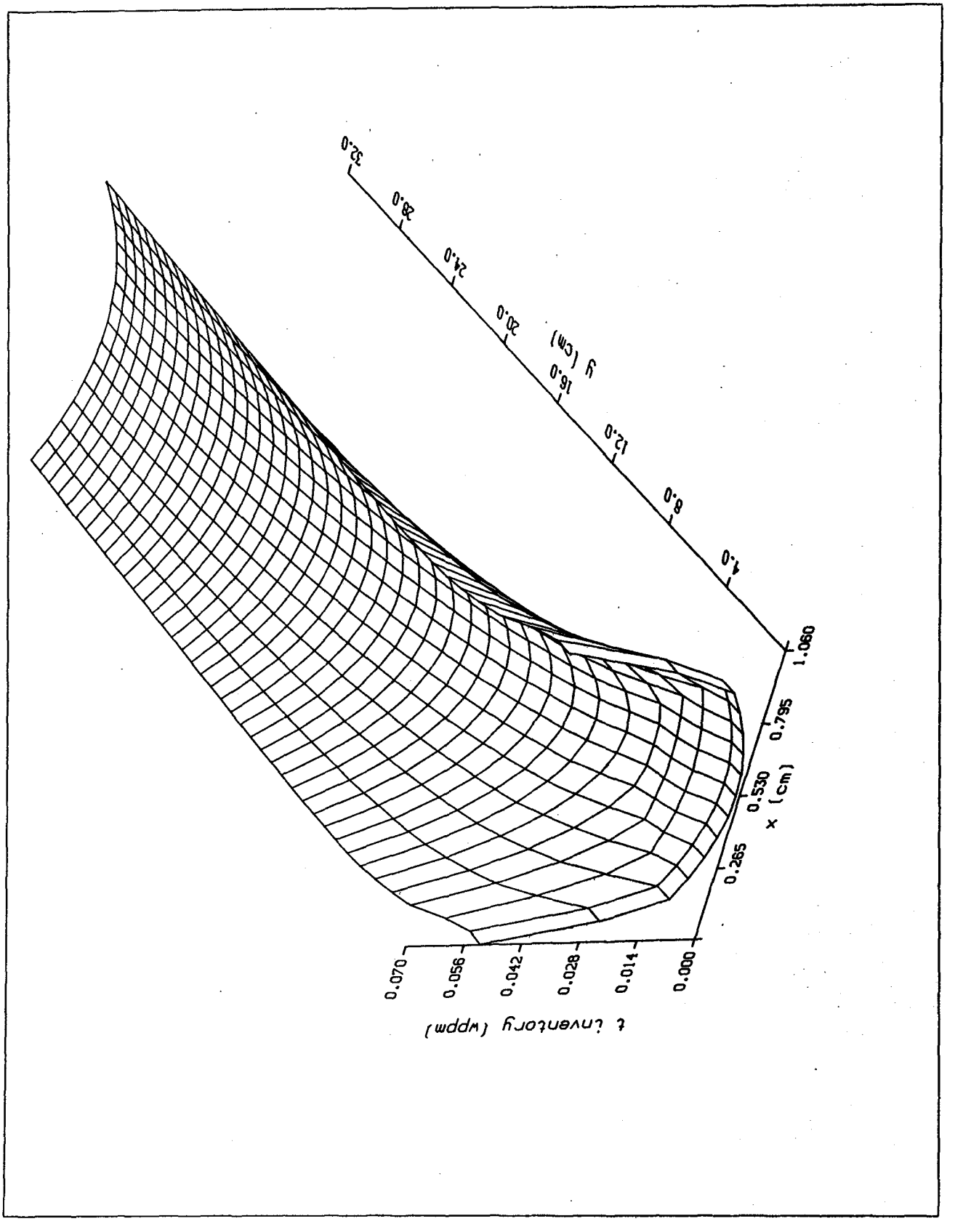


Figure 2.3-29 Plate surface adsorption tritium inventory distribution for the $LiAlO_2$+Be case

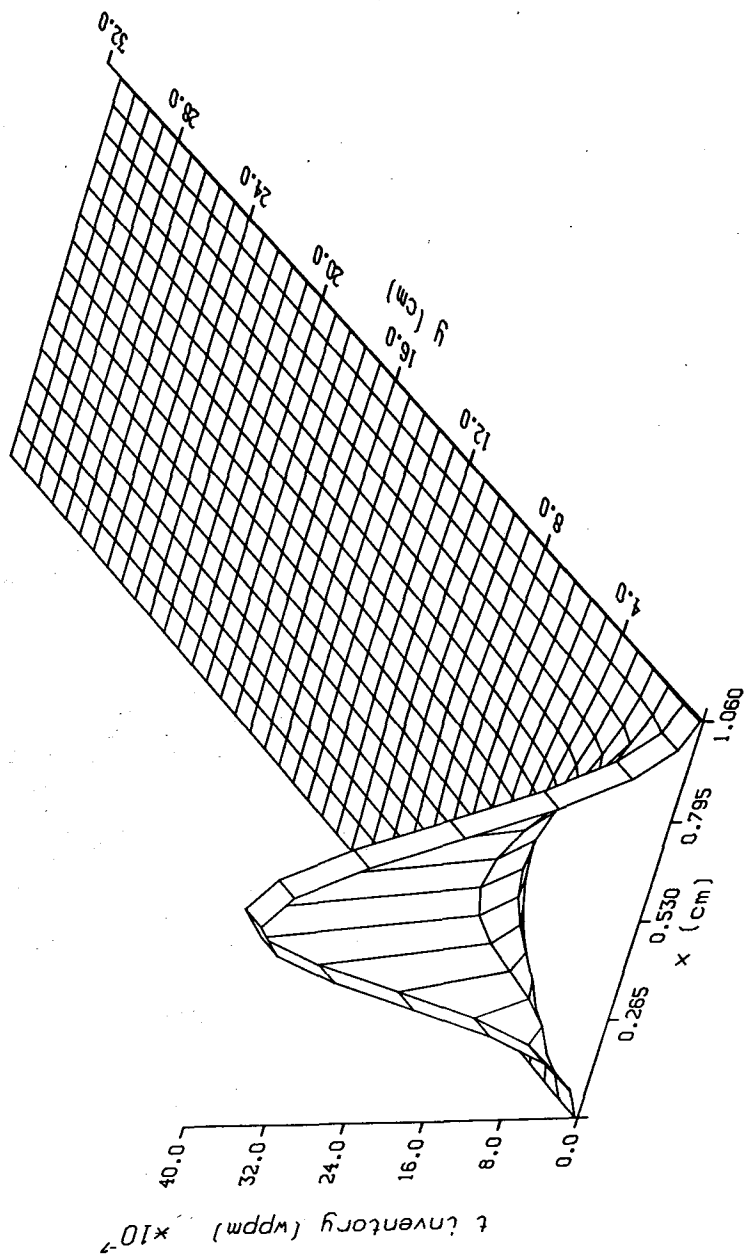


Figure 2.3-30 Plate solubility tritium inventory distribution for the $LiAlO_2$+Be case

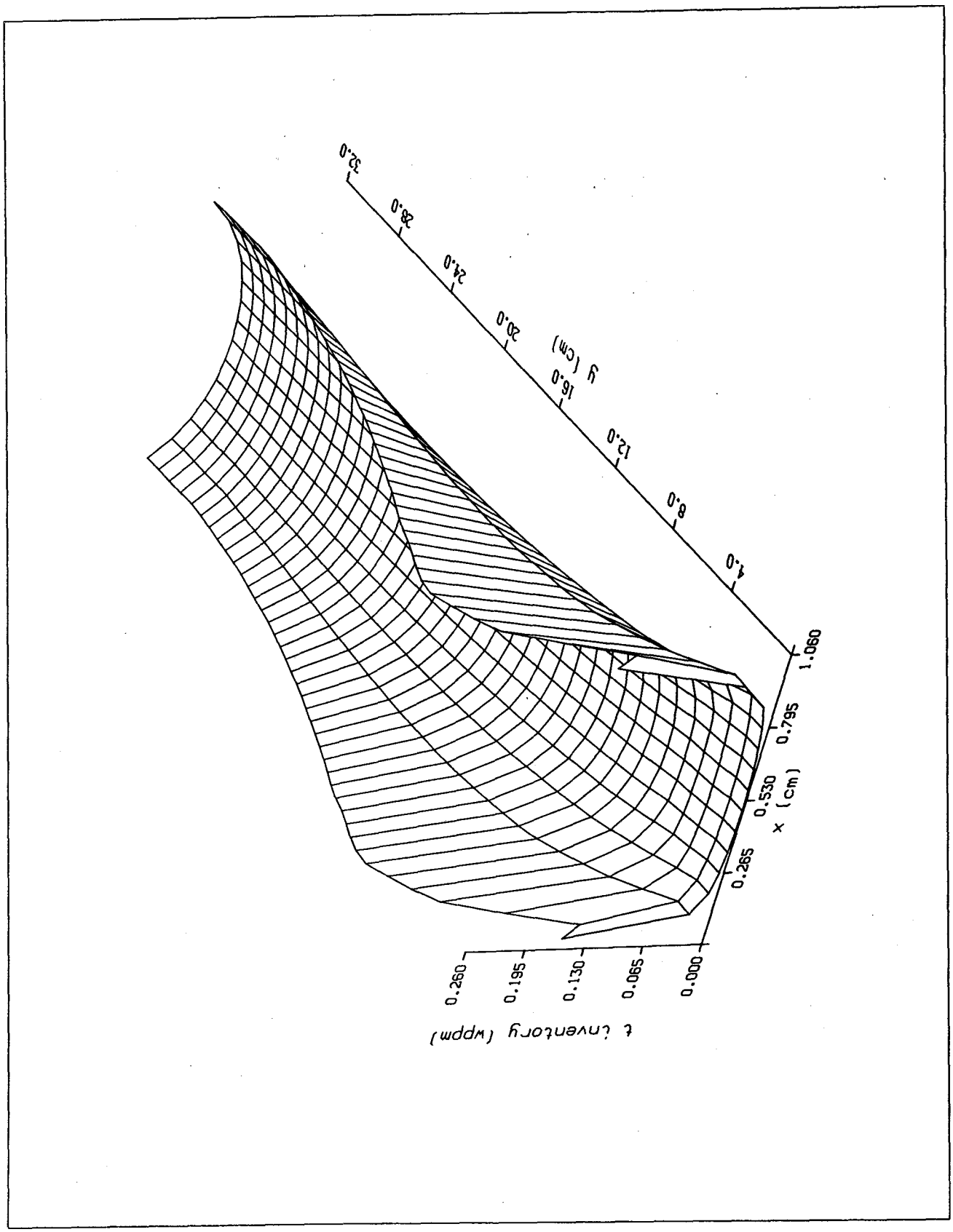


Figure 2.3-31 Plate total tritium inventory distribution for the $LiAlO_2$ case

Table 2.3-14 Tritium Inventory Results for the Different Cases

Case	I_d (wppm)	I_a (wppm)	I_s (wppm)	Lower Limit	I_{tot} (wppm) Average	Upper Limit	I_{tot} (gm)
Cases Without a Multiplier							
Li_2O	2.80×10^{-6}	8.47×10^{-2}	6.42×10^{-2}	1.45×10^{-2}	1.45×10^{-2}	1.45	5.6
Li_2ZrO_3	2.19×10^{-5}	8.63×10^{-2}	1.07×10^{-7}	8.63×10^{-3}	8.63×10^{-2}	8.65×10^{-1}	8.58×10^{1}
Li_8ZrO_6	2.55×10^{-5}	8.63×10^{-2}	3.63×10^{-8}	8.63×10^{-3}	8.63×10^{-2}	8.66×10^{-1}	8.52×10^{1}
$Li_2Be_2O_3$	1.17×10^{3}	8.63×10^{-2}	2.83×10^{-8}	1.17×10^{1}	1.17×10^{3}	1.17×10^{5}	5.52×10^{5}
Li_7Pb_2	4.86×10^{-7}	8.63×10^{-2}	1.45	1.55×10^{-1}	1.55	1.55×10^{1}	1.59×10^{3}
Cases With a Homogeneous SB/M Mixture							
$LiAlO_2$/Be	1.89	8.96×10^{-2}	3.03×10^{-8}	3.87×10^{-1}	1.98	10.3	2.30×10^{2}
$LiAlO_2$/BeO	4.82×10^{-1}	8.96×10^{-2}	1.89×10^{-7}	1.86×10^{-2}	5.72×10^{-1}	1.14	7.65×10^{1}
Li_2O/Be	6.16×10^{-5}	8.47×10^{-2}	4.83×10^{-8}	8.50×10^{-3}	8.47×10^{-2}	8.47×10^{-1}	8.1
Li_2O/BeO	3.14×10^{-5}	8.47×10^{-2}	9.57×10^{-8}	8.49×10^{-3}	8.47×10^{-2}	8.47×10^{-1}	9.5
Cases With A Separate Multiplier Region							
Li_2O	3.16×10^{-6}	8.47×10^{-2}	7.83×10^{-2}	1.63×10^{-2}	1.63×10^{-1}	1.63	4.39×10^{1}
$LiAlO_2$	5.67×10^{-2}	4.74×10^{-2}	1.46×10^{-7}	1.61×10^{-2}	1.04×10^{-1}	7.31×10^{-1}	3.64×10^{1}
Li_5AlO_4	2.53×10^{-2}	6.10×10^{-2}	2.14×10^{-8}	8.63×10^{-3}	8.63×10^{-2}	8.63×10^{-1}	2.30×10^{1}
Li_2SiO_3	3.61×10^{-5}	3.09×10^{-2}	2.99×10^{-8}	3.09×10^{-3}	3.09×10^{-2}	3.09×10^{-1}	9.6
Li_4SiO_4	1.08×10^{-3}	3.04×10^{-2}	4.05×10^{-8}	3.15×10^{-3}	3.15×10^{-2}	3.15×10^{-1}	9.2
Li_2ZrO_3	4.44×10^{-5}	8.63×10^{-2}	8.52×10^{-8}	8.63×10^{-3}	8.63×10^{-2}	8.67×10^{-1}	4.70×10^{1}
Li_8ZrO_6	4.78×10^{-5}	8.63×10^{-2}	3.57×10^{-8}	8.63×10^{-3}	8.63×10^{-2}	8.68×10^{-1}	4.54×10^{1}
Li_2TiO_3	8.49×10^{-5}	1.16×10^{-2}	9.75×10^{-8}	1.16×10^{-3}	1.17×10^{-2}	1.25×10^{-1}	4.1

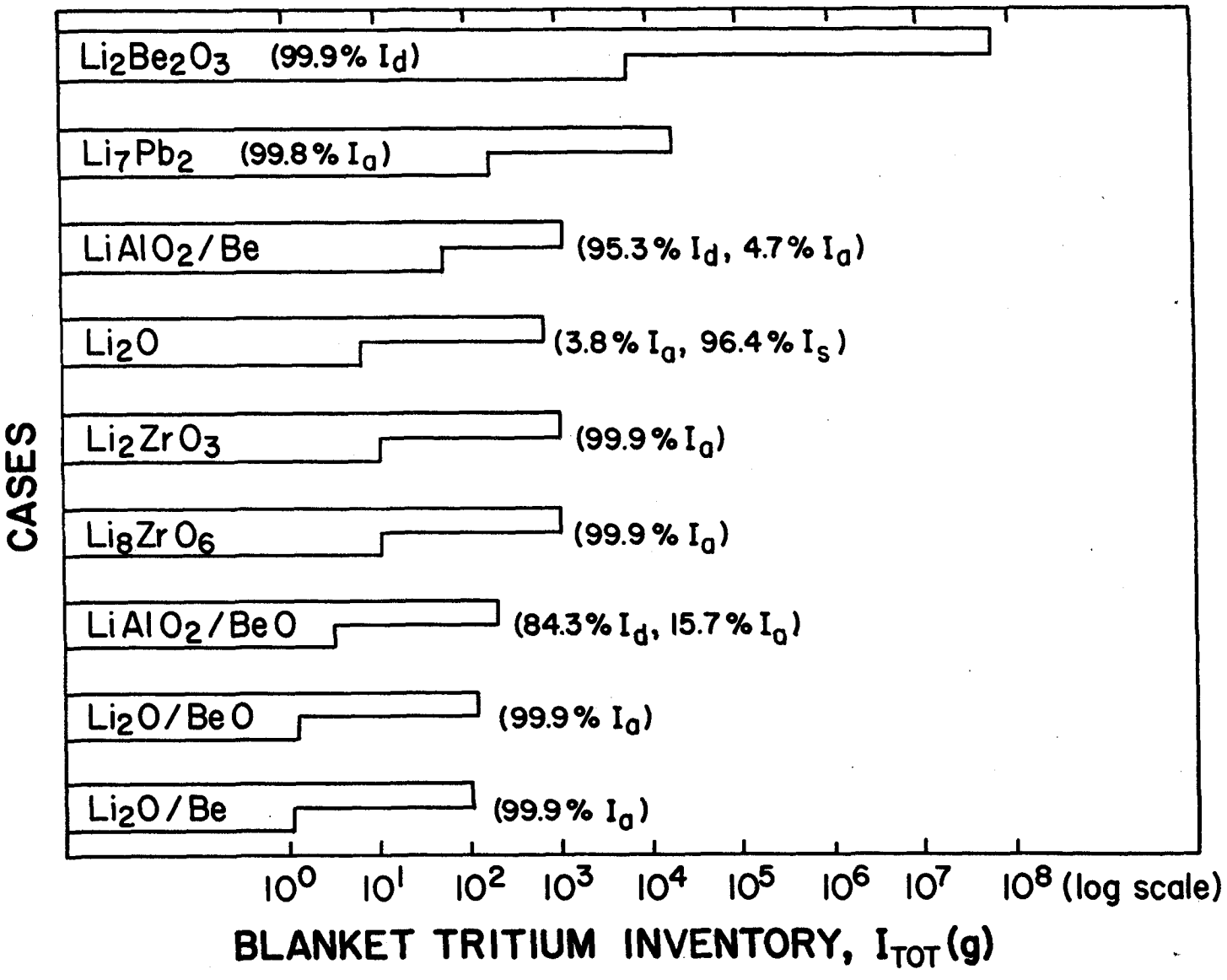


Figure 2.3-32 Upper and lower limits of calculated tritium inventory for the cases without a multiplier and for the homogeneous SB/M mixture cases

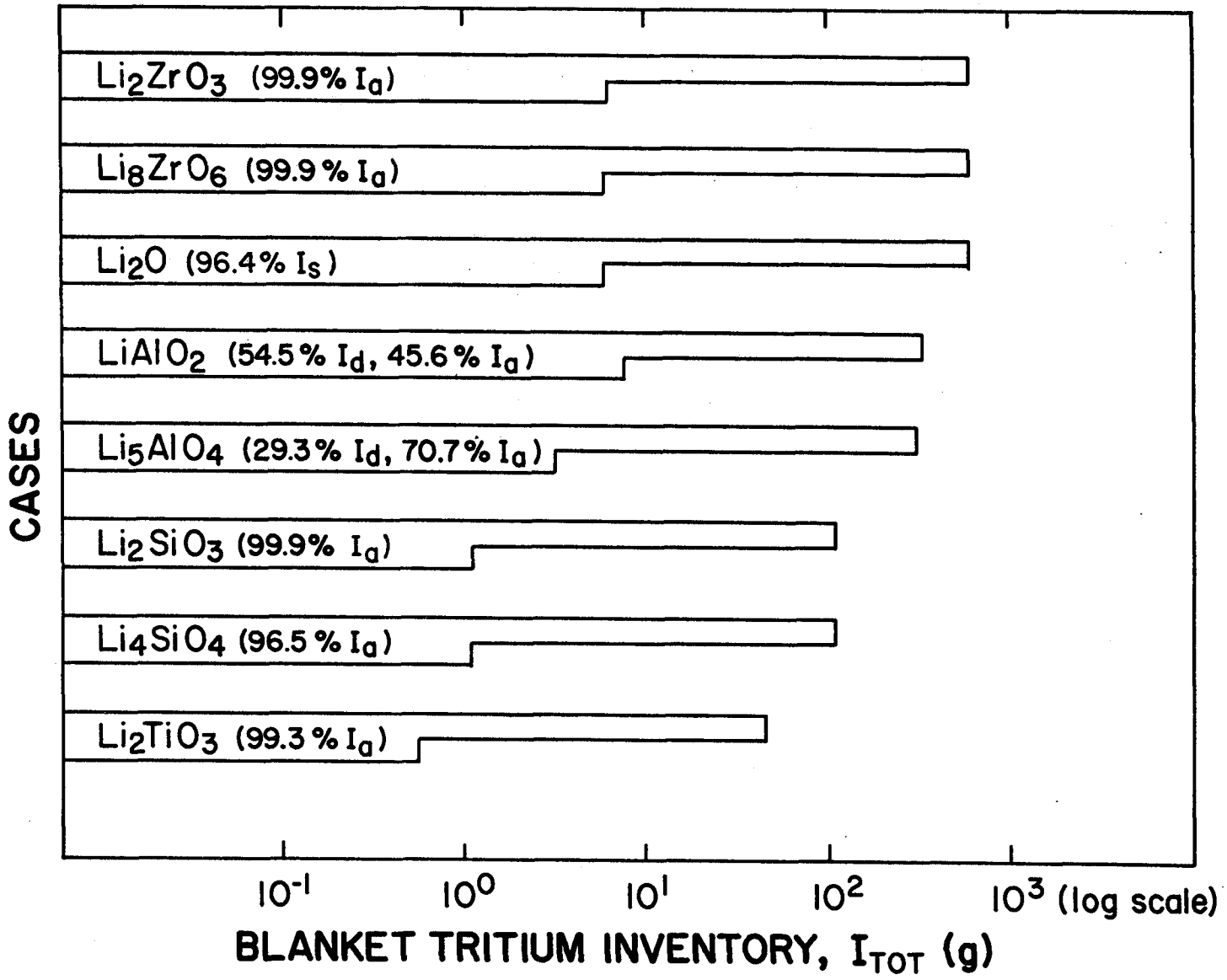


Figure 2.3-33 Upper and lower limits of calculated tritium inventory for cases with a separate Be multiplier region

on BeO data) is correct. Li_7Pb_2 also tends to have high inventories (due to tritium solubility) and so does $LiAlO_2$/Be (due to diffusion). Apart from these, it is hard to differentiate between the other cases within the uncertainty range. Except for the $LiAlO_2$ cases where the diffusive inventory is significant and for the Li_7Pb_2 and Li_2O cases where the solubility inventory is dominant, the total inventory for all the other cases consists mainly of the surface adsorption component. By further increasing the isotope swamping of the purge flow, these surface adsorption inventories could be further reduced beyond the 0.01 factor already used. This indicates the need for further experimental data related to the adsorption mechanism and to the effect of isotope swamping. The effect of large protium additions on tritium permeation and tritium recovery must also be considered in a blanket design context.

Sensitivity analyses were performed to determine the effect on the plate temperature and/or tritium inventory of: 1) a temperature dependent (instead of constant) thermal conductivity; 2) including the size variation of the breeder grains; and 3) a crack in the sintered-block breeder.

Expressions for temperature-dependent thermal conductivity for sintered and unirradiated $LiAlO_2$, Li_4SiO_4, Li_8ZrO_6, and Li_2ZrO_3 are given in Section 2.2. For each of these cases with a separate multiplier region, the diffusive inventories obtained using an average and a temperature-dependent thermal conductivity were compared. The already low diffusive inventories for the two zirconate cases barely changed, while that of Li_4SiO_4 increased by about 24%, which is not too significant since the inventory is low. For the $LiAlO_2$ case, though, the diffusive inventory is important (45% of the relatively high total inventory) and the observed 27% increase when using a temperature-dependent thermal conductivity is significant. Note that these temperature-dependent thermal conductivities were used where possible in this study.

Data on the pore size distribution of $LiAlO_2$ was obtained from Ref. [53]. The grain radius distribution was then obtained using a typical equation relating the grain radius, r_g, to the corresponding pore radius, r_p, for a given porosity, ε.

$$r_g = 6.5 \left(\frac{r_p}{\varepsilon}\right)^{0.27} \qquad (2\text{-}36)$$

It was found that using the grain radius distribution over the plate instead of an average grain radius increases the tritium diffusive inventory by 11% for the $LiAlO_2$+Be case. This is an interesting observation, showing that grain size distribution could only have a significant effect on the tritium diffusive inventory estimation (> 11%) if the distribution is abnormally irregular. To avoid any such effect on tritium release due to abnormal grain size distribution, it seems prudent to have the grain size distribution determined for all solid breeder materials considered for tritium experiments.

Table 2.3-15 shows the effect of a crack in the solid breeder plate, assuming sintered-block form, for $LiAlO_2$+Be and Li_2O. Note that cracking is expected to occur if a sintered block form is used, as indicated by the thermal stress calculations reported in the thermo-mechanics section. Cracking is arbitrarily assumed to occur at the tip of the plate at 5 mm from the plate center, with a length of 0.076 cm extending radially into the plate. Even though the crack is assumed to be filled with helium (with a thermal conductivity of 0.43 W/m-K), the changed temperature profile barely affects the total tritium inventory in the case of $LiAlO_2$+Be. The tritium inventory increases from 0.104 to 0.108 wppm only, due mostly to an increase in the diffusive inventory. However, for the case of Li_2O, the total inventory is increased by a factor of 2.2 (2.6 to 5.7 wppm), due mostly to an increase in the solubility inventory. In both cases, the maximum temperature is raised appreciably by the presence of the crack (from 1273 K to 1412 K for $LiAlO_2$, and from 1073 K to 1286 K for Li_2O). Sintering occurring at these higher temperatures could close pores, making diffusion more difficult and further increasing the tritium inventories. Figures 2.3-34 to 2.3-38 show how the temperature and tritium inventory distributions are affected by the presence of such a crack. For comparison purposes, Table 2.3-15 also shows how the temperature and tritium inventories are increased in the extreme lower case of a crack with a 0.043 w/m K thermal conductivity.

Tritium Inventory in Multiplier

Figure 2.3-39 shows the diffusive inventory, I_{d_m}, in the separate multiplier region as a function of the multiplier diffusion coefficient. The equation used was:

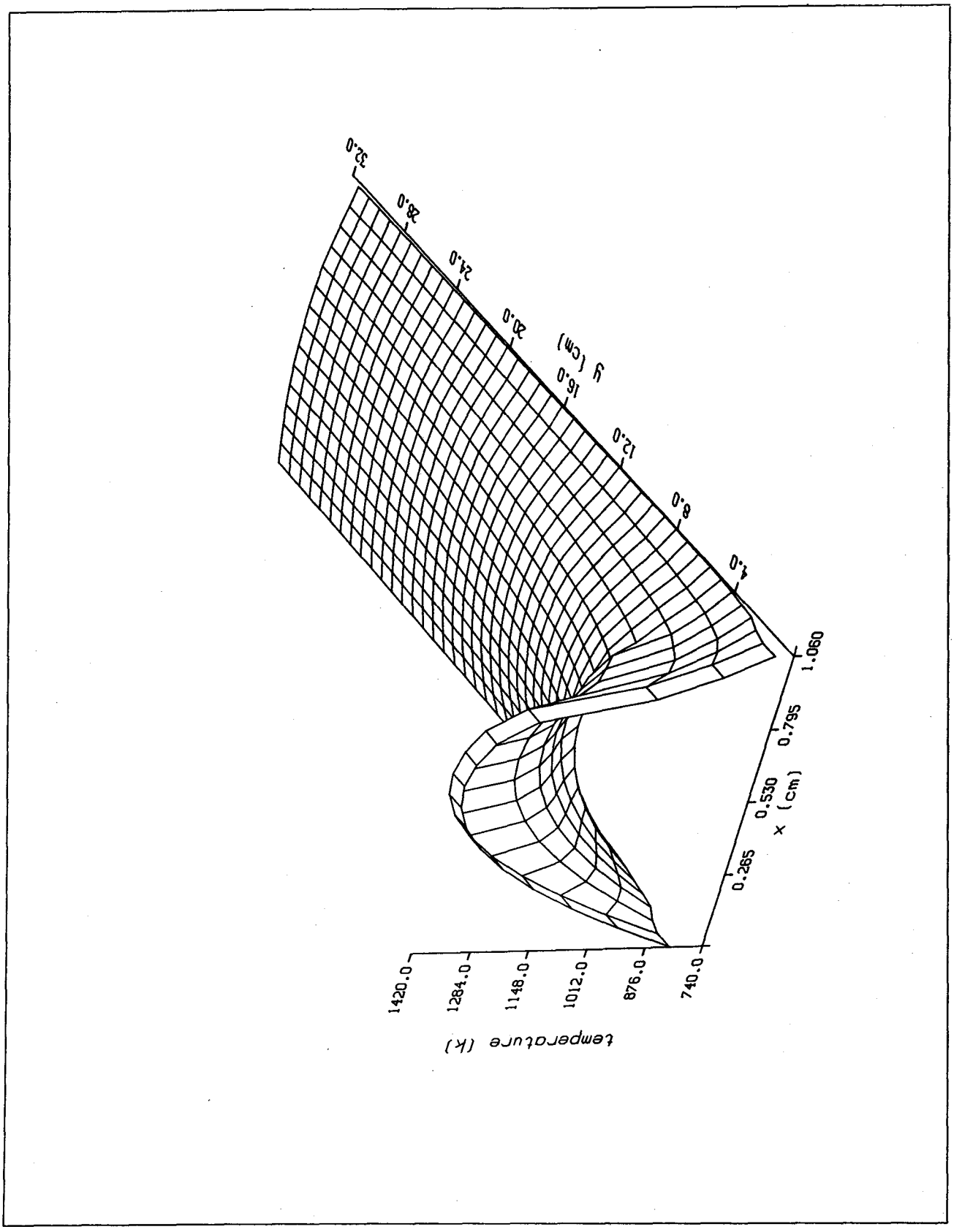


Figure 2.3-34 Plate temperature distribution for $LiAlO_2$+Be case with a 0.076 cm thick crack at x = 0.95 cm and y = 0 to 3.9 cm; k_{crack} = 0.43 W/m-K

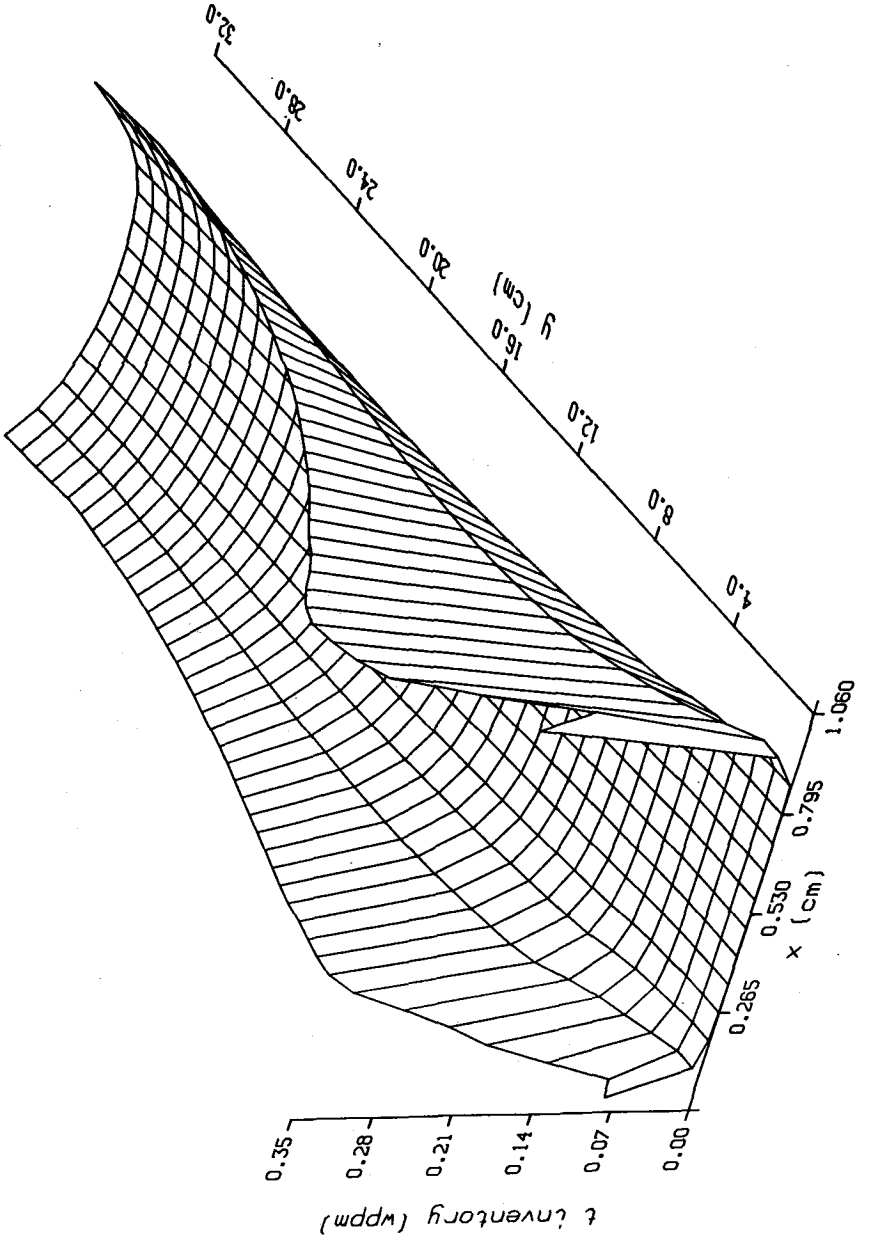


Figure 2.3-35 Plate diffusive tritium inventory distribution for LiAlO2+Be case with a 0.076 cm thick crack at x = 0.95 cm and y = 0 to 3.9 cm; k_{crack} = 0.43 W/m-K

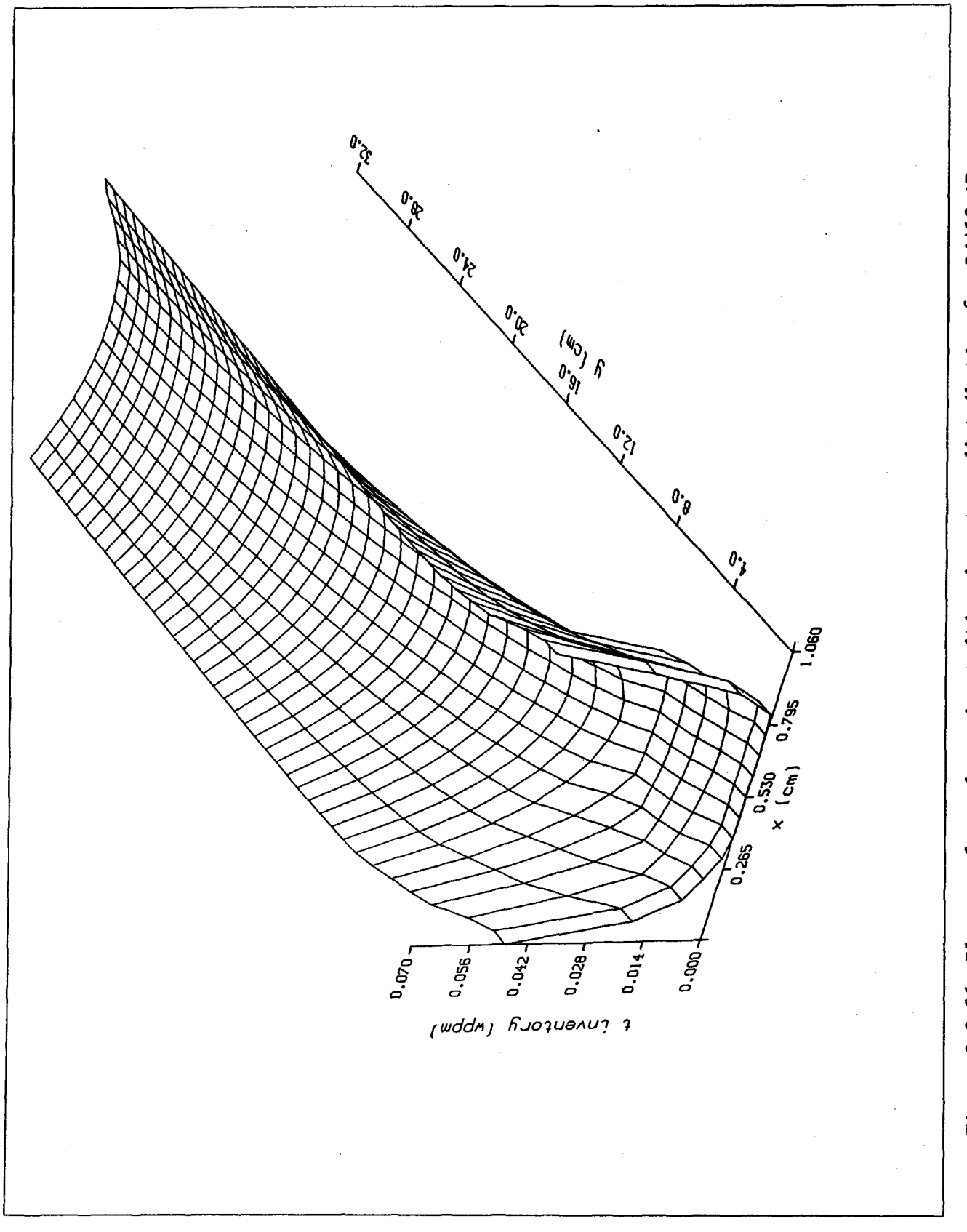


Figure 2.3-36 Plate surface adsorption tritium inventory distribution for $LiAlO_2$+Be case with a 0.076 cm thick crack at x = 0.95 cm and y = 0 to 3.9 cm; k^2_{crack} = 0.43 W/m-K

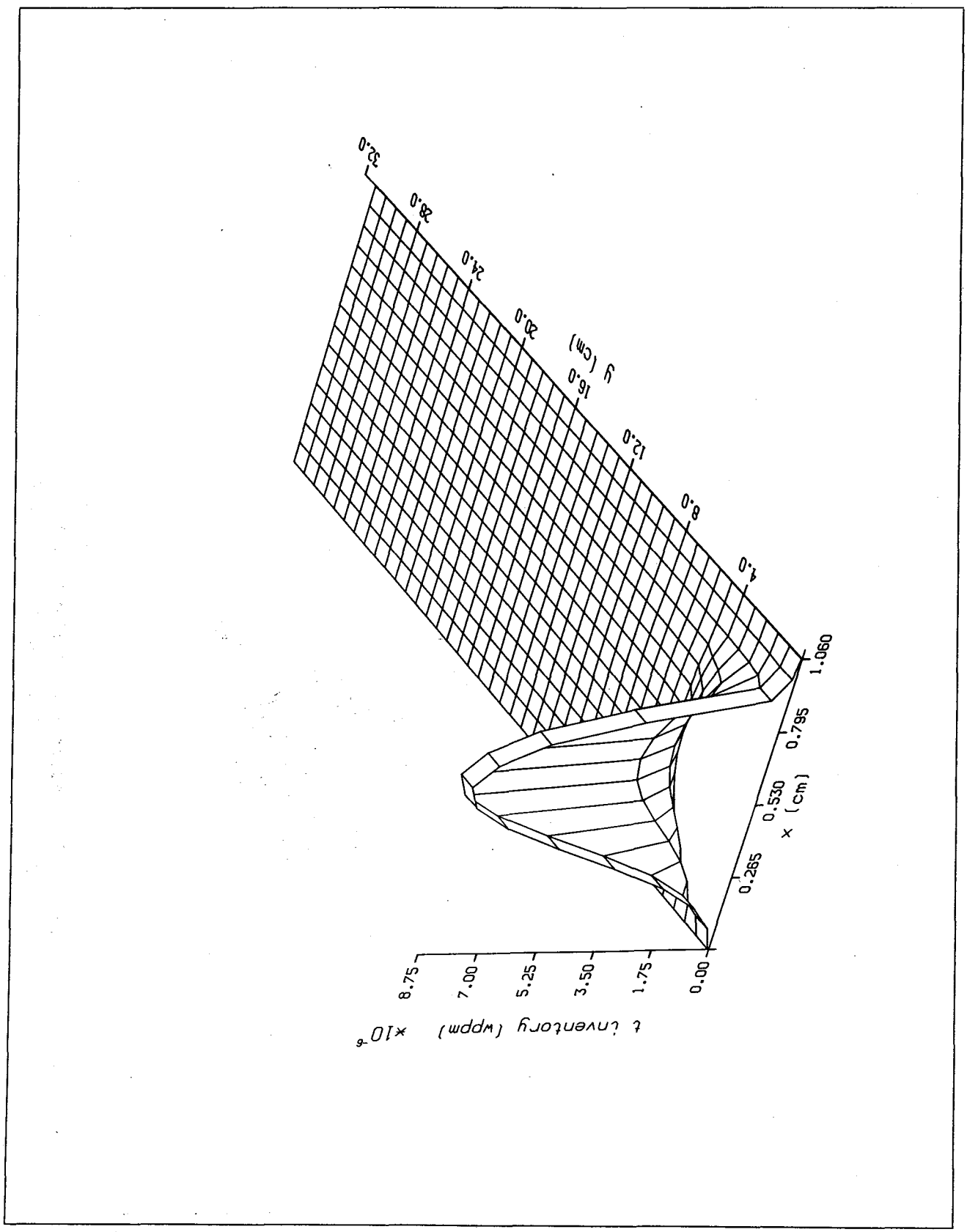


Figure 2.3-37 Plate solubility tritium inventory distribution for $LiAlO_2$+Be case with a 0.076 cm thick crack at x = 0.95 cm and y = 0 to 3.9 cm; k_{crack} = 0.43 W/m-K

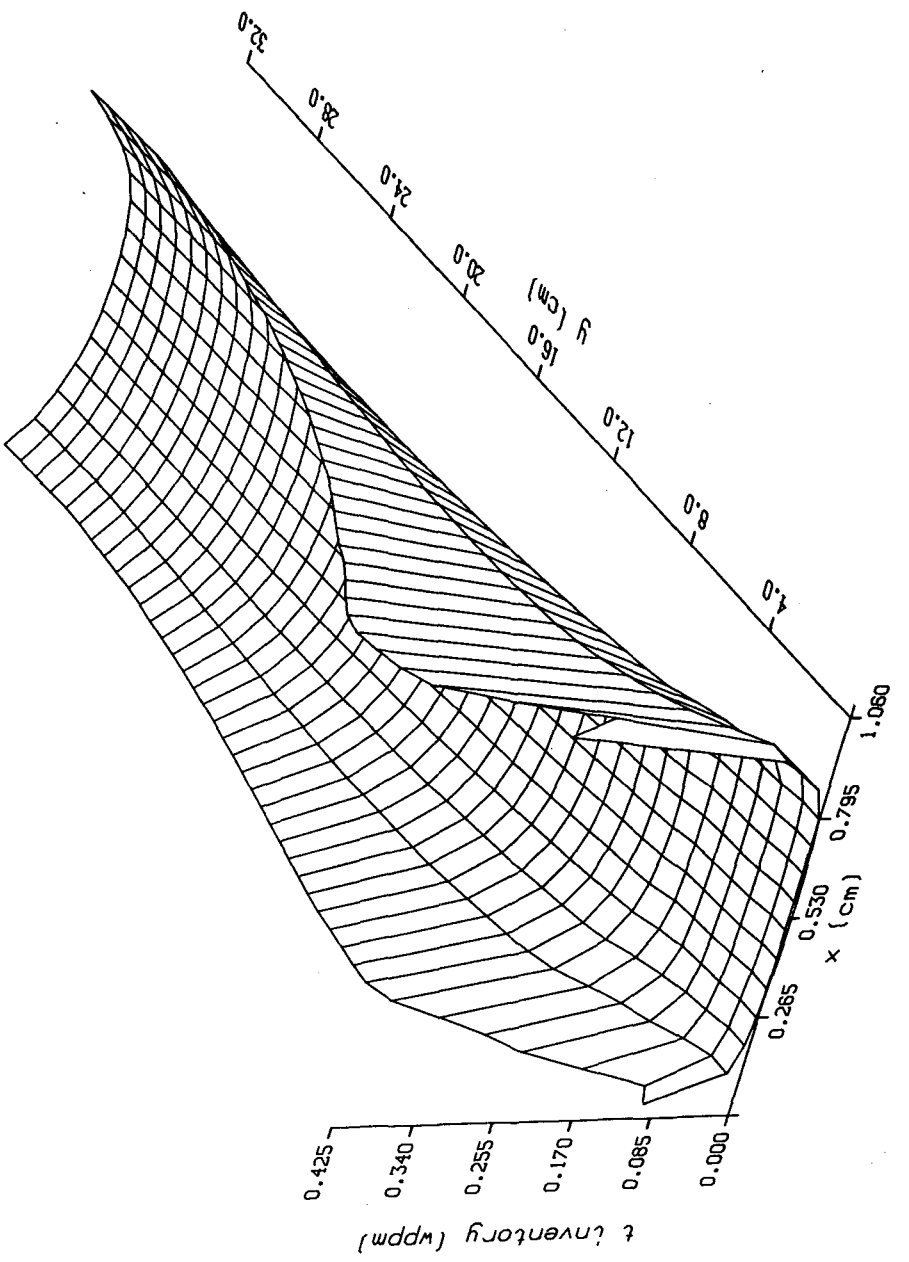


Figure 2.3-38 Plate total tritium inventory distribution for $LiAlO_2$+Be case with a 0.076 cm thick crack at x = 0.95 cm and y = 0 to 3.9 cm; k_{crack} = 0.43 W/m-K

Table 2.3-15 Effect of a Crack with Low Thermal Conductivity on the Plate Maximum Temperature and Tritium Inventory (crack location is at x = 0.95 cm, y = 0 to 3.9 cm)

Case	k_{crack} (W/m-k)	Max Temp (K)	Tritium Inventory (wppm)			
			I_d	I_a	I_s	I_t
$LiAlO_2$+Be	No crack	1273	5.67×10^{-2}	4.74×10^{-2}	1.47×10^{-7}	1.05×10^{-1}
	0.43*	1412	6.06×10^{-2}	4.64×10^{-2}	2.85×10^{-7}	1.08×10^{-1}
	0.043	1858	6.96×10^{-2}	4.58×10^{-2}	1.41×10^{-6}	1.15×10^{-1}
Li_2O	No crack	1073	2.80×10^{-6}	8.47×10^{-2}	6.42×10^{-2}	1.49×10^{-1}
	0.43*	1286	2.80×10^{-6}	8.47×10^{-2}	1.44×10^{-1}	2.29×10^{-1}
	0.043	1755	3.01×10^{-6}	8.47×10^{-2}	5.68×10^{-1}	6.53×10^{-1}

* = Conductivity of helium

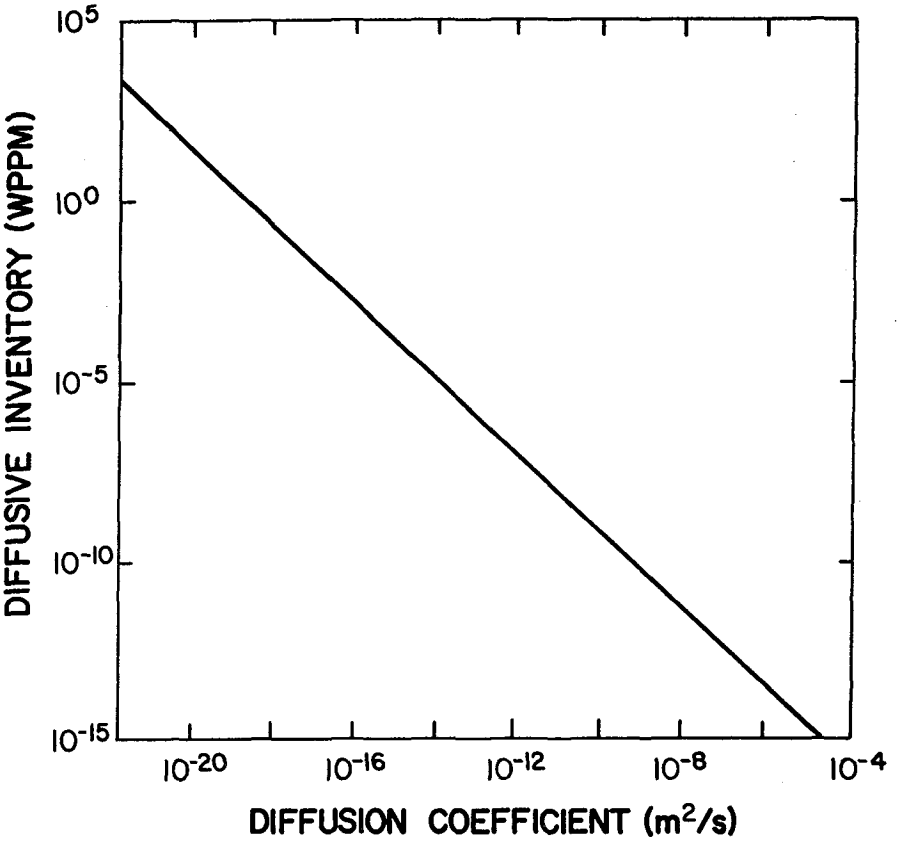


Figure 2.3-39 Diffusive inventory in multiplier region as a function of the diffusion coefficient

$$I_{d_m} \text{ (wppm)} = \left(\frac{G_m \, r_{g_m}^2}{15D \, (0.8\rho_m)}\right) \times 10^6 \qquad (2\text{-}38)$$

where the factor of 0.8 accounts for the material being of 80% theoretical density, the factor of 10^6 converts from weight fraction to wppm, and where

G_m = tritium generation rate in the multiplier material

= 2.0×10^{-6} g/m^3-s (average value for multiplier region from neutronics calculation)

r_{g_m} = multiplier grain radius = 1 μm

ρ_m = multiplier density = 1.8×10^6 g/m^3 for Be

The multiplier diffusion coefficient, D_m, is calculated from:

$$D_m = D_{O_m} \exp(-E_{A_m}/RT) \quad (2\text{-}39)$$

where, from Section 2.2,

D_{O_m} = 3.1×10^{-11} m^2/s for Be
1.0×10^{-6} m^2/s for BeO

and E_{A_m} = 18 kJ/mol for Be
220 kJ/mol for BeO

and R = 8.314×10^{-3} kJ/mol-K

At 700 K, D = 1.5×10^{-12} m^2/s for Be and 3.8×10^{-23} m^2/s for BeO.

From Figure 2.3-39, the diffusive inventory in Be at the temperature given above is low ($\simeq 10^{-7}$ wppm or about 8×10^{-6} g per blanket). However, it would be huge if BeO was used as a separate multiplier ($\simeq 10^{4}$ wppm or 8×10^{5} g per blanket at equilibrium). Note that the corresponding tritium diffusion time constant is about 1500 years because of the low diffusion coefficient of BeO, which means that equilibrium will not be reached during the blanket life. The diffusive inventory will then be lower than that at steady state but will still be large, of the order of 10^{9} g probably). Even if the inventory was reduced by a factor of 100 (by using 0.2-μm BeO grains, for example), the inventory would still be very high. This clearly shows the disadvantage of using BeO.

Another important issue associated with tritium production in the multiplier is whether or not to use a tritium permeation barrier around the multiplier rods. If a barrier is used, the two following options exist for tritium recovery: using a separate tritium purge flow (which produces about 8 g tritium/day per reactor) or letting the tritium accumulate in the multiplier and recovering it at the end of life (8.76 kg after 3 FPY) which poses safety problems. If a permeation barrier is not included, then the tritium permeating from the multiplier to the main flow (along with tritium permeating through the breeder cladding, as shown in the next section) must be extracted from the coolant flow. The choice does not necessarily mean to choose one alternative and exclude the others; a compromise whereby some tritium is allowed to permeate to the main flow and a reasonable amount is allowed to accumulate in the multiplier for removal at the end of life is conceivable.

For the purpose of this study, the results show that the design issue posed by the tritium generated in the separate multiplier region is a disadvantage for those cases with a separate multiplier region when compared to those without a separate multiplier region.

For the homogeneous breeder and multiplier mixture, the tritium inventory and removal from the multiplier is not an issue since the same purge flow is used for the breeder and multiplier. However, the diffusive inventory in the multiplier was estimated for each case to see how it compares to the inventory in the solid breeder.

Equation (2-38) was again used for the calculations. Since the 1-D neutronics computations only give tritium generation rate values for the breeder/multiplier mix, it was assumed that 1% of the total tritium generation rate occurs in the multiplier based on the tritium generation values in the breeder and multiplier for the separate multiplier cases. The results for the maximum and average tritium generation rate and for three different temperatures are shown in Table 2.3-16 for each of the four cases.

For the two cases with Be, even at the lowest temperature, the diffusive inventory in the multiplier is low ($\simeq 10^{-8}$ wppm or about 5×10^{-6} g per blanket) when compared to that of the breeder (see Table 2.3-14). However, for the two cases with BeO, the diffusive inventory at equilibrium is very high, particularly at the lowest temperature (100-500 wppm or about 140 kg per blanket), indicating again the problem of using BeO. Thus, for breeder/multiplier mixtures, although the chemical compatibility of BeO with the solid breeder might be better than that of Be, the above results indicate that only the two cases with Be should be further considered.

Tritium Permeation

Permeation of tritium from the solid breeder into the coolant is a significant release pathway for tritium.[5] The permeation rate is a function of the tritium form and partial pressure, and the cladding area, thickness and temperature. Of these factors, the cladding surface area is most clearly affected by the choice of solid breeder material for a given blanket concept. This area is a function of the breeder region thickness, which depends on the particular breeder temperature limits and thermal conductivity.

Table 2.3-16 Tritium Diffusive Inventory in the Muliplier for the Four Homogeneous Breeder/Multiplier Mixture Cases

Solid Breeder/ Multiplier	$G_m(\frac{g}{m^3-s})$ x 10^{-7}	T(K)	Multiplier $D(\frac{m^2}{s})$	Multiplier I_d(wppm)
$LiAlO_2$/BeO	6.95	1273	1.02×10^{-15}	2.34×10^{-5}
		861	5.17×10^{-20}	4.64×10^{-1}
		700	4.54×10^{-23}	5.28×10^{2}
	2.0	1273	1.02×10^{-15}	6.73×10^{-6}
		861	5.17×10^{-20}	1.33×10^{-1}
		700	4.54×10^{-23}	1.52×10^{2}
$LiAlO_2$/Be	9.96	923	3.06×10^{-8}	1.87×10^{-8}
		771	1.93×10^{-8}	2.98×10^{-8}
		700	1.45×10^{-8}	3.97×10^{-8}
	4.89	923	3.06×10^{-8}	9.21×10^{-9}
		771	1.93×10^{-8}	1.47×10^{-8}
		700	1.45×10^{-8}	1.94×10^{-8}
Li_2O/BeO	8.26	1073	2.18×10^{-17}	1.31×10^{-3}
		811	7.84×10^{-21}	3.64
		700	4.54×10^{-23}	6.28×10^{2}
	3.0	1073	2.18×10^{-17}	4.75×10^{-4}
		811	7.84×10^{-21}	1.32
		700	4.54×10^{-23}	2.29×10^{2}
Li_2O/Be	11.7	923	3.06×10^{-8}	2.20×10^{-8}
		772	1.93×10^{-8}	3.48×10^{-8}
		700	1.45×10^{-8}	4.66×10^{-8}
	6.48	923	3.06×10^{-8}	1.22×10^{-8}
		772	1.93×10^{-8}	1.93×10^{-8}
		700	1.45×10^{-8}	2.58×10^{-8}

The chemical form of tritium depends on many factors and may vary between breeder materials.[68] However, present experimental data are ambiguous. Furthermore, H_2 addition to the purge stream effectively forces the released tritium into the HT form, and also virtually eliminates (by isotopic exchange) tritium adsorbed onto the breeder surface.

The addition of H_2 at 100:1 (H:T) is assumed here for the reference blanket. This and other design choices would affect the tritium permeation magnitude, but generally not the relative permeation rate between the solid breeder materials. The difference in TBR between the breeder materials for the same blanket thickness is neglected assuming any blanket is likely to be adjusted so as to produce no more tritium than necessary. This adjustment may be most cost-effective, if met by reducing the amount of Be or ^6Li rather than decreasing the blanket thickness, because the magnet shielding requirements are unchanged.

For the solid breeder properties given in Section 2.2 and the blanket described in Section 2.3.2, the breeder plate thickness and total breeder plate surface area are given in Table 2.3-17. For 2 m axial length and 0.3 m width per module (Table 2.3-2), 1125 blanket modules implies 5.4 GWth reactor power at 5 MW/m^2 neutron wall load and 1.28 energy multiplication factor. The tritium production rate with a breeding ratio of 1.05 is then 0.0078 g T/s or 674 g T/d.

For protium swamping by a factor of 100:1, the hydrogen flow rate is 0.26 g/s. At a helium purge of 15 m^3/s at 0.6 MPa, the hydrogen partial pressure is 56 Pa. If all the tritium is removed as HT, then P_{HT} = 1.1 Pa.

Permeation rates for HT9 were obtained from Ref. [5] and evaluated at an average cladding temperature of 750 K. Although there was some variation in cladding temperature along the coolant flow path, across the blanket, and between breeder materials, it was not that large. Assuming HT9 clad material and an oxide barrier factor of 100, the clad permeability is 6.6×10^{-11} g $T/m\text{-}s\text{-}Pa^{0.5}$. This permeability is uncertain by about an order of magnitude, primarily because of the uncertainty in the surface conditions and associated barrier factor.

Table 2.3-17 gives the resulting permeation rates from the solid breeder into the helium coolant. The rates range between 1-3 g/d for a 1.6 GWe reactor,

Table 2.3-17 Tritium Permeation for Solid Breeder Blankets

	Number of Plates/ Module	Cladding Area (m^2)	Permeation Rate into the Coolant	
			Breeder (g T/d)	Multiplier (g T/d)
Cases without a Multiplier				
Li_2O	17	43400	1.4	-
Li_2ZrO_3	21	53600	1.8	-
Li_8ZrO_6	24	61300	2.0	-
$Li_2Be_2O_3$	28	71500	2.4	-
Li_7Pb_2	35	89400	2.9	-
Cases With a Homogeneous SB/M Mixture				
$LiAlO_2$/Be	26	66400	2.2	-
$LiAlO_2$/BeO	16	40900	1.3	-
Li_2O/Be	27	69000	2.3	-
Li_2O/BeO	19	48500	1.6	-
Cases With a Separate Be Multiplier Region				
Li_2O	25	35800	1.2	7.5
$LiAlO_2$	24	34400	1.1	7.5
Li_5AlO_4	41	58800	1.9	7.5
Li_2SiO_3	36	51600	1.7	7.5
Li_4SiO_4	32	45900	1.5	7.5
Li_2ZrO_3	28	40100	1.3	7.5
Li_8ZrO_6	33	47300	1.6	7.5
Li_2TiO_3	23	33000	1.1	7.5

similar to the 2 g/d estimated for the BCSS $LiAlO_2$/He/Be blanket.[5] The effect of solid breeder choice is thus roughly a factor of three due to differences in clad area related to breeder temperature limits and thermal conductivity.

Tritium is produced in the multiplier at about 1% of its production rate in the solid breeder, or 7.5 g T/d in a 5.4 GWth reactor. For mixed breeder/multiplier materials, the additional tritium would not affect the tritium permeation. If the multiplier is separate and unclad, however, this tritium

will eventually permeate into the coolant and would dominate over any tritium permeating through the breeder cladding, regardless of the solid breeder material. Such a permeation rate into the coolant may be unacceptably large, and require cladding on the multiplier.

Given the uncertainties in the permeation coefficient and barrier factor (a factor of ten), the factor of three variation in permeation rate (Table 2.3-17) among the different solid breeder materials is probably not significant. The magnitude of the permeation rate, however, is large enough to be of concern, particularly for an unclad multiplier.

2.3.3.4 Activation

Waste Disposal Rating, Biological Hazard Potential and Recycling Hazard

The activation of six solid breeder materials (including impurities) was calculated for two different neutron energy spectra, one with a beryllium multiplier and one without. Also calculated for the former case was the activation of the beryllium multiplier. The fluxes used in the calculation correspond to the front of the breeder region. It was found that the results were similar for both spectra and only one set of results is reported here, namely the one corresponding to the neutron spectrum for the unmultiplied Li_2O case.

The materials and their impurities are shown in Section 2.2. Since many of the conclusions are driven by the amount of certain impurities assumed to be in the material, those amounts are crucial in understanding the results. This is particularly true for those sensitive impurities (e.g., bismuth, niobium, and others) whose concentrations in several candidate breeder materials are assumed to be zero.

The activation calculations were performed with the REAC code system with its expanded cross-section and decay data libraries.[69] The REAC code system has been used to study fusion first wall and magnet activation, the transmutation of materials in facilities used for fusion material testing, the shielding for accelerators, and for transport of radioactive substances. Cross-sections are based on ENDF/B-V and on the LLNL ACTL library[70] wherever possible. Because of the hard spectrum encountered in these calculations, some of the cross-sections may be incorrect by an order of magnitude, but most

cross-sections should be accurate to 50%. Decay data were taken from ENDF/B-V and the Table of Isotopes.[71]

The calculations were performed for each of the 40 elements listed in the breeder impurity table in Section 2.2, except uranium, and the results added to obtain values for the solid breeder material. To include the effects of multi-step reactions, the three-year (5 MW/m^2) exposure was divided into six time steps of six months each. The results for ten hours and ten years cooling will be presented here. Biological hazard potential (BHP) values for each isotope were taken from the Environmental Protection Agency's "The Radioactivity Concentration Guides",[72] using the most conservative figure for the given isotope. BHP values give the maximum concentration of the radioisotopes which meets EPA standards. As geometric dilution, plateout, and holdup (all of which are element-dependent) depend on an accident scenario, these effects were not considered and hence it was assumed that all radioisotopes remain in the original volume. Dose rates at one meter through air were calculated using the decay data information and ANSI standard for conversion from photon flux to dose rates and calculating shielding through use of the energy absorption coefficient. Near surface burial limits were determined using the Nuclear Regulatory Commission's rules as published in the Code of Federal Regulations (10 CFR 61). For some isotopes not covered by 10 CFR 61, limits have been estimated by Kennedy.[73]

For short cooling times, the measures of interest are radiation dose which indicates the recycling hazard, and biological hazard. These values after 3-year irradiation and 10-hour cooling are summarized in Table 2.3-18.

Depending on the material, impurities can either be the driving force (e.g., $Li_2Be_2O_3$), be completely unimportant (e.g., Li_2TiO_3, Li_2ZrO_3, Li_7Pb_2), or be important, depending upon whether BHP or dose is being considered (e.g., Li_2O, $LiAlO_2$, Li_2SiO_3). Table 2.3-19 gives the elements which are the greatest contributors to BHP and dose for each material.

To give a measure of the amount of radiation dose, the Department of Energy (DOE) limit on exposure to workers is 2.5 mR/hr, which implies that only gram (or lower) amounts could be handled without shielding. Thus, all these blanket materials would need to be shielded, although Li_2ZrO_3 generates the largest dose. It is difficult to provide an absolute measure for the

Table 2.3-18 Activation After Three Year Irradiation at 5 MW/m^2 for Reference Design at Front of Breeder Region

	Cooling 10 Hours		Cooling 10 Years	
Material	Dose Rate at 1 Meter (REM/hr/g)	Air BHP (10^{14})	Dose Rate at 1 Meter (10^{-5} REM/hr/g)	Class C Limit
Li_2O	0.0029 (1.00)	0.0177 (0.10)	3.2 (1.00)	0.22 (0.045)
$LiAlO_2$	7.10 (0.0017)	0.99 (0.90)	55.0 (0.98)	9.1 (0.22)
Li_2SiO_3	0.140 (0.051)	8.80 (1.00)	57.0 (1.00)	0.23 (0.061)
Li_2TiO_3	5.60 (0.0011)	2.10 (0.001)	5.2 (1.00)	0.18 (0.089)
Li_2ZrO_3	24.1 (0.0004)	8.75 (0.0064)	8.8 (1.00)	96.0 (0.75)
$Li_2Be_2O_3$	0.031 (1.00)	0.0116 (0.53)	14.0 (1.00)	8.2 (0.96)
Li_7Pb_2	2.64 (0.0072)	20.2 (0.0017)	59.0 (1.00)	32.0 (0.066)
Be	0.0034 (1.00)	0.017 (0.88)	33.0 (1.00)	19.0 (1.00)

NOTE: Numbers in parentheses are the fractional amount contributed by assumed impurities. All gases (including H-3) are assumed to be retained.

Table 2.3-19 Elements Providing Greatest Contribution to Activation After 3 Year Irradiation, 10 h Cooling for Reference Design at Front of Breeder Region

Material	Air BHP	Dose Rate at 1 Meter
Li_2O	Li	(Mn, Ni)
$LiAlO_2$	(Bi)	Al
Li_2SiO_3	(Bi)	Si, (Al)
Li_2TiO_3	Ti	Ti
Li_2ZrO_3	Zr	Zr
$Li_2Be_2O_3$	Li, (Ni)	(Mg)
Li_7Pb_2	Pb	Pb

NOTE: Impurities are enclosed in parentheses. Li contribution is through tritium, which was assumed to be retained.

biological hazard since the actual exposure is so scenario-dependent. However, it can be seen from Table 2.3-18 that the low Z materials generate the lowest numbers.

For long cooling times, waste disposal and recycling are the main concerns. These values after 3-year irradiation and 10-year cooling are also given in Table 2.3-18. The Nuclear Regulatory Commission has established limits on the radioactivity that can be present at burial in a near-surface disposal area. The class of waste allowing the highest amount of activity in such a disposal area is known as class C. The waste may be diluted so that the radioactivity per volume does meet the limits. The values in Table 2.3-18 assume no dilution and indicate that $LiAlO_2$, Li_2ZrO_3, $Li_2Be_2O_3$, and Li_7Pb_2 would have to be diluted before disposal. Note that these calculations were for the point of highest flux in the blanket, so for the entire blanket these materials may not need dilution. It can also be seen from Table 2.3-18 that the radiation dose has decreased by many orders of magnitude when comparing the 10 hour cooling values to the 10 year cooling values.

The elements providing the greatest contribution to BHP, dose, and waste disposal limitations are given in Table 2.3-20. Nickel and cobalt are the primary contributors to radiation dose at long times. Per weight, niobium has by far the greatest contribution to waste disposal limitations, but as seen

Table 2.3-20 Elements Providing Greatest Contribution to Activation After 3 Year Irradiation, 10 y Cooling for Reference Design at Front of Breeder Region

Material	Air BHP	Dose Rate at 1 Meter	Class C Limit
Li_2O	Li, (Cu)	(Na, Ni)	0
$LiAlO_2$	(Co)	(Co)	Al, (Mo)
Li_2SiO_3	Li	(Ni)	0, (Cu)
Li_2TiO_3	(Cu, Ni)	(Ni)	0, (Cu)
Li_2ZrO_3	Zr	(Co, Ni)	Zr, (Nb)
$Li_2Be_2O_3$	Li	(Ni, Cu)	(Nb, Mo)
Li_7Pb_2	Pb	(Co)	Pb, (Mo)

NOTE: Impurities are enclosed in parentheses.

from the composition table in Section 2.2, few materials are assumed to have any niobium. However, it should also be noted that when disposal is a concern, the bulk of the limitation comes from a major constituent of the material.

Afterheat

Decay heat values were calculated by assuming that the only contributions were from products of the primary elements. Contributions from products of impurity elements were ignored. The decay heat values were generated by taking the decay rate results from the REAC runs and multiplying by the total average decay energy (gamma and beta) per decay. The total average decay energy in most cases was taken from ENDF/B-V; in other cases, it was estimated from the decay scheme presented in the Table of Isotopes.[71]

The decay heat values, H, one hour after shutdown were then used in combination with the average steady-state temperature at the tip of the solid breeder plate, $\overline{T}$, the maximum allowable temperature, T_{max} (usually based on the sintering limit), of the solid breeder and the solid breeder heat capacity, C_{Br}, to obtain the time t_{cr}, to reach the maximum allowable temperature after shutdown with no coolant flow and under adiabatic conditions.

$$t_{cr} = \frac{C_{Br}(T_{max} - \overline{T})}{H} \tag{40}$$

For the homogeneous SB/M mixtures, the breeder and multiplier heat capacities, volume fractions and densities and the multiplier decay heat must be factored in to obtain the effective heat capacity and decay rate. The results are shown in Table 2.3-21, together with the values used for T_{max}, $\overline{T}$, C_{Br} and H for each case. Based on these results, Li_2O and $Li_2Be_2O_3$ are very attractive (with t_{cr} of 7.6 and 2.3 days, respectively) and, to a lesser extent, so are the two silicates (with t_{cr} of the order of 1 day). Li_2TiO_3, $LiAlO_2$ and possibly Li_5AlO_4 are adequate (with t_{cr}'s of 5, 2.5 and 0.5 hours respectively). However, the two zirconates and Li_7Pb_2 show times of about 1.5-3 minutes to reach the maximum allowable temperature and, if for some reason a loss of coolant accident occurs, this leaves very little time to have the system fixed again before the solid breeder is ruined and needs replacement.

Table 2.3-21 Time After Shutdown to Reach the Solid Breeder Maximum Allowable Temperature

	T_{max} (K)	$\overline{T}$ (K)	C (kJ/kg-K)[a]	H (kW/kg)[b]	t_{cr} (secs)
Cases Without a Multiplier					
Li_2O	1073	908	2.8	0.0007	6.6×10^5
Li_2ZrO_3	1273	993	1.05	1.7	173
Li_8ZrO_6	1033	877	1.85	1.7	170
$Li_2Be_2O_3$	943	834	1.3	0.0007	2.02×10^5
Li_7Pb_2	693	688	0.475	0.027	88.0
Cases with a Homogeneous SB/M Mixture					
$LiAlO_2$/Be	923	823	1.5	0.040	1.96×10^4
$LiAlO_2$/BeO	1273	1013	1.575	0.040	7.26×10^4
Li_2O/Be	923	826	2.725	0.0007	1.50×10^6
Li_2O/BeO	1073	1014	2.87	0.0007	3.38×10^6
Cases with a Separate Be Multiplier Region					
Li_2O	1073	954	2.825	0.0007	4.80×10^5
$LiAlO_2$	1273	1038	1.575	0.040	9.25×10^3
Li_5AlO_4	873	825	1.525	0.040	1.83×10^3
Li_2SiO_3	973	875	1.65	0.0021	7.62×10^4
Li_4SiO_4	1003	897	1.775	0.0021	8.96×10^4
Li_2ZrO_3	1273	1034	1.05	1.7	148
Li_8ZrO_6	1033	915	1.84	1.7	128
Li_2TiO_3	1203	1002	1.43	0.016	1.80×10^4

[a]For the homogeneous cases, C_{Be} = 2.25 kJ/kg-K and C_{BeO} = 1.95 kJ/kg-K are also included in the calculations.

[b]For the homogeneous cases, the decay heat after one hour for Be only is zero. The decay heat for BeO is assumed similar to that for $Li_2Be_2O_3$.

2.3.3.5 Economics

The material cost of the solid breeder and multiplier, the thermal efficiency of a power plant coupled to the blanket, and the pumping power required for the coolant flow and purge flow are considered in this section. Also included is the power leakage at the back of the blanket, which would raise the cost by requiring additional shield to insulate the superconducting magnets.

Material Cost

The material unit costs estimated in Section 2.2 were used to determine the comparative fabrication costs for blankets containing the various breeder and multiplier materials. These costs include both material and fabrication. The highest unit costs are associated with the beryllium and with ^6Li enrichment at \$400/kg Be and \$1500/kg ^6Li.

The material weight per module was calculated from the product of the material density (assuming an 80% theoretical density) and of its volume, which was determined from the number of plates per module. The material weight per module was multiplied by 1125 modules per blanket to obtain the total cost of the blanket. Table 2.3-22 lists the breeder, multiplier (if applicable) and total costs per module and per reactor for each case. The total costs per module for all the cases, ranked in descending order, are shown on the bar chart in Figure 2.3-40, along with the percentage ^6Li enrichment for each case (the ^6Li content was from optimized TBR results).

In order not to excessively penalize the four homogeneous (20/80) breeder/multiplier mixture cases for the cost calculations, the homogeneous mixture is assumed to be contained in the first 20 cm of breeder region with breeder only in the second 37 cm breeder region. This will reduce the amount of expensive beryllium, while the lower neutronics performance can be afforded (TBR is reduced from 1.87 to 1.75 for the Li_2O/Be case and from 1.80 to 1.59 for $LiAlO_2$/Be).

The highest costs are associated with the unmultiplied $Li_2Be_2O_3$ and Li_7Pb_2 cases, with most of the other cases showing costs between about \$60,000 to \$95,000 per module. The cost for the unmultiplied Li_2O case, however, is appreciably lower than those of all the other cases (\$25,000 per module), making unmultiplied Li_2O quite attractive on this basis.

Table 2.3-22 Blanket Material and Fabrication Costs

Breeder Material	^{6}Li Enrich. (%)	Costs Per Module			Total Cost for Reactor[c] (M$)
		Breeder Cost[a] (k$)	Multiplier Cost[b] (k$)	Total Cost (k$)	
Cases Without a Multiplier					
Li_2O	natural	25	0	25	28
L_2ZrO_3	29	94	0	80	90
Li_8ZrO_6	natural	48	0	48	54
$Li_2Be_2O_3$	natural	119	0	119	134
Li_7Pb_2	29	109	0	99	111
Cases With a Homogeneous SB/M mixture[d]					
$LiAlO_2$/Be	36	45	55	92	104
$LiAlO_2$/BeO	40	45	40	85	96
Li_2O/Be	natural	17	48	65	73
Li_2O/BeO	14	17	39	72	81
Cases With a Separate Be Multiplier Region					
Li_2O	20	29	22	60	67
$LiAlO_2$	62	45	22	67	75
Li_5AlO_4	30	38	22	60	68
Li_2SiO_3	50	47	22	69	78
Li_4SiO_4	33	41	22	63	71
Li_2ZrO_3	58	64	22	64	72
Li_8ZrO_6	26	35	22	81	91
Li_2TiO_3	51	46	22	68	77

[a]Breeder Region: 32 cm thick for separate multiplier cases, 57 cm thick for all other cases

[b]12 cm thick multiplier region with 54% multiplier volume fraction

[c]1125 modules per reactor (5.4 GWth)

[d]20/80 SB/M in first 20 cm; SB only in next 37 cm

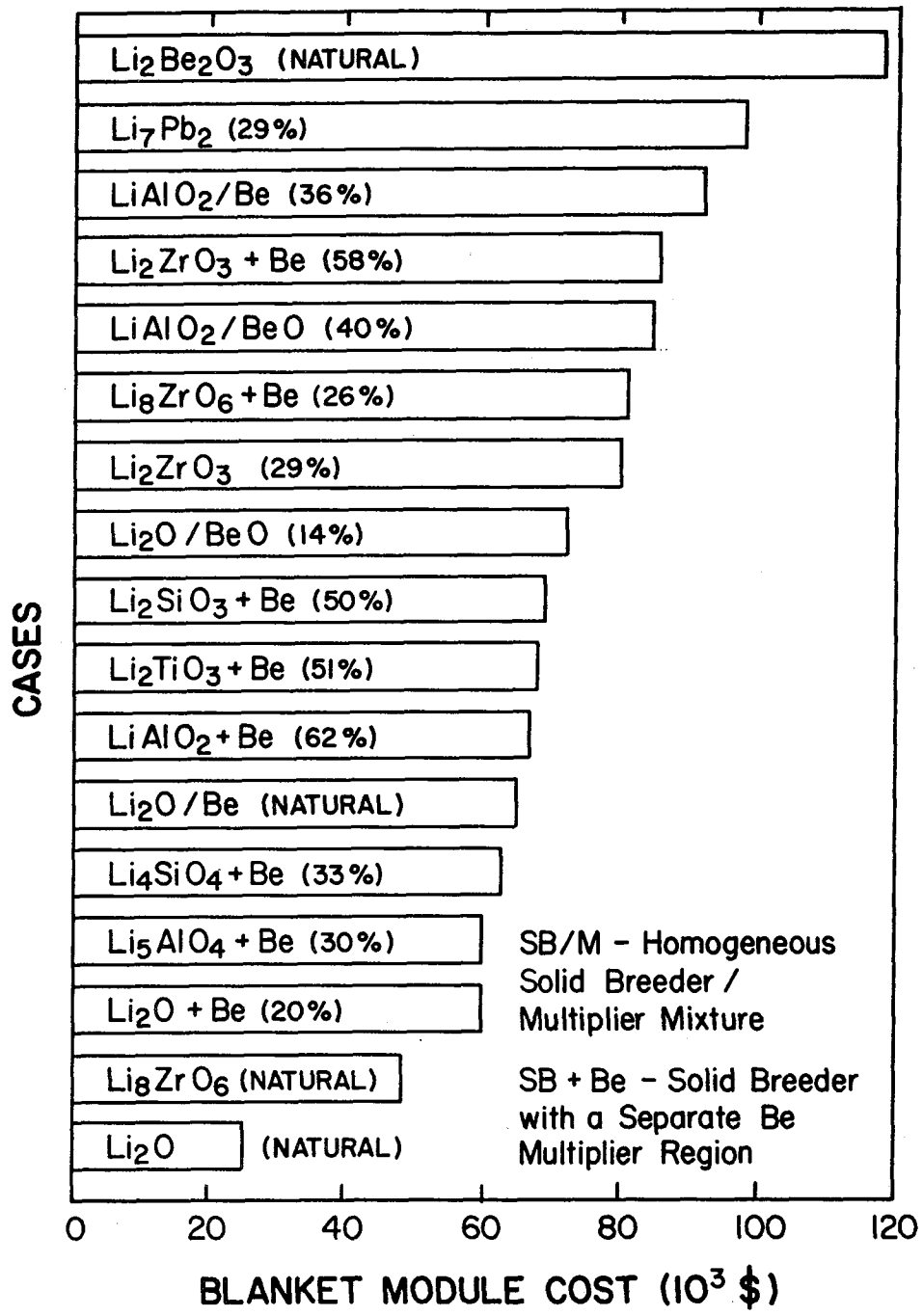


Figure 2.3-40 Cost per module for the different solid breeder cases (the chosen ^{6}Li enrichment for each case is shown in between parentheses)

To verify the importance of the multiplier and breeder costs relative to the structure (cladding, first wall) costs, these were also estimated for HT9 as structural material (at $45/kg including fabrication).[5] The cost of the structure is about $12,300 per module, which is equivalent to about 50% of the total module cost of the unmultiplied Li_2O case and about 16% of the total module cost for the unmultiplied Li_2BeO_3 case. This means that the breeder and multiplier costs are a significant fraction of the total module cost.

Thermal Efficiency and Pumping Power

The thermal efficiency, η_{th}, of the steam cycle coupled to the blanket was calculated from the helium bulk temperature at the exit of the blanket, $T_{B_{out}}$ (obtained from the mass flow rate, fusion power and multiplication factor). The steam cycle was based on the one described in Ref. [74] with a corresponding steam temperature of 311 K in the condenser.

For this cycle, η_{th} was found to be 68% of the ideal Carnot efficiency. If, as an upper limit, the maximum temperature in the steam cycle is assumed to be equal to $T_{B_{out}}$, then η_{th} is given by the following expression:

$$\eta_{th} = 0.68 \left[1 - \frac{311}{T_{B_{out}}}\right] \tag{2-41}$$

For the pumping power calculations, both the pressure drop across the multiplier region (if applicable) and the pressure drop across the breeder plates were considered. Estimates for the pressure drop in the helium circuit outside the breeder were obtained from Ref. [5] to give the total blanket pressure drop. The other components include the inlet manifold, distribution channel, the side flow path, the grooved first wall, the collection channel, and the outlet manifold, with a combined 48 kPa pressure drop.

The pressure drop across the array of multiplier rods, ΔP_m, were calculated,[75] assuming a staggered array of longitudinal pitch, S_L = 1.90 cm, transverse pitch, S_T = 2.2 cm, rod diameter, d_r = 2 cm, and inter-rod spacing, t_s = 2 mm. Therefore,

$$\Delta P_m = 2\, f\, \rho v_{max}^2\, N_r \tag{2-42}$$

where ρ is the helium density, v_{max} is the maximum velocity at the minimum

area, N_r is the number of rows in the array, and f is the empirical friction factor given by:[75]

$$f = \left[0.25 + \frac{0.118}{\left[\frac{S_T - d_r}{d_r}\right]^{1.08}}\right] Re_{max}^{-0.16} \qquad (2\text{-}43)$$

where Re_{max} is the Reynolds number based on the maximum velocity and the rod diameter.

The pressure drop across the breeder region, ΔP_{br}, was calculated in a similar way:[75]

$$\Delta P_{br} = \frac{\rho v^2}{2}\left[\frac{2fL_c}{d_h} + 1\right] \qquad (2\text{-}44)$$

where L_c is the length of a channel, ρ is the helium density, v is the helium velocity, d_h is the hydraulic diameter of the channel between two plates, and f is the friction factor given by:[76]

$$f = 0.184\ Re_d^{-0.2} \qquad (2\text{-}45)$$

where Re_d is the Reynolds number based on the hydraulic diameter. The sum of entry and exit losses was assumed to be equal to the dynamic pressure of the flow, as shown in Eq. (2-44). Note that the pressure drop calculations for this study were done for the chosen reference design under the assumption of constant mass flow rate for all the different material combination cases. One should be cautious not to generalize these results to other designs and assumptions without carefully evaluating their effects on the calculations.

The cycle thermal efficiency and pressure drop results are summarized in Figure 2.3-41. The total pressure drop, ΔP_{TOT}, has been converted to a pumping power ratio (PPR), which is equivalent to the pumping power required divided by the electric power generated by the heat transported out of the blanket by the helium mass flow.

$$PPR = \left(\frac{\dot{m}}{\eta_p}\frac{\Delta P_{TOT}}{\rho}\right)/\left(\dot{m}\, C_p \Delta T_{He} \eta_{th}\right) \qquad (2\text{-}46)$$

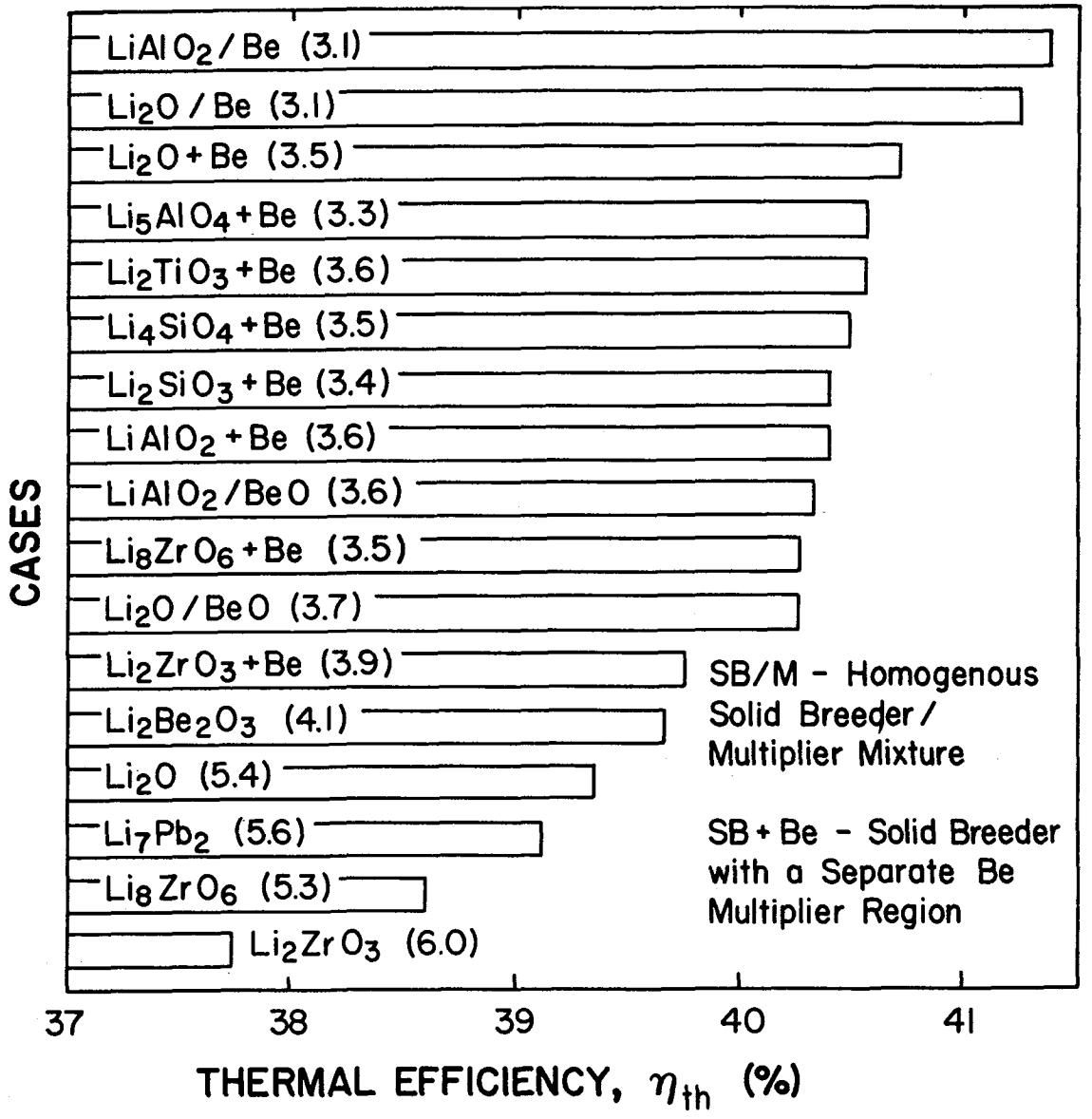


Figure 2.3-41 Thermal efficiency for the different cases
(The PPR for each case is also shown in brackets)

where $\dot{m}$ is the helium mass flow rate, η_p is the pump efficiency (0.9), C_p is the helium specific heat and ΔT_{He} is the helium bulk temperature rise.

From Figure 2.3-41, the gross thermal efficiency (without including pumping power) can be seen to vary from 37.8% for the unmultiplied Li_2ZrO_3 case to 41.3% for the $LiAlO_2$ homogeneous mixture case. Apart from the unmultiplied Li_2ZrO_3 case, all the cases have similar thermal efficiencies (within a small 2.7% range).

The main coolant pumping power ratio tends to vary inversely with thermal efficiency, and shows a maximum of 6% for the unmultiplied natural Li_2ZrO_3 case and a minimum of 3.1% for the $LiAlO_2$ homogeneous case. However, the variation is mostly due to the number of plates in the design; the fewer the plates, the fewer the channels and the larger the pumping power for a given mass flow rate. The mass flow rate here is fixed by the first wall design. For blankets where the coolant does not first flow through the first wall the PPR could be changed. Also, since the neutronics are rather insensitive to small changes in the breeder volume fraction, as shown in Table 2.3-8, it is conceivable that a fixed number of plates of the same size be used for all the cases, which will then have essentially the same pumping power requirements.

For the breeder material in sphere-pac form, the pumping power required for the purge flow through the sphere-pac in the plate will be a function of the sphere sizes only for a given volume flow rate.

For 20% porosity, ε, in the solid breeder material, the pressure drop, ΔP_{purge}, was calculated from the following expression:[76]

$$\Delta P_{purge} = \frac{f_c L S \rho V_0^2}{\varepsilon^2} \tag{2-47}$$

where, for viscous flow (Re < 2) the friction factor, f_c, is given by:

$$f_c = 5/Re \tag{2-48}$$

$$Re = \frac{\rho V_0}{\mu S} \tag{2-49}$$

$$S = 6(1 - \varepsilon) \sum W_i/D_{P_i} \tag{2-50}$$

The variables are defined as follows:

D_{P_i} = particle diameter of species i

W_i = weight fraction of species i in the sphere pac

L = "depth" of sphere pac (in the flow direction) = 2 m

S = particle surface area per unit volume of packing

V_0 = superficial velocity based on an empty plate cross-section

ρ = helium density = 0.61 kg/m^3 at 1 MPa and 800 K

μ = helium viscosity = 3.9 x 10^{-5} kg/m-s at 800 K

η_p = the estimated efficiency of the pump = 0.8

Q = the volume flow rate for the reactor (total purge flow)

$1/\sum W_i/D_{P_i}$ = the effective particle diameter.

The total pumping power, PP_{purge}, can then be calculated from the following expression.

$$PP_{purge} = \frac{Q\ \Delta P_{purge}}{\eta_p} \qquad (2\text{-}51)$$

Figure 2.3-42 shows the results for a plate thickness of 1 cm. When compared to the electrical power produced by a typical reactor (of the order of 2000 MW), the purge flow pumping power is small for a typical effective particle diameter of 1.1 mm (corresponding to the BCSS[5] particle sizes of 1200, 300 and 30 microns), varying from about 150 kW for a flow rate of 5 m^3/s to about 3 MW for a flow rate of 20 m^3/s.

The particle sizes are usually chosen based on tritium diffusion considerations. However, the choice of particle sizes is constrained by the inlet pressure of the purge flow which limits the total allowable pressure drop even if the required pumping power is acceptably small. For example, for a purge flow inlet pressure of 1 MPa and a volume flow rate of 15 m^3/s, the effective particle diameter must be about 400 microns or larger. If the purge flow pressure is lower (e.g., 0.1 MPa), the effective particle diameters are further limited (> 1 mm).

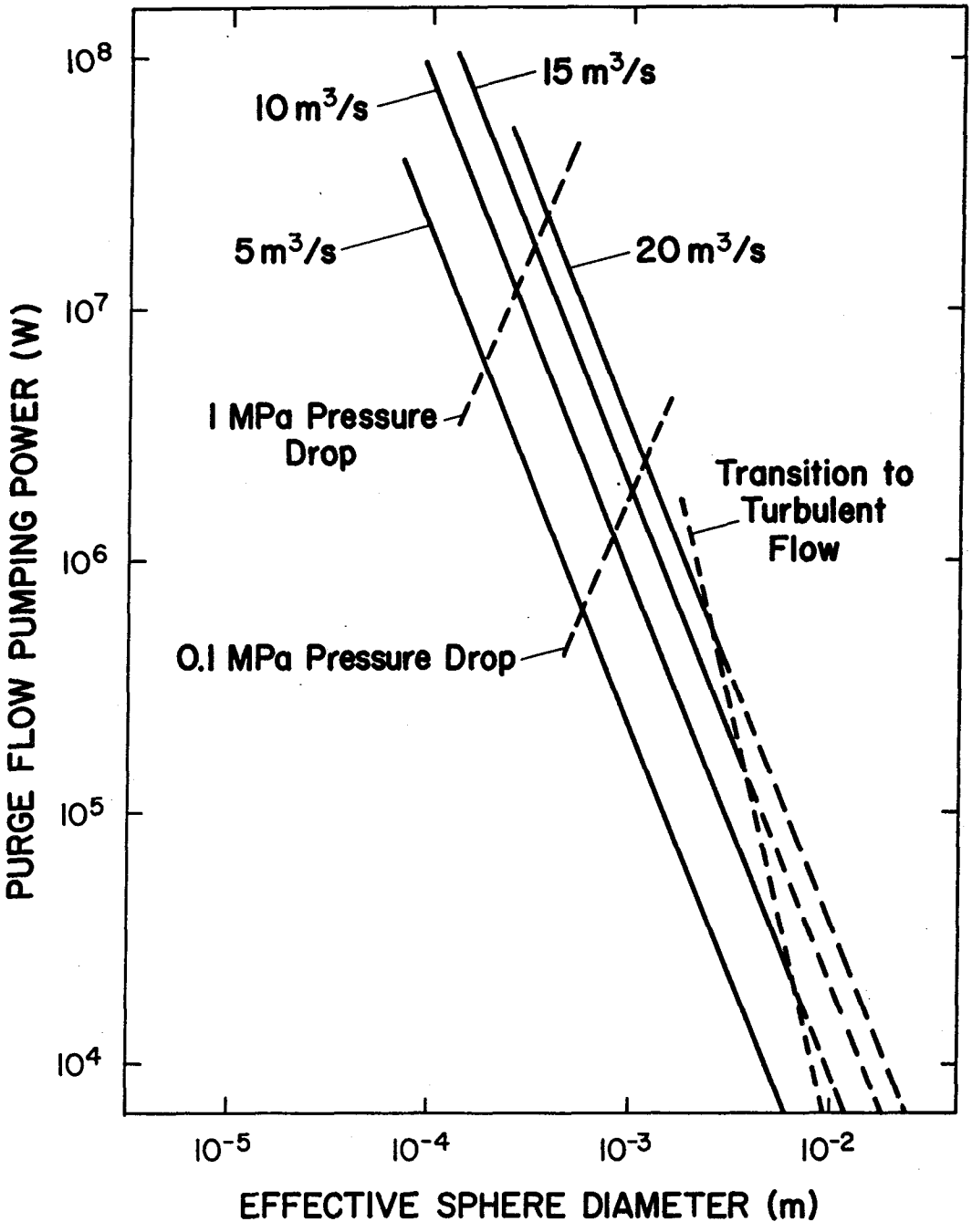


Figure 2.3-42 Pumping power required for the purge flow as a function of plate thickness for different purge flow total volume flow rates

If the plate thicknesses for the different cases are allowed to differ, the pumping power required for the purge flow will also differ for each case. To determine the sensitivity of the pumping power to changes in plate thickness, a low value of 0.5 cm and a high value of 1.3 cm for the plate thickness were selected for further calculations. The effects of these changes were a reduction of approximately 17% in the pumping power for the 1.3 cm case and an increase of about 12% for the 0.5 cm case. This shows that variation in the plate thickness has a relatively minor effect on the required purge flow pumping power for the range of plate thicknesses considered in this study.

Power Leakage

The power leakage can be calculated from the neutron flux and the neutron energy at the back of the 30 cm partial shield (see Figs. 2.3-2 and 2.3-3). The results give an idea of the amount of additional shield required to protect the superconducting magnets from neutron radiation and heat generation. This additional shield requires space and is also an additional capital cost factor.

The results are summarized in Table 2.3-23. There is a variation of a factor of 6 in the leakage power for the different cases, except for Li_7Pb_2, which, with a leakage power of about 14.9 MW for the whole blanket, shows the highest value. The values for the other cases all fall within the range 1.2 to 7.1 MW for the whole blanket, with Li_2O showing the lowest value.

A factor of 2 to 3 increase in power leakage typically requires about 5 cm of additional shield thickness. The importance of power leakage can be minimized for a tokamak-type reactor by limiting the shield increase to the outboard region where space is less restricted. In the inboard region, where space is critical, the blanket thickness can be reduced by a few centimeters without seriously reducing the TBR. In general, though, the cases with lower power leakage are preferred, and, in this respect, the Li_7Pb_2 case is certainly less attractive than the others.

2.3.4 Conclusions and R&D Priorities

The performance of a solid breeder blanket was analyzed for a wide range of present candidate breeder materials. The performance parameters considered

Table 2.3-23 Total Power Leakage at the Back of the 30 cm Partial Shield for the Different Cases

Case	Total Power Leakage (MW)
Cases Without a Multiplier	
Li_2O	5.6
Li_2ZrO_3	4.1
Li_8ZrO_6	4.2
$Li_2Be_2O_3$	3.4
Li_7Pb_2	14.9
Cases With a Homogeneous SB/M Mixture	
$LiAlO_2$/Be	7.1
$LiAlO_2$/BeO	6.1
Li_2O/Be	4.7
Li_2O/BeO	3.8
Cases with a Separate Be Multiplier Region	
Li_2O	1.2
$LiAlO_2$	2.5
Li_5AlO_4	2.5
Li_2SiO_3	2.6
Li_4SiO_4	2.5
Li_2ZrO_3	2.4
Li_8ZrO_6	2.1
Li_2TiO_3	3.2

are listed in Table 2.3-3. The results, as described in Section 2.3.3, are summarized in Table 2.3-24.

The performance parameters are not of equal importance. TBR is the most important parameter for a fundamental reason: tritium self-sufficiency is a requirement. Safety concerns dictate that the tritium inventory is also of high importance. However, the magnitude of the uncertainties in the tritium-related property data tends to make a comparison between the different cases difficult.

Table 2.3-24 Summary of the Performance Results for All Cases

Solid Breeder	Effective TBR[a]	Power Mult.	Peak Li Burnup (at.%)	Gross η_{th} (%)	Power Leakage (MW)	Blanket SB & M Cost ($M)	Breeder Total T Inventory (g)	Breeder Permeation Rate (g T/d)	Pumping Power Ratio (%)	Dose Rate at 1 m[c] (REM/hr-g)	Afterheat Time to Reach T_{max} (hr)
Cases Without a Multiplier											
Li_2O	1.08 (nat)	1.22	2.9	39.4	5.6	28	5.6	1.4	5.4	0.0029	183
Li_2ZrO_3	0.93 (29)	1.02	6.1	37.8	4.1	90	85.8	1.8	6.0	24.1	0.048
Li_8ZrO_6	0.98 (nat)	1.12	3.7	38.6	4.2	54	85.2	2.0	5.3	24.1	0.047
$Li_2Be_2O_3$	1.09 (nat)	1.31	5.4	39.7	3.4	135	552,000	2.4	4.1	0.031	56
Li_7Pb_2	1.22 (29)	1.18	5.0	39.1	14.9	110	1,590	2.9	5.6	2.64	0.024
Cases With a Homogeneous SB/M Mixture											
$LiAlO_2$/Be	1.51 (36)	1.51	46.8	41.4	7.1	104	230	2.2	3.1	1.86	5.4
$LiAlO_2$/BeO	1.09 (40)	1.36	35.3	40.3	6.1	96	76.5	1.3	3.6	1.27	20
Li_2O/Be	1.57 (nat)	1.52	19.5	41.2	4.7	73	8.1	2.3	3.1	0.0033	420
Li_2O/BeO	1.14 (14)	1.36	14.3	40.3	3.8	81	9.5	1.6	3.7	0.027	940
Cases With a Separate Be Multiplier Region											
Li_2O	1.24 (20)	1.42	15.8	40.7	1.2	68	43.9	1.2	3.5	0.0029	130
$LiAlO_2$	1.09 (62)	1.39	37.8	40.4	2.5	75	36.4	1.1	3.6	7.1	2.6
Li_5AlO_4	1.17 (30)	1.40	23.2	40.6	2.5	68	23	1.9	3.3	7.1	0.51
Li_2SiO_3	1.10 (50)	1.37	31.2	40.4	2.6	78	9.6	1.7	3.4	0.14	21
Li_4SiO_4	1.14 (33)	1.38	24.9	40.5	2.5	71	9.2	1.5	3.5	0.14	2.5
Li_2ZrO_3	1.17 (58)	1.27	31.8	39.7	2.4	97	47	1.3	3.9	24.1	0.041
Li_8ZrO_6	1.22 (26)	1.34	21.2	40.3	2.1	91	45.4	1.6	3.5	24.1	0.036
Li_2TiO_3	1.12 (51)	1.39	32.9	40.6	3.2	77	4.1	1.1	3.6	5.6	5

[a] % ^6Li enrichment corresponding to optimum TBR is shown in parentheses; (nat) is for natural lithium (7.25% ^6Li).
[b] At 0.5 cm from tip of breeder plate.
[c] After 3-year irradiation and 10-hour cooling.
For the separate multiplier cases, the dose rate for Be is 0.0034 REM/hr-g and is due entirely to impurities.
For the homogeneous SB/M mixture cases, the dose rate for the multiplier (0.0034 REM/hr-g for Be and ≃ 0.03 REM/hr-g for BeO) have been included in these figures.

Other important parameters include activation, afterheat, power multiplication and material cost. The dose rate after 3-year irradiation and 10-hour cooling, which gives an indication of the recycling hazard, is the activation parameter considered in this section. It is not as dominated by impurities (which arguably can be removed at a cost) as the other activation parameters. The time to reach the maximum allowable temperature after shutdown with no coolant flow can be calculated from the decay heat. It is also an important parameter since it indicates how much time is available to restart the cooling system, in case of accidental shutdown, without damaging the solid breeder and/or multiplier. Power multiplication and material cost are included here as the basic power and economic parameters.

The limitation of the peak lithium burnup after 3 full-power years is uncertain. It is generally believed that high burnup is a disadvantage since the chemical change caused by accelerated burnup could affect the characteristics and performance of the material, but the exact effect is unclear. This points out the need for high burnup testing of solid breeders with subsequent material analysis to determine how the material is affected. In general, though, the cases showing higher burnups are less attractive than those showing lower burnups.

The power leakage factor can be important for space-limited reactors since higher power leakage implies the need for additional shielding. However, the importance of power leakage can be minimized in a tokamak-type reactor by limiting this additional shield increase to the outboard region where space is less restricted. On the inboard region, where space is very important, the blanket thickness can be reduced by a few centimeters without seriously reducing the TBR.

Note that the relative behavior among the candidate breeder materials for all the above-mentioned parameters (TBR, tritium inventory, dose rate, afterheat time to reach the maximum allowable temperature, power multiplication, material cost, Li burnup and power leakage) tends to be independent of the geometric details of the design (although for the tritium inventory and the cost, this applies only if the blanket mass of breeder and multiplier is fixed for all designs).

In contrast, the pumping power requirements and the thermal efficiency tend to be design-dependent. Furthermore, for the reference design of this

study it was found that, since the neutronics calculations are rather insensitive to small changes in the volume fractions, the same plate thickness and number of plates can be used in each case. The pressure drop experienced will then be the same for all cases for a given coolant volume flow rate. The thermal efficiency for a given flow rate and inlet temperature, as is the case in this study, is essentially dependent on M only and will only serve to slightly amplify the relative difference between the different cases based on M. For these reasons, the pumping power ratio and thermal efficiency are not considered as important parameters here.

The deflection of and/or stresses in the clad are also not considered here since their importance as a comparison criterion is very much design-dependent and will be much lessened if it is assumed that some means of allowing for swelling and thermal expansion can be found. Such a means could be the use of a bellow-type arrangement or added breeder porosity. Nevertheless, one should keep in mind that the higher swelling and thermal expansion of Li_2O compared to the other solid breeders is a potential disadvantage for the Li_2O cases. The thermal stress calculations for the solid breeder highlight the problem associated with the sintered block form. The high thermal stresses will lead to cracking which can cause the breeder temperature to reach the sintering limit and the tritium inventory to increase. Based on this, the sphere pac form is preferred to the sintered block form for the solid breeder.

The six major parameters of importance can be classified in pairs based on the indications that they give about tritium (TBR and tritium inventory), economics (M and material cost), and safety (dose rate and afterheat time to reach the maximum allowable breeder temperature). Graphical representations of the comparison of the various cases based on these three pairs of major parameters have been made. Figure 2.3-43 shows a point graph of the effective TBR and of the reciprocal of solid breeder tritium inventory for the seventeen cases. This choice of variable means that the more attractive cases will show up in the top right hand corner of the plot. It should be noted that the comparison is made more difficult by the magnitude of the uncertainties in the tritium inventories, which strongly indicates the need for better property data on the solid breeder tritium-related properties. On the TBR side, the results were obtained from 1-D neutronics calculations and adjusted by a factor of 0.85 for 3-D effects.

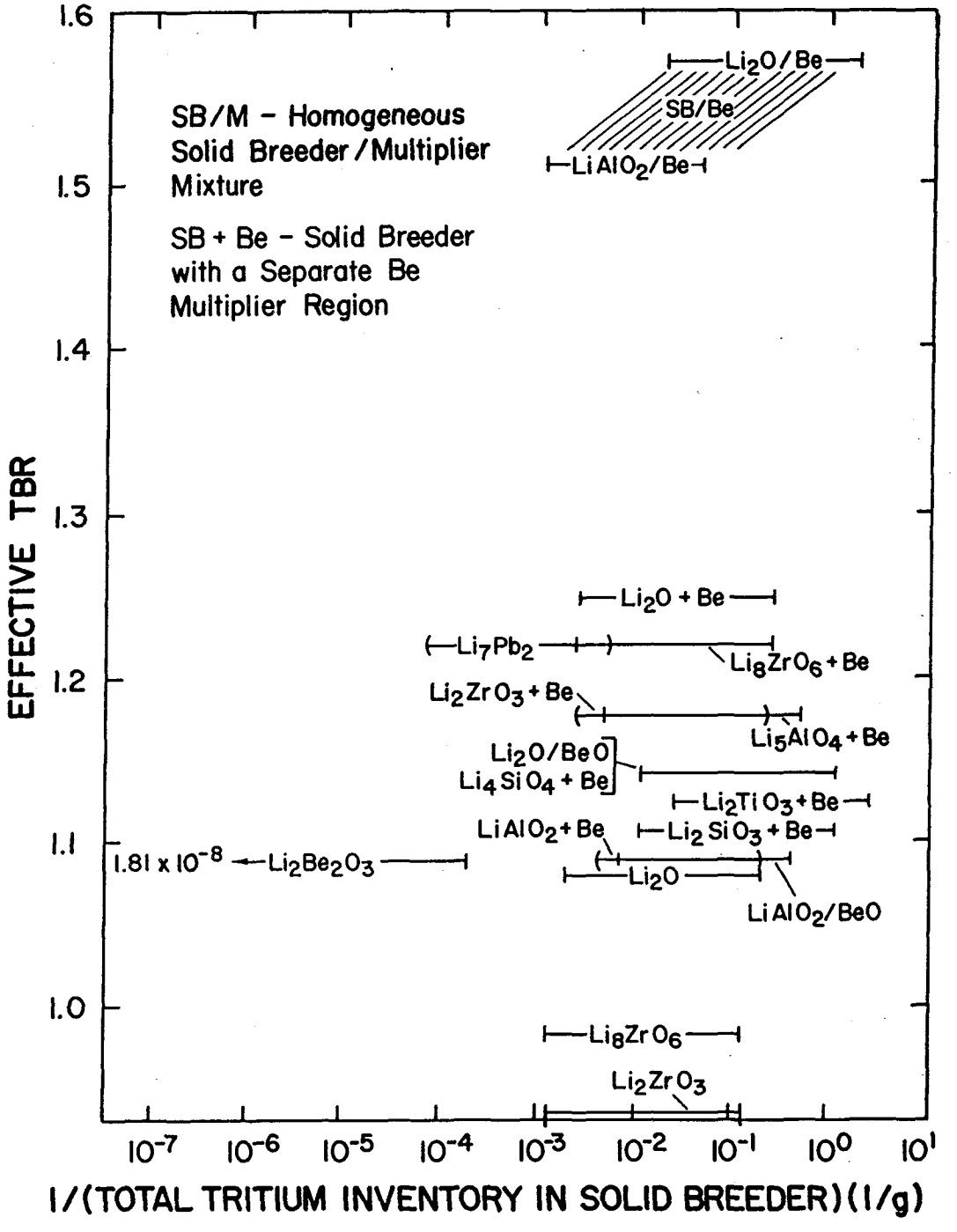


Figure 2.3-43 Point graph of the effective tritium breeding ratio and of the reciprocal of the total tritium inventory in the solid breeder for the different cases

There are considerable uncertainties[77] in the basic data, modeling and calculations for TBR. The required TBR depends on many factors[77] such as achievable plasma burnup and desired doubling time. For the purposes of this study, a reference value of 1.05 for the required TBR is assumed. Based on this, cases with an effective TBR of 1.05 or less are unattractive. These include the unmultiplied cases of Li_2ZrO_3 and Li_8ZrO_6 (and all other unmultiplied ternary ceramics considered in this study). Cases with effective TBR's between 1.05 and 1.10 are marginal and consist, in order of increasing TBR, of unmultiplied Li_2O and $Li_2Be_2O_3$, $LiAlO_2$+Be and $LiAlO_2$/BeO. $Li_2Be_2O_3$, though, shows a high tritium inventory and is thus unattractive. There are six cases with effective TBR's between 1.10 and 1.20 (Li_2SiO_3+Be, Li_2TiO_3+Be, Li_4SiO_4+Be, Li_2O/BeO, Li_5AlO_4+Be, Li_2ZrO_3+Be), but a ranking of these cases is difficult since, in general, the cases with higher TBR's tend to have slightly higher tritium inventories as well. However, calculations based on the tritium diffusion coefficient data in Section 2.2 indicate that there is a large tritium diffusive inventory associated with BeO (not shown in Figure 2.3-43) and the Li_2O/BeO and $LiAlO_2$/BeO cases are thus unattractive. The five remaining cases which show effective TBR's higher than 1.20 are Li_2O+Be and Li_8ZrO_6+Be with similarly attractive TBR's (1.24 and 1.22) and tritium inventories (about 45 g per blanket each), Li_7Pb_2 (with an effective TBR of 1.22),and the homogeneous mixture cases of ternary ceramic/Be and Li_2O/Be with very high TBR's (1.5 to 1.6). However, Li_7Pb_2 has a much higher tritium inventory than the four other cases (2 kg compared to 10-100 g), which makes it less attractive.

To summarize, consideration of TBR and tritium inventory indicates the need for ^6Li enriched solid breeders to be tested in conjunction with Be multiplier. In particular, the cases of Li_2O and Li_8ZrO_6 with a separate Be region are attractive, as are the cases of a homogeneous mixture of Be and Li_2O (or any ternary ceramic which minimizes the chemical compatibility problem with Be). Be is strongly preferred to BeO as a multiplier because of its much better neutronics performance and the high tritium diffusive inventory associated with BeO. Unmultiplied Li_2O has the advantage of simpler and less costly design and is the only unmultiplied case which should still be considered even though its 1.08 effective TBR is in the high risk category.

Figure 2.3-44 shows a point graph of the reciprocal of the solid breeder and multiplier material cost per blanket module and of the power multiplication for the different cases. Again, the choice of variables was made so that the attractive cases would appear in the top right hand corner of the graph. Note that the power multiplication is a more important economics parameter than the material cost. For example, a 10% increase in power multiplication will reduce the cost per unit power for a typical commercial reactor by about 10% while a 10% increase in the breeder material cost will result in less than 1% increase in the reactor cost per unit power. From the figure, the unmultiplied cases of Li_2ZrO_3, Li_8ZrO_6, and Li_7Pb_2 exhibit low power multiplication and do not show any particular advantage on a material cost basis either. The unmultiplied Li_2O case also shows poor power performance, but has by far the lowest associated cost (3 times lower than the average cost and half the cost of the next lowest case). The $Li_2Be_2O_3$ and Li_2ZrO_3+Be cases tend to have low power multiplication and only average cost figures. The other cases, with the exception of the two homogeneous mixture cases with Be, show comparable cost and power performance, with the Li_2O+Be case being slightly more attractive overall and the homogeneous mixture cases with BeO being slightly less attractive due to their high cost. The two homogeneous cases, Li_2O/Be and $LiAlO_2$/Be, exhibit very good power performance but slightly higher than average costs due to the higher unit cost of Be.

Figure 2.3-45 shows a point graph of the afterheat time to reach the maximum allowable temperature with no coolant flowing and of the reciprocal of the dose rate after 3 year irradiation and 10 hour cooling. The four Li_2O cases (Li_2O, Li_2O+Be, Li_2O/Be and Li_2O/BeO) are very attractive both on the basis of dose rate and afterheat time to reach T_{max}; so are $Li_2Be_2O_3$ and the two silicate cases with Be (albeit to a lesser extent). The two zirconates (with or without Be) and the Li_7Pb_2 case are very poor with respect to both variables. The aluminates, particularly for the separate multiplier cases, and the Li_2TiO_3+Be case have rather high dose rates, but average afterheat time to reach T_{max}.

On the whole, the conclusions drawn from the tritium inventory and TBR considerations regarding the choice of materials recommended for the test program are unchanged, except for Li_8ZrO_6, which does not look as attractive based on the activation results. Basically, only multiplied solid breeders

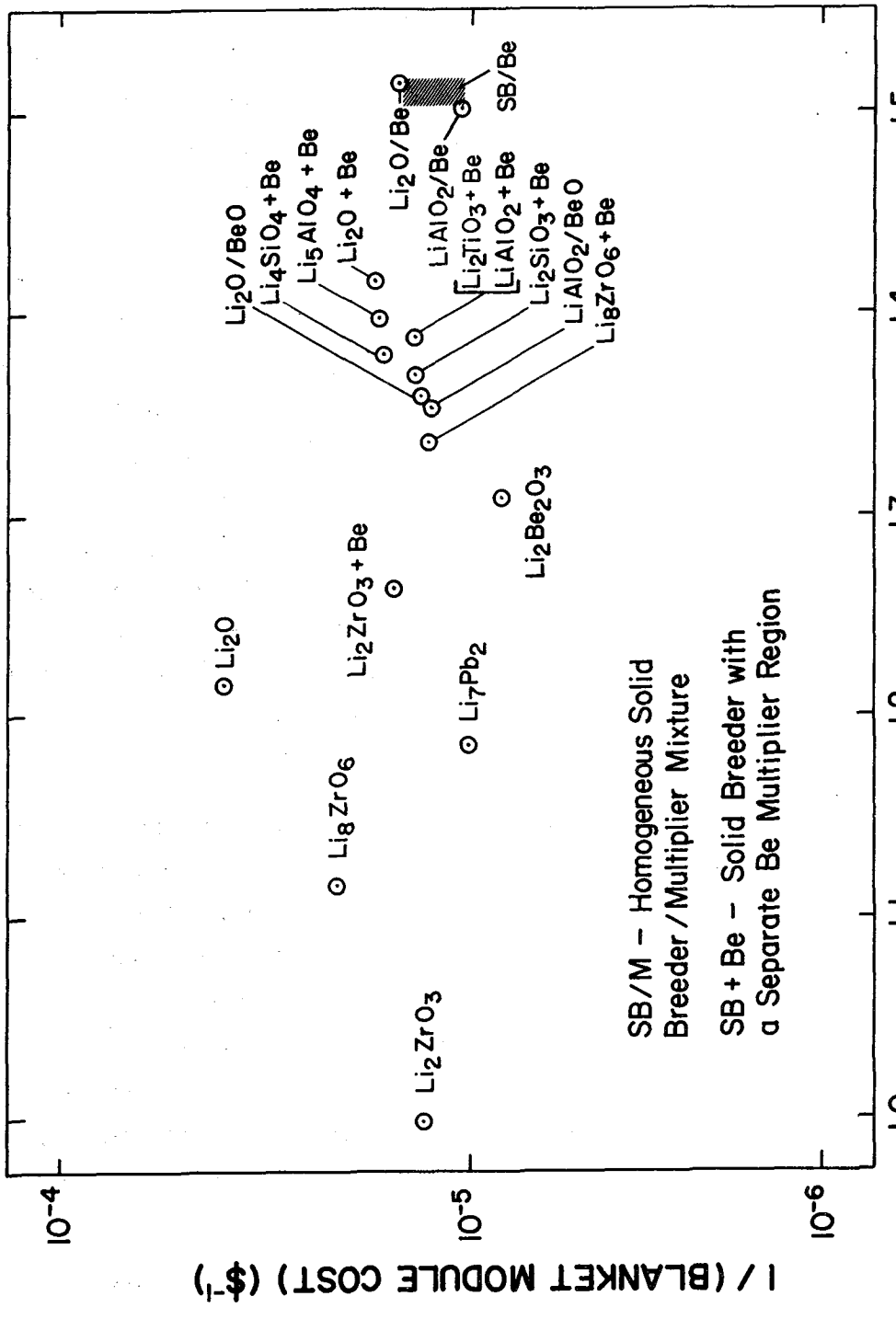


Figure 2.3-44 Point graph of the reciprocal of material cost for a blanket module and of the power multiplication for the different cases

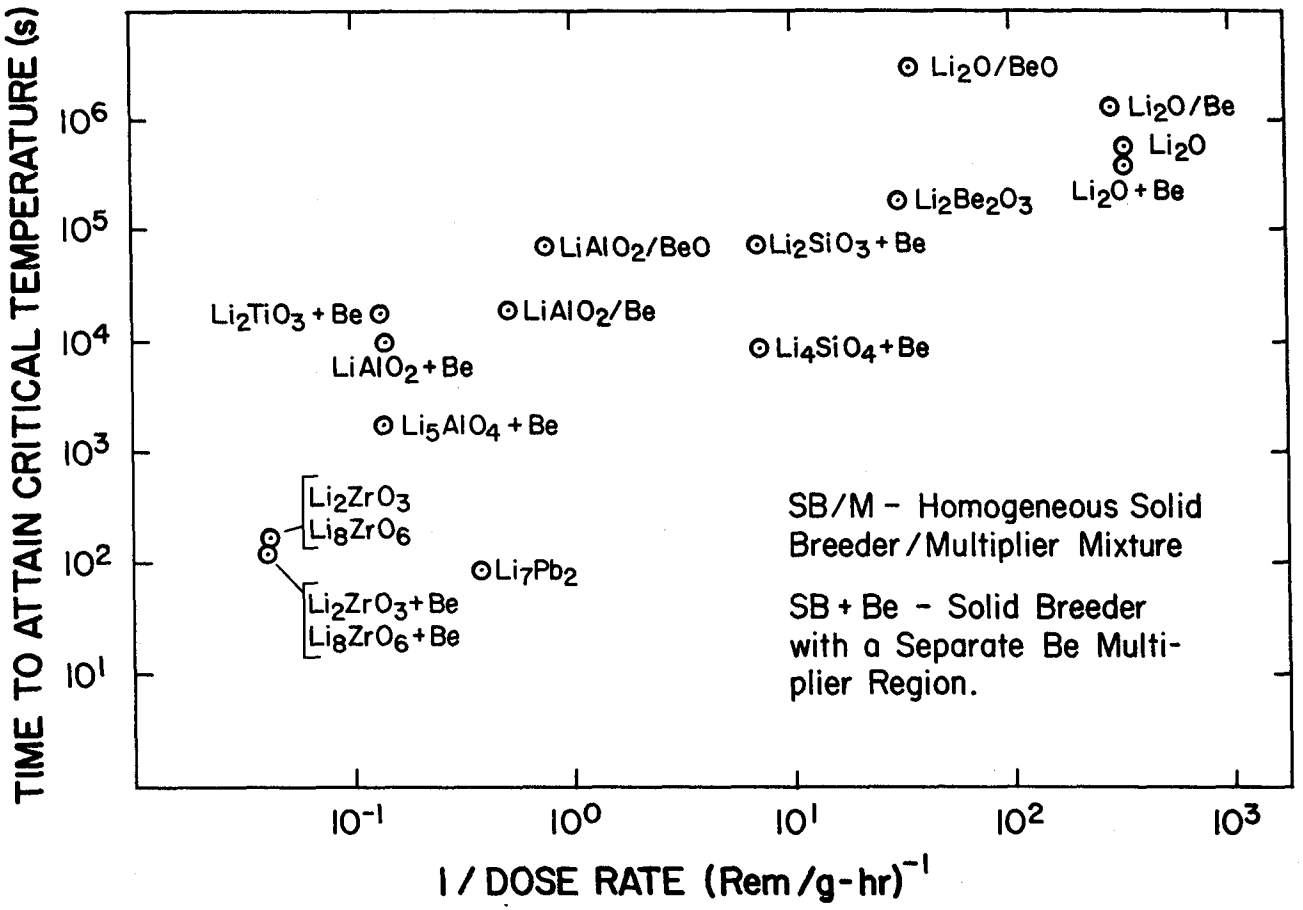


Figure 2.3-45 Point graph of the afterheat time to reach the maximum allowable temperature and of the reciprocal of the dose rate after 3-year irradiation and 10-hour cooling for the different cases

are attractive except, possibly, for natural Li_2O which exhibits very low cost and dose rate, and very high afterheat time to reach the maximum allowable breeder temperature, but marginal TBR and M. Li_2O, with its good overall performance, is also the preferred choice for the separate multiplier case. The other preferred solid breeders to be considered with a separate Be multiplier region, based on their adequate TBR and favorable cost, power multiplication and activation results, are Li_4SiO_4 and Li_2SiO_3 (to a lesser extent). Li_5AlO_4+Be shows reasonably good neutronics performance but fares poorly based on activation while Li_2TiO_3+Be tends to rank in the average for each performance parameter. These two cases are thus not particularly attractive but could be backup candidates if the front-runners do not make it for one reason or another. The homogeneous mixture cases with Be should be considered due to their extremely high TBR and power multiplication values, and if there are no compatibility problems the Li_2O/Be case is the preferred choice.

2.4 Fission Reactor Evaluation for Advanced Solid Breeder Testing

2.4.1 Introduction

Fission reactor testing will play a major role in the development of solid breeder blanket technology. Specific tests have been proposed utilizing fission reactors since testing in these facilities appears to currently offer the best simulation of the fusion environment. The major advantage of fission reactor testing is the ability to provide a neutron flux over a moderately large test volume and, in particular, to directly breed tritium while providing bulk heating and radiation damage effects to the experiment. In earlier work, specific requirements were identified for fission reactor facilities used for advanced solid breeder testing: appropriate neutron energy flux/spectrum, on-line instrumentation capability, and adequate test volume.[78] Typical instrumentation requirements for advanced solid breeder testing would include thermocouples and an on-line sweep gas monitoring system to measure tritium release. The test fission reactor facility must also have adequate test volume to accommodate the test specimen/submodule and its instrumentation.

The most important parameters in choosing a given fission reactor for material testing are its spectrum and flux. The neutron spectrum impacts both the tritium production and heat generation rates within the solid breeder material. The neutron flux establishes the tritium generation rate and the achievable lithium burnup during the test. Microscopic calculations have been performed to estimate the tritium production and heat generation rates for representative fission reactors. These results were compared to the anticipated fusion environments for several blanket concepts.[1,79] The results for the Li_2O/He/HT9 and $LiAlO_2$/H_2O/HT9 blanket concepts are shown in Figures 2.4-1 and 2.4-2, respectively. These calculations indicate that it is possible to match the initial tritium production rates or the heating rates, but not within the same test. Also, the achievable lithium burnups will be moderate.

The objective of this section is to explore the ability of fission reactor testing to match the tritium production and temperature profiles anticipated in macroscopic specimens having sufficient size to address solid breeder performance issues (as distinct from property data). These issues include performance in macroscopic samples with purge flow and temperature gradients.

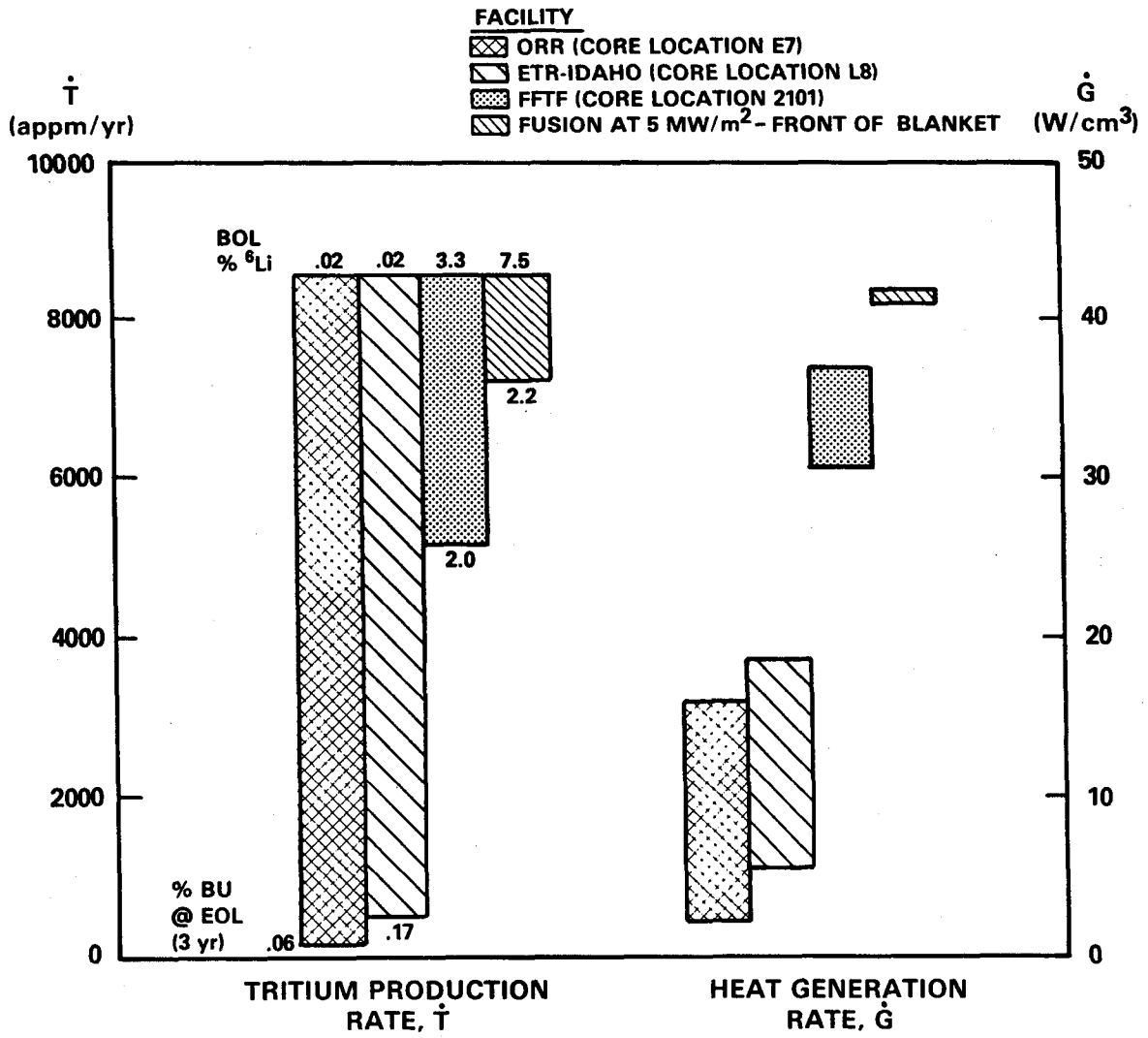


Figure 2.4-1 Microscopic neutronics calculations for representative Light Water Reactor (LWR) and Fast Test Reactors (FTR) compared to anticipated tritium production and heat generation rates for the Li_2O/He/HT9 blanket concept

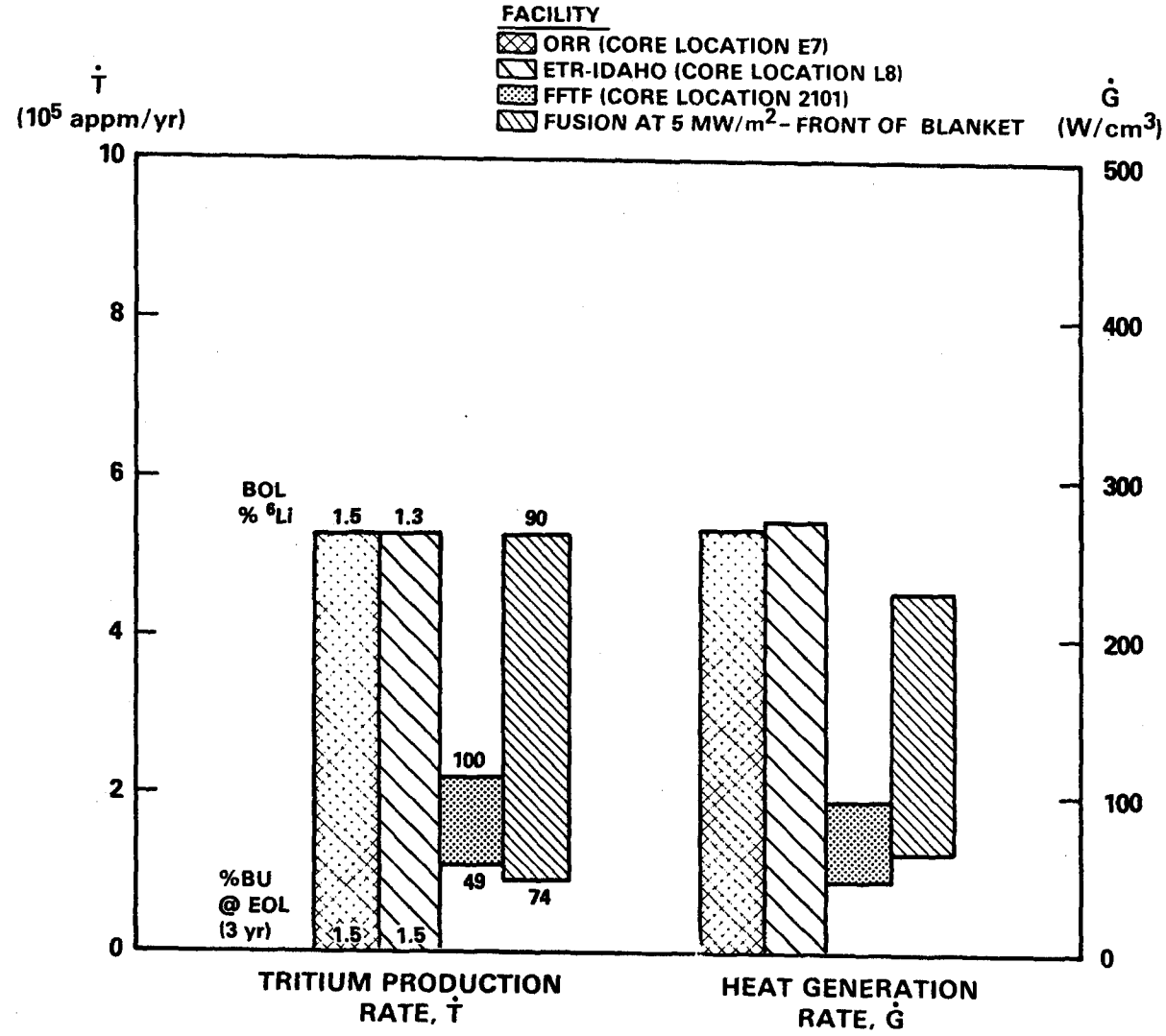


Figure 2.4-2 Microscopic neutronics calculations for representative Light Water Reactor (LWR) and Fast Test Reactors (FTR) compared to anticipated tritium production and heat generation rates for the $LiAlO_2/H_2O$/HT9 blanket concept

These advanced solid breeder tests will allow exploration of behavior under combined test conditions not available in previous tests that can closely simulate the fusion environment in many important respects.

There are four major test variables that affect the degree of simulation: neutron spectrum, neutron flux, ^{6}Li enrichment, and breeder geometry or size. These effects interact with one another; for example, increasing the ^{6}Li enrichment may make the tritium and heat generation more reactor-relevant if the neutron flux is otherwise too small. However, the degree of simulation and the extent of these interactions have not previously been quantified, in general.

Since these are important and moderately expensive tests, it is important to establish the optimum test device or test module conditions. To accomplish this, three reactors were considered which have significantly different neutron spectra. Selected solid breeder cylindrical geometries and sizes were considered, as were various ^{6}Li enrichments. Results were calculated for Li_2O and can be extrapolated to other breeder materials. Tritium production and neutron heating rates were calculated as a function of position within the solid breeder material. Temperature gradients within the test samples were also calculated. Finally, the tritium production rate distributions within the solid breeder material were calculated as a function of test time for selected geometries and ^{6}Li enrichments.

2.4.2 Representative Reactor Conditions

Three test fission reactors were chosen for investigation: The Fast Flux Test Facility (FFTF) at Hanford, the High Flux Isotope Reactor (HFIR) at Oak Ridge, and the National Reactor Universal (NRU) at Chalk River, Canada. These reactors have quite a different neutron spectra. The FFTF reactor is a fast neutron spectrum source. The HFIR reactor has a neutron spectrum which is significantly softer than the typical fast spectrum associated with liquid metal reactors, although it still has a significant non-thermal neutron flux. The NRU reactor is a thermal reactor with a significant thermal neutron flux, but with the local spectrum modified by the use of fast neutron producing fuel rods. The calculations for the NRU reactor were for a test position designed to optimize the neutron energy spectrum for an epithermal flux. The fast and

thermal flux components for these three reactors are summarized in Table 2.4-1. Also, a comparison of their normalized neutron energy spectra, shown in Figure 2.4-3, illustrates the important differences. These relative neutron energy spectra are normalized by the total neutron flux for each reactor.

The FFTF is a liquid metal (sodium) cooled reactor which has a relatively high energy neutron spectrum when compared to light water reactors. Other reactors in this generic class include: EBR-II (U.S.), JOYO (Japan), BR-2 (Belgium), Phenix/SuperPhenix (France), and KNK (Germany). The FFTF was chosen for analysis because of its relatively large available test volume when compared to these other reactors and the availability of core model codes. The FFTF was designed for testing and therefore includes in-core instrumentation capabilities. The FFTF runs with typical cycle lengths (i.e., times at which the reactor is at power) of 60-150 days. Present experimental irradiation programs include: the liquid metal reactor, space power, and fusion programs. The largest available position for instrumented testing would be a hexagonal position measuring 12 cm (4.73 in) flat-to-flat. The axial length of the core region is 91.4 cm (36 in). The space above the core region could also be utilized for testing if desired. The normalized neutron energy spectrum for the FFTF for a row four position at core midplane is shown in Figure 2.4-3.

Table 2.4-1 Fission Reactor Capabilities Reactor Characteristics

Reactor	Reactor Power (MWth)	Flux ($\times 10^{15}$ n/cm^2-sec)		Core Materials Structure/Fuel/Coolant
		Thermal	Fast	
FFTF	300-400	small	4.3	316 SS/UO_2/Na
HFIR	100	2.3	1.5	SS/UO_2/H_2O
NRU	125	0.24	0.04	Zr/UO_2D_2O

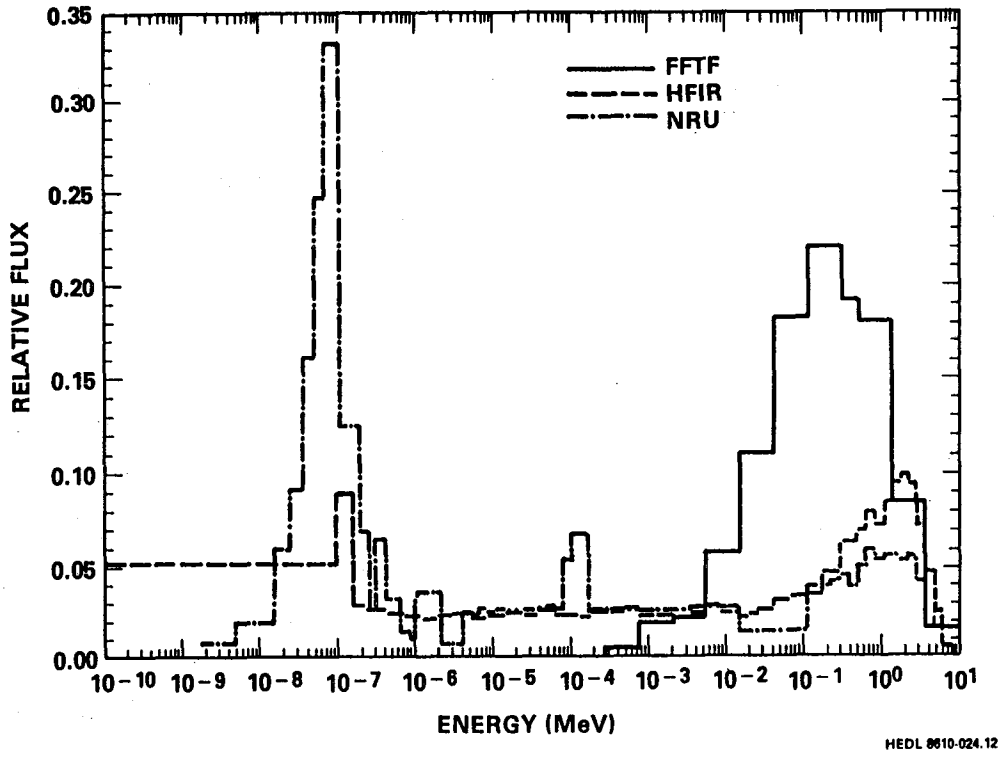


Figure 2.4-3 Comparison of neutron spectra for the FFTF, NRU, and HFIR reactors normalized to their total flux

The HFIR is a water-cooled reactor and has a softer neutron energy spectrum when compared to the liquid metal reactors. The HFIR is presently in the process of increasing its instrumentation capabilities through refitting. The HFIR runs with typical cycle lengths of 21-23 days. The reactor is presently utilized for isotope production and materials testing for the Fusion Program. The largest available position for instrumented testing at present would be a circular position measuring 3.7 cm (1.5 in) in diameter. The axial length of the core region is 51 cm (20 in). The normalized neutron energy spectrum for the HFIR at an instrumented position is shown in Figure 2.4-3.

The NRU is a water-cooled "thermal" reactor which has a relatively modest non-thermal component of its flux. Other reactors of this class include: ATR (U.S.), JMTR (Japan), and SILOE (France). The NRU reactor can accommodate

instrumented in-core tests. The NRU runs with typical cycle lengths of 14-30 days. Presently, the reactor is also being used for isotope production, fuel/loop testing, fission reactor safety tests, and the CRITIC solid breeder experiment. The largest available position for instrumented testing would be a cylindrical position with a diameter of 10 cm (3.9 in). The axial length of the core is 300 cm (118 in). The flux and energy spectrum for the NRU reactor chosen for investigation are for the fast neutron MK-IV rod position. This is a spectrally tailored position within the core chosen to increase the relative fast component of the neutron energy spectrum from NRU (although it decreases the local thermal flux). The relative neutron energy spectrum for this NRU position at core midplane is shown in Figure 2.4-3.

2.4.3. Evaluation

A simple cylindrical model was used for calculating the tritium production and neutron heating rates in Li_2O for each of the representative test reactors. The model consists of a cylindrical test design containing the Li_2O surrounded by a boundary zone specific to the reactor. The approach of using simple cylindrical models with a boundary source was taken for several reasons. First, present and next generation fission reactor experiments utilize a cylindrical geometry for the solid breeder material and are located within the reactor core region. This approach avoided detailed reactor descriptions and permitted a large number of Monte Carlo calculations to be made in exploring the effects of the test pin design on the tritium production and heat generation rates. The boundary source approximation assumes the neutron source term is equivalent to the total neutron flux, but neglects the potential effect of the test pin on the local flux and on the core's reactivity. The boundary zone in the model is the first attempt at accounting for the boundary source term perturbation caused by the test pin. With full reactor models it would have been difficult to compute spatial data in the pins. Finally, use of the same approach for the three different reactors was chosen in an attempt to ensure consistent comparisons between the three reactors.

Details of this one-dimensional model are shown schematically in Figure 2.4-4. Specifically, each cylindrical test specimen consists of a solid or annular solid breeder pellet surrounded by a stainless steel jacket. A gas gap exists between this first stainless steel jacket and the second jacket

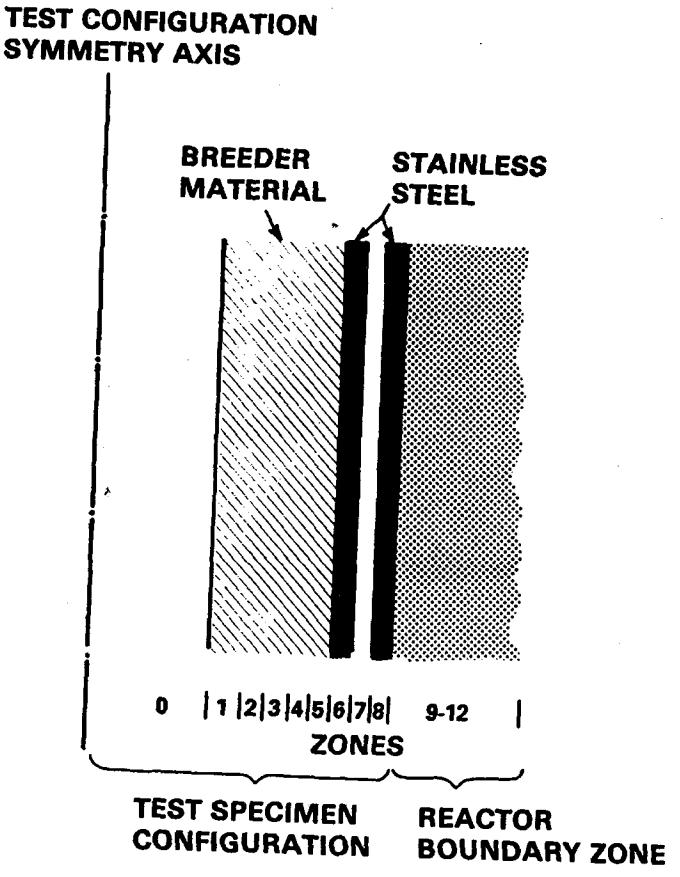


Figure 2.4-4 Schematic of one-dimensional model used to calculate tritium production and heat generation rates

which serves as a boundary between the reactor environment and the test configuration. The gas gap was included in the test configuration to permit some temperature control and the potential for tritium permeation measurements. The calculational models for FFTF, HFIR and NRU are described in Table 2.4-2. The same Li_2O test pin geometries were used in each reactor for consistency and are described in Table 2.4-3. Consistent with present experiments, both solid and annular test pin geometries were considered. Atom densities for all materials used are given in Table 2.4-4. As shown in Table 2.4-2, the solid breeder region was divided into five equal volume zones. This was done to enable spatial distributions through the pins to be computed. The buffer

Table 2.4-2 Calculational Models for HFIR and NRU and FFTF

Zone	Outer Radius (cm)	FFTF	HFIR	NRU
0-8	1.487	Li_2O Test Specimen+		
9	2.120	36% SS/64% Na	H_2O	H_2O
10	2.730	36% SS/64% Na	H_2O	Zr
11	3.240	36% SS/64% Na	H_2O	H_2O
12	6.335	36% SS/64% Na		

+The geometry of the test specimens are given in Table 2.4-3. Material compositions are given in Table 2.4-4.

Table 2.4-3 Calculational Model of Lithium Oxide Fusion Blanket Test Pin Geometries

Zone	Test Configuration Type 1 Solid Pellet		Test Configuration Type 2 Annular Pellet	
	Outer Radius (cm)	Material	Outer Radius (cm)	Material
0			0.640	void
1	0.572	Li_2O	0.810	Li_2O
2	0.810	Li_2O	0.949	Li_2O
3	0.991	Li_2O	1.071	Li_2O
4	1.145	Li_2O	1.180	Li_2O
5	1.280	Li_2O	1.280	Li_2O
6	1.306	316 SS	1.306	316 SS
7	1.357	void	1.357	void
8	1.487	316 SS	1.487	316 SS

Table 2.4-4 Material Atom Densities

Material	Alloy/ Element/Isotope	Atom Density[+] Atoms/barn-cm
Lithium Oxide	^{6}Li	0.06834*E
	^{7}Li	0.06834*(1-E)
	O	0.3467
Structure	316 SS	0.0820
	Zr	0.0430
Coolant	H	0.06693
H_2O	O	0.03347
Sodium	Na	0.0225

[+]E = enrichment fraction

regions around the blanket pins were used to partially account for flux depressions in the vicinity of the blanket pins caused by ^{6}Li absorptions. Without the buffer regions, the flux at the pin boundary would have been significantly overestimated, particularly for higher enrichments in NRU and HFIR due to the very high thermal neutron absorption rates. The flux could still be too high in these cases. For the FFTF reactor, selected full core model calculations were performed for naturally enriched Li_2O. The resulting tritium and nuclear heat generation rates were consistent with the one-dimensional model (differences less than 5%).

All calculations were made using the MCNP program. A neutron source was applied at the outer boundary of each calculational model. The sources were computed from neutron spectrum data for the three reactors. For the FFTF, a spectrum at the core midplane in the Materials Open Test Assembly (MOTA) was obtained from a three-dimensional diffusion theory 3DB calculation. The total flux at this location was 4.5×10^{15} n/cm^2-sec. For HFIR, the total neutron flux is 5.8×10^{15} n/cm^2-sec. For NRU, a spectrum in MARK-IV Fast Neutron rod was used. The total flux at this location was 3.1×10^{14} n/cm^2-sec. Energy distributions of the boundary sources for FFTF, HFIR, and NRU are listed in Tables 2.4-5 through 2.4-7, respectively. In these tables, the total fluxes are normalized to a value of 1.0. The normalized spectra are compared in

Figure 2.4-3. The method used was validated by comparing the results obtained for FFTF with the results of an earlier analysis[1] that was based on full core model.

The model described above has several limitations. The calculations which are reported here do not take into consideration the incident photon flux for each of the three reactor types. For the FFTF, the photon heating is approximately 1-5 W/cm^3 for 85% T.D. (theoretical density) Li_2O, depending upon axial position within the core. For NRU, the photon heating is approximately 2 W/cm^3 for 90% T.D. Li_2O. Therefore, the total heating rates in the test specimen will be somewhat higher than the neutron heating values given here, and the spatial distribution of this component will be different than the neutron heating spatial distribution. Based upon the estimates for the photon heating rates given above, however, this contribution to the total heating is typically less than 10% of the nuclear heating calculated with our model, except at the very lowest enrichments (< 0.5% Li^7). The model does not explicitly take into account the perturbation in the flux/spectrum due to the presence of the solid breeder material. The use of a boundary zone is an

Table 2.4-5 Spectrum of FFTF Boundary Source[a]

Group	Lethargy Width (ΔU)	Upper Energy Bound (MeV)	$\phi(U) \cdot \Delta U$	ϕU
1	9.999	2.750×10^{-4}	6.153×10^{-4}	6.154×10^{-5}
2	1.001	7.480×10^{-4}	4.955×10^{-3}	4.952×10^{-3}
3	0.998	2.030×10^{-3}	1.967×10^{-2}	1.970×10^{-2}
4	1.00	5.530×10^{-3}	2.284×10^{-2}	2.279×10^{-2}
5	0.998	1.500×10^{-2}	5.815×10^{-2}	5.827×10^{-2}
6	1.003	4.090×10^{-2}	1.115×10^{-1}	1.112×10^{-1}
7	0.999	1.111×10^{-1}	1.836×10^{-1}	1.837×10^{-1}
8	1.000	3.020×10^{-1}	2.211×10^{-1}	2.211×10^{-1}
9	0.500	4.979×10^{-1}	9.625×10^{-2}	1.925×10^{-1}
10	1.000	1.353	1.806×10^{-1}	1.806×10^{-1}
11	1.000	3.679	8.427×10^{-2}	8.424×10^{-2}
12	1.000	10.00	1.650×10^{-2}	1.650×10^{-2}

[a]Lower energy bound of Group 1 is 1.250×10^{-8} MeV.

Table 2.4-6 Spectrum of HFIR Boundary Source[a]

Group	Lethargy Width (ΔU)	Upper Energy Bound (MeV)	$\phi(U) \cdot \Delta U$	ϕU
1	6.829	9.240×10^{-8}	3.513×10^{-1}	5.144×10^{-2}
2	0.498	1.520×10^{-7}	4.438×10^{-2}	8.916×10^{-2}
3	0.502	2.510×10^{-7}	1.446×10^{-2}	2.883×10^{-2}
4	0.500	4.140×10^{-7}	1.321×10^{-2}	2.640×10^{-2}
5	0.501	6.830×10^{-7}	1.239×10^{-2}	2.475×10^{-2}
6	0.495	1.120×10^{-6}	1.162×10^{-2}	2.349×10^{-2}
7	0.507	1.860×10^{-6}	1.098×10^{-2}	2.165×10^{-2}
8	0.498	3.060×10^{-6}	1.165×10^{-2}	2.340×10^{-2}
9	0.499	5.040×10^{-6}	1.189×10^{-2}	2.383×10^{-2}
10	0.500	8.310×10^{-6}	1.086×10^{-2}	2.172×10^{-2}
11	0.500	1.370×10^{-5}	1.143×10^{-2}	2.286×10^{-2}
12	0.501	2.260×10^{-5}	1.261×10^{-2}	2.519×10^{-2}
13	0.501	3.730×10^{-5}	1.217×10^{-2}	2.428×10^{-2}
14	0.498	6.140×10^{-5}	1.301×10^{-2}	2.609×10^{-2}
15	0.498	1.010×10^{-4}	1.196×10^{-2}	2.403×10^{-2}
16	0.503	1.670×10^{-4}	1.179×10^{-2}	2.344×10^{-2}
17	0.499	2.750×10^{-4}	1.263×10^{-2}	2.532×10^{-2}
18	0.501	4.540×10^{-4}	1.253×10^{-2}	2.498×10^{-2}
19	0.501	7.490×10^{-4}	1.316×10^{-2}	2.629×10^{-2}
20	0.496	1.230×10^{-3}	1.155×10^{-2}	2.328×10^{-2}
21	0.501	2.030×10^{-3}	1.206×10^{-2}	2.408×10^{-2}
22	0.167	2.400×10^{-3}	3.804×10^{-3}	2.272×10^{-2}
23	0.168	2.840×10^{-3}	3.753×10^{-3}	2.229×10^{-2}
24	0.165	3.350×10^{-3}	3.787×10^{-3}	2.293×10^{-2}
25	0.501	5.530×10^{-3}	1.242×10^{-2}	2.478×10^{-2}
26	0.500	9.120×10^{-3}	1.446×10^{-2}	2.891×10^{-2}
27	0.498	1.500×10^{-2}	1.230×10^{-2}	2.473×10^{-2}
28	0.283	1.990×10^{-2}	6.117×10^{-3}	2.164×10^{-2}
29	0.248	2.550×10^{-2}	5.843×10^{-3}	2.356×10^{-2}
30	0.472	4.090×10^{-2}	1.253×10^{-2}	2.651×10^{-2}
31	0.500	6.740×10^{-2}	1.578×10^{-2}	3.159×10^{-2}
32	0.499	1.110×10^{-1}	1.667×10^{-2}	3.342×10^{-2}

Table 2.4-6 Spectrum of HFIR Boundary Source[a] (Continued)

Group	Lethargy Width (ΔU)	Upper Energy Bound (MeV)	$\phi(U) \cdot \Delta U$	ϕU
33	0.500	1.830×10^{-1}	1.953×10^{-2}	3.907×10^{-2}
34	0.501	3.020×10^{-1}	2.365×10^{-2}	4.720×10^{-2}
35	0.251	3.880×10^{-1}	1.585×10^{-2}	6.325×10^{-2}
36	0.250	4.980×10^{-1}	1.583×10^{-2}	6.343×10^{-2}
37	0.249	6.390×10^{-1}	1.748×10^{-2}	7.011×10^{-2}
38	0.251	8.210×10^{-1}	1.988×10^{-2}	7.931×10^{-2}
39	0.302	1.110×10^{-2}	2.176×10^{-2}	7.215×10^{-2}
40	0.196	1.350×10^{-2}	1.650×10^{-2}	8.430×10^{-2}
41	0.254	1.740×10^{-2}	2.416×10^{-2}	9.520×10^{-2}
42	0.248	2.230×10^{-2}	2.467×10^{-2}	9.945×10^{-2}
43	0.252	2.870×10^{-2}	2.382×10^{-2}	9.440×10^{-2}
44	0.249	3.680×10^{-2}	1.799×10^{-2}	7.237×10^{-2}
45	0.301	4.970×10^{-2}	1.422×10^{-2}	4.733×10^{-2}
46	0.200	6.070×10^{-2}	5.260×10^{-3}	2.631×10^{-2}
47	0.199	7.410×10^{-2}	2.862×10^{-3}	1.435×10^{-2}
48	0.150	8.610×10^{-2}	1.030×10^{-3}	6.861×10^{-3}
49	0.150	1.000×10^{-3}	4.387×10^{-4}	2.931×10^{-3}

[a]Lower energy bound of Group 1 is 1.000×10^{-10} MeV.

Table 2.4-7 Spectrum of NRU Boundary Source[a]

Group	Lethargy Width (ΔU)	Upper Energy Bound (MeV)	$\phi(U) \cdot \Delta U$	ϕU
1	1.079	5.000×10^{-9}	8.511×10^{-3}	7.889×10^{-3}
2	1.099	1.500×10^{-8}	2.194×10^{-2}	1.997×10^{-2}
3	0.511	2.500×10^{-8}	3.034×10^{-2}	5.939×10^{-2}
4	0.336	3.500×10^{-8}	3.063×10^{-2}	9.104×10^{-2}
5	0.357	5.000×10^{-8}	5.759×10^{-2}	1.615×10^{-1}
6	0.293	6.700×10^{-8}	7.260×10^{-2}	2.481×10^{-1}
7	0.400	1.000×10^{-7}	1.331×10^{-1}	3.324×10^{-1}
8	0.588	1.800×10^{-7}	7.343×10^{-2}	1.249×10^{-1}
9	0.329	2.500×10^{-7}	2.246×10^{-2}	6.838×10^{-2}
10	0.182	3.000×10^{-7}	4.876×10^{-3}	2.674×10^{-2}
11	0.065	3.200×10^{-7}	8.601×10^{-3}	1.333×10^{-1}
12	0.223	4.000×10^{-7}	1.438×10^{-2}	6.444×10^{-2}
13	0.446	6.250×10^{-7}	1.436×10^{-2}	3.217×10^{-2}
14	0.307	8.500×10^{-7}	4.628×10^{-3}	1.505×10^{-2}
15	0.111	9.500×10^{-7}	1.257×10^{-3}	1.130×10^{-2}
16	0.047	9.960×10^{-7}	7.088×10^{-4}	1.499×10^{-2}
17	0.024	1.020×10^{-6}	6.930×10^{-4}	2.911×10^{-2}
18	0.024	1.045×10^{-6}	6.840×10^{-4}	2.825×10^{-2}
19	0.025	1.071×10^{-6}	2.048×10^{-3}	8.331×10^{-2}
20	0.071	1.150×10^{-6}	8.307×10^{-3}	1.167×10^{-1}
21	0.602	2.100×10^{-6}	2.160×10^{-2}	3.588×10^{-2}
22	0.644	4.000×10^{-6}	5.079×10^{-3}	7.883×10^{-3}
23	0.232	5.043×10^{-6}	5.869×10^{-3}	2.532×10^{-2}
24	0.250	6.476×10^{-6}	6.185×10^{-3}	2.474×10^{-2}
25	0.228	8.135×10^{-6}	6.366×10^{-3}	2.791×10^{-2}
26	0.272	1.068×10^{-5}	6.705×10^{-3}	2.463×10^{-2}
27	0.250	1.371×10^{-5}	6.705×10^{-3}	2.685×10^{-2}
28	0.250	1.760×10^{-5}	6.592×10^{-3}	2.639×10^{-2}
29	0.250	2.260×10^{-5}	6.614×10^{-3}	2.645×10^{-2}
30	0.250	2.902×10^{-5}	6.795×10^{-3}	2.718×10^{-2}
31	0.250	3.727×10^{-5}	6.817×10^{-3}	2.725×10^{-2}
32	0.250	4.785×10^{-5}	6.885×10^{-3}	2.755×10^{-2}
33	0.250	6.144×10^{-5}	7.359×10^{-3}	2.944×10^{-2}

Table 2.4-7 Spectrum of NRU Boundary Source[a] (Continued)

Group	Lethargy Width (ΔU)	Upper Energy Bound (MEV)	$\phi(U) \cdot \Delta U$	ϕU
34	0.250	7.889×10^{-5}	6.863×10^{-3}	2.745×10^{-2}
35	0.250	1.013×10^{-4}	1.382×10^{-2}	5.526×10^{-2}
36	0.500	1.670×10^{-4}	3.413×10^{-2}	6.826×10^{-2}
37	1.500	7.485×10^{-4}	4.154×10^{-2}	2.769×10^{-2}
38	1.500	3.355×10^{-3}	4.063×10^{-2}	2.709×10^{-2}
39	1.500	1.503×10^{-2}	4.190×10^{-2}	2.793×10^{-2}
40	1.500	6.738×10^{-2}	2.235×10^{-2}	1.490×10^{-2}
41	0.500	1.111×10^{-1}	7.788×10^{-3}	1.558×10^{-2}
42	0.250	1.426×10^{-1}	8.578×10^{-3}	3.432×10^{-2}
43	0.250	1.832×10^{-1}	8.714×10^{-3}	3.485×10^{-2}
44	0.250	2.352×10^{-1}	9.662×10^{-3}	3.865×10^{-2}
45	0.250	3.020×10^{-1}	1.054×10^{-2}	4.217×10^{-2}
46	0.250	3.877×10^{-1}	1.129×10^{-2}	4.515×10^{-2}
47	0.250	4.979×10^{-1}	9.391×10^{-3}	3.756×10^{-2}
48	0.250	6.393×10^{-1}	1.278×10^{-2}	5.111×10^{-2}
49	0.250	8.208×10^{-1}	1.488×10^{-2}	5.951×10^{-2}
50	0.250	1.054×10^{-2}	1.341×10^{-2}	5.364×10^{-2}
51	0.250	1.353×10^{-2}	1.370×10^{-2}	5.480×10^{-2}
52	0.250	1.738×10^{-2}	1.413×10^{-2}	5.654×10^{-2}
53	0.250	2.231×10^{-2}	1.332×10^{-2}	5.327×10^{-2}
54	0.250	2.865×10^{-2}	1.388×10^{-2}	5.554×10^{-2}
55	0.250	3.679×10^{-2}	1.036×10^{-3}	4.144×10^{-2}
56	0.250	4.724×10^{-2}	8.714×10^{-3}	3.485×10^{-2}
57	0.250	6.065×10^{-2}	4.289×10^{-3}	1.716×10^{-2}
58	0.250	7.788×10^{-2}	1.926×10^{-3}	7.702×10^{-3}
59	0.250	1.000×10^{-3}	6.705×10^{-4}	2.682×10^{-3}

[a]Lower energy bound of Group 1 is 1.700×10^{-9} MeV.

attempt to take this effect locally into account. Nevertheless, the perturbation to the source term cannot be completely assessed without a more sophisticated core model for each representative reactor. For this reason, the absolute values for the calculated parameters should not be strictly compared between the different reactor types. Finally, the model cannot address the impact of the solid breeder test upon the reactivity of the reactor. The quantity of ^{6}Li in the test could be limited in a given test reactor for this reason.

The results from the calculations for the FFTF are summarized in Table 2.4-8. Only the calculation for the 2.54 cm (1.0 in) diameter Li_2O are shown. Calculations at 7.5 and 80% ^{6}Li enrichment are reported for: total neutron flux, neutron heating rate, tritium production rate, and the ^{6}Li capture rate. The total flux decreases by ~ 15% at the center of the test specimen configuration when the ^{6}Li enrichment is increased from 7.5 to 80%. The integrated neutron heating rate within the Li_2O increases from 25.3 to 891 W/cm of axial length. Also, the integral tritium production rate increases from 13 to 105 x 10^{13} T/s/cm of axial length. When the ^{6}Li enrichment is increased from 7.5% to 80%, the total tritium production rate also increases but is 24% lower than anticipated from linearly interpolating the value for the 7.5% ^{6}Li enrichment case (self-shielding). This result suggests that while the total neutron flux suppression was only 15%, the larger suppression in the tritium production rate is due to the preferential absorption of the lower energy neutrons from the neutron flux. The radial gradients within the solid breeder material were very modest, even for the one-inch diameter pellet for FFTF testing. Given the uncertainty in the calculations, there was no radial gradient for a 7.5% ^{6}Li enrichment. At 80% ^{6}Li, there was a 10% relative difference in both the tritium production and neutron heating rates when comparing the inner and outer zones.

The results from the calculations for HFIR are summarized in Tables 2.4-9 and 2.4-10 for the two test pin geometries. For the solid pellet test geometry, the neutron heating and tritium production rates are almost an order of magnitude higher than FFTF for a given enrichment. The change in the total cross-sectionally integrated neutron heating and tritium production rates as a function of ^{6}Li enrichment are shown in Figures 2.4-5 and 2.4-6, respectively. For the HFIR, neither the neutron heating nor the tritium production rates

Table 2.4-8 Neutronic Results for Solid Li_2O Test Pin Geometry in FFTF

Zone	Outer Radius (cm)	Material	Total Flux (10^{15} n/cm^2-s)		Neutron Heating (W/cm^3)		T Production Rate (10^{13} atoms/cm^3/s)		^{6}Li Capture Rate (10^{-9} s/atom)	
			Li Enrichment (%)		Li Enrichment (%)		Li Enrichment (%)		Li Enrichment (%)	
			7.5	80	7.5	80	7.5	80	7.5	80
1	0.572	Li_2O	4.49	3.92	31.1	169	2.54	19.9	4.80	3.64
2	0.810	Li_2O	4.46	3.96	30.8	171	2.53	20.3	4.79	3.71
3	0.991	Li_2O	4.46	3.99	31.2	174	2.55	20.5	4.82	3.75
4	1.145	Li_2O	4.48	4.01	31.3	179	2.59	21.2	4.89	3.87
5	1.280	Li_2O	4.49	4.05	31.9	186	2.61	21.9	4.93	4.01
6	1.306	SS-316	4.50	4.09	2.9	2.8				
7	1.357	void	4.50	4.13						
8	1.487	SS-316	4.47	4.14	2.9	2.8				
9	6.335	MOTA	4.45	4.35						
Total[a]					158	891	13.0	105		

[a]Total represents the total cross-sectionally integrated values over only the solid breeder materials for neutron heating rate (W/cm^3) and tritium production rate (10^{13} atoms/cm^3-s).

Table 2.4-9 Neutronics Results for Solid Li_2O Test Pin Geometry in HFIR

Zone	Outer Radius (cm)	Material	Total Flux (10^{15} n/cm^2-s)				Neutron Heating (W/cm^3)				T Production Rate (10^{13} atoms/cm^3-s)				^{6}Li Capture Rate (10^{-9}/s/atom)			
			Li Enrichment (%):				Li Enrichment (%):				Li Enrichment (%):				Li Enrichment (%):			
			0.5	7.5	20	80	0.5	7.5	20	80	0.5	7.5	20	80	0.5	7.5	20	80
1	0.572	Li_2O	4.08	2.34	2.09	1.71	267	161	136	138	35.4	20.4	16.6	16.6	1063	40.8	12.0	3.0
2	0.810	Li_2O	4.12	2.37	2.08	1.69	288	247	174	158	38.7	33.0	21.7	19.2	1126	64.1	15.7	3.5
3	0.991	Li_2O	4.18	2.48	2.14	1.75	293	395	256	214	39.1	52.4	32.2	26.3	1142	102	23.5	4.8
4	1.145	Li_2O	4.23	2.63	2.23	1.82	306	709	535	323	41.2	96.1	68.9	40.7	1201	186	50.3	7.4
5	1.280	Li_2O	4.25	2.92	2.51	2.00	319	1509	2354	3056	42.6	205	306	398	1242	399	223	72.6
6	1.306	SS-316	4.31	3.32	3.14	2.91	35.6	20.5	19.6	19.2								
7	1.357	void	4.39	3.42	3.25	3.03												
8	1.487	SS-316	4.45	3.57	3.42	3.22	38.3	24.6	23.9	23.4								
9	2.120	H_2O	4.89	4.23	4.12	3.98												
10	2.730	H_2O	5.28	4.86	4.80	4.70												
11	3.240	H_2O	5.41	5.19	5.15	5.08												
Total (see Table 2.4-8)							1493	3062	3501	3941	200	412	451	508				

Table 2.4-10 Neutronics Results for Annular Li_2O Test Pin Geometry in HFIR

Zone	Outer Radius (cm)	Material	Total Flux (10^{15} n/cm^2-s)				Neutron Heating (W/cm^3)				T Production Rate (10^{13} atoms/cm^3-s)				^{6}Li Capture Rate (10^{-9}/s/atom)			
			Li Enrichment (%):				Li Enrichment (%):				Li Enrichment (%):				Li Enrichment (%):			
			0.5	7.5	20	80	0.5	7.5	20	80	0.5	7.5	20	80	0.5	7.5	20	80
1	0.572	Li_2O	4.34	2.41	2.10	1.74	345	332	197	190	44.3	42.1	24.6	23.4	1290	82.0	17.9	4.3
2	0.810	Li_2O	4.36	2.45	2.13	1.76	351	422	247	226	45.1	53.7	31.2	28.1	1315	104	22.7	5.1
3	0.991	Li_2O	4.36	2.57	2.19	1.82	345	615	377	292	44.3	79.1	48.1	36.7	1293	154	35.1	6.7
4	1.145	Li_2O	4.41	2.73	2.31	1.88	356	968	310	460	45.7	125	104	58.5	1334	243	76.3	10.7
5	1.280	Li_2O	4.38	2.98	2.60	2.07	358	1746	2806	3924	46.0	227	365	510	1341	442	267	93.4
6	1.306	SS-316	4.42	3.32	3.16	2.94	38.3	20.5	19.8	19.3								
7	1.357	void	4.49	3.43	3.27	3.06												
8	1.487	SS-316	4.57	3.57	3.42	3.24	41.1	24.9	24.0	23.5								
9	2.120	H_2O	4.99	4.25	4.13	4.00												
10	2.730	H_2O	5.33	4.87	4.80	4.72												
11	3.240	H_2O	5.45	5.19	5.15	5.09												
Total (see Table 2.4-8)							1334	3103	3372	3870	171	400	435	499				

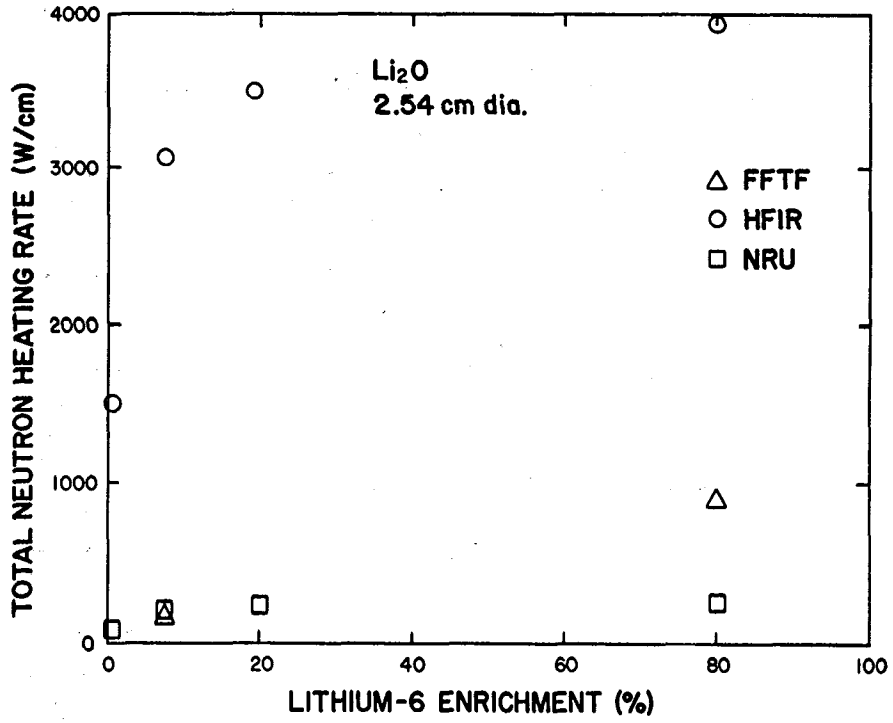


Figure 2.4-5 Total neutron heating rate as a function of ^{6}Li enrichment for the representative reactors

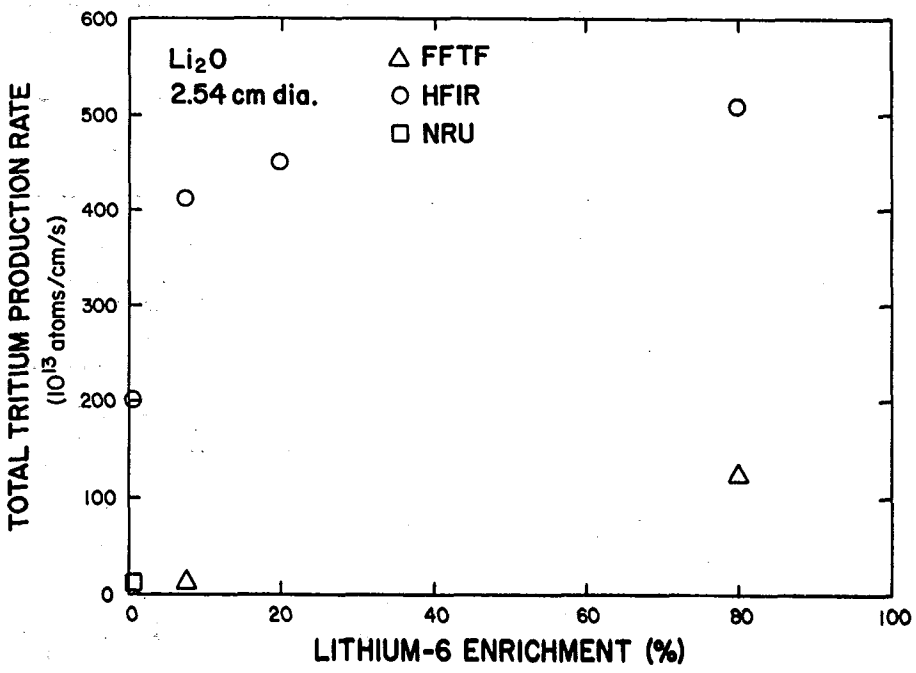


Figure 2.4-6 Total tritium production rates as a function of ^{6}Li enrichment for the representative reactors

increase linearly with ^{6}Li enrichment. This behavior is due to the self-shielding occurring in test specimens of this size. The ratio of the neutron heating to the tritium production rates are fairly constant, which implies that the neutron heating contribution from elastic and inelastic scattering is relatively small. The radial gradients for both heating and tritium production rates become quite large for ^{6}Li enrichments greater than 0.5%, with the radial gradient increasing with increasing enrichment. The annular pellet test geometry results given in Table 2.4-10 show the same behavior. The cross-sectionally integrated neutron heating and tritium production rates are only slightly smaller than for the solid pellet.

Finally, the results from the calculations for NRU are summarized in Tables 2.4-11 and 2.4-12 for the two test geometries. For the solid pellets, the integrated neutron heating and tritium production rates are comparable to those for the FFTF. However, the change in these rates is not a linear function of ^{6}Li enrichment. This behavior is similar to that observed for the HFIR. Again, the ratio of the neutron heating to tritium production rates is fairly constant, which implies the neutron heating contribution from elastic and inelastic scattering is relatively small. As with the HFIR results, the radial gradients become quite large for ^{6}Li enrichments greater than 0.5% (see Figs. 2.4-5 and 2.4-6). The annular pellet test geometry results given in Table 2.4-12 show a similar behavior with the cross-sectionally integrated neutron heating and tritium production rates only slightly smaller than those for the solid pellet.

The neutron heating rates were transformed into radial temperature profiles. As a reference case, it was assumed that the outer radius of the Li_2O pellet is maintained at 400°C, that the pellet reaches thermal steady state, and that heat transfer occurs radially. A thermal conductivity of 2.5 W/cm-°C was assumed independent of temperature. The temperature profiles were then calculated using curves interpolated through the calculated heat generation rates for each of the five equal volume zones. The anticipated temperature profiles for the 2.54 cm (1 in) diameter Li_2O pellet with 7.5% ^{6}Li enrichments for the three reactors are shown in Figure 2.4-7. Both the FFTF and NRU have acceptable temperature profiles for a one-inch diameter pellet. Testing of such a pellet size in the HFIR reactor would lead to unacceptable temperatures

Table 2.4-11 Neutronics Results for Solid Li_2O Test Pin Geometry in NRU

Zone	Outer Radius (cm)	Material	Total Flux (10^{15} n/cm^2-s) Li Enrichment (%):				Neutron Heating (W/cm^3) Li Enrichment (%):				T Production Rate (10^{13} atoms/cm^3-s) Li Enrichment (%):				^{6}Li Capture Rate (10^{-9}/s/atom) Li Enrichment (%):			
			0.5	7.5	20	80	0.5	7.5	20	80	0.5	7.5	20	80	0.5	7.5	20	80
1	0.572	Li_2O	0.215	0.110	0.093	0.072	16.5	10.9	7.8	7.8	2.12	1.38	0.97	0.96	61.8	2.68	0.71	0.17
2	0.810	Li_2O	0.220	0.113	0.094	0.073	17.2	16.3	10.0	9.7	2.24	2.09	1.07	1.20	65.3	4.07	0.92	0.22
3	0.991	Li_2O	0.223	0.112	0.096	0.074	18.0	26.5	16.1	12.3	2.30	3.40	2.05	1.53	67.1	6.62	1.50	0.28
4	1.145	Li_2O	0.226	0.128	0.103	0.078	19.1	47.6	35.5	19.7	2.47	6.17	4.62	2.50	71.9	12.0	3.38	0.46
5	1.280	Li_2O	0.230	0.147	0.121	0.090	20.2	99.1	149	199	2.61	12.8	12.8	25.8	76.1	25.0	14.2	4.72
6	1.306	SS-316	0.234	0.174	0.163	0.150	2.1	1.2	1.2	1.1								
7	1.357	void	0.238	0.178	0.170	0.156												
8	1.487	SS-316	0.240	0.188	0.178	0.168	2.2	1.5	1.4	1.4								
9	2.120	H_2O	0.267	0.230	0.223	0.215												
10	2.730	H_2O	0.285	0.262	0.258	0.254												
11	3.240	H_2O	0.290	0.275	0.272	0.268												
Total (see Table 2.4-8)							92	203	221	252	11.9	25.8	28.6	32.4				

Table 2.4-12 Neutronics Results for Annular Li_2O Test Pin[a] Geometry in NRU

Zone	Outer Radius (cm)	Material	Total Flux (10^{15} n/cm^2-s) Li Enrichment (%):				Neutron Heating (W/cm^3) Li Enrichment (%):				T Production Rate (10^{13} atoms/cm^3-s) Li Enrichment (%):				^{6}Li Capture Rate (10^{-9}/s/atom) Li Enrichment (%):			
			0.5	7.5	20	80	0.5	7.5	20	80	0.5	7.5	20	80	0.5	7.5	20	80
1[a]	0.572	Li_2O	0.234	0.121	0.100	0.076	20.1	23.1	13.0	12.1	2.60	2.98	1.66	1.53	75.9	5.80	1.21	0.28
2	0.810	Li_2O	0.235	0.122	0.100	0.076	20.2	28.6	15.9	13.4	2.60	3.68	2.03	1.68	76.2	7.16	1.49	0.31
3	0.991	Li_2O	0.236	0.127	0.102	0.077	20.4	39.7	25.8	16.4	2.64	5.13	3.33	2.09	76.9	9.99	2.42	0.38
4	1.145	Li_2O	0.236	0.135	0.109	0.081	21.0	61.5	53.5	27.5	2.71	7.98	6.94	3.53	79.1	15.5	5.08	0.65
5	1.280	Li_2O	0.238	0.153	0.095	0.095	21.6	109	177	254	2.78	14.1	23.2	33.0	81.3	27.6	17.0	6.04
6	1.306	SS-316	0.243	0.177	0.151	0.151	2.2	1.2	1.1	1.1								
7	1.357	void	0.245	0.182	0.158	0.158												
8	1.487	SS-316	0.248	0.190	0.169	0.169	2.4	1.5	1.4	1.4								
9	2.120	H_2O	0.272	0.231	0.216	0.216												
10	2.730	H_2O	0.287	0.264	0.254	0.254												
11	3.240	H_2O	0.292	0.276	0.273	0.269												
Total (see Table 2.4-8)							78.5	199	217	246	10.1	25.7	28.2	31.8				

[a]The void radius is 0.64 cm.

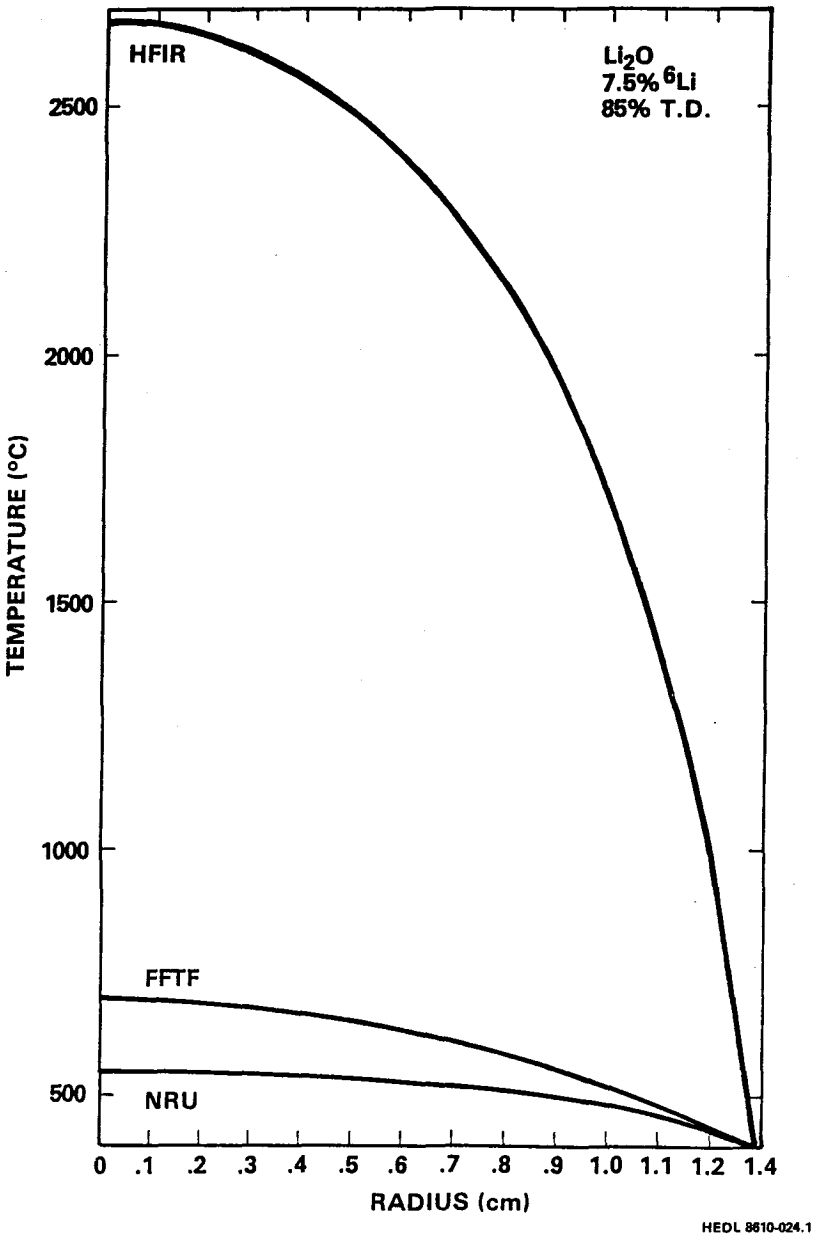


Figure 2.4-7 Anticipated temperature profiles in FFTF, HFIR, and NRU reactors

in the center of the pellet. The impact of lithium enrichment on the temperature difference achieved in a one inch diameter pellet in NRU is summarized in Figure 2.4-8. Note that the center line temperature decreases with increasing ^{6}Li enrichment in both NRU and HFIR due to the self-shielding, leading to significant energy deposition at the outer radii.

Finally, the impact of testing time and the associated lithium burnup are considered. For FFTF, the ^{6}Li absorption rate is fairly independent of radius, even at 80% ^{6}Li enrichment. Therefore, the lithium burnup remains fairly constant with time within the entire volume of the breeder material. However, for the HFIR and NRU reactors, the large ^{6}Li absorption rate radial gradients lead to changes in the radial tritium production rate profiles with time. The following approach was used to estimate the radial tritium production rate

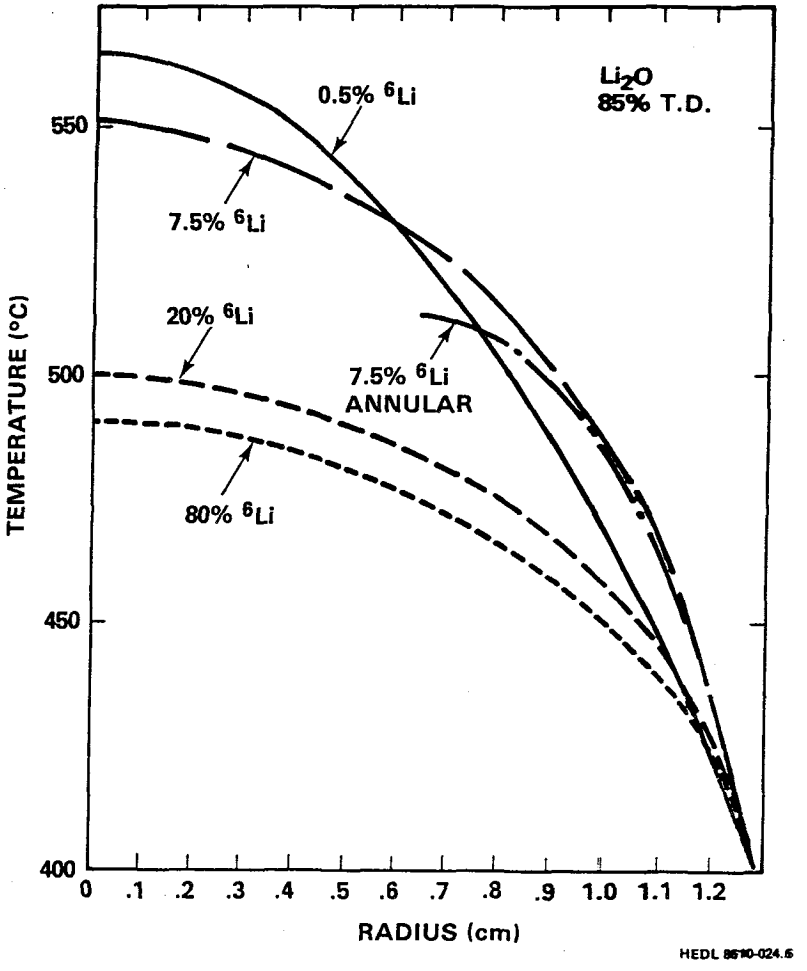


Figure 2.4-8 Influence of ^{6}Li enrichment on temperature profile in the NRU reactor

profile in the Li_2O as a function of testing time for the HFIR and NRU reactors. First, the radial profiles at time zero were fit with an exponential function to approximate the effect of self-shielding in the specimen. A suitable time interval was chosen during which the change in the ^6Li atom density in a given zone did not change by more than 20%. The 5 zones were divided into 15 regions for these calculations. The ^6Li burnup was calculated for each region and new ^6Li atom densities calculated for each zone. This revised ^6Li atom distribution was used for the next time increment calculations. These calculations assume that the structural integrity of the pellet remains the same as ^6Li burnout occurs and that the self-shielding does not change with time. The first assumption is felt to be valid for moderate ^6Li enrichments (< 10% ^6Li). At higher enrichments, the extreme radial peaking in the heating rates in the outer radii may lead to localized surface cracking and loss of dimensional stability in the specimen, leading to a loss of material on the outer surface. Also, the impact of swelling is neglected. The second assumption, however, is probably not valid for large ^6Li burnups where the spectrum will undoubtedly be perturbed. Therefore, the calculations were terminated when the integrated tritium production rate decreased by more than 15%.

The change in the radial distribution for the tritium production rate for the HFIR testing is shown in Figure 2.4-9. This specific calculation is shown for the 2.54 cm diameter solid breeder test geometry with 7.5% ^6Li enrichment. As anticipated, the region of peak tritium production moves radially inward as a function of test time. The calculations for HFIR for this ^6Li enrichment extend only to eight weeks, since at that point the total tritium production with the sample has dropped by ~ 15% (see Fig. 2.4-10). A similar behavior is seen in the NRU testing of a similar test specimen configuration and ^6Li enrichment. Due to the lower flux associated with the NRU reactor, however, calculations for up to three years of testing remain valid (see Fig. 2.4-11).

2.4.4 Conclusions

A series of detailed macroscopic neutron calculations were performed for three representative reactors to assess their viability as fission test facilities for advanced solid breeder materials testing. The three classes of reactors represented by the FFTF, HFIR, and NRU reactors are a fast flux

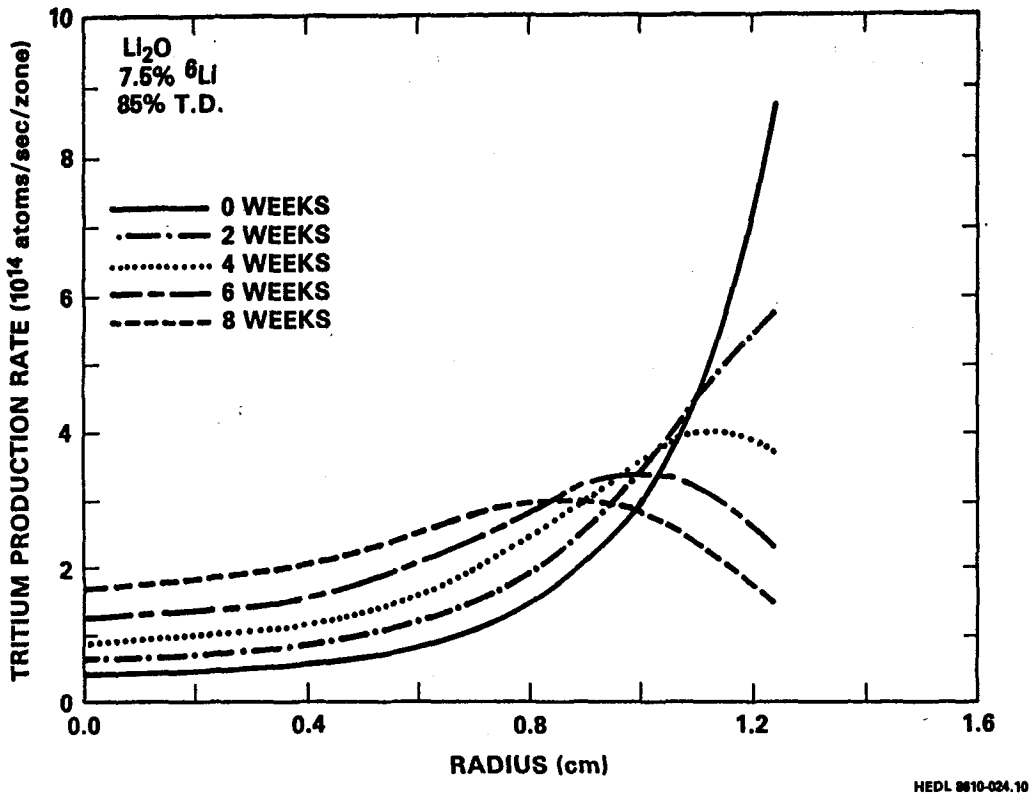


Figure 2.4-9 Time evaluation of tritium production rates in the HFIR reactor

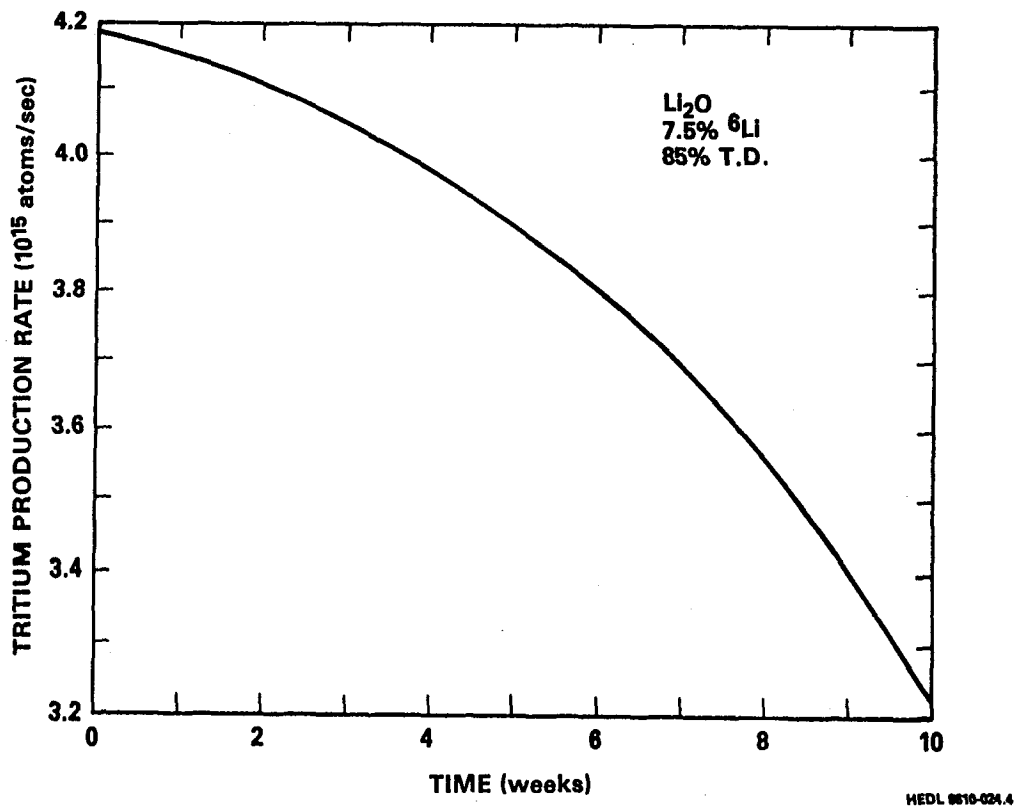


Figure 2.4-10 Decrease in total tritium production as a function of test time in the HFIR reactor

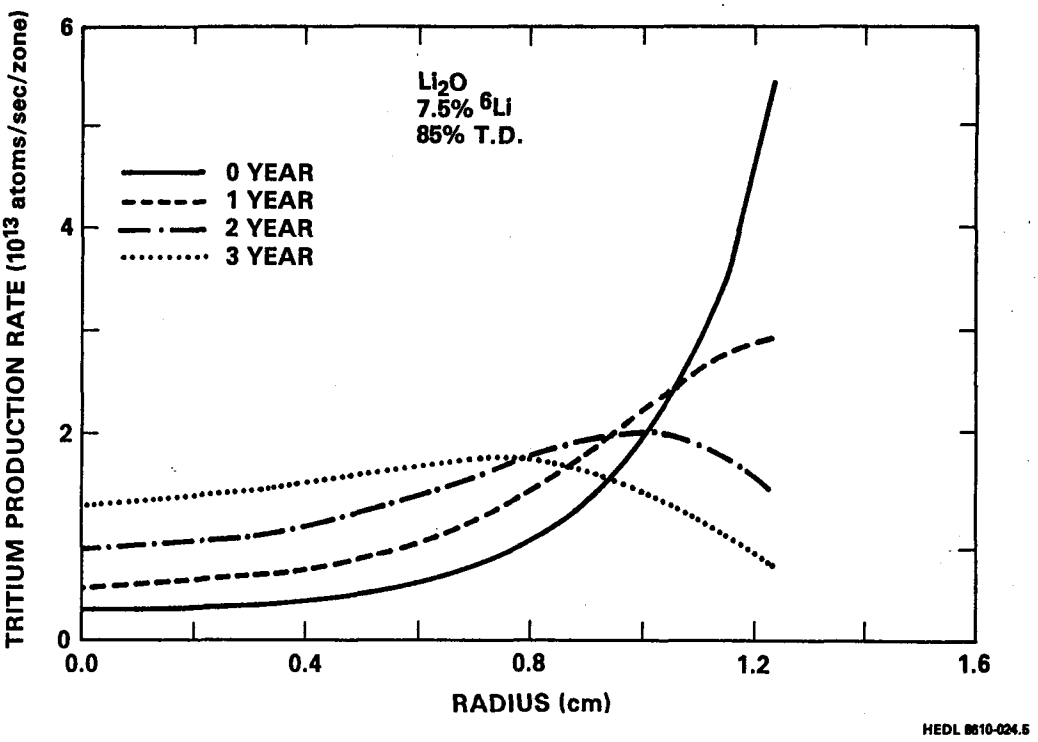


Figure 2.4-11 Time evaluation of tritium production rates in the NRU reactor

spectrum and two tailored fluxes associated with thermal reactors. The calculations indicated that the spatial gradients for both the heat generation and tritium production rates are more favorable in a fast flux spectrum when compared to the steeper gradients obtained in the thermal or modified thermal spectra, such as those for HFIR and NRU. To achieve reasonable gradients across the test specimens in these two reactors, the ^6Li enrichment must be kept to less than 10%. Although the spectra for the HFIR and NRU reactors are different, the calculated heat generation and tritium production rates are quite similar if the differences in flux between the two reactors is used to normalize the results. This is not surprising since these rates depend predominately upon the thermal portion of the spectrum. The temperature differences for either a 2.5 cm diameter cylindrical or 1.2 cm thick annulus become too large, even in the FFTF, if the enrichment is much higher than 20% ^6Li. For both the NRU and HFIR reactors, these temperature differences are prohibitively high unless the Li enrichment is kept below 1-2% and the specimen width

is small. Finally, the impact of burnup as a function of test time was explored. It was found that the peak tritium production rates in both HFIR and NRU move radially inward with test time due to lithium burnup in the outer zones for ^{6}Li enrichments greater than about 7%. For FFTF, the tritium production rate across the test pin, (and therefore, the burnup) is uniform over the test time for ^{6}Li enrichments up to 80%.

The analysis suggests the following general conclusions regarding the different capabilities offered by the spectra of existing fission reactors for solid breeder testing. For basic material property testing, fission reactors with either predominately fast or mixed energy neutron spectra can be utilized. Care must be taken to choose the appropriate ^{6}Li enrichment and specimen size to achieve the desired test environment in a given test reactor. For "prototypic" solid breeder testing with relevant temperature and tritium production gradients, the choice of an appropriate reactor for testing becomes more difficult. Fission reactors with significant thermal neutron flux are limited to small test specimen dimensions or low reaction rates due primarily to self-shielding effects. Reasonable gradients for the initial tritium production and temperature within the test specimens can be obtained only for small test specimens with ^{6}Li enrichments of less than 2-3%. Also, the selective ^{6}Li burnup within the sample is quite severe and leads to a change in the tritium production gradient within the specimen as a function of the test time. Fission reactors with fast neutron spectra are less susceptible to self-shielding issues, and therefore, larger specimen sizes and higher burnup rates can be explored. High tritium production rates and acceptable temperature gradients within the test specimens can be obtained for larger diameter specimens ($\geq$ 2.5 cm in diameter) and higher ^{6}Li enrichments (up to 20%) with minimal change in the tritium production gradients with test time. The major limitation of fast neutron reactors is that the lowest achievable test temperature in the specimen is $\sim$ 360°C. Lower temperatures ($\sim$ 260°C) are possible only at significantly higher cost.

2.5 Liquid Breeder Facilities

2.5.1 Introduction

The presence of a strong magnetic field in a liquid metal-cooled blanket increases substantially the pressure needed to drive the coolant through the blanket and affects the heat and mass transfer in the liquid metal. The large MHD body force which causes the increase in required pumping pressure affects indirectly the heat and mass transfer by suppressing turbulence and altering, in some cases drastically, the flow distribution within the blanket.

Understanding the nature and the consequences of the interaction of liquid metal flows with strong magnetic fields, and development of an appropriate experimental data base and predictive tools are necessary before detailed designs of liquid metal-cooled blankets can be developed. The activities towards attainment of this goal, as well as those pertaining to design evaluation, screening, and final testing can be divided into three phases.

The first phase involves analytical, experimental, and numerical investigations of the structure of flow in typical components of flow networks (ducts, manifolds, expansions, contractions, etc.). Because of the laminar nature of MHD flows in very strong magnetic fields, knowledge of the flow field and use of any of a large variety of existing computational tools renders the calculation of heat transfer parameters a straightforward matter. For this reason, heat transfer experiments at this stage will be of confirmatory nature, providing further support to the adequacy of the experimental or analytical mapping of the flow field and the heat transfer predictive capability. On the other hand, the effect of MHD flow distribution on mass transfer may be much more difficult to assess because it may be obscured by much stronger effects related to loop chemistry. For this reason, experimental investigation of MHD effects on corrosion must be preceded by thorough testing in ordinary forced convection loops with well controlled impurity levels.

The initial phase of MHD experiments involving measurements of flow structure and heat transfer in individual flow network components is followed by experiments carried out on more complex test modules simulating key features of leading blanket designs. Because of the electrical coupling between individual ducts in the blanket, the use of test modules of representative size scale and complexity is necessary. For such experiments, facilities with

more powerful magnets to achieve test parameters with values approaching those prevailing in the blanket and, more importantly, increased working magnetic field volume are needed. Data obtained during this second phase will be used to validate predictive capability for pressure drop and heat transfer and to obtain design data for blanket configuration screening and further development. The development would include exploration of techniques for MHD pressure drop reduction and/or heat transfer enhancement at relevant parameter ranges close to those of the blanket environment.

The second phase also includes mass transfer (corrosion) testing, to be carried out after the flow field and temperature distributions are established either analytically and/or experimentally. The corrosion tests, which involve measurement of dissolution and deposition rates, require long operating times per experiment in loops of prototypic temperatures, temperature differences, structural and coolant materials, and impurity levels.

The final phase involves testing of modules with actual materials and geometry and with operating conditions as close to prototypic as possible. Engineering design data of the overall thermomechanical performance of the blanket modules and their corrosion characteristics will be obtained during this phase. Information pertaining to design reliability in a non-neutronic environment will also be gathered.

Work on the first phase is already being carried out at ALEX (Argonne Liquid-metal Engineering Experiment). The ALEX facility has been designed and built for the purpose of providing experimental validation of analytical and numerical tools for the prediction of MHD flow structure either existing or currently under development, and for providing a data base for those cases for which predictive capability is not expected in the near future.[80] Heat transfer tests are also within the capability of the facility. The range of possible experiments at ALEX is limited by the magnetic flux density available (2.1 T) and the separation between the two pole faces of the magnet (15 cm). Although a low cost upgrade of the facility can increase the values of these parameters to 2.5 T and 30 cm, a future facility is needed. The facility named LMF (Liquid Metal Flow Facility) provides a bridge between the first and second phases of testing. In addition to LMF, the second phase requires an additional facility, MHDM, (MHD Mass Transfer Facility) to explore the interaction between MHD and corrosion. These facilities, as well as the facilities

for the third phase, the Thermomechanical Integration Facility, TMIF, and the Partially Integrated Test Facility, PITF, do not have to be separate. They may very well share the same site with support hardware (cranes, etc.) and water and power supplies, the same magnet, and the same instrumentation and data acquisition system. Inasmuch as the tests to be carried out at LMF, MHDM, TMIF, and PITF are sequential, sharing of facilities and hardware should not cause any scheduling problems. A possible exception is testing at MHDM, which requires long operating times per test (on the order of months). Such testing will require dedicated use of the magnet and will interfere with all other MHD-related activities.

Table 2.5-1 summarizes the features and the objectives of the major liquid breeder experiments. In the following, the LMF facility, test articles, instrumentation, and types of tests to be performed are covered in more detail.

Before defining the operating parameters of LMF, a discussion of the required similarity between blanket prototypical conditions and test conditions is in order. For a given geometry, the equations governing MHD flow, when cast in non-dimensional variables, involve three non-dimensional parameters: the Hartmann number, M, the interaction parameter, N, and the wall conductance ratio, C. Achieving values for these parameters in an experiment identical to those in the blanket ensures full prototypicality of MHD flow. Figure 2.5-1a shows the expected M and N space for tokamak blankets similar to those considered in the BCSS and TPSS studies ($5 \times 10^3 \leq M \leq 10^5$, $10^3 \leq N \leq 2 \times 10^5$).[81,82] If attention is to be focused on the crucial first wall coolant channels, the parameter space is considerably smaller ($5 \times 10^3 \leq M \leq 2 \times 10^4$ and $10^3 \leq N \leq 10^4$). Figure 2.5-1a also shows the area in the parameter spaces that can be covered by a facility such as ALEX. Figures 2.5-1b and 2.5-1c show the progressively larger portion of the operating parameters space that can be covered by ALEX Upgrade and LMF.

The interaction parameter is a measure of the relative importance of the electromagnetic forces to the inertial forces in the liquid metal. As such, there is always a critical value of N, N_{cr}, depending in general on M and C, beyond which inertial effects are negligible. For most of the cases of interest to blanket engineering, N_{cr} is expected to be considerably lower than the value of interaction parameter in the blanket. For such cases, there is no

Table 2.5-1 Features and Objectives of Major Liquid Breeder Experiments

ALEX[a]/ALEX Upgrade	LMF[b]	MHDM[c]	TMIF[d]	PITF[e]
• Testing of flow network components	• Testing of segments of blanket modules	• Basic elements of relevant geometry	• Actual materials and geometry	• Prototypic blanket module
• Working fluid: NaK	• Working fluid: NaK	• Relevant materials combination		
• Loop structural material: austenitic stainless steel	• Loop structural material: austenitic stainless steel	• Transport loop	• Transport loop	• Transport loop
• Magnetic flux density: 2-2.5 T	• Magnetic flux density: 4-6 T	• Relevant T, ΔT, impurities, V	• Relevant environmental and operating conditions	• Prototypic environmental and operating conditions
• Available dimension in B-field direction: 15-30 cm	• Available dimension in B-field direction: 120 cm	• Long operating time per experiment		
• Measurement of velocity, pressure, temperature, and electric potential distributions	• Measurement of velocity, pressure, temperature, and electric potential distributions	• Measurement of dissolution and deposition rates	• Measurement of integral quantities (ΔP, T, corrosion, and deposition rates)	• Measurement of integral quantities
• Develop and test instrumentation for local measurements in NaK environment	• Develop and test instrumentation in NaK environment	• Develop and test instrumentation in relevant environments	• Design data for blanket test module	• Engineering design data
• Validate MHD flow, pressure, and heat transfer predictive capability for individual flow network components	• Validate MHD flow, pressure, and heat transfer predictive capability for segments of blanket modules	• Design data on MHD heat and mass transfer	• Confirm and refine configurations	• Reliability data in non-fusion environment
• Obtain design data for flow network components	• Obtain design data for segments of blanket modules	• Verify techniques to reduce corrosion and corrosion effects		
	• Explore techniques to reduce pressure drop and enhance heat transfer			

[a]Exists (ANL)
[b]Liquid Metal Flow Facility
[c]MHD Mass Transfer Facility
[d]ThermoMechanical Integration Facility
[e]Partially Integrated Test Facility (may be upgrade of TMIF)

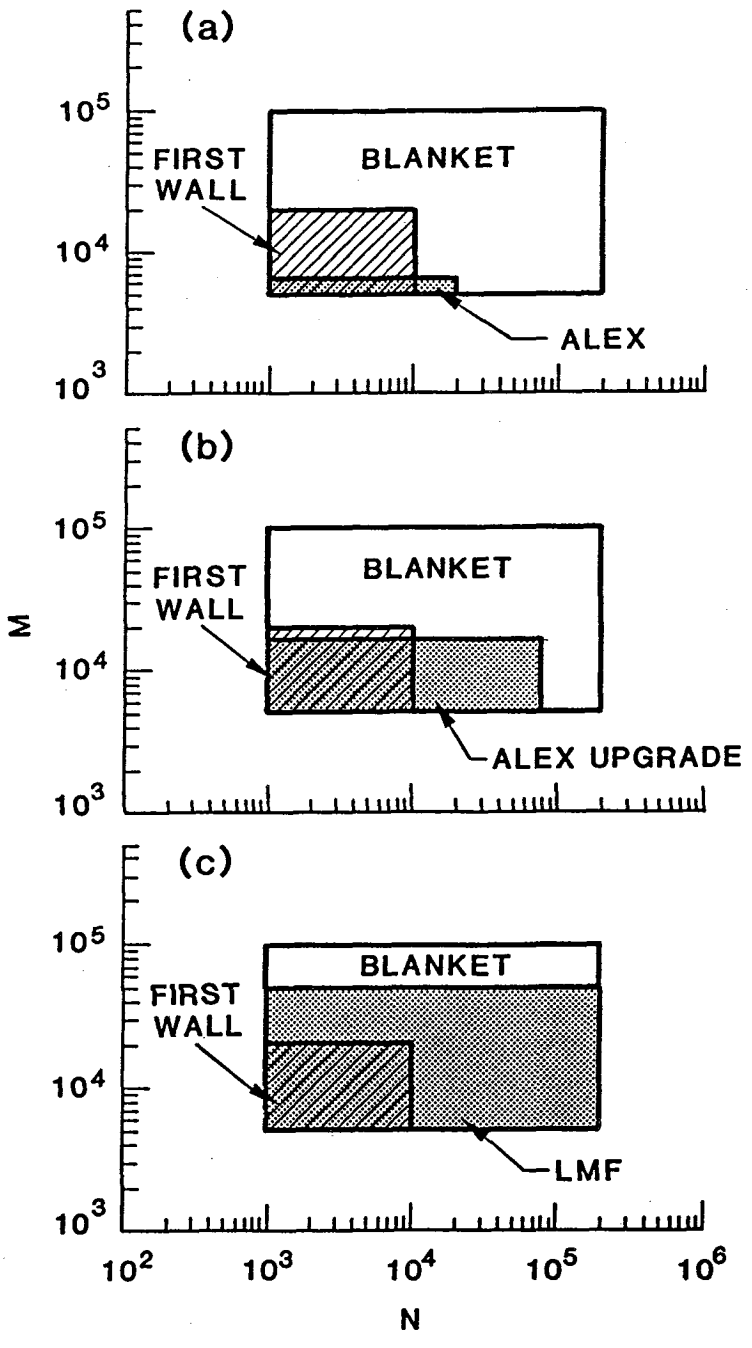


Figure 2.5-1 Hartmann number, M, and interaction parameter, N, ranges for the blanket, in general, and the first wall coolant channels, in particular. The portion of the parameter space which can be covered by testing at ALEX, ALEX Upgrade, and LMF (with a 5 T magnet) is also shown.

foreseeable reason to strive for prototypicality in N. In other words, if an experiment at lower magnetic flux density values has established that inertial effects for the cases studied are unimportant, increasing the magnetic flux density and thus increasing the electromagnetic forces will render the inertial forces even less important.

The Hartmann number is a measure of the relative importance of the electromagnetic forces to the viscous forces in the liquid metal. Its magnitude determines the thickness of boundary layers at the duct walls and of shear layers which can exist, under certain conditions, in the liquid metal. For the Hartmann numbers which prevail in the blanket, the thickness of these layers is very small. If the total flow quantity can be predicted, the effect of these layers on heat transfer can be calculated independently of the detailed velocity distribution. This may not be true for mass transfer which exhibits very small diffusion scale lengths. The effect of these layers on the core flow is usually negligible in thin conducting ducts. Boundary layers play a larger role in non-conducting ducts, but in this case the issues of MHD pressure drop and heat transfer are so reduced that their importance in the test program is much less than for thin conducting ducts. As a result, for most cases of interest, heat transfer and fluid flow experiments at Hartmann numbers smaller than the blanket prototypic values will probably provide the engineering information required.

The above discussion points to the fact that the need for prototypicality in M and N needs to be considered carefully. This is particularly important because, unlike the interaction parameter whose upper limit during a test is determined by instrumentation resolution in velocity and pressure drop measurement, prototypical Hartmann numbers can only be achieved with prototypical magnetic flux density values and prototypical sizes of the test articles. Given the fact that a major cost item of any test facility is the cost of the magnet system, and the fact that the cost of the magnet system is a strong function of the magnetic flux density and the available volume, insistence on full prototypicality in Hartmann number may result in a facility whose cost is several fold higher than what is now thought to be adequate. A more prudent approach would be to design the LMF facility in such a way as to represent a meaningful increase in parameter ranges over ALEX or ALEX Upgrade. The need for further increase in parameter range beyond those of LMF should be consid-

ered an open question that must be settled in the future rather than being taken for granted.

The definition of the facility involves largely the definition of the required magnet. The required flux density and, more importantly, the required pole face separation is a strong function of the reactor parameters and, even more so, of the particular blanket design. Since these are questions that have not been settled yet, the magnet parameters are chosen so that testing relevant to a range of different type of commercial fusion reactors can be carried out.

2.5.2 LMF Facility Description

The major components of the facility are: a) the flow loop which supplies a flow of liquid metal at specified conditions to the test article, b) the magnet system, which establishes a magnetic field of required magnetic flux density and spatial distribution, c) the instrumentation and data acquisition system, which collects and stores data for subsequent and/or real time analysis and display, and d) the test article.

2.5.2.1 Test Article

The articles to be tested in the facility, must be discussed first because they largely determine the design and functional requirements of the facility. The most important test articles are those which represent suitable simulation of blanket modules. Because the blanket modules are subjected to a strong toroidal field, the test articles should have sufficiently large dimensions along the magnetic field lines for adequate simulation. This is a most important requirement which necessitates magnets with considerably larger pole face separation than ALEX or ALEX Upgrade.

In addition to the aforementioned blanket modules, the facility must be able to accommodate a great variety of other test articles, each of which is designed to address a particular design issue related to MHD. Some of these articles will be similar to those already tested at ALEX or ALEX Upgrade. Such testing may be necessary if there is reason to believe that the increase in M and N which is possible in LMF will reveal additional information of engineering relevance. In fact, it is desirable that the facility be able to accept the identical test articles tested previously at lower M and N.

Although views on what constitutes an important design issue may evolve with the blanket designs, current thinking has identified the transition from the poloidal manifolds to the toroidal first wall coolant channels as the most important MHD-related issue of the BCSS blanket. Similarly, the manifold feeding the poloidal coolant tube bank of the TPSS blanket is the most prominent design issue for that particular design. As a minimum, the LMF must be able to address satisfactorily these design issues with appropriate test articles. Such test articles, incorporating the most important geometric features of the BCSS and the TPSS blanket, are shown in Figs. 2.5-2 and 2.5-3. It should be stressed that these are only conceptual designs and that the nominal dimensions are meant to provide the size scale of the articles. As the figures show, the modules can be used for heat transfer experiments with the addition of heat flux at appropriate surfaces.

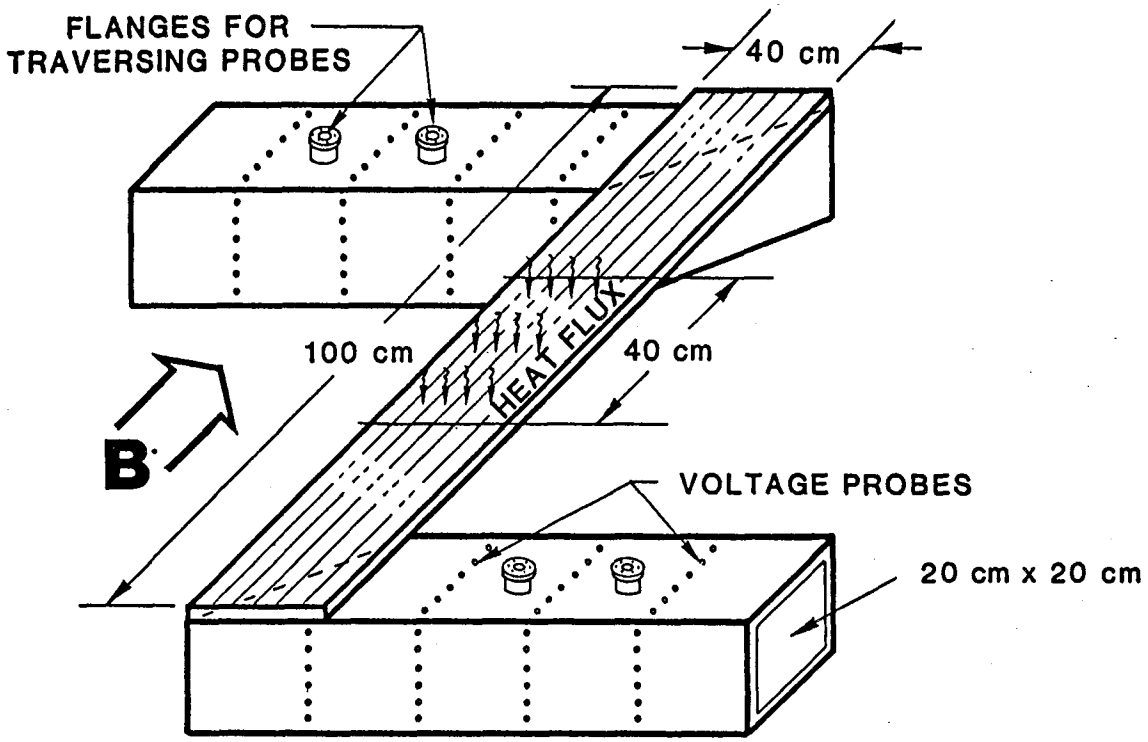


Figure 2.5-2 Conceptual design of a test section simulating the salient features of the BCSS liquid metal-cooled blanket design

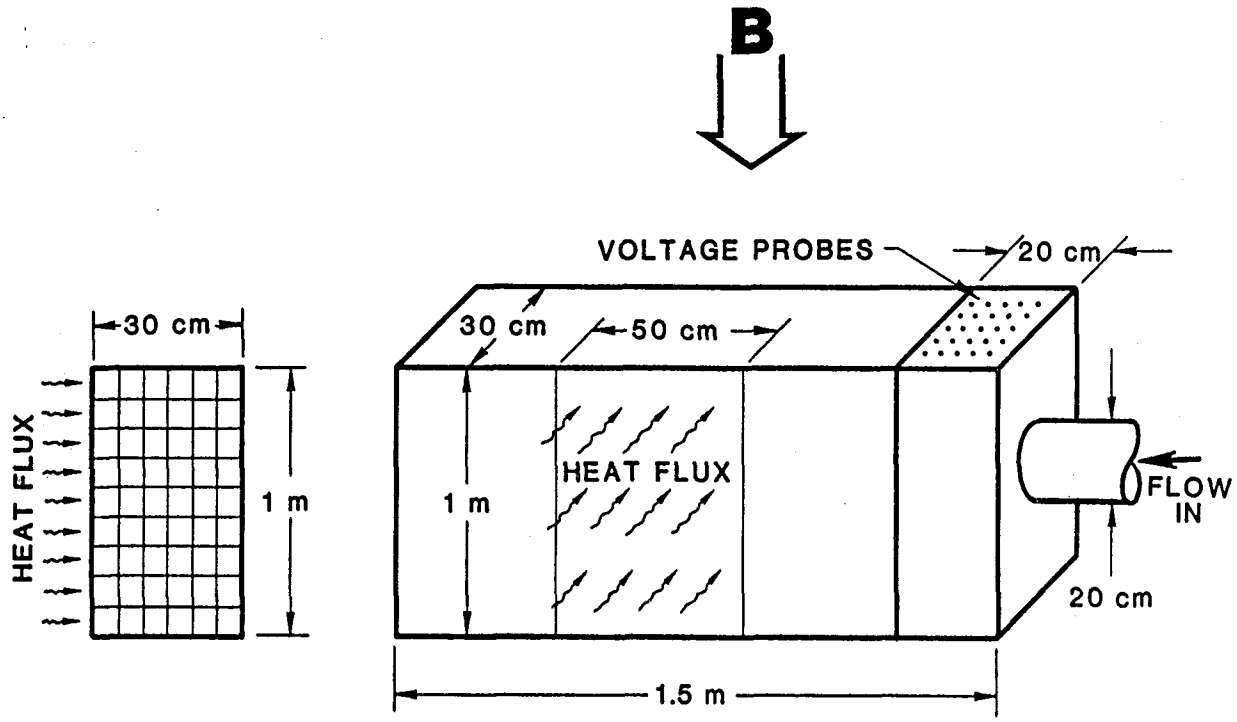


Figure 2.5-3 Conceptual design of a test section simulating the inlet (or outlet) manifold of the TPSS design. Flows in each of the individual ducts fed from the manifold can be measured with individual EM flow meters.

In terms of magnet requirements, the most important dimension in Figs. 2.5-2 and 2.5-3 is the one in the direction of the applied magnetic field. This dimension corresponds to a requirement of the pole face separation of about 1 m. For a superconducting magnet with a circular warm bore, a diameter of about 1.2 m will be required to accommodate a fully instrumented and insulated test module.

2.5.2.2 Flow Loop

A schematic of the flow loop is shown in Fig. 2.5-4. The proposed working fluid is the eutectic NaK alloy. The fact that the working fluid is liquid at room temperature not only simplifies the loop design, but, most importantly, facilitates the operation of the loop and the conduct of the tests, alleviates safety concerns, and ultimately enables the acquisition of

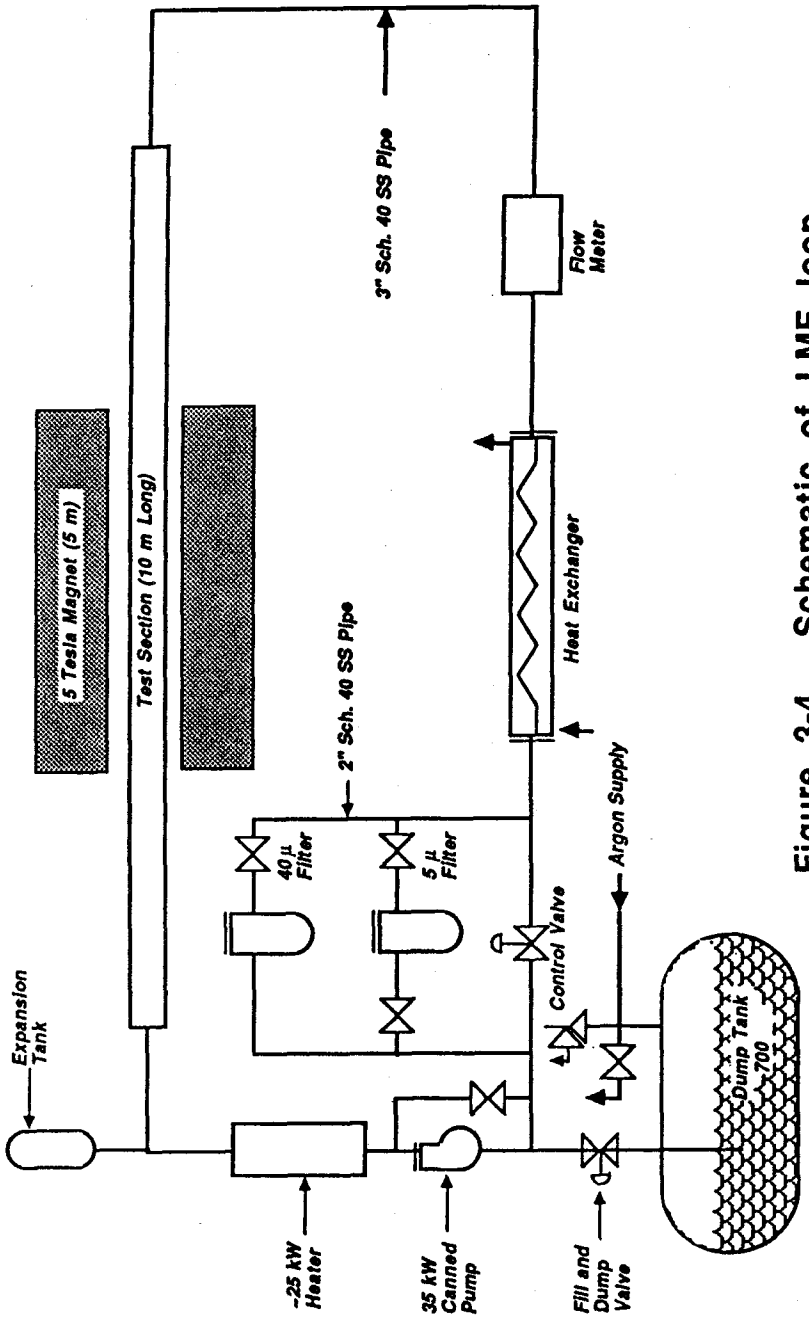


Figure 3-4. Schematic of LMF loop.

Figure 2.5-4 Schematic of LMF loop

data of higher quality and greater variety than would be possible with a high temperature loop. Use of lithium as a working fluid is, of course, a sine qua non for liquid metal corrosion testing. But because corrosion tests require careful control of loop chemistry, a multipurpose loop may not be appropriate for corrosion studies. Other than corrosion studies, the only other advantage of lithium over NaK is that, at identical test conditions, the Hartmann number testing with lithium is 50% higher than that for testing with NaK, whereas the interaction parameter is 100% higher. The interaction parameters can be made identical if NaK testing is conducted at 1/2 the velocity values of lithium testing. The advantage in Hartmann number for testing with lithium is not high enough to compensate for the limitations in the quality and the variety of test data brought about by the high temperature operation.

The schematic of Fig. 2.5-4 shows the major components of the loop. The NaK inventory of 700 liters kept in the dump tank is forced into the loop by pressurizing the argon cover gas in the dump tank. Once the loop is filled, the canned (or EM) pump circulates the working fluid through the test section, the heat exchanger which removes the heat imparted to the fluid either by the pump or by heaters during the heat transfer tests, and the control valve (or the filter during impurity filtering operation). Flow rate through the loop is controlled by a combination of pump speed through a pump speed controller, control valve setting, and proportion of total flow flowing in the bypass loop.

Although testing will be conducted at or near room temperature, the loop must have the capability of operation at 300°C for brief periods of time (of the order of few hours). Such operation, which will take place at low flow rates and pressures, reduces the oxide at the inner surfaces of the test section and minimizes the effects of interfacial electrical resistance on the test results. A small auxiliary EM pump may be incorporated into the loop design for pumping during high temperature operation for conditioning the test article. Heating of the loop is accomplished through a 25 kW electric heater.

Precise control of the test parameters and safe operation of the loop require appropriate loop instrumentation, safety interlocks, leak detectors, alarms, controllers, etc. Such hardware and supporting software are specified during the detailed design of the loop. They are not peculiar to the proposed loop, and should be part of any well-engineered liquid metal facility.

Since loop chemistry is not crucial, all loop piping is 300 series stainless steel, as are most of the loop components. Other materials for NaK wetted component parts are acceptable, provided, of course, that they are compatible with NaK at the design temperature of the component. Fouling of the working fluid by sodium and potassium oxides may interfere with component operation and test article instrumentation. It is imperative, therefore, to implement loop fabrication and operation procedures which will minimize as much as possible an introduction of oxygen into the loop. In addition, regularly scheduled filtering of the working fluid must be carried out. A summary of the loop parameters is given in Table 2.5-2.

The cost of the loop is estimated to be about $\$10^6$. This estimate refers, of course, to a stainless steel, room temperature loop. Loops operating at high temperature or loops made of different materials for corrosion studies will be considerably more expensive. With the exclusion of the magnet, the estimate includes all loop hardware and engineering. It is assumed that the loop will be sited in an existing building with existing cranes and other support hardware, utility hookups, exhaust stacks, etc.

Table 2.5-2 LMF Loop Parameters

Working Fluid	NaK Eutectic
Inventory of Working Fluid	700 liters
Loop Materials	Predominantly 300 Series S/S
Volumetric Flow Rate Through Test Article	1-25 liters/sec
Pump Outlet Pressure	1 MPa
Pump Outlet Temperature	$\leq$ 100°C
Test Article Conditioning Temperature (at low pressure and flow rate)	300°C
Overall Length of Test Article (between flanges for test section replacement)	$\sim$ 10 m

2.5.2.3 Magnet System

The major options for a magnet system are iron core versus superconducting and dipole versus solenoid.

A conventional iron core electromagnet, as opposed to a superconducting magnet, requires no maintenance and supervision between tests, can be energized in a much shorter time, and its design, operation, modification, or repair is much more straightforward. On the other hand, the power supply and cooling water requirements are so demanding, that for the size and magnetic flux density magnitude envisioned for the LMF, the use of conventional iron core magnets is all but precluded.

A superconducting magnet does have a non-negligible standby cost, traced mainly to manpower required for supervision, and replenishment for losses of liquid helium and liquid nitrogen. The standby cost is estimated to be equivalent to the cost for a staff employee. Increased effort and increased liquid helium and electric power consumption in preparation for a test result is a total cost for a 24-hour test, exceeding somewhat the monthly standby cost. For continuous testing periods, the weekly cost of operating the superconducting magnet is equivalent to the monthly cost for a staff employee.

Although design and fabrication of a superconducting magnet such as the one envisioned for the LMF facility is a challenging task, the required technology and expertise exist and have been demonstrated in the construction of a 6 T superconducting dipole magnet, by far the largest of its kind. That magnet, designed and constructed at ANL for DOE's plasma MHD energy conversion program, has dimensions and magnetic flux densities close to those deemed necessary for the LMF facility. It is shown in Fig. 2.5-5 as an example of the size scale and configuration required for a dipole LMF magnet. The desired dimensions and field uniformity for an LMF dipole magnet are as follows: a warm bore of a diameter of 1.2 m and a transverse field uniform within $\pm$ 5% over a volume 1 m x 0.3 m x 3 m (the 1.0 m dimension is in the field direction). The overall length of the magnet warm bore is approximately 5 m.

A solenoid candidate magnet for the LMF, shown in Fig. 2.5-6, would have a larger volume for the same test article testing capability. For this reason, although solenoid magnets are, in general, less costly than dipoles, the cost of an LMF solenoid would be about 25% higher than would be the cost of an

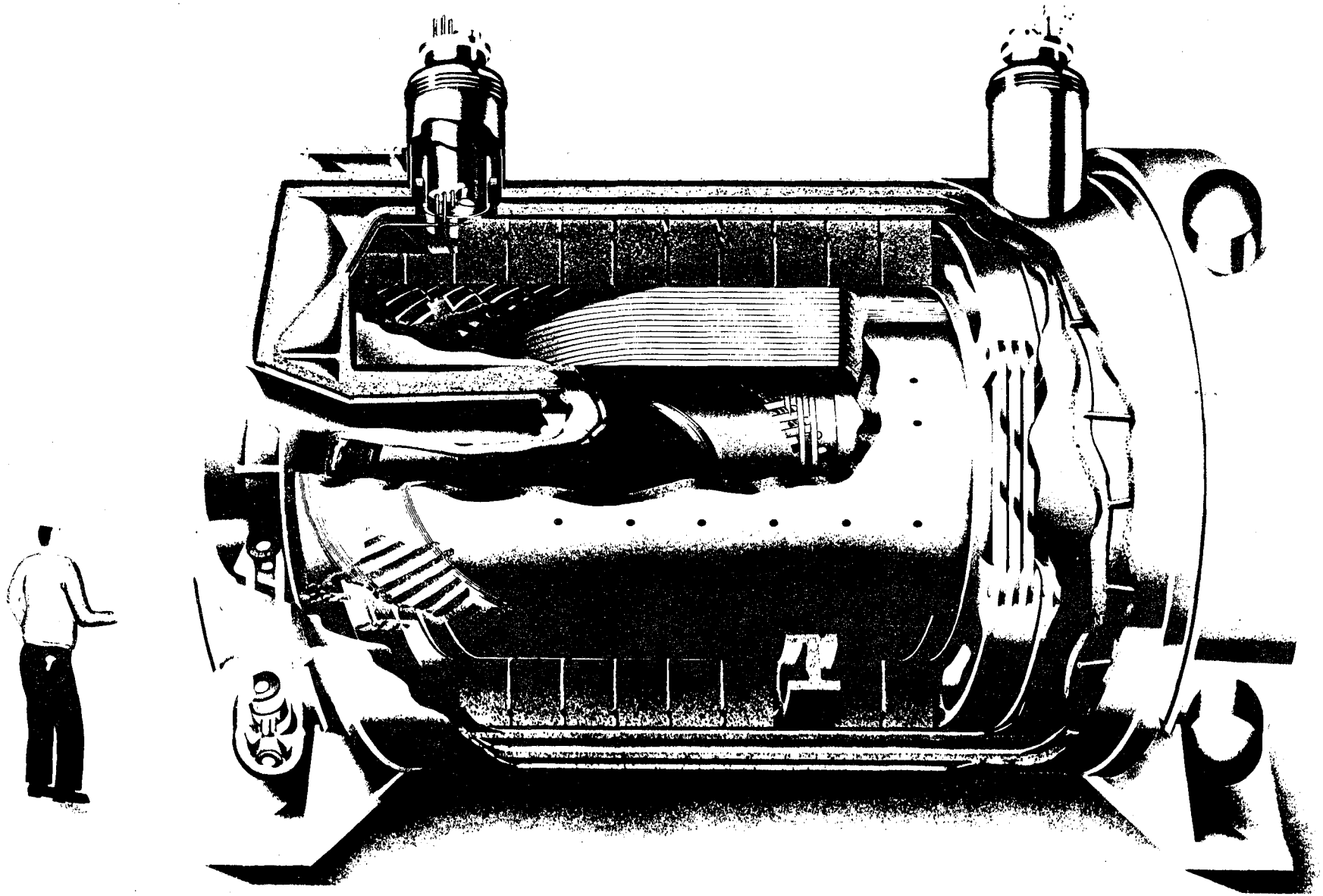


Figure 2.5-5 An example of a superconducting dipole magnet of the scale required for LMF. The magnet shown was built for DOE's Plasma MHD Energy Conversion Program and has a tapered field with a peak value of 6 T, a tapered warm bore with a maximum diameter of 109 cm and minimum diameter of 80 cm, and a warm bore length of 640 cm. It weighs 172 metric tons.

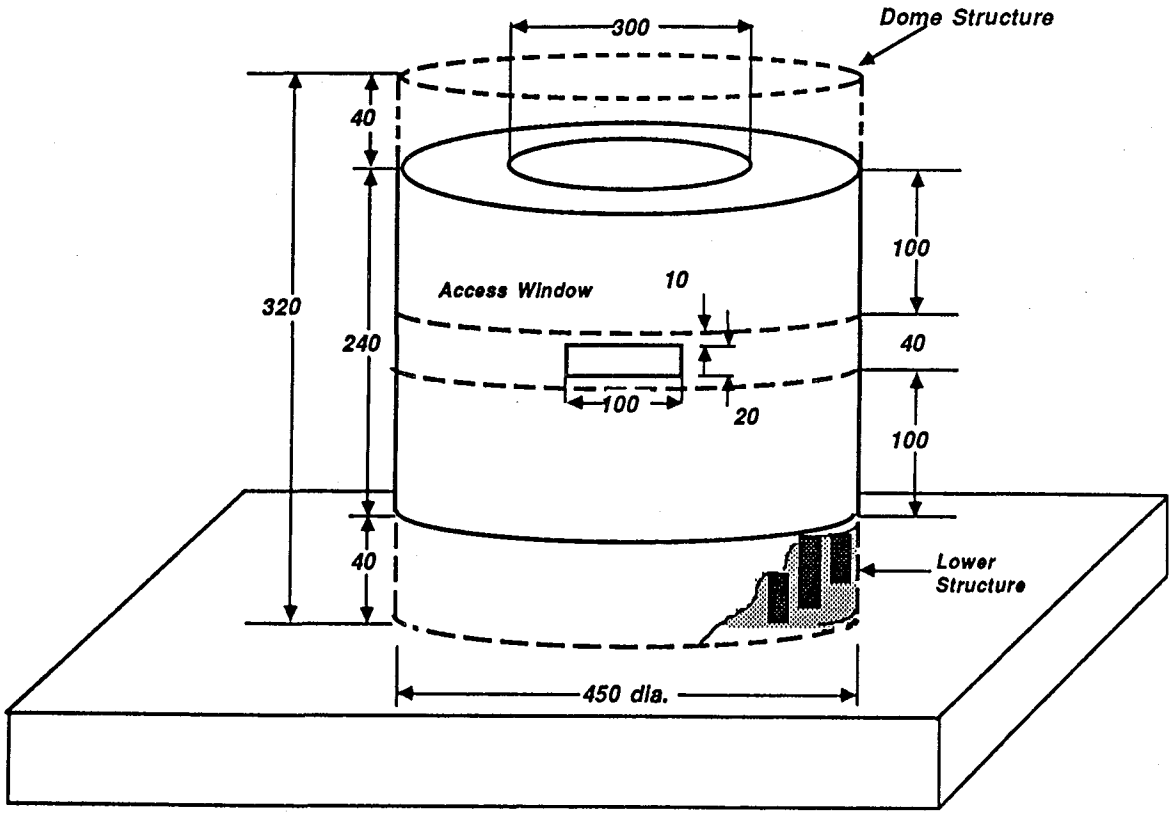


Figure 2.5-6 Solenoid magnet for LMF (all dimensions in centimeters)

LMF dipole. The estimated costs for dipole and solenoid magnets for a peak field of 5 T is \$12 x 10^6 and \$15 x 10^6. For the same type of magnet, the cost scales roughly with the magnetic flux density and the magnet volume.

Although a solenoid magnet may, at first, appear to be preferable because it simulates geometrically a segment of a tokamak torus, the fact remains that, for testing with predominantly transverse fields, the solenoid magnet has severe test volume access limitations. Radial access to the test volume can only be allowed at a very limited number of windows. This limits the type and variety of test articles that can be tested. Although additional attention must be paid to this question, as well as to the final cost differential between the two magnet types, it appears that a dipole magnet is preferable.

2.5.2.4 Instrumentation

Measurements of direct engineering importance gathered during a test are velocity, pressure, and temperature distributions. Voltage distributions, although of limited engineering importance by themselves, are in fact invaluable in that, under certain conditions, they are directly related to the flow distribution. Even for those cases where such a relation is not firmly established, the voltage distributions provide an additional dimension in the comparison between analysis and experiment. The test articles in Figs. 2.5-2 and 2.5-3 show the possible locations of voltage probes for the measurement of voltage distributions. Such probes are nothing more than wires welded to the surface of the test article. Given the fact that the voltage differences to be measured may be quite small, care must be taken to eliminate sources of error and/or noise (e.g., minimize thermoelectric effects).

The measurement of velocity distributions is most important, in as much as such distributions can be quite unusual by conventional fluid mechanical standards and can strongly affect heat and mass transfer coefficients. Most common instruments for measuring velocities are Pitot probes and hot film anemometers. The former are of very limited use for the low velocities relevant to MHD testing at high interaction parameters. They are also quite susceptible to plugging by the fine oxide particles suspended in the liquid metal or formed within the pressure tubes themselves.

Hot film anemometry has been used successfully in the past for liquid metal MHD studies. However, calibration shift due to sensor contamination and reduced sensitivity due to heat transfer inhibition brought about by the presence of a strong magnetic field make such measurements extremely tedious. The shortcoming of reduced sensitivity is experienced by all heat transfer-based measuring instruments. The fact that the magnetic field affects the calibration curve requires that these instruments be calibrated in the prevailing magnetic fields. This adds considerably to the complexity of the measuring process.

Velocity measuring instruments based on time-of-flight present another option, but their successful liquid metal MHD use has yet to be demonstrated.

By far the most attractive velocity measuring instrument to date is the LEVI (Liquid Metal Electromagnetic Velocimeter Instrument).[83] The idea of

using Ohm's law in moving media for the measurement of velocity is not, of course, new. Earlier attempts to use such an instrument met with very limited success because, in general, in addition to the local voltage gradient, the current density must also be known before the velocity can be computed. What is new is the realization that, for a great majority of flows of relevance to blanket engineering, the current density can be neglected, thus leading to a simple and accurate means of velocity measurement. Such a capability has already been demonstrated.[84] The spatial resolution of a LEVI is 1-2 mm. The measured velocity is actually an average of the velocity over the distance of the spatial resolution. The magnitude of the lowest velocities that can be measured with such an instrument is inversely proportional to the local magnetic flux density and the spatial resolution. Measurements of velocities as low as 3 cm/s at flux densities as low as 0.5 T and spatial resolution of 1.5 mm have been reported.[84] Clearly, at higher magnetic flux densities measurement of velocities of a few mm/sec is certainly possible. No other method either currently available or under development is able to measure such low velocities.

An added advantage of the LEVI is that it requires no calibration. In addition, its temporal response is only limited by the electronics used to amplify and read the induced voltages. It can therefore be used for the measurement of fluctuating as well as steady state velocities.

The limitations of the LEVI stem from its principle of operation. Clearly, it can only be used in the presence of a magnetic field, and can only measure velocity components transverse to the externally applied magnetic flux density vector. Also, its accuracy diminishes as the wall conductance ratio, C, or certain fractional powers of C approach the value of one. For these reasons, the user should be familiar with the salient points of 3-D MHD flows at high M and N to ensure that the limits of applicability of the LEVI are not exceeded.

No matter what the measuring instrument, mapping of the flow distribution is a challenging task. Carefully designed traversing mechanisms must be used and special care must be taken to ensure that neither the traversing mechanism itself nor the probe holder affects the electrical configuration of the test article. Modification of the quantity to be measured by the measurement process itself is, of course, a standing issue in all measurements. The point

to be made here is that, because the distribution of the flows under investigation is almost entirely determined by electrical considerations, particular attention must be paid to the disturbance of the electrical parameters of the system. This situation is entirely different from that which prevails in an ordinary fluid mechanical situation. Experience and guidelines developed for ordinary fluid mechanic velocity measurements are of little use here.

Because of the complexities of the velocity distribution measurements, it is unrealistic to expect that the flow field within a complex test article would be completely mapped. It is important, therefore, to carefully select the locations of velocity profile measurements to obtain the most important information. Such locations can be selected only after a detailed design of the test article has been developed and all MHD implications have been thoroughly analyzed. There would undoubtedly be cases (the first wall coolant channels in either the TPSS or BCSS designs) where, because of the small sizes of the ducts, reliable detailed velocity profiles would be exceedingly difficult to obtain. In such cases, the flow structure can be deduced indirectly by carefully designed heat transfer experiments. In such experiments, information about the flow distribution can be obtained by measuring the temperature distribution with fine thermocouples strategically placed on the surface of the test article and within the flow ducts. In fact, heat transfer experiments should be viewed as much as a means for obtaining information about the flow structure and distribution as for measuring of overall heat transfer parameters. Examples of such heated zones in the test articles are shown in Figs. 2.5-2 and 2.5-3.

The final measurement of engineering importance is the measurement of pressure distribution. Measurement of overall pressure drop through the test article is important and easily performed. Measurement of pressure distribution throughout the test section is much more challenging. Such pressure distributions will be measured with differential pressure transducers. Resolutions of the order of 300 Pa are available. The available resolution of the instruments, the available flux density, the wall conductance ratio and the nature of the case under investigation will determine the available spatial resolution. Desirable spatial resolution is determined by the characteristic dimension, which, of course, changes over a complex test article. For the magnetic flux densities anticipated for the LMF, and wall conductance ratios

of the order of 0.01 and higher, the measurement of detailed pressure distribution does not appear to be limited by the resolution of the available instrumentation. For much lower wall conductance ratios corresponding to laminated ducts, or for insulating walls, the measurement of detailed pressure distribution throughout the test article may not be a realistic goal. This, of course, will not invalidate the experiment. It will simply make the pressure distribution "coarser" with fewer data points more widely spaced. The challenging problems associated with pressure distribution measurement are related to the minimization of the current short circuit paths and corresponding local electrical disturbances brought about by the pressure lines themselves. Such considerations become more important for small wall conductance ratios. The obvious solution is to minimize the size of the pressure lines. This solution has practical limits resulting from the tendency of the pressure lines to get plugged by oxides possibly forming in the lines themselves. The problem of liquid metal freezing in the lines of high temperature loops is even harder to solve in small size lines. The pressure system must be designed so as to make routine flushing and purging of the lines possible.

2.5.3 Experimental Program

Both isothermal and heat transfer tests will be carried out at LMF. The heat transfer tests will be conducted at bulk fluid temperatures not much above room temperature. What matters in heat transfer is, of course, the temperature differences involved. The absolute temperature level of the coolant/structure has a very limited effect on heat transfer, arising primarily from the dependence of material properties on temperature. Given the shortcomings of performing tests at elevated temperatures, the measurement of such second order effects related to the absolute temperature level does not seem to be justified. This is particularly so because, as adequate simulation of neutronic heating is impossible in the proposed experiments, much more important effects related to volumetric heat deposition have been left out.

Figure 2.5-1c presents the range of achievable parameters at LMF with an available flux density of 5 T and test articles similar to those shown in Figs. 2.5-2 and 2.5-3. Of course, testing will not be limited to just the two test articles discussed here. All components of existing or future blanket designs for which there are unresolved MHD-related issues can be tested in

LMF. The priority for such testing will be determined by the impact of the particular issue on the overall blanket design and performance.

The measurements to be performed will be similar for all test articles. They will involve the measurement of velocities, pressures, and voltages at selected locations. The selection of the number of desirable locations is a strong function of the details of the particular test article and the goals of the test. In general, the testing methodology will be similar to the one currently followed in the ALEX tests.[84]

During heat transfer tests, in addition to the previously discussed measurements, temperature distributions will also be obtained. Heat transfer measurements fall into two categories. In the first category, heat transfer is used as a diagnostic tool for the study of flow distribution for those cases for which direct measurement of flow structure is not possible. In this case, the heat transfer parameters need not be prototypic. In the second category, heat transfer parameters at or near prototypic conditions are obtained for direct confirmation of predictive calculational tools and/or for the creation of an empirical data base.

As discussed earlier, the flow structure in the test articles is expected to be prototypic. Under these conditions, prototypicality of the laminar flow heat transfer depends mainly on the relative magnitude of the thermal diffusion length in the liquid metal compared to the length scale of the test article. Because thermal diffusivities in the blanket at 500°C and room temperature NaK are similar, as are the length scales of relevance, it is easy to achieve heat transfer prototypicality by requiring that the ratio of L/V in the blanket and the test article are the same. Here, L is the heated length in the flow direction and V is the average velocity. Although this is the only requirement for prototypicality of the heat transfer processes, it is desirable to conduct the tests at values of individual parameters close to those prevailing in the blanket. Such a set of parameters is as follows: surface heat flux = 0.1 - 0.3 MW/m^2, heated length: 0.5 m, average velocity: 0.2 m/s. Under such conditions and assuming plug flow, the peak interface temperature is 100°C higher than the inlet bulk flow temperature. The total heat input to the test article is of the order of 30 kW.

References for Chapter 2

1. M.A. Abdou, et al., "FINESSE: A Study of the Issues, Experiments, and Facilities for Fusion Nuclear Technology Research and Development (Interim Report)," PPG-821, UCLA-ENG-84-30, University of California, Los Angeles (1984). See also, M.A. Abdou, et al., "Technical Issues and Requirements of Experiments and Facilities for Fusion Nuclear Technology (FINESSE Phase I Report)," PPG-909, UCLA-ENG-85-39, University of California, Los Angeles (1985).

2. "Technical Planning Activity Final Report," ANL/FPP-87-1, Argonne National Laboratory (1987).

3. IAEA Advisory Group, "Chemical Aspects of Fusion Technology-1982," Nucl. Fusion, 23:7, 955-973 (1983).

4. D.J. Suiter, "Lithium Based Oxide Ceramics for Tritium Breeding Applications," MDC E2677, McDonnell Douglas Aerospace Corp. (1983).

5. "Blanket Comparison and Selection Study, Final Report," ANL/FPP-84-1, Argonne National Laboratory (1984). See also "Blanket Comparison and Selection Study," ANL/FPP-83-1, Argonne National Laboratory (1983).

6. P.P. Turner and S.F. Bartram, "Tentative Phase Diagram of Beryllia-Lithia System," Inorganic Chemistry, 6:4, 833 (1967).

7. R. Weast (ed.), CRC Handbook of Chemistry and Physics, 56th Edition, CRC Press, Cleveland (1975).

8. T. McCarville, et al., "Technical Issues for Beryllium Use in Fusion Blanket Applications," UCID-20319, Lawrence Livermore National Laboratory (1985).

9. M. Dalle Donne, S. Dorner and D.F. Lupton, "Fabrication and Properties of Zr_5Pb_3, A New Neutron Multiplier Material for Fusion Blankets," J. Nucl. Mat., 141-143, 369-372 (1986).

10. C. Denuziere and N. Roux, "Data and Properties of Lithium Aluminate $LiAlO_2$," Commissariat a L'Energie Atomique, C.E.N. Saclay (1984).

11. S.W. Tam, L. Leibowitz, Y.Y. Liu, R. Blomquist and C.E. Johnson, "Saturation Phenomena and Percolative Transitions in the High Temperature Thermal Conductivity of γ-$LiAlO_2$," J. Nucl. Mat., 133-134, 234-237 (1985).

12. Y.Y. Liu and S.W. Tam, "Thermal Conductivity for Sintered and Sphere-Pac Li_2O and Gamma-$LiAlO_2$ Solid Breeders With and Without Irradiation Effects," Fusion Tech., 7, 399-410 (1985).

13. S.W. Tam and C.E. Johnson, "The Thermal Conductivity of Mixed Beryllia/Li Ceramic in Sphere-Pac Forms," J. Nucl. Mat., 141-143, 348-352 (1986).

14. B. Schultz and H. Wedemuier, "Preparations, Characterizations and Thermal Diffusivity of γ-$LiAlO_2$," J. Nucl. Mat., 139, 35-41 (1986).

15. P. Cooke and P. Reynolds, "A Demo Tokamak Reactor, Aspects of the Conceptual Design," CLM-R254, UKAEA Culham Laboratory (1985).

16. G.W. Hollenberg and P.E. Baker, "Thermal Properties of Li_8ZrO_6," Hanford Engineering Development Laboratory, memorandum, February 10, 1984.

17. "Metals Handbook, 9th ed., Vol. 2, Properties and Selection: Nonferrous Alloys and Pure Metals," American Society of Metals, Ohio (1979).

18. D.L. Smith, et al., "Chapter X, Nuclear," U.S. INTOR Data Base & Design, USA INTOR/85-1 (1985).

19. R.F. Mattas, et al., "Chapter III, Impurity Control Engineering," U.S. INTOR Critical Issues, Phase-2A, Part 1, USA INTOR/85-1 (1985).

20. J.F. Lynch, et al. (eds.), "Engineering Properties of Selected Ceramic Materials," American Ceramics Society, Columbus, Ohio (1966).

21. G.W. Hollenberg, "Planning Document for FUBR-1B Experiment, Second Insertion," Hanford Engineering Development Laboratory (1984).

22. J. Davis (ed.), "Materials Handbook for Fusion Energy Systems," U.S. Dept. of Energy (1984).

23. Barin-Knacke, Thermochemical Properties of Inorganic Substances, Verlag, Berlin (1978).

24. Y.S. Touloukian (ed.), "Specific Heat of Non-Metallic Solids in Thermophyscial Properties of Matter," Vol 5, IFI/Plenum, New York (1970).

25. D. Finken (ed.), "Fusion Technology Programme, Semi-Annual Report October/1985-March/1986," KfK-4076, Kernforschungszentrum Karlsruhe (1986).

26. P. Groner and W. Seifritz, "Ceramic Lithium Compounds for Solid Breeder Concepts for Fusion Reactors," Nucl. Tech./Fusion, 5, 169-177 (1984).

27. C.E. Johnson and A.K. Fischer, "Blanket Materials for Fusion Reactors: Comparisons of Thermochemical Performance," J. Nucl. Mat., 130, 445-453 (1985).

28. H. Ihle and C. Wu, "Chemical Thermodynamics of Fusion Reactor Breeding Materials and Their Interaction with Tritium," J. Nucl. Mat., 130, 454-464 (1985).

29. L. Yang, et al., J. Nucl. Mat., 103-104, 585-590 (1981).

30. H. Ohno, et al., "Electrical Conductivity of a Sintered Pellet of Octalithium Zirconate," J. Nucl. Mat., 132, 222-230 (1985).

31. M. Dalle Donne, "Tritium Release from a Lithium Ceramic: Interpretation of the TRIO Experiment," Fusion Tech., 9, 503-505 (1986).

32. F. Botter, et al., "Out of Pile Tritium Release from Various Lithium Materials," 14th Symposium on Fusion Technology (SOFT), Avignon, France (Sept. 1986).

33. D.L. Baldwin and G.W. Hollenberg, "Measurements of Tritium and Helium in Fast Neutron Irradiated Lithium Ceramics Using High Temperature Vacuum Extraction," J. Nucl. Mat., 141-143, 305-310 (1986).

34. H. Werle, et al., "The LISAl Experiment: In-Situ Tritium Release Investigations," J. Nucl. Mat., 141-143, 321-326 (1986).

35. I.J. Hastings, et al., "Irradiation of Lithium Based Ceramics for Fusion Blanket Applications," AECL-9187/CFFTP-86-G-003, Chalk River Nuclear Laboratories (1986).

36. R. Clemmer, et al., "The TRIO Experiment," ANL-84-55, Argonne National Laboratory (1984).

37. W. Shmayda, "Tritium Interactions With Materials," Course Notes, Tritium Safe Handling Course, Canadian Fusion Fuels Technology Project, September 17, 1984.

38. J.D. Fowler, B. Chandra, T.S. Elleman, A.W. Payne, and K. Verghese, J. Am. Ceramics Soc., 60, 155 (1977).

39. V.G. Vasilyev, "Tritium Release from Neutron Irradiated Li_7Pb_2 and $Li_{17}Pb_{83}$," 14th Symposium on Fusion Technology (SOFT), Avignon, France (Sept. 1986).

40. A.R. Palmer, D. Roman and H.J. Whitfield, "The Diffusion of Tritium from Irradiated Beryllium Oxide Powders," J. Nucl. Mat., 14, 141-146 (1964).

41. M.A. Abdou, et al., "Chapter VIII, Tritium and Blanket," U.S. FED-INTOR, Phase 1, FED-INTOR/TRIT/82-5 (1982).

42. M. Tetenbaum, A.K. Fisher, and C.E. Johnson, "An Investigation of the Solubility of LiOH in Solid Li_2O," Fusion Tech., 7, 53-56 (1985).

43. J. H. Norman and G. R. Hightower, "Measurements of the Activity Coefficient of LiOH Dissolved in $Li_2O(s)$ for an Evaluation of Li_2O as a Tritium Breeder Material," J. Nucl. Mat., 122-123, 913-920 (1984).

44. V.G. Vasilyev, "Thermodynamic and Kinetic Research of $LiAlO_2$-H_2O Systems," Second International Conf. on Fusion Reactor Materials, Chicago (April 1986).

45. M.A. Abdou, J.J. Wittenberg and C.W. Maynard, "A Fusion Design Study of Nonmobile Blankets With Low Lithium and Tritium Inventories," Nucl. Tech., 26, 400-419 (1975).

46. M.C. Billone, "Influence of Surface Desorption on Tritium Recovery in Fusion Solid Breeders," J. Nucl. Mat., 141-143, 316-320 (1986).

47. A.K. Fisher, J.A. McDaniel and C.E. Johnson, "Studies of Surface Adsorption on $LiAlO_2$," J. Nucl. Mat., 141-143, 344-347 (1986).

48. M.C. Billone, et al., "Elastic and Creep Properties of Li_2O," J. Nucl. Mat., 141-143, 282-288 (1986).

49. F. Botter, et al., "Effects of Radiation on Lithium Aluminate Samples Properties," J. Nucl. Mat., 141-143, 364-368 (1986).

50. D. Finken (ed.), "Fusion Technology Programme Semi-Annual Report, April/1985-September/1985," KfK-3379, Kernforschungszentrum Karlsruhe (1985).

51. P.H. Perry and D. Green, Perry's Chemical Engineering Handbook, Sixth Edition, McGraw-Hill (1984).

52. R.E. Williford, "A Cracked-Fuel Constitutive Equation," Nucl. Tech., 67, 208 (1984).

53. "The Development and Testing of Ceramic Breeder Materials, Progress Report," EURFU/XII-849/FT.BM1, NET Report (1984).

54. R.M. Tennent (ed.), Science Data Book, Oliver & Boyd, Manchester, England (1971).

55. Samsonov (ed.), The Oxide Handbook, Second Edition (1982).

56. H. Kwast, et al., "In-Pile Tritium Release from $LiAlO_2$, Li_2SiO_3 and Li_2O in EXOTIC Experiments 1 and 2," J. Nucl. Mat., 141-143, 300-304 (1986).

57. C. Alvani, et al., "The ENEA Selected Fabrication Processes of $LiAlO_2$ Ceramic Pellets for Tritium Breeding Experiments in Fusion Technology," VI-CIMTEC, Milano (June 1986).

58. A.J. Flipot and P. Diels, "Relationship Between Fabrication Parameters and Structural Characteristics of Sintered Lithium Metasilicate," J. Nucl. Mat., 141-143, 339-343 (1986).

59. Project Staff, "TFTR Lithium Blanket Module Program Final Design Report, LBM Lithium Oxide Pellet Fabrication," Vol. IV, GA-A17467, General Atomic Co. (1983).

60. C. Johnson, Argonne National Laboratory, private communication (July 1986).

61. W.R. Spears, "The SCAN-2 Cost Model," EUR-FU/XII-80/86/62, NET Report (1986).

62. J. Ortman and E. Larsen, "The Preparation, Characterization and Melting Point of Li_2O," UWFDM-449, University of Wisconsin (1982).

63. J.M. Beeston, "Beryllium Metal as a Neutron Moderator and Reflector Material," Nucl. Eng. & Design, 14, 445-474 (1970).

64. KBI Product Specifications, Be Standard Nuclear Grade HP-20SNG, File #302 19-SP9 (1977).

65. S.A. Urry, Solution of Problems in Strength of Materials, Second Edition, Pitman Paperbacks, Bath, Great Britain (1976).

66. R.B. Bird, et al., Transport Phenomena, John Wiley & Sons, New York, 559 (1960).

67. T. Morimoto, et al., "The Adsorption of Water on SiO_2, Al_2O_3, and $SiO_2 \cdot Al_2O_3$. The Relation Between the Amounts of Physisorbed and Chemisorbed Water," Bulletin of the Chemical Society of Japan, 44, 1282-1288 (1971). See also T. Morimoto, et al., "Desorbability of Chemisorbed Water on Metal Oxide Surfaces. I. Desorption Temperature of Chemisorbed Water on Hematite, Rutile and Zinc Oxide," Bulletin of the Chemical Society of Japan, 41, 1533-1537 (1968).

68. A.K. Fisher and C.E. Johnson, "Thermodynamics of Li_2O and Other Breeders for Fusion Reactors," J. Nucl. Mat, 133-134, 186-191 (1985).

69. F.M. Mann, "Transmutations of Alloys in MFE Facilities as Calculated by REAC (A Computer Code System for Activation and Transmutation)," HEDL TME 81-37, Hanford Engineering Development Laboratory (1981). See also, F.M. Mann, "Cross Sections for Activation Studies," in Damage Analysis and Fundamental Studies Quarterly Progress Report, October-December 1984, DOE/ER-0046/20, U.S. Department of Energy (1985).

70. R. Kinsey, Compiler, "ENDF/B Summary Documentation (ENDF-201)," Third Edition (ENDF/B-V), BNL-NCS-17541, Brookhaven National Laboratory (1979). Version V.2 was released in 1982-3.

71. C.M. Lederer and V.S. Shirley (eds.), Table of Isotopes, Seventh Edition, John Wiley & Sons, New York (1978).

72. K.F. Eckerman, et al., "A New Calculation of Derived Limits for the 1960 Radiation Protection Guides Reflecting Updated Models for Dosimetry and Biological Transport," EPA 520/1-84-010, U.S. Environmental Protection Agency (1984).

73. W.E. Kennedy, Jr. and R.A. Peloquin, "Potential Low-Level Waste Disposal Limits for Activation Productions from Fusion," PNL-4844, Pacific Northwest Laboratory (1983).

74. R.F. Bourgue, Note for BCSS Progress Meeting, Argonne National Laboratory, Illinois (May 1984).

75. F. Kreith, Principles of Heat Transfer, Third Edition, Harper & Row, New York (1973).

76. Perry (ed.), Chemical Engineer's Handbook, McGraw-Hill, New York, 393-394 (1950).

77. M.A. Abdou, et al., "DT Fuel Self-Sufficiency in Fusion Reactors," Fusion Tech., 9, 250-285 (1986).

78. P. Gierszewski and R. Puigh, "Testing Needs and Experiments for Solid Breeder Blankets," J. Nucl. Mat., 141-143, 311-315 (1986).

79. P.J. Gierszewski, M.A. Abdou and R.J. Puigh, "Fission Reactor Experiments for Solid Breeder Blankets," Fusion Tech., 10, 1097-1101 (1986).

80. C.B. Reed, B.F. Picologlou and P.V. Dauzvardis, "Experimental Facility for Studying MHD Effects in Liquid Metal Cooled Blankets," Fusion Tech., 8, 257-263 (1985).

81. Y.S. Cha, et al., "Design of Self-Cooled Liquid-Metal Blankets for Tokamak and Tandem Mirror Reactors," Fusion Tech., 8, 90-113 (1985).

82. B.F. Picologlou, Y.S. Cha, and S. Majumdar, "Lithium-Cooled Blankets for Advanced Tokamaks," Fusion Tech., 10, 848-853 (1986).

83. C.B. Reed, B.F. Picologlou, P.V. Dauzvardis and J.L. Bailey, "Techniques of Measurement of Velocity in Liquid-Metal MHD Flows," Fusion Tech., 10, 813-821 (1986).

84. B.F. Picologlou, C.B. Reed, P.V. Dauzvardis and J.S. Walker, "Experimental and Analytical Investigations of Magnetohydrodynamic Flows Near the Entrance to a Strong Magnetic Field," Fusion Tech., 10, 860-865 (1986).

3. FUSION TESTING ISSUES

TABLE OF CONTENTS

Page

3. Fusion Testing Issues....3-1

3.1 Introduction....3-1

3.2 Test Requirements....3-3

3.2.1 Summary of Test Requirements....3-3

3.2.2 Analysis of the Effects of Cyclic Operation....3-5

3.2.2.1 Solid Breeder Thermal and Tritium Behavior....3-11

3.2.2.2 Unsteady Liquid Metal Flow Behavior....3-21

3.2.2.3 Unsteady Liquid Metal Blanket Temperature Response....3-35

3.3 External Tritium Supplies....3-42

3.3.1 Natural Tritium....3-42

3.3.2 Bomb Test Tritium....3-42

3.3.3 Fission Reactions....3-42

3.3.4 Heavy Water Absorption....3-43

3.3.5 Lithium Absorption....3-44

3.3.6 Helium-3 Absorption....3-46

3.3.7 Fusion Reactions....3-47

3.3.8 Summary....3-47

3.4 ETR Tritium Breeding Blanket Availability and Testing Requirements....3-48

3.4.1 Introduction....3-48

3.4.2 Blanket MTBF Requirements....3-49

3.4.3 Testing Time and Performance Confidence Levels....3-54

3.4.4 Parallel Testing As a Means of Achieving Performance Confidence....3-58

3.4.5 Conclusion....3-59

LIST OF FIGURES

		Page
3.2-1	Tritium and thermal diffusion time constants as a function of temperature - Li_2O	3-13
3.2-2	Tritium and thermal diffusion time constants as a function of temperature - γ-$LiAlO_2$	3-14
3.2-3	Tritium and thermal diffusion time constants as a function of temperature - Li_4SiO_4	3-15
3.2-4	Solid breeder temperature profiles under pulsing	3-17
3.2-5	Transient tritium release rate from 0.2 μm grain $LiAlO_2$ (for 200-s burn, 50-s dwell, and 12-s ramp times)	3-19
3.2-6	$LiAlO_2$ diffusive tritium concentration profiles with 200-s burn, 50-s dwell, and 12-s ramp times (microscopic calculation)	3-20
3.2-7	Channel geometry for transient MHD fluid flow calculation	3-23
3.2-8	Grid nodes	3-24
3.2-9	Unsteady velocity profile with no magnetic field	3-26
3.2-10	Effect of magnetic field on velocity profile at two instants of time	3-28
3.2-11	Induced magnetic field profiles at two instants of time	3-29
3.2-12	Effect of magnetic Prandtl number on transient mean velocity	3-30
3.2-13	Pulsed magnetic field	3-31
3.2-14	Effect of a pulsed magnetic field on mean velocity vs. time	3-32
3.2-15	Effect of a pulsed magnetic field on mean velocity for different Pr_m	3-33
3.2-16	Single coolant channel geometry	3-36
3.2-17	Transient first wall temperatures of a liquid metal blanket cooling channel at 5 m from the inlet for different velocity profiles	3-38
3.2-18	Transient first wall temperature for a slug velocity profile, 5:1 duty cycle	3-40
3.2-19	Transient first wall temperature for a skewed velocity profile, 5:1 duty cycle	3-40

3.2-20 Transient first wall temperature for a slug velocity profile, 5:2 duty cycle.....3-41

3.2-21 Transient first wall temperature for a skewed velocity profile, 5:2 duty cycle.....3-41

3.4-1 Failure rate over component life.....3-51

3.4-2 Tritium breeding ratio and replacement tritium cost.....3-52

3.4-3 MTBF for tritium breeding module (at various values of MTTR) necessary to achieve a blanket availability goal of 0.8 as a function of the number of tritium breeding modules (and tritium breeding ratio).....3-53

3.4-4 Required module MTBF (meeting 0.8 blanket availability goal) as a function of the number of modules per sector.....3-54

3.4-5 Confidence level versus testing time and number of failures.....3-56

3.4-6 Minimum (zero failures) required testing time versus goal MTBF and confidence level.....3-56

3.4-7 Minimum required testing time (at various confidence levels) to achieve a blanket availability of 0.8 as a function of the number of tritium breeding modules and tritium breeding ratio. Also shown is the cost of external tritium supply as a function of the breeding ratio.....3-57

3.4-8 Cost of purchased tritium as a function of the minimum required testing time at several confidence levels.....3-58

3.4-9 The effect of parallel testing on the minimum time (zero failures) required to achieve a confidence level of 0.9.....3-59

LIST OF TABLES

		Page
3.2-1	Device Parameters: Reference Conditions and Recommended Values	3-4
3.2-2	General Effects of Fusion Test Device Parameters on Blanket Performance	3-6
3.2-3	Some Time Constants for Blanket Behavior at Reactor Conditions	3-8
3.2-4	Reference Burn Cycle Times (in seconds)	3-10
3.2-5	Examples of Threshold Effects in a Fusion Blanket	3-11
3.3-1	Potential Tritium Sources	3-48
3.4-1	Representative ETR Parameters Considered in the Reliability Analysis	3-50

3. FUSION TESTING ISSUES

3.1 Introduction

Integrated testing is essential for concept verification and demonstration of fusion nuclear components. It has been shown previously in the FINESSE study[1] that only a fusion facility can provide the proper combination of environmental conditions to adequately perform integrated testing. The importance of fusion testing also has been clearly recognized in the Magnetic Fusion Program Plan.[2]

The fusion nuclear technology testing mission will strongly affect the design and operation of any fusion engineering test reactor. It places requirements on many of the key device parameters, including neutron wall loading, accessible first wall test area, burn time, and availability. For example, as the neutron wall load is decreased, it becomes increasingly difficult to maintain the correct temperature distributions within the blanket test module. This also impacts many related phenomena activated by temperature. The test requirements for fusion testing are treated further in Section 3.2 and Ref. [1].

Besides the physical characteristics of the reactor, fusion testing also impacts the operation of the facility. Examples of these impacts are:

1. Requirements on operating time. The fluence and availability goals for the test reactor are driven in large part by nuclear testing. Some nuclear tests involving tritium transport, corrosion, and radiation effects may require test times as long as weeks or months. The exploration of neutron interactive effects (i.e., processes which are affected by the presence of neutrons) is essential for concept verification and component performance tests. Test times required for end-of-life radiation effects are normally much longer, but may not be needed for concept verification and performance tests.

2. Safety implications. Test modules and associated systems must be included in the safety analysis of the test reactor. For example, if a liquid lithium cooled test module is required, then water cooling of the reactor components may become a critical issue. Special safety systems may be needed for protection against accidental chemical reactions, and measures

must be taken to prevent damage to the reactor components and site equipment and personnel in the event of a test module failure.

3. Equipment associated with the test program. Any integrated test of a component will necessarily include the subsystems which influence component performance. As an example, the blanket system includes external heat transport equipment and cooling system components (pumps, piping, etc.), tritium extraction and processing equipment, impurity control and chemical systems, cooling system volume control, safety systems, and possibly others. The presence of these auxiliary systems and the need for reliable operation will affect the cost and operation of the facility.

4. Tritium supply requirements. Because of the fluence and availability requirements imposed by nuclear component testing, large amounts of tritium will be consumed. The source of this tritium for an engineering test facility is still uncertain, and depends to a large extent on the exact quantities needed. Some (or all) of the fuel requirement might be satisfied by external sources, such as tritium produced in fission reactors (especially the CANDU reactors). However, if the external supplies are insufficient, on-site tritium breeding will be needed. If tritium breeding blankets are required, they may have a significant impact on device availability, since prior fusion testing of blankets will not exist. In either case, the cost of providing tritium could be a sizeable fraction of the device operating budget.

In this chapter, the various impacts of fusion testing on a fusion engineering test reactor are examined. Further analysis can be found in Refs. [1] and [3]. Three specific areas are emphasized here. First, in Section 3.2, test requirements are reviewed. The test requirements are restrictions on the acceptable device parameter ranges which provide adequate testing for nuclear issues. An emphasis is placed on the effects of cyclic operation and on restrictions on operating time parameters. Detailed analysis is shown in the areas of solid breeder tritium transport/thermal behavior and liquid breeder heat transfer/fluid flow.

The second issue, addressed in Section 3.3, is tritium supply requirements. A nuclear testing mission requires much higher neutron fluence than a

physics or system integration mission. Even without material testing, fluences greater than 1-2 MW-yr/m^2 will probably be required in order to provide data on interactive nuclear effects and early failures. This, in turn, requires either large external supplies of tritium and/or the presence of an internal tritium breeding blanket. Section 3.3 reviews the potential external sources of tritium.

If a breeding blanket is required for local tritium generation, then its availability will have an impact on the overall test reactor availability. Section 3.4 examines issues related to blanket availability. While it is difficult to evaluate the expected reliability of breeding blankets, requirements can be determined from overall system availability requirements. These requirements may be very difficult to meet without any prior fusion testing of blanket components.

3.2 Test Requirements

3.2.1 Summary of Test Requirements

The most important test requirements are those related to the major parameters of the test facility. The device parameters which most strongly affect the blanket are listed in Table 3.2-1. Previous analyses in the FINESSE project[1,4] have been performed to establish preliminary guidelines for the fusion engineering test reactor parameters. These are summarized in Table 3.2-1.

Requirements on the test facility parameters are related to the assumed reference conditions for a commercial reactor. Table 3.2-1 provides a set of reference conditions based on a survey of recent tokamak reactor and reactor blanket design studies.[5-8] Two bounds are given for the test requirements: minimum and recommended values. The minimum values are based on detailed analysis of the important blanket phenomena under altered test conditions. One can show that test device parameters below the minimum value in any category will seriously limit the usefulness of nuclear testing for at least one identifiable phenomenon. There is a high probability that results could not be extrapolated to reactor conditions under these circumstances. Future analysis of additional phenomena will generally produce more stringent minimum

Table 3.2-1 Device Parameters: Reference Conditions and Recommended Values

Parameter	Test Facility		Reference Reactor
	Minimum	Recommended	
Neutron Wall Load (MW/m^2)	1	2-3	5
Surface Heat Load on First Wall (MW/m^2)	0.2	0.2-0.5	1
Fluence at Test Module[a] ($MW-yr/m^2$)	2	3-6	15-20[b]
Plasma Burn Time (s)	500	>1000[c]	steady state
Plasma Dwell Time (s)	<100	<50	--
Continuous Operating Time	days	weeks	months
Availability (%)	20	30-50	70
Test Port Size (m^2 x m)	0.5x0.3	1x0.5	--
Total Test Surface Area (m^2)	5	10-20	--
Magnetic Field Strength (T)	3	5	7

[a]Fluence at test module. Required test device lifetime is greater (by about a factor of two).
[b]Blanket lifetime.
[c]Steady state is preferred.

test requirements, due to an increased understanding of the complexities of blanket behavior. Only if the reference device parameters are reduced is it likely that the minimum parameter values will be reduced.

While the minimum parameter ranges provide values below which there is confidence that results cannot be extrapolated to reactor conditions, the recommended parameter ranges provide values above which there is confidence that results could be extrapolated to reactor conditions. The recommended values are determined partly from analysis and partly from engineering judgement. While testing at prototypical values is clearly most beneficial, the large majority of nuclear issues can still be adequately addressed if these recommended parameters are achieved. However, since we do not fully understand engineering phenomena under fusion reactor conditions, a judgement is required based on typical experience in scaling for other technologies. Operation at the recommended set of parameters gives no guarantee that the results will be fully valid at full reactor parameters.

For both the minimum and recommended values, further analysis is needed to refine the estimates in Table 3.2-1 and explore additional effects due to scaled operation. Precise specification of the requirements on test device parameters is difficult. In general, the physical behavior in nuclear components varies gradually with the device parameters, showing threshold effects only in a limited number of cases (such as the transition from laminar to turbulent flow, or from elastic to plastic strains). The determination of test requirements must be constructed from analyses of the many phenomena which are affected by varying device parameters, and from an informed engineering judgement on how far the conditions can be extrapolated in order to confidently predict behaviors under full reactor conditions.

Exact simulation of all the conditions in the blanket (including temperature profiles, radiation damage profiles, and geometric boundary conditions) is not possible under scaled device parameters. Therefore, it is important to define the degree to which imperfect simulation of the reactor conditions can be tolerated, based on whether or not the needed data can still be obtained. In addition, modifications to the test modules themselves can be partially successful in recovering reactor relevant behavior under scaled conditions. The process of altering test module characteristics to enhance the value of testing is called Engineering Scaling.

Table 3.2-2 shows the effects that the fusion test device parameters have on blanket performance. The test parameters from Table 3.2-1 are grouped into four areas: 1) neutron wall loading, which is the primary device parameter in determining the heat sources (surface and bulk heating), nuclear reaction rates, and accumulated fluence; 2) plasma burn time and pulsing, which represents effects related to non-steady-state operation; 3) device geometry and test volume; and 4) magnetic field strength and geometry. Relationships also exist among the performance parameters; for example, the thermal condition of the blanket strongly impacts structural, corrosion, and tritium behaviors. These secondary relationships are not explicitly defined in Table 3.2-2.

3.2.2 Analysis of the Effects of Cyclic Operation

In this section, a number of new calculations are described relating to transient behavior of solid and liquid breeder blankets. These calculations provide input to the determination of test requirements on operating time and burn cycle characteristics.

Table 3.2-2 General Effects of Fusion Test Device Parameters on Blanket Performance

	Neutronics	Thermal	Structural	Flow/Corrosion	Tritium
Neutron Wall Load:					
Heat Source (Surface and Bulk Heating)	nuclide density and geometric changes due to thermal expansion and cracking	temperature profiles, heat transfer coefficient, thermophysical properties	thermal stresses, material properties, thermal creep, temperature-dependent radiation damage profiles	mass transport/ corrosion rates and profiles, coolant properties, wall electrical conductivity (LM)	diffusion and other transport processes, solubility and surface adsorption, mass transfer, grain growth, porosity changes (sintering)
Reaction Rates	R.R.	R.R.	R.R.	R.R.	tritium production rate
Fluence	transmutations, activation	thermophysical properties, gap conductance	material properties, swelling, ductility, creep	degradation of MHD insulators, radiation-enhanced corrosion	tritium generation, trapping, burn-up related thermochemistry changes (SB), effect on permeation barriers
Plasma Burn Time and Pulsing	--	transient temperature profiles	fatigue, crack growth, ratchetting, creep/fatigue	corrosion equilibrium	inventory and recovery equilibrium; permeation rate and barrier characteristics
Device Geometry and Test Volume	neutronic boundary conditions, extrapolation to full blanket coverage, deep penetrations	thermal boundary conditions, MHD heat transfer, thermal entrance effects	component sizes (especially aspect ratios)	MHD velocity profiles and pressure drop entrance effects, MHD mass transfer, spatial profiles of corrosion	tritium breeding and inventory
Magnetic Field (Strength and Geometry)	--	MHD heat transfer	steady and transient forces, MHD pressure stresses	MHD fluid flow and corrosion	--

Operating time requirements are based on analysis of the time dependent responses of all the important blanket phenomena. These include thermal-hydraulic, corrosion, structural, tritium, and neutronic performance. The unsteady behavior of the blanket is usually very complex, but often the evaluation of burn cycle requirements can be related to relatively basic time constants for the processes involved. A partial list of basic time constants is given in Table 3.2-3. The time constants are evaluated using blanket characteristics from the reference designs described in Ref. [1]. Three major classes of time constants which recur frequently are:

1. Diffusive processes governed by a diffusivity and scale length, $\tau_d = L^2/D$. This includes primarily thermal diffusion and mass diffusion.
2. Convective processes governed by a velocity and scale length, $\tau_c = L/v$. This applies primarily to various residence times.
3. Bulk changes governed by inventory and rate of change. Examples are bulk temperature rise and tritium build-up rate.

Table 3.2-4 shows the range of burn cycle times considered here for the fusion test reactor. To understand the relationship between unsteady responses and the test requirements, it is helpful to consider three possible situations for the time constant of a given process:

1. Time constant much shorter than the burn time. A good example of this is MHD velocity profiles, which have a time constant of the order of 1 s or less. In this case, the process reaches a true equilibrium within a single burn time. If the duty cycle of the machine is high, then the conditions in the blanket are prototypical most of the time.
2. Time constant much longer than the dwell time. A good example of this is corrosion, which normally takes weeks to months to become developed. In this case, the process reaches a quasi-equilibrium, with conditions changing very little during a single burn cycle. If the duty cycle is high, then the quasi-equilibrium will be close to the true equilibrium condition.
3. Time constant roughly equal to the burn or dwell time. A good example of this might be temperature responses, particularly in solid breeder blankets (which possess relatively low thermal conductivities). This condition is the most problematic, and requires detailed analysis to determine the nature of the responses that depend on temperature.

Table 3.2-3 Some Time Constants for Blanket Behavior at Reactor Conditions

FLOW	
Solid breeder blanket purge residence time	6 s
Liquid breeder blanket flow residence time	10-30 s
Liquid metal cooling circuit transit time	60 s
THERMAL	
First wall conduction	3-5 s
First wall bulk temperature rise	15-30 s
Liquid breeder conduction (Li)	30 s
Solid breeder conduction ($\frac{1}{2}$-cm plate)	50-100 s
(1-cm plate)	200-400 s
200 K coolant bulk temperature rise (4000 MW_t):	
Liquid Li blanket	100 s
Liquid LiPb blanket	1500 s
Solid breeder bulk temperature rise ($LiAlO_2$, 300-1000°C):	
Front (near plasma)	120 s
Back (away from plasma)	1800 s
MATERIAL INTERACTIONS	
Dissolution time for Fe in Li (500°C)[a]	40 days
TRITIUM	
Diffusion through Structure[b]	
V, 800 K	1.7 hours
V, 600 K	2.5 hours
316SS, 800 K	10 days
316SS, 600 K	150 days
Solid Breeder (water-cooled $LiAlO_2$, 0-2 μm grain)	
Solubility response	8-200 s
Diffusion:[c]	
1250 K	8-200 s
750 K	13-300 hours
Overall release rate:[d]	
67% of equilibrium	60 s
99% of equilibrium	2 months
Surface adsorption[e] (isotopic exchange)	3-10 hours
Inventory:[d]	
67% of equilibrium	6 months
99% of equilibrium	4 years
Liquid Breeder[f]	
Molten salt extractor ^3H residence	10-20 min
Tritium inventory (0.5 kg/day burnup):	
LiPb	30 min
Li	20-40 days

Footnotes for Table 3.2-3

[a]D. R. Olander, "Fundamental Aspects of Nuclear Reactor Fuel Elements," TID-26711-P1 (1976).

[b]B.L. Doyle and D.K. Brice, "Steady State Hydrogen Transport in Solids Exposed to Fusion Reactor Plasma, Part II: Applications of Theory," J. Nuclear Materials, 122-123, 1523-1530 (1984). (Note: Oxide layers may slow down transport into the metal.)

[c]See Section 2.2 of this report.

[d]Ref. [1], Section 5.2.3.2.

[e]R.G. Clemmer, et al., "The TRIO Experiment," ANL-84-55, Argonne National Laboratory (1984).

[f]"Blanket Comparison and Selection Study - Interim Report," ANL/FPP-83-1, Argonne National Laboratory (1983), p. VII-99.

Table 3.2-4 Reference Burn Cycle Times (in seconds)

Burn Time	
<200	Short Burn
>5,000	Long Burn
>10,000	Quasi-steady State
Plasma Startup/Shutdown	
15	
Dwell Time	
20	Minimum Time to Evacuate
100	Relaxed Requirements on Vacuum Pumps, Ducts, Etc.

There are two situations which cannot be accommodated by this simplified structure: threshold effects and interrelated processes with different time constants. Structural responses provide good examples of important threshold effects. For example, irradiation of ferritic steels generally increases the transition temperature from ductile to brittle behavior (DBTT). If the blanket temperature falls below the DBTT due to plasma cycling, then the test module structural response could be dominated by low temperature effects unlike a reactor blanket. Another example is high cycle fatigue, which might not be important in a continuous burn reactor. Table 3.2-5 lists some of the known time-dependent threshold effects.

Interrelated time constants also complicate the definition of test requirements. For example, even though corrosion is dominated by long time constant processes, it is also strongly affected by blanket temperatures, which have relatively short time constants. The cyclic effects on temperature could result in significantly different corrosion behavior, such as temperature-sensitive chemical reactions and redeposition. Another example is temperature-dependent swelling. It is difficult to predict all of the effects of cycling because of the large number of important interrelationships between phenomena which exist in a blanket.

Table 3.2-5 Examples of Threshold Effects in a Fusion Blanket

Temperature-dependent chemical reactions
High-cycle fatigue, fracture mechanics
DBTT - low temperature embrittlement
Solid breeder thermal fracture
Plastic deformations, especially ratchetting

In Section 3.2.2.1, transient tritium transport and inventory are modeled using a finite difference numerical solution. Because of the strong dependence of tritium behavior on temperature, a transient thermal calculation is coupled to the analysis.

In Section 3.2.2.2, transient MHD fluid flow is modeled. This analysis considers primarily the response of the fluid to rapid changes in the magnetic field strength.

In Section 3.2.2.3, transient thermal behavior in liquid metal blankets is discussed. Thermal time constants are generally much longer than hydrodynamic time constants.

3.2.2.1 Solid Breeder Thermal and Tritium Behavior

The transient thermal and tritium behavior of solid breeders are analysed in this section and their effect on the test operating time requirements is discussed. The aim is to find out what requirements are imposed on the test operation by the need to observe these behaviors at experimental conditions appropriately approximating reactor conditions.

Time constants can be computed to give an indication of the transient responses for thermal and tritium diffusion in solid breeders under unsteady conditions. The time constant for thermal diffusion is calculated from $\delta^2 \rho C_p / k$, where δ, ρ, C_p, and k are the solid breeder diffusion length, density, specific heat capacity and thermal conductivity respectively. Similarly, the time constant for tritium intra-granular diffusion is calculated from δ^2/D where D is the tritium diffusion coefficient for the solid breeder. Note that the tritium diffusion time constants are based on experimentally-determined

values of the diffusion coefficient which have a wide range of uncertainty, as shown in Section 2.2.

Figures 3.2-1 through 3.2-3 show the time constants for tritium diffusion and thermal diffusion as a function of temperature for three different solid breeders: Li_2O, γ-$LiAlO_2$ and Li_4SiO_4. Because of the uncertainties associated with the tritium diffusion coefficient, the corresponding time constant is shown within an uncertainty band which is narrowest for Li_2O and widest for Li_4SiO_4. The uncertainty in the thermal diffusion time constant is not shown as it is relatively small, the major component being the uncertainty of about 30% in the thermal conductivity data. The tritium diffusion coefficient for $LiAlO_2$ is significantly lower than those of Li_2O and Li_4SiO_4 but the time constants shown are of the same order. This is because the grain size used for $LiAlO_2$ (0.2 μm) is much smaller than those used for Li_2O (3 μm) and Li_4SiO_4 (2 μm). These grain sizes are consistent with those practically achievable and with the magnitude of the diffusion coefficient. For the test program, it is conceivable that the grain sizes of the Li_2O and Li_4SiO_4 cases could be reduced, thereby reducing the time constant. In this respect, $LiAlO_2$ is at a disadvantage since it would be very hard to further reduce its grain size.

A number of comments can be made from the curves in Figures 3.2-1 through 3.2-3 with respect to the fusion test requirements if the time constants are assumed to give an indication of the burn times necessary to achieve steady state during one cycle of operation.

1. The time needed to reach steady state is virtually always governed by tritium diffusion, except at higher temperatures where both the tritium and thermal time constants are of the same order.
2. Reducing the temperature from 1000 K to 700 K, which might be the range of temperature in a test section, causes a slight decrease in the thermal diffusion time constant but an increase of orders of magnitude in the tritium diffusion time constant.
3. The lowest test section temperature will determine the time required to reach steady state and for a time constant of the order of 100-500 s, the lowest temperature should be about 1000 K, 1100 K and 900 K for Li_2O, $LiAlO_2$ and Li_4SiO_4 respectively, based on the average tritium diffusion time constant.

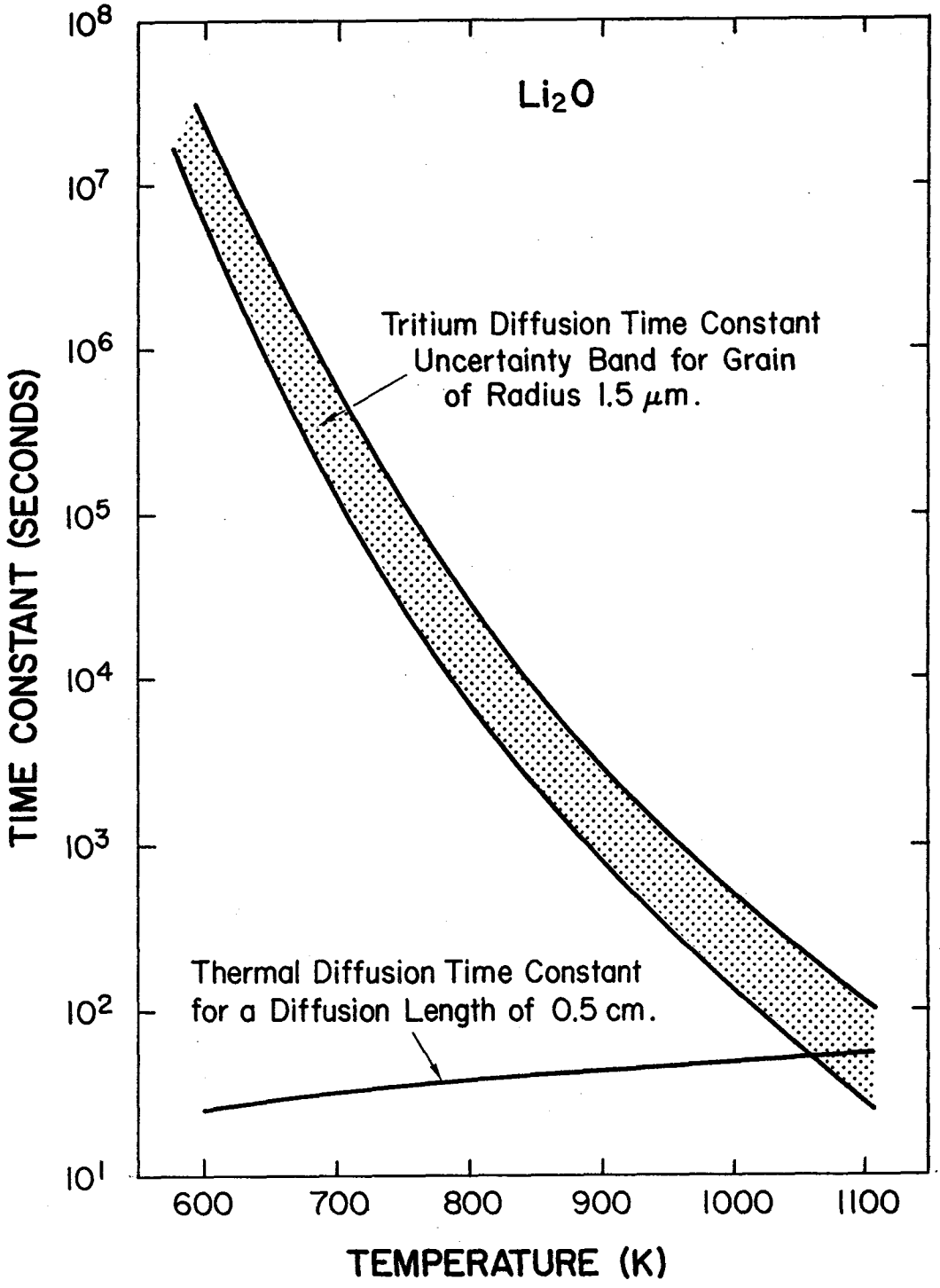


Figure 3.2-1 Tritium and thermal diffusion time constants as a function of temperature - Li_2O

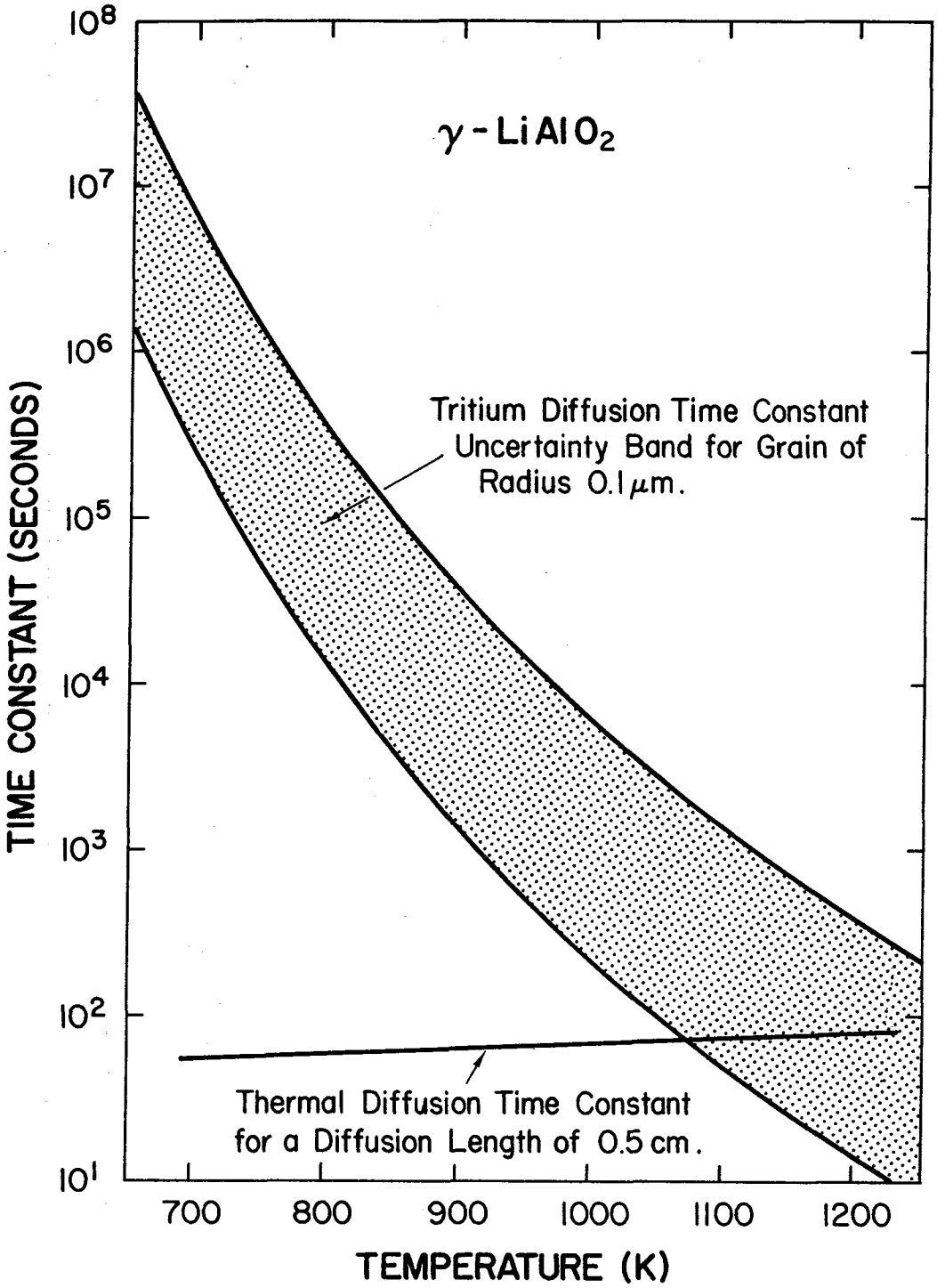


Figure 3.2-2 Tritium and thermal diffusion time constants as a function of temperature - γ-$LiAlO_2$

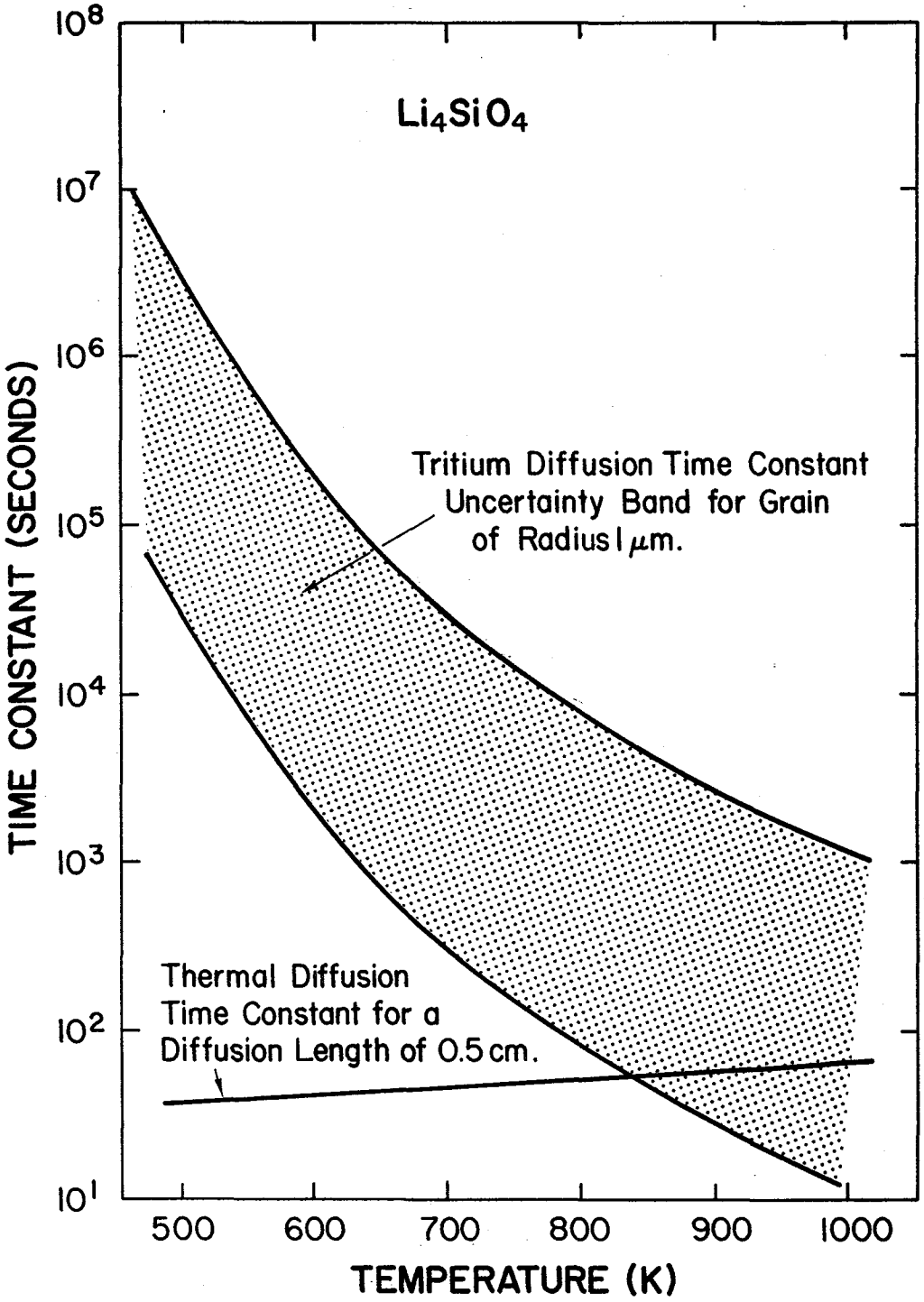


Figure 3.2-3 Tritium and thermal diffusion time constants as a function of temperature - Li_4SiO_4

Time constants for other tritium processes, such as solubility and surface adsorption, can be estimated from experimental results or from an understanding of the mechanisms involved in the process. Results from the TRIO[9] and LISA[10] experiments, for instance, suggest that the time response for surface adsorption (based on isotopic exchange) is of the order of 1-10 hours. The solubility time response is assumed to be of the same order as that for intra-granular diffusion assuming it is controlled by the diffusion of the soluble species in the lattice.

To illustrate the effect of cyclic operation on the temperature distribution and tritium behavior, use was made of the code described in Section 4.6. The code solves the transient heat conduction equation using the Alternating Direction Implicit finite difference technique for a typical solid breeder plate of rectangular cross-section with helium coolant flowing on each side radially away from the plasma. The results give the temperature distribution over the plate as a function of time, which can then be used as input for the tritium modeling. The tritium modeling yields the tritium concentration along the tritium transport stages which consist of intragranular diffusion, grain boundary diffusion and pore diffusion. Tritium solubility and surface adsorption are also included for the purpose of this calculation by considering them as source terms for the grain and grain boundary diffusion respectively. The aim is to obtain an indication of the time responses of the different tritium diffusion mechanisms and of how they interact with the other tritium processes when operating in pulses.

Figure 3.2-4 shows the temperature distribution over half the plate thickness at the plate front end for four cycles of operation. The solid breeder considered is $LiAlO_2$ whose property data are listed in Section 2.2 and the nuclear heat generation is 65 W/cm^3. The burn time is 200 seconds, the dwell time 50 seconds and the ramp-up and down times 12 seconds each. It can be seen from the figure that the temperature distribution over each cycle is essentially the same, which means that the response time is quite fast (of the order of 25 seconds as expected from Figure 3.2-2). Since the response time is fast, the temperature also falls quickly during the dwell time which means that, on average, the temperature is significantly lower than the maximum temperature at each location (by about a third or a fourth). Thus, although the maximum temperature in the test reactor would be prototypic, the

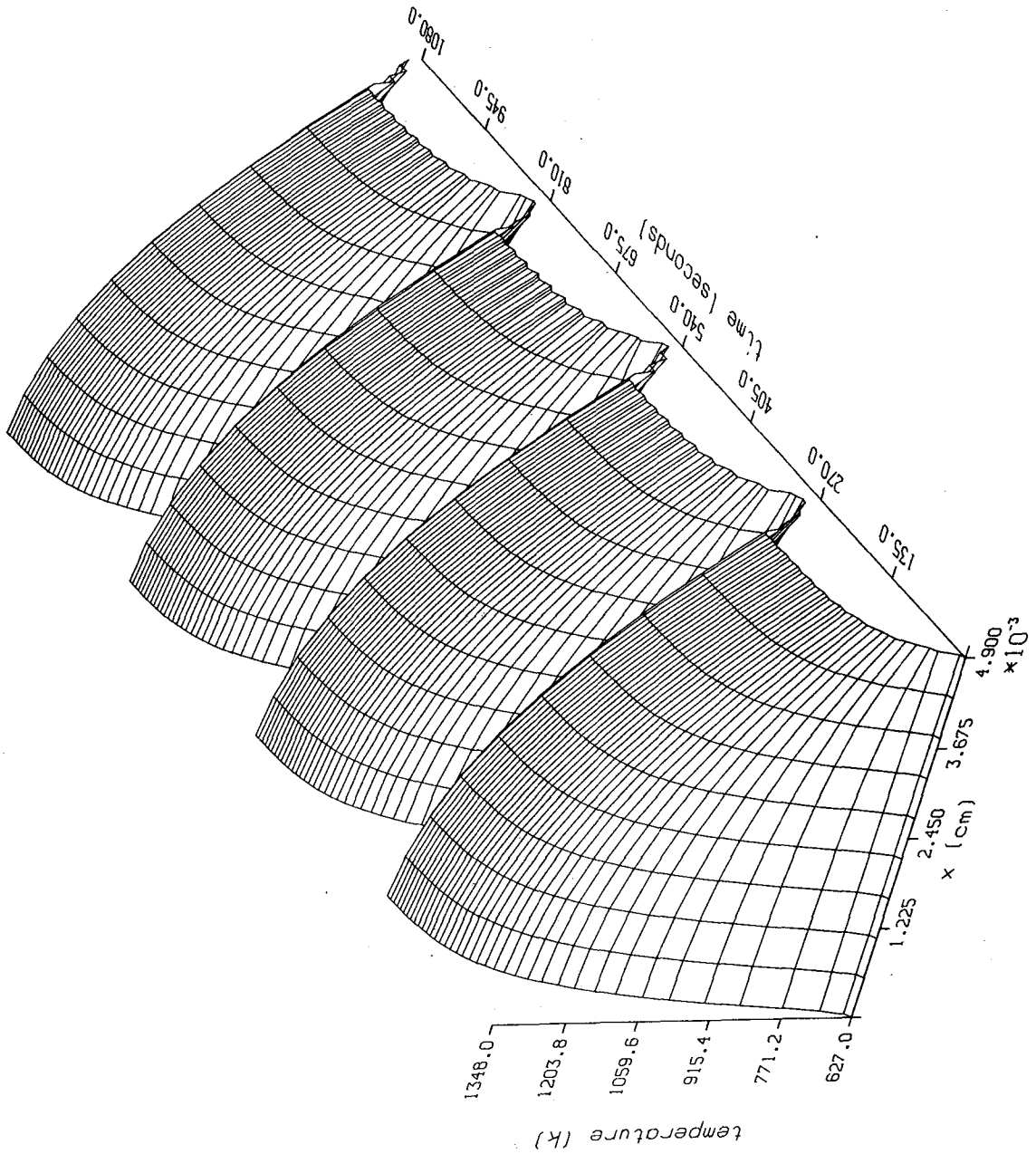


Figure 3.2-4 Solid breeder temperature profiles under pulsing

experimental measurement of temperature dependent phenomena (tritium release) in such a pulsed test reactor would reflect lower than prototypic temperatures.

Figure 3.2-5 shows the corresponding tritium diffusive concentration (based on the tritium generation in one grain) in the grain, grain boundary and pore as a function of time for a $LiAlO_2$ grain located at the center of the plate front end (at x=0 in Figure 3.2-4). A non-dimensional effective radius is used as a variable corresponding to the diffusion path lengths (0-1.0 represents intra-granular diffusion, 1.0-2.0 grain boundary diffusion and 2.0-3.0 pore diffusion). The grain boundary diffusion and pore diffusion are assumed to be much faster than intra-granular diffusion. Figure 3.2-5 indicates that, based on the parameters considered for this calculations, it takes about four cycles for the maximum tritium concentration in the grain to be achieved. Since surface adsorption equilibrium was assumed to occur over hours, it did not affect the tritium diffusive concentration over the time period shown here.

Figure 3.2-6 shows the tritium release rate from one grain to the purge flow (at an effective non-dimensional radius of 3.0) as a function of time. The tritium generation rate in the grain is also shown in the figure and illustrates the burn, dwell and ramp times considered for each cycle. The release rate takes about three cycles to reach its short-term maximum value. The tritium release per cycle is not equal to the corresponding tritium generation rate in the grain for the time period shown because of the long surface adsorption response time. It is anticipated that at times of the order of the surface adsorption response time (1-10 hours), the surface adsorption process will reach some type of quasi-steady state and that the tritium released per cycle will then approach the tritium generated per cycle. The release rate shows two peaks per cycle. This is an interesting behavior observed for the 100-second solubility time response assumed in the calculations. The release rate first begins to decrease due to dissolution. The second peak occurs when the dissolution mechanism saturates.

To summarize, the thermal time constants for solid breeders tend to be shorter than the tritium time constants. The maximum breeder temperature is reached during each cycle for a test reactor operating in pulses with typical burn, dwell and ramp times of 200, 50 and 12 seconds respectively. However, at

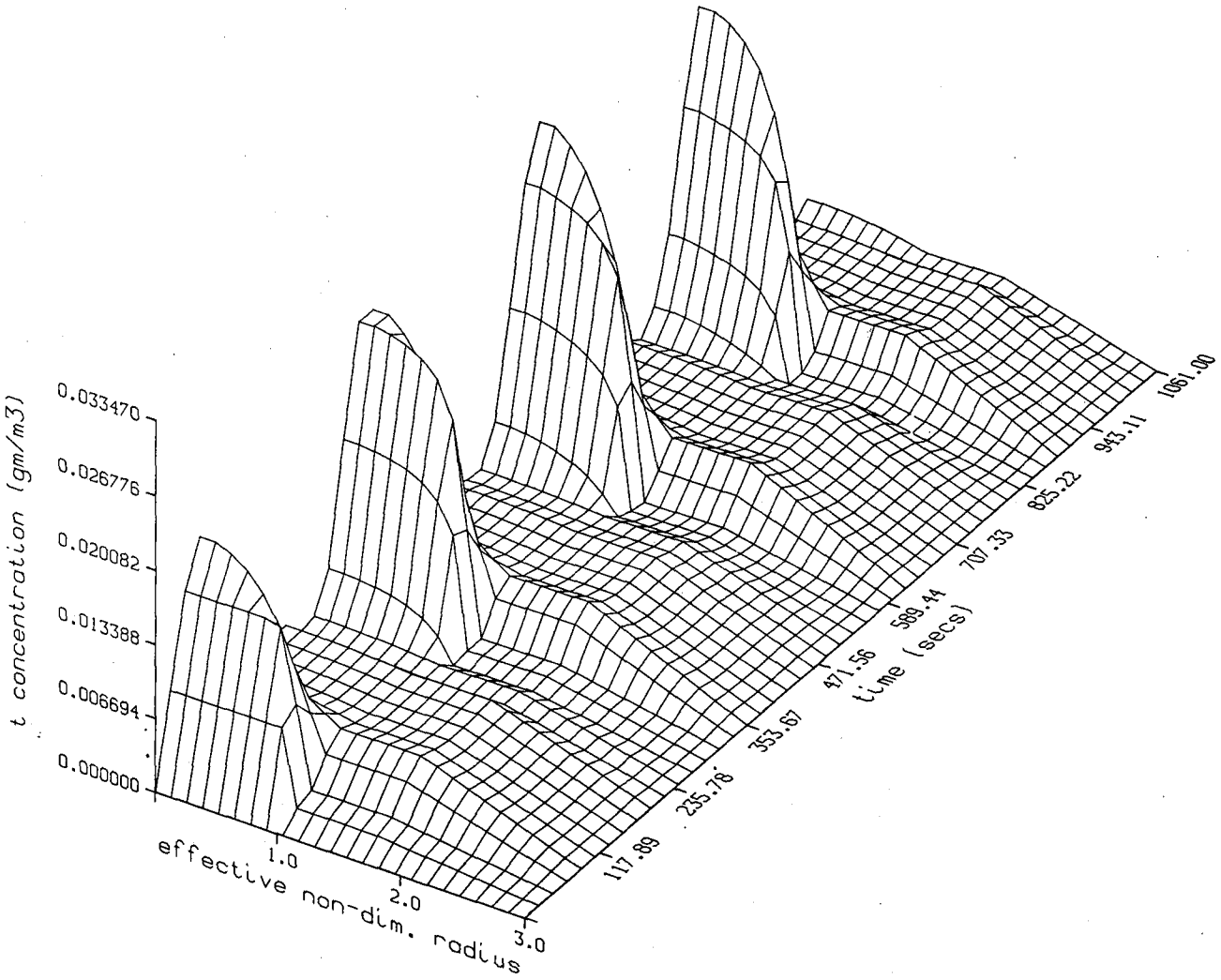


Figure 3.2-5 Transient tritium release rate from 0.2 μm grain $LiAlO_2$ (for 200-s burn, 50-s dwell, and 12-s ramp times)

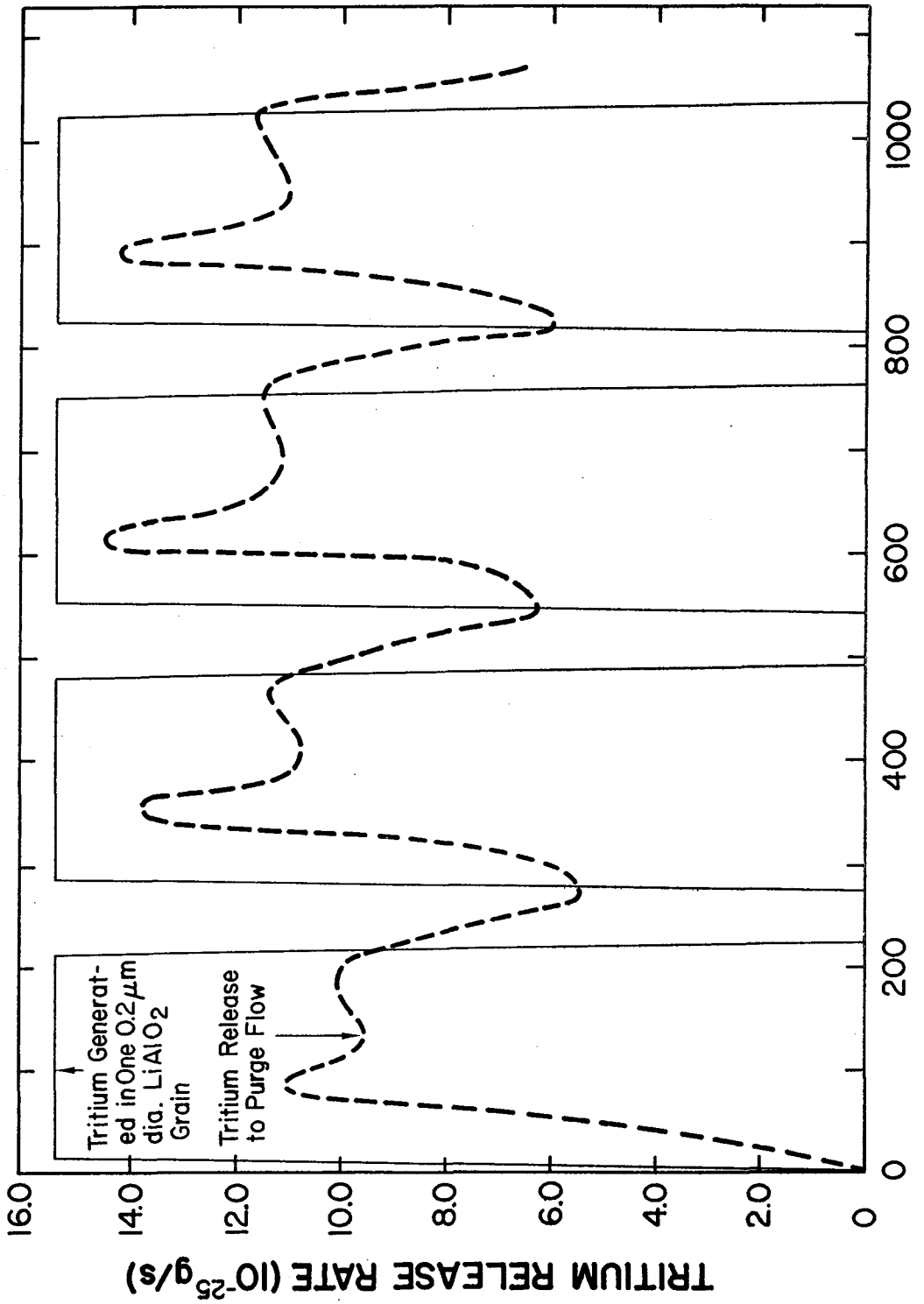


Figure 3.2-6 $LiAlO_2$ diffusive tritium concentration profiles with 200-s burn, 50-s dwell, and 12-s ramp times (microscopic calculation)

any solid breeder location, the effective average temperature over the cycle is significantly lower than the corresponding temperature during steady state operation. The tritium diffusive concentration and release rate to the purge flow for the above cyclic operation reach their maximum after 3 or 4 cycles. The tritium solubility inventory should also reach its maximum value after about the same number of cycles since the solubility time response is assumed to be of the same order as that for diffusion. However, it will take on the order of 1-10 hours for the surface adsorption inventory to reach its maximum value because of its much slower time response and this will determine the necessary test reactor operating time (for steady or pulsed operations) to allow the tritium processes to reach steady or quasi-steady state. The significance of the above discussion with regard to the test operating mode selection (pulsed or steady state) is not clear since it could be argued that understanding and modeling tritium behavior can be achieved under either test mode. It should be stated, though, that the only way to account for any unpredicted changes, in particular in the material properties, which could affect the thermal and tritium behavior of the solid breeder, is to operate the test reactor at prototypic conditions (i.e. in steady state).

3.2.2.2 Unsteady Liquid Metal Flow Behavior

Numerous studies exist for steady MHD flow through ducts[11-13] but only a few studies are available that deal with unsteady MHD flows. Results of such studies are of interest in the design of liquid metal blankets in fusion reactors during startup or shutdown. Also, while a future fusion reactor is intended to operate in steady state, it is likely that a blanket test facility will be pulsed. The power cycling may lead to temperature fluctuations[14] which affect the temperature distribution. It is also probable that the poloidal magnetic field in a test facility will be pulsed. This could have a considerable effect on the coolant velocity profile.

Unsteady MHD flows in channels have been studied analytically under time dependent pressure gradients. Yen and Chang[15] analyzed MHD channel flow with a sudden applied magnetic field, coupled with either a step, periodic or impulsive change in pressure gradient. Singer[16] examined the unsteady forced and natural convective MHD channel flow in a transverse magnetic field. The unsteadiness was caused by prescribed variations in the axial

pressure gradient and/or the wall temperature. He solved the system of linear partial differential equations analytically using Fourier and Laplace transformations.

In most of the transient MHD channel flow studies in a transverse magnetic field, the pressure gradient and/or the wall temperature were the external sources of unsteadiness. The present analysis deals with the unsteady flow of an electrically conducting fluid through a channel in a transverse magnetic field. The analysis considers unsteadiness caused by a prescribed variation in the applied magnetic field and/or the axial pressure gradient.

In this section, 1-D transient MHD flow is studied. The problem can be described by a set of coupled linear partial differential equations which are solved numerically using the finite difference method.

Mathematical Formulation

The equations which describe the one-dimensional flow of an incompressible, unsteady, viscous and conducting liquid are;[16]

$$\frac{\partial u}{\partial t} = -\frac{1}{\rho}\frac{\partial p}{\partial x} + \nu \frac{\partial^2 u}{\partial y^2} + \frac{B_o}{\rho \mu_o}\frac{\partial b}{\partial y} \qquad (3\text{-}1)$$

$$\frac{\partial b}{\partial t} = B_o \frac{\partial u}{\partial y} + \lambda \frac{\partial^2 b}{\partial y^2} \qquad (3\text{-}2)$$

where $u(y,t)$, $b(y,t)$ are the velocity and induced magnetic field in the x-direction (see Figure 3.2-7). B_o is the applied magnetic field in the y-direction. The variables ρ, ν, p, μ_o and λ are the density, kinematic viscosity, pressure, magnetic permeability and magnetic diffusivity ($\lambda = \frac{1}{\mu_o \sigma}$), where σ is the electrical conductivity.

If the channel walls are assumed to be fully insulating, Eqs. (3-1) and (3-2) can be solved subject to the following initial and boundary conditions;

$$u(y,0) = 0.0 \ , \ b(y,0) = 0.0$$
$$u(h,t) = 0.0 \ , \ u(-h,t) = 0.0$$
$$b(h,t) = 0.0 \ , \ b(-h,t) = 0.0$$

and $\frac{\partial p}{\partial x} = \text{constant} = G$

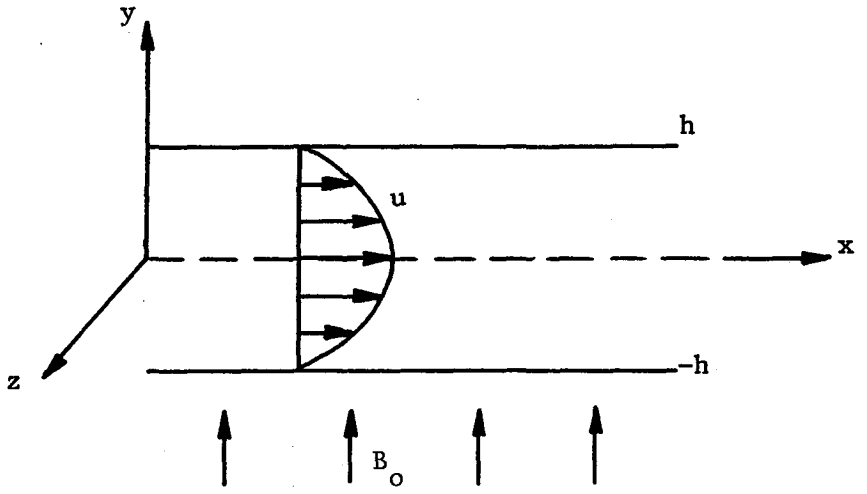


Figure 3.2-7 Channel geometry for transient MHD fluid flow calculation

For a steady fully developed laminar conducting flow in a channel with no transverse magnetic field, the velocity is given by the Hagen-Poiseuille profile;

$$u = \frac{Gh^2}{2\mu}\left(1 - \frac{y^2}{h^2}\right) \tag{3-3}$$

The following non-dimensional quantities can be defined;

$$U = \frac{u}{\left(\frac{G\,h^2}{2\mu}\right)}\ , \quad Y = \frac{y}{h}\ , \quad Ha = B_o h \left(\frac{\sigma}{h}\right)^{1/2}$$

$$R_m = \frac{\mu_o\, \sigma\, h^3\, G}{2\mu}\ , \quad B = \frac{b}{B_o\, R_m}\ , \quad T = \frac{\nu\, t}{h^2} \quad \text{and} \quad Pr_m = \frac{\nu}{\lambda}$$

where Ha = Hartmann number, R_m = magnetic Reynolds number and Pr_m = magnetic Prandtl number.

Finite Difference Equations

To derive the discretization equations of (3-1) and (3-2), we first overlay the region of interest with a computational grid, whose nodal points (each of which is surrounded by its own control volume or "cell") represent the locations at which the velocities and induced magnetic fields will be

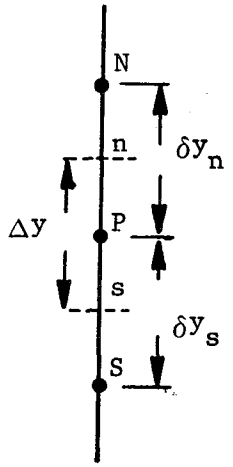


Figure 3.2-8 Grid nodes

calculated. Figure 3.2-8 shows a grid-point cluster of the one dimensional problem.

Attention is focused on the grid point (P) which has the points N (north) and S (south) as its neighbours. The dashed lines show the faces of the control-volume denoted by (n) and (s). For the one-dimensional problem under consideration, the volume of the cell is $\Delta y \times 1 \times 1$, assuming unit thickness in x and z directions. Integrating Eqs. (3-1) and (3-2) over the control volume and over the time interval from (t) to $(t + \Delta t)$, we get;

$$(u_p - u_p^o)\,\Delta y = -\frac{1}{\rho}\frac{\partial p}{\partial x}\,\Delta t\,\Delta y + \nu\left[\left(\frac{\partial u}{\partial y}\right)_n - \left(\frac{\partial u}{\partial y}\right)_s\right]\Delta t + \frac{B_o}{\rho\mu_o}(b_n - b_s)\,\Delta t \qquad (3\text{-}4)$$

$$(b_p - b_p^o)\,\Delta y = B_o(u_n - u_s)\,\Delta t + \lambda\left[\left(\frac{\partial b}{\partial y}\right)_n - \left(\frac{\partial b}{\partial y}\right)_s\right]\Delta t \qquad (3\text{-}5)$$

It is assumed that the new values of u and b prevail over the time step, i.e. a fully implicit scheme is utilized. u_p^o and b_p^o are the values of u and b at the old time step. Linear interpolation functions are used between the grid points to evaluate the derivatives of u and b. Hence, the resulting discretization equations can be written as;

$$u_P a_P = a_N u_N + a_S u_S + S_u \qquad (3\text{-}6)$$

$$b_P a'_P = a'_N b_N + a'_S b_S + S_b \qquad (3\text{-}7)$$

where a_s and a'_s are the coefficients of u and b equations and are given by;

$$a_N = \frac{\nu}{(\delta y)_n}, \quad a_S = \frac{\nu}{(\delta y)_s}, \quad a_P = a_N + a_S + \frac{\Delta y}{\Delta t}$$

and

$$S_u = u_P^o \frac{\Delta y}{\Delta t} - \frac{1}{\rho}\frac{\partial p}{\partial x}\Delta y + \frac{B_o}{\rho\mu_o}(b_n - b_s)$$

Coefficients for Eq. (3-7) can be derived in a similar fashion.

The characteristic times for Eqs. (3-1) and (3-2) are:

$$T_1 = \frac{h^2}{\nu} \quad \text{and} \quad T_2 = \frac{h^2}{\lambda}$$

where T_1 is the time it takes the momentum information to diffuse across the flow and T_2 is the time it takes the magnetic flux to diffuse across the flow. For liquid lithium in a 10-cm channel, $T_1 \sim 10^5$ seconds and $T_2 \sim 1$ second.

The ratio $T_2/T_1 = \nu/\lambda$, which is termed the magnetic Prandtl number, (Pr_m), indicates how fast the magnetic field penetrates the fluid as compared to viscous diffusion. From the characteristic times shown above, it can be seen that the magnetic Prandtl number is very small. In other words, momentum disturbances take a much longer time to diffuse through the flow than magnetic disturbances, which can be assumed to occur instantaneously. Therefore, the choice of the time step is important to resolve physically the momentum information and to obtain a stable solution if the explicit or the Crank-Nicholson procedures are adopted. In the present analysis the fully implicit solution procedure is used, which ensures a stable solution and physically satisfactory behavior. It can be seen that, as $\Delta t \to \infty$, Eqs. (3-6) and (3-7) reduce to the steady-state discretization equations.

The solution of the discretization equations is obtained by the Gaussian-elimination method.

Results and Discussion

Figure 3.2-9 shows the unsteady velocity profile at zero Hartmann number

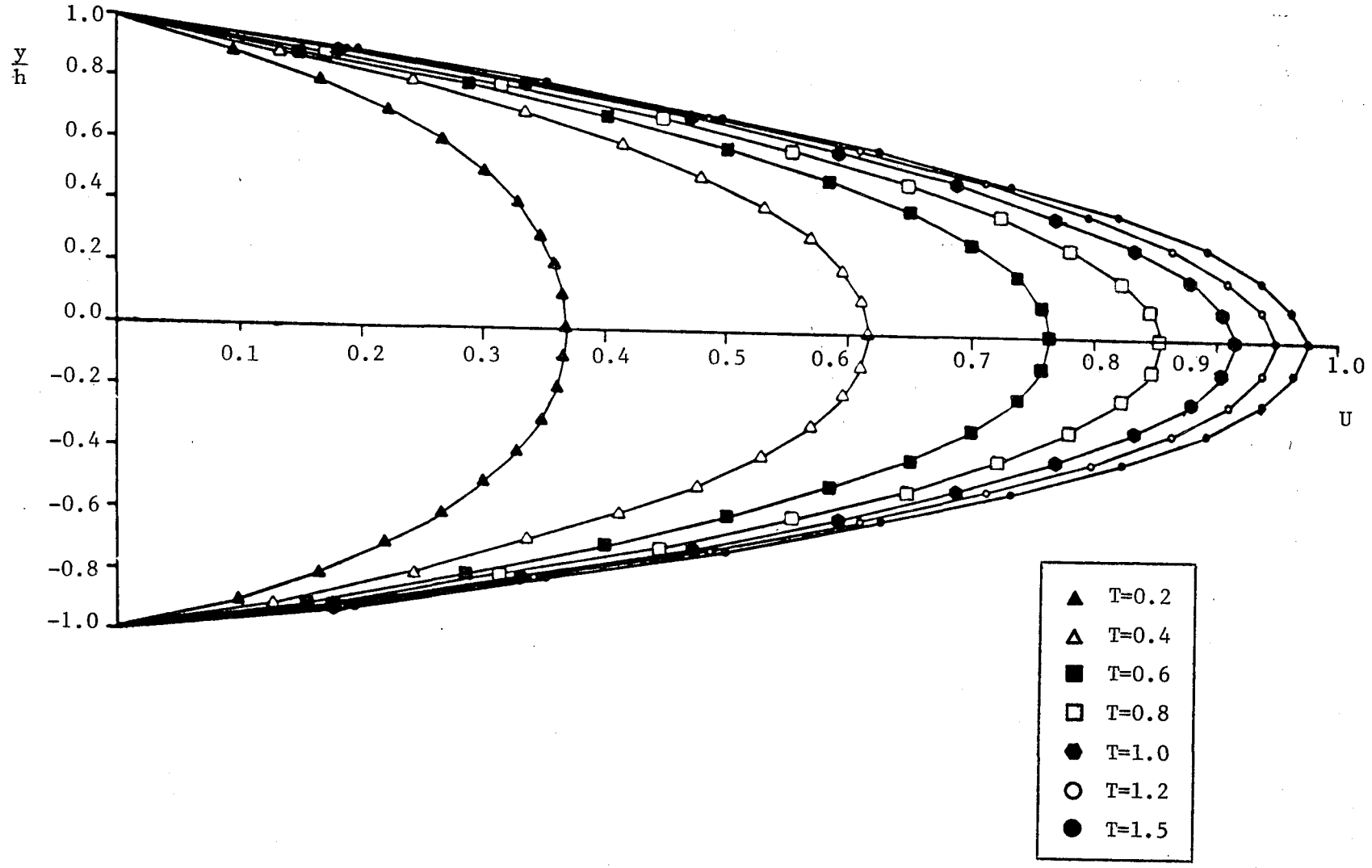


Figure 3.2-9 Unsteady velocity profile with no magnetic field

for a suddenly applied pressure gradient. Initially the fluid is at rest and at time zero, the pressure gradient is suddenly increased to some constant level. The fluid is then set into motion and the velocity asymptotically approaches the steady value. The effect of the magnetic field upon the velocity profile is shown on Figure 3.2-10 for Pr_m=10. In this case the external magnetic field is instantaneously turned on along with the pressure gradient. The effect of the magnetic field applied normal to the channel is to retard the flow. It is noticable in this high Pr_m case that there is a delay between applying the magnetic field and the effect being felt by the fluid, as a result the velocity is larger at T=0.3 than at T=0.8. The variation of the induced magnetic field across the channel is shown on Figure 3.2-11 at two different instances of time. Although the induced field is not and important engineering parameter, it is an integral part of the solution.

The effect of the magnetic Prandtl number on the transient mean velocity can be seen from Figure 3.2-12. Initially the fluid is at rest; at zero time the pressure gradient is suddenly increased to some constant level along with the magnetic field. For Pr_m = 10 (i.e. relatively small magnetic diffusivity) the magnetic field is delayed in penetrating the fluid and as a result an overshoot and oscillation are observed. For flows with relatively large magnetic Prandtl number it is necessary to establish the magnetic field before changing the pressure gradient to avoid these oscillations. As Pr_m is decreased (i.e. increasing the magnetic diffusivity), the magnetic field penetrates the fluid faster and the oscillations are eliminated.

The effects of pulsing the magnetic field are considered next. Figure 3.2-13 shows a typical pulsed magnetic field. Figures 3.2-14 and 3.2-15 show the effects of a pulsed field on the transient mean velocity for different duty factors, d_f, and magnetic Prandtl numbers, Pr_m. The duty factor is defined as

$$d_f = \frac{\text{operating time}}{\text{operating time + dwell time + ramp times}}$$

For higher Pr_m, penetration of the magnetic field is slow and the mean velocity decreases to the steady value corresponding to a steady applied magnetic field. For low values of Pr_m the decrease in velocity is faster. During the

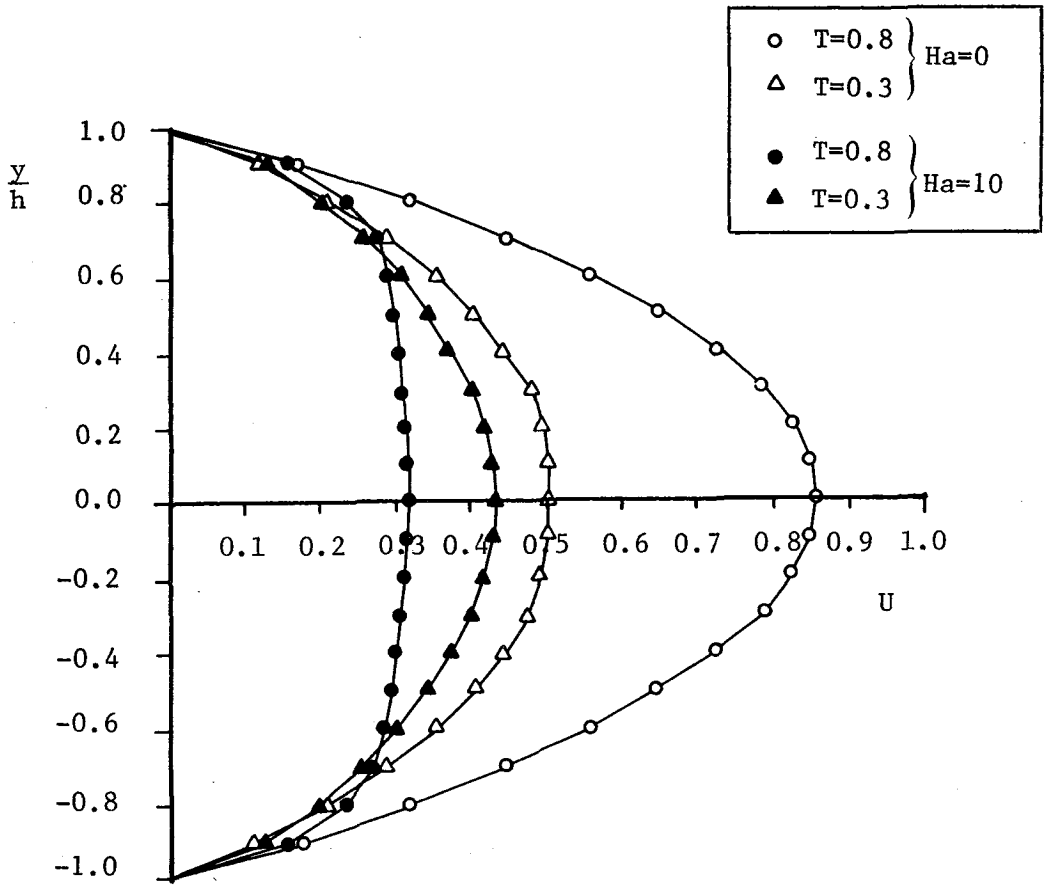


Figure 3.2-10 Effect of magnetic field on velocity profile at two instants of time

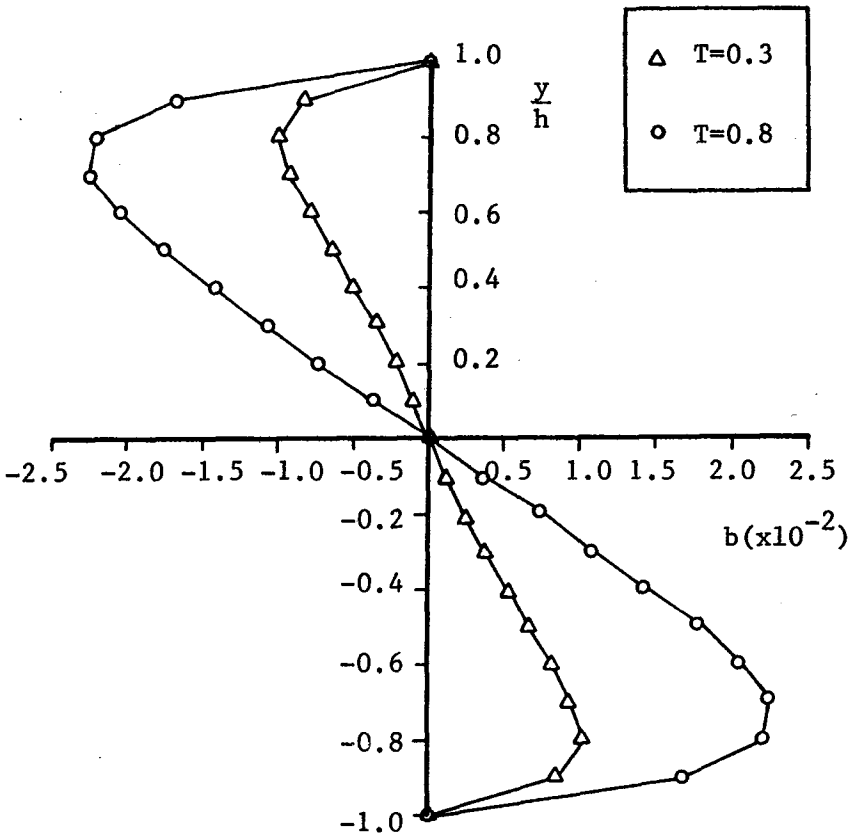


Figure 3.2-11 Induced magnetic field profiles at two instants of time

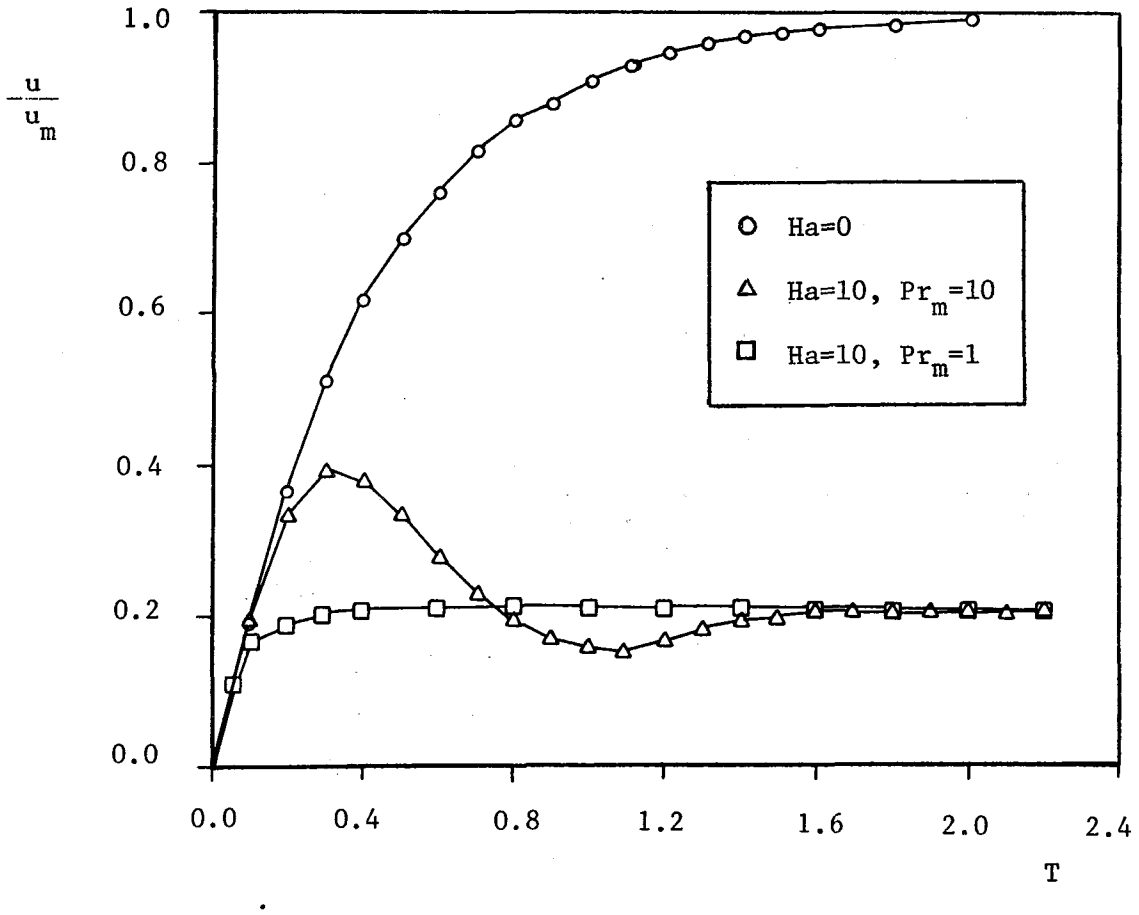


Figure 3.2-12 Effect of magnetic Prandtl number on transient mean velocity

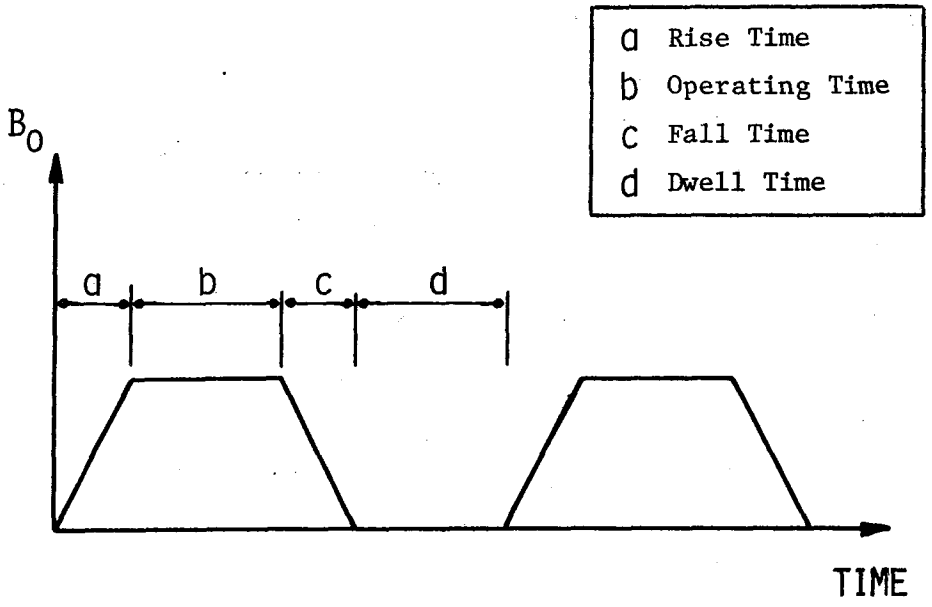


Figure 3.2-13 Pulsed magnetic field

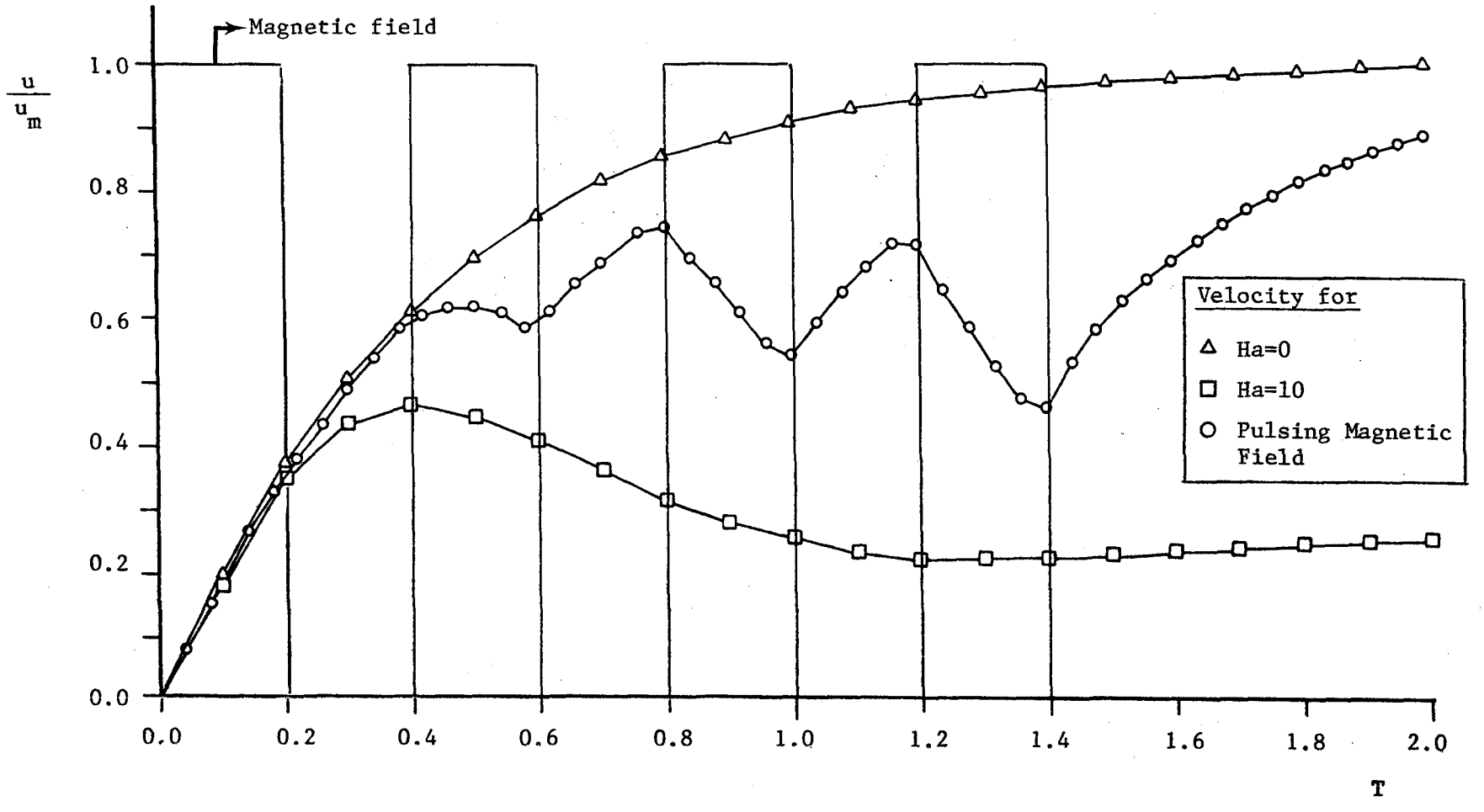


Figure 3.2-14 Effect of a pulsed magnetic field on mean velocity vs. time

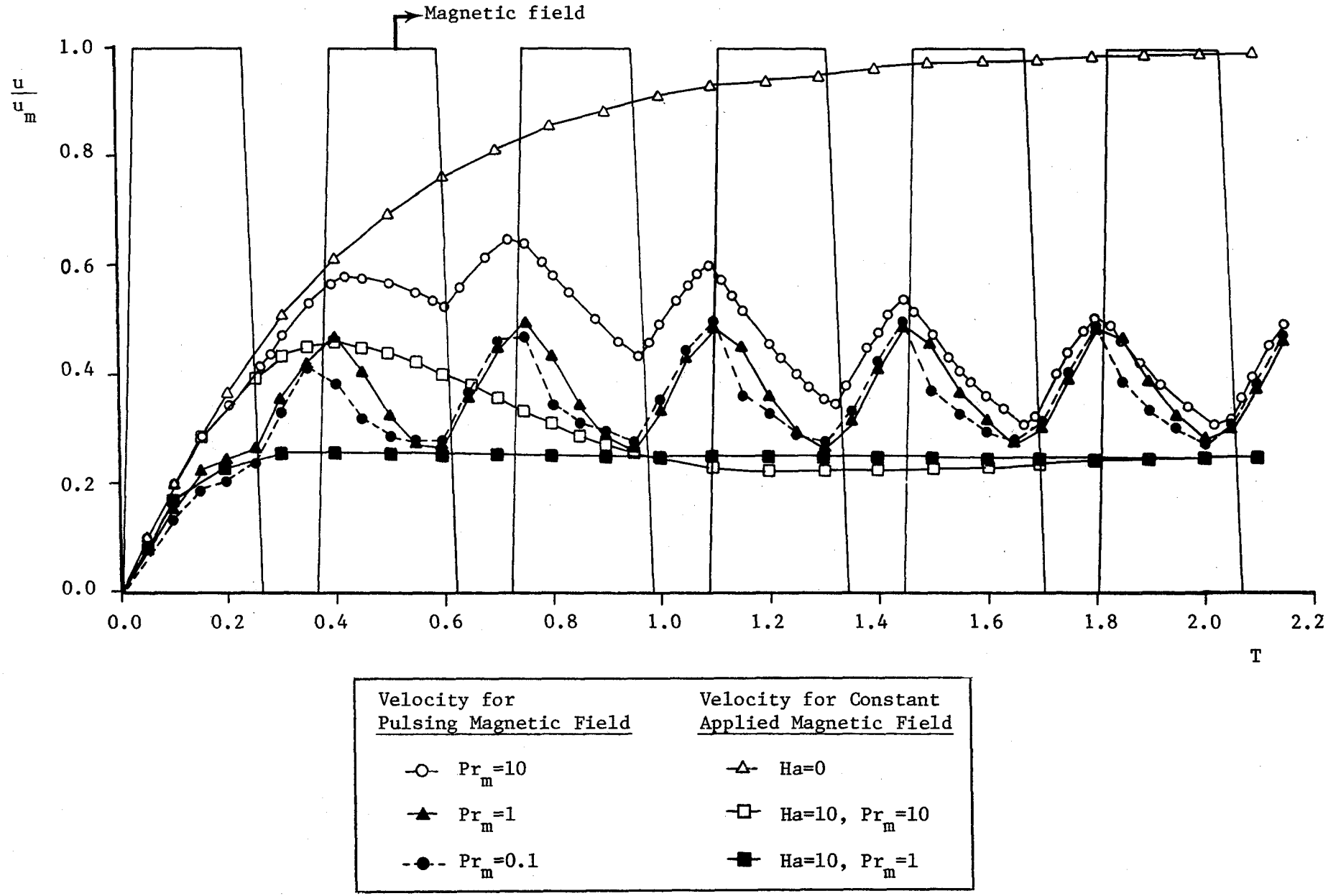


Figure 3.2-15 Effect of a pulsed magnetic field on mean velocity for different Pr_m

dwell time, the mean velocity rises slowly to reach the steady state when there is no magnetic field. However, the rate of velocity rise during the dwell time is independent of Pr_m.

Summary

The effects of a transverse magnetic field and fluid diffusive properties upon the unsteady, fully-developed laminar flow of an electrically conducting fluid through an insulated parallel-plate channel has been numerically analyzed. An oscillatory approach to steady state occurs whenever the magnetic field and pressure gradient are simultanously turned on in a fluid of large magnetic Prandtl number (>10). These oscillations are largely damped by the diffusive character of the fluid when the magnetic diffusivity is increased. Also, if the magnetic field is allowed to become established before the fluid is put in motion, the oscillations can be damped.

If the magnetic field is pulsing at low frequency (i.e., long pulses compared with times to reach steady conditions between a maximum, B_{max}, and a minimum, B_{min}), then the flow will oscillate between a maximum corresponding to an applied field B_{min} and a minimum corresponding to an applied field B_{max}. However, high frequency pulsing (i.e., short pulses compared with times to reach steady conditions) will induce flow oscillations with smaller differences between the maximum and minimum values.

In the present analysis the flow was assumed fully developed, i.e., the fluid inertia was neglected. However, two-dimensional or three-dimensional analysis with the fluid inertia included, may reveal interesting transient behaviors, especially when the flow tries to adjust itself to a pulsing magnetic field.

3.2.2.3 Unsteady Liquid Metal Blanket Temperature Response

It is assumed that future fusion devices will operate under steady neutron wall loads. However, near-term experimental devices may operate under pulsed neutron wall loads. A pulsed neutron wall load directly affects the

blanket temperatures which in turn affects the blanket thermal stresses, tritium permeation and inventory, corrosion and heat recovery. In this section, the effect of cyclic operation on the thermal behavior of a liquid metal blanket is investigated. This analysis is applicable to full scale testing of reference blankets as well as the operation and design of act-alike test modules.

Blanket Characteristic Times

In the FINESSE interim report,[1] the following characteristic times were reported.

1. Coolant residence time (τ_r). This is the time it takes a fluid particle to travel through the blanket. It is an important time scale since it indicates the thermal memory of the blanket. The coolant residence time is given by:

$$\tau_r = \sum_i L_i/u_{b,i}$$

where i = channel segment and L_i = length of channel.

2. Coolant conduction time (τ_c). This is the time it takes the coolant temperature profile across the channel to become quasi-steady:

$$\tau_c = \frac{a^2}{\alpha_c}$$

where a is a characteristic length scale (channel half width) and α_c is the thermal diffusivity of the coolant. In a typical reactor blanket, $\tau_c > \tau_r$, which indicates that the coolant temperature profile is never fully developed within the blanket.

3. First wall conduction time τ_{fw}. This is the time it takes any thermal information to diffuse across the first wall.

$$\tau_{fw} = \frac{a_{fw}^2}{\alpha_{fw}}$$

where α_{fw} is the thermal diffusivity of the first wall. For most fusion blankets, $\tau_{fw} < \tau_r < \tau_c$ in the metallic first wall, which means that a quasi-steady first wall temperature profile is very easy to achieve. If τ_{fw} and τ_r were comparable, then the thickness of the first wall would have to be considered in the analysis.

Analysis

The analysis is carried out by solving the unsteady energy equation. The following assumptions are made:

1. The flow is fully developed.
2. Axial conduction is neglected.
3. Volumetric heat generation is uniform throughout the fluid.

Figure 3.2-16 shows a single coolant channel with constant cross-section. The unsteady energy equation in cartesian coordinates can be written as:

$$\frac{\partial T}{\partial t} = - u \frac{\partial T}{\partial x} + \frac{k}{\rho C_p} \frac{\partial^2 T}{\partial y^2} + \frac{\dot{Q}}{\rho C_p} \qquad (3\text{-}8)$$

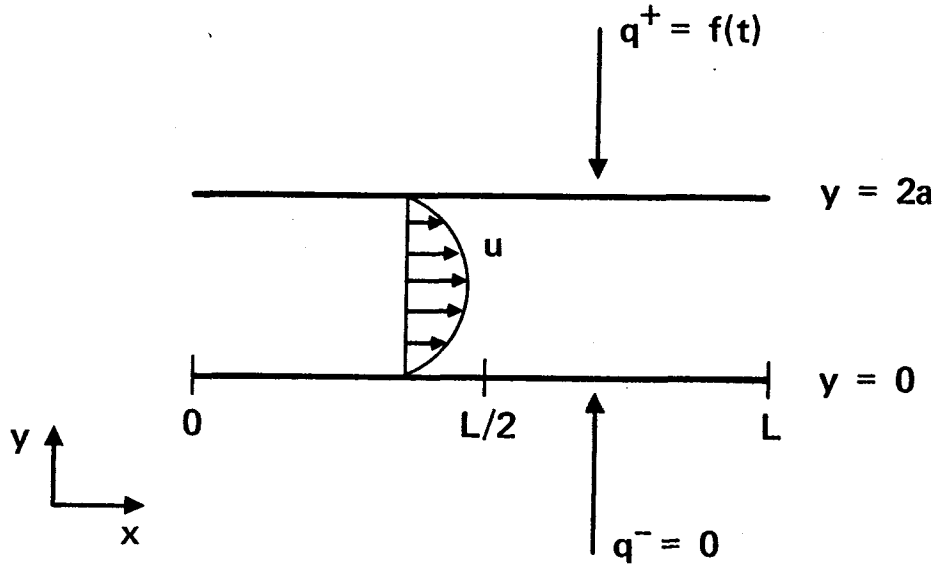


Figure 3.2-16 Single coolant channel geometry

where T is the temperature

Q is the volumetric heat source

u is the coolant velocity

ρ, k, and C_p are the coolant density, thermal conductivity, and specific heat, respectively. The boundary conditions are;

$$\text{upper channel wall, } K \frac{\partial T}{\partial y} = q_w^+ (t)$$

$$\text{lower channel wall, } K \frac{\partial T}{\partial y} = 0$$

where $q_w^+(t)$ is the surface heat flux at the first wall. Using the following non-dimensional parameters;

$$\tilde{\tau} = \frac{t}{L/u} , \quad \tilde{u} = \frac{u}{\langle u \rangle} , \quad \tilde{x} = \frac{x}{L} , \quad \tilde{y} = \frac{y}{2a}$$

$$\Theta = \frac{T - T_o}{\dot{q}\ L/K} , \quad \langle u \rangle = \frac{\int_0^{2a} u\ dy}{2a}$$

The energy equation (3-8) can then be written as:

$$\frac{\partial \Theta}{\partial \tilde{\tau}} = -\tilde{u} \frac{\partial \Theta}{\partial \tilde{x}} + \frac{\alpha}{2a\langle u \rangle} \frac{\partial^2 \Theta}{\partial \tilde{y}^2} + \frac{\dot{Q}\ \alpha}{q\ \langle u \rangle} \qquad (3\text{-}9)$$

with the boundary conditions

$$\frac{\partial \Theta}{\partial \tilde{y}} = 1 \ (\text{at } \tilde{y}=2), \text{ and } \frac{\partial \Theta}{\partial \tilde{y}} = 0 \ (\text{at } \tilde{y}=0)$$

T_o is the inlet coolant temperature = 300°C. The velocity profile u(y) is a specified function of y only. The width of the channel is 4.5 cm and the length of the channel is 10 meters. Equation (3-9) is solved using a fully implicit finite-difference numerical procedure.

Figure 3.2-17 shows the variation with time of the first wall temperature at x=L/2 for a slug, skewed and parabolic velocity profiles in lithium. The first wall in this case is subjected to a constant uniform heat flux of 0.5 MW/m^2 and no volumetric heating. It is noticable that the wall temperature

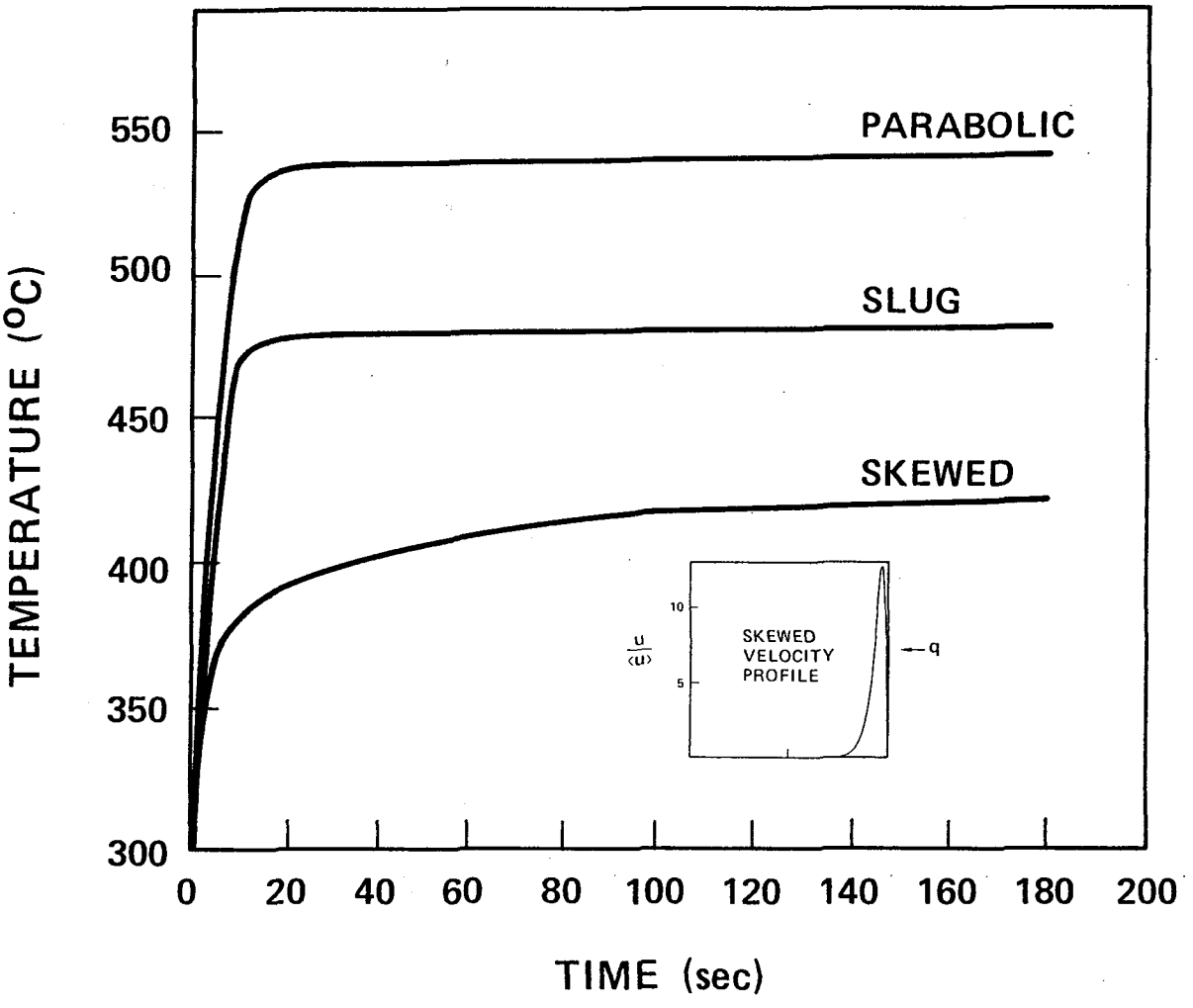


Figure 3.2-17 Transient first wall temperatures of a liquid metal blanket cooling channel at 5 m from the inlet for different velocity profiles

for the slug profile reaches a steady-state much faster than the skewed profile. However, the skewed profile achieves lower first wall temperatures than the slug or parabolic profiles. The reason for this is that most of the flow is through a very narrow region at the first wall, hence the convective capability of the flow is larger near the wall.

Figures 3.2-18 and 3.2-19 show the first wall temperature response (at the middle and end of the channel) to pulsed operation of the wall heat flux for a slug and skewed profiles respectively. The ratio of burn to dwell times is 5:1. Again the slug profile reaches a quasi-steady response much faster than the skewed profile.

Figures 3.2-20 and 3.2-21 show the first wall temperature response to pulsed wall heat flux for a slug and skewed profiles. The ratio of burn to dwell times is 5:2.

Summary

The convective heat transfer capability of the coolant is closely related to the hydrodynamics of the flow. The assumption that slug flow correctly represents high Hartmann number flows is valid provided the thermal boundary layer is sufficiently thick. In cases where this approximation is not valid, there may be significant effects on heat transfer. In liquid metal blankets, Hartmann numbers are of the order of 10^4-10^6, resulting in hydrodynamic boundary layer thicknesses of the order of microns -- much thinner than normal thermal diffusion scale lengths.

Regarding heat transfer at high heat flux operation (regardless of whether the neutron wall loading is cyclic or continuous), the slug profile will usually yield the lowest first wall temperatures. However, Hartmann profiles will result in slightly higher first wall temperatures than those obtained by assuming a slug profile, since at the walls the axial convection is zero due to the no-slip boundary condition. For profiles which are skewed towards the first wall (as in the flow turning from a poloidal direction to a toroidal direction in the BCSS[5] blanket design) the first wall temperature would be lower than that obtained from a slug profile.

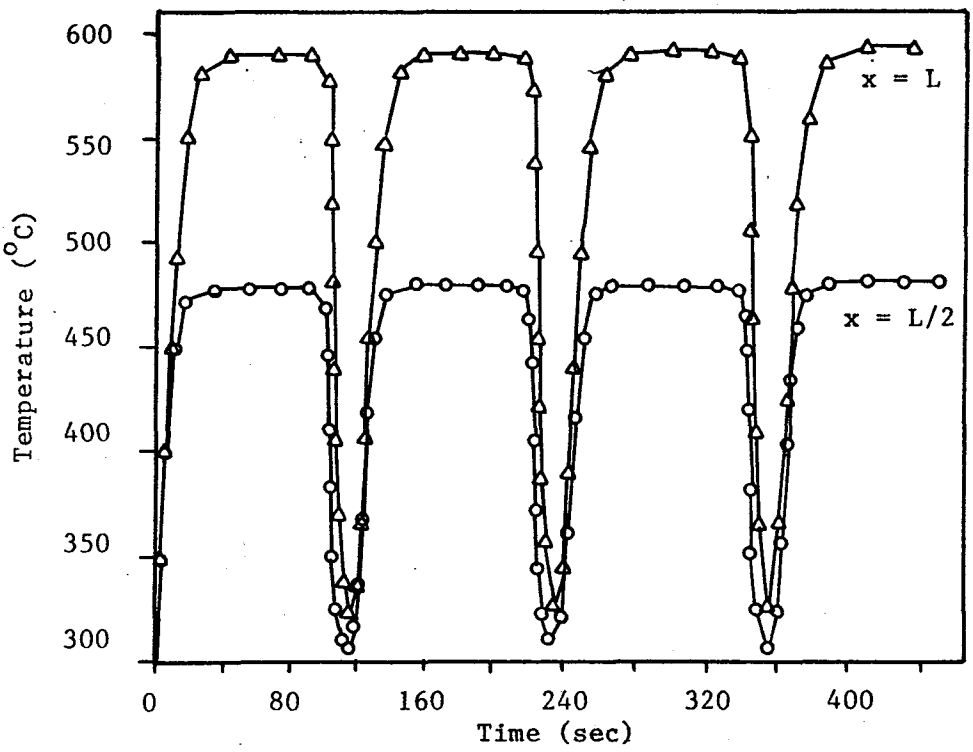


Figure 3.2-18 Transient first wall temperature for a slug velocity profile, 5:1 duty cycle

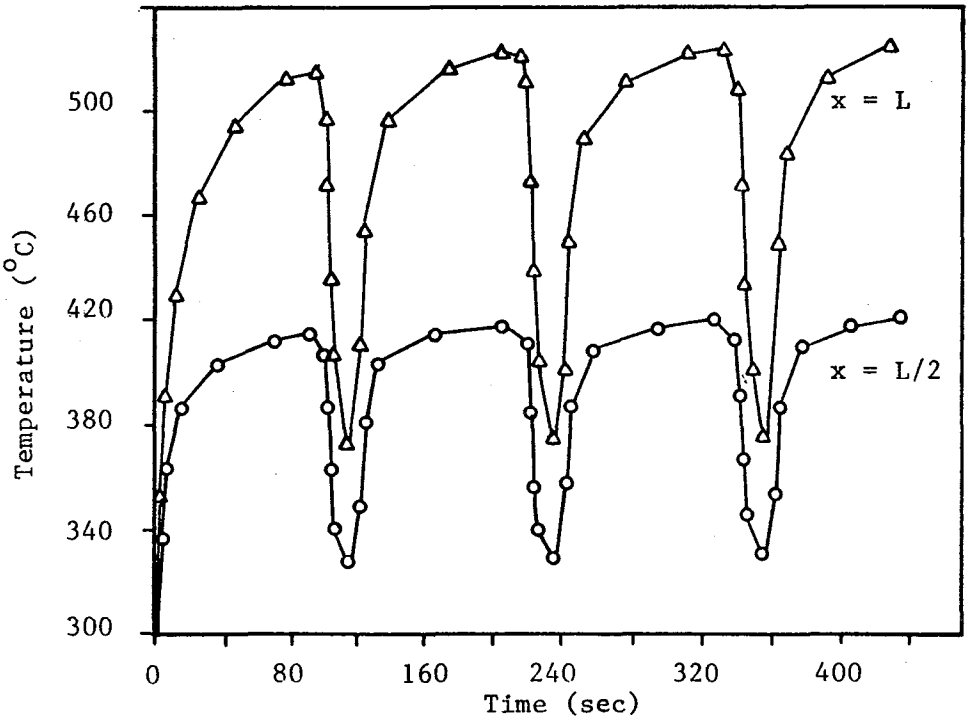


Figure 3.2-19 Transient first wall temperature for a skewed velocity profile, 5:1 duty cycle

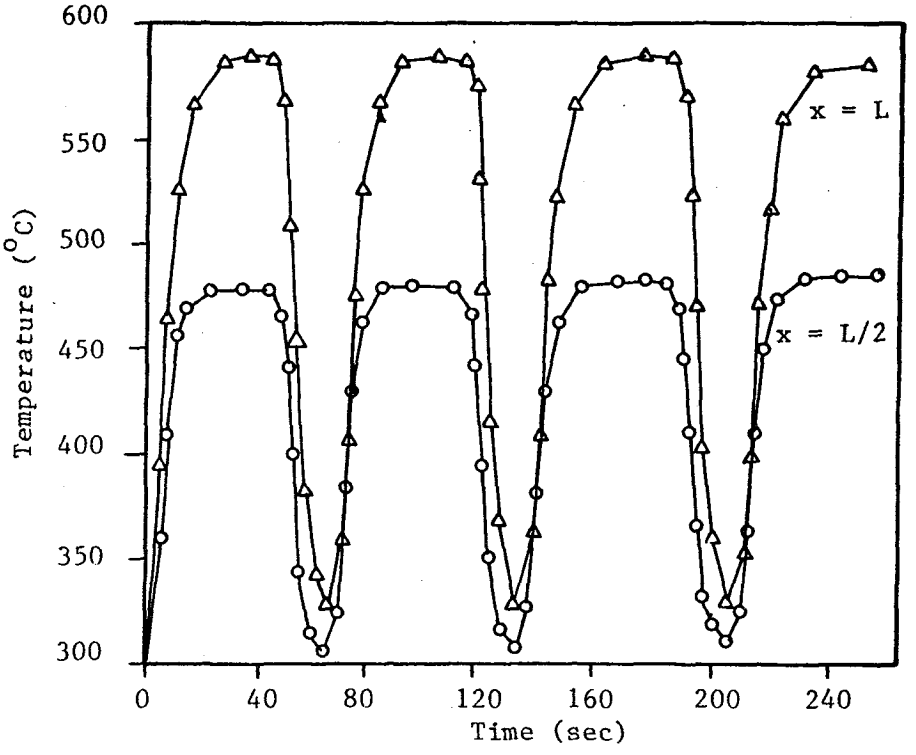


Figure 3.2-20 Transient first wall temperature for a slug velocity profile, 5:2 duty cycle

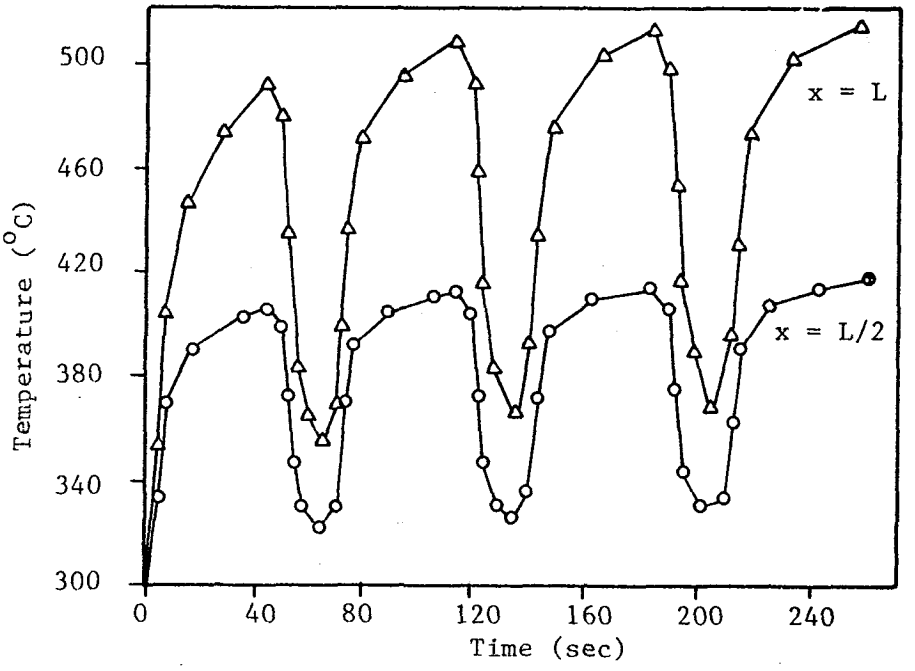


Figure 3.2-21 Transient first wall temperature for a skewed velocity profile, 5:2 duty cycle

3.3 External Tritium Supplies

The availability of tritium is a significant concern for next generation fusion devices. For example, NET (600 MWf) would require about 6 kg/yr of tritium averaged over a 10-15 year operating life,[17] with projected DT startup in 1998. The various external tritium sources that could contribute to the tritium supply for this and similar devices are summarized here.

3.3.1 Natural Tritium

With a half-life of 12.3 years, any tritium in the terrestrial environment is due to recent or chronic natural sources. The primary natural source is through the interaction of cosmic ray particles with the N_2 and O_2 of the upper atmosphere, and the accretion of tritons emitted during solar flares. Tritium produced through fission of natural uranium ores is a much smaller source (a few percent) and leads to tritium that is bound in the earth's crust and inaccessible.[18]

The atmospheric bomb tests in the late 1950's swamped the natural tritium and have made it very difficult to estimate the natural production rate. It is generally accepted as 0.25 atoms/cm^2-s, or 0.18 kg/yr, with a global inventory of 3.6 kg.[18]

3.3.2 Bomb Test Tritium

Atmospheric bomb tests in the late 1950's and early 1960's released about 500 kg of tritium into the atmosphere. This has essentially stopped since 1962, with about 145 kg remaining in 1986 as this tritium decays. Since the oceans are a large sink for hydrogen (by isotopic exchange), the present distribution of the total environmental tritium is: 0.6 kg atmosphere, 18 kg continental waters, and 129 kg oceans.

3.3.3 Fission Reactions

Tritium is produced in fission reactions at about 0.3-2 g/GWe-yr (10^{-4} T/fission ^{235}U).[19,20] For a typical fuel lifetime of 3 years, the total tritium inventory in a light water reactor (LWR) is 1-6 g (100 Mg U fuel) since generally less than 1% of this tritium is lost by permeation in zircaloy clad fuel.[20] This fission tritium is fairly evenly distributed between the fuel matrix and the zirconium cladding.[19]

This tritium could be recovered in fuel reprocessing. In voloxidation processes, the fuel is heated and most of the fuel matrix tritium would be released as HT. In dissolution processes, the fuel (and cladding) are dissolved in acids, and any tritium would be released as HTO and diluted in the solution. Tritium and other fission products would normally be scrubbed from the effluents.

A 1000 Mg U/yr reprocessing plant would process about 10 full LWR fuel loads per year. At a fuel burnup of 35 GWd/Mg U (about 5×10^{-5} kg T/Mg U[19]), the total potential tritium production would be 0.05 kg/yr (0.1 kg T/yr assuming the cladding is also processed). Presently, around 300 Mg U/yr of commercial fuel is reprocessed. The La Hague facility in France, for example, processed 220 Mg U in 1983.[21] The projected commercial reprocessing capacity includes: 1600 Mg U/yr at La Hague, France (800 Mg U/yr in 1988, another 800 Mg U/yr in 1991), 800 Mg U/yr at JNFS, Japan (1995), 350 Mg U/yr at DWK, West Germany (1994) and 120 Mg U/yr at Eurochemie, Belgium (1989).[21] These facilities could in principle supply 0.1-0.3 kg T/yr.

3.3.4 Heavy Water Absorption

In heavy-water moderated reactors such as CANDUs, some neutrons are absorbed in the heavy-water (D_2O) moderator, leading to production of tritium from $D(n,\gamma)T$ reactions. In present CANDU reactors, this occurs at about 0.23 kg T/GWe-yr.[20] There is presently about 12 GWe of CANDU reactor capacity in the Ontario Hydro electric grid, 3.6 GWe under construction in Ontario, and a further 4 GWe of CANDU (and other) heavy-water moderated reactors elsewhere.[22]

This heavy-water produced tritium normally remains in the moderator water. When the tritium concentration becomes a significant radiological or operational hazard, it is reduced by replacing or diluting the moderator with fresh D_2O. At Ontario Hydro, the continuing startup of newly commissioned reactors has provided the opportunity to reduce the peak concentrations by spreading the tritiated heavy water around the new reactors. Tritium concentrations in the older CANDU reactors (Pickering A and Bruce A) are 20-30 Ci/L in the moderator and 1.5-2 Ci/L in the primary coolant.[20] The present inventory of tritium in Ontario Hydro CANDU reactors is roughly 8 kg, and growing by about 2 kg/yr.

Facilities for extraction of tritium from heavy-water moderator exist at Grenoble (France), and possibly Savannah River (US). Large facilities are being commissioned at Darlington (Canada) and Chalk River (Canada) to remove tritium from CANDU heavy water moderator. The latter facilities are able to process 370 kg D_2O/hr and 20 kg D_2O/hr respectively, at typical concentrations of 3-30 Ci/kg with 95-97% removal efficiency.[20] Initially, there will be a large amount of tritium produced as the present high tritium concentrations are reduced. In steady-state with Canadian CANDU reactors, these facilities will yield 2-2.5 kg T/yr.

For Ontario Hydro with the Darlington tritium removal facility, tritium production will equilibrate at 2.3 kg/yr by 1991, and the total by 2001 will be roughly 23 kg (decay corrected). If a second facility were built by 1993, the equilibrium levels would be further reduced, the equilibrium tritium production would be 2.8 kg/yr, and 29 kg would have accumulated by 2001.[20]

3.3.5 Lithium Absorption

It is possible to modify fission reactors to directly produce tritium by replacing fuel or absorber material with lithium. The (n,T) reaction has a very high thermal neutron cross-section in ^6Li (7.5% natural isotropic abundance). ^7Li, with 92.5% natural abundance, will also undergo a (n,T) reaction, but has a reaction threshold around a few MeV.

Dedicated military production reactors use $LiAlO_2$ or LiAl "fueled" rods to achieve very high tritium production rates. Although the exact values are not available, the total international production of tritium for weapons purposes (primarily in the U.S. and U.S.S.R.) is probably on the order of 30-50 kg/yr. Most of the present world tritium supply for commercial processes is obtained from these sources.

Tritium can also be produced as a by-product in a power reactor if some fuel channels or some absorber/control rods were replaced with lithium-bearing materials. The exact amount is limited by requirements on criticality and flux distribution. Since the lithium has a very high cross-section, it tends to burn out very quickly. This means that the lithium must be located where it can be readily removed, or that the associated reactor reactivity change must be compensated by substantial movement of control rods during operation.

LWRs normally operate steadily for as long as possible between shutdowns--typically every 1-1.5 years in present machines. Replacing lithium rods or control/absorber rods more frequently than this would be a major expense. Estimates of enhanced tritium production as LWR by-product are about 0.1 kg T/GWe-yr, at a cost of 2-3 times the current commercial market rate.

CANDU power reactors are much better suited to enhanced tritium production because of the active reactor flux control and material replacement capability available through on-line refueling. This makes it reasonably convenient to replace lithium-bearing elements on a frequent basis, using lithium-bearing rod bundles in some of the channels.

The possibility of using lithium in absorbers, and lithium bundles in several fuel channels in CANDU reactors has been considered.[23] The major requirement was that tritium production would not affect power production. The solution was to use the lithium bundles to provide flux flattening, normally provided by external absorber rods and fuel management strategies. Flux flattening allows all fuel channels to operate at comparable power levels near their operating limits, rather than the entire reactor being limited by the few hottest channels. Flux flattening can be provided by using lithium bundles in the central channels. The operation of the reactor, including flux profile and power levels, could be virtually identical with that without tritium production. The lithium bundles would be moved through the channels at rates slightly slower than the regular fuel bundles, so it would not impose any additional wear on the fueling machines. These lithium bundles could be allowed to cool off and then processed (e.g., vacuum degassing) to remove the tritium. This procedure could produce about 0.2 kg/GWe-yr, at costs comparable to, or possibly less than, current commercial rates.

Although there are a large number of reactors, the major practical limitations are the several years required to adequately develop and test a new "fuel" bundle[24] and electric utility resistance to anything that might possibly interfere with their electricity production. There is precedence, however, in that CANDU reactors presently produce ^{60}Co for commercial markets. A realistic estimate for tritium production in modified power reactors is probably no more than 1 kg/yr by the year 2000.

3.3.6 Helium-3 Absorption

Helium-3 is an isotope of helium that, like lithium-6, has a very high (n,T) neutron absorption cross-section. However, while lithium is a reasonably common natural element on earth, ^3He is not. Presently, helium is obtained from natural gas wells, where helium has accumulated over millions of years from natural radioactive decay (apparently there are a few gas wells with up to several percent helium content). Helium is also a very minor constituent of the atmosphere (about 5 ppm). These sources amount to about 4000 Mg ^3He in the atmosphere, and 0.2 Mg ^3He in U.S. natural gas wells.(25) Since natural helium is mostly ^4He, with about 1 ppm ^3He, extraction of this ^3He would be expensive (1000 $/g).

Helium-3 is widely available in the solar system, with estimates of 10^6 Mg within the first 2 m of the lunar surface and 10^{20} Mg in Jupiter, for example.(25) However, such sources are also not economically accessible over the next 20 years.

The most practical source is from the decay of tritium. About 5% of the tritium decays each year into ^3He. ^3He supplies from the decay of tritium stockpiles for weapons programs are estimated as up to 300 kg by the year 2000 if the ^3He were accumulated, with a post-2000 production rate of 15 kg ^3He/yr.(25) ^3He from the decay of tritium from CANDU reactors is about 0.4 kg/yr now, and potentially 1 kg/yr post-2000 if all the tritium were simply stored. At present, this CANDU helium is not recovered, although some is reconverted into tritium anyway because it remains in the moderator for some time before escaping.

If ^3He is collected and placed into a neutron environment, it can be reconverted back into tritium. Some considerations for enhanced tritium production by reinjection of ^3He gas in CANDU reactors have been reported.(26) The advantages of helium rather than lithium as the raw material result are that helium is gaseous, so it can be used in a flow-through system, and the resulting tritium is easily separated. The disadvantages are that it is correspondingly more difficult to prevent leakage of the helium and tritium from the reactor vessel. Tritium leakage would not be a significant problem in CANDUs because of their background tritium levels, but could be a factor in LWRs. In general, however, the cost, complexity and practical supply limits are similar to those for enhanced tritium production from lithium.

3.3.7 Fusion Reactions

Tritium is produced in half of the D-D fusion reactions. Present tokamak experiments have produced up to 10^{18} DD fusion reactions in one shot, but typically much less. At an average level of 10^{15} DD/shot, and 10^{4} deuterium shots per year, the total tritium production is 10^{-5} g/year. This is dispersed at very low concentrations in hydrogen/deuterium, and not worth recovering.

A fusion power reactor would consume about 120 kg T/GWe-yr if based on the D-T fusion reaction. In-situ tritium production is necessary to meet this consumption. If the in-situ tritium breeding is designed to exceed the operating requirements by 1%, then the uncommitted tritium supply would be about 1 kg/GWe-yr. Of course, operating fusion power reactors are not expected before the year 2000.

3.3.8 Summary

The various potential sources of tritium are summarized in Table 3-6. Overall, there is a reasonable assured supply of 2-2.5 kg/yr from CANDU reactors, and potential for an additional 1 kg/yr from modified power reactors and fuel reprocessing. If military needs for tritium were reduced, much larger amounts of tritium could be made available. Although not discussed here, the market for commercial uses of tritium is presently about 0.2-0.5 kg/yr, with potential expansion to 1-1.5 kg/yr by the year 2000.

Table 3.3-1 Potential Tritium Sources

Source	Supply Rate (kg/yr)	Inventory (kg 1986)
Atmosphere/oceans		
Cosmic rays	0.2	4
Atmospheric bomb tests	0.	145
Unmodified power reactors		
PWR/BWR (1 GWe)	0.002	0.006
CANDU (12 GWe)	2.5	8
Modified power reactors		
PWR/BWR (1 GWe)	0.1	0
CANDU (1 GWe)	0.5	0
Fuel reprocessing plant		
1000 Mg U/yr capacity	0.05-0.1	--
Military production reactors		
US/USSR/UK/France/China	30-40(?)	--

3.4 ETR Tritium Breeding Blanket Availability and Testing Requirements

3.4.1 Introduction

The objective of this section is to investigate the implications of ETR tritium breeding relative to blanket module availability and pre-operational testing requirements. Parametric studies have been performed to 1) calculate the required blanket module Mean Time Between Failure (MTBF) as a function of module Mean Time to Repair (MTTR) and blanket availability goal, 2) determine the necessary pre-operational testing time to insure confidence in required MTBFs, and 3) investigate parallel testing as a means of accelerating the component development process. Required MTBFs and testing times are also related to the ETR tritium breeding ratio and the yearly cost of replacement tritium.

The main implication of ETR tritium breeding is that both replacement tritium costs and component (i.e. tritium breeding blanket module) development requirements are important in ETR planning. Tritium costs for a 300 MW_f device at 30-50% availability would be \$60-90M/year (5-8 kg/year of tritium is required). Module development requirements may include testing times as long

as one million hours, depending on the total number of modules deployed and the desired level of confidence in the module MTBF. Regardless of how developmental testing is performed, the ETR tritium breeding blanket testing program will have a great impact on both the cost and the timetable of fusion demonstration and application.

3.4.2 Blanket MTBF Requirements

The availability of an ETR is difficult to predict and will depend on many factors. However, desirable operational characteristics, including availability, can be applied as design goals. This approach is used here, and it is assumed that the ETR operational goal is an availability of 50% and that the tritium breeding blanket availability goal is 80%. Reactor tritium breeding module requirements can be based on these goals through the use of an availability model which relates module characteristics to the blanket goal availability. A simple availability model for tritium breeding blanket modules is presented here.

In the case of the tritium breeding blanket, the availability goal of 80% can be met if each of n identical modules has an availability of a_m which satisfies the following relationship:

$$A_b = (a_m)^n = 0.80 \tag{3-10}$$

where a_m is defined by the MTBF and MTTR as:

$$a_m = \frac{MTBF}{MTBF + MTTR} \tag{3-11}$$

Given an MTTR, the MTBF can be found simply from Eqns. 3-10 and 3-11 as follows:

$$MTBF = \frac{MTTR\ (A_b)^{1/n}}{1 - (A_b)^{1/n}} \tag{3-12}$$

This MTBF can be thought of as module design requirement such that the availability goal of the tritium breeding blanket as a whole is satisfied. Note that this model implicitly assumes that module failure occurs randomly--a

process that can be described by an exponential distribution of failure times. The exponential distribution failure rate, λ, is just the reciprocal of the MTBF (λ=1/MTBF). This type of failure is characteristic of the operational phase (useful life period) of deployed components, as shown in Figure 3.4-1. The burn-in or wear-out phases are not considered here. If the modules are deployed such that burn-in or wear-out failures occur, then the blanket availability will be lower. Essentially, there is an implicit requirement that components undergo pre-operational developmental testing to discover basic design and fabrication problems, and to validate module lifetime. Pre-operational testing will also be necessary to determine if modules are capable of meeting MTBF requirements.

For the ETR, MTBF requirements depend on the parameters of the machine. These are summarized in Table 3.4-1. At 300 MW_f, the tritium consumption is 8.4 kg per year (50% reactor availability). Full breeding (a TBR of 1.05) is assumed to occur over 58 modules in the 60 module configuration with 2 modules being reserved for testing purposes. If fewer modules are deployed, then makeup tritium must be purchased. Figure 3.4-2 shows the effective tritium breeding ratio and the yearly cost of replacement tritium as a function of the number of tritium breeding modules. If no tritium is bred in ETR, the yearly cost (at $10,000/g) is $84M.

Table 3.4-1 Representative ETR Parameters Considered in the Reliability Analysis

Fusion Power	300 MW
ETR Availability Goal	0.5
Blanket Availability Goal	0.8
Number of Blanket Sectors	12
Number of Modules per Sector	5
Total Number of Modules	60
Number of Test Modules	2 minimum[a]
Full Coverage TBR	1.05
Tritium Consumption Rate	8.4 kg/FPY
Tritium Cost	$84 M/FPY
Blanket Module MTTR	336 hours (nominal)
Blanket Module MTBF	calculated

[a]Two test modules are provided even for the "full coverage" case. The number of test modules can be increased for lower coverage cases.

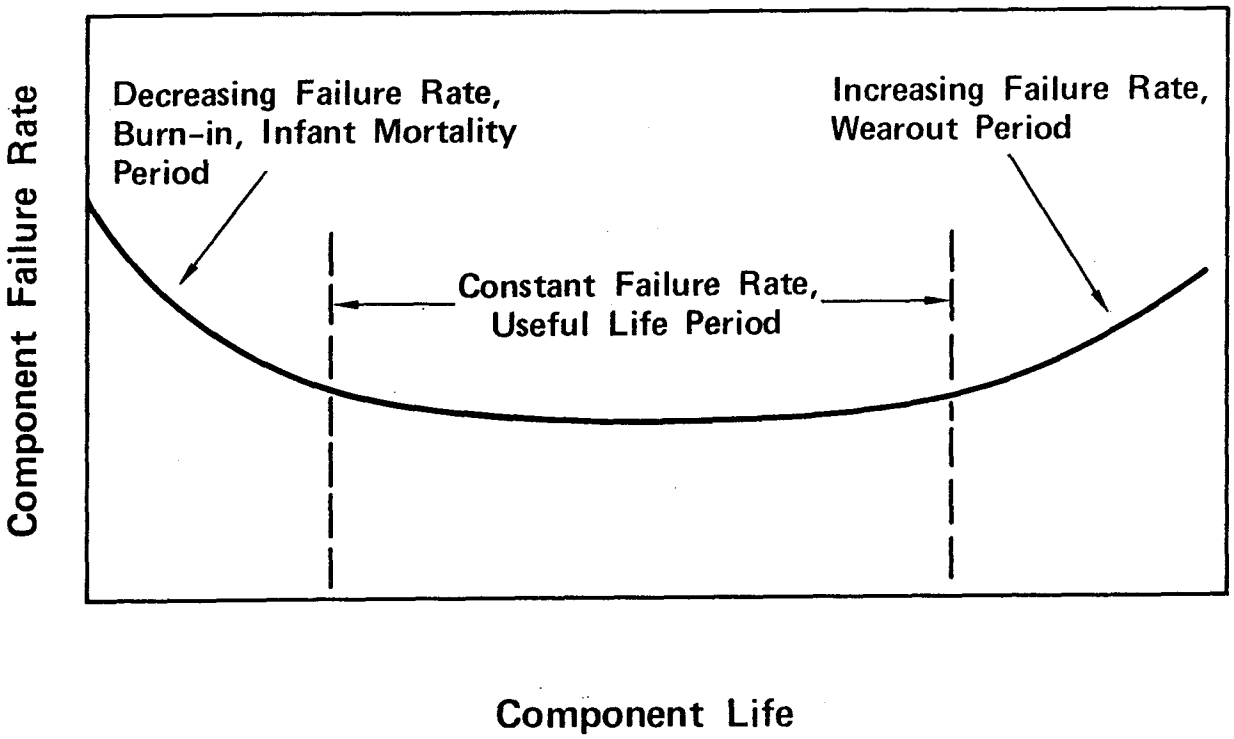


Figure 3.4-1 Failure rate over component life

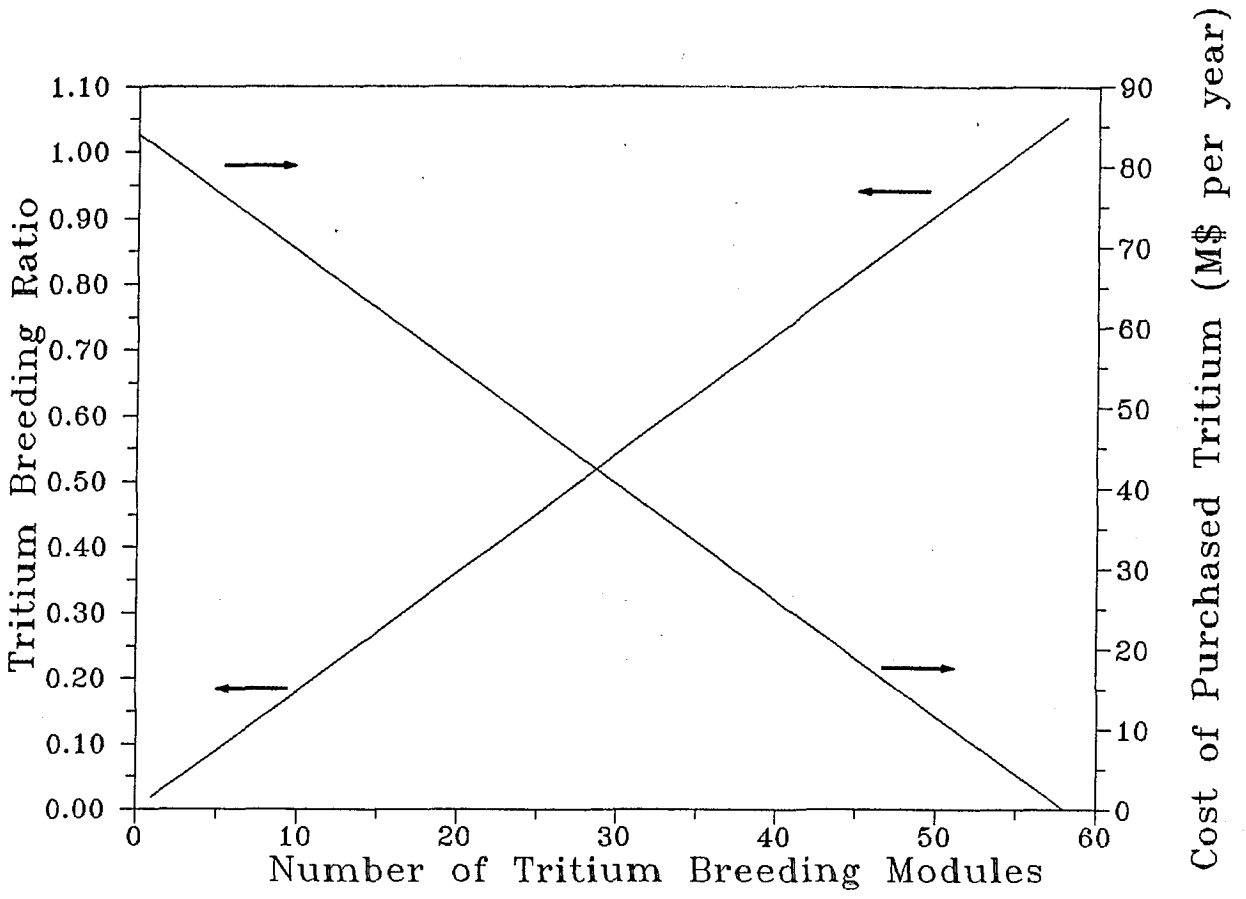


Figure 3.4-2 Tritium breeding ratio and replacement tritium cost

Corresponding to the number of tritium breeding modules in ETR is a particular module MTBF requirement, as related by Eq. (3-12). Figure 3.4-3 presents the module MTBF requirement as a function of the number of modules (meeting the blanket availability goal of 80%) and the MTTR. For full tritium breeding and an MTTR of 2 weeks (336 hours), the required MTBF is about 87,000 hours (10 years). To restate the definition of MTBF, the 87,000 hour requirement means that, on average, the time between failures for any single module in a large sample of identical modules should be 10 years (87,000 hours).

Equation (3-12) and Figure 3.4-3 show the MTBF requirement as a function of the number of modules. If there are fewer modules per sector (larger modules), then the MTBF requirement per module is smaller. This is illustrated

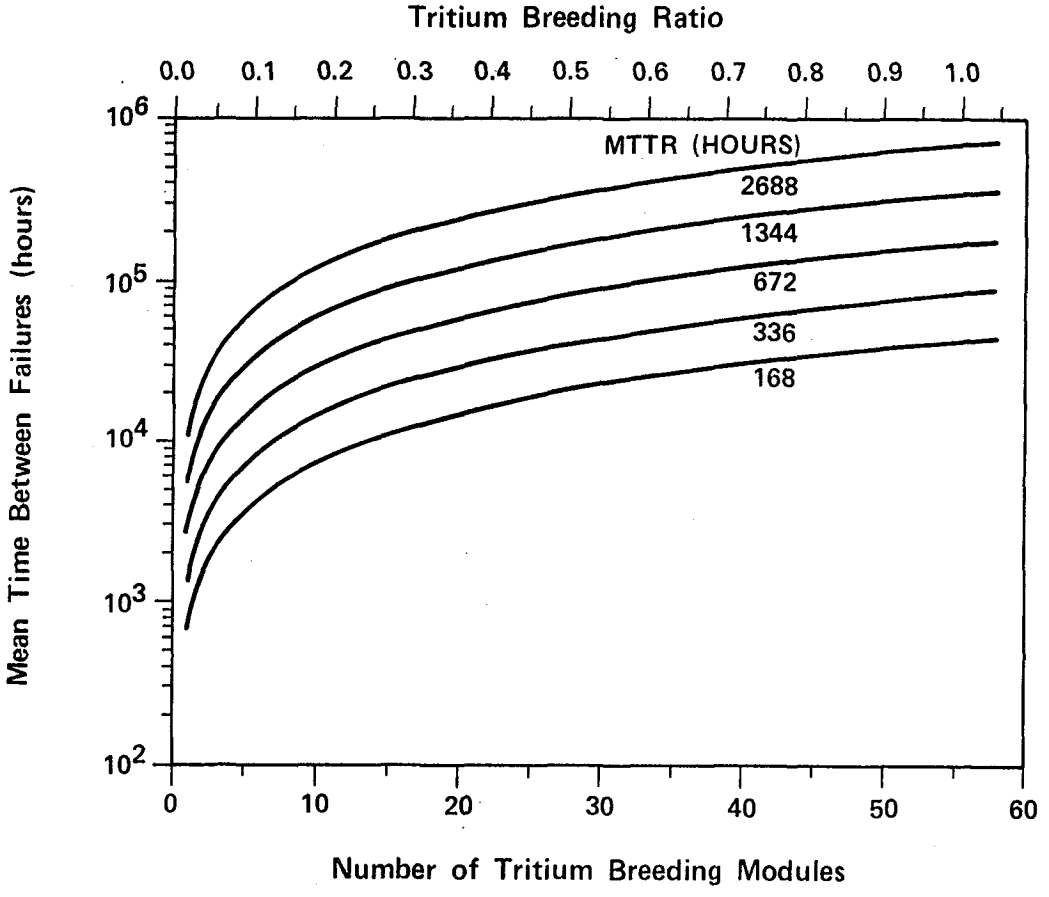


Figure 3.4-3 MTBF for tritium breeding module (at various values of MTTR) necessary to achieve a blanket availability goal of 0.8 as a function of the number of tritium breeding modules (and tritium breeding ratio)

in Figure 3.4-4 which plots the required MTBF against the total tritium breeding (neglecting test modules). An apparent conclusion from these results is that larger modules have inherently easier design goals in terms of MTBF. However, since a larger module includes essentially all of the material and complexity of several smaller modules, it would generally have a lower achievable MTBF as well. At least to first approximation, the goals for small or large modules are effectively equivalent per unit of TBR. Further results here are based on small modules (five per blanket sector), with TBR per module of 1.05/60.

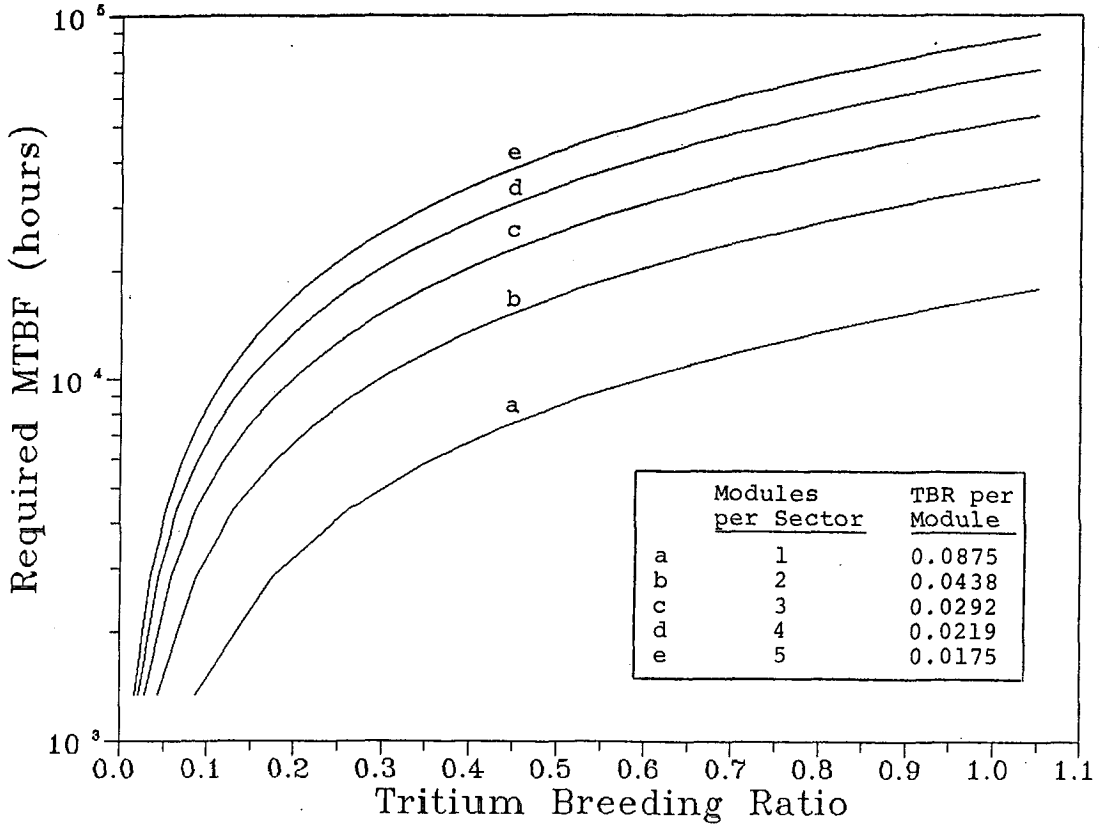


Figure 3.4-4 Required module MTBF (meeting 0.8 blanket availability goal) as a function of the number of modules per sector

3.4.3 Testing Time and Performance Confidence Levels

Fusion component testing will be necessary to discover design flaws (as well as infant mortality phenomena), validate wear-out mechanisms and component lifetimes, and develop estimates of component failure rates (during the constant failure rate operational period). The concern here is with pre-operational testing as a means to determine component failure rates in the constant failure rate regime.

If blanket module testing is viewed as a series of time-terminated trials, then the occurrence of module failures can be described as a Poisson process.[27] For a test of duration t, of a component with failure rate given by $\lambda=(1/MTBF)$, the probability of seeing r failures is:

$$f(r) = \frac{\alpha^r}{r!} e^{-\alpha} \tag{3-13}$$

where $\alpha = \lambda t$ is the mean number of failures during time t. The normalization of this distribution is of the form:

$$\sum_{r=0}^{\infty} f(r) = 1 \tag{3-14}$$

In a component test where r module failures are actually observed, r may be used as an estimate of the true value of α in Eq. (3-13):

$$\hat{\alpha} = r \tag{3-15}$$

where $\hat{\alpha}$ is the estimated value of α. As an unbiased estimator of the true value of α in Eq. (3-13), $\hat{\alpha}$ is also Poisson-distributed. An upper confidence limit can be obtained for α from $\hat{\alpha}$ as follows:[27]

$$c = \sum_{j=\hat{\alpha}+1}^{\infty} f(j) \tag{3-16}$$

where, on average, $\alpha < \hat{\alpha}$ (the actual mean number of failures is less than the number observed) with a confidence level given by c. Using the normalization property, this can be restated as:

$$c = 1 - \sum_{j=0}^{\hat{\alpha}} f(j) = 1 - \sum_{j=0}^{\hat{\alpha}} \frac{(\lambda t)^j}{j!} e^{-\lambda t} \tag{3-17}$$

Figure 3.4-5 shows the confidence level c as a function of $\hat{\alpha}$, the number of test failures, and the product λT (remember that $\lambda = 1/\text{MTBF}$). λT is just the total testing period in integral MTBFs. This illustrates that longer test times are required to achieve higher confidence levels and that test failures degrade the confidence in any given MTBF. Figure 3.4-6 restates Eq. (3-17) by showing the minimum test time (zero failures) required to develop confidence in a given MTBF. A similar set of curves results when component failures are seen. In actuality, the testing sequence typically follows a route such as illustrated by the bold arrows shown in Figure 3.4-5.

It was shown in Section 3.4.2 that the greater the number of modules, the greater the MTBF requirement. These MTBF requirements can be matched to pre-operational testing time requirements through Eq. (3-17). This is done in

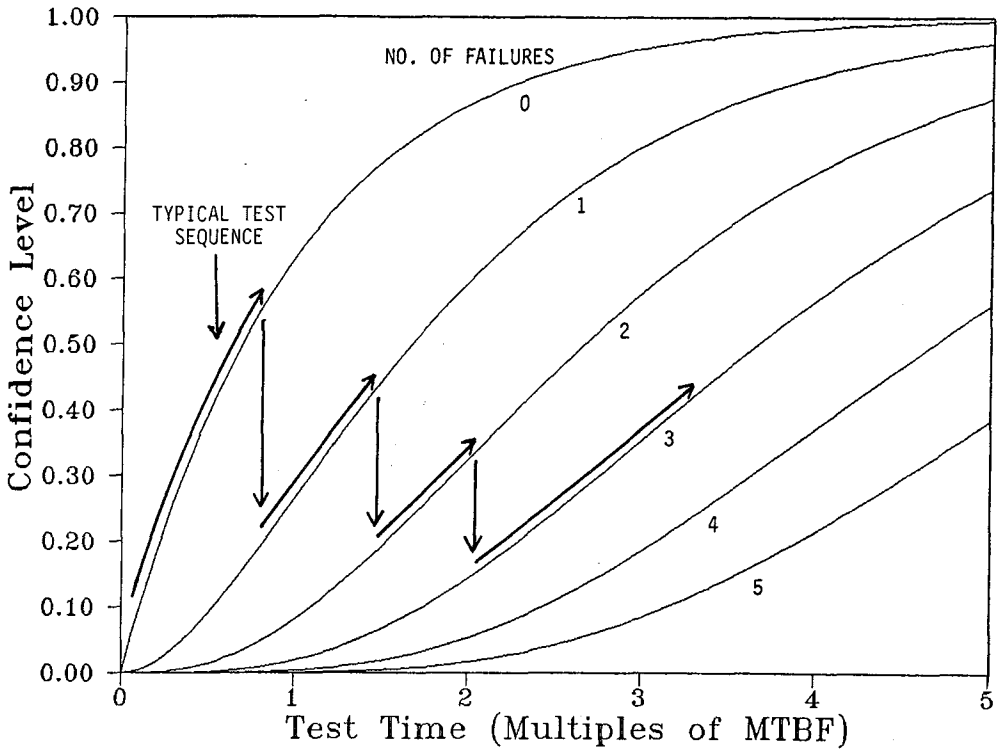


Figure 3.4-5 Confidence level versus testing time and number of failures

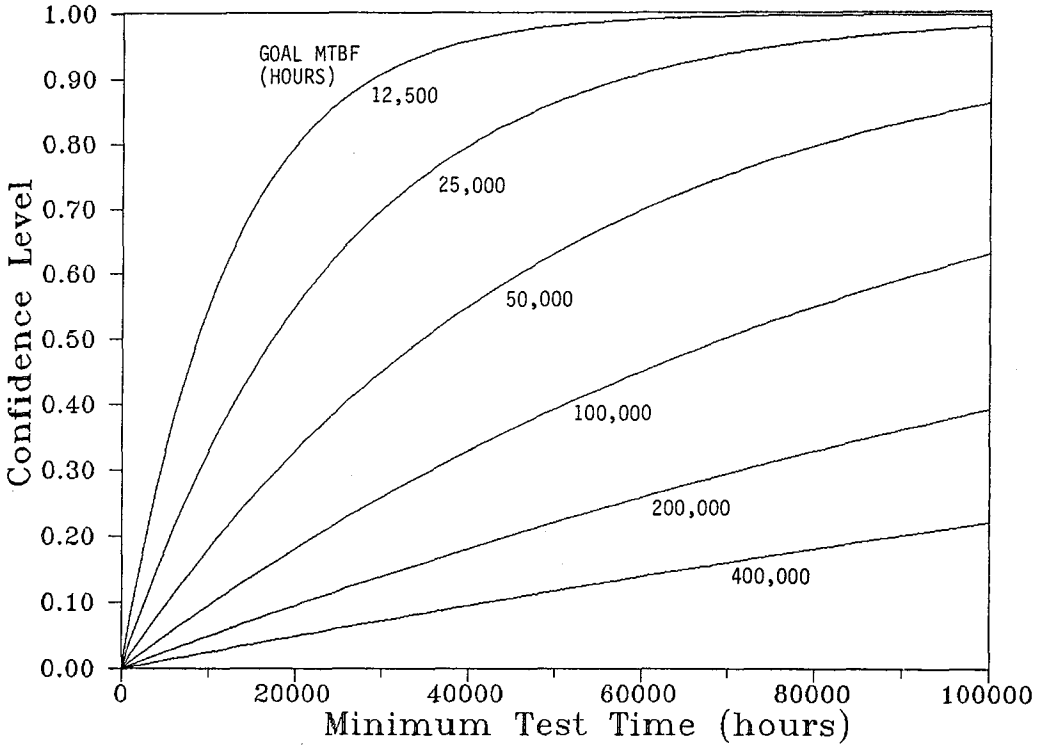


Figure 3.4-6 Minimum (zero failures) required testing time versus goal MTBF and confidence level

Figure 3.4-7 where $\hat{\alpha}$ in Eq. (3-17) is set equal to zero to give the minimum testing time. Figure 3.4-7 also shows the tritium breeding ratio and the cost of purchased tritium corresponding to any particular number of tritium breeding modules. Several confidence levels are shown.

Figure 3.4-7 can be used in a variety of ways. The key point is that there is a relationship between required testing time, operational confidence in module MTBF, and the cost of purchased tritium. This is presented in a different way in Figure 3.4-8 where the yearly cost of purchased tritium is shown as a function of confidence level and minimum testing time. Presented in this manner, it is clear that higher confidence levels are more expensive while operational testing times reduce the yearly tritium cost in the ETR. Testing costs are not developed here, but clearly the longer pre-operational testing times will incur greater testing costs.

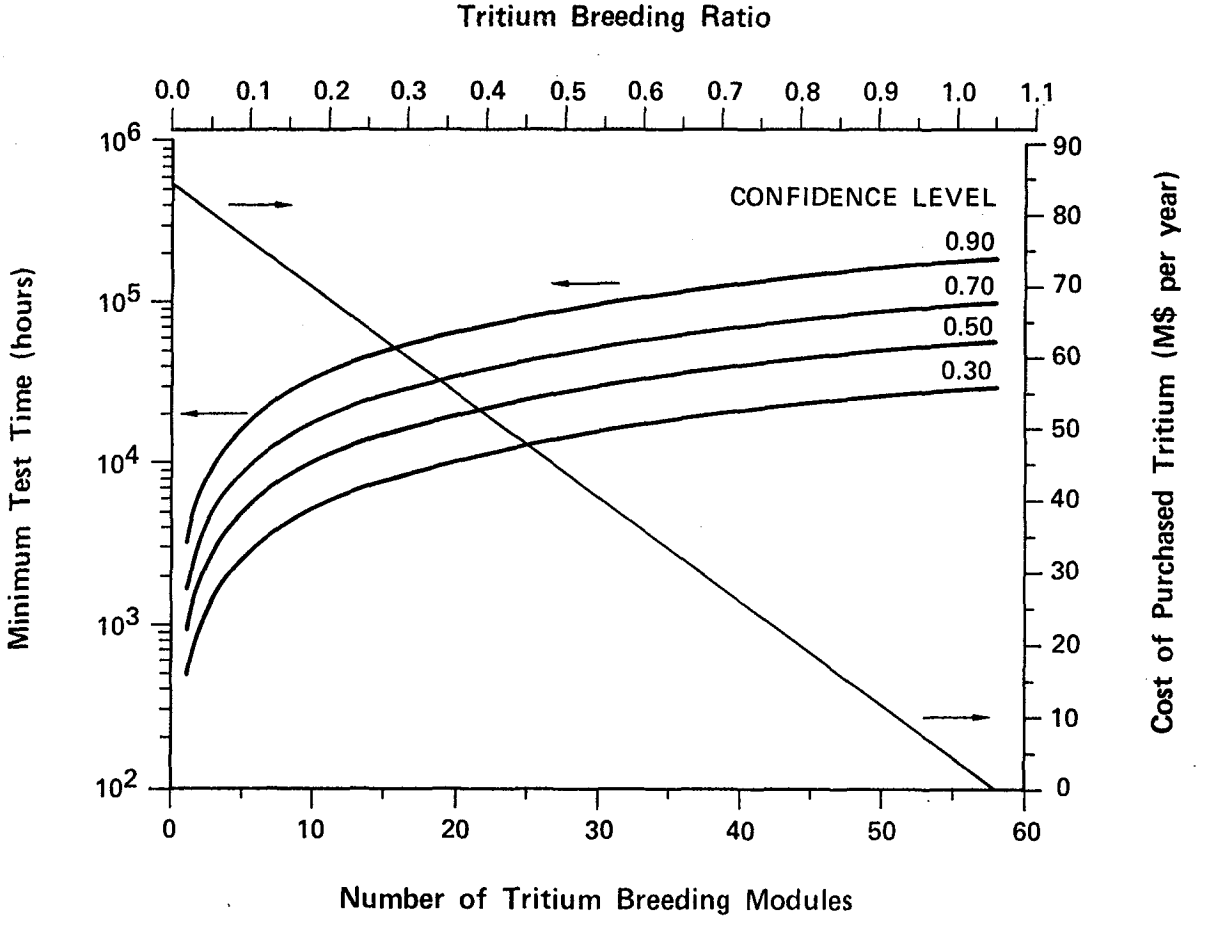


Figure 3.4-7 Minimum required testing time (at various confidence levels) to achieve a blanket availability of 0.8 as a function of the number of tritium breeding modules and tritium breeding ratio. Also shown is the cost of external tritium supply as a function of the breeding ratio.

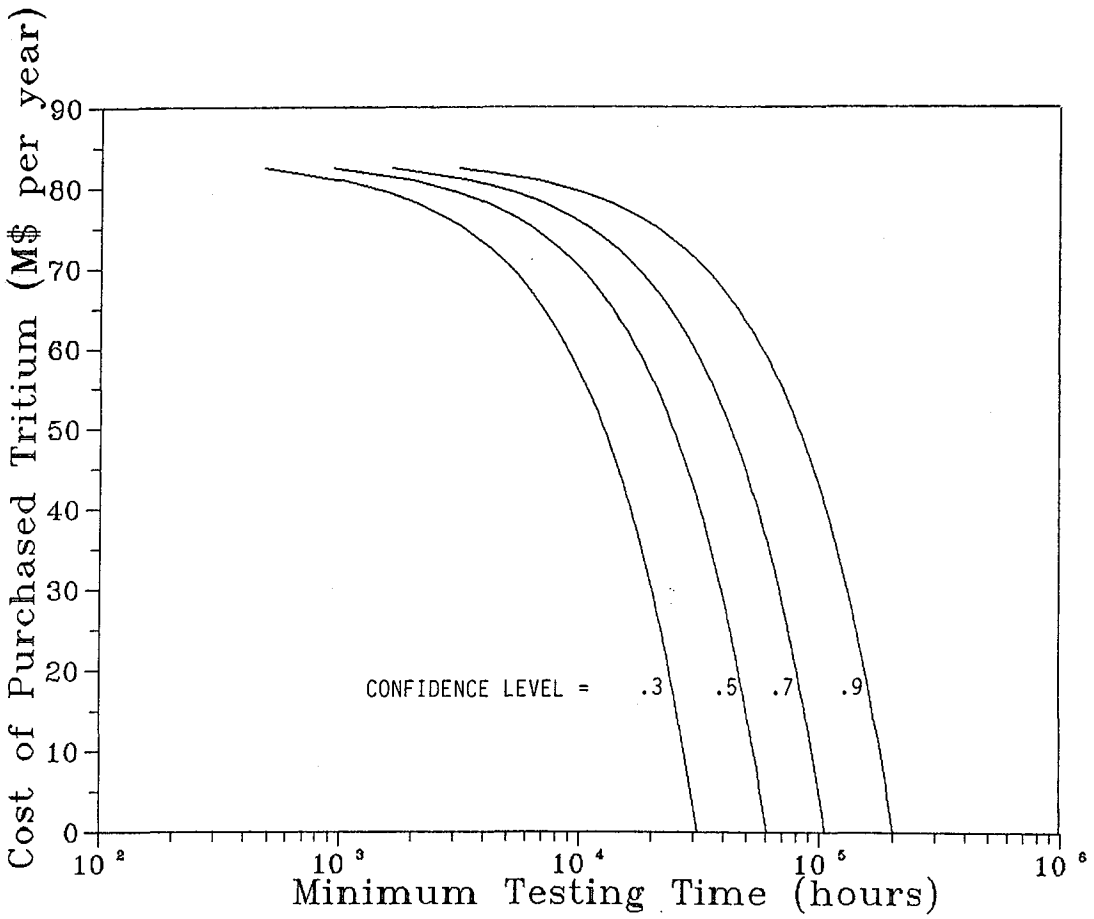


Figure 3.4-8 Cost of purchased tritium as a function of the minimum required testing time at several confidence levels

3.4.4 Parallel Testing As a Means of Achieving Performance Confidence

The previous sections developed tritium breeding module MTBF requirements and related these to pre-operational testing times and confidence levels. It is clear from these results that very long testing times (> 10 years) are required to develop high confidence in module MTBF at higher TBRs. Parallel testing is one means of compressing the actual calandar time required. Parallel testing requires that identical components are tested at the same time under identical conditions. Figure 3.4-9 shows the effect of parallel testing on calendar time (the minimum testing time required to achieve a 90% confidence level is shown). Note that for a single test, calendar time and testing time exactly correspond. n parallel tests reduce the total minimum testing time to T/n.

In terms of a real testing program, parallel testing can be thought of as being more aggressive and potentially more costly than a single track program. The model (Figure 3.4-9) predicts that higher confidence levels can be achieved much sooner. In this way, a potential ten-year development program could be significantly reduced. Of course, the actual testing and development of tritium breeding modules will be a much more complex undertaking, but parallel testing is a general approach for accomplishing component development in a more timely manner.

3.4.5 Conclusion

These analyses have addressed the following aspects of tritium breeding in an ETR:

- module MTBF requirements as a function of TBR (coverage)
- corresponding pre-operational testing time requirements
- parallel testing as a more aggressive developmental approach

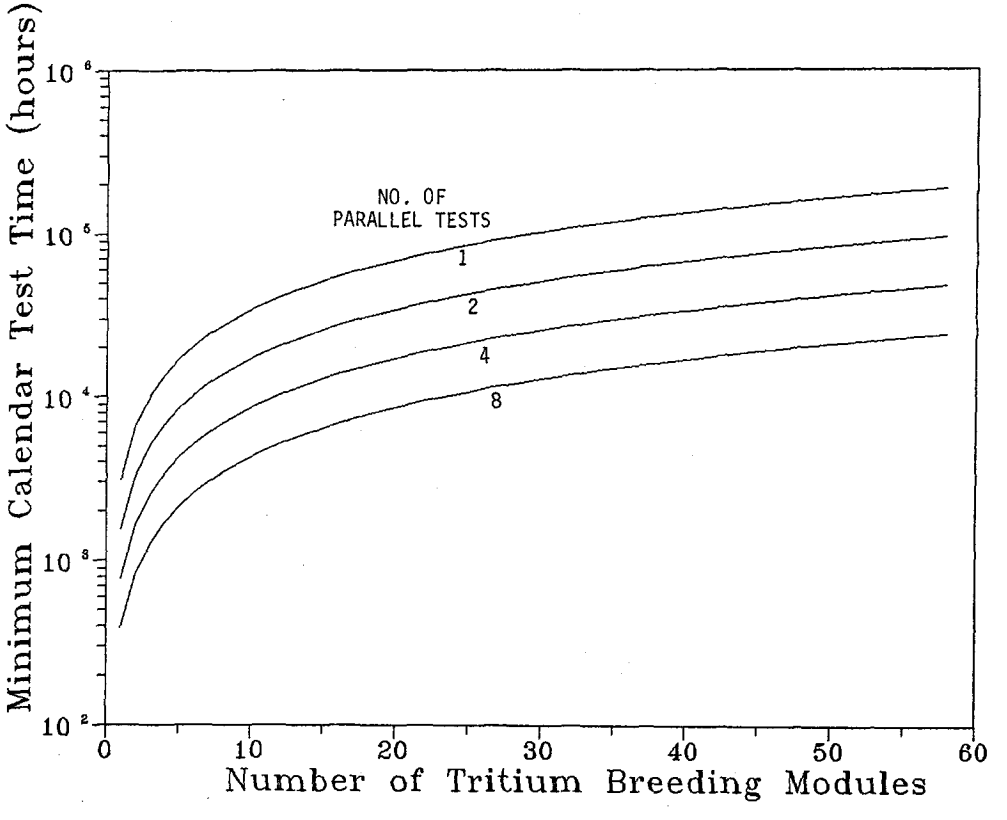


Figure 3.4-9 The effect of parallel testing on the minimum time (zero failures) required to achieve a confidence level of 0.9

It has been found that for a 300 MW_f ETR (50% availability) with a potential yearly cost of tritium as high as $84M, a tritium breeding blanket availability goal of 80% will result in module MTBF requirements as high as 90,000 hours, depending on the module replacement time (MTTR). High confidence (90%) in this level of module performance will require testing times which are at a minimum several times the required MTBF. One means of achieving such test times is by parallel testing of identical components. Under the set of assumption used in this analysis, parallel testing reduces the calendar time in direct proportion to the number of parallel tests.

The intent of these analyses is not to specify the exact test requirements of any tritium breeding module. Rather, the objective is to illustrate, in a quantitative way, some of the cost and development implications of tritium breeding in an ETR. It is very probable that if significant breeding is attempted in the future ETR, the modules will not have demonstrated, in a statistical sense, an idealized high level of confidence at some required MTBF. Most likely, engineering judgement will be the major basis of module design. Lengthy testing time will in all likelihood not be available. Nevertheless, the demonstrated MTBF and module testing requirements presented here are indicative of the serious developmental issues that must be faced in the design of future fusion facilities.

References for Chapter 3

1. M.A. Abdou, et al., "FINESSE: A Study of the Issues, Experiments, and Facilities for Fusion Nuclear Technology Research and Development (Interim Report)," PPG-821, UCLA-ENG-84-30, University of California, Los Angeles (1984).

2. "Magnetic Fusion Program Plan," DOE/ER-0214, U.S. Department of Energy, Office of Energy Research (1985).

3. M.A. Abdou, et al., "Technical Issues and Requirements of Experiments and Facilities for Fusion Nuclear Technology (FINESSE Phase I Report)," PPG 909, UCLA-ENG-85-39, University of California, Los Angeles (1985).

4. P. Gierszewski, et al., "Engineering Scaling and Quantification of the Test Requirements for Fusion Nuclear Technology," Fusion Tech., 8, 1100-1108 (1985).

5. "Blanket Comparison and Selection Study - Final Report," ANL/FPP-84-1, Argonne National Laboratory (1984).

6. C.C. Baker, et al., "Tokamak Power Systems Studies - FY 1985," ANL/FPP-85-2, Argonne National Laboratory (1985).

7. C.C. Baker, et al., "STARFIRE - A Commercial Fusion Tokamak Power Plant Study," ANL/FPP-80-1, Argonne National Laboratory (1980).

8. M.A. Abdou, et al., "A Demonstration Tokamak Power Plant Study (DEMO)," ANL/FPP-82-1, Argonne National Laboratory (1982).

9. R.G. Clemmer, et al., "The TRIO Experiment," ANL-84-55, Argonne National Laboratory (1984).

10. H. Werle, et al., "The LISA-1 Experiment In Situ Tritium Release Investigations," J. Nucl. Mat., 141-143, 321-326 (1986).

11. J. Hartmann, "Hg-Dynamics I," kgl. Danske videnskab. selskab, Mat-Fys. Medd., vol. 15, no. 6 (1937).

12. J. Shercliff, J. Fluid Mech., 1, 644-666 (1956).

13. C. Chang and T. Lundgren, Proc. 1959 Heat Transfer Fluid Mech. Inst., pp. 41-54 (1959).

14. G. Deis, "Thermal Cycling Effects in Tokamak Reactor Blanket Components," Proc. 9th Symposium on Engineering Problems of Fusion Research, IEEE Pub. No. 81CH1715-2 NPS, Vol. II, p. 1783 (1981).

15. J. Yen and C. Chang, Phys. Fluids, 4, 1355-1361 (1961).

16. R. Singer, "Transient Magnetohydrodynamic Flow and Heat Transfer," ZAMP, 16 (1965).

17. The NET Team, "NET Status Report," NET Report 51 (1985).

18. B. Brown, "Tritium in the Environment," CRNL-2739-4, Chalk River Nuclear Laboratories (1986).

19. A. Bleier, R. Kroebel, K.H. Neeb and E. Schneider, "Tritium Inventories and Behavior in Zircaloy Cladding of Spent Light Water Reactor Fuel Rods," Proc. Fuel Reprocessing and Waste Management Conference, Vol. 1, pp. 238-248 (1984).

20. K.Y. Wong, et al., "Canadian Tritium Experience," Ontario Hydro, 1984.

21. J. Couture, "Status of the French Reprocessing Industry," Proc. Fuel Reprocessing and Waste Management Conference, Vol. 1, pp. 33-45 (1984).

22. "World List of Nuclear Power Plants," Nuclear News (1985).

23. Internal Reports, Canadian Fusion Fuels Technology Project.

24. I. Hastings, Chalk River Nuclear Laboratory, private communication (1986).

25. L.J. Wittenberg, J.F. Santarius and G.L. Kulcinski, "Lunar Source of ^{3}He for Commercial Fusion Power," Fusion Tech., 10, 167-178 (1986).

26. G.F. Thomas and S.J. Brereton, "Enhanced Tritium Production for Fusion Reactors via $^{3}He(n,p)^{3}H$ in the Heavy Water Moderator of a CANDU Reactor," J. Fusion Energy, 4, 27-44 (1985).

27. A.E. Green and A.J. Bourne, Reliability Technology, Wiley Interscience, London (1972).

4. THEORY AND MODELING

TABLE OF CONTENTS

Page

4.1 Introduction....4-1

4.2 Computational Methods in Liquid Metal MHD....4-13

4.2.1 Introduction....4-13

4.2.2 Finite Difference Method....4-18

4.2.2.1 Entry Length Effects in MHD Duct Flow....4-22

4.2.2.2 Sensitivity Analysis of MHD Heat Transfer....4-29

4.2.2.3 MHD Flow in a Sudden Duct Enlargement....4-37

4.2.2.4 Concluding Remarks....4-49

4.2.3 Finite Element Method....4-51

4.2.3.1 Introduction....4-51

4.2.3.2 Basic Equations....4-53

4.2.3.3 Illustration of Self-Adaptive Mesh Refinement in the 1-D Hartmann Problem....4-55

4.2.3.4 Two-Dimensional Fully Developed Duct Flow....4-60

4.2.3.5 Extensions and Recommendations....4-87

4.3 Analytic Treatment of MHD Flow in a Curved Pipe....4-88

4.3.1 Introduction....4-88

4.3.2 Analytic Approach....4-90

4.3.3 Results and Discussion....4-94

4.4 MHD Pressure Drop....4-99

4.4.1 Introduction....4-99

4.4.2 Pressure Drop Due to Magnetic Field Entrance or Exit....4-99

4.4.2.1 Background....4-99

4.4.2.2 Description of Methodology....4-101

4.4.2.3 Application to Fusion Reactor....4-116

4.5 Heat Transfer in Flow Over a Wedge or a Cylinder Under the Condition of Heat Generation....4-118

4.5.1 Introduction....4-118

4.5.2 Analysis....4-120

4.5.3 Limiting Cases of $Pr \to 0$ and $Pr \to \infty$....4-125

4.5.4 Analysis for a Cylinder in Cross Flow....4-128

4.5.5 Experimental Apparatus and Procedure....4-130
4.5.5.1 Apparatus....4-130
4.5.5.2 Procedure....4-134
4.5.6 Results and Discussion....4-136
4.5.7 Summary and Conclusions....4-144
4.6 Liquid Metal/Structural Material Interactions Research....4-147
4.6.1 Introduction....4-147
4.6.2 Analytical Approach to Mass Transport....4-148
4.6.3 Liquid Phase Transport Modeling....4-149
4.6.4 Particle Mass Transport Modeling....4-153
4.6.5 Solid Phase Mass Transport Modeling....4-156
4.6.6 Chemical Reactions for Lithium/HT9....4-158
4.6.7 Experimental Investigations of Mass Transport in Lithium/HT9 Systems....4-159
4.6.7.1 Introduction....4-159
4.6.7.2 Thermal Convection Loop Program for Lithium/HT9....4-161
4.6.8 Summary and Future Experimental Work....4-166
4.7 Tritium Transport in Solid Breeders....4-167
4.8 Design Window for a Liquid-Metal-Cooled Limiter....4-170
4.8.1 Introduction....4-170
4.8.2 Design Approach....4-170
4.8.3 Design Constraints....4-171
4.8.4 Choice of Limiting Values and Material Properties....4-172
4.8.5 Geometrical Configuration....4-172
4.8.6 Thermal and Stress Analysis....4-173
4.8.6.1 Analysis of the Flat Face Channel Without Coating....4-174
4.8.6.2 Identifying Maximum Permissible Heat Flux for Flat Face Channel Without Coating....4-177
4.8.6.3 Analysis of the Flat Face Channel with Coating....4-179
4.8.6.4 Defining Maximum Permissible Heat Flux for a Limiter Center Channel with Coating....4-186
4.8.6.5 Analysis of the Channel at the Leading Edge....4-186
4.8.7 Design Window for Limiter Without Coating....4-187
4.9 Thermal and Stress Analysis of Limiters....4-193
4.9.1 Introduction....4-193
4.9.2 Geometric Configuration....4-193

4.9.3 Mathematical Formulation.....4-194
4.9.3.1 Thermal Analysis.....4-194
4.9.3.2 Stress Analysis.....4-196
4.9.3.3 Boundary Conditions.....4-202
4.9.4 Results.....4-205
4.9.5 Concluding Remarks.....4-212

LIST OF FIGURES

		Page
4.1-1	Types and role of experiments and facilities for Fusion Nuclear Technology	4-1
4.1-2	Thermomechanical design window	4-4
4.1-3	Hartmann number (M) and interaction parameter (N) ranges for existing data and reactor conditions	4-4
4.1-4	Liquid metal MHD modeling logic	4-6
4.1-5	Tritium systems model	4-10
4.2-1	Location of flow variables on the finite-difference grid: (1) control volume for u, (2) control volume for v, and (3) control volume for p and T	4-20
4.2-2	Control volume in two-dimensional geometry	4-20
4.2-3	Pipe flow configuration	4-23
4.2-4a	Velocity vectors for a developing pipe flow	4-24
4.2-4b	Temperature contours (degrees Celsius)	4-24
4.2-5	Effect of a horizontal magnetic field on the centerline velocity	4-25
4.2-6	Local Nusselt number for the entrance region of a pipe	4-26
4.2-7	Velocity profile at channel exit	4-28
4.2-8	Local Nusselt number for the entrance region of a channel	4-30
4.2-9	Effect of magnetic field on entry length heat transfer (parabolic inlet profile and constant wall temperature)	4-31
4.2-10	Channel flow configuration	4-32
4.2-11	Development of the velocity profile along a channel for different values of Hartmann (Ha) numbers	4-34
4.2-12	Fully developed velocity profiles used in the sensitivity study	4-36
4.2-13	Local Nusselt number for different velocity profiles (constant wall temperature)	4-38
4.2-14	Local Nusselt number for different velocity profiles (constant wall heat flux)	4-39

4.2-15 Temperature development for different velocity profiles (constant wall temperature).....4-40

4.2-16 Temperature development for different velocity profiles (constant wall heat flux).....4-41

4.2-17 Configuration of the pipe expansion and a definition sketch.....4-43

4.2-18 Characteristics of the annular eddy as a function of Reynolds number at different Hartmann numbers; L_1/D_o, relative eddy length; L_2/D_o, relative location of eddy center.....4-46

4.2-19 Effect of axial magnetic field on the development of the velocity profile along the pipe.....4-47

4.2-20 Velocity vectors showing the effects of an axial magnetic field on the flow in a sudden pipe enlargement (note: velocities in the upper half of the pipe are magnified).....4-48

4.2-21 Effect of axial magnetic field on the wall pressure distribution along the pipe at different Hartmann numbers.....4-49

4.2-22 Geometry for the 1-D Hartmann problem.....4-56

4.2-23 Solution of the Hartmann problem using linear and quadratic shape functions.....4-58

4.2-24 Residual errors for the Hartmann problems.....4-61

4.2-25 Illustration of self-adaptive mesh refinement for the Hartmann problem.....4-62

4.2-26 Geometry for the fully developed 2-D channel flow problem.....4-63

4.2-27 Rectangular element configuration.....4-64

4.2-28 Illustration of the 2-D linear shape function.....4-66

4.2-29 Velocity profile in the non-conducting duct, Ha=10.....4-69

4.2-30 Electric scalar potential in the non-conducting duct, Ha=10.....4-70

4.2-31 Electric current density in the non-conducting duct, Ha=10.....4-71

4.2-32 Velocity profile in the non-conducting duct, Ha=100.....4-72

4.2-33 Electric scalar potential in the non-conducting duct, Ha=100.....4-73

4.2-34 Electric current density in the non-conducting duct, Ha=100.....4-74

4.2-35 Velocity profile in the duct with conducting side walls, Ha=100.....4-76

4.2-36 Electric scalar potential in the duct with conducting side walls, Ha=100....4-77

4.2-37 Electric current density in the duct with conducting side walls, Ha=100....4-78

4.2-38 Symmetry conditions for the duct with conducting side walls....4-79

4.2-39 High accuracy solution for the velocity profile in the duct with conducting side walls, Ha=100....4-80

4.2-40 Comparison of finite element solution with analytic solution....4-81

4.2-41 Illustration of transition nodes....4-84

4.2-42 Residuals for the duct with non-conducting walls, Ha=100....4-85

4.2-43 Residuals for the duct with conducting side walls, Ha=100....4-86

4.3-1 Simplified representation of a poloidal circular coolant pipe in a toroidal magnetic field....4-89

4.3-2 Coordinate system....4-90

4.3-3 First perturbed axial velocity profile due to the effect of Dean number (K=20), together with Poiseuille profile (K=0)....4-95

4.3-4 First perturbed axial velocity profile due to the effect of Hartmann number (Ha=1), along with Poiseuille profile (Ha=0)....4-97

4.3-5 First perturbed axial velocity profile due to the combined effects of Dean and Hartmann numbers (K=20, Ha=1), together with Poiseuille profile....4-97

4.3-6 First perturbed stream function (576 Ψ/K) due to the effect of Dean number....4-98

4.3-7 Second perturbed stream function (-1327104 Ψ/K^3) for the first quadrant due to the effect of Dean number....4-98

4.4-1 Electrical current flow as a result of changing B field....4-102

4.4-2 Pressure gradients due to interaction of electrical currents with B field....4-102

4.4-3 Geometry used in calculation of MHD pressure drop....4-104

4.4-4 Quadrant in which potential distribution is calculated....4-105

4.4-5 Velocity profiles assumed in analysis....4-106

4.4-6 Eddy current distribution due to abruptly changing B field, non-conducting walls, slug flow....4-107

4.4-7 Eddy current distribution due to abruptly changing B field, non-conducting walls, parabolic flow.....4-107

4.4-8 Eddy current distribution due to abruptly changing B field, conducting walls (ϕ=0.07), slug flow.....4-113

4.5-1 Flow over a wedge.....4-121

4.5-2 Comparison between the temperature and velocity fields in boundary layer for very small and very large Prandtl number fluids.....4-125

4.5-3 Equivalent wedge for a segment dx on the cylinder.....4-128

4.5-4 Schematic drawing of the experimental set-up.....4-131

4.5-5 Boundary layer temperature profile for flow over a flat plate.....4-136

4.5-6 Variation and location of maximum temperature as a function of the Prandtl number.....4-137

4.5-7 Temperature gradient at the wall for flow over a wedge as a function of the Prandtl number.....4-139

4.5-8 Boundary layer temperature profile in flow over a flat plate for the Prandtl number PR=0.....4-139

4.5-9 Boundary layer temperature profile for flow over a flat plate for the case of Pr $\rightarrow \infty$.....4-140

4.5-10 Change in local Nusselt number around the circular cylinder up to the point of separation for Pr=0.01.....4-141

4.5-11 Change in average Nusselt number due to volumetric heat generation for flow over a cylinder.....4-142

4.5-12 Ratio of local ΔNu_d to local Nu_d^0 at different angles on the cylinder for Pr=0.7.....4-143

4.6-1 Block diagram of mass transport processes.....4-148

4.6-2 Schematics for liquid- and solid-phase models.....4-151

4.6-3 Schematic of thermal convection loop.....4-162

4.6-4 Comparison of flow geometries.....4-163

4.8-1 Geometrical configuration of the limiter.....4-172

4.8-2 Details of the leading and center channel.....4-173

4.8-3 Thermal and stress boundary conditions for the limiter channel.....4-174

4.8-4 Description of elements for coolant channel without coating....4-175

4.8-5 Maximum allowable heat flux vs. wall thickness of the channel....4-176

4.8-6 Allowable heat flux vs. spacing between channels....4-176

4.8-7 Variation of stresses with increasing back wall thickness....4-178

4.8-8 Dependence of total stress on the width of channel at different pressure....4-178

4.8-9 Dependence of total stress on channel breadth at different pressure....4-179

4.8-10 Maximum heat flux vs. channel cross-section for different channel spacing....4-180

4.8-11 Maximum heat flux vs. channel cross-section for different channel spacing....4-180

4.8-12 Description of elements for coolant channel with coating....4-181

4.8-13 Variation of stresses with increasing back wall thickness....4-182

4.8-14 Variation of stresses with increasing back wall thickness....4-182

4.8-15 Variation of stresses with increasing back wall thickness....4-183

4.8-16 Variation of stresses with increasing back wall thickness....4-183

4.8-17 Variation of stresses with increasing back wall thickness....4-184

4.8-18 Variation of stresses with increasing back wall thickness....4-184

4.8-19 Multiplication factor vs. total front wall thickness....4-185

4.8-20 Maximum permissible heat flux for different cross-sectional areas....4-186

4.8-21 Maximum permissible heat flux for different cross-sectional areas....4-187

4.8-22 Design margin with untapered conduits at 4 and 5 MW/m^2 heat flux....4-189

4.8-23 Design margin with tapered conduit at 4 and 5 MW/m^2 heat flux....4-190

4.8-24 Design window with tapered conduit at 4 MW/m^2 heat flux....4-191

4.8-25 Design window with tapered conduit at 5 MW/m^2 heat flux....4-191

4.8-26 Design window with insulated conduit at 4 MW/m^2 heat flux.....4-192

4.8-27 Design window with insulated conduit at 5 MW/m^2 heat flux.....4-192

4.9-1 Geometric configuration of the limiter.....4-194

4.9-2 Three-dimensional mesh of a limiter specimen.....4-195

4.9-3 Equivalent nodal forces on an element.....4-201

4.9-4 Different possible deformations of the limiter element.....4-202

4.9-5 Limiter section.....4-203

4.9-6 Maximum temperature at the limiter surface vs. wall heat flux.....4-206

4.9-7 Maximum primary stresses vs. water coolant pressure.....4-206

4.9-8 Maximum stress on the surface of a copper limiter vs. wall heat flux.....4-207

4.9-9 Maximum surface temperature vs. wall heat flux for a vanadium limiter.....4-208

4.9-10 Maximum primary stress on the surface of vanadium limiter vs. Li coolant pressure.....4-209

4.9-11 Maximum stress for a vanadium limiter vs. wall heat flux.....4-209

4.9-12 Temperature distribution.....4-210

4.9-13 Stress distribution.....4-211

4.9-14 Von Mises stress distribution (σ_{ss}).....4-211

LIST OF TABLES

		Page
4.2-1	Non-Dimensional Numbers in Liquid Metal MHD	4-15
4.2-2	Thermal Entrance Lengths for Different Geometries and Boundary Conditions	4-42
4.2-3	Mean Nusselt Number for Different Velocity Profiles and Two Boundary Conditions	4-42
4.4-1	Contributors to MHD Pressure Drop	4-100
4.4-2	Pressure Drop Due to Abruptly Increasing B for Various Velocity Profiles	4-108
4.4-3	Pressure Drop Due to Slug Flow in Linearly Increasing B	4-108
4.4-4	Experimental Results of Pressure Drop Due to Varying B	4-112
4.4-5	Pressure Drop for Slug Flow in Thin-Walled Duct with Abruptly Changing B Field	4-114
4.4-6	Pressure Drop for Slug Flow in Thin-Walled Duct with Linearly Changing B Field	4-114
4.5-1	Properties of the Liquid Metal	4-132
4.5-2	Specifications of Hot Flim Anemometer Probe	4-132
4.5-3	Specifications of the Anemometer Unit	4-133
4.5-4	Experimental Observations	4-135
4.5-5	Change in Nusselt Number Due to Heat Generation for a Pr=0 Flow Over a Cylinder	4-144
4.8-1	Dimensions of the Channels	4-188

4. THEORY AND MODELING

4.1 Introduction

Development of theory and analytical and numerical models is a critical element in the R&D plan for fusion nuclear technology.[1,2] Successful development of predictive capabilities is necessary to design, construct, and operate fusion nuclear components, and requires a highly interactive program of theory, modeling, and experiments. In the early stages of R&D, theory and models are used to anticipate scientific and engineering phenomena, to define performance parameter ranges of interest, and to characterize uncertainties. Thus, theory and modeling are necessary in planning and designing useful experiments. Results from experiments are then used to verify analytical and numerical models.

The coupling between experiments and modeling efforts is shown more clearly in Figure 4.1-1. Whereas the ultimate goal of the experimental pro-

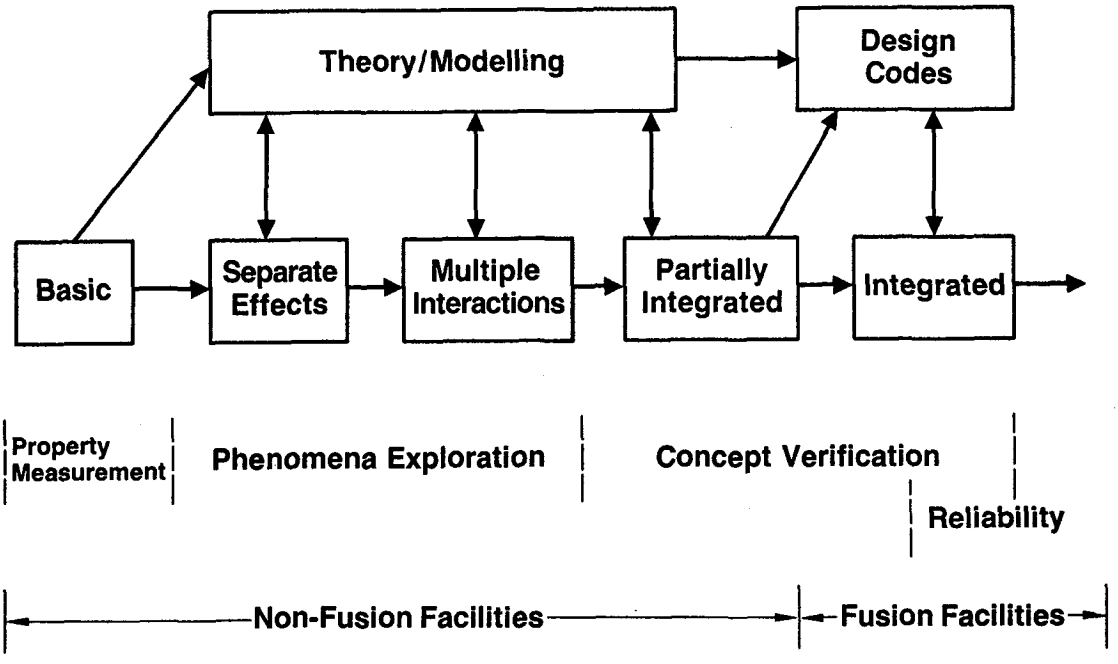


Figure 4.1-1 Types and role of experiments and facilities for Fusion Nuclear Technology

gram is fusion integrated testing, the ultimate goal of the modeling program is a design code for overall predictions of the performance of fusion nuclear components. This design code may consist of a combination of analytical, numerical, and empirical components.

The major components of interest in fusion nuclear technology are the blanket, tritium and vacuum systems, plasma-interactive components, and radiation shielding. The modeling needs for each of these components have some unique characteristics. The blanket and PIC provide multiple functions under some of the most severe environmental conditions of any fusion component. As such, the modeling issues are most complicated, involving many of the technical disciplines in science and engineering. These include, for example, fluid mechanics, heat transfer, mass transfer, material science, thermodynamics, and neutron transport. The blanket has received the largest amount of attention in this study. Particular emphasis has been placed on liquid metal blankets because they provide an excellent example of an area for which: 1) the present level of understanding and ability to predict blanket thermomechanics, particularly MHD effects, are poor; and 2) the potential for advancement in predictive capabilities and the planning of effective experiments through theory and model development is great.

Liquid Metal Blankets

Several recent design studies have adopted self-cooled liquid metal blankets because of their many attractive features.[3-5] A key advantage is due to the combination of coolant and breeding material so that the blanket design can be much simpler. Both Li and 17Li-83Pb have excellent neutronic properties, and tritium breeding is not considered to be a major issue. Since tritium recovery is usually accomplished outside the blanket, there are more degrees of freedom to design an efficient recovery system.

A large number of uncertainties exist in the behavior of liquid metal blankets, leading to the uncertainties in their feasibility and attractive ness. One of the key issues is the interaction of the magnetic field with the liquid metal and the resulting thermomechanical behavior of the blanket system. The magnetic field creates a large body force which results in a large MHD pressure drop. This pressure drop increases pumping power requirements and, much more importantly, requires a large internal operating pressure in

the blanket, which causes large stresses. The pressure drop in a straight channel with constant magnetic field can be calculated. However, in the complicated magnetic configuration and flow geometry existing in typical blankets, the accuracy of the pressure drop calculations is uncertain.

MHD effects will also have a strong impact on heat and mass transfer. One of the key effects of the magnetic field in a fusion reactor blanket is flow laminarization which tends to reduce the heat transfer coefficient. Other limits on structure temperature result from degraded structural properties at high temperature and under irradiation. Blanket temperature is further limited by corrosion and mass transport.

A reduction in the heat transfer coefficient will increase the film temperature drop of the coolant. Therefore, if the maximum structure temperature is fixed, the exit bulk temperature of the coolant must be reduced, which will adversely impact the efficiency of energy conversion. If the heat transfer coefficient is much worse than expected, the available coolant temperature rise will also be limited. To compensate for this, an increased flow rate is required, which causes larger MHD pressure drops.

The effect of MHD on corrosion is less clear. The dissolution of the material in the liquid can be controlled either by solid state diffusion, by interface reactions, or by liquid phase mass transfer. Only if the dissolution is controlled by liquid phase mass transfer will MHD flow patterns have an important impact on mass transfer.

Figure 4.1-2 shows an example of the design window for a typical self-cooled Li/Li/V-alloy blanket.[1,6] It can be seen that approximately a 20% uncertainty in the pressure drop, heat transfer coefficient, or structure temperature limit can cause the available design margin to disappear. The uncertainty in these predictions is currently much larger than the available design margin. The importance of better understanding and predictive capabilities for MHD effects is thus clear.

Figure 4.1-3 shows the parameter region where available MHD experimental results exist, as well as the parameter region at which fusion reactor blankets will operate.[7-10] Except for very recent experiments, the existing data are a few orders of magnitude away from fusion conditions. Furthermore, data are available only for a few very simple configurations.

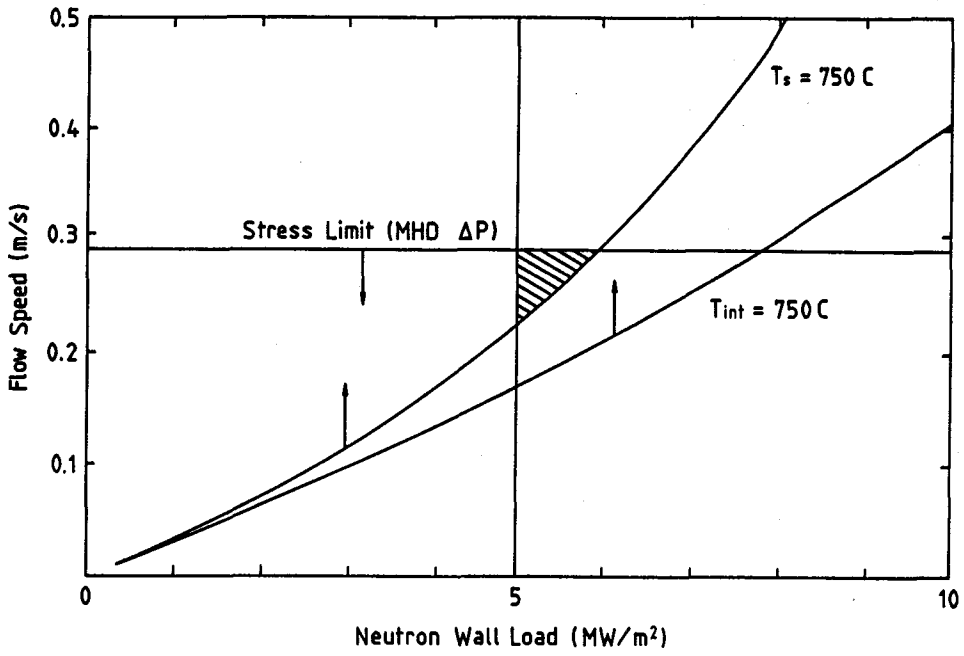


Figure 4.1-2 Thermomechanical design window

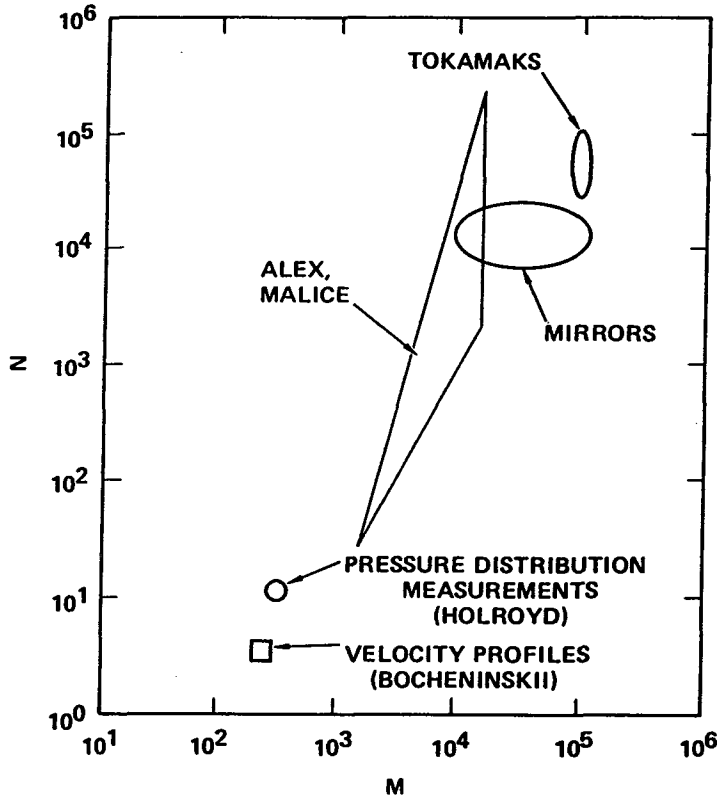


Figure 4.1-3 Hartmann number (M) and interaction parameter (N) ranges for existing data and reactor conditions

ALEX (Argonne National Laboratory), MALICE (Mol, Belgium), and other similar experiments are expected to provide data to help in the development of modeling tools. The experimental investigations in ALEX are aimed toward measurement of detailed flow characteristics in simple configurations attaining Hartmann numbers and interaction parameters in the range of 10^3 to 10^4, as can be seen in Figure 4.1-3. An Alex upgrade which will have the capability to test more complex configurations with limited heat transfer capabilities is presently under consideration. Beyond ALEX, an advanced MHD experiment, LMF1, has been defined in FINESSE to provide the capability to test prototypical elements of reactor blankets under realistic parameter ranges (see Section 2.5).

Numerical solutions of MHD should be closely associated with the experimental program. Experimental results are required to calibrate the numerical solution, while the numerical solution can be used to extrapolate experimental results to non-experimental conditions of interest. Therefore, each part alone has only limited value. Unfortunately, numerical solutions for the type of problem fusion faces are far from simple. A logical step is to develop the numerical techniques using a number of simple problems for which solutions are available. This is useful to assure that the techniques being developed are valid. The development of an MHD code for fusion application will require years of concentrated effort. The results reported here include only preliminary efforts on code development. Much work remains to be done.

Figure 4.1-4 shows a logic diagram for model development which is analogous to the experimental test plans that were developed in our previous work.[1] Three primary modeling tasks are indicated: theory and analytic method development, numerical methods, and analysis. The intimate ties with the experiments are illustrated in the figure. Also shown is the interaction with conceptual design studies. The modeling plan consists of three phases which are associated with the experimental test plan phases. In the first phase, preliminary designs are developed, simple geometry benchmark experiments are performed, and both numerical and analytical methods are explored. This phase is already underway. Analysis of separate effect experiments will aid in the design of improved blanket configurations as well as providing valuable input to the development of models.

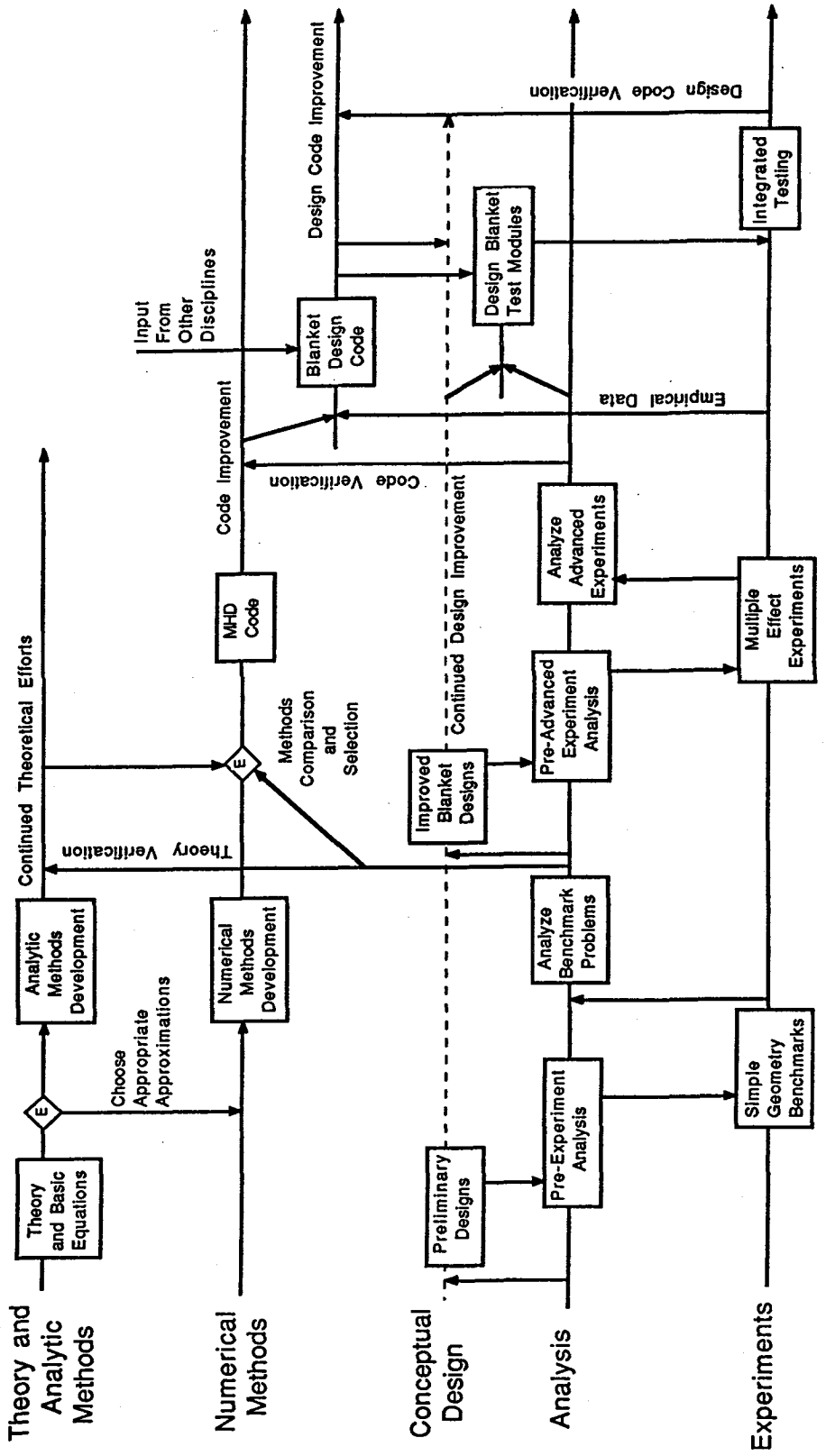


Figure 4.1-4 Liquid metal MHD modeling logic

During the second phase, choices will have to be made in order to focus the effort to develop an MHD code. The numerical method must be chosen and appropriate approximations will be determined. The required capabilities of this code are still uncertain, since we do not yet know the required prediction accuracy for fusion blankets. Also during this period, advanced MHD experiments will be performed (such as LMF1, described in Section 2.5). Analysis of these advanced experiments will provide for verification and improvement of the MHD code. This code, together with similar models developed in other areas, such as heat transfer, mass transfer, and structural analysis, will provide the basis for an overall liquid metal blanket design code. Partially integrated and/or multiple effect tests performed during this period will help to develop the design code. This code is expected to be the primary tool in the design of blanket test modules for fusion integrated testing.

Solid Breeder Blankets

The most important uncertainties for solid breeder blankets generally relate to tritium transport and inventory. A number of experiments are underway to investigate the tritium behavior in solid breeders. Tritium modeling is needed as a complement to these experiments in order to determine the tritium-related properties of solid breeders. In the past, the tritium transport processes in the solid breeders have been modeled separately. It would be useful to integrate these different processes into one complete model based on physical laws (e.g., for calculating tritium diffusion), chemical laws (e.g., for determining the tritium species and solubility) and past experimental data (e.g., for estimating such processes as surface adsorption). The modeling should also include a transient computation capability since some experiments operate in an unsteady mode. Furthermore, in view of the discussions concerning whether the next fusion test facility should operate in pulsed mode or in steady state, the modeling of tritium transport in the transient state will provide data on the predicted tritium behavior during pulsed operation, which could help in the choice of the operating mode. Section 4-7 summarizes the proposed tritium model which is being developed as part of the FINESSE effort.

Plasma-Interactive Components

Plasma-interactive components (PIC), such as limiters, divertor plates and channels, and rf antennas, provide a crucial interface between the plasma and the reactor engineering system. Many of the issues involve a variety of technical disciplines of physics and engineering. Therefore, advances in modeling of PIC will require the combined effort of many experts whose knowledge and experience cover this diversity of technical disciplines.

An appreciation of the modeling needs for PIC can be gained by examining the PIC issues. These can be divided into the following categories: 1) particle exhaust, erosion and recycling; 2) high heat flux removal and thermo-mechanical response; 3) disruptions; 4) tritium permeation and retention; and 5) irradiation effects.

Modeling of particle exhaust, erosion and recycling is intimately related to plasma physics. Modeling effort in this area has been underway for several years; see Refs. [1] and [2] for examples. These modeling efforts have contributed greatly to improving our understanding of plasma-material interaction, the effect of plasma edge temperature, and the importance of selection of plasma-side materials. Furthermore, these modeling-related activities have uncovered and quantified important phenomena such as redeposition of eroded materials.

One critical area that has not received much effort in the past is modeling of the thermo-mechanical response of PIC. This is a critical area because: 1) PIC receives about 20% of the fusion energy and, therefore, efficient heat removal and recovery is important for the reactor economics, and 2) the steady state and transient thermomechanical loads, including the high heat flux and electromagnetic forces, make the design of efficient and reliable systems very difficult. While many of the technical disciplines involved here are similar to those in the blankets, the detailed problems and modeling needs are substantially different.

The issue of tritium permeation and retention is discussed below as part of the tritium systems. Irradiation effects need to be addressed for the plasma-side and heat sink materials. Many of these materials are different from those used in the blanket. At present, prediction of radiation effects relies primarily on experimental data. Additional modeling effort will pro-

vide better understanding and enable extrapolation of experimental data.

Tritium Systems

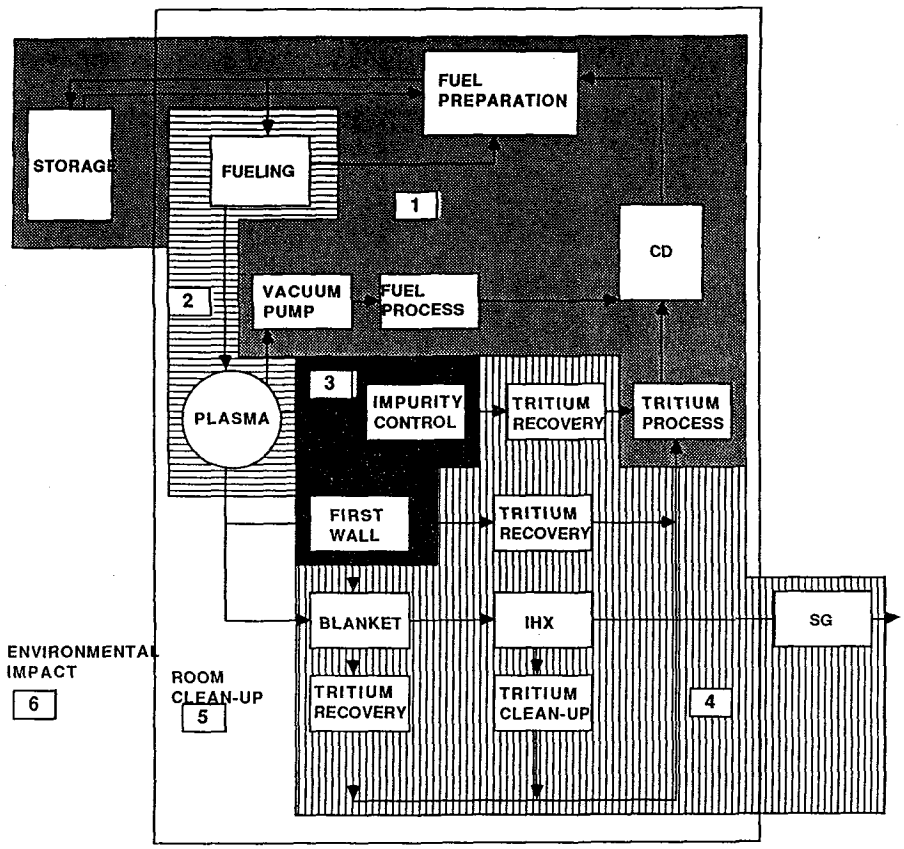
In an operating fusion reactor, tritium moves intentionally and unintentionally through a large number of subsystems. For a variety of reasons, including economics, safety, machine availability, tritium accounting, and tritium breeding requirements, it is important to understand quantitatively this movement of tritium and the resulting tritium inventories resident in subsystems. A comprehensive model of the total tritium systems is needed to provide this understanding. Pieces of the model have already been developed and used to address particular issues, but further work is needed in the overall analysis of tritium movement and inventories for specific reactor concepts.

A total tritium systems model may be structured conceptually as shown in Figure 4.1-5. The necessary outputs are tritium flows into and out of each box shown and the inventories in each box. Computer codes and data sources exist to provide estimates of these quantities. Overall integration and analysis is needed. Questions to be addressed by analysis are of two kinds:

1. Questions of steady-state operation, for example:
   - Which components or subsystems are most important from the standpoint of tritium handling cost, inventories, and losses?
   - How do these parameters vary with reactor concept and design?
2. Questions of transient or off-normal operation, for example:
   - What is the time for tritium flows and inventories to reach steady-state values after startup?
   - What is the effect on reactor safety and availability of limited outages in subsystems such as cryopumps, plasma exhaust processing, breeding blanket extraction or processing, and water detritiation systems?
   - What tritium movement is anticipated or required during maintenance operations? Related issues are pre-treatment of equipment for maintenance, outgassing during maintenance, and tritium control in maintenance cells.

Radiation Shield

The capabilities required for the design of radiation shield consist



1. John Bartlit, LANL
2. P. Cook, UCLA
3. R. Martin, UCLA and R. Bastasz, Sandia
4. D. Sze, ANL - Lithium System
   P. Gierszewski, CFFTP - Water Systems
5. P. Gierszewski, CFFTP
6. C. Wong, GA

Figure 4.1-5 Tritium systems model

of: 1) a library of basic nuclear data, 2) a library of nuclear responses (e.g., kerma factors, atomic displacement function) generated by special purpose codes, 3) a set of radiation protection criteria for components and personnel, and 4) codes for predicting neutron and photon transport. Thanks to intensive efforts by the fission reactor industry and other nuclear-related activities over the past several decades, there exists today some sophisticated capabilities for general shielding design. However, additional development is required to address fusion-specific problems.

The fusion system has many radiation-sensitive components, and hence there is a definite need for accurate prediction of radiation transport. However, the fusion shield has three key characteristics that make prediction of radiation transport difficult. The first is very deep radiation penetration; typically six orders of magnitude attenuation are required in the nuclear island plus an additional four orders of magnitude in the biological shield. The second is the complex geometry of the reactor system, and the third is the presence of many penetrations. Three-dimensional representation of the reactor geometry is necessary. The only practical method available is Monte Carlo. However, the statistical nature of this method makes it very difficult, and in some cases practically impossible, to get accurate solutions at all required locations. On the other hand, the Discrete Ordinates method is deterministic and provides, in general, accurate solutions everywhere, but its application is practically limited to 1- and 2-D problems. There are needs for further development to improve the accuracy and efficiency of radiation transport calculations. An example is better variance reduction techniques to improve Monte Carlo codes. Another is more rigorous, efficient and automated techniques for coupling Monte Carlo and Discrete Ordinates codes that allow different methods to be used in various regions of the fusion system.

Some modeling effort is also required in the area of response functions. Experimental data is required about the tolerable radiation levels in the many components of the fusion reactor system. Integral shielding experiments with an intense neutron source will permit validation of data, methods and codes.

Chapter Overview

The bulk of this chapter deals with the initial results of modeling liquid metal blanket phenomena. Section 4.2 provides detailed numerical analysis for a variety of simple MHD fluid flow and heat transfer problems. Both the finite difference and finite element methods are used. Geometries which are treated include simple 2-dimensional pipe flow and channel flow with magnetic fields aligned either parallel or perpendicular to the direction of the main flow. Developed, developing, and orifice flows are considered.

Analytic solutions for MHD flow are included in Section 4.3. Flow in a circular pipe flowing around a bend in the plane perpendicular to a magnetic

field is investigated using an asymptotic expansion in the Dean and Hartmann numbers.

In Section 4.4, the MHD pressure drop is studied at a magnetic field entrance/exit region. The validity of approximate solutions to the pressure drop is explored using assumed velocity profiles. Results are compared with existing data and analytic solutions from the literature.

Section 4.5 describes a continuing effort to determine the effects of bulk heating on heat transfer in liquid metal blankets. In this work, heat transfer near a wedge or cylinder is studied. This work helps define the validity of probe measurements under the condition of bulk heating, as well as having general relevance to heat transfer over plates.

Section 4.6 describes efforts to develop models for predicting corrosion and mass transport in the lithium-HT9 system. Early development of a general modeling tool is described. This model takes into account solid phase, liquid phase, and interface processes in a comprehensive way. In addition, a set of two thermal convection loops have been designed in order to provide data to assist in the model development as well as to provide basic empirical data.

Some work on areas other than liquid metal blankets has been performed and is described in Sections 4.7-4.8. In Section 4.7, preliminary development of a model for predicting tritium transport and inventory in solid breeders is described. This model attempts to account for a variety of processes including solubility, grain diffusion, grain boundary diffusion, desorption, pore diffusion, and purge flow convection.

Section 4.8 discusses thermomechanical modeling of limiters. Because of the safety impacts of liquid lithium cooling in blankets, plasma-interactive components may be required to operate with non-water coolants. In this section, a complete thermal-hydraulic and structural analysis are described for evaluating the design window for liquid metal cooled limiters. A three-dimensional finite element code was developed to calculate thermomechanical stresses in a limiter and the results are discussed in Section 4.9.

4.2 Computational Methods in Liquid Metal MHD

4.2.1 Introduction

Theoretical studies over the past 10-20 years have greatly advanced our understanding of the unusual characteristics involved in liquid metal MHD fluid flow. Exact and/or approximate analytic solutions now exist for various classes of straight pipe and duct flow with uniform and varying cross sections and magnetic fields.[11-13] The existence and nature of narrow MHD fluid flow layers, which have a major influence on the characteristics of the core flow, have also largely been determined.

However, the ability of closed form solutions to predict the velocity profiles in more complex geometries is limited. Fusion blankets often include the simultaneous existence of multiple electrically connected flow paths, spatially and temporally variable magnetic fields, changes in flow directions, and manifolding. If an ability is needed to predict velocity profiles in situations such as these, then a numerical solution may be the only hope. The nature of the optimum numerical method and the degree to which theoretical information can be coupled to the solution are both unknown at this time.

Liquid metals flowing in high magnetic fields can result in changes to the coolant flow profile and an increase in pressure drop. This will influence heat transfer, corrosion rate of structural materials, and drastically increase the pressure losses. Therefore, there is a need to assess the influence of the magnetic field on the behavior of liquid metals. In this section, numerical solutions are provided to the magnetohydrodynamic (MHD) equations, which describe the transport of momentum and energy of a conducting liquid in the presence of a magnetic field.

To model MHD problems, both Navier-Stokes equations and Maxwell's equations must be considered. MHD flow is usually laminar due to the strong damping effect of the magnetic field on turbulence.[14] If the field and the flow are aligned, laminarization is a dissipative process. Larger eddies, perpendicular to the field, are destroyed due to electrical resistivity and the smaller ones due to the viscous dissipation. When the field and the flow are perpendicular to one another, laminarization is predominantly due to the domination of magnetic forces over Reynold's stress gradients across the boundary.

The MHD equations, which describe the transport of momentum and energy of an incompressible, constant property, conducting laminar fluid in the presence of a magnetic field, are given in dimensionless vector form as follows:

$$\text{continuity equation } \vec{\nabla} \cdot \vec{V} = 0 \tag{4-1}$$

$$\text{momentum equation } \left(\frac{\partial \vec{V}}{\partial t} + (\vec{V} \cdot \vec{\nabla})\vec{V}\right) = -\vec{\nabla}P + \frac{1}{Re}\nabla^2 \vec{V} + Al\ (\vec{J} \times \vec{B}) \tag{4-2}$$

$$\text{Maxwell's equation } \frac{\partial \vec{B}}{\partial t} = \vec{\nabla} \times (\vec{V} \times \vec{B}) + \frac{1}{Re_m}\nabla^2 \vec{B} \tag{4-3}$$

$$\text{Ohm's Law } \vec{J} = Re_m \left[\vec{E} + \vec{V} \times \vec{B}\right] \tag{4-4}$$

$$\text{energy equations } \frac{\partial T}{\partial t} + \vec{V} \cdot \vec{\nabla}T = \frac{1}{Re\ Pr}\nabla^2 T + Q_V \tag{4-5}$$

The primary variables $\vec{V}$, P, $\vec{B}$, $\vec{J}$, $\vec{E}$, and T are, respectively: fluid velocity, pressure, magnetic field, electric current density, electric field and temperature, and Q_V is the internal heat source due to ohmic heating, all in dimensionless form. The body force $\vec{J} \times \vec{B}$ is generated by the interaction of the applied magnetic field with the moving conducting liquid. The dimensionless parameters which govern the equations are Reynold's number (Re), Alfven number (Al), Hartmann numbers (Ha), magnetic interaction parameter (N), magnetic Reynold's number (Re_m) and Prandtl number (Pr).

Definitions of each of these parameters can be found in Branover[15] and Schlichting[16] and are listed in Table 4.2-1. V is a characteristic velocity, L is a characteristic length and B_o is a characteristic magnetic-field induction. ρ, ν, C_p, k, σ and μ_o are the fluid density, kinematic viscosity, specific heat, thermal conductivity, electrical conductivity and magnetic permeability, respectively. ν is the kinematic viscosity (μ/ρ) and ν_m is the magnetic diffusivity ($1/\mu_o\sigma$).

Equations (4-1) through (4-5), along with the appropriate boundary and initial data, constitute a system of coupled, non-linear partial differential equations (PDE's) which must be solved simultaneously for the dependent variables V, P, B and T to fully describe the momentum and energy in the conducting fluid.

Table 4.2-1. Non-Dimensional Numbers in Liquid Metal MHD

Non-dimensional Number	Symbol	Definition	Physical Meaning
Reynolds Number	Re	VL/ν	$Re = \frac{\text{inertia force}}{\text{viscous force}}$
Hartmann Number	Ha	$B_o L \sqrt{\frac{\sigma}{\mu}}$	$Ha^2 = \frac{\text{magnetic force}}{\text{viscous force}}$
Magnetic Reynolds Number	Re_m	$\sigma \mu_o VL$	$Re_m = \frac{\text{induced magnetic field}}{\text{applied magnetic field}}$
Magnetic Interaction parameter	N	$\frac{\sigma B_o^2 L}{\rho V}$	$N = \frac{\text{magnetic force}}{\text{inertia force}}$
Magnetic Prandtl Number	Pr_m	$\frac{\nu}{\nu_m}$	$Pr_m = \frac{\text{momentum diffusivity}}{\text{magnetic diffusivity}}$
Thermal Prandtl Number	Pr	$\frac{\nu}{\alpha}$	$Pr = \frac{\text{momentum diffusivity}}{\text{thermal diffusivity}}$
Alfven Number	Al	$\frac{B_o^2}{\mu_o \rho V^2}$	$Al = \frac{\text{magnetic energy}}{\text{kinetic energy}}$

Although we are able to write these governing equations and boundary/initial conditions for many of the problems of interest to fusion reactor blankets, it cannot be proven mathematically that solutions to such a system of non-linear partial differential equations exist. If the methods of classical mathematics were to be used for solving these equations, there would be little hope of predicting any phenomena of practical interest. Simplification and approximation of the equations are necessary, with subsequent application of numerical or analytical methods to the resulting simplified set of equations, preferably one that combines the benefits of the analytical and numerical approaches.

Experimental investigations are important activities and the only activities that can observe the realities of the physical phenomenon being studied. Theoretical investigations, on the other hand, are useful only when the mathematical models which describe the physics of the process are valid, and depend on the availability of numerical methods to solve the resulting set of differential equations.

Computer models are built, debugged, adjusted and exercised for comparison with experimental data. The goal of a computational effort should be to

produce results which consistently and accurately predict observed experimental behavior and phenomena. Once confidence is gained in the ability to predict the phenomena, models become a design tool. Modeling allows the designer to evaluate the impact of design changes without building an experiment. It is doubtful that a fusion reactor device will ever be designed using only computer predictions. However, modeling should be used to increase the effectiveness of an experimental program by eliminating and highlighting design needs prior to building the experiments.

Examples of theoretical analysis to simplified subsets of the MHD equations aimed mainly for flows at high interaction parameters can be found in the work of Hunt[17] and Walker, et al.[18] Walker and Ludford,[19] and Petrykowski and Walker[20] have employed asymptotic techniques to analyze large interaction parameter and high Hartmann number MHD flows. However, flows at moderate Hartmann numbers and interaction parameters involve the complete governing equations and require the use of numerical techniques. Some benefits can be obtained from the long experience and actual achievements of the science of computational fluid mechanics. One of the pioneering works was the development of the MAC (Marker and Cell) method[21], followed by the SIMPLE (Semi-Implicit Method of Pressure Linked Equations) method[22] which is widely used at present for ordinary-hydrodynamic (OHD) flows. Numerical solutions to MHD flows have been applied recently with moderate successes.[23,24]

Two numerical techniques, finite difference methods (FDM's) and finite element methods (FEM's), have been investigated as methodologies by which the MHD equations could be solved. Both techniques have attractive features and, depending on the particular problem, boundary conditions and geometry, it may or may not be easier or faster to implement one or the other of these techniques. Both methods approximate the behavior of the continuous physical system by concentrating the variables into discrete lumps. They connect together the values of field variables for a finite set of locations (grid nodes) by linear (or linearized) algebraic equations called the discretization equations. These equations are derived from the differential equations describing the physical process and thus express the same physical information as the differential equations. As the number of grid points becomes very large, the solution of the discretization equations is expected to approach the exact

solution of the corresponding differential equations.

For a given differential equation, the possible discretization equations are not unique. The different types arise from the differences in the profile assumptions and in the methods of derivation. The distinction between the finite-difference method and the finite-element method results from the ways of choosing the profiles and deriving the discretization equations.

FDM's approximate the dependent variables by discrete values of the variable at selected points of the independent variable or grid points. The exact nature of the algebraic combination depends on the methods of deriving the discretization equations (e.g. forward, backward or central differencing). The FEM subdivides the calculational domain into elements. The discretization equations are usually derived by the use of a variational principle when one exists or by the Galerkin method, which is a special case of the method or weighted residuals. In the derivation, a shape function or profile assumption is used to describe how the dependent variable ϕ varies over an element.

The analysis of MHD flows presented in this section utilizes the SIMPLE method[22] developed by Patankar and Spalding, and the FEM based on the method of weighted residuals. It should be pointed out that the formulation of the SIMPLE method is another special case of the method of weighted residuals, where a shape function is used to describe the variations of the dependent variable between two grid points. It so happens that these shape functions are locally one-dimensional, necessitating the use of an orthogonal set of grid lines. More details of the calculational procedure can be found in subsequent sections.

After deriving the discretization equations, the problem is reduced to solving an algebraic system of equations. Limitations on computer storage capacity typically restrict the total number of grid points. Techniques which minimize grid or element size in regions in which the gradients and errors are large can be implemented (see self-adaptive technique in the FEM section of this chapter), which tends to alleviate these problems in some cases.

In general, problems involving variable body forces are difficult to solve numerically whether it be in OHD or MHD flows; the reason is the double interaction between the momentum equations for the velocities and the magnetic field in MHD flows. Therefore, in an iterative pressure correction procedure,

such as the SIMPLE method, the adjustment procedure may be continually over-correcting, prohibiting the attainment of a converged solution. Under-relaxation may be helpful, but at higher Hartmann numbers an alternative correction procedure must be used to account for the correction in the electromagnetic forces as well as inertia forces which would be small at high interaction numbers.

At present, we are able to obtain solutions to problems with dimensionless parameters in the range of 100 to 200. Typical fusion reactor blanket parameters are more on the order of 1000 to 10000. In order to extend numerical studies to these levels, it will be necessary to concentrate on developing new solution algorithms, possibly based on FDM or FEM, which are able to address these difficulties. The material in this section is intended to give an introduction and direction to future model development efforts.

4.2.2 Finite Difference Method

In this section, the SIMPLE method is used to investigate the development of the two-dimensional velocity and temperature profiles for a conducting fluid in the presence of a magnetic field in straight and suddenly expanding ducts. The partial-differential equations for the momentum and energy which describe the flow of steady, viscous, incompressible, electrically conducting fluid in two-dimensional geometry are solved by a finite difference calculational procedure.

The flow field in liquid metal blankets of conceptual fusion reactors are three-dimensional with regions of varying geometry and/or non-uniform applied magnetic fields. However, because of the difficulties in dealing with three-dimensional flows, we have restricted our calculations to two-dimensional geometries with the magnetic field in the plane of the flow.

Solution Procedure

The calculational procedure is aimed at solving the steady, incompressible coupled nonlinear Navier-Stokes equations in two dimensions. The problems analyzed numerically include developing flow in ducts with the magnetic field in the plane of the flow aligned with the main flow direction or perpendicular to it. The continuity, momentum, and energy equations which describe the transport of momentum and energy in two dimensions are:

$$\frac{\partial}{\partial x}(\rho u) + \frac{1}{y^r}\frac{\partial}{\partial y}(y^r \rho v) = 0 \tag{4-6}$$

$$\rho\frac{\partial}{\partial x}(u^2) + \frac{\rho}{y^r}\frac{\partial}{\partial y}(y^r uv) - \frac{\partial}{\partial x}\left(\mu\frac{\partial u}{\partial x}\right) - \frac{1}{y^r}\frac{\partial}{\partial y}\left(y^r \mu\frac{\partial u}{\partial y}\right) = -\frac{\partial p}{\partial x} + S_u \tag{4-7}$$

$$\rho\frac{\partial}{\partial x}(uv) + \frac{\rho}{y^r}\frac{\partial}{\partial y}(y^r v^2) - \frac{\partial}{\partial x}\left(\mu\frac{\partial v}{\partial x}\right) - \frac{1}{y^r}\frac{\partial}{\partial y}\left(y^r \mu\frac{\partial v}{\partial y}\right) = -\frac{\partial p}{\partial y} + S_v \tag{4-8}$$

$$\rho\frac{\partial}{\partial x}(uT) + \frac{\rho}{y^r}\frac{\partial}{\partial y}(y^r vT) - \frac{\partial}{\partial x}\left(\frac{k}{C_p}\frac{\partial T}{\partial x}\right) - \frac{1}{y^r}\frac{\partial}{\partial y}\left(y^r \frac{k}{C_p}\frac{\partial T}{\partial y}\right) = S_T \tag{4-9}$$

where u, v, p and T are the dependent variables, velocities in x and y-directions, pressure and temperature, respectively. ρ, μ, k and C_p are density, dynamic viscosity, thermal conductivity and specific heat of the fluid, respectively. The index r is given by

r = 0 for plane geometry,

r = 1 for axisymmetric geometry.

S_u, S_v and S_T are body source terms which include the electromagnetic forces ($\vec{J} \times \vec{B}$) in the momentum equations and the volumetric heating term (J^2/σ) in the energy equation.

The finite-difference equations are obtained by integrating the differential equations over the control volumes surrounding the location of the flow variables. The locations and the control volumes for the individual variables are shown in Figure 4.2-1. The velocities u, v in the x and y-directions, respectively, are staggered between two grid nodes. The other flow variables (pressure and temperature) are located at the intersection of the grid lines, as shown in Figure 4.2-2.

Consider the two-dimensional partial differential equation for the transport of a variable (Ψ):

$$\frac{\partial}{\partial x}(G_x\Psi) + \frac{1}{y^r}\frac{\partial}{\partial y}(y^r G_y\Psi) = \frac{\partial}{\partial x}(\Gamma_\Psi\frac{\partial\Psi}{\partial x}) + \frac{1}{y^r}\frac{\partial}{\partial y}(y^r \Gamma_\Psi\frac{\partial\Psi}{\partial y}) + S_\Psi \tag{4-10}$$

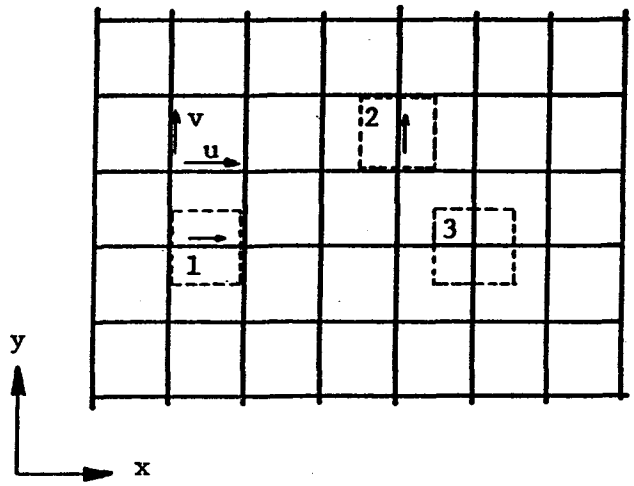


Figure 4.2-1 Location of flow variables on the finite-difference grid: (1) control volume for u, (2) control volume for v, (3) control volume for p and T

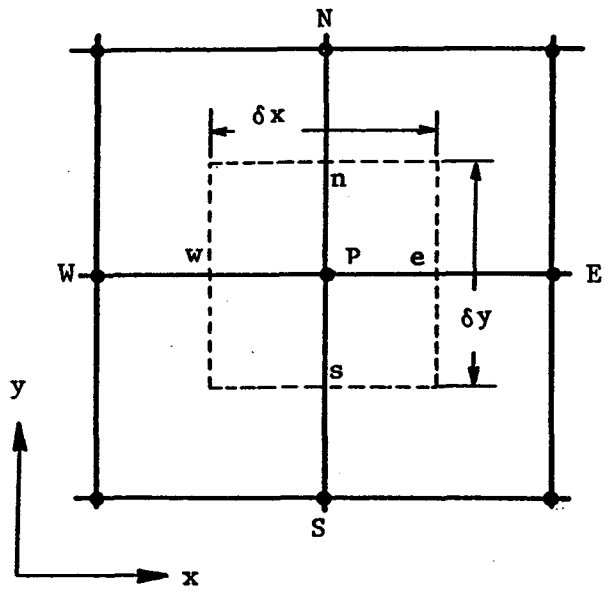


Figure 4.2-2 Control volume in two-dimensional geometry

Ψ takes the value of 1 for the continuity equation u, v for the momentum equations in x and y directions, respectively, and T for the energy equation. G_x and G_y are mass fluxes ρu and ρv, respectively. Γ_Ψ is an exchange coefficient. S_Ψ is a source term and assumes different forms:

for momentum equation: $S_\Psi = -\nabla P + J \times B$

and for energy equation: $S_\Psi = \frac{J^2}{\sigma}$

The difference equation relating Ψ_P to the surrounding Ψ's is obtained by integrating Eq. (4-10) over the control volume enclosing P:

$$\int_s^n \left[G_x \Psi - \Gamma_\Psi \frac{\partial \Psi}{\partial x}\right]_w^e dy + \int_w^e \left[G_y \Psi - \Gamma_\Psi \frac{\partial \Psi}{\partial y}\right]_s^n dx - \int_s^n \int_w^e S_\Psi \, dx \, dy = 0 \tag{4-11}$$

The quantities in square brackets represent the local fluxes of Ψ due to the combined effects of convection and diffusion. After expressing the convection and diffusion fluxes by upwind and central differencing, and after collecting the discrete values, we obtain the general expression:

$$A_P \Psi_P = A_N \Psi_N + A_S \Psi_S + A_E \Psi_E + A_W \Psi_W + S^\Psi \tag{4-12}$$

where the coefficients A_P, A_N, A_S, A_E and A_W contain contributions from convective and diffusive fluxes, and link values at Ψ_N, Ψ_S, etc. with Ψ_P. S^Ψ represents the integral of the source S_Ψ over the control volume. For the momentum equation, the difference equations can be written as:

$$A_P u_P = \sum_n A_n u_n + \delta y \, (P_W - P_P) + S^u \tag{4-13}$$

$$A_P v_P = \sum_n A_n v_n + \delta x \, (P_S - P_P) + S^v \tag{4-14}$$

Here the summations are over the four neighboring velocities. To complete the

transformation to difference form, the continuity equation is expressed as:

$$(G_e - G_w)\,\delta y + (G_n - G_s)\,\delta x = s_m \qquad (4\text{-}15)$$

where s_m is a residual mass which must be driven to a negligible value through appropriate pressure adjustments. This is the essence of the SIMPLE procedure which solves the set of Eqs. (4-13) to (4-15) by a cyclic series of guess and correct operations until s_m is made very small. The velocities are first calculated using the momentum equations for a guessed pressure field, then a new corrected pressure is calculated from the pressure correction equation formed by linking the pressure correction with the residual mass. The velocities are later adjusted to satisfy continuity. Variable fields are computed successively along each line while iterating through the calculational domain.

4.2.2.1 Entry Length Effects in MHD Duct Flow

Development of 2-D velocity and temperature profiles is explored for a conducting fluid in the entrance region of straight ducts in the presence of a magnetic field. The partial-differential equations for the momentum and energy are solved by a finite difference calculational procedure. In laminar flow parallel to the magnetic field, the magnetohydrodynamic (MHD) force is seen to enhance heat transfer slightly due to the suppression of velocity profile development. In laminar flow perpendicular to the magnetic field, higher fields enhance heat transfer by increasing the flow rate near the wall.

Flow Parallel to the Magnetic Field

Consider a circular pipe with the magnetic field aligned with the axis of the pipe (Fig. 4.2-3). The velocity component parallel to the field generates no MHD effects; however, the transverse component, v, resulting from the development of the velocity profile, leads to an electromotive force (Bv) generated in the circumferential direction. Due to the symmetry, no charge build-up occurs and the electric field, **E**, is zero everywhere. Assuming further that the induced magnetic fields are negligible, there is a body force in the radial direction given by $-\sigma B^2 v$, where v is the radial velocity component.

In the entry region of a pipe, fluid is decelerated near the wall, and a secondary velocity component from the boundary layer and transverse to the

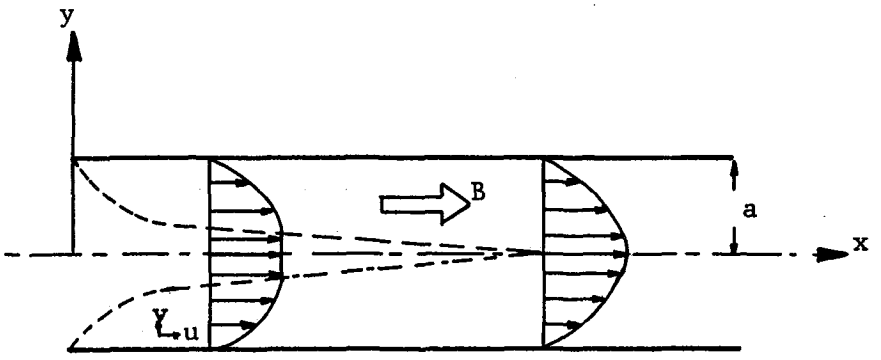


Figure 4.2-3 Pipe flow configuration

field is produced. Figures 4.2-4a and 4.2-4b show the development of the velocity and temperature profiles in the pipe. The flow entering from the left is at a temperature of 200 °C and the temperature at the pipe wall is kept at 695 °C. The effect of an axial magnetic field produces a body force from the interaction with the transverse velocity component which suppresses the growth of the viscous wall layer and thus lengthens the entry region. Figure 4.2-5 shows the development of the dimensionless centerline velocity with dimensionless distance along the pipe for a range of values of N/R_e, where N is the interaction parameter and Re is the Reynolds number. For N/R_e=30 the center line velocity is about 47% lower than the non-magnetic case at x/aR_e of 0.2 and the entry length is about 3.5 times that of the non-magnetic entry length. These results compare favorably with the results of D'Arcy and Schmidt.[25]

Since in an axial magnetic field there is no interaction between a parallel field and a fully developed laminar velocity field, no change in heat transfer is expected. However, for a developing flow the effect is to delay the full flow development which leads to an increase in heat transfer. Figure 4.2-6 shows how the Nusselt number changes along the non-dimensional axial

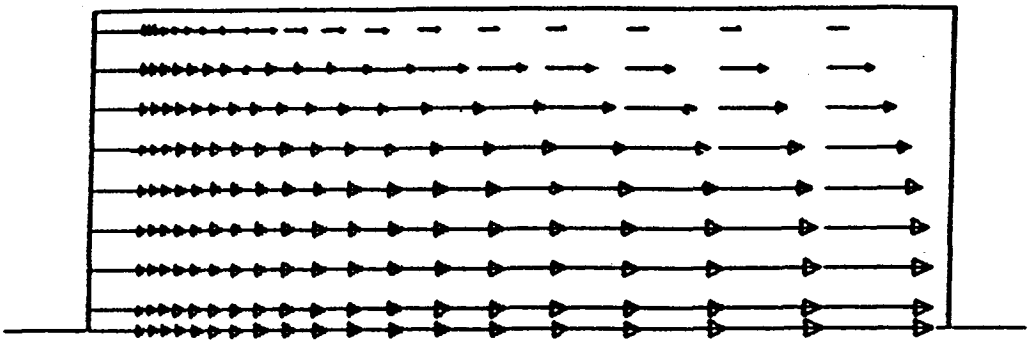


Figure 4.2-4a Velocity vectors for a developing pipe flow

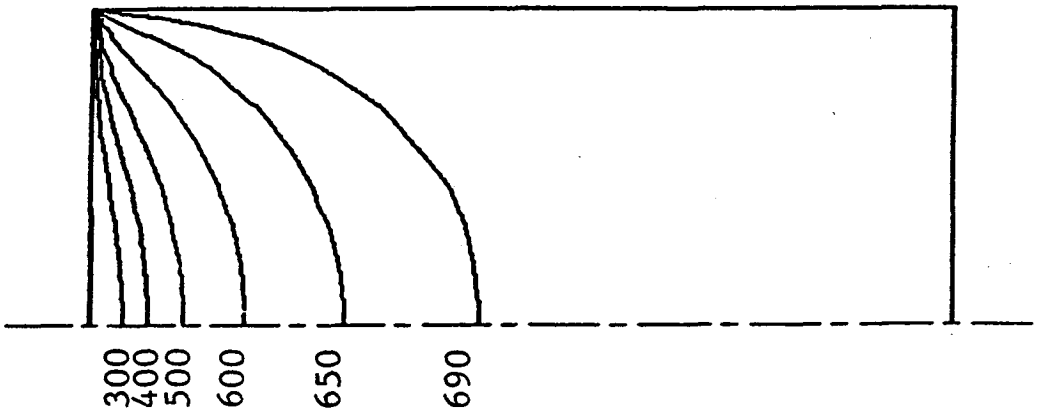


Figure 4.2-4b Temperature contours (degrees Celsius)

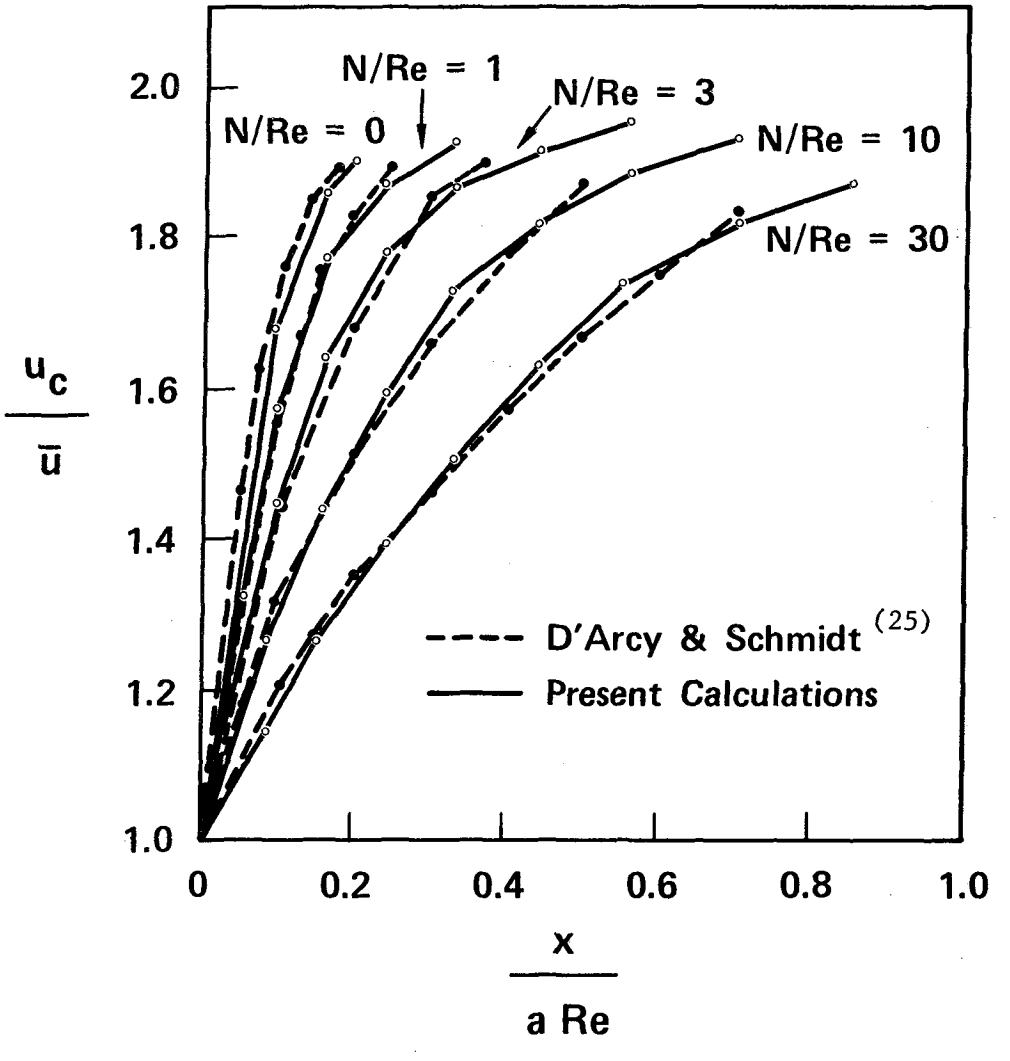


Figure 4.2-5 Effect of a horizontal magnetic field on the centerline velocity

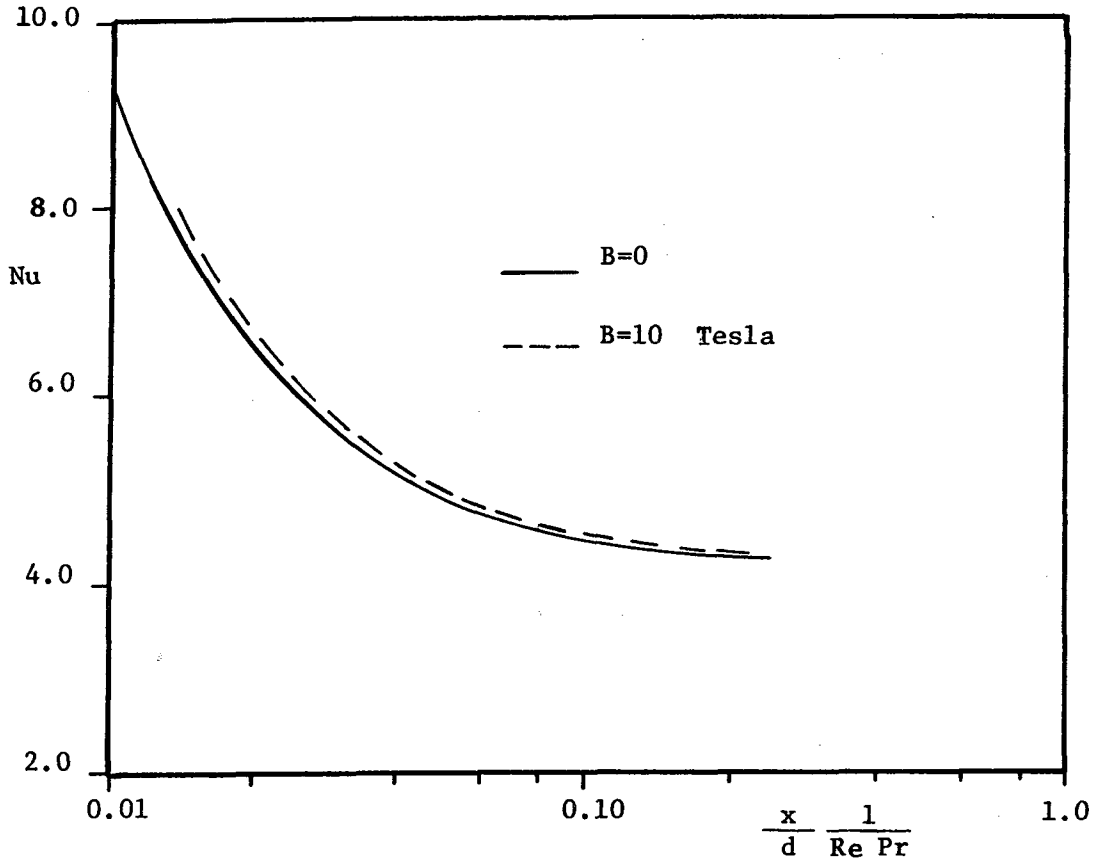


Figure 4.2-6 Local Nusselt number for the entrance region of a pipe

distance. The Nusselt number is defined by:

$$Nu = hd/k \tag{4-16}$$

where h is the heat transfer coefficient, d is the pipe diameter and k is the thermal conductivity. The heat transfer coefficient is calculated from

$$h = q_w/(t_b - t_w) \tag{4-17}$$

where q_w is the heat flux at the wall, t_b is the fluid bulk temperature defined as

$$t_b = \frac{\int_o^a utrdr}{\int_o^a urdr} \tag{4-18}$$

and t_w is the wall temperature. The Nusselt number decreases with x and approaches a value of about 4.0, which is comparable to the value reported by Eckert and Drake.[26] The effect of an axial magnetic field is to increase the Nusselt number by a small amount due to the interaction of the magnetic field with the transverse velocity field. This interaction reduces the transverse component of the velocity, thus increasing the axial velocity component near the wall.

For an order of magnitude estimate of the entrance region effects in fusion reactor design, consider lithium coolant flowing in a pipe of 10 cm in diameter with a mean velocity of 0.5 m/sec in the presence of a toroidal field of 10 Tesla. For these conditions we obtain $Re \approx 5 \times 10^4$ and $N/Re \approx 1$. From Figure 4.2-5, $x/aRe \approx 0.3$ and the entry length is about 750 m. This is certainly longer than coolant pipes in practical blanket designs and means that the flow in a reactor blanket duct aligned with the field will never reach full development. The implication for heat transfer is that the Nusselt number is about two to three times higher than the fully developed conditions. In an actual reactor blanket design, perpendicular fields will almost always exist. The effect of these perpendicular fields will result in much more rapid flow development than indicated here.

Flow Perpendicular to the Magnetic Field

Consider an MHD flow with a magnetic field (B), applied perpendicular to a channel with infinite parallel plates, located at $y = \pm a$. The induced electromotive force (uB) leads to current flow given by Ohm's Law:

$$j_z = \sigma(E_z + uB) \tag{4-19}$$

To determine the constant electric field intensity E_z, assume there is no external electric circuit, then:

$$\int_{-(a+\delta)}^{(a+\delta)} j_z \, dy = 0 \tag{4-20}$$

where $\delta \equiv$ channel wall thickness. Substituting from Ohm's law and integrating, we obtain

$$E_z = -\phi \, \bar{u} \, B$$

where

$$\bar{u} = \frac{\int_{-a}^{a} u\,dy}{2a} \quad \text{and} \quad \phi = \frac{1}{1 + c}$$

and

$$c \equiv \text{conductance ratio} = \frac{\sigma_w \delta}{\sigma_f a} .$$

σ_w and σ_f are the wall and fluid electrical conductivities, respectively. Equation (4-20) is then written as:

$$j_z = \sigma B \left(-\phi \bar{u} + u\right)$$

and the electromagnetic force JxB becomes:

$$-\sigma B^2 \left(-\phi \bar{u} + u\right) \tag{4-21}$$

In the following, we assume fully insulating walls such that $\phi = 1$. Results are presented in Figure 4.2-7 for the normalized velocity $(u/\bar{u})$ as a function

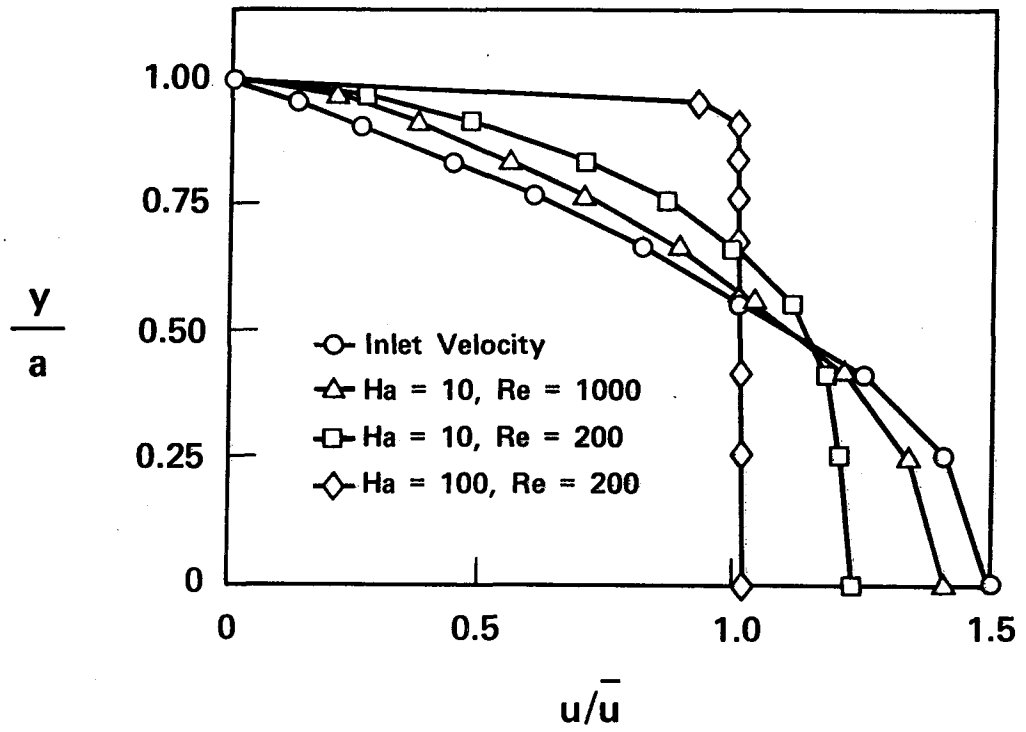


Figure 4.2-7 Velocity profile at channel exit

of the normalized location across the channel (y/a). At the exit of the channel, a distance of (3.3a) from the inlet, velocity profiles are shown for Ha=10 and 100. For Ha=10 and Re=200, the profile is developed at the exit. However, for Ha=10 and Re=1000, the profile is not yet fully developed.

Finite difference solutions for very high Hartmann numbers (Ha > 100) are difficult to obtain. In these calculations, we employ a spatially uniform mesh, which leads to increasingly poor convergence as the Hartmann number increases. This is a result of the vanishing role of velocity-dependent terms in the momentum equations.

Heat transfer was also examined in the case of perpendicular flow. In this case, the Nusselt number is given by

$$Nu = ha/k \qquad (4\text{-}22)$$

where 'a' is the channel half-width. Constant temperature boundary conditions were applied.

Figure 4.2-8 shows the temperature profile development for four cases: slug flow and parabolic flow inlet velocity profiles with Ha=0 and Ha=100. The ultimate Nusselt number is the same for a given Hartmann number, but the approach towards the ultimate Nu is slower for a slug inlet profile. The higher Hartmann number produces better heat transfer due to the enhanced flow rate near the walls.

Figure 4.2-9 supports this conclusion. Increasing Hartmann number yields increasing heat transfer coefficients.

4.2.2.2 Sensitivity Analysis of MHD Heat Transfer

In laminar flow heat transfer, the convective capability of the flow depends on the velocity profile. In self-cooled liquid metal blankets of a fusion reactor, the presence of a magnetic field results in steep velocity gradients near the walls. In many locations in the blanket, such as where the flow turns around a bend or where the flow area of the channel and the direction of the magnetic field change, large changes in velocity gradients occur. These result in large changes in the first wall and blanket temperature distribution, and substantially affect blanket performance.

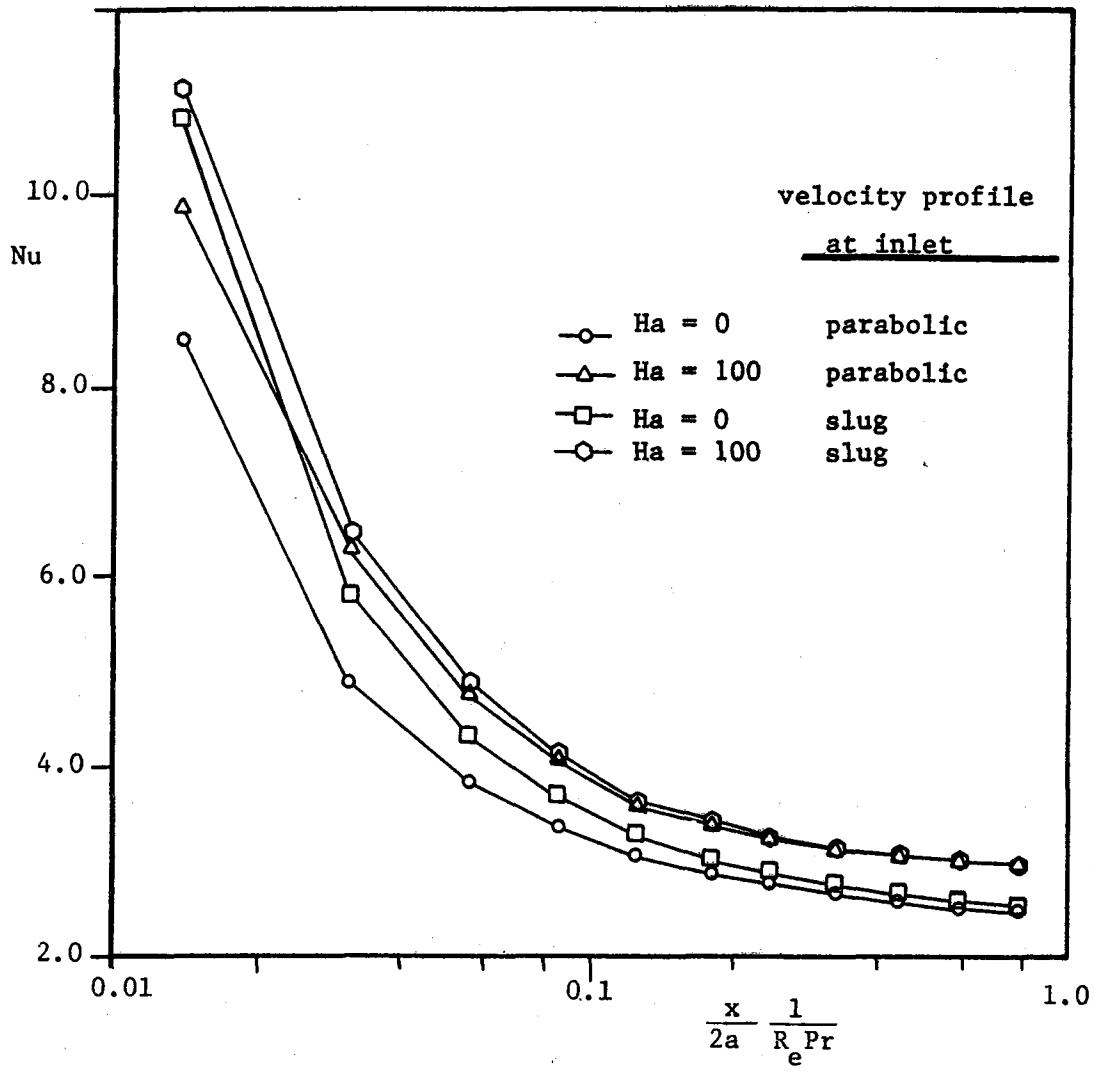


Figure 4.2-8 Local Nusselt number for the entrance region of a channel

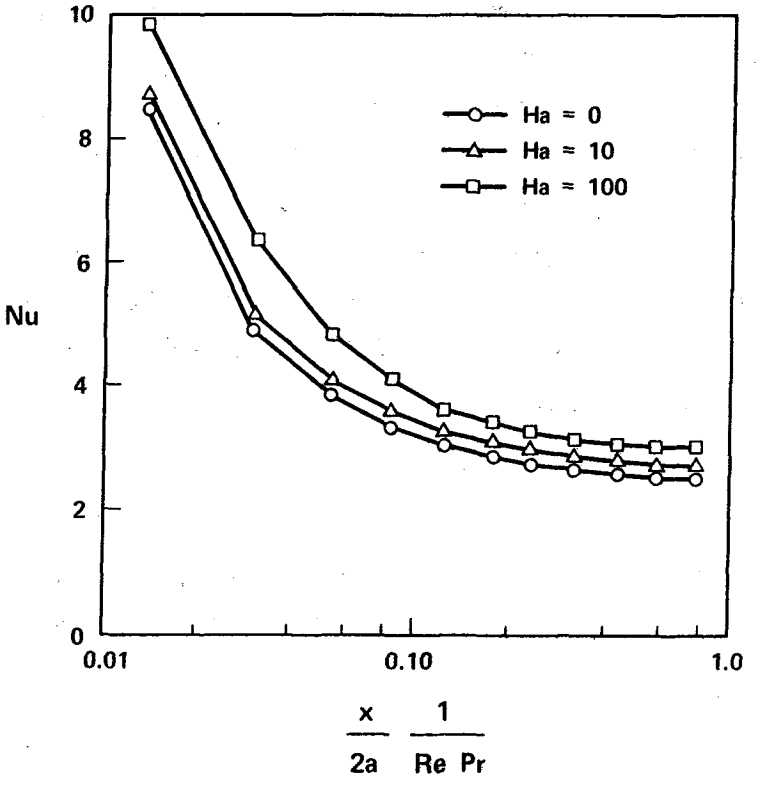


Figure 4.2-9 Effect of magnetic field on entry length heat transfer (parabolic inlet profile and constant wall temperature)

Numerical calculations were performed for the flow of an electrically conducting fluid in a plane channel in a magnetic field aligned with the direction of the main flow. Velocity and temperature variations across the duct were evaluated for different assumed velocity profiles at the inlet. It is shown that the presence of the magnetic field retards the development of the velocity profile. The solution of the energy equations for slug, parabolic and skewed velocity profiles shows that the highest heat transfer coefficients are obtained with the latter profile, which has the largest velocity gradient near the wall.

Analysis

Figure 4.2-10 illustrates the channel configuration and the coordinate system used (x,y,z).

The velocity at the entrance is either a slug profile or a skewed one. Viscous effects bring the fluid to rest at the wall, causing the formation of

a region where the longitudinal velocity varies from zero at the walls to some nearly uniform value in the core of the channel. Since the longitudinal mass flux is less in the boundary layer than in the core region, continuity requires the generation of a transverse fluid velocity away from the walls. This transverse velocity component causes, first, an increase in the uniform longitudinal core velocity, and second, the transverse component (normal to the applied magnetic field B_0) interacts with the field and results in a Lorentz force which impedes the growth of the boundary layer.

From Ohm's Law the current density is given by

$$j_z = \sigma(E - vB_0) \tag{4-23}$$

To determine the constant electric field intensity E_z, assume that there is no external electrical circuit, i.e., the total current through the fluid and walls in each section is zero.

$$\int_0^{2(a+\delta)} j_z \, dy = 0 \tag{4-24}$$

where δ is the channel wall thickness.

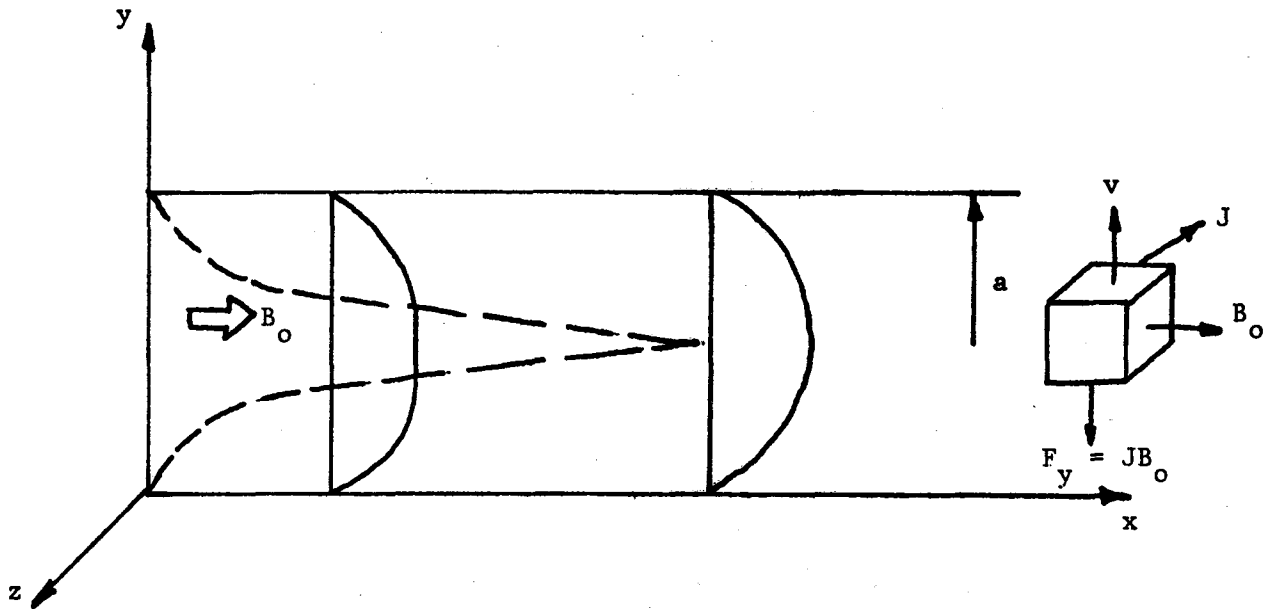


Figure 4.2-10 Channel flow configuration

Substituting from Eq. (4-23) for j_z into Eq. (4-24) and integrating, we get

$$j_z = \sigma B_0(\phi \langle v \rangle - v) \tag{4-25}$$

where

$$\langle v \rangle = \frac{\int_0^{2a} v \, dy}{2a} \text{ and } \phi = \frac{\sigma_f \, a}{\sigma_f \, a + \sigma_w \delta}$$

and where σ_w is the wall conductivity. For insulating channel walls, $\phi = 1$ and the electromagnetic force is

$$J_z B_0 = \sigma B_0^2 (\langle v \rangle - v) \tag{4-26}$$

The effect of this electromotive force is to reduce the transverse velocity component and therefore increase the momentum development length. Figure 4.2-11 shows the development of the velocity profile along the channel for different values of Hartmann numbers (Ha):

$$Ha = B_0 \, a \sqrt{\frac{\sigma_f}{\mu}} \tag{4-27}$$

For Ha=0 and Ha=100, the velocity is fully developed at $\frac{x}{2a} = 50$ for both the slug and the skewed inlet profiles. At Ha=1000, the velocity profile at $\frac{x}{2a} = 50$ is still developing. At higher Ha numbers, the development of the velocity profile will be delayed further. Fusion blankets have Hartmann numbers of about 5×10^4 to 5×10^5.

The energy equation in cartesian coordinates can be written as

$$\rho C_p \, u \frac{\partial T}{\partial x} = K \left(\frac{\partial^2 T}{\partial x^2} + \frac{\partial^2 T}{\partial y^2}\right) + \mu \left(\frac{\partial u}{\partial y}\right)^2 + \frac{J_z^2}{\sigma} \tag{4-28}$$

The viscous dissipation term is negligible when compared to the first wall heat flux. The axial conduction term can be shown to be negligible for high Peclet number flows.[27] Therefore, the energy equation can be written simply as:

$$u \frac{\partial T}{\partial x} = \frac{K}{\rho C_p} \frac{\partial^2 T}{\partial y^2} + \frac{j_z^2}{\sigma} \tag{4-29}$$

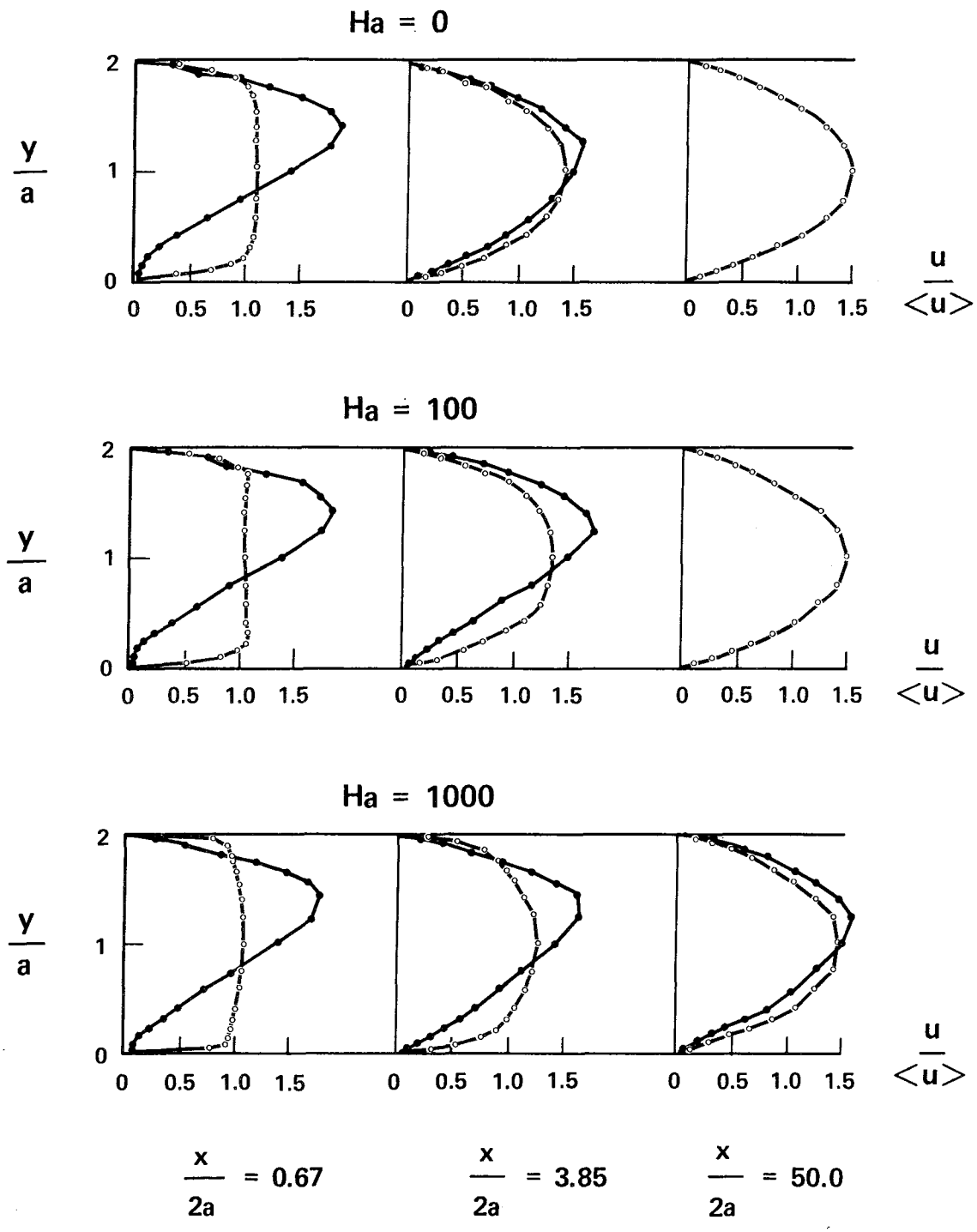


Figure 4.2-11 Development of the velocity profile along a channel for different values of Hartmann (Ha) numbers

The above equation can yield solutions for the sensitivity analysis once the approximation of a developed velocity profile is made. Evaluating the temperature T using assumed developed velocity profiles will provide a conservative estimate of blanket heat transfer. In the present analysis, a Reynolds number of 10^6 and a Peclet number of 4.4×10^4 were used. In reality, the flow may not be fully developed if the flow and the field are parallel, and hence the local heat transfer coefficient would be higher.

The assumed velocity profiles are:

$$\frac{u}{\langle u \rangle} = \left(\frac{n+1}{n}\right) \left(\frac{y}{2a}\right)^n \left[1 - \left(\frac{y}{2a}\right)^n\right] \tag{4-30}$$

for symmetric power profile, and

$$\frac{u}{\langle u \rangle} = \left(\frac{n+1}{n}\right)(2n + 1)\left(\frac{y}{2a}\right)^n \left[1 - \left(\frac{y}{2a}\right)^n\right] \tag{4-31}$$

for skewed profile, where

$$\langle u \rangle = \frac{\int_0^{2a} u \, dy}{2a} .$$

Figure 4.2-12 shows the different velocity profiles used. Equation (4-29) is solved for two cases: first, constant, but different wall temperatures, and second, constant heat flux.

let T_+ = first wall constant temperature,
T_- = second wall constant temperature,
and T_0 = coolant bulk temperature at inlet.

The boundary conditions considered for the first case are $T_+ = 600$ °C, $T_- = 300$ °C and $T_0 = 200$ °C. The non-dimensional temperature, Θ, is given by $\Theta = \frac{T - T_0}{T_- - T_0}$. The boundary conditions for the second case are constant heat flux at the first wall (q_+) and zero heat flux at the second wall ($q_- = 0$). The first and second wall temperatures are given by

$$\Theta_+ = \frac{K}{q_+ h} (T - T_0) = 1$$

$$\Theta_- = 0$$

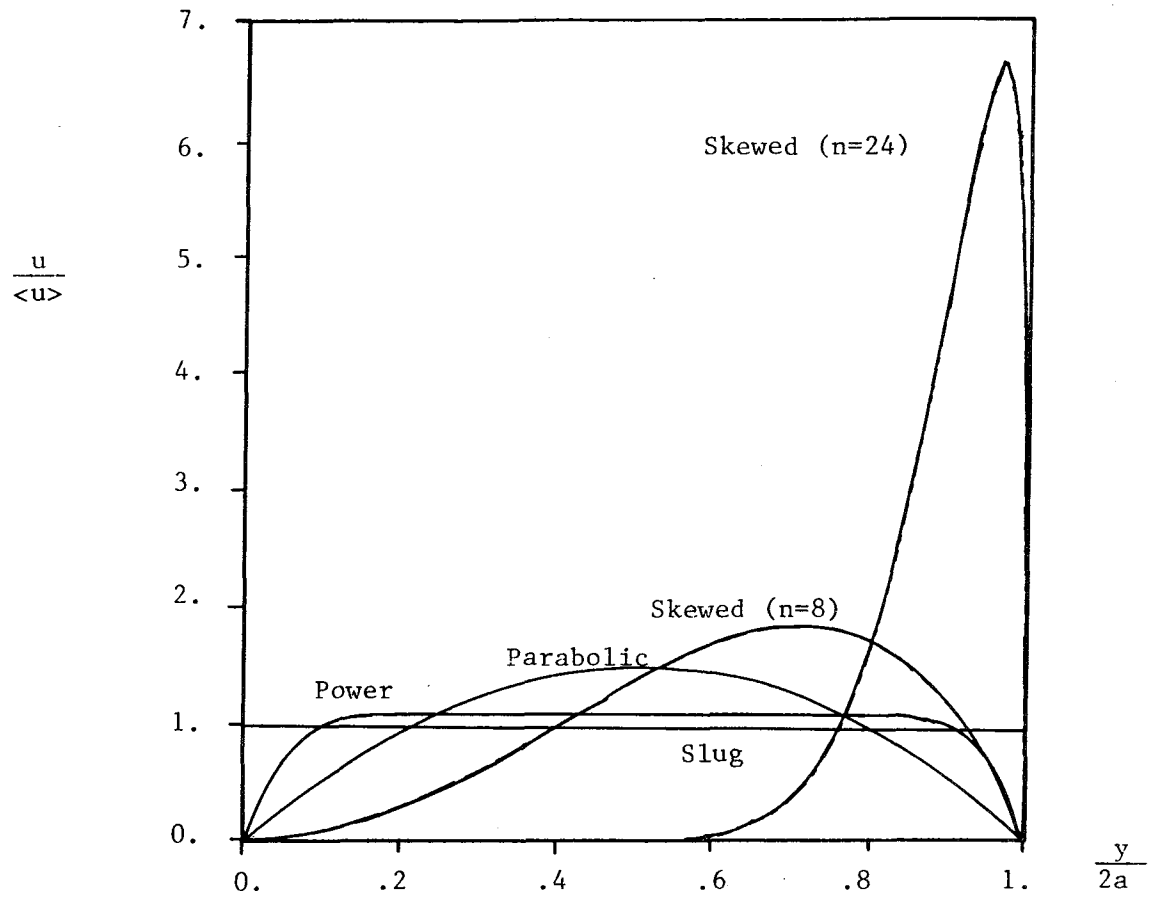


Figure 4.2-12 Fully developed velocity profiles used in the sensitivity study

where h = width of the channel. The local Nusselt number evaluated at the first wall is

$$Nu_x^+ = \frac{-\left.\frac{\partial T}{\partial y}\right|_{y=2a} D_H}{T_b - T_w} \qquad (4\text{-}32)$$

where

$$T_b = \frac{\int_0^{2a} u\,T\,dy}{\int_0^{2a} u\,dy}$$

Figure 4.2-13 shows the variation of the local Nusselt number Nu_x along the channel for the constant wall temperature case. It is seen that the skewed profile gives the highest local Nusselt numbers. Figure 4.2-14 for the constant heat flux case shows similar behavior, but the local values of Nu_x are higher than the former. Figures 4.2-15a and 4.2-15b show the temperature across the channel at different locations along the channel for the constant wall temperature case. Figures 4.2-16a and 4.2-16b show the temperature across the channel for the constant heat flux case. The thermal entrance length L^*_{th} is defined as the duct length required to achieve a value of local Nu_x equal to 1.05 Nu for fully developed flow. The dimensionless thermal entrance length is:

$$L^*_{th} = \frac{L_{th}}{D_h P_e}$$

where $D_h \equiv$ hydraulic diameter.

The thermal entrance length L^*_{th} has been evaluated for particular forms of the energy equation (neglecting viscous and source terms). Shah and London[28] have tabulated thermal entrance lengths for various boundary conditions and geometries. Table 4.2-2 shows the thermal entrance lengths for two different geometries and boundary conditions. The flow is assumed fully developed and the axial conduction is neglected.

For fusion blanket analysis, an appropriate boundary condition is one of a constant wall heat flux. Figures 4.2-13 and 4.2-15 show that the local Nusselt number increases as the velocity profile is skewed towards the first wall. Table 4.2-3 shows the constant value that the Nusselt number reaches along the channel for the different velocity profiles. The constant wall heat flux condition shows higher Nusselt numbers than the constant wall temperature. In practical fusion blankets, the flow is in the thermal entry region.

4.2.2.3 MHD Flow in a Sudden Duct Enlargement

Results of calculations of MHD laminar, viscous flow through an abrupt expansion of a circular channel with a magnetic field aligned to the direction

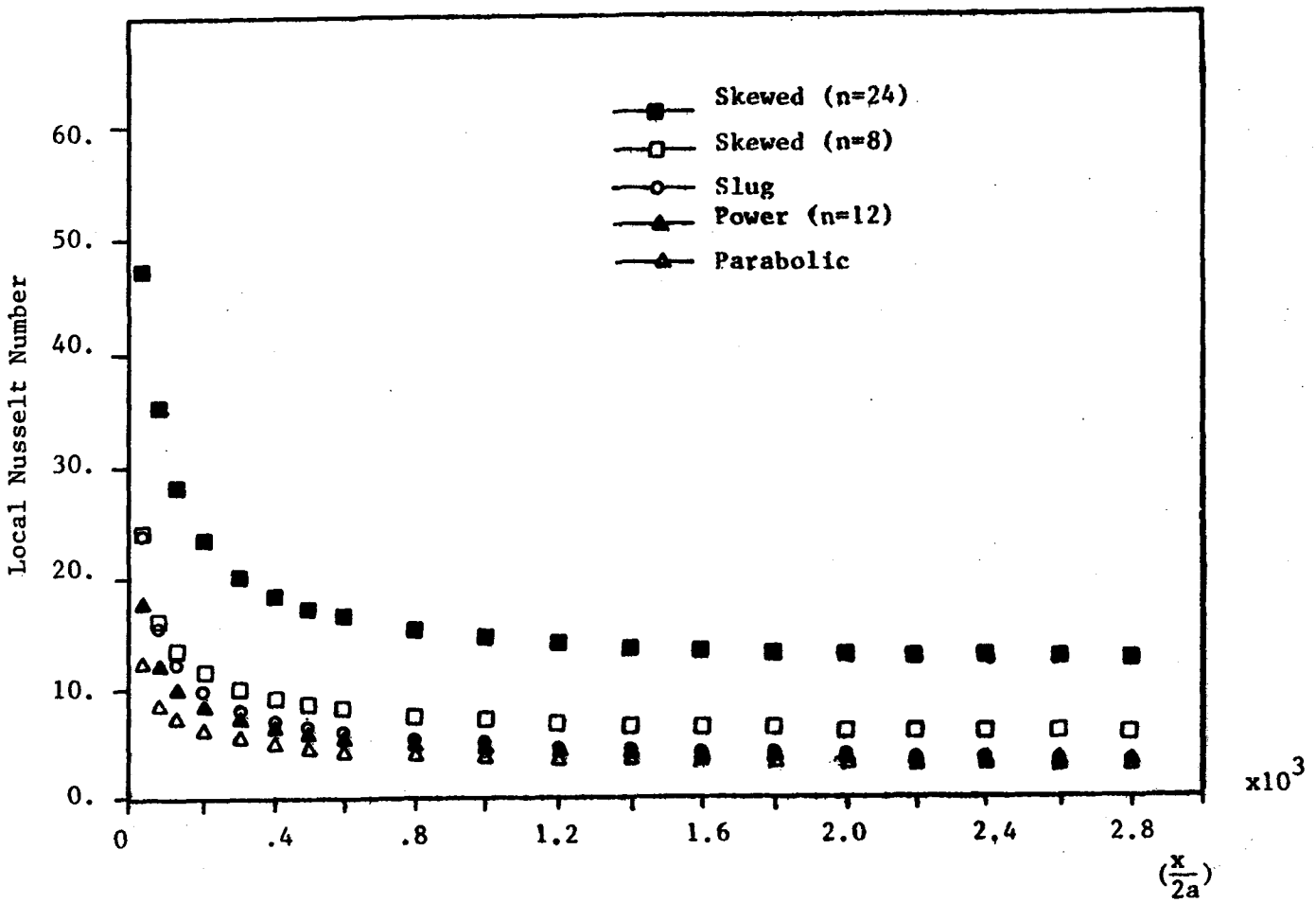


Figure 4.2-13 Local Nusselt number for different velocity profiles (constant wall temperature)

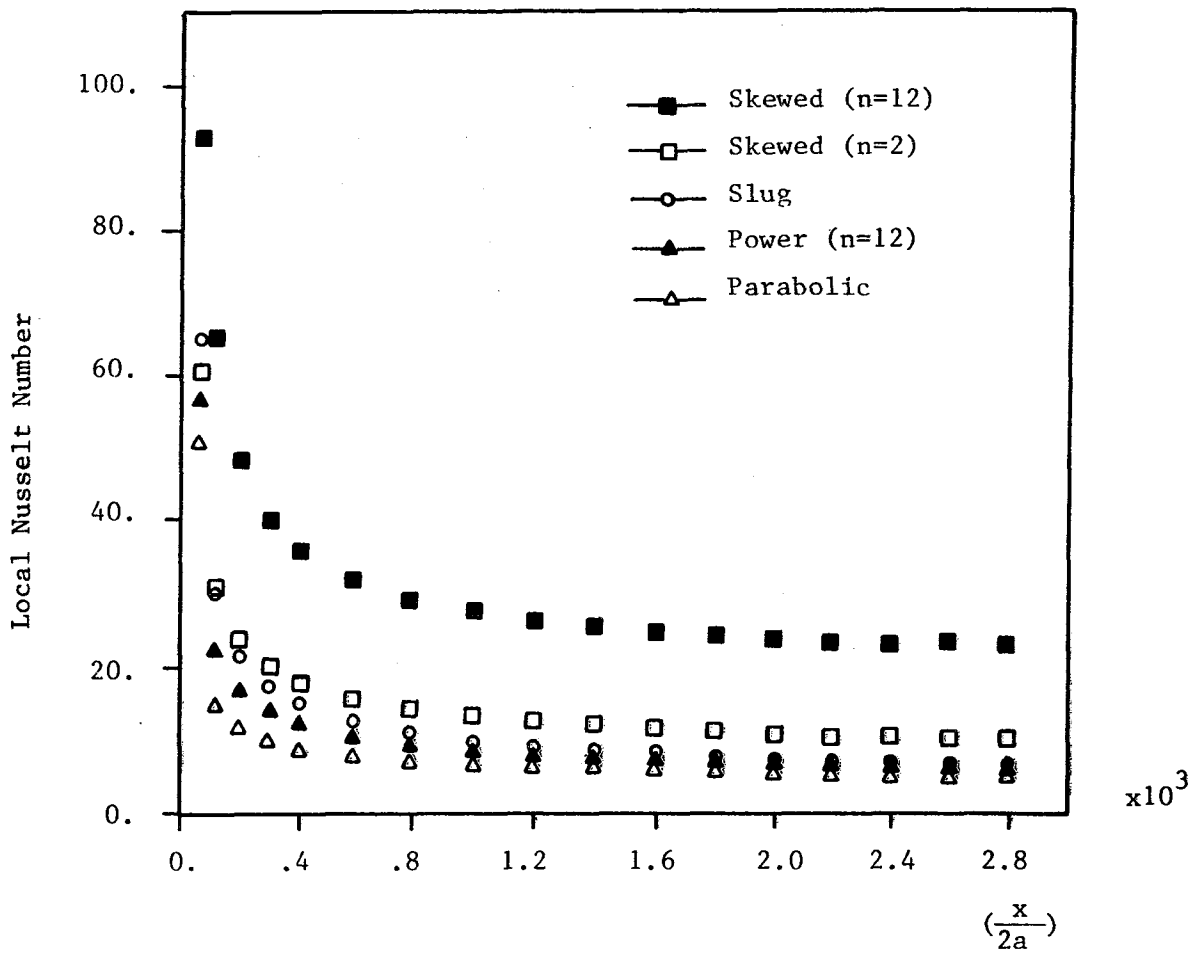
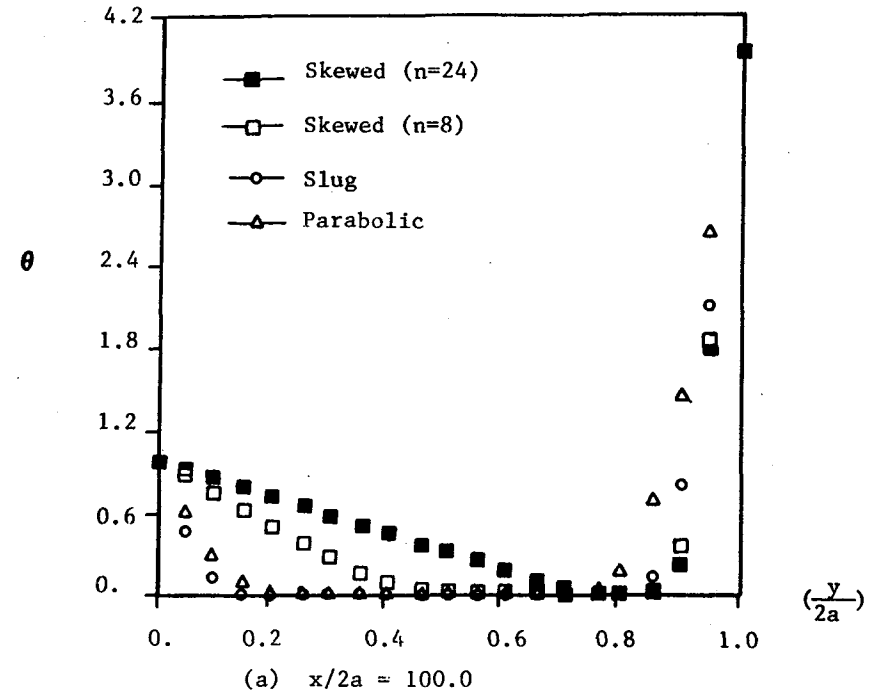
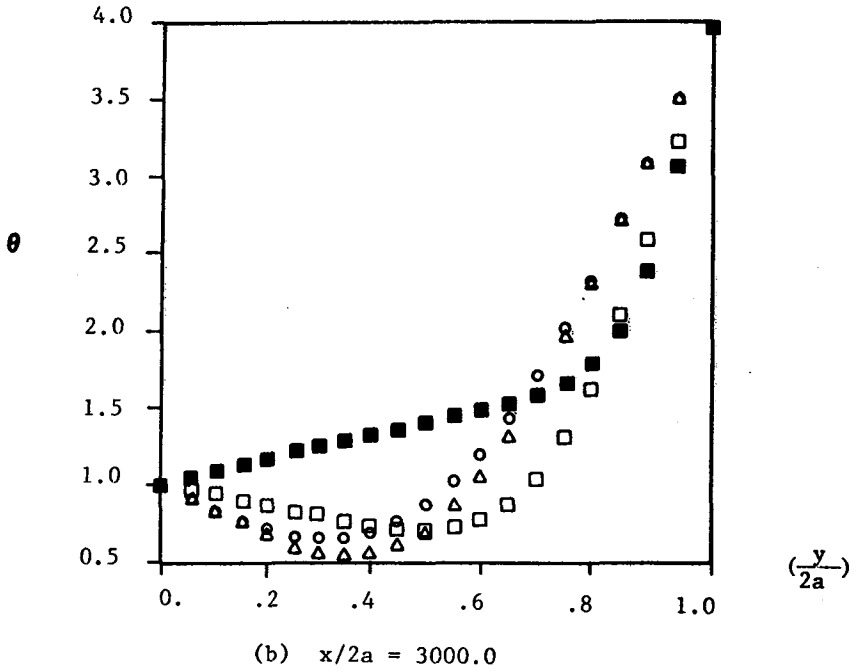


Figure 4.2-14 Local Nusselt number for different velocity profiles (constant wall heat flux)



(a) x/2a = 100.0

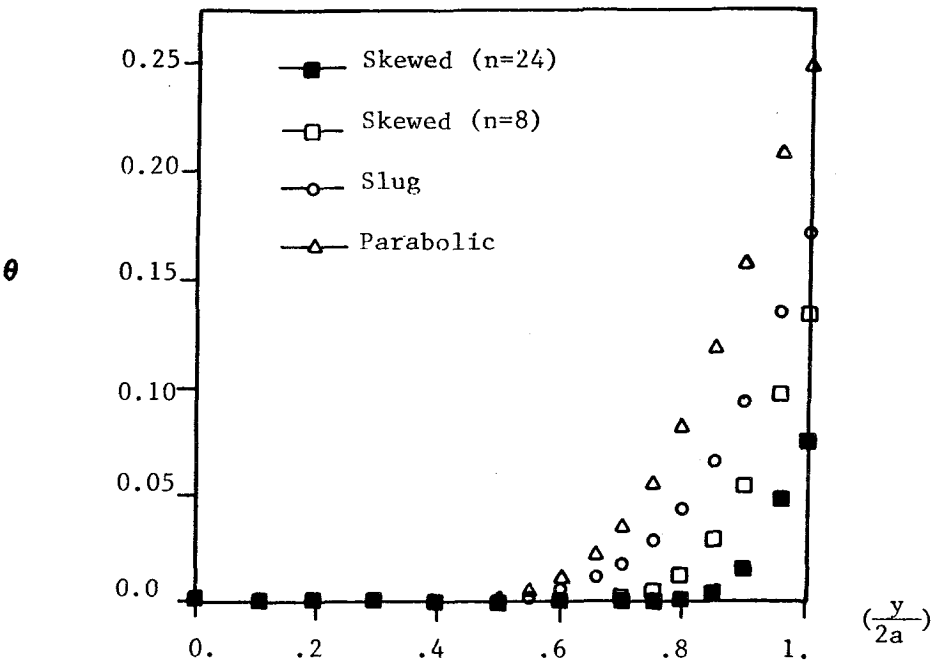
Figure 4.2-15a



(b) x/2a = 3000.0

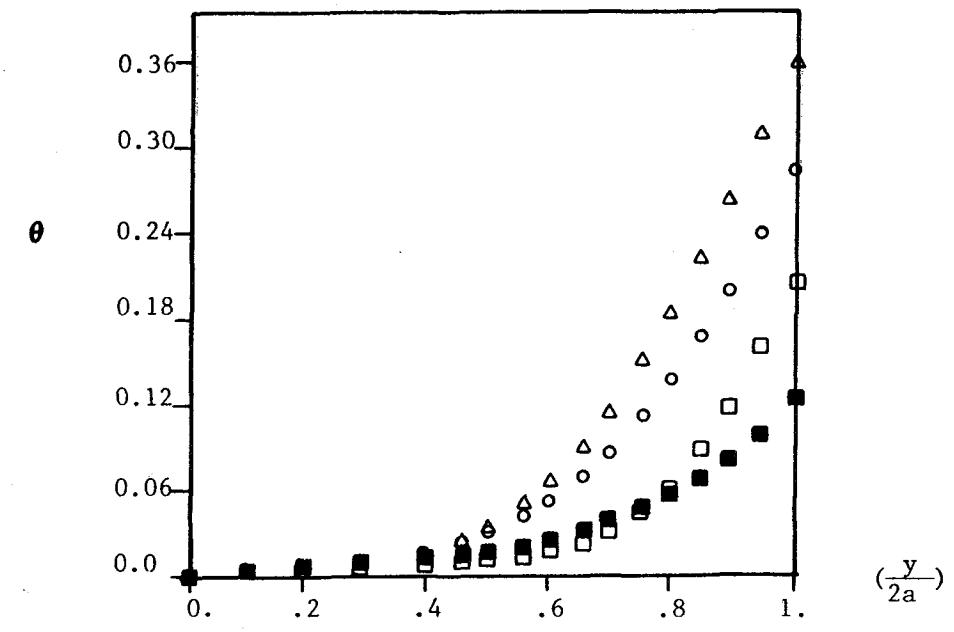
Figure 4.2-15b

Figure 4.2-15 Temperature development for different velocity profiles (constant wall temperature)



(a) x/2a = 100.0

Figure 4.2-16a



(b) x/2a = 3000.0

Figure 4.2-16b

Figure 4.2-16 Temperature development for different velocity profiles (constant wall heat flux)

Table 4.2-2 Thermal Entrance Lengths for Different Geometries and Boundary Conditions

Geometry	Boundary Conditions	L_{th}^{a}	Hydraulic Diameters
Parallel Plate		$\sim 0.0508^{a}$	2236
Parallel Plate		~ 0.045	1980
Circular Pipe	Specified wall temperature different from inlet temperature	0.0335	1472
Circular Pipe	Specified wall heat flux	0.043	1894

Table 4.2-3 Mean Nusselt Number for Different Velocity Profiles and Two Boundary Conditions

Profile	Constant Temp. Boundary Condition	Constant Heat Flux Condition
Slug	5.40768	11.14368
Parabolic	3.97543	6.95077
n = 4	4.35336	7.80441
n = 12	4.92338	9.35026
Skewed		
n = 2	5.25836	
n = 4	7.56256	14.11627
n = 6	9.70375	18.33974
n = 12	15.81046	29.32225

[a]from present analysis

the main flow are reported. The dynamic interaction between the magnetic field and the conducting liquid is analyzed numerically using the SIMPLE method described earlier in Section 4.2.2. The effects of the interaction on the recirculating eddy were analyzed and show that for laminar flow, the magnetic field creates body forces which act in the opposite direction to the vortex eddy. This tends to weaken the eddy, creating an almost stagnant region near the wall behind the opening.

Figure 4.2-17 shows the arrangement of the problem considered. For a non-conducting fluid, the flow pattern can be described as a main stream that has generated an annular eddy between itself and the walls.

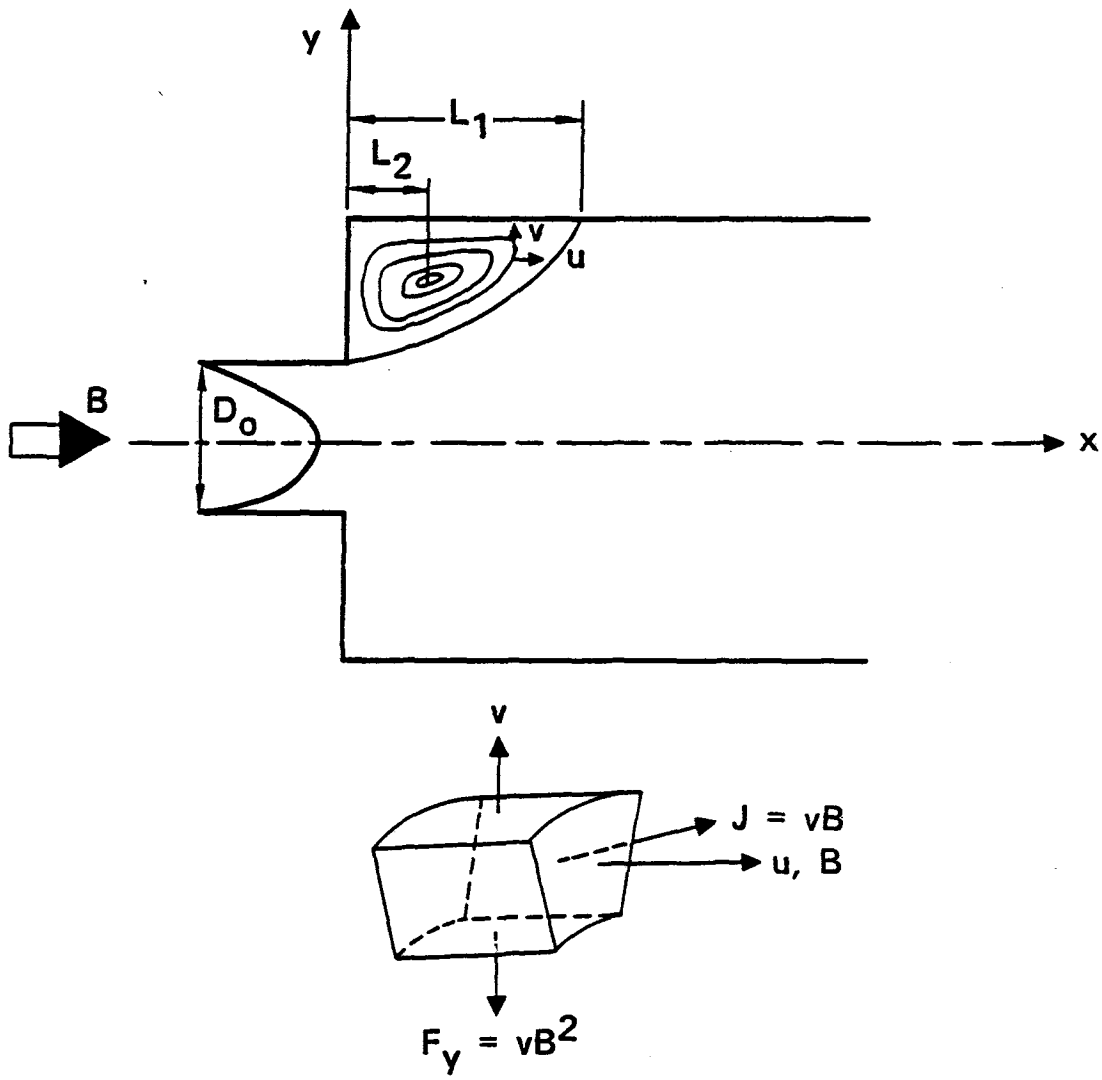


Figure 4.2-17 Configuration of the pipe expansion and a definition sketch

The effect of an axial magnetic field downstream of a sudden expansion is to generate azimuthal electric currents when the flow crosses magnetic field lines. These currents interact with the magnetic field to produce magnetic body forces in the radial direction, as shown in Figure 4.2-17. The interaction between the flow variables and magnetic variables are governed by a coupled system of non-linear equations which are not analytically tractable in the general case.

Macagno and Hung[29] studied the behavior of a captive eddy in non-conducting flow both experimentally and numerically. They showed that at relatively small Reynolds numbers the re-attachment location moves downstream with increasing Reynolds number. McMichael and Deutsch[30] obtained an analytical solution using asymptotic expansion techniques for a conducting flow in slowly varying tubes in the presence of an axial magnetic field. They showed the appearance of flow separation along the wall in both converging and diverging regions of the tube. Their results, however, are limited to slowly varying tube radius.

In the present analysis, we assume steady laminar conducting flow in a tube with a sudden enlargement at the inlet, as shown in Figure 4.2-17. The abrupt circular conduit expansion had a diameter ratio of 2:1, with a parabolic velocity profile at the inlet. Reynolds (Re) and Hartmann (Ha) numbers are defined as

$$Re = \frac{\rho u_o D_o}{\mu} \text{ and } Ha = B_o D_o \sqrt{\frac{\sigma}{\mu}}$$

where u_o is the mean inlet velocity. The applied magnetic field (B_o) is uniform and directed along the tube axis. The assumption of small magnetic Reynolds number is frequently made to decouple Maxwell's equations from the hydrodynamic equations. In this case, the induced magnetic field is neglected and the magnetic body force is linearly related to the velocity field through Ohm's law.

As shown in Figure 4.2-17, the velocity component parallel to the field generates no MHD effects; however, the transverse component (V) leads to an electromotive force (BV) generated in the circumferential direction. No charge buildup occurs and the electric field is zero everywhere due to symmetry. Therefore, there is a body force generated in the radial direction given

by $(-\sigma B_o^2 V)$, as shown in the figure. The body force acts in opposite directions to the radial velocity direction. The electric conductivity of the pipe walls remains arbitrary and has no effect on the fluid dynamics.

Results

The flow characteristics of a conducting fluid through a sudden pipe expansion in the presence of a horizontal magnetic field is studied at different Reynolds numbers up to 200. Figure 4.2-18 shows the relative location of the re-attachment region (L_1/D_o) and the center of the eddy (L_2/D_o) as a function of Reynolds and Hartmann numbers. When the applied magnetic field is zero, the results show good agreement with the experiments of Macagno and Hung.[29] The line for the relative eddy length (L_1/D_o) is very nearly straight and increases with increasing Reynolds numbers and similarly for the relative location of the eddy center (L_2/D_o). When a horizontal magnetic field is applied, the re-attachment point moves downstream.

The effect is more pronounced at lower Reynolds numbers. For higher Reynolds numbers, the length of the recirculating region is not changed significantly from the zero Hartmann number case. Figure 4.2-19 show the effect of the axial magnetic field on the development of the velocity profile along the pipe. Figure 4.2-20 shows velocity vectors for the flow behind the sudden enlargement for Re=200 at different values of Hartmann number. The top half of the plot is magnified to show the recirculating flow behind the enlargement. It can be seen from the figure that, as Hartmann number increases, the length of the recirculating zone increases and the intensity of the eddy decreases. This creates an almost stagnant region behind the enlargement, which can have a great effect on heat transfer from the first wall in the presence of obstacles in liquid metal coolant ducts. Therefore, it seems necessary to streamline the sharp edges of obstacles in coolant ducts aligned with a strong magnetic field if they cannot be avoided.

Figure 4.2-21 shows the wall pressure distribution along the pipe at different Hartmann numbers. In the non-magnetic case, large adverse pressure gradients develop downstream of the enlargement. Magnetic forces, however, tend to decrease the maximum pressure gradients downstream of the enlargement and shift the maximum further downstream.

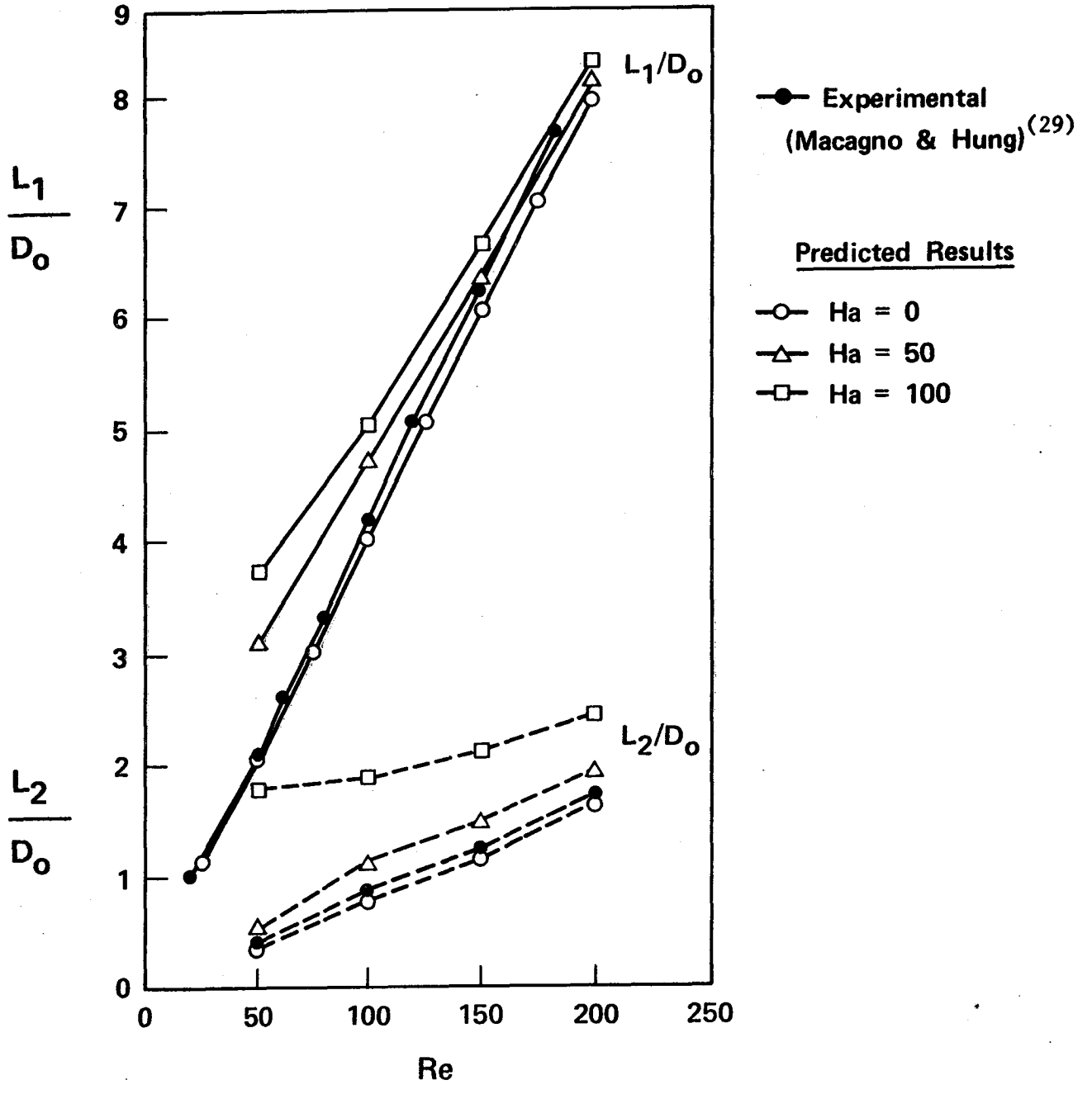


Figure 4.2-18 Characteristics of the annular eddy as a function of Reynolds number at different Hartmann numbers; L_1/D_o, relative eddy length; L_2/D_o, relative location of eddy center.

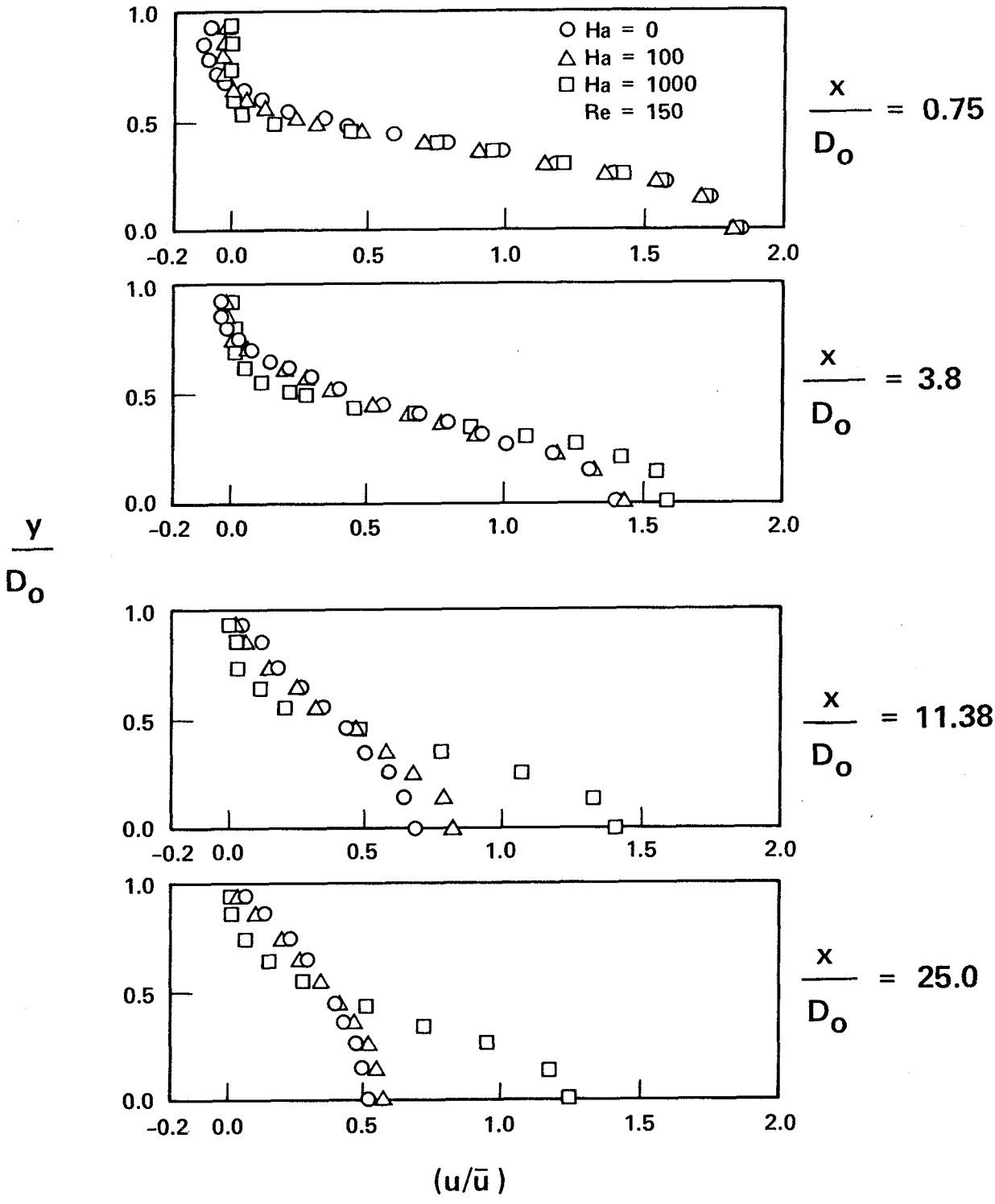
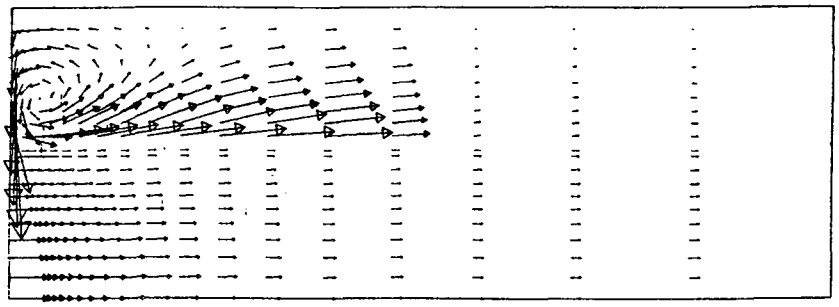


Figure 4.2-19 Effect of axial magnetic field on the development of the velocity profile along the pipe

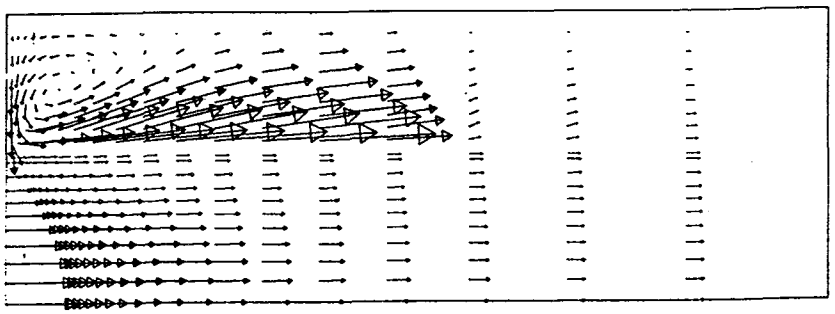
Re = 200.0

Ha = 0.0



Re = 200.

Ha = 100.



Re = 200.

Ha = 200.

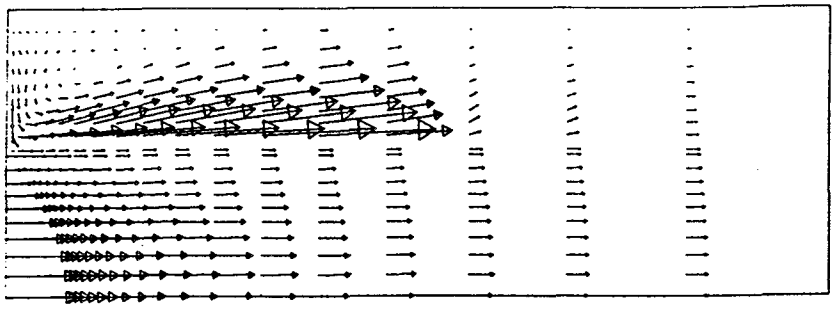


Figure 4.2-20 Velocity vectors showing the effects of an axial magnetic field on the flow in a sudden pipe enlargement (note: velocities in the upper half of the pipe are magnified).

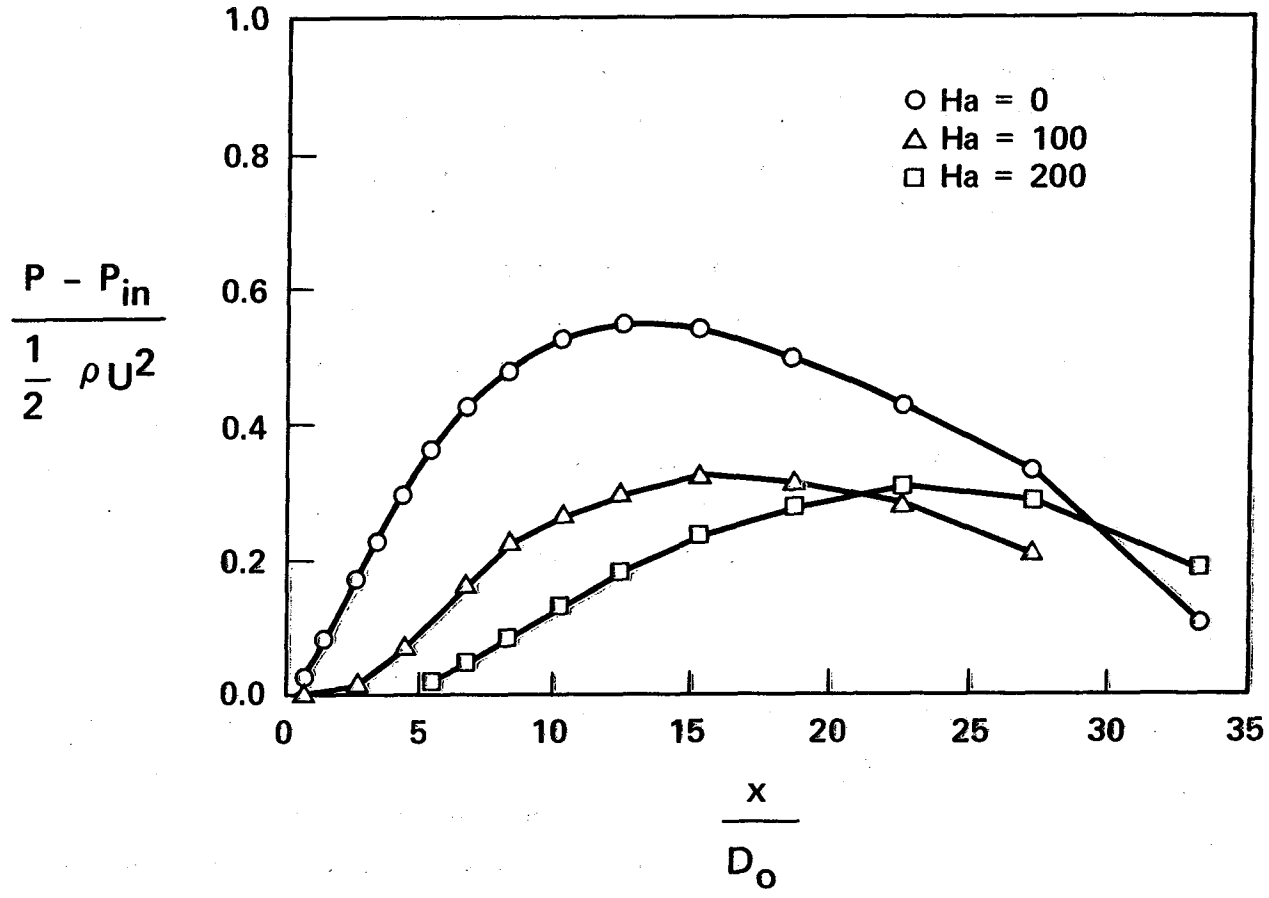


Figure 4.2-21 Effect of axial magnetic field on the wall pressure distribution along the pipe at different Hartmann numbers

4.2.2.4 Concluding Remarks

A two-dimensional numerical study of MHD flow in ducts has been presented. The velocity and temperature distributions were calculated for a magnetic field in a plane parallel to the flow field. It was shown that the interaction of a magnetic field aligned to the main flow direction with the transverse velocity component in the developing duct causes a delay in full flow development. For a laminar flow, this delay leads to a slight improvement in heat transfer. In laminar channel flow perpendicular to the field, the flow develops in a few channel widths and attains a flat profile characteristic of Hartmann flow. This flattening of the velocity profile serves to increase heat transfer due to the increased velocity gradients near the wall.

For an MHD flow through a sudden pipe enlargement, it was shown that a horizontal magnetic field interacts with the recirculating flow behind the expansion and tends to weaken the eddy strength, and at the same time increases its length. This almost stagnant region behind the expansion reduces the convective capability of the flow to remove heat from the first wall. Thus, there is a need to avoid flow separation, if possible, by reducing the number of such orifices, especially in flows which are aligned with the toroidal magnetic field in a fusion blanket. Also, avoiding sharp edge obstacles by streamlining them can help to reduce flow separation and avoid stagnant regions. Conversely, MHD flows behind an obstacle in a strong, perpendicular magnetic field tend to be separationless, with a tendency to flow in a thin layer at the wall parallel to the magnetic field. Preliminary results which show this effect were obtained and further analysis is planned.

Numerical Problems

The essence of most solution procedures of the non-linear Navier-Stokes equations relies on an iterative process of pressure and velocity corrections until mass continuity is satisfied, (i.e., the residual mass is made very small). In the SIMPLE method, the guess and correct operation utilizes the convective terms, which are small compared to the magnetic terms in a strong magnetic field. Therefore, for a more effective solution method, the iterative process must account for corrections in the electromagnetic forces as well.

Consider the combined Navier-Stokes and Maxwell's equations which describe MHD flows. The coupled non-linear partial-differential equations which govern the flow of a steady, constant property conducting fluid in a magnetic field can be written as;

$$\rho \frac{\partial}{\partial x_j}(u_i u_j) - \frac{1}{\mu_o}\frac{\partial}{\partial x_j}(b_i b_j) = -\frac{\partial}{\partial x_i}\left(p + \frac{|\vec{b}|^2}{2\mu_o}\right) + \mu \frac{\partial^2 u_i}{\partial x_j \partial x_j} \qquad (4\text{-}33)$$

where u_i and b_i are the velocity and magnetic field components in x_i-space ($i=1,2,3$). The other equation which governs the magnetic field can be written as:

$$\frac{\partial}{\partial x_j}(u_j b_i) - \frac{\partial}{\partial x_j}(u_i b_j) = \frac{1}{\mu_o \sigma}\frac{\partial^2 b_i}{\partial x_j \partial x_j} \qquad (4\text{-}34)$$

The velocity and magnetic fields must satisfy the continuity equations:

$$\frac{\partial u_i}{\partial x_i} = 0 \quad \text{and} \quad \frac{\partial b_i}{\partial x_i} = 0 \tag{4-35}$$

Equations (4-33 to 4-35) fully describe any MHD flow. As can be seen from Eq. (4-33), the pressure term $(|\vec{b}|^2/2\mu_o)$ is added, which must be accounted for in any pressure correction scheme. A solution method would therefore iterate between Eqs. (4-33) and (4-34) to calculate intermediate values of u_i and b_i. Then, using continuity equations, a pressure correction can be constructed which can correct the velocities and, hence, the induced magnetic field. The process can be repeated until the residual errors in Eq. (4-35) are made very small. This seems a preferred method of solving MHD flows and further work is being pursued in this direction.

Other finite difference solution methods[23,31] use a time splitting technique, where the time evolution of the flow is followed in order to arrive at the steady-state solution. This method seems needlessly expensive when the only solution of interest is the steady state. It seems, therefore, that to develop an efficient algorithm for MHD flows at high Hartmann numbers, ways of improving the pressure correction method by including corrections due to electromagnetic terms must be sought. Dynamic grid adaptive techniques can be used to resolve small regions of large gradients. This can improve the resolution of the variable field, but it will still suffer from convergence problems when applied to non-linear problems at high Hartmann numbers. However, using an adaptive grid technique in the improved pressure correction scheme can improve the efficiency and resolution of the solution field.

4.2.3 Finite Element Method

4.2.3.1 Introduction

In this section, a fully numerical approach is described, based on the finite element method. This formulation takes no advantage of a priori knowledge of the spatial details of the flow which may be anticipated from theoretical studies. After the characteristics and ultimate capabilities of numerical techniques are better understood, then any existing knowledge of the flow patterns can be better utilized.

Applications of the finite element method to fluid flow problems have become increasingly common in recent years.[32-34] Several authors have treated particular problems in liquid metal MHD fluid flow,[35-38] however, these are generally limited to simple geometries and often lack the ability to treat problems with fusion relevant parameters (primarily the Hartmann number and interaction parameter).

The difficulties encountered in numerical solutions of laminar MHD fluid flow problems generally stem from the disparate spatial scale lengths involved. These disparate scale lengths arise due to the dominance of the MHD body force in the momentum equation. Throughout most of the flow area, viscous and inertial effects are negligible and the flow is potential. The solution is determined primarily by the electrical characteristics of the containing walls and the flow characteristics in narrow inertial and viscous layers (e.g., Hartmann layers and shear layers). Simultaneous modeling of the core flow and the thin "boundary" layers requires special treatment of these different regions.

One possible approach, which is often used in analytic solutions, is to seek separate solutions in the core flow and the "boundary" layers. These two solutions are coupled at their interface. (For details on the analytic treatment of MHD channel flow problems using matched asymptotic expansions, see, for example, Ref. [39]). If the location and relative size of boundary layers can be predicted a priori, then a numerical solution could proceed by defining a much finer mesh in the boundary layers.

A different approach has been attempted in the present analysis. Using the finite element method, the location and size of boundary layers is determined as an integral part of the solution. The technique of self-adaptive mesh refinement is employed, in which local errors in a coarse mesh solution are calculated, and then a new mesh is constructed to increase the spatial resolution in regions of large error. The mesh refinement procedure can be iterated until a sufficiently accurate solution is obtained. In this way, a unique optimum mesh is produced for each problem.

In this section, the fundamentals of self-adaptive mesh, finite element solutions of MHD fluid flow equations are described and demonstrated by example. The examples are simplified problems, which are intended to demonstrate the method. The ultimate goal is to provide a solution technique for

geometrically complex problems at high Hartmann number and interaction parameter. However, at this time, the analyses has been restricted to simple one- and two-dimensional duct flow problems.

4.2.3.2 Basic Equations

It has been known for many years that the magnetic field has a strong laminarizing effect on liquid metal MHD fluid flow.[40-43] When a transverse magnetic field exists, the transition from laminar to turbulent flow is given approximately by:

$$Ha_{\perp} > \frac{Re}{500} \tag{4-36}$$

For flow parallel to the magnetic field, this transition Hartmann number is reduced to approximately Re/60. Given the Hartmann and Reynolds numbers of actual reactor blankets, the flow is virtually always laminarized.

This laminarizing effect significantly reduces heat transfer, which can be a factor in closing the liquid metal blanket design window. Experimental studies[42,43] have shown that a small residual level of turbulence may exist, but at a level too low to make substantial changes to the velocity or temperature profiles (1-2%). Very recent results suggest a mechanism for generating and sustaining two-dimensional turbulence in transverse flow.[44,45] However, the results were obtained at relatively low parameters and will require verification at Hartmann numbers and interaction parameters closer to actual fusion conditions.

Assuming the flow is laminarized and steady state, and the magnetic Reynolds number is small (it is usually less than $\sim 10^{-2}$), the full set of non-dimensionalized 3-D MHD equations can be written as follows:

$$u \frac{\partial u}{\partial x} + v \frac{\partial u}{\partial y} + w \frac{\partial u}{\partial z} = - \frac{\partial p}{\partial x} + \frac{1}{Re} \nabla^2 u + N \, (\underline{j} \times \underline{B})_x \tag{4-37}$$

$$u \frac{\partial v}{\partial x} + v \frac{\partial v}{\partial y} + w \frac{\partial v}{\partial z} = - \frac{\partial p}{\partial y} + \frac{1}{Re} \nabla^2 v + N \, (\underline{j} \times \underline{B})_y \tag{4-38}$$

$$u \frac{\partial w}{\partial x} + v \frac{\partial w}{\partial y} + w \frac{\partial w}{\partial z} = - \frac{\partial p}{\partial z} + \frac{1}{Re} \nabla^2 w + N \, (\underline{j} \times \underline{B})_z \tag{4-39}$$

$$\nabla^2 \phi = B_x \left(\frac{\partial w}{\partial y} - \frac{\partial v}{\partial z}\right) + B_y \left(\frac{\partial u}{\partial z} - \frac{\partial w}{\partial x}\right) + B_z \left(\frac{\partial v}{\partial x} - \frac{\partial u}{\partial y}\right) - u \left(\frac{\partial B_z}{\partial y} - \frac{\partial B_y}{\partial z}\right) - v \left(\frac{\partial B_x}{\partial z} - \frac{\partial B_z}{\partial x}\right) - w \left(\frac{\partial B_y}{\partial x} - \frac{\partial B_x}{\partial y}\right) \tag{4-40}$$

$$\frac{\partial u}{\partial x} + \frac{\partial v}{\partial y} + \frac{\partial w}{\partial z} = 0 \tag{4-41}$$

$$(\underline{j} \times \underline{B})_x = \left(\frac{\partial \phi}{\partial z} B_y - \frac{\partial \phi}{\partial y} B_z\right) - u \, (B_y^2 + B_z^2) + v \, B_x B_y + w \, B_x B_z \tag{4-42}$$

$$(\underline{j} \times \underline{B})_y = \left(\frac{\partial \phi}{\partial x} B_z - \frac{\partial \phi}{\partial z} B_x\right) - v \, (B_x^2 + B_z^2) + w \, B_y B_z + u \, B_x B_y \tag{4-43}$$

$$(\underline{j} \times \underline{B})_z = \left(\frac{\partial \phi}{\partial y} B_x - \frac{\partial \phi}{\partial x} B_y\right) - w \, (B_x^2 + B_y^2) + u \, B_x B_z + v \, B_y B_z \tag{4-44}$$

where Eqs. (4-37 to 4-39) represent the Navier-Stokes equation in Cartesian coordinates, Eq. (4-40) is derived from Ohm's law and current conservation, Eq. (4-41) is the continuity equation, and definitions for all variables appear at the end of this chapter.

Several 2-dimensional simplifications of these equations result in interesting problems. These include:

1. 2-D developing flow with the magnetic field (B_z) perpendicular to both components of velocity (u,v) and $\partial/\partial z = 0$:

$$\frac{\partial u}{\partial x} + \frac{\partial v}{\partial y} = 0 \tag{4-45}$$

$$u \frac{\partial u}{\partial x} + v \frac{\partial u}{\partial y} = - \frac{\partial p}{\partial x} + \frac{1}{Re} \left(\frac{\partial^2 u}{\partial x^2} + \frac{\partial^2 u}{\partial y^2} \right) - N B_z^2 u - N B_z \frac{\partial \phi}{\partial y} \tag{4-46}$$

$$u \frac{\partial v}{\partial x} + v \frac{\partial v}{\partial y} = - \frac{\partial p}{\partial y} + \frac{1}{Re} \left(\frac{\partial^2 v}{\partial x^2} + \frac{\partial^2 v}{\partial y^2} \right) - NB_z^2 v + NB_z \frac{\partial \phi}{\partial x} \quad (4\text{-}47)$$

$$\frac{\partial^2 \phi}{\partial x^2} + \frac{\partial^2 \phi}{\partial y^2} = B_z \left(\frac{\partial v}{\partial x} - \frac{\partial u}{\partial y} \right) + v \frac{\partial B_z}{\partial x} - u \frac{\partial B_z}{\partial y} \quad (4\text{-}48)$$

2. 2-D developing flow with the magnetic field (B_y) in the direction of one component of the velocity (u,v) and $\partial/\partial z=0$ except for a constant electric field ($\partial\phi/\partial z=k$):

$$\frac{\partial u}{\partial x} + \frac{\partial v}{\partial y} = 0 \quad (4\text{-}49)$$

$$u \frac{\partial u}{\partial x} + v \frac{\partial u}{\partial y} = - \frac{\partial p}{\partial x} + \frac{1}{Re} \left(\frac{\partial^2 u}{\partial x^2} + \frac{\partial^2 u}{\partial y^2} \right) + NB_y \frac{\partial \phi}{\partial z} - NB_y^2 u \quad (4\text{-}50)$$

$$u \frac{\partial v}{\partial x} + v \frac{\partial v}{\partial y} = - \frac{\partial p}{\partial x} + \frac{1}{Re} \left(\frac{\partial^2 v}{\partial x^2} + \frac{\partial^2 v}{\partial y^2} \right) \quad (4\text{-}51)$$

$$\frac{\partial^2 \phi}{\partial x^2} + \frac{\partial^2 \phi}{\partial y^2} = 0 \quad (4\text{-}52)$$

3. 2-D fully developed channel flow with the magnetic field parallel to one component of velocity. (This case is derived in detail later in this section).

4.2.3.3 Illustration of Self-Adaptive Mesh Refinement in the 1-D Hartmann Problem

Solving simultaneous equations in more than one dimension using the finite element method can be very cumbersome. In order to develop and illustrate the techniques to be used on more sophisticated problems, a simple one-dimensional Hartmann problem was first analyzed. The classical Hartmann problem consists of two infinite plates with the magnetic field aligned in a perpendicular direction, as shown in Figure 4.2-22. The one-dimensional steady Navier-Stokes equation can be written in the following form, assuming

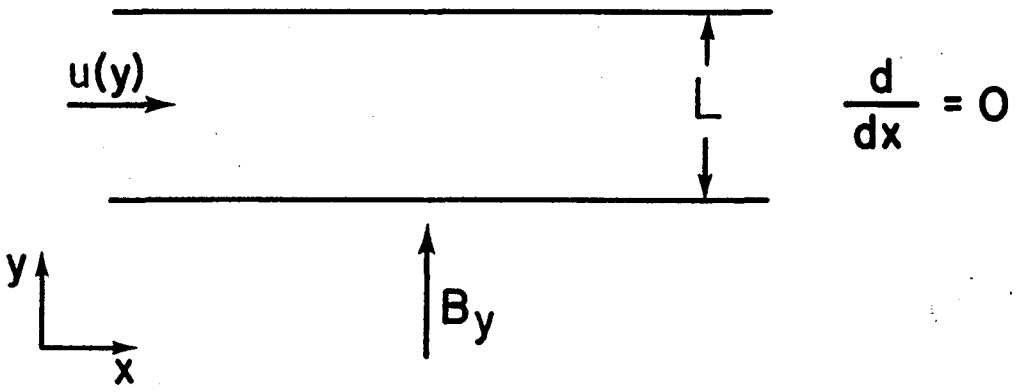


Figure 4.2-22 Geometry for the 1-D Hartmann problem

perfectly conducting walls (zero electric field):

$$\frac{d^2u}{dy^2} - H^2u + k = 0 \qquad (4\text{-}53)$$

where k represents the constant pressure gradient, u is the x-directed velocity, and H is the Hartmann number ($H = aB\sqrt{\sigma/\mu}$, where a is the channel half-width, B is the magnetic field strength, σ and μ are the fluid conductivity and viscosity). The form of the equation is unchanged in the case of finite wall conductivity, where the electric field is a constant and can be combined with the pressure drop term.

The boundary conditions on u are:

$$u=0 \text{ at } y=0,L \qquad (4\text{-}54)$$

The solution of Eq. (4-36) proceeds by developing a variational statement of the problem, as shown in detail in Ref. [46]. The basis function representation of u is given by:

$$u(x) = \sum_n \psi_n(x)\, U_n \qquad (4\text{-}55)$$

where ψ is the basis, or shape function. This form is substituted for u in Eq. (4-53), multiplied by a weighting function (in this Galerkin approximation, the weighting function is the same as the basis function), and integrated over the global domain, τ:

$$\int_{\tau} \psi_m \left[\sum_n \frac{d^2\psi_n}{dy^2} U_n - \sum_n H^2 \psi_n U_n + k \right] = 0 \qquad (4\text{-}56)$$

In the finite element formulation, the basis function consists of a sum of locally defined functions which are usually simple polynomials. These polynomials are given the property that their value is equal to unity at one node and zero at all others. Equation (4-56) then becomes equivalent to a linear matrix equation in which the unknowns are the values of velocity at the node points. In matrix notation, we can write:

$$\sum_n A_{nm} U_n + B_m = 0 \qquad (4\text{-}57)$$

where

$$A_{nm} = \int_{\tau} \psi_m \left[\frac{d^2\psi_n}{dy^2} - \psi_n H^2 \right] dy \qquad (4\text{-}58)$$

and

$$B_m = \int_{\tau} k \, \psi_m dy \qquad (4\text{-}59)$$

In this problem (and many others) the order of the first term in Eq. (4-58) can be reduced using a standard technique of integration by parts:

$$\int_a^b \psi_m \frac{d^2\psi_n}{dy^2} dy = \psi_m \frac{d\psi_n}{dy} \Big|_a^b - \int_a^b \frac{d\psi_n}{dy} \frac{d\psi_m}{dy} dy \qquad (4\text{-}60)$$

In most cases (including the present one), the first term on the right hand side of Eq. (4-60) vanishes at the boundaries.

Because of the reduction in order, linear basis functions can be used here. These are simpler to employ, but generally provide less accurate results as compared to higher order polynomial basis functions.[47] In this study, both linear and quadratic basis have been used. Good results have been obtained with linear basis functions for all cases studied.. However, quadra-

tic shape functions often exhibit oscillatory behavior and poorer convergence following mesh refinement. This behavior is unexpected and requires further study to determine the cause.

Figure 4.2-23 compares the numerical solution using 20 nodes with the exact analytic solution at a Hartmann number of 10 for both linear and quadratic shape functions. The solution using linear shape functions provides a very good fit, whereas the solution using quadratic shape functions shows large oscillations.

Once the solution is obtained, the local error can be estimated from the residuals. The element mean residual is given by:

$$\bar{r} = \left(r^2/h\right)^{1/2} \tag{4-61}$$

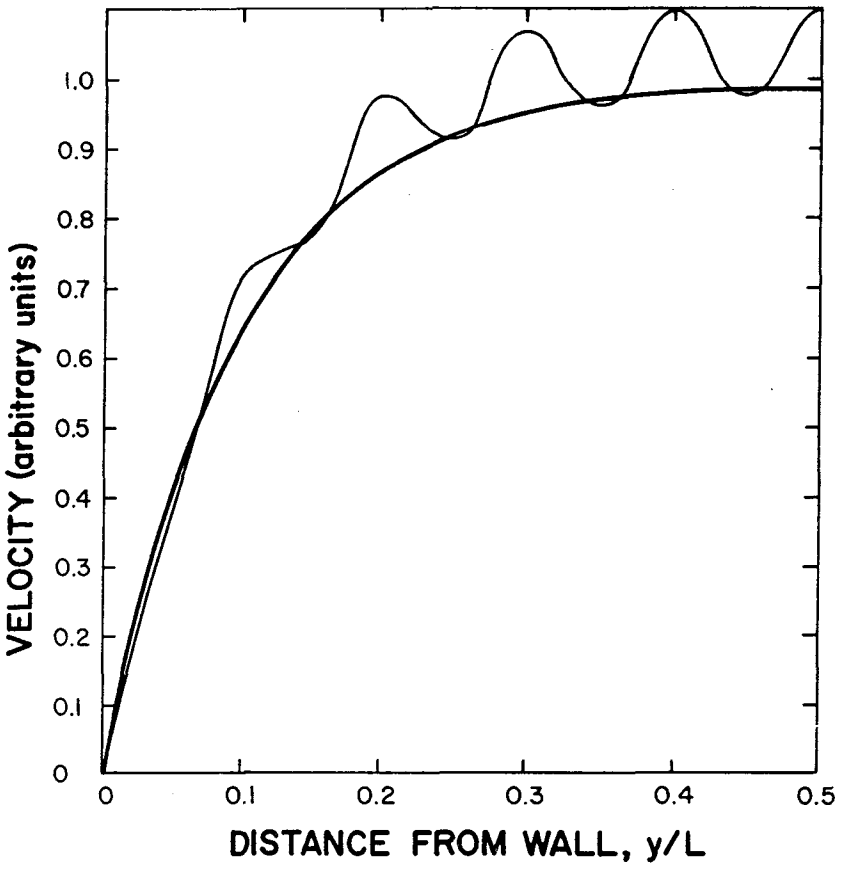


Figure 4.2-23 Solution of the Hartmann problem using linear and quadratic shape functions

where r is the root mean square of the local error (or the degree to which the original equation is satisfied) obtained by replacing u with its basis function representation, and h is the size of the element. From Eq. (4-53) we obtain:

$$r^2 = \int_{\Omega_E} \left(\frac{d^2u}{dy^2} - H^2u + k \right)^2 dy \tag{4-62}$$

In the case of linear basis functions, the second derivative vanishes, leaving:

$$r^2 = \int_{\Omega_E} (H^2u - k)^2 dy \tag{4-63}$$

Integrating, we obtain:

$$r^2 = h \left(\frac{a^2}{3} + ab + b^2 \right) \tag{4-64}$$

where

$$a = H^2(U_2 - U_1) \tag{4-65}$$

$$b = H^2U_1 - k \tag{4-66}$$

and U_1 and U_2 are the values of velocity at the endpoints of each element.

If quadratic basis functions are utilized, then Eq. (4-62) gives:

$$r^2 = h \left(\frac{2}{5} a^2 + \frac{4}{3} ac + \frac{2}{3} b^2 + 2c^2 \right) \tag{4-67}$$

where

$$a = -\frac{H^2}{2} (U_1 - 2U_2 + U_3) \tag{4-68}$$

$$b = -\frac{H^2}{2} (U_3 - U_1) \tag{4-69}$$

$$c = k + (U_1 - 2U_2 + U_3) - H^2U_2 \tag{4-70}$$

and U_1-U_3 are the values of velocity at the three element nodes.

Figure 4.2-24 shows the residual errors obtained for the solutions provided in Figure 4.2-23.

In order to test the ability of the method to treat very high Hartmann numbers, linear shape functions were employed together with iterative mesh refinement. Results for H=1000 are presented in Figure 4.2-25. The initial solution was obtained using 5 elements. Successive meshes were obtained by examining the element averaged residuals and comparing them to the mean residual for the entire domain. Each element with a residual higher than the mean was divided into n_{std} pieces, where n_{std} is the number of standard deviations above the mean.

In Figure 4.2-25, 5 iterations were performed, using 4, 8, 12, 20, and 30 nodes, respectively. The highest residual error was always found in the outermost element, resulting in rapid convergence. Note that the two curves at the right side of the figure use an expanded scale in the region adjacent to the wall.

4.2.3.4 Two-Dimensional Fully-Developed Duct Flow

The solution of the one-dimensional Hartmann problem indicates that mesh self-adaptation may be an efficient method to extend the range of Hartmann numbers which can be analyzed numerically. In order to develop the techniques which will be used in more general problems, a simple two-dimensional duct flow problem was analyzed. Figure 4.2-26 shows the geometry, which includes a rectangular duct with its cross section entirely in the x-y plane, fully developed velocity in the z-direction, and the magnetic field uniform throughout the channel, directed along the y-axis.

The non-dimensionalized MHD equations for this simplified geometry reduce to the following:

Navier-Stokes Equation:

$$\frac{\partial^2 v}{\partial x^2} + \frac{\partial^2 v}{\partial y^2} - H^2\left(v + \frac{\partial \phi}{\partial x}\right) - Re\,\frac{dp}{dz} = 0 \qquad (4\text{-}71)$$

Ohm's Law with Current Conservation Applied:

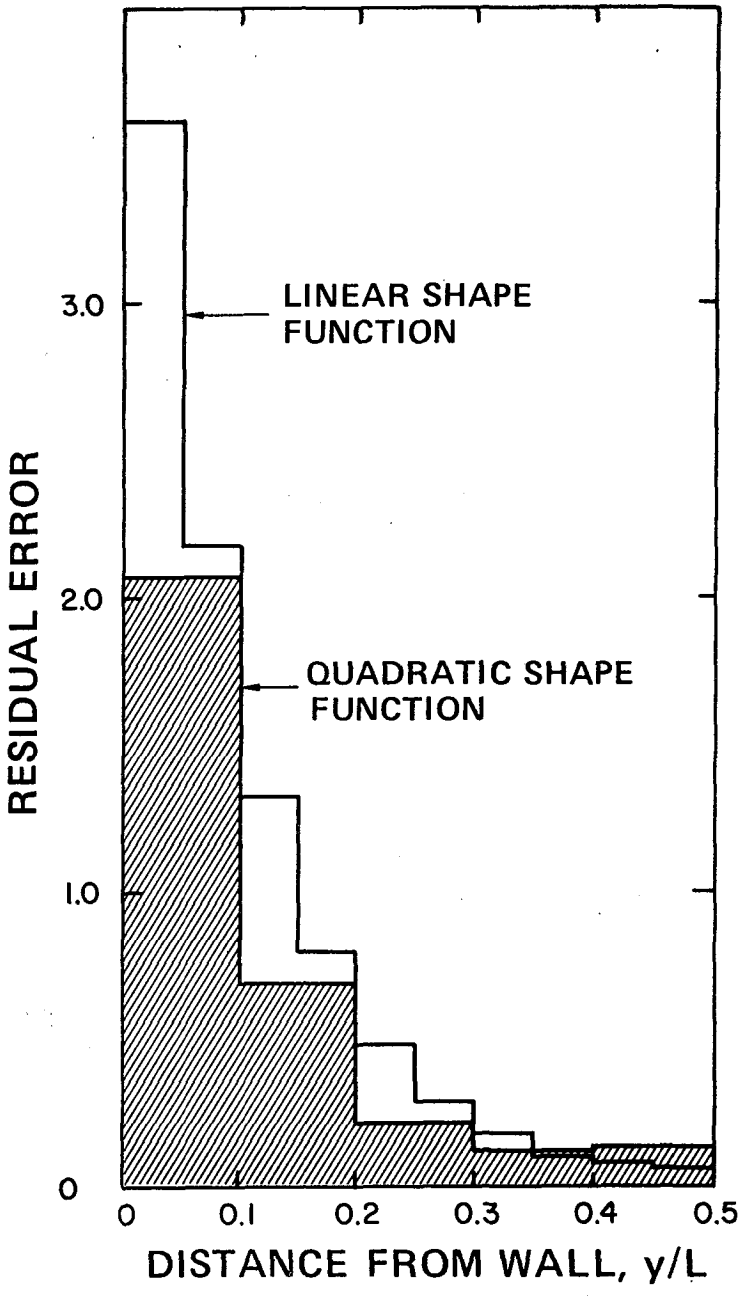


Figure 4.2-24 Residual errors for the Hartmann problem

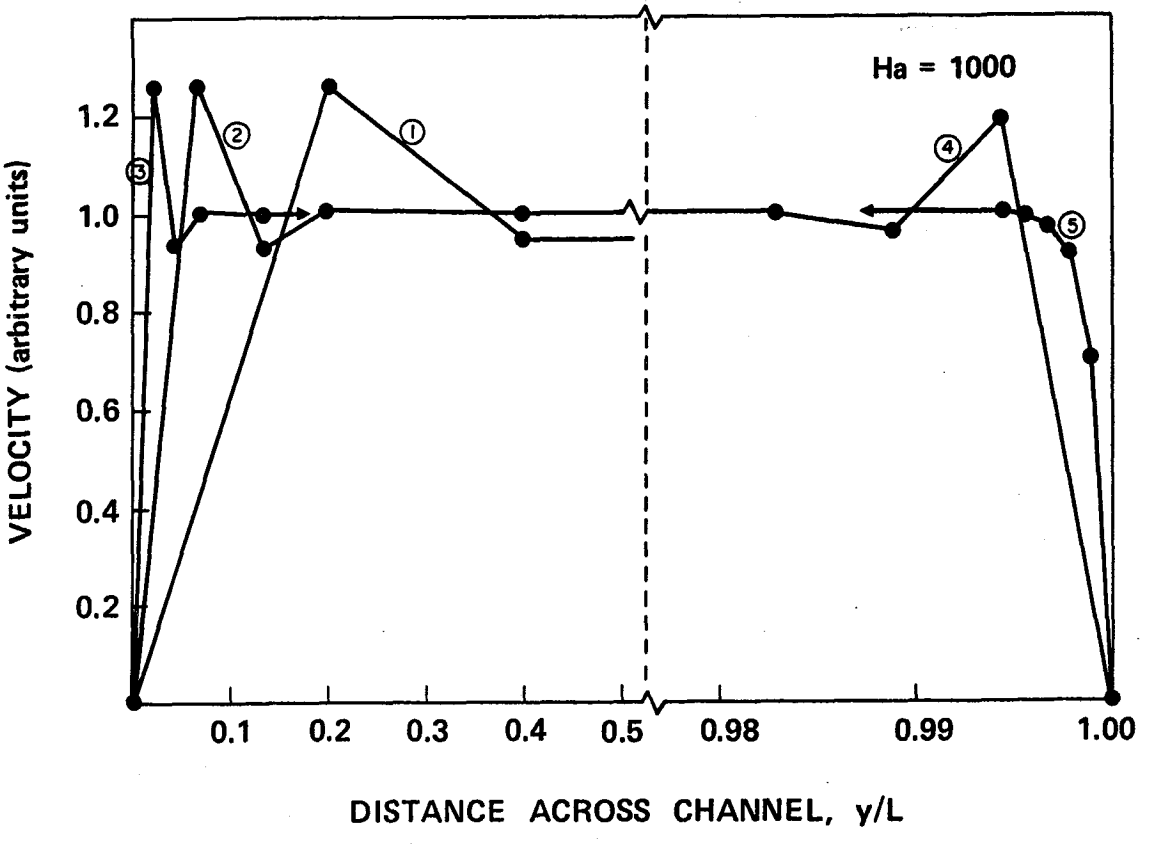


Figure 4.2-25 Illustration of self-adaptive mesh refinement for the Hartmann problem

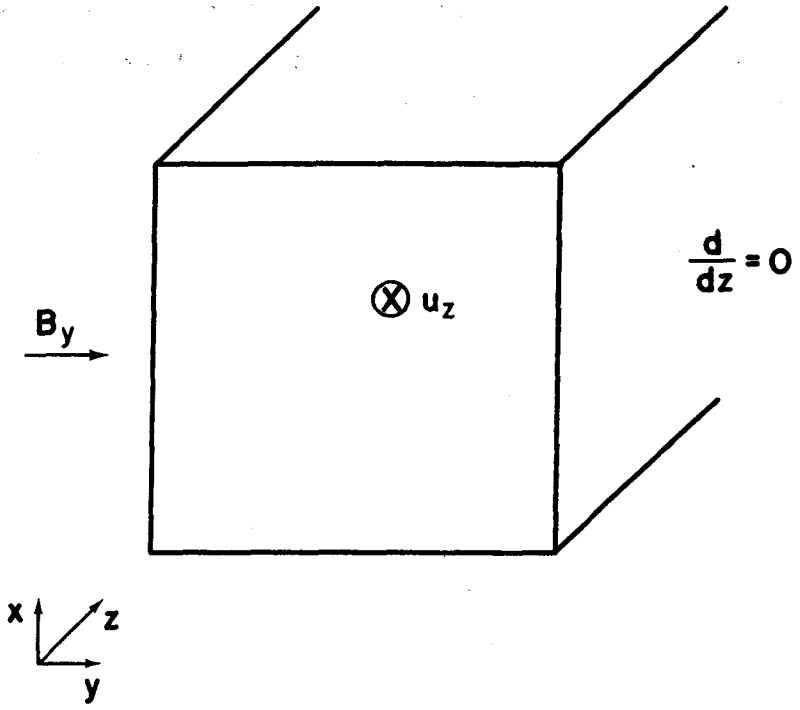


Figure 4.2-26 Geometry for the fully developed 2-D channel flow problem

$$\frac{\partial^2 \phi}{\partial x^2} + \frac{\partial^2 \phi}{\partial y^2} + B \frac{\partial v}{\partial x} = 0 \qquad (4\text{-}72)$$

The boundary conditions which have been treated at this time include

$$v=0 \text{ or } \frac{\partial v}{\partial n} = 0 \quad \text{at each wall}$$
$$\phi=0 \text{ or } \frac{\partial \phi}{\partial n} = 0 \quad \text{at each wall} \qquad (4\text{-}73)$$

These allow symmetric channels to be modeled with as little as 1/4 of the channel in the actual mesh.

The Finite Element Method Applied to the 2-D Problem

In this subsection, the basis functions are presented, the global system of equations is derived, and some of the numerical techniques are described. Calculation of residuals, mesh refinement algorithms, and results from mesh

self-adaptation are presented in the following subsection.

In the fully developed channel flow problem, both the z-directed velocity (v) and the electric scalar potential (ϕ) must be determined. Linear basis functions of the same form are used for both v and ϕ:

$$v = \sum_i \psi_i(x,y)\, V_i \tag{4-74}$$

$$\phi = \sum_i \psi_i(x,y)\, \Phi_i \tag{4-75}$$

ψ is defined within each element as:

$$\Psi_1 = (r/\delta_x)\,(s/\delta_y) \tag{4-76}$$

$$\Psi_2 = (1 - r/\delta_x)\,(s/\delta_y) \tag{4-77}$$

$$\Psi_3 = (1 - r/\delta_x)\,(1 - s/\delta_y) \tag{4-78}$$

$$\Psi_4 = (r/\delta_x)\,(1 - s/\delta_y) \tag{4-79}$$

where Fig. 4.2-27 shows the element configuration and ψ is composed of the sum

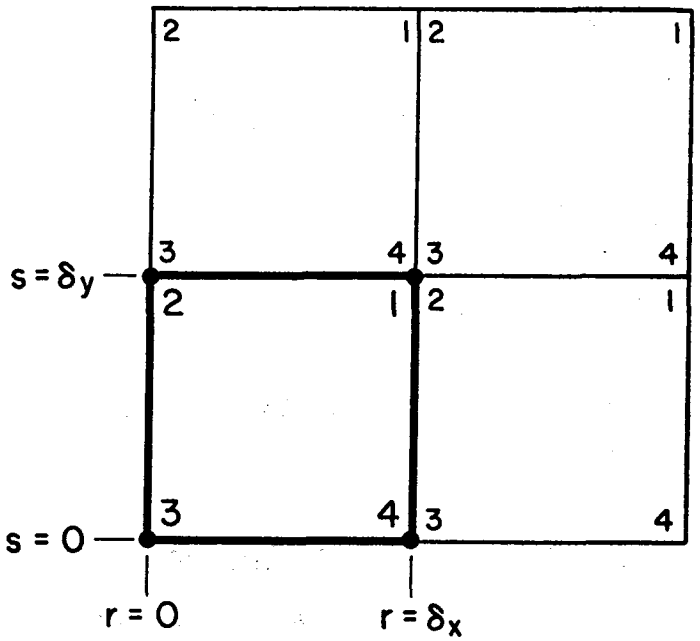


Figure 4.2-27 Rectangular element configuration

of Ψ_i over the four elements neighboring any given node. The element contribution to the basis function at one node is pictured in Fig. 4.2-28. A complete basis function consists of four of these; one for each element which neighbors the node to which the basis function is applied. Rectangular elements were used here to simplify the evaluation of the matrix coefficients. With rectangular elements, the transformation between the local element coordinate system (r,s) and the global coordinate system (x,y) is trivial.

Equations (4-71) and (4-72) can be written in terms of their basis function representations as follows:

$$\sum_n (A_{nm} V_n + B_{nm} \Phi_n) + C_m = 0 \tag{4-80}$$

$$\sum_n (D_{nm} \Phi_n + E_{nm} V_n) = 0 \tag{4-81}$$

where A, B, C, D, and E are given by:

$$A_{nm} = \int\int \left(\frac{\partial\psi_n}{\partial x}\frac{\partial\psi_m}{\partial x} + \frac{\partial\psi_n}{\partial y}\frac{\partial\psi_m}{\partial y} + H^2\psi_n\psi_m\right) dx\, dy \tag{4-82}$$

$$B_{nm} = H^2 \int\int \psi_m \frac{\partial\psi_n}{\partial x}\, dx\, dy \tag{4-83}$$

$$C_m = Re \frac{dp}{dz} \int\int \psi_m\, dx\, dy \tag{4-84}$$

$$D_{nm} = -\int\int \left(\frac{\partial\psi_n}{\partial x}\frac{\partial\psi_m}{\partial x} + \frac{\partial\psi_n}{\partial y}\frac{\partial\psi_m}{\partial y}\right) dx\, dy \tag{4-85}$$

$$E_{nm} = \int\int \psi_m \frac{\partial\psi_n}{\partial x}\, dx\, dy \tag{4-86}$$

Once the integrals in Eqs. (4-82 to 4-86) are evaluated and element contributions to each node are correctly taken into account, Eqs. (4-80) and (4-81) can be solved using any linear matrix system solver. The structure of the matrix is banded for the first iteration (before mesh refinement). The band width is roughly equal to the number of nodes in a single row of nodes. However, after the mesh is refined, it becomes difficult to retain a clean banded structure.

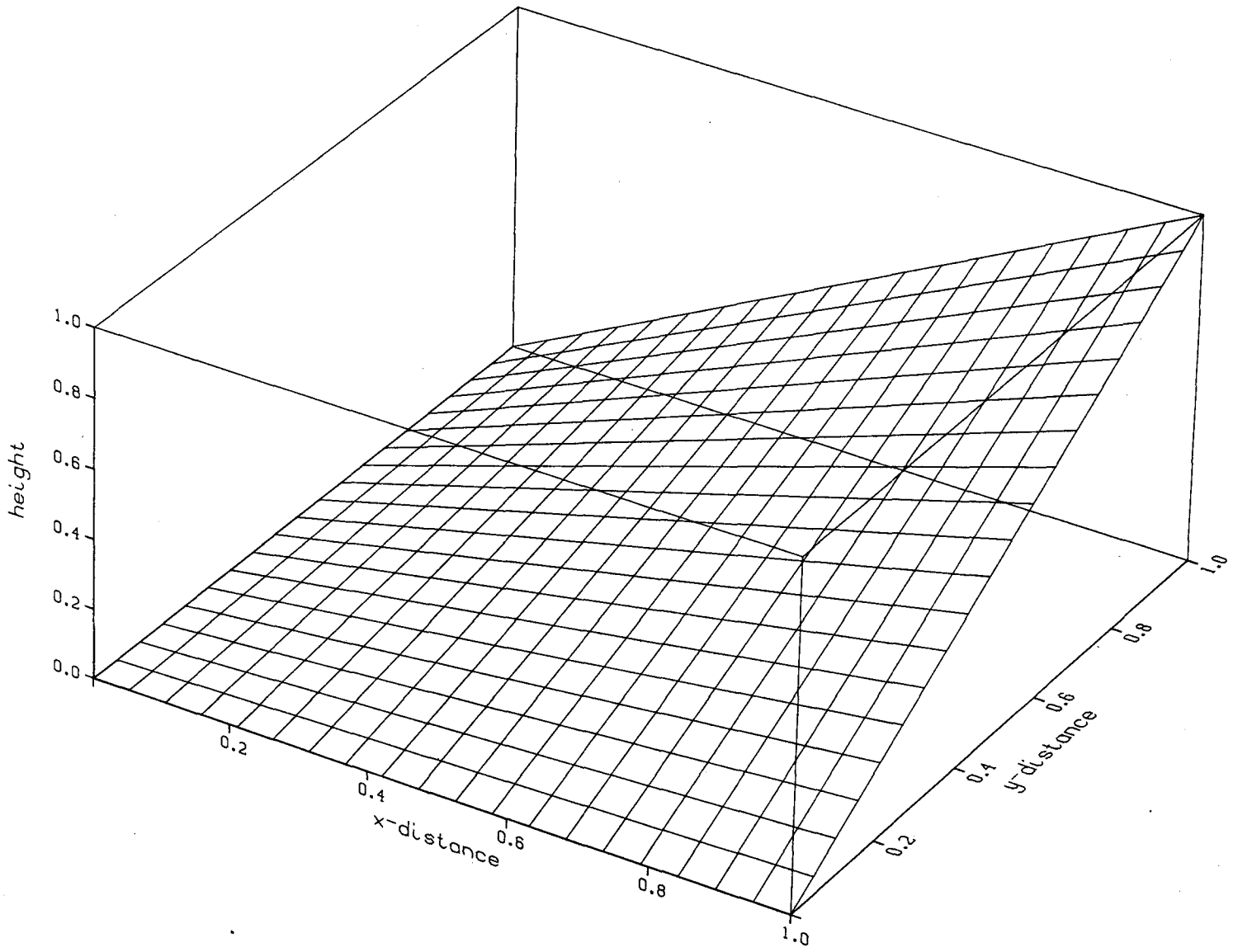


Figure 4.2-28 Illustration of the 2-D linear shape function

It is anticipated that a sparse matrix solution technique will eventually be applied to solving this set of equations. This technique would store only non-zero elements in the matrix, thus allowing the solution of much larger problems. For the purpose of demonstrating the techniques in these example problems, a full matrix inversion routine has been used. The number of equations which can be solved in this way is limited to approximately 1000.

Boundary conditions treated here include both zero function and zero normal derivative. These are both relatively simple boundary conditions to apply. In the case of zero function value, the equation corresponding to a fixed node is removed from the system and all terms referring to the function at the fixed node in the remaining equations are set to zero. This is equivalent to removing the row and column corresponding to the value at the fixed node. In the numerical routines, node elimination is accomplished by shifting the columns and rows in the coefficient matrices over (and up) to fill the space. Since many nodes are on the boundaries, the elimination of equations can significantly reduce the size of the system which must be solved.

Zero normal derivative is also a simple boundary condition to apply. No alterations are necessary to either the coefficient matrix or the load vector.

After solution of the system of equations, it is desirable to construct the electric current density from the velocity and electric scalar potential values. The current density is obtained from Ohm's Law:

$$\underline{j} = \sigma \, (\underline{E} + \underline{v} \times \underline{B}) \tag{4-87}$$

In component form:

$$j_x = - \frac{\partial \phi}{\partial x} - v_z B_y \tag{4-88}$$

$$j_y = - \frac{\partial \phi}{\partial y} \tag{4-89}$$

Linear basis functions do not guarantee continuity of derivatives across element boundaries, so it is inappropriate to evaluate $\underline{j}$ at the node points. Instead, the current density is evaluated at the element interior using:

$$\frac{\partial \phi}{\partial x} = \sum_{i=1}^{4} \frac{\partial \Psi_i}{\partial x} \Phi_i \tag{4-90}$$

At the element centroids this reduces to simply:

$$j_x = -(\phi_1 - \phi_2 - \phi_3 + \phi_4)/(2\,\delta_x) - (v_1 + v_2 + v_3 + v_4)/4 \qquad (4\text{-}91)$$

$$j_y = -(\phi_1 + \phi_2 - \phi_3 - \phi_4)/(2\,\delta_y) \qquad (4\text{-}92)$$

Results are presented here using two types of boundary conditions. In Case 1, non-conducting walls are used at all sides of the duct and no symmetry is applied. Non-conducting walls require zero perpendicular current, which also implies that $\partial\phi/\partial n=0$ (where n is the direction normal to the wall). The velocity is fixed to zero at all walls (the no-slip condition). In Case 2, the side walls perpendicular to the magnetic field are perfectly conducting and the walls parallel to the field are perfectly insulating. The gradient of the potential along perfectly conducting walls is zero, which can also be applied by setting the potential at the walls equal to a constant. The potential along the non-conducting walls is the same as Case 1, and the velocity is also set to zero at all walls.

Results for Case 1 are shown in Figs. 4.2-29 to 4.2-34. In Figs. 4.2-29 to 4.2-31, the velocity profile, electric scalar potential, and electric current density are plotted using a 10x10 mesh which models the entire channel. Note that the magnetic field is directed along the y-axis, leading to the main direction of current along the x-axis. In the vector plot for current density, the arrows represent the local direction of current, where the length of the arrows indicates the normalized magnitude of the current density. In each succeeding current density plot, the normalization for the current density magnitude is different.

Fig. 4.2-29 shows only slight flattening as a result of the Hartmann effect; however, the current density clearly shows the recirculation pattern characteristic of non-conducting ducts.

Figs. 4.2-32 to 4.2-34 show the same parameters for a Hartmann number of 100. The velocity profile is quite flat throughout the majority of the channel as expected. With a uniform 10x10 mesh, this case is poorly solved in the Hartmann boundary layers, which occupy only ~ 1% of the channel nearest the perpendicular walls. The velocity profile overshoots in a manner very similar to the one-dimensional problem described above. The current density vector

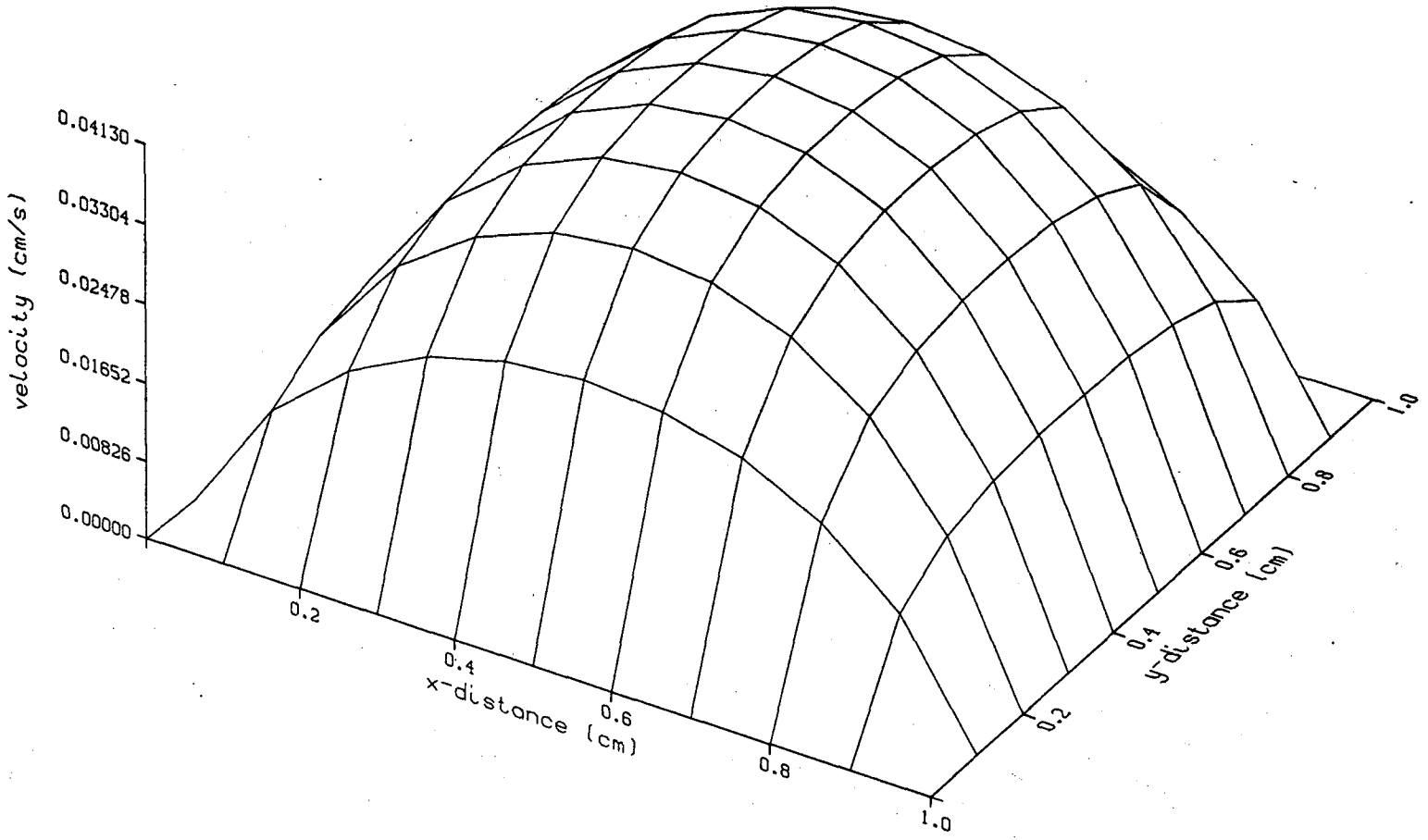


Figure 4.2-29 Velocity profile in the non-conducting duct, Ha=10

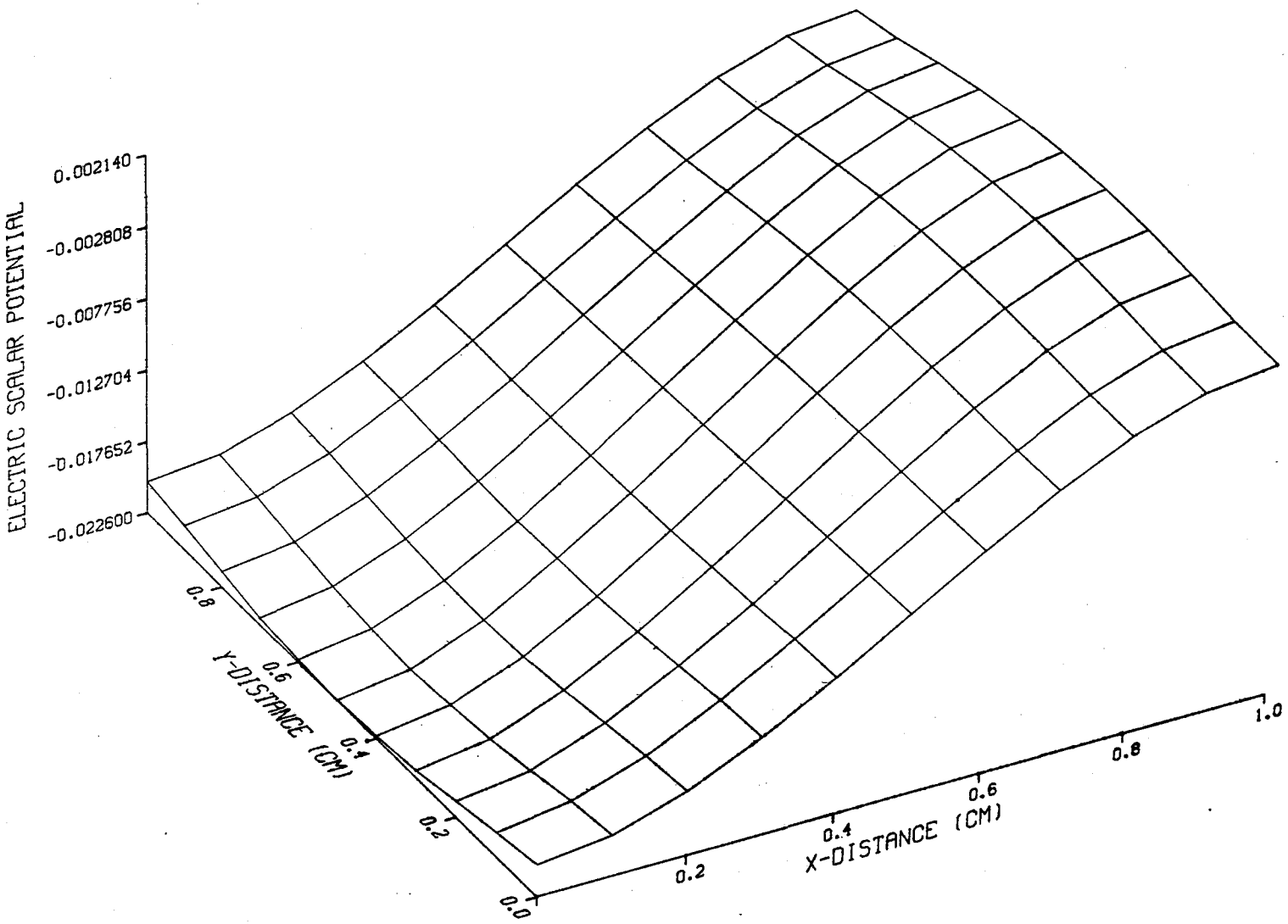


Figure 4.2-30 Electric scalar potential in the non-conducting duct, Ha=10

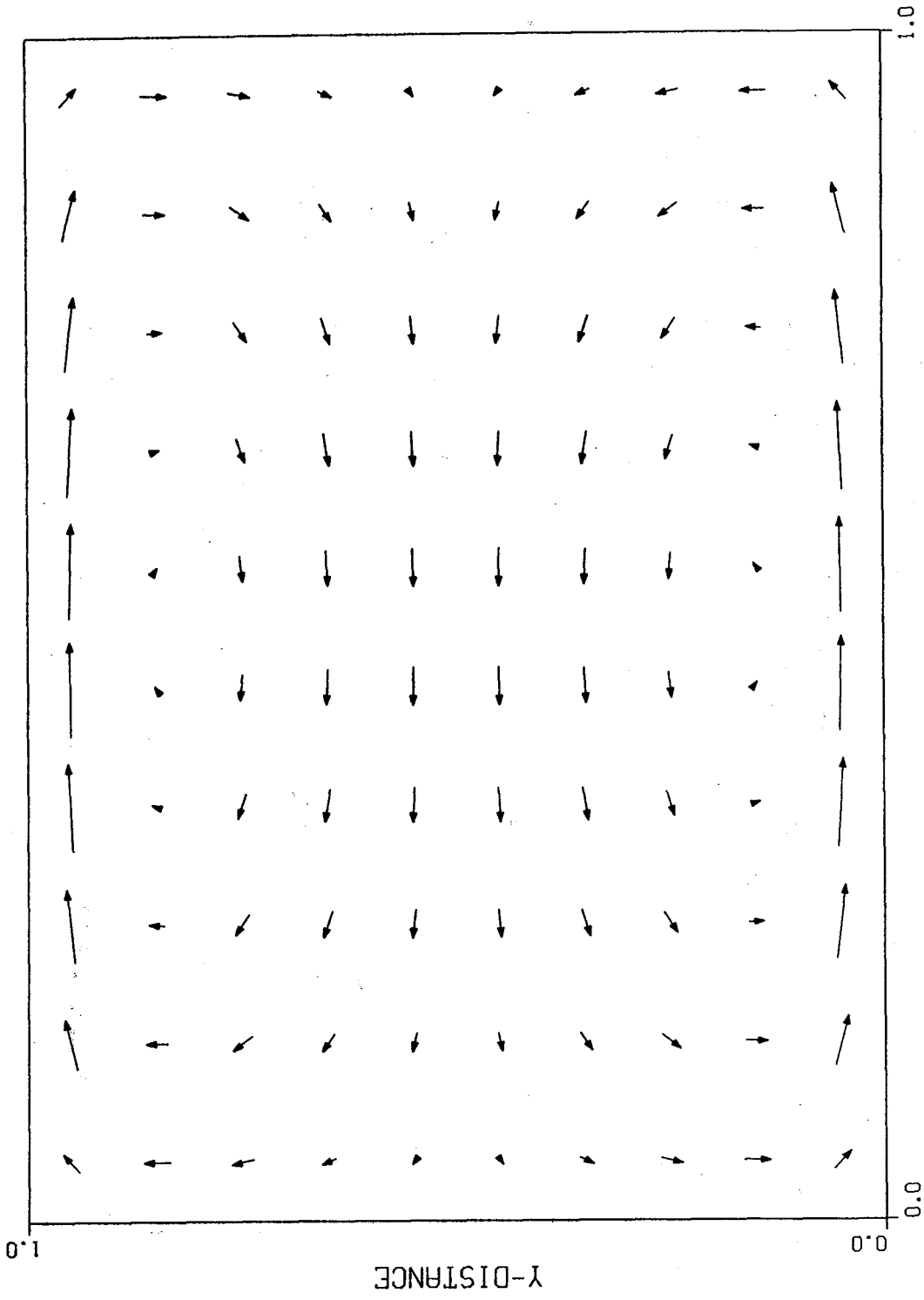


Figure 4.2-31 Electric current density in the non-conducting duct, Ha=10

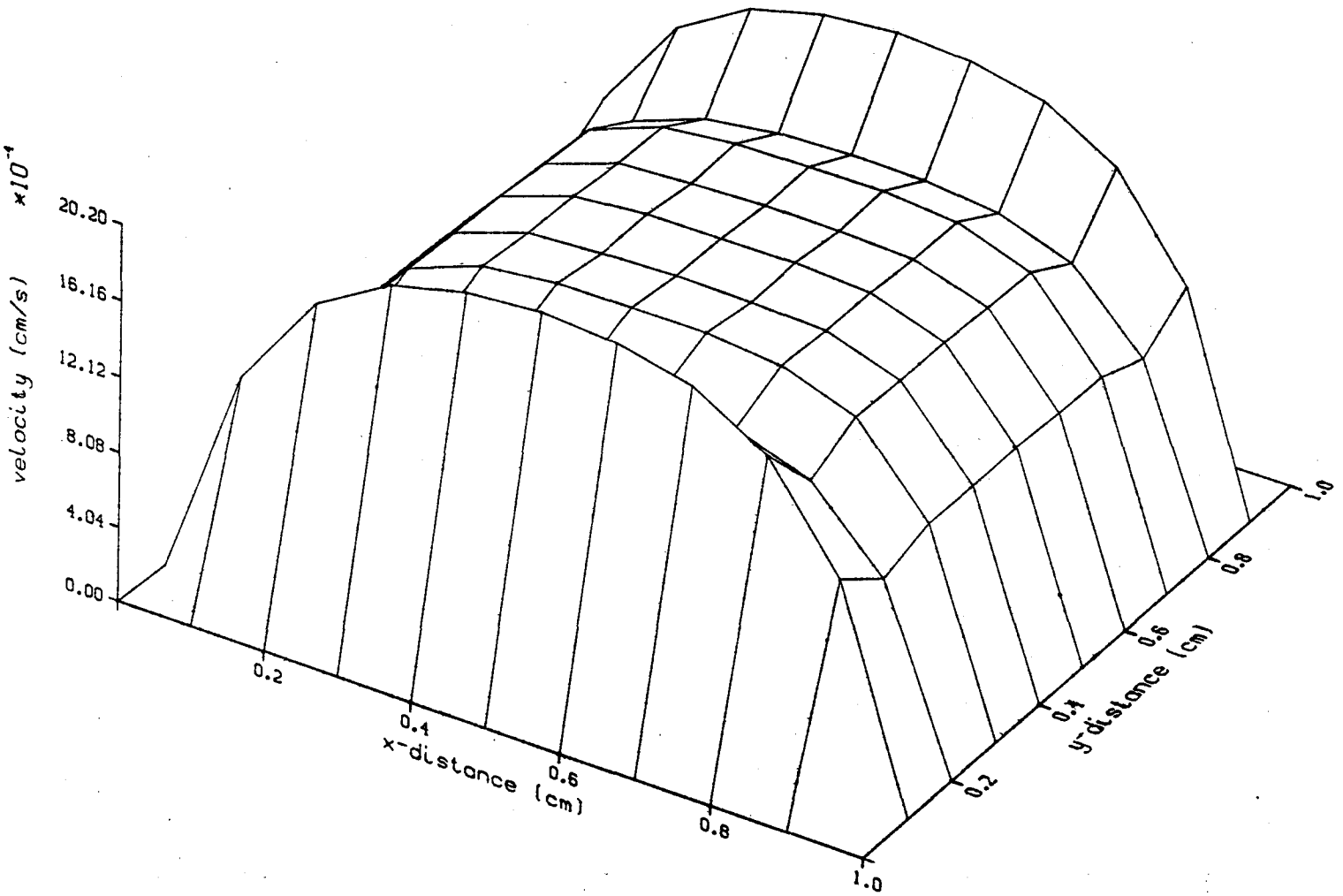


Figure 4.2-32 Velocity profile in the non-conducting duct, Ha=100

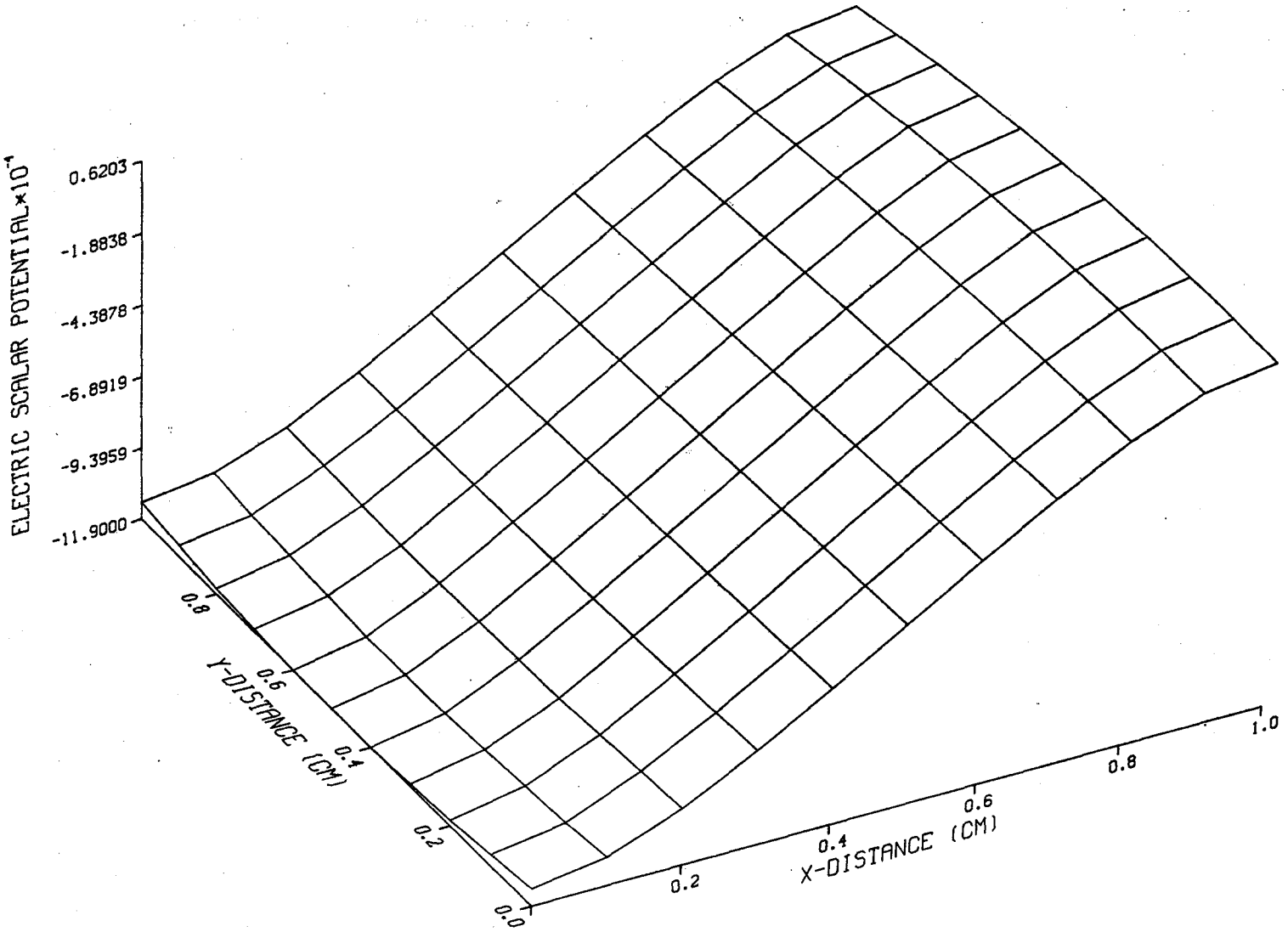


Figure 4.2-33 Electric scalar potential in the non-conducting duct, Ha=100

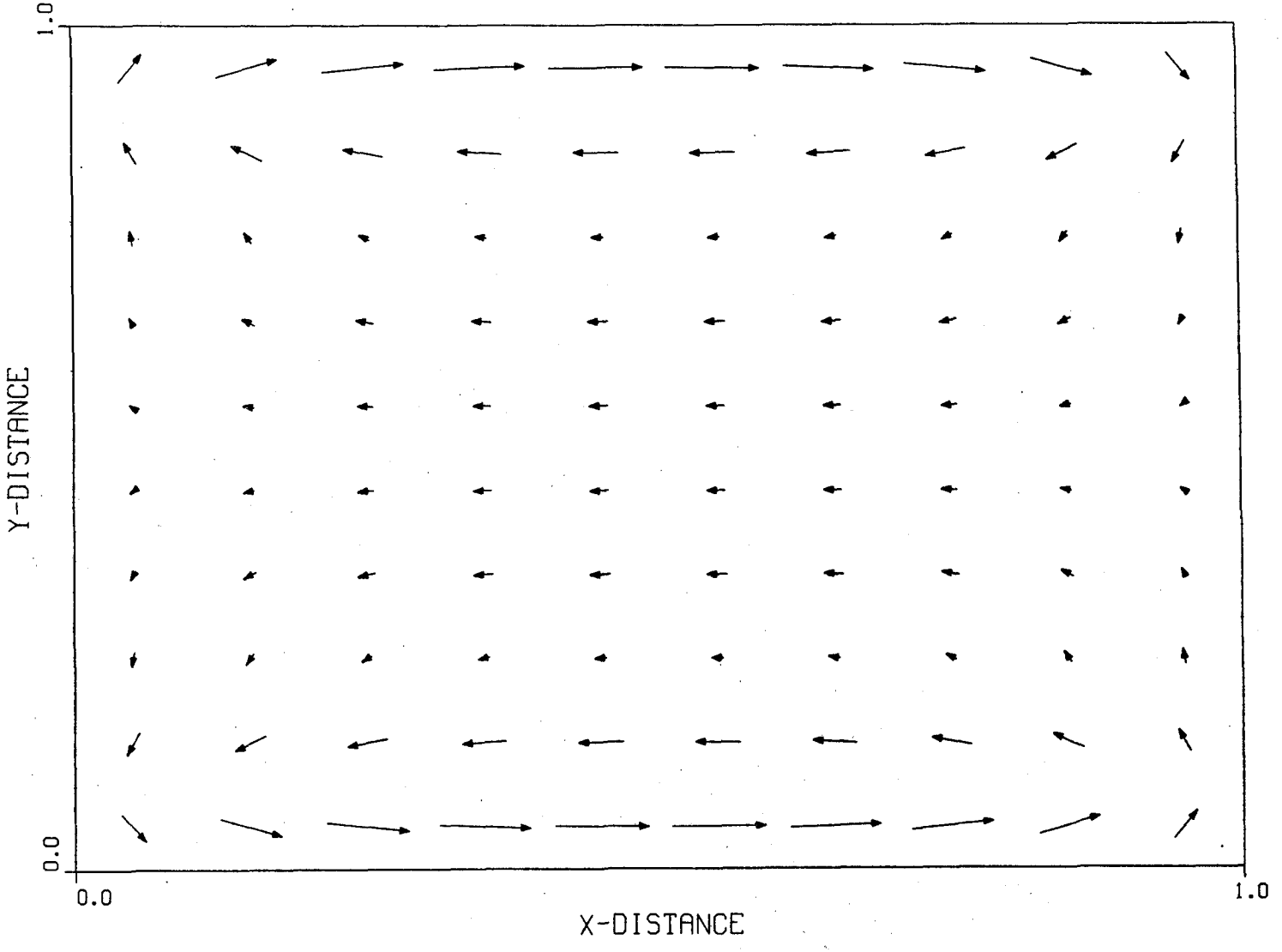


Figure 4.2-34 Electric current density in the non-conducting duct, Ha=100

plot also shows narrowing of the boundary layer as well as the overshooting effect. Careful observation of Fig. 4.2-34 shows an oscillatory behavior in the current density magnitude near the perpendicular walls.

Results for Case 2 are shown in Figs. 4.2-35 to 4.2-39. Figs. 4.2-35 to 4.2-37 show the velocity profile, electric scalar potential, and electric current density vector plot for Ha=100 and a 10x10 mesh which models the entire channel. The most notable feature in the velocity profile is the large wall jets near the parallel walls. This feature is a result of the fact that the electric current turns parallel to the field near the insulating parallel walls. This significantly reduces the MHD body force in those regions as compared to the bulk of the channel. The existence of conducting perpendicular walls also allows these wall jets to form, as they control the magnitude of the total circulating current.

Another notable feature of the velocity profile with conducting perpendicular walls is the overshoot in the Hartmann layers. This is the same effect observed with the non-conducting duct. The plot of the electric scalar potential clearly indicates the effect of the boundary condition. The potential is forced to be constant along the perfectly conducting walls. The current density is nearly constant throughout most of the channel, returning through the conducting perpendicular walls near the parallel side walls.

This same problem was analyzed with a finer mesh (20x20) and four-fold symmetry. The symmetry conditions are indicated in Fig. 4.2-38. Using a finer mesh, together with symmetry, increases the effective resolution by a factor of 4 in each direction. Figure 4.2-39 shows the velocity profile for this case. The wall jets are much more clearly defined and their magnitude has increased. The overshoot at the Hartmann layers is also significantly reduced.

In order to test the accuracy of these calculations, the results were compared with the analytic theory of Hunt.[17] The geometry Hunt used is exactly the same as shown in Fig. 4.2-26: a rectangular channel with uniform magnetic field perpendicular to the perfectly conducting walls and parallel to the non-conducting walls. However, the variables he treated were velocity and magnetic field, rather than velocity and the electric scalar potential. In principle, these two formulations are equivalent, related through the induction equation:

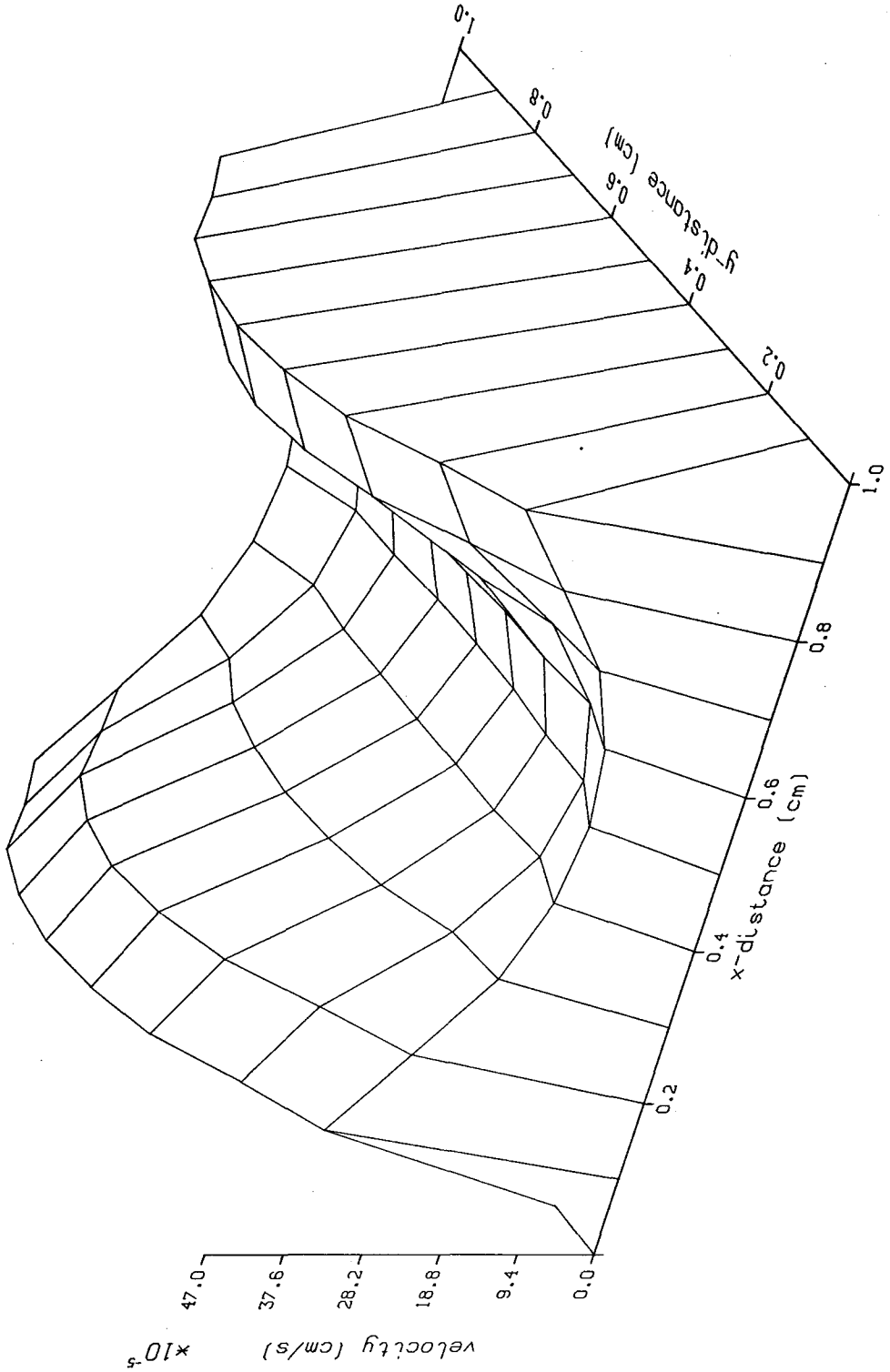


Figure 4.2-35 Velocity profile in the duct with conducting side walls, Ha=100

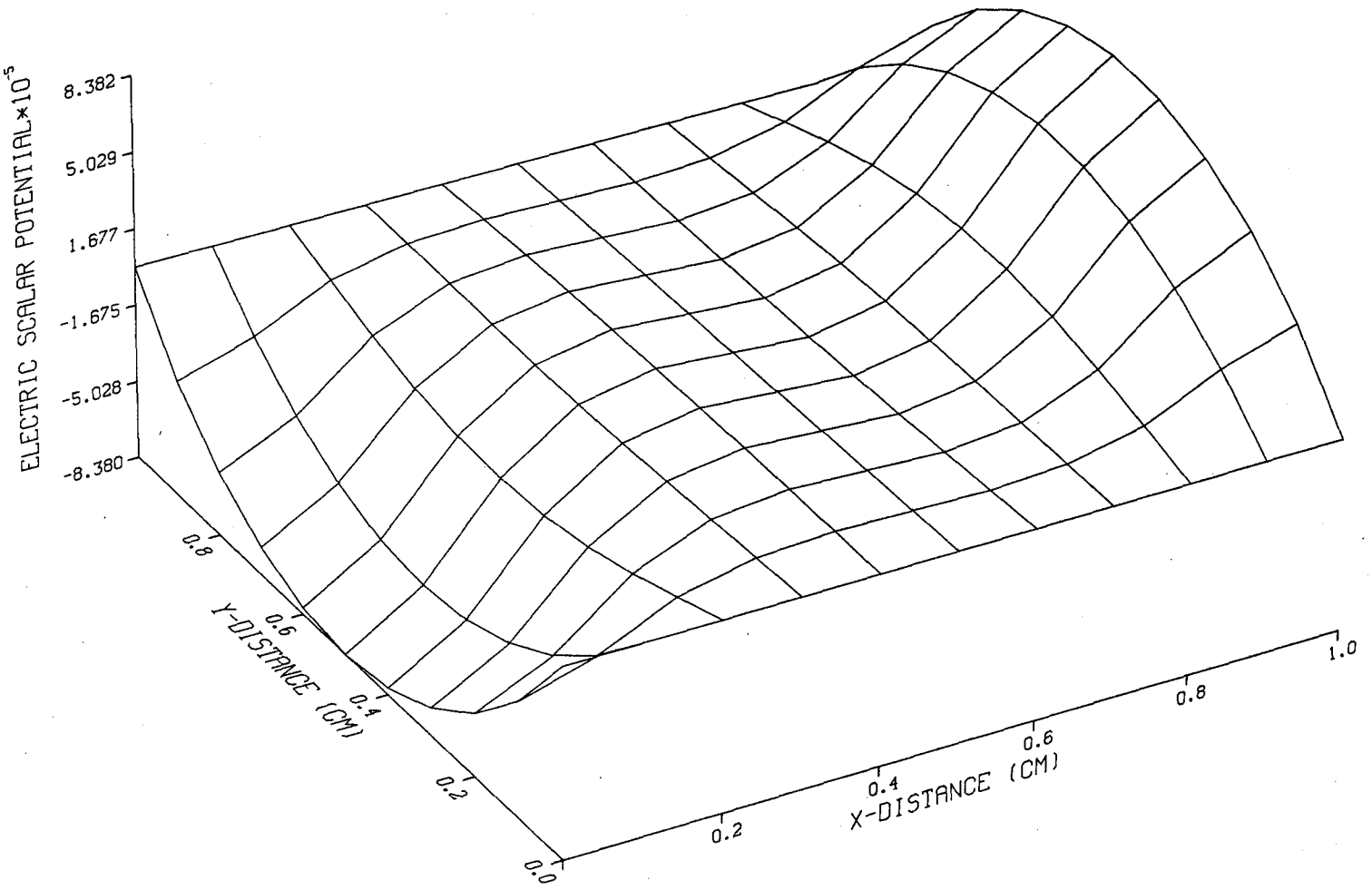


Figure 4.2-36 Electric scalar potential in the duct with conducting side walls, Ha=100

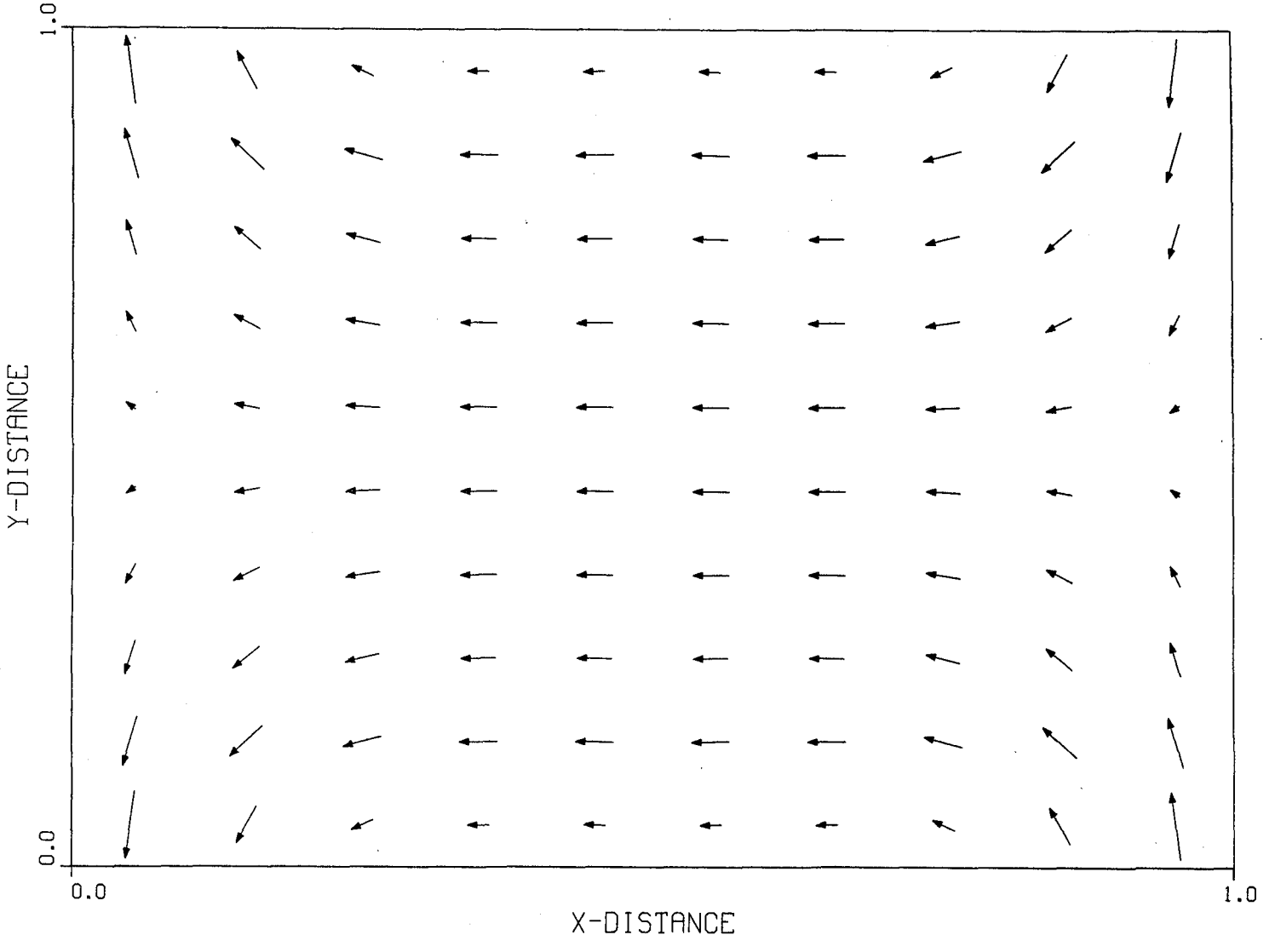


Figure 4.2-37 Electric current density in the duct with conducting side walls, Ha=100

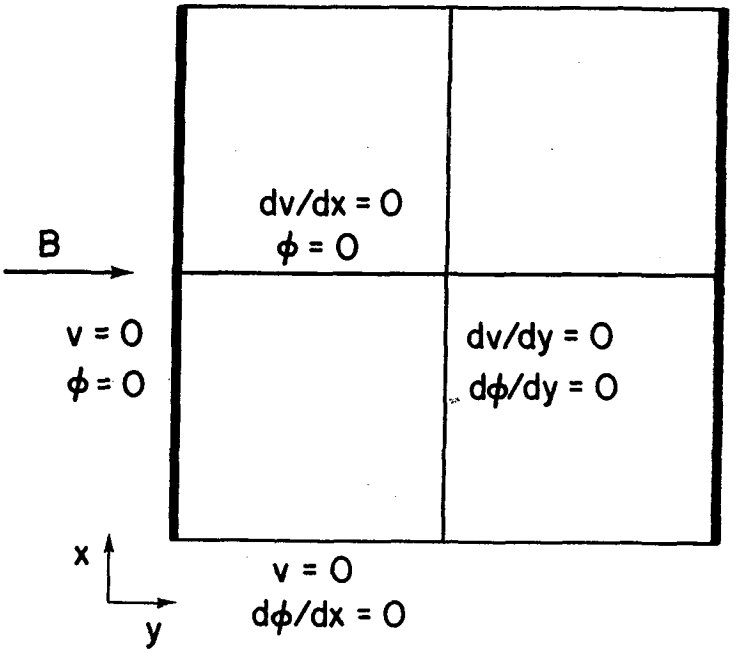


Figure 4.2-38 Symmetry conditions for the duct with conducting side walls

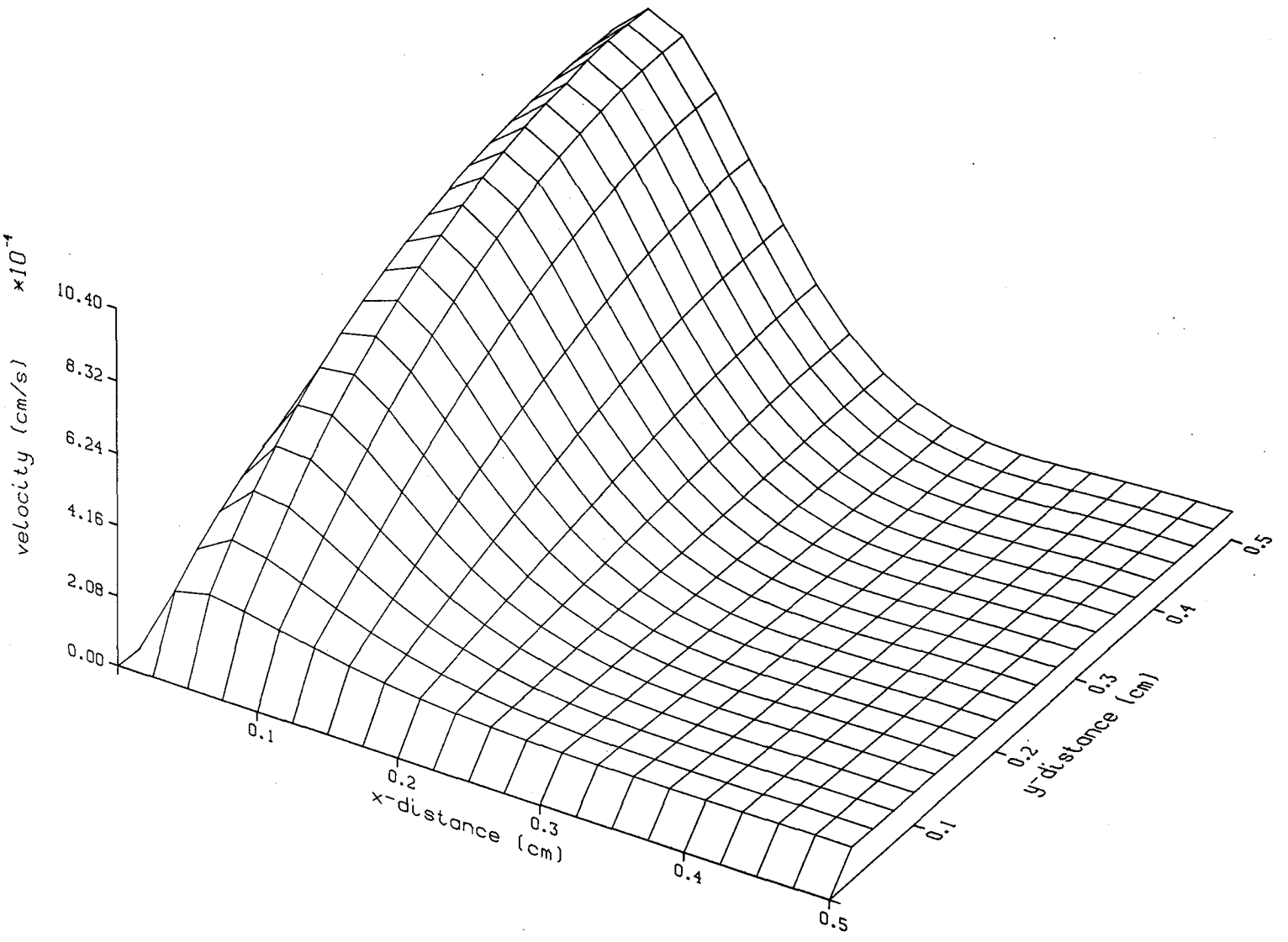


Figure 4.2-39 High accuracy solution for the velocity profile in the duct with conducting side walls, Ha=100

$$\nabla \times \underline{B} = \mu_0 \underline{j} \qquad (4\text{-}93)$$

The analytic solution was obtained by expanding the velocity and magnetic field in Fourier series, then solving a set of two coupled partial differential equations component by component.

Figure 4.2-40 shows Hunt's analytic solution for the velocity along the axis y=0 and compares it with finite element calculations using 10x10, 20x20, and 40x40 meshes. The velocity in this figure is normalized with respect to the channel average velocity. Increasingly finer meshes clearly show a trend towards matching the analytic solution. However, convergence towards this solution is relatively slow. Even though the solution in Fig. 4.2-39 appears quite smooth in the wall jets, it is likely that inadequate mesh refinement in the Hartmann layer continues to affect the accuracy of the solution. In order to better match the analytic solution, better mesh refinement is clearly needed.

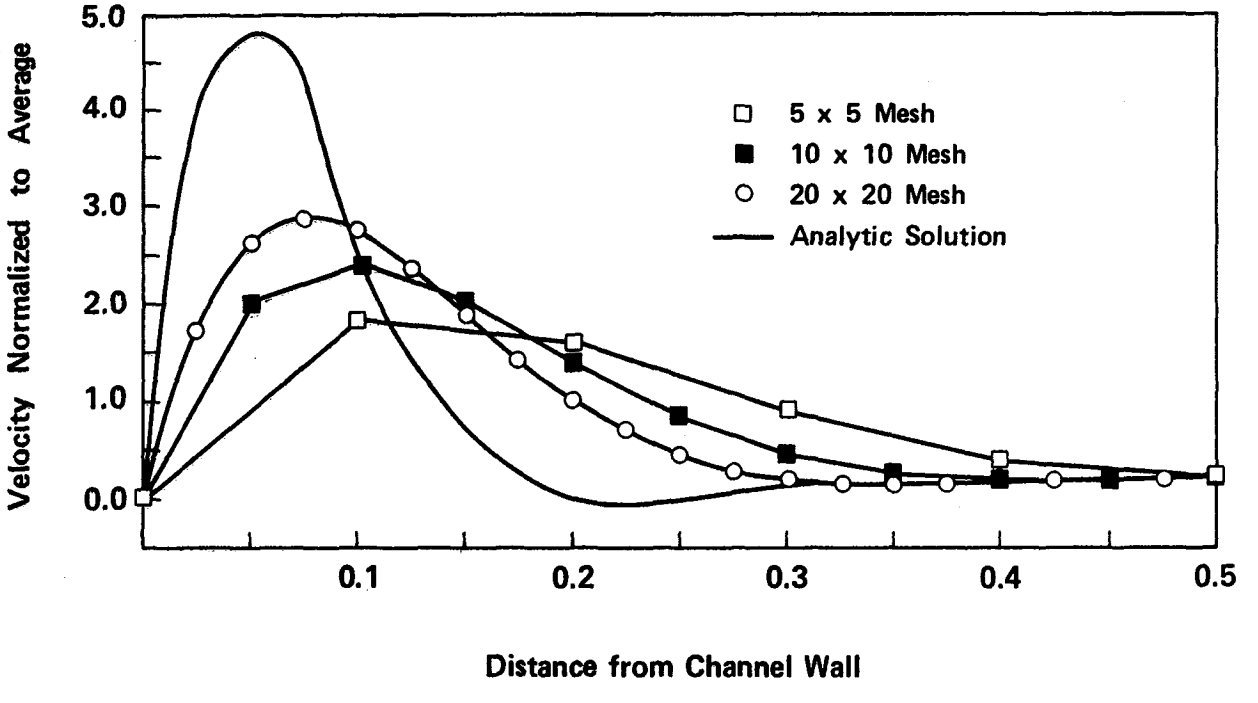


Figure 4.2-40 Comparison of finite element solution with analytic solution

Calculation of Residual Errors

For this linear problem, the global system of equations can be solved uniquely. The resulting coefficients for the basis functions represent a solution which minimizes the average weighted error over the global domain. While the globally averaged error is zero, the local errors can be large and may vary considerably across the solution domain. These errors are easily computed by replacing each variable in the original equations with its basis function representation, and then checking the degree to which the equations are satisfied in each element.

Since order reduction was applied to allow the use of linear basis functions, all second derivatives evaluate to zero. The errors for Eqs. (4-71) and (4-72) are thus given by:

$$r_1^2 = \int_{\Omega_E} \left[H^2\left(v + \frac{\partial \phi}{\partial x}\right) + Re \frac{\partial p}{\partial z} \right]^2 dx\, dy \tag{4-94}$$

$$r_2^2 = \int_{\Omega_E} \left(\frac{\partial v}{\partial x} \right)^2 dx\, dy \tag{4-95}$$

After substituting the basis function representations for v and ϕ, the following equations are obtained:

$$\frac{r_1^2}{H^4} = \int_0^{\delta_y} \int_0^{\delta_x} \left[\frac{rsv_1}{\delta_x \delta_y} + \frac{sv_2}{\delta_y}(1 - r/\delta_x) + v_3(1 - r/\delta_x)(1 - s/\delta_y) + \frac{rv_4}{\delta_x}(1 - s/\delta_y) + \frac{s\phi_1}{\delta_x \delta_y} - \frac{s\phi_2}{\delta_x \delta_y} - \frac{\phi_3}{\delta_x}(1 - s/\delta_y) + K \right]^2 dr\, ds \tag{4-96}$$

where $K = \dfrac{Re \dfrac{\partial p}{\partial z}}{H^2}$, and

$$r_2^2 = \int_0^{\delta_x} \int_0^{\delta_y} \left[\frac{v_1 s}{\delta_x \delta_y} - \frac{v_2 s}{\delta_x \delta_y} - \frac{v_3}{\delta_x}(1 - s/\delta_y) + \frac{v_4}{\delta_x}(1 - s/\delta_y) \right]^2 dr\, ds \tag{4-97}$$

The element average residual error is computed from

$$\bar{r} = \left(r^2/\delta_x \delta_y\right)^{1/2} \tag{4-98}$$

The second residual, $\bar{r}_2$, is fairly straightforward to evaluate:

$$r_2^2 = \frac{\delta_y}{3} \left[(v_1 - v_2)^2 + (v_3 - v_4)^2 + (v_1 - v_2)(v_4 - v_3) \right] \tag{4-99}$$

The first residual requires lengthy algebraic manipulation, which results in:

$$\begin{aligned} r_1^2 = {} & K^2 dx\, dy + \frac{K}{2} dx\, dy\, (v_1 + v_2 + v_3 + v_4) + K\, dy\, (p_1 + p_4 - p_3 - p_2) \\ & + \frac{dx\, dy}{9} \left[(v_1^2 + v_2^2 + v_3^2 + v_4^2) + (v_1 + v_3)(v_2 + v_4) + \frac{1}{2}(v_1 v_3 + v_2 v_4) \right. \\ & + dy/6 \left[(v_1 + v_2)(2p_1 - 2p_2 + p_4 - p_3) + (v_3 + v_4)(2p_4 - 2p_3 + p_1 - p_2) \right] \\ & \left. + \frac{dy}{3dx} \left[(p_1 - p_2)^2 + (p_3 - p_4)^2 + (p_2 - p_1)(p_3 - p_4) \right] \right] \end{aligned} \tag{4-100}$$

There are a number of possible ways to use these two residual errors. Initially, a simplified approach has been used in which only the residual from the Navier-Stokes equation is utilized. As with the one-dimensional problem described earlier, the element averaged residual is computed for each element. A global average is determined, and then for each element the number of standard deviations above the mean error is determined. In this case, only one element division is made if the error exceeds the average by at least one standard deviation. Accelerated refinement has not yet been attempted.

An element is refined by splitting it into four equal parts. This results in 5 additional nodes. However, the nodes on boundaries with undivided elements present a potential problem. Referring to Figure 4.2-41, the shape functions for the undivided element vary linearly from point A to point C, whereas the shape functions for the neighboring divided element consist of two linear functions from A to B and from B to C. In order to prevent this discontinuity in the solution, the transition nodes between divided and undivided elements are computed as the mean value between the nodes at the corners of the nearest undivided element. These transition nodes can be eliminated from the system of equations and evaluated after solving the system. In this way, there is no "overhead" paid by their existence.

Figures 4.2-42 and 4.2-43 show the residual errors calculated from the Navier-Stokes equation in the first iteration for both the nonconducting duct

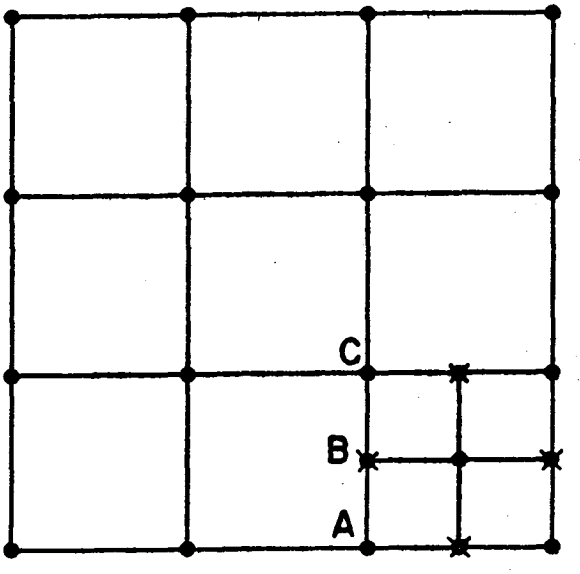


Figure 4.2-41 Illustration of transition nodes

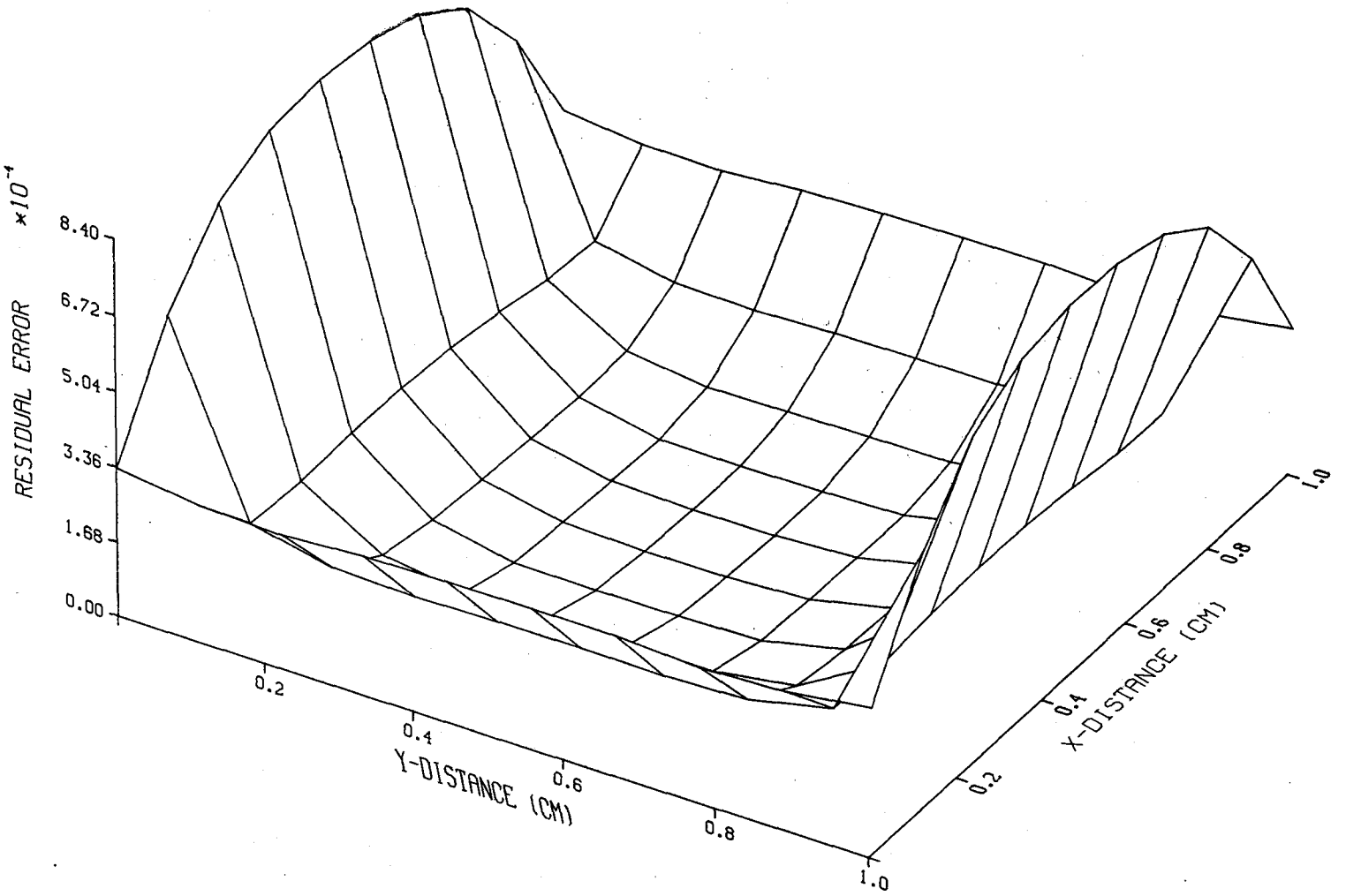


Figure 4.2-42 Residuals for the duct with non-conducting walls, Ha=100

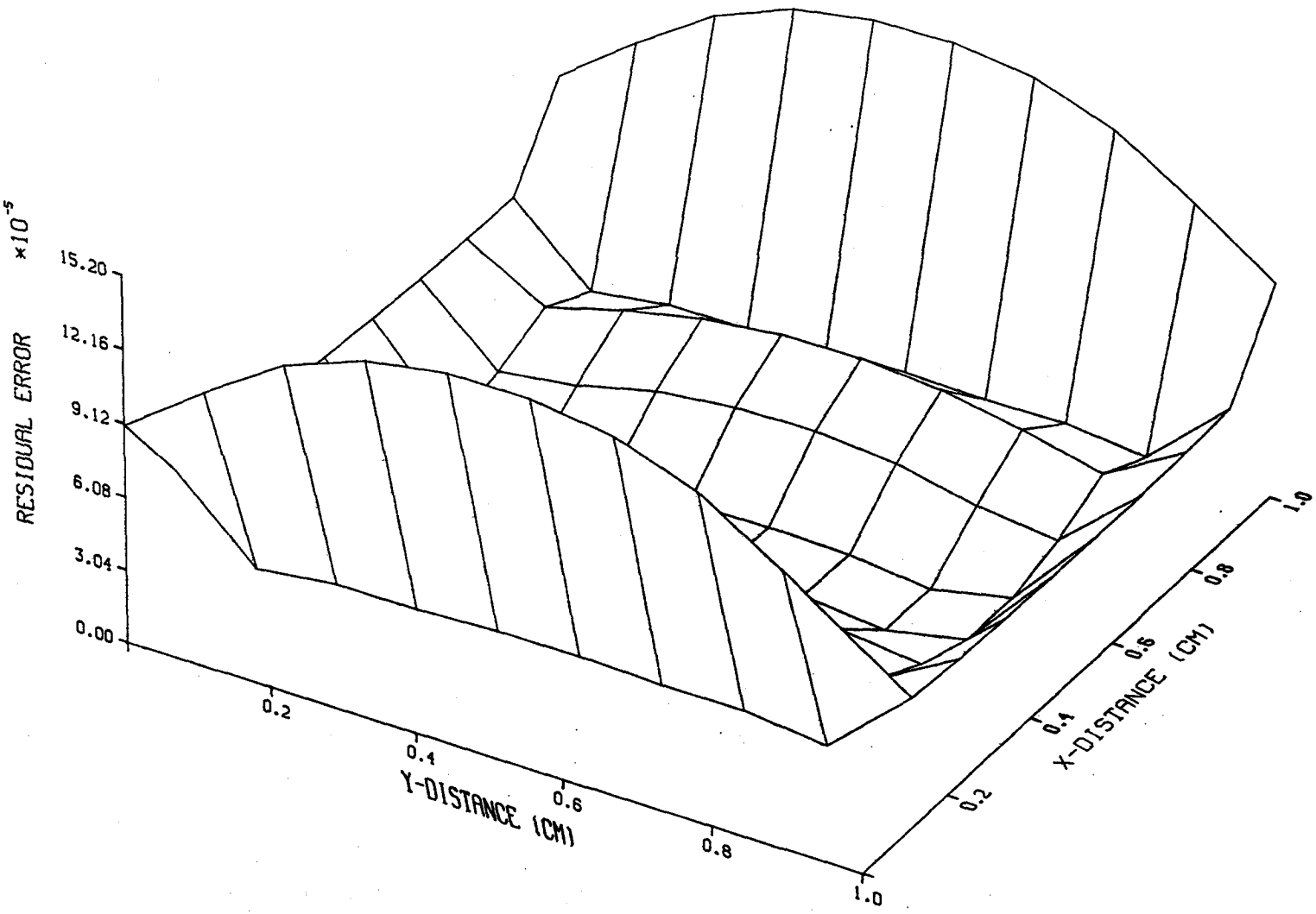


Figure 4.2-43 Residuals for the duct with conducting side walls, Ha=100

and the duct with perfectly conducting side walls. There are clearly much larger errors in the Hartmann layers and wall jet regions.

4.2.3.5 Extensions and Recommendations

The calculations described in this section are a preliminary attempt to explore the advantages and disadvantages of the finite element method for solving MHD fluid flow problems. In this regard, they have proven very effective for certain classes of problems. However, much more development will be required to improve the mesh refinement technique and numerical methods. At this time, only very simple problems have been solved using numerically inefficient algorithms.

The solutions obtained using a uniform mesh are consistantly well-conditioned. However, the accuracy is extremely limited using a uniform mesh for problems with high Hartmann number. It is essential for the success of the finite element method at high Hartmann number to further refine the mesh adaptation procedure.

For expediency, very simple numerical techniques have been employed for solving the global system of equations. In order to solve larger problems -- i.e., finer meshes, more complex geometries, and more complex systems of equations -- a more efficient system solver will need to be applied. Sparse matrix techniques appear very attractive for problems with complex, adapted meshes, which are difficult to formulate in a banded structure.[48,49] Improvements in the area of numerical methods will greatly extend the range of problems which can be treated.

Finally, as mentioned in Section 4.2.3.2, the fully developed channel flow problem is one of the simplest two-dimensional problems which could be treated. A much better test to determine the ultimate applicability of these techniques will be developing flow (Eqs. 4-45 through 4-52). The presence of inertia and a pressure gradient in the equations may significantly affect the success of the solution technique.

4.3 Analytic Treatment of MHD Flow in a Curved Pipe

4.3.1 Introduction

Velocity and temperature profiles for ordinary hydrodynamic (OHD) flow in curved pipes are of importance to many engineering problems, such as cooling and heating coils used in heat exchangers and refrigeration equipment, turbomachinary equipments, etc. However, the flow of a conducting fluid in curved pipes under an intense magnetic field has its applications mainly in self-cooled liquid metal blankets in fusion reactors.

Axisymmetric flow in a straight pipe is two-dimensional in character. The flow in a curved pipe, however, exhibits a three-dimensional nature due to the centrifugal force acting normal to the main direction of the flow, causing a secondary flow pattern in the pipe cross-section. As a result, the point of maximum axial velocity shifts to the outside. One of the early theoretical analyses was made by Dean,[50] who used a perturbation technique to analyze the secondary flow field as a deviation from Poiseuille flow. Other researchers, (e.g., McConalogue and Srivastava[51]) utilized Fourier-series method to solve the fully developed flow in a curved pipe. The developing laminar flow in a curved pipe was calculated by Patanker, Pratap and Spalding[52] using the finite-difference method.

Although the literature on laminar OHD flow in curved pipes is quite extensive, there have been very few investigations of MHD laminar flow in a curved pipe under the influence of a magnetic field. For a uniform magnetic field acting normal to the plane of the pipe, the combined effects of centrifugal force acting normal to the main flow direction and electromagnetic forces acting in a direction opposite to the main flow direction create an interesting behavior which is worth analyzing. Holroyd[53] analyzed experimentally the flow in a uniform magnetic field perpendicular to the plane of an elbow. Walker[54] presented analytical solutions for MHD flow in two straight pipes connected by a smooth elbow under a strong magnetic field acting perpendicular to the flow direction. He showed that, if the magnetic field is sufficiently strong (where inertia and viscous forces are negligable), then the flow tends towards the inside surface of the elbow, closer to the center of curvature.

The present theoretical analysis attempts to examine the fully developed

flow of a conducting liquid in a highly conducting, loosely coiled pipe under a magnetic field which is perpendicular to the plane of the pipe, as shown in Figure 4.3-1. Using the perturbation technique, the MHD flow field is analyzed as a deviation from Poiseuille flow. These preliminary results show the secondary flow pattern which is manifested by centrifugal forces (Dean number) when the applied magnetic field is zero. The first perturbed term in the electromagnetic force effect shows that at small values of Hartmann numbers O(1) the flow is slightly retarded for straight pipes. The combined effect of Dean number (K=20) and Hartmann number (Ha=1) is to retard the flow and shift the point of maximum axial velocity towards the outside of the pipe away from the pipe center of curvature. These results are obtained for small values of the non-dimensional parameters -- perhaps more terms are needed in the expansion to show the realistic flow behavior.

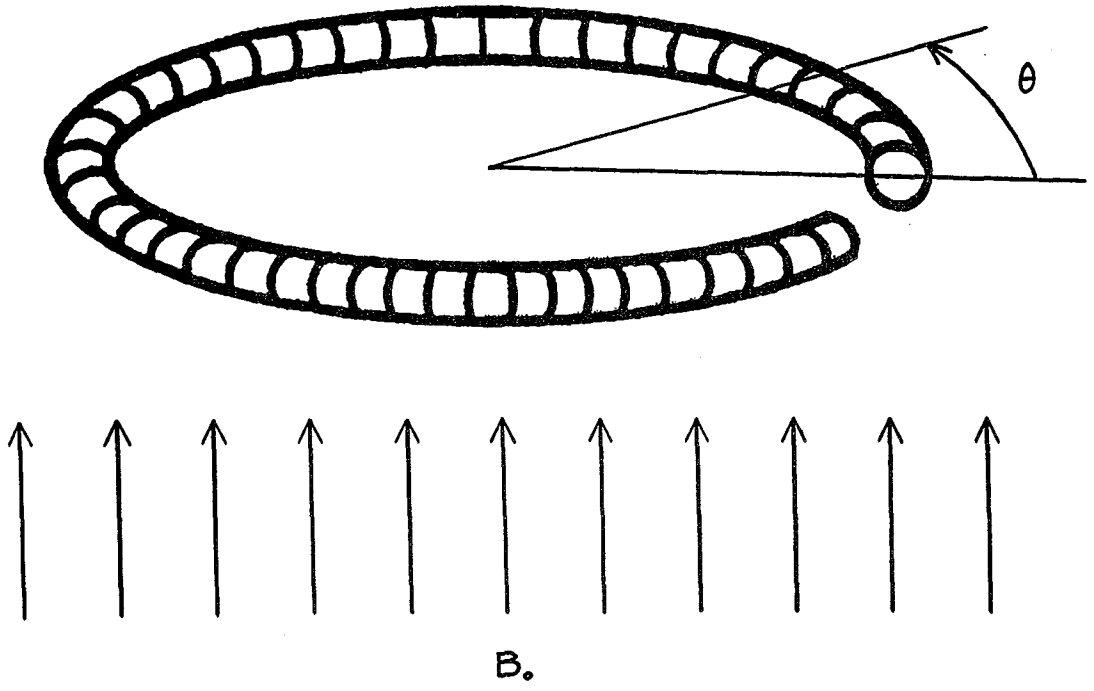


Figure 4.3-1 Simplified representation of a poloidal circular coolant pipe in a toroidal magnetic field

4.3.2 Analytic Approach

Consider a circular pipe with cross-sectional radius (a) coiled in a circle of radius (R), as shown in Fig. 4.3-2. The toroidal coordinate system (r',α,θ) is introduced, where r' denotes the distance from the center of the circular cross-section of the pipe, α the angle between the radius vector and the plane of symmetry, and θ the angular distance of the cross-section from the entry of the pipe. The corresponding velocity components are (u',v',w'). The following non-dimensional variables are defined

$$r = \frac{r'}{a},\quad s = \frac{R\theta}{a},\quad \vec{q} = \frac{\vec{q}'}{\bar{w}_o},\quad p = \frac{p'}{\rho \bar{w}_o^2},\quad \vec{B} = \frac{\vec{B}'}{B_o} \tag{4-101}$$

where primes are dimensional quantities, unprimed quantities are dimensionless, $\vec{q} = (u,v,w)$, p is the pressure, ρ the density, $\bar{w}_o$ the mean axial velocity in the pipe, and $\vec{B} = (B_r,B_\alpha,B_\theta)$ is the magnetic field vector. B_o is the strength of the characteristic magnetic vector field.

The continuity, momentum, and induction equations in vector forms are as follows, with primes on the variables denoting dimensional quantities:

$$\nabla' \cdot \vec{V}' = 0 \tag{4-102}$$

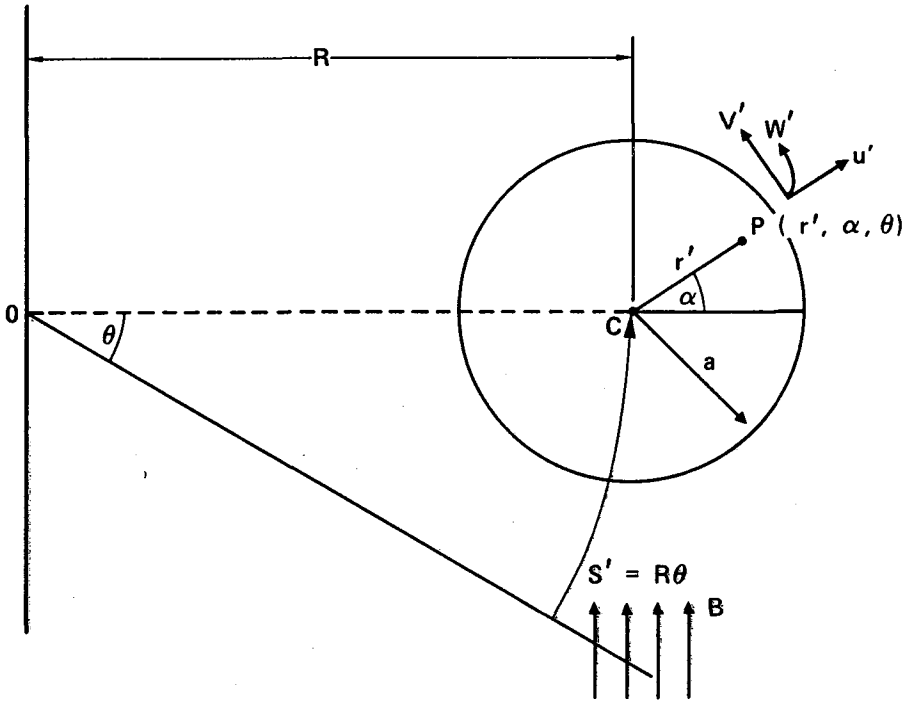


Figure 4.3-2 Coordinate system

$$\rho(\vec{V}' \cdot \nabla')\vec{V}' = -\nabla' p' + \rho \nu \nabla'^2 \vec{V}' + \sigma(\vec{V}' \times \vec{B}') \times \vec{B}' \tag{4-103}$$

$$\frac{1}{\mu o} \nabla'^2 \vec{B}' + \nabla' \times (\vec{V}' \times \vec{B}') = 0 \tag{4-104}$$

In the process of non-dimensionalizing Eqs. (4-102) and (4-103) the following non-dimensional quantities are obtained:

$$\delta = \frac{a}{R} \qquad k = \left(\frac{a}{R}\right)^{1/2} \frac{2a \overline{w}_o}{\nu} \tag{4-105}$$

where δ is small for loosely coiled pipe.

Before dropping the $0(\delta)$ terms compared with $0(1)$ terms in (4-103), it is necessary to rescale the velocities to make the centrifugal force terms of the same order of magnitude as the viscous and inertia terms, as it is the centrifugal force that drives the secondary motion. The transformation that accomplishes this is:

$$(u, v, w) \rightarrow (\delta^{1/2} u, \delta^{1/2} v, w) \tag{4-106}$$

It is also convenient to rescale the axial distance as follows:

$$S = \frac{R\theta}{a} = \delta^{-1/2} z \tag{4-107}$$

For small δ, we may expand the pressure as follows:

$$p = p_o(z) + \delta p_1(r, \alpha, z) + \ldots \tag{4-108}$$

This shows that the major contribution to the axial pressure gradient may be separated from the cross-sectional component.

Using the non-dimensional variable shown above, the governing equations can be written as:

$$\text{continuity: } 0 = \frac{\partial u}{\partial r} + \frac{u}{r} + \frac{1}{r}\frac{\partial v}{\partial \alpha} \tag{4-109}$$

momentum equation:

$$u\frac{\partial u}{\partial r} + \frac{v}{r}\frac{\partial u}{\partial \alpha} - \frac{v^2}{r} - w^2 \cos\alpha$$

$$= -\frac{\partial p_1}{\partial r} - \frac{2}{k}\frac{1}{r}\frac{\partial}{\partial \alpha}\left(\frac{\partial v}{\partial r} + \frac{v}{r} - \frac{1}{r}\frac{\partial u}{\partial \alpha}\right) + N_\delta^* \left(V B_\alpha B_r - B_\alpha{}^2 u\right) \qquad (4\text{-}110a)$$

$$u\frac{\partial v}{\partial r} + \frac{v}{r}\frac{\partial v}{\partial \alpha} + \frac{uv}{r} + w^2 \sin\alpha$$

$$= -\frac{1}{r}\frac{\partial p_1}{\partial \alpha} + \frac{2}{k}\frac{1}{r}\frac{\partial}{\partial \alpha}\left(\frac{\partial v}{\partial r} + \frac{v}{r} - \frac{1}{r}\frac{\partial u}{\partial \alpha}\right) + N_\delta^*(u B_r B_\alpha - v B_r{}^2) \qquad (4\text{-}110b)$$

$$u\frac{\partial w}{\partial r} + \frac{v}{r}\frac{\partial w}{\partial \alpha} = -\frac{\partial p_0}{\partial z} + \frac{2}{k}\left\{\left(\frac{\partial}{\partial r} + \frac{1}{r}\right)\frac{\partial w}{\partial r} + \frac{1}{r^2}\frac{\partial^2 w}{\partial \alpha^2}\right\} - N_\delta^* \; w(B_r{}^2 + B_\alpha{}^2) \qquad (4\text{-}110c)$$

induction equation;

$$\nabla^2 \vec{B} + R_m \nabla x \left(\vec{V} \times \vec{B}\right) = 0 \qquad (4\text{-}111)$$

where k is the Dean number, N_δ^* the modified interaction parameter, R_m magnetic Reynolds number, defined respectively as:

$$k = 2\delta^{1/2}\, Re = \left(\frac{a}{R}\right)^{1/2} \frac{2a\bar{w}_o}{\nu}$$

$$N_\delta^* = \frac{\sigma a B_o{}^2}{\rho \bar{w}_o \delta^{1/2}} \qquad (4\text{-}112)$$

$$R_m = \sigma \mu_o a \bar{w}_o$$

with σ electrical conductivity, and μ_o magnetic permeability of the fluid. Boundary conditions for no slip at the pipe wall are

$$u = v = w = 0 \text{ at } r = \frac{r'}{a} = 1 \qquad (4\text{-}113)$$

while the corresponding condition for magnetic field for highly conducting pipe is:

$$\frac{\partial B}{\partial n} = 0 \text{ at } r = 1 \tag{4-114}$$

The magnetic Reynolds number is considered to be very small, therefore the induction equation can be reduced to:

$$\nabla^2 \vec{B} = 0 \tag{4-115}$$

With the magnetic boundary condition expressed above, the simple result will be given as:

$$\vec{B} = \text{const} \tag{4-116}$$

which is valid all through the given domain.

From the Eqs. (4-110a,b,c) one can see that two parameters, K and N_δ^*, characterize the flow in curved pipe. The Dean number K is equal to the ratio of the square root of the product of the inertial and centrifugal forces to the viscous force. Since the secondary flow is induced by centrifugal forces and their interaction primarily with viscous forces, K is a measure of the magnitude of the secondary flow, while the parameter δ is a measure of the effect of geometry and the extent to which the centrifugal forces varies on the cross-section.

The modified interaction parameter N_δ^* is a measure of the magnitude of the magnetic force which resists the flow of the conducting fluid.

Equation (4-109) can be satisfied automatically by introducing a stream function ψ for the secondary flow, defined by:

$$u = \frac{\partial \psi}{\partial \alpha}, \quad v = -\frac{\partial \psi}{\partial r} \tag{4-117}$$

Substitution into Eq. (4-110c) yields:

$$\nabla_1^2 w - \frac{k}{2}\frac{\partial p_o}{\partial z} = \frac{k}{2r}(\psi_\alpha w_r - \psi_r w_\alpha) + Ha^2 w \tag{4-118a}$$

while cross-differentiation of Eqs. (4-110a,b) and elimination of the pressure term give:

$$\nabla_1^4\psi + \frac{k}{2}\frac{1}{r}\left(\psi_r \frac{\partial}{\partial\alpha} - \psi_\alpha \frac{\partial}{\partial r}\right)\nabla_1^2 \psi - Ha^2 \nabla_2^2 \psi$$

$$= -kw\left(\sin\alpha\, w_r + \frac{\cos\alpha}{r} w_\alpha\right) \tag{4-118b}$$

where Ha is the Hartmann number, ∇_1^2 and ∇_2^2 operators defined respectively as

$$Ha = B_o a \sqrt{\frac{\sigma}{\mu}}$$

$$\nabla_1^2 \equiv \frac{\partial^2}{\partial r^2} + \frac{1}{r}\frac{\partial}{\partial r} + \frac{1}{r^2}\frac{\partial^2}{\partial\alpha^2} \tag{4-119}$$

$$\nabla_2^2 \equiv \cos^2\alpha\, \nabla_1^2 - \cos 2\alpha \frac{\partial^2}{\partial r^2} + \sin 2\alpha \frac{1}{r}\frac{\partial^2}{\partial r \partial\alpha} - \sin 2\alpha \frac{1}{r^2}\frac{\partial}{\partial\alpha}$$

The boundary conditions are

$$\psi = \psi_r = w = 0 \text{ at } r = 1 \tag{4-120}$$

For small values of Dean and Hartmann numbers, series solution can be sought by expanding the solution in a series in powers of Dean and Hartmann numbers:

$$w = \sum_{n=0}^{\infty}\sum_{m=0}^{\infty} K^{2n}\, Ha^{2m}\, w_{n,m}(r,\alpha), \quad \psi = \sum_{n=0}^{\infty}\sum_{m=0}^{\infty} K^{2n+1}\, Ha^{2m}\, \psi_{n,m}(r,\alpha) \tag{4-121}$$

The leading term for w, w_{oo}, is Poiseuille flow in a straight pipe, while the leading term for ψ has the order O(K). This series expansion in k and Ha means perturbing the equivalent Poiseuille flow and calculating the effects of the secondary flow and the magnetic force, respectively, by successive approximation.

4.3.3 Results and Discussion

From the expansion in Eq. (4-121) series solution for the axial velocity, w, can be obtained as

$$w(r,\alpha) = (1 - r^2)\left(-\frac{\partial \overline{P}_o}{\partial z}\right) + \frac{K^2}{138240}$$

$$\{3r^9 - 30r^7 + 90r^5 - 120r^3 + 57r\}\left(-\frac{\partial \overline{P}_o}{\partial z}\right)^3 \cos\alpha$$

$$+ \frac{Ha^2}{16}(-r^4 + 4r^2 - 3)\left(-\frac{\partial \overline{P}_o}{\partial z}\right) + \ldots \qquad (4\text{-}122)$$

where

$$-\frac{\partial \overline{P}_o}{\partial z} = \frac{k}{8}\left(-\frac{\partial P_o}{\partial z}\right) \qquad (4\text{-}123)$$

The order of magnitude of w has been considered to be one. Therefore, $\left(-\frac{\partial \overline{P}_o}{\partial z}\right)$ is of the same order from the leading term and one can have

$$-\frac{\partial \overline{P}_o}{\partial z} = 1 \qquad (4\text{-}124)$$

The effect of Dean number is indicated in Fig. 4.3-3, which shows that the point for the maximum axial velocity is shifted outside and that there is no change in the volume flow rate due to the first-perturbed term in Dean

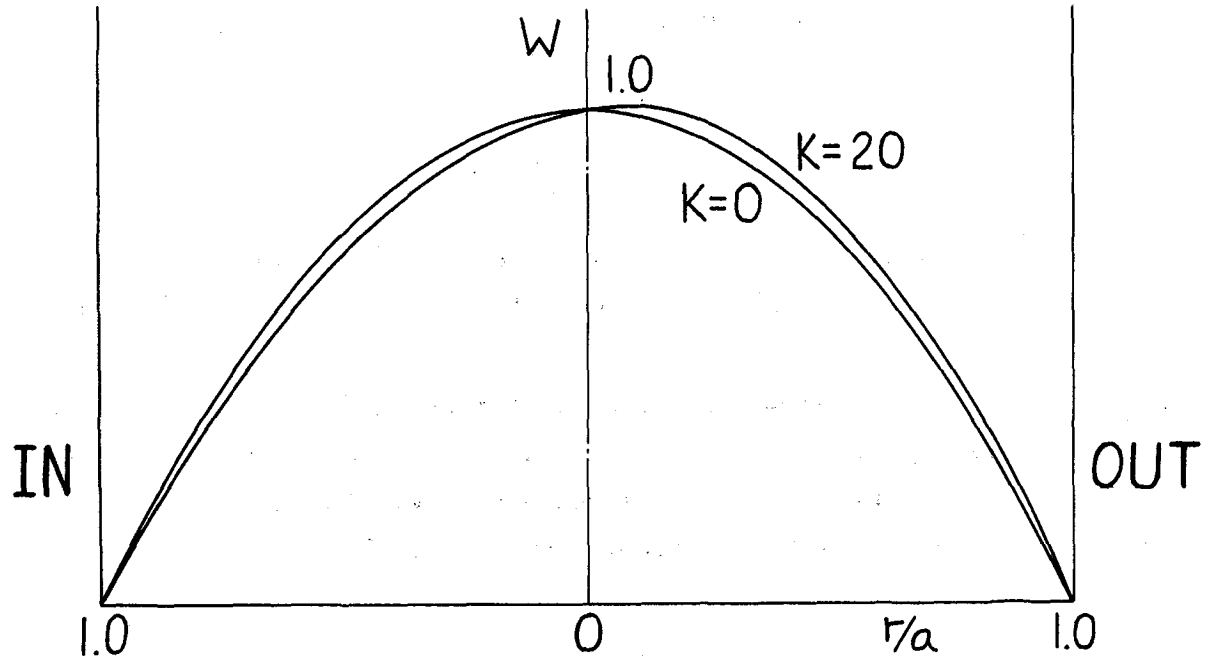


Figure 4.3-3 First perturbed axial velocity profile due to the effect of Dean number (K=20), together with Poiseuille profile (K=0)

number. Fig. 4.3-4 shows that the axial velocity is reduced for the equivalent pressure gradient, which gives reduced flow rate without biased velocity profile due to the first-perturbed term in Hartmann number.

Now, the change in volume flow rate due to the first perturbation in Ha can be expressed as

$$\frac{Q}{\pi a^2 \bar{w}_o} = 1 - \frac{7}{15} Ha^2 + \ldots \qquad (4\text{-}125)$$

where Q is the actual flow rate, and $\bar{w}_o$ the mean axial velocity for the straight pipe for the equivalent pressure gradient.

The combined effects of Dean number and Hartmann number is shown in Fig. 4.3-5, exhibiting the biased velocity profile and the reduced flow rate due to the above two numbers, respectively.

It is expected that the second-perturbed term in Dean number will affect the volume flow rate, and that the corresponding term in Hartmann number will indicate the shift of the maximum axial velocity. Further study on this is being done.

Series solution for stream function of the secondary flow, ψ, is obtained as:

$$\psi(r,\alpha) = \frac{K}{576}(-r^7 + 6r^5 - 9r^3 + 4r)\sin\alpha$$

$$+ \frac{K^3}{1327104}(1.714 \times 10^{-3} r^{14} - 5.143 \times 10^{-2} r^{12} + 0.375 r^{10} - 1.60 r^8 + 4.05 r^6 + 19.74 r^4 - 22.52 r^2)\sin 2\alpha + \ldots \qquad (4\text{-}126)$$

Figures 4.3-6 and 4.3-7 show the first-perturbed and the second-perturbed terms in Dean number, respectively. These show that more terms are needed to have a realistic flow pattern of the secondary flow. Further study is being pursued, including the effect of Hartmann number.

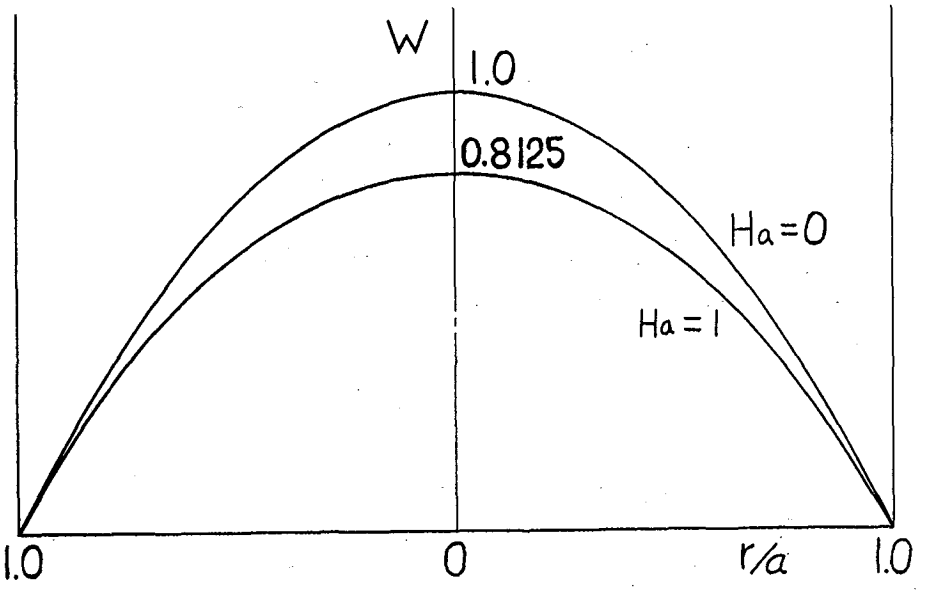


Figure 4.3-4 First-perturbed axial velocity profile due to the effect of Hartmann number (Ha=1), along with Poiseuille profile (Ha=0)

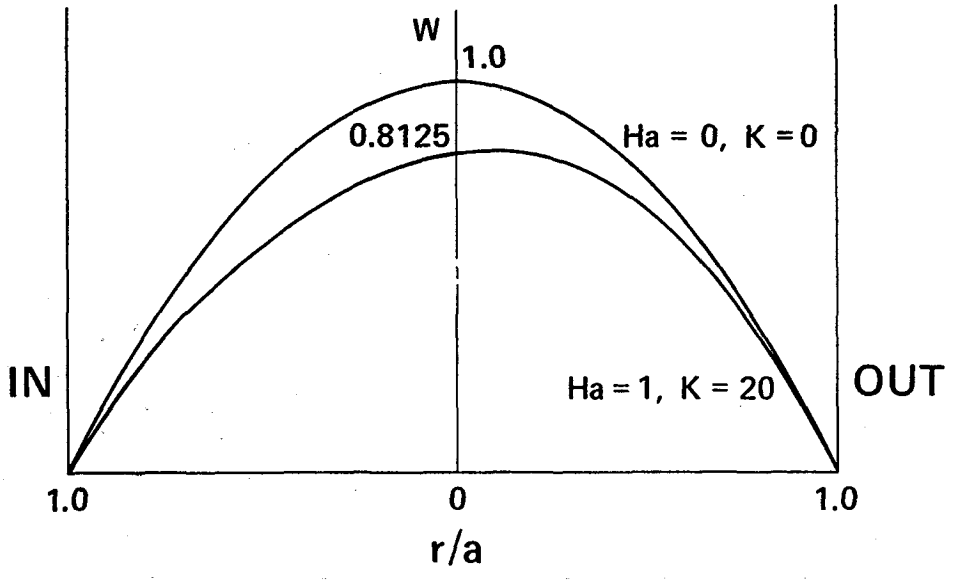


Figure 4.3-5 First-perturbed axial velocity profile due to the combined effects of Dean and Hartmann numbers (K=20, Ha=1), together with Poiseuille profile

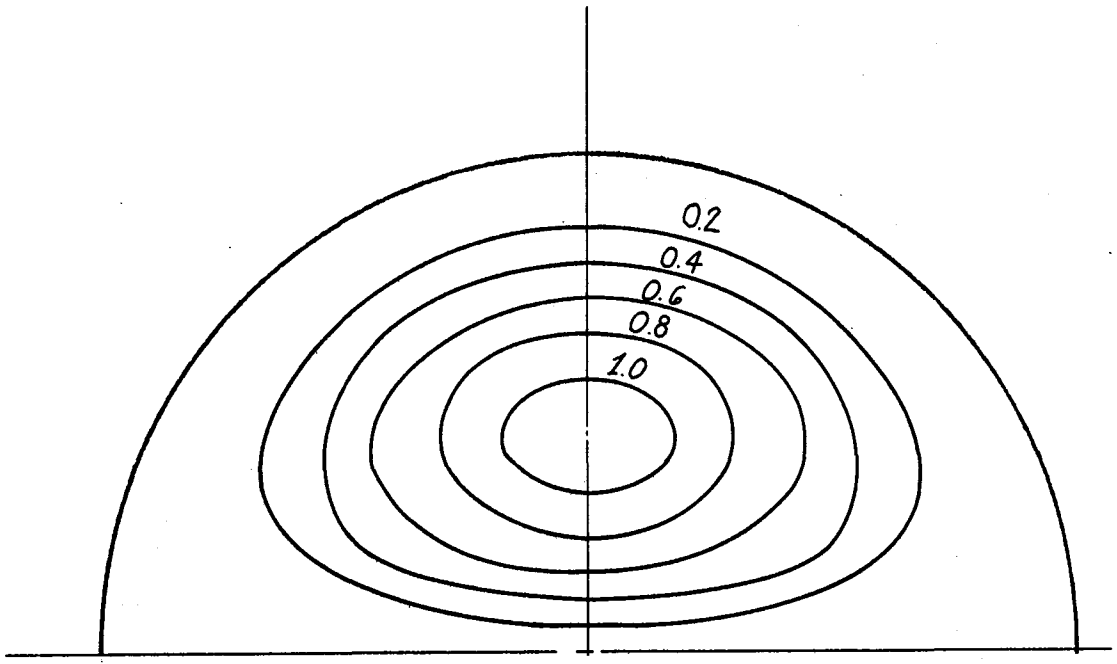


Figure 4.3-6 First perturbed stream function (576 Ψ/K) due to the effect of Dean number

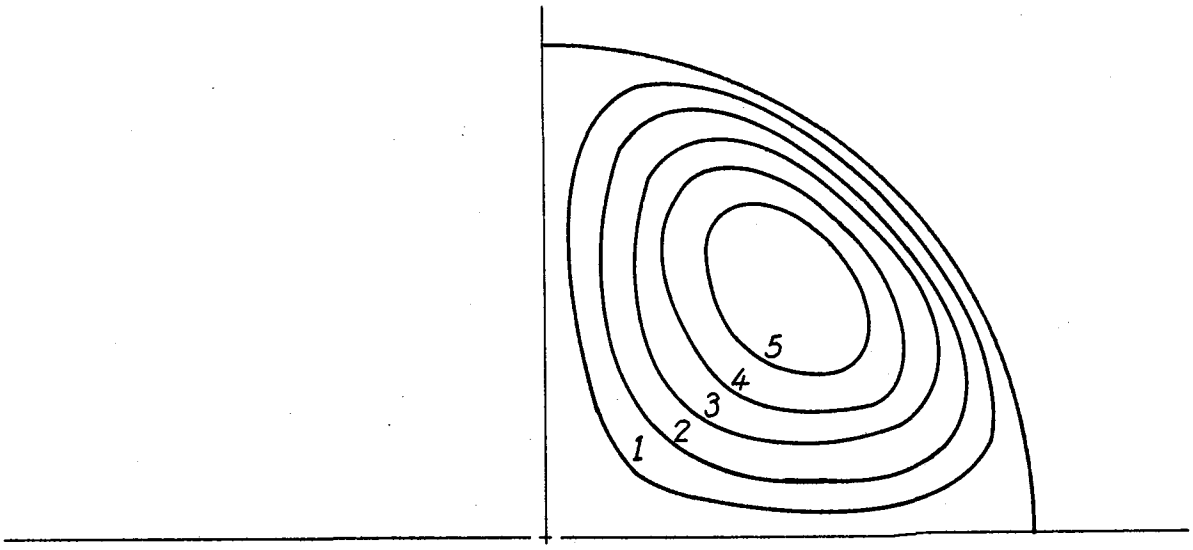


Figure 4.3-7 Second perturbed stream function (-1327104 Ψ/K^3) for the first quadrant due to the effect of Dean number

4.4 MHD Pressure Drop

4.4.1 Introduction

An important part of assessing the viability of a particular self-cooled liquid metal blanket involves calculating the MHD pressure drop. A high pressure drop means high pressure stresses. It is also desirable to reduce the pressure drop for economical reasons, namely, to reduce the ratio of pumping power to electric power output of the power plant. However, the stresses resulting from the MHD pressure drop pose more fundamental feasibility problems.

The MHD pressure drop in a straight duct for fully developed flow is well understood, but the fusion blanket design will necessarily cause many deviations from straight duct flow in order to satisfy the many conflicting requirements and constraints, such as flow distribution requirements, heat transfer, material temperature limits and allowable stresses. In addition, the magnetic field is spatially varying. In Table 4.4-1, an attempt has been made to list the various contributors to the MHD pressure drop which may be found in a fusion blanket and give an idea of how well each is understood. As can be seen in the table, much work remains to be done in the area of MHD pressure drop.

One contributor to MHD pressure drop is due to a varying magnetic field. In a liquid metal fusion reactor blanket, this is unavoidable because the fluid must enter and exit the magnetic field as tritium and heat extraction will be done outside of the field. In the following sections, the pressure drop due to a varying B field is discussed and results of a numerical analysis of this phenomenon are presented.

4.4.2 Pressure Drop Due to Magnetic Field Entrance or Exit

4.4.2.1 Background

When a conducting fluid flows in a direction perpendicular to a magnetic field, the free charges in the fluid feel a force proportional to $q(\underline{V} \times \underline{B})$, the Lorentz force, where q is the charge, V is the velocity, and B is the magnetic field. In regions of non-uniform magnetic field, the product $\underline{V} \times \underline{B}$ changes in a streamwise direction. The magnitude of the charge separation,

Table 4.4-1. Contributors to MHD Pressure Drop

Type of Pressure Drop	Design Dependent	Well Understood	Some Work Done/More Work Needed	Not Yet Studied/Very Little Work	If Not Understood Potentially Important
Global effects					
Intra-Channel	X			X	X
Manifolding				X	
Bends					
In plane $\perp$ to B				X	
In plane $\parallel$ to B				X	X
Helical Flow Paths	X			X	X
Mixing Vanes	X			X	X
Entrance and Exit			X		
Flow not Entirely $\perp$ or $\parallel$ to B				X	
Varying B			X		
Contractions, Expansions	X		X		
Nonuniform Wall Thickness	X		X		
Straight Duct		X			
Mixed $\parallel$, $\perp$ components				X	
Turbulence Enhancement				X	
Flow Tailoring				X	

and therefore the induced potential, will vary longitudinally, causing eddy currents to flow in the plane perpendicular to the B field (Fig. 4.4-1).

There will be a net body force due to these longitudinal currents whether the duct walls are conducting or non-conducting. In this situation, the electromotive force will be in such a direction as to cause a positive pressure gradient at one end of the current loop, and a negative pressure gradient at the other end, accelerating and decelerating the flow (Fig. 4.4-2). The net effect, however, is negative because the positive pressure gradient occurs in the region where the magnitude of the magnetic field (and thus the force on the fluid) is less than that in the region with the negative pressure gradient.

Entrance and exit effects are a special case of flow in a non-uniform field. In this case, the eddy currents may return in regions with little or no magnetic field.

4.4.2.2 Description of Methodology

Although this problem contains 3-D effects, a 2-D analysis was employed due to the complexity of a 3-D analysis. The effect this has on the results of the analysis will be discussed.

The following assumptions were made in solving this problem: a) the velocity profile is given; b) the induced magnetic field is negligible; c) the duct is rectangular; d) the problem is 2-D; and e) viscous terms are negligible.

The equations which must be solved are:

$$\underline{j} = \sigma(\underline{E} + \underline{V} \times \underline{B})$$

where

$$E = - \underline{\nabla}\phi \tag{4-127}$$

$$\underline{\nabla} \cdot \underline{j} = 0 \tag{4-128}$$

$$\rho \frac{D\underline{V}}{Dt} + \underline{\nabla}p = \eta \nabla^2 \underline{V} + \underline{j} \times \underline{B} \tag{4-129}$$

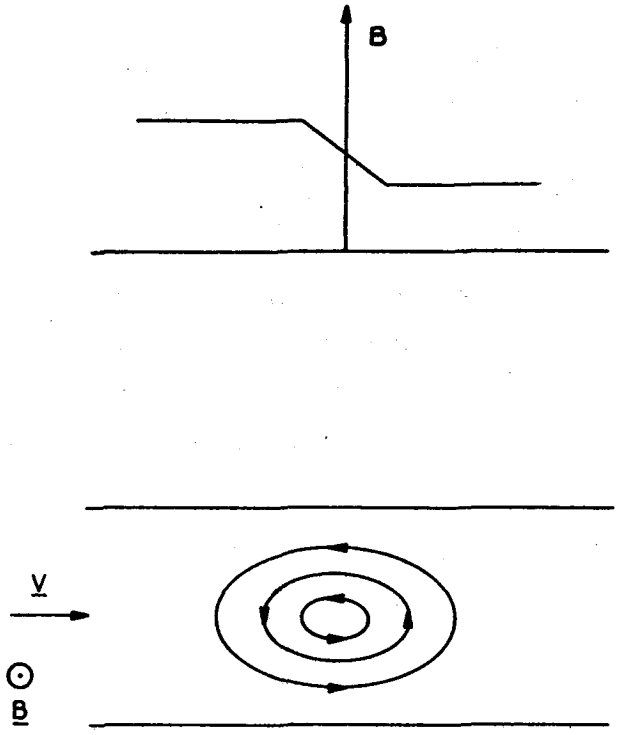


Figure 4.4-1 Electrical current flow as a result of changing B field

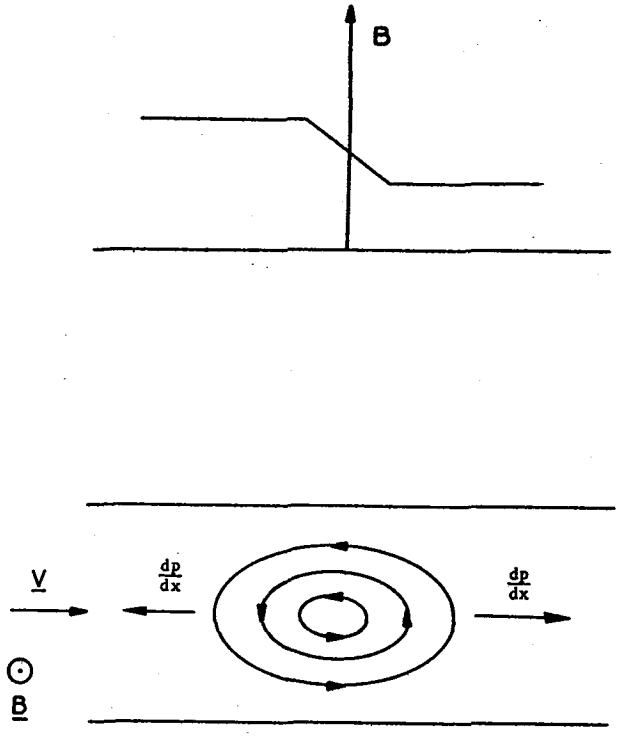


Figure 4.4-2 Pressure gradients due to interaction of electrical currents with B field

where j is the electrical eddy current density, σ is the wall conductivity, ϕ is the electric potential, p is the pressure, and η is the fluid viscosity. Because the fluid velocity is assumed constant and viscous terms are neglected, the Navier-Stokes equation reduces to

$$\underline{\nabla} p = \underline{j} \times \underline{B} \tag{4-130}$$

In dimensionless form, these equations are:

$$\underline{j}^* = - \underline{\nabla}\phi^* + \underline{V}^* \times \underline{B}^* \tag{4-131}$$

$$\underline{\nabla} \cdot \underline{j}^* = 0 \tag{4-132}$$

$$\underline{\nabla} p^* = \underline{j}^* \times \underline{B}^* \tag{4-133}$$

where $j^* = j/\sigma u_m B_o$, $\phi^* = \phi/a u_m B_o$, $V^* = V/u_m$, $B^* = B/B_o$, $p^* = p/\sigma a u_m B_o^2$. B_o is the maximum magnetic field, u_m is the mean velocity, and a is the duct half-width. The asterisks will be dropped for convenience.

In the investigation of MHD problems, slug flow is sometimes assumed in order to simplify calculations. In this analysis, various velocity profiles are assumed in order to get an idea of how the velocity profile affects the pressure drop. This is an approximation, whose validity remains to be demonstrated.

The geometry for this problem is shown in Figure 4.4-3. In this two-dimensional problem, Eqs. (4-131)-(4-133) reduce to

$$j_x = \frac{-\partial\phi}{\partial x} \tag{4-134}$$

$$j_y = \frac{-\partial\phi}{\partial y} - VB \tag{4-135}$$

$$\frac{\partial j_x}{\partial x} + \frac{\partial j_y}{\partial y} = 0 \tag{4-136}$$

$$\frac{dp}{dx} = j_y B \tag{4-137}$$

Equations (4-134) and (4-135) may be used in Eq. (4-136) to yield

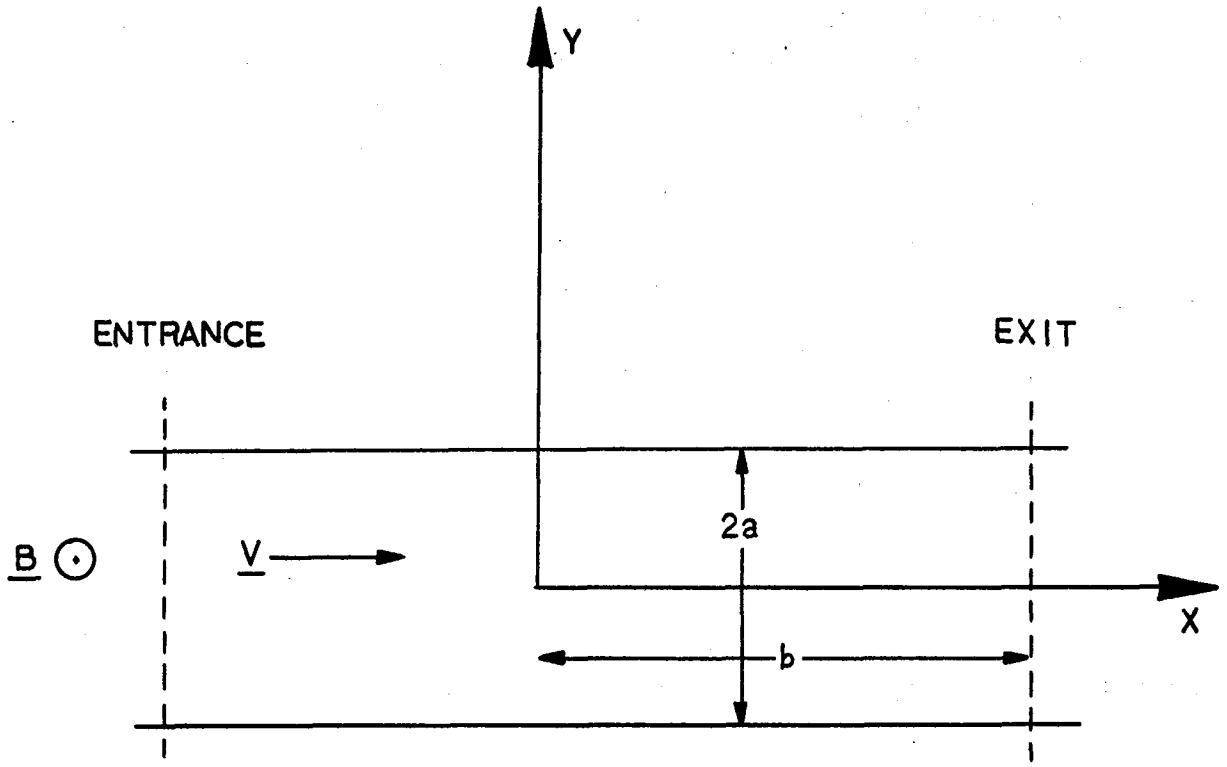


Figure 4.4-3 Geometry used in calculation of MHD pressure drop

$$\frac{\partial^2\phi}{\partial x^2} + \frac{\partial^2\phi}{\partial y^2} + B\frac{\partial V}{\partial y} = 0 \qquad (4\text{-}138)$$

The potential distribution is found by iterating on the finite difference form of Eq. (4-138) using successive over-relaxation (SOR). Once the potential distribution is known, the pressure drop can be calculated from:

$$\frac{dp}{dx} = \left(\frac{-\partial\phi}{\partial y} - VB\right)B \qquad (4\text{-}139)$$

which is the result of substitution of Eq. (4-135) into Eq. (4-137).

The symmetric nature of the problem was utilized in order to save computing time. The problem is symmetric about the y-axis, and if a zero potential is assumed along the x-axis (this can be done without any loss of generality), the problem is anti-symmetric about the x-axis. Thus, the potential distribution need only be calculated in one quadrant.

Figure 4.4-4 shows the quadrant in which the potentials were calculated. At boundaries a, b, and c, the boundary conditions are the same for conducting and non-conducting ducts. At boundary a, the condition which applies is:

$$\phi \to 0 \text{ as } x \to \infty \tag{4-140}$$

This implies there are no longitudinal eddy currents far downstream from the exit from the B field. At boundary b, the potential is assumed to be zero, and at boundary c, the condition is:

$$\frac{\partial \phi}{\partial x} = 0 \tag{4-141}$$

This specifies symmetry about the y-axis. The boundary condition at d depends upon whether the duct walls are conducting or insulating. These boundary conditions will be discussed in their respective sections.

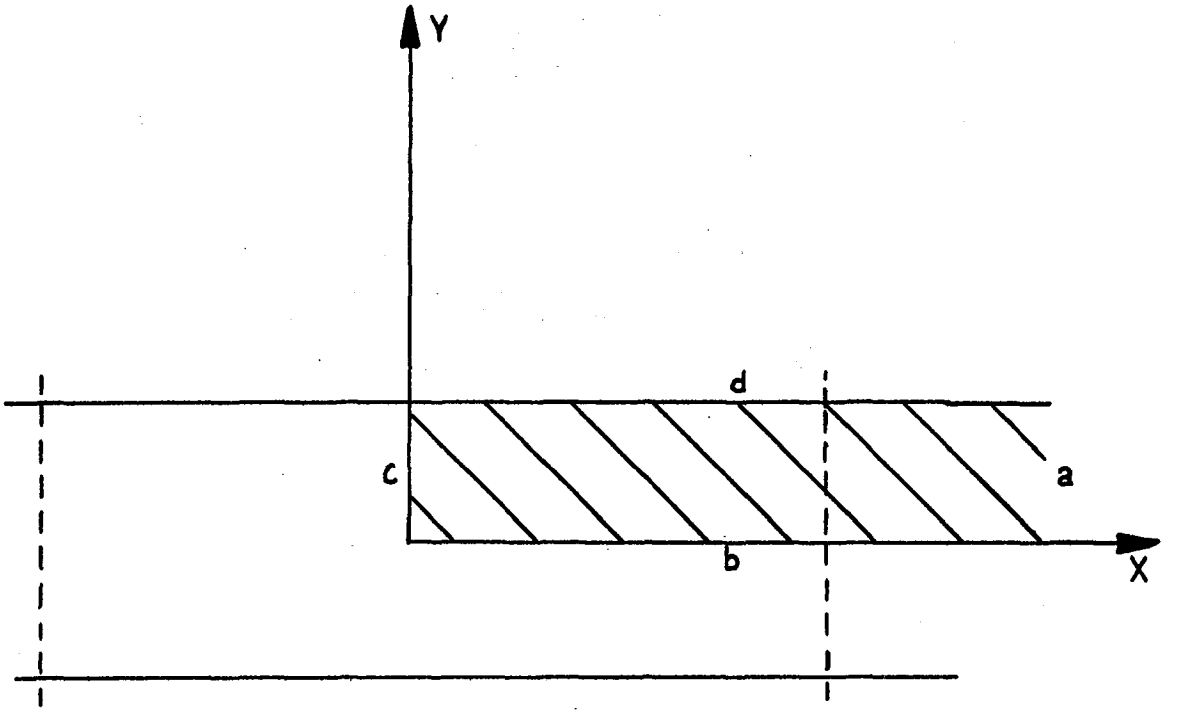


Figure 4.4-4 Quadrant in which potential distribution is calculated

Non-conducting Ducts

The pressure drop was calculated for non-conducting ducts. In this case, the condition applied at boundary d was:

$$\frac{\partial \phi}{\partial y} = 0 \tag{4-142}$$

The velocity profiles used were of the form:

$$V/u_m = \frac{n+1}{n}\left(1 - \left(\frac{y}{a}\right)^n\right) \tag{4-143}$$

The problem was solved for slug flow, and Eq. (4-143) with n=2 (parabolic flow) and n=4. Figure 4.4-5 shows these velocity profiles. When slug flow is assumed, Eq. (4-138) reduces to the 2-D Laplace Equation:

$$\frac{\partial^2 \phi}{\partial x^2} + \frac{\partial^2 \phi}{\partial y^2} = 0 \tag{4-144}$$

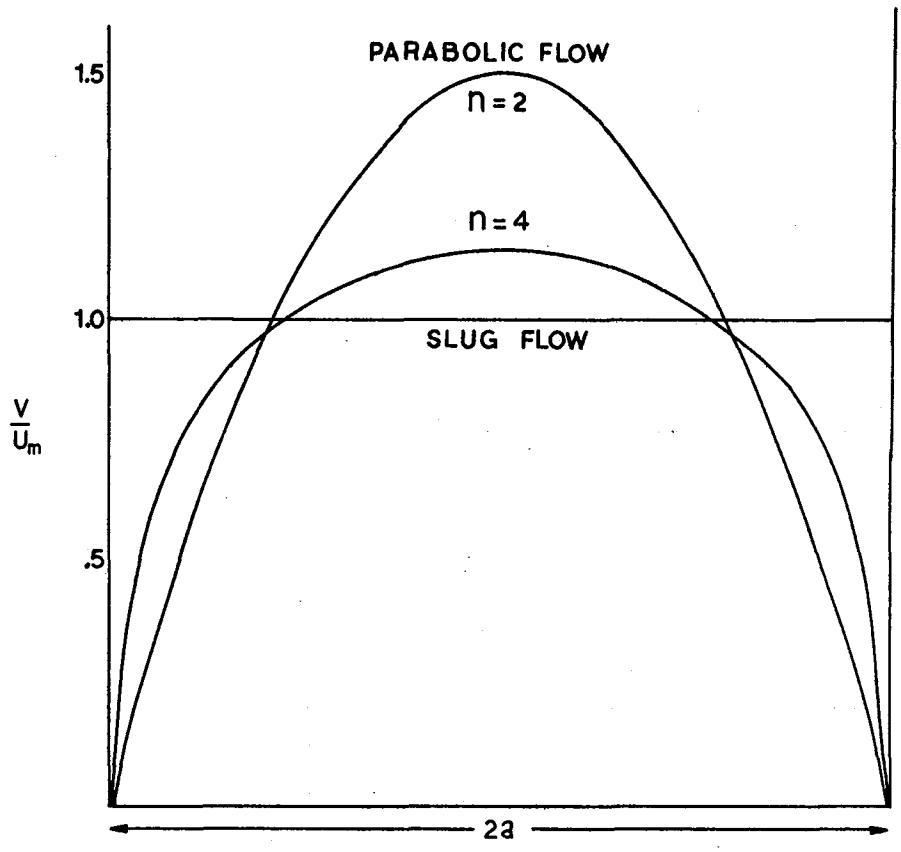


Figure 4.4-5 Velocity profiles assumed in analysis

The electrical eddy current distributions due to an abruptly increasing B field for two velocity profiles are shown in Figs. 4.4-6 and 4.4-7. The pressure drops are shown in Table 4.4-2.

The pressure drop was also found for the case of slug flow in a linearly increasing B field. These results are shown in Table 4.4-3.

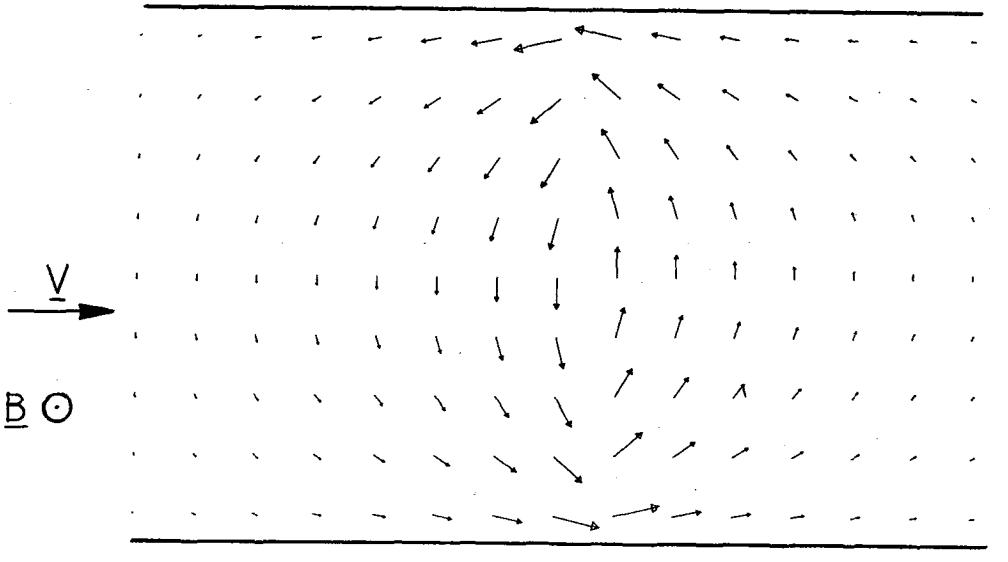


Figure 4.4-6 Eddy current distribution due to abruptly changing B field, non-conducting walls, slug flow

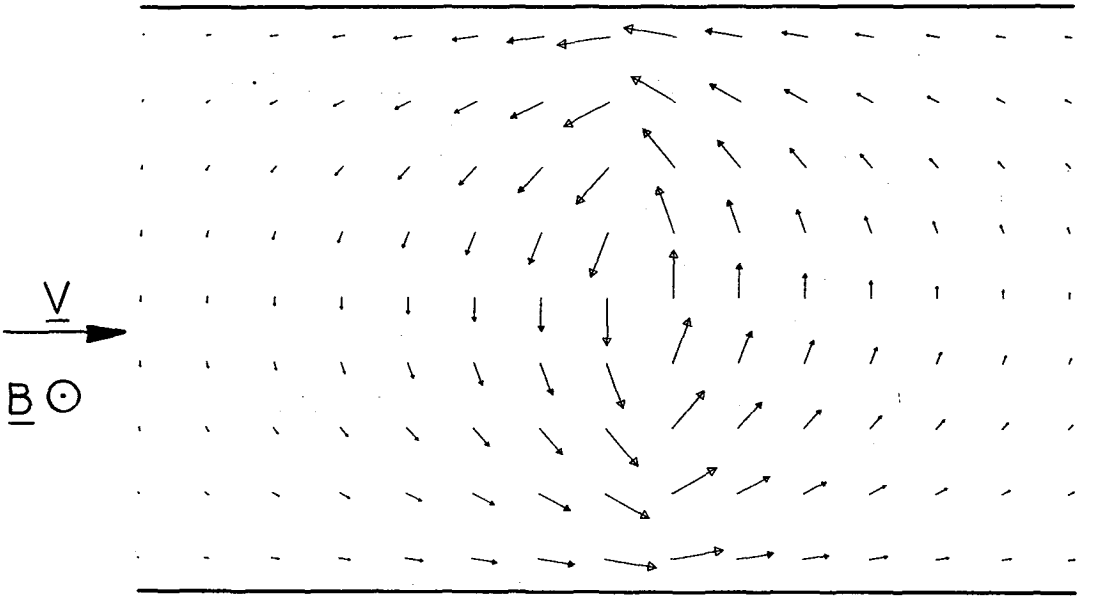


Figure 4.4-7 Eddy current distribution due to abruptly changing B field, non-conducting walls, parabolic flow

Table 4.4-2 Pressure Drop Due to Abruptly Increasing B for Various Velocity Profiles

Velocity Profile	Non-Dimensional Pressure Drop
slug	.27
n = 2 (parabolic)	.298
n = 4	.296

Table 4.4-3 Pressure Drop Due to Slug Flow in Linearly Increasing B

Length over which B Changes	Non-Dimensional Pressure Drop
a	.17
2a	.12
3a	.088
4a	.070
5a	.058
6a	.050
7a	.043
8a	.038

Discussion and Comparison to Analytical and Experimental Results

Equation (4-144), representing the case of slug flow, can be solved analytically.[55] The dimensionless potential is represented by:

$$\phi = \left[\frac{-y}{a} - \frac{8}{\pi^2} \Sigma \frac{(-1)^{(n-1)/2}}{n^2} \cosh \frac{n\pi x}{2a} \exp\left(\frac{-n\pi b}{2a}\right) \sin \frac{n\pi y}{2a}\right] \text{ for } |x| < b \tag{4-145}$$

$$\phi = \frac{8}{\pi^2} \Sigma \frac{(-1)^{(n-1)/2}}{n^2} \sinh \frac{n\pi b}{2a} \exp\left(\frac{-n\pi |x|}{2a}\right) \sin \frac{n\pi y}{2a} \text{ for } |x| > b \tag{4-146}$$

where the summations are over all odd positive integral values of n. The j_y current can then be found from Eq. (4-135):

$$j_y = \frac{4}{\pi} \Sigma^{(-1)} \frac{(n-1)/2}{n} \cosh \frac{n\pi x}{2a} \exp\left(\frac{-n\pi b}{2a}\right) \cos \frac{m\pi y}{2a} \text{ for } |x| < b \quad (4\text{-}147)$$

In order to calculate the pressure gradient, the only current that must be known is the j_y current for $|x| < b$. The analytical solution for the pressure drop is found to be:

$$\Delta p = .25 \quad (4\text{-}148)$$

In dimensional form, this equation is:

$$\Delta p = .25\, \sigma a V B^2 \quad (4\text{-}149)$$

The scaling of Eq. (4-149) comes directly from Eq. (4-130).

A comparison of the numerical results with Eq. (4-148) shows the numerical solution to be correct within 8%. This error could possibly be eliminated by using smaller mesh size, but the additional computation time would not be worth the small gain in accuracy.

In the numerical calculation of the pressure drop, the pressure drop appeared to vary with duct half-width for velocity profiles other than slug. The pressure drop for non-slug flow was always greater than that for slug flow. The pressure drops shown in Table 4.4-2 were all calculated for the same duct half-width. It is not clear why the pressure drop should vary with duct half-width. This should be investigated further.

It is not surprising that the pressure gradient for parabolic flow is greater than that for slug flow. Electrical currents will follow the path of least resistance. In slug flow, the electromotive force, $\underline{V} \times \underline{B}$ is constant along the y-axis. With parabolic flow, the electromotive force, and therefore the induced potential, decreases in the y-direction. The current density will be greater with parabolic flow because the currents feel less resistance in the boundary layers. In flow with n=4, the velocity gradient is not as steep, and thus the maximum electromotive force is less than for parabolic flow. It follows that the integral value of $\underline{j} \times \underline{B}$ will therefore be less for this flow than parabolic flow, although the difference is not as great as that when compared with slug flow.

There has been some work done with which to compare these results.

Holroyd and Walker[56] did a theoretical investigation of the problem of a change in the magnetic field and found the pressure drop to be:

$$\Delta p = C\ \sigma a V B^2\ M^{-1/2} \tag{4-150}$$

where C varies with the magnitude of B_{min}/B_{max}.

This equation was derived in order to predict the pressure drop due to a changing magnetic field, the field always being non-zero. This is different from the entrance effect in that longitudinal currents will return in regions of non-zero magnetic field. It is not likely that this would affect the functional form of the equation, but it would most likely affect the coefficient. In this case, the pressure drop should be somewhat lower than in the entrance case because of the positive force on one side of the current loop (see Fig. 4.4-2). Experimental results of Holroyd[7] support this assumption. There is an obvious difference in the scaling of Eqs. (4-149) and (4-150). An expansion technique neglecting inertial terms was used to arrive at Eq. (4-150) without reducing the problem to two dimensions. Reducing the problem to two dimensions decouples the effects due to the Hartmann currents (those which flow in the plane perpendicular to the bulk flow) and the longitudinal currents. As can be seen from Figs. 4.4-6 and 4.4-7, Hartmann currents do not flow; only longitudinal currents can flow. It has been shown that the longitudinal currents and Hartmann currents are probably not discrete.[56]

In order to get a better idea of the applicability of Eqs. (4-149) and (4-150) comparison with experimental results is necessary. Unfortunately, there appears to be only one experiment directly applicable to this problem.[57] This experiment was performed explicitly to calculate the pressure drop due to entrance (or exit) effects. The pressure drop was found to be

$$\Delta p = .062\ \sigma a V B^2 \tag{4-151}$$

The functional form of Eq. (4-149) was assumed, and the experiment was carried out to evaluate the coefficient.

This experiment, however, was done in such a way that inertial and viscous forces were not present. The annular volume of a plastic wheel was filled with mercury and the wheel was rotated to move the mercury through a

magnetic field. The annulus had a dam which prevented the mercury from circulating inside the wheel. The mercury, therefore, acted much like a solid -- it could not move, so there were no inertial or viscous forces.

Because Eq. (4-149) was derived under the assumption that viscous and inertial terms are negligible, it makes sense that the experimental results fit this functional form. Comparing the coefficients in Eqs. (4-149) and (4-151) one sees that the numerical result for slug flow yielded a pressure drop four times greater than that of the experiment. One reason the numerical result is larger is that the magnetic field was assumed to change abruptly. It has been shown that a gradually decreasing magnetic field will cause less of a pressure drop than a rapidly decreasing one.[55] In the experiment, the B field decreased over a distance of about 1.5 a. The numerically calculated pressure drop for this fringe length is about twice that of the experimentally measured pressure drop. The exact variation of the B field was not given in the experimental results, and because this will affect the pressure drop, it is not surprising there is some discrepancy. In addition, if the Hartmann currents and longitudinal currents are not actually discrete, the calculated pressure drop will be somewhat inaccurate. Particularly, if the longitudinal currents are forced to stay in the plane perpendicular to the B field (as they are in the case of a 2-D analysis), the pressure drop calculated due to the varying magnetic field will be somewhat high.

Experiments have been conducted to investigate the pressure drop due to a changing magnetic field.[7] The functional form of Eq. (4-150) was assumed. The pressure drop due to entering the magnetic field was measured. Table 4.4-4 shows the results of the experiments and compares the coefficients of Eq. (4-150) to the coefficients which would have been obtained had the functional form of Eq. (4-149) been assumed. As expected, the pressure drop due to entering the B field was larger than that due to the changing B field. Comparison of the entrance pressure drop measurement with that of the experiment described previously shows it to be somewhat smaller. This could, in part, be due to different rates of increase of B field, and the fact that fully developed flow was not achieved in Holroyd's experiment because of relatively short lengths of uniform B field regions.[7] In addition, the ducts in Holroyd's experiment were round. The pressure drop for a round duct will be less than that of a rectangular duct with corresponding half-width.[55]

Table 4.4-4 Experimental Results of Pressure Drop Due to Varying B[7]

Coefficient if Functional Form of Coefficient of Eq. (4-150)	Eq. (4-149) Used
.458	.026
.289	.018
.435	.031
.856*	.049

*Actual measurement of entrance pressure drop

Conclusions

The numerical solution predicts a pressure drop of the same order of magnitude as that measured in experiments. The two experiments discussed measured pressure drops of the same order of magnitude. The variation of the B field in the experiments was not given, and this variation is known to affect the pressure drop. It was shown that the velocity profile has some affect on the calculated value of the pressure drop. The velocity profile in an entrance region will actually not be constant, but will be affected by the force produced through the interaction of the longitudinal eddy currents with the B field.[56] The affect of this changing velocity profile should be numerically investigated, possibly by employing an iterative procedure. Once the potential distribution is calculated, the velocity profile could be adjusted using this information. A new potential distribution would then be calculated, and the process repeated until convergence occurs.

More experimental results are necessary before definitive conclusions are drawn. Experiments with various duct half-widths should be done for a range of Hartmann numbers. Although it would seem that the functional form of Eq. (4-150) should be more correct than that of Eq. (4-149) because less simplifications were made in its derivation, there is a lack of experimental evidence to support this claim.

Thin Conducting Ducts

Calculating the pressure drop in thin conducting walls requires a different condition on boundary d. Shercliff formulated a boundary condition to represent this situation.[55] Assuming no contact resistance between the

fluid and the wall,

$$\frac{\partial \phi}{\partial y} + VB = \Phi \frac{\partial^2 \phi}{\partial x^2} \qquad (2\text{-}152)$$

where Φ is the conductance ratio, $\Phi = \frac{\sigma_w t}{\sigma_f a}$.

The pressure drop was calculated for slug flow with various conductance ratios. The electrical eddy current distribution for one case is shown in Figure 4.4-8. The results of the pressure drop calculations for an abruptly increasing B field are shown in Table 4.4-5. The results for a linearly increasing B field are shown in Table 4.4-6.

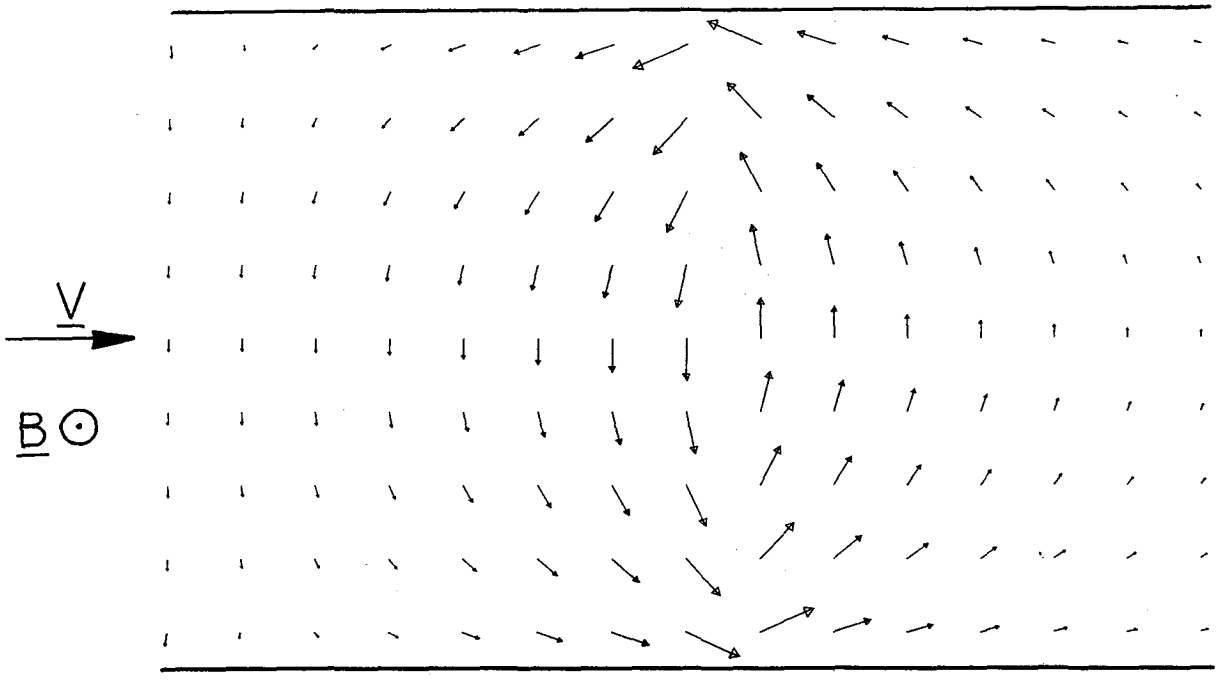


Figure 4.4-8 Eddy current distribution due to abruptly changing B field, conducting walls (Φ=0.07), slug flow

Table 4.4-5 Pressure Drop for Slug Flow in Thin-Walled Duct with Abruptly Changing B Field

Conductance Ratio	Non-Dimensional Pressure Drop
.001	.27
.01	.28
.03	.34
.05	.42
.07	.51

Table 4.4-6 Pressure Drop for Slug Flow in Thin-Walled Duct with Linearly Changing B Field

Distance Over Which B Varies	Non-Dimensional Pressure Drop
a	.31
2a	.26
3a	.23
4a	.21

Discussion and Comparison to Analytical and Experimental Results

Holroyd and Walker examined the problem of the pressure drop in a thin-walled duct due to a non-uniform B field, the B field always being non-zero.[56] Again, an expansion method was employed neglecting inertial effects, without reducing the problem to 2-D, and the pressure drop was found to be

$$\Delta p = C\ aVB^2\ \phi^{1/2} \tag{4-153}$$

where C varies with the ratio of B_{min}/B_{max}. The functional form here is different from that found in this author's numerical analysis due to the different assumptions made. This analysis, however, is not directly applicable to the entrance problem because the currents will circulate in regions of non-zero B field. It would be expected then, that the pressure drop in

this situation be less than in the entrance problem.

Experiments were carried out to validate Eq. (4-156).[53] Two ducts were used, one with $\Phi = .2$ and one with $\Phi = 8.7$. In the weakly conducting duct, the pressure drop was found to be:

$$\Delta p = .053\ \sigma a V B^2\ \Phi^{1/2} \tag{4-154}$$

If this is put in the same functional form as Eq. (4-151) the result is:

$$\Delta p = .024\ \sigma a V B^2 \tag{4-155}$$

This is an order of magnitude less than the pressure drop found in the numerical analysis. Part of this discrepancy is due to the fact that the experiments were done with round ducts. Also, the purpose of this experiment was to measure the pressure drop due to a changing magnetic field, the B field always being non-zero. As explained in the beginning of the section, the pressure drop in this situation should be somewhat less than in the entrance problem. The numerical result was for $\Phi = .01$, while the experimental result was for $\Phi = .2$. Intuition suggests that the pressure drop for a more highly conducting duct would be greater than that of the duct with lower conductivity. It has been shown that this is not necessarily the case.[56] In order for Eq. (4-153) to be valid, the following "thin-wall" condition should be satisfied

$$M^{-1/2} \ll \Phi^{1/2} \ll 1 \tag{4-156}$$

This ensures that the longitudinal currents will flow in the fluid to cross the duct instead of being short-circuited through the duct walls in the plane transverse to the bulk flow direction. Experiments done by Holroyd in the highly conducting duct ($\Phi = 8.7$) show little, if any, pressure drop due to longitudinal currents.[53]

Because of this phenomenon, the 2-D code would not be at all valid for ducts not meeting the "thin-wall" criteria. The 2-D code forces the currents to flow across the duct. At high conductance ratios, the problem bears no resemblance to a 2-D problem, a 3-D analysis would have to be done.

As can be seen in Table 4.4-6, the problem with a conductance ratio of

.001 yielded the same results as for a non-conducting duct. The problem was not solved for conductance ratios greater than .07 because numerical problems developed at higher conductance ratios. Alternative numerical techniques should be explored to try to alleviate this problem.

Conclusions

The numerical solution gives a pressure drop an order of magnitude greater than that measured in related experiments. In actuality, the velocity profile will be influenced by the interaction of the B field with the longitudinal currents, and will not be constant. The effect of this on the pressure drop should be investigated.

Experimental measurements of the entrance pressure drop are needed in order to more accurately assess the validity of the pressure drop calculations given in Table 4.4-6. The experiments should be done with ducts of varying conductivity over as wide a range of M as possible. This would help one to better assess the validity of Eq. (4-153) and the numerically calculated pressure drop.

4.4.2.3 Application to Fusion Reactor

A very conservative estimate of the pressure drop in a non-conducting duct can be calculated using Eq. (4-149). Typical values in a fusion reactor would be $\sigma = 3 \times 10^6\ (\Omega\text{-m})^{-1}$, a = .35 m, V = .12 m/s, and B = 4T. The pressure drop calculated using Eq. (4-149) is .51 MPa. Using Eq. (4-150) and the coefficient from Holroyd's entrance pressure drop measurement, the pressure drop is found to be .075 MPa. It is likely that the pressure drop in a fusion reactor will be somewhere between these values if non-conducting ducts are used.

If conducting ducts are utilized, a conservative estimate of the pressure drop can be found usng the results of Table 4.4-6. For Φ = .01, the calculated pressure drop is .56 MPa. As a comparison, the pressure drop calculated from Eq. (4-153) is .034 MPa. The coefficient used in Eq. (4-153) is from the theory of Holroyd and Walker, corresponding to a 50% change in the magnetic field.[56] This was the largest coefficient -- it was used to offset the fact that the pressure drop calculated from Eq. (4-153) will probably be somewhat less than that in the entrance problem pressure drop.

There is much uncertainty in the calculation of the pressure drop due to entrance to or exit from the magnetic field. It could be a significant contribution relative to the 4-5 MPa pressure drop expected in a fusion reactor blanket. More analysis and experimentation are necessary to better understand and quantify this pressure drop.

4.5 Heat Transfer in Flow Over a Wedge or a Cylinder Under the Condition of Heat Generation[a]

4.5.1 Introduction

Heat transfer in liquid metals with volumetric heat generation presents a unique and interesting heat transfer situation. This section treats the special features of heat transfer in liquid metals that result from the presence of volumetric heating. One of the primary purposes of this work is to determine how heat generation affects the use of hot film probes used to measure velocity profiles in the coolant. However, the analysis is also directly applicable to heat transfer in the entrance region of coolant channels where the boundary layer is developing.

Fluid flow and heat transfer play a crucial role in the performance of liquid metal cooled fusion reactor blankets. Much of the thermomechanical behavior of blanket components depends directly on the temperature profiles, including thermal stresses, high temperature properties (under irradiation), and material interactions. Heat transfer plays a prominent role in optimizing designs; thus, it is important to minimize uncertainties in its prediction.

Volumetric heating arises from neutron and gamma radiation that originates in the plasma or is produced by nuclear reactions in the blanket. The effects of internal heat generation are coupled to the effects of unusual MHD velocity profiles to create a unique heat transfer situation. Volumetric heat generation causes the bulk temperature of the coolant to rise. In addition, it can alter the temperature profile and, hence, the heat transfer coefficient. Volumetric heat generation has normally been found to decrease the heat transfer coefficient[(58)] and, as a result, cause an increase in the wall temperature.

It has been found that most of the flow in liquid metal fusion blankets is in the developing region[(59)] where the velocity profiles are not well known. It is known that highly nonuniform velocity profiles exist in liquid metal flow in the cooling blankets due to the presence of magnetic fields.[(56)]

[a]Partial support for this work was received from the University of Kentucky 1986 Summer Faculty Research Fellowship.

The presence of volumetric heat generation in addition to unpredictable velocity profiles causes an uncertainty in the prediction of coolant and wall temperatures. As a result, it has been proposed to test the velocity profiles in test reactors by using delicate instruments like hot film anemometers before implementing a full scale fusion reactor.[59] A hot film anemometer is used for measuring the velocity of a fluid at a point. This instrument consists of a resistor wire that is heated up by passing electrical current through it. The fluid is then allowed to flow over the wire. The heat loss due to the flow of the fluid is a function of the fluid velocity at that point. If this function is known, the fluid velocity may then be calculated by measuring the energy input into the wire. Therefore, in order to use a hot film anemometer in heat generating fluids, the effect of volumetric heat generation on the heat transfer coefficient should be studied.

This study is aimed at investigating the effect of volumetric heat generation on the heat transfer characteristics of flow over surfaces -- especially wedge type flows -- and flow over a circular cylinder as it pertains to the use of hot film anemometers.

The effect of magnetic field on hot film probes has been studied by Lykoudis and Dunn.[60] It was shown that the presence of a magnetic field reduces the heat transfer coefficient. This reduction was observed to be more pronounced for flows with Reynolds number higher than 10. That study, however, did not discuss the effect of heat generation on the hot film performance.

Past investigations into the effect of heat generation on heat transfer have dealt with a variety of hydrodynamic situations. Ostrach[61] has considered a situation of uniform and constant source or sink distribution with natural and forced laminar convection flows between two plane parallel surfaces. Hallman[62] later extended the analysis to a cylindrical duct. Poppendick[63] has dealt with forced convection in laminar or turbulent flows in plane and cylindrical channels. In all these studies, the flow was assumed to be fully developed thermally and hydrodynamically. These analyses, therefore, are not applicable to developing flows.

Sparrow and Siegal[64] have studied the heat transfer characteristics for laminar flow of a heat generating fluid in a circular tube. The internal heat generation is permitted to vary in an arbitrary manner. They obtained the

results for developing temperature profiles but assumed fully developed velocity profiles. The analysis was done by converting the energy equation into a Sturm-Liouville type equation and expressing the result in the form of a series solution.

Taghavi, et al.[58], have investigated the effect of volumetric heat generation on heat transfer for various types of velocity profiles for flow between parallel plates. The thermal entrance region is studied by transforming the three-dimensional convection equation into a two-dimensional transient conduction equation. Analytical results for Nusselt number have been given for the fully developed case. It is found that, due to volumetric heat generation, the Nusselt number is generally reduced. It has also been concluded that the shape of the temperature profile is very much sensitive to the fluid velocity profile.

Chambre[65] analyzed the case of a generalized source or sink in a laminar flow over a flat plate. The surface temperature of the plate and the heat source are taken as an arbitrarily prescribed function of distance and are expressed in the form of series. Similarity transformation has been used to convert the partial differential equations to a series of ordinary differential equations. These equations have been solved for the particular case of the Prandtl number equal to one. No discussion or result is available on how the heat transfer solution depends on the Prandtl number.

The present work employs a technique similar to that of Chambre[65] and applies it to the case of flow over a wedge with uniform heat generation in the fluid and constant temperature of the surface. A similarity transformation has been used to transform the partial differential equations to ordinary differential equations. These equations were solved numerically for different Prandtl numbers. The temperature distribution in the boundary layer is given for different Prandtl numbers for the special case of flow over a flat plate. An expression for local Nusselt number is given and its variation with the Prandtl number is presented. This analysis has then been extended to the situation of a cylinder in cross flow.

4.5.2 Analysis

An analysis for the laminar thermal boundary layer is developed for a wedge of an arbitrary angle. This analysis does not solve the MHD velocity

profiles. It attempts to estimate the effect of volumetric heat generation on the thermal behavior of a hot film probe without magnetic field effects. Further study is needed to investigate the combined and nonlinear effects of heat generation and magnetic field on the heat transfer problem.

The mathematical model is shown in Figure 4.5-1. In doing this analysis, the Falkner-Skan solution for the momentum equations has been used.[66] For the flow over a wedge, the stream velocity is given by:

$$U(x) = Cx^m \tag{4-157}$$

where $m = \beta/(2-\beta)$. In Eq. (4-157), m is the wedge parameter and β is the wedge angle in radians. The similarity parameter has been defined as:

$$\eta = y\left[\frac{m+1}{2}\frac{U(x)}{2\nu x}\right]^{1/2} \tag{4-158}$$

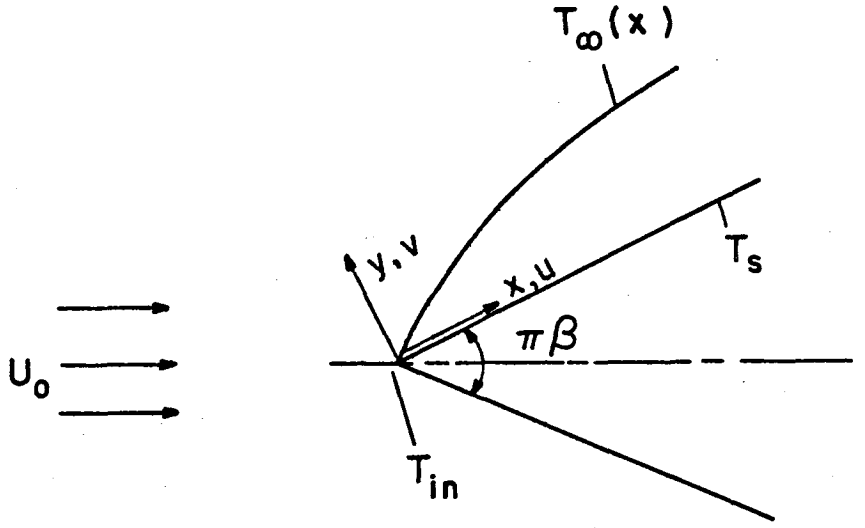


Figure 4.5-1 Flow over a wedge

The Falkner-Skan analysis for the wedge flow yields the following equations for the velocity components:

$$u = U(x)f' \tag{4-159}$$

$$v = -\left[\frac{m+1}{2}\frac{\nu U(x)}{2}\right]^{1/2}\left[f + \frac{(m-1)\eta f'}{m+1}\right] \tag{4-160}$$

where the directions for u and v are shown in Figure 4.5-1. The function f has been used in the stream function definition in the Falkner-Skan solution for the momentum equation. The function f satisfies the following equation:

$$f''' + ff'' + \beta(1-f'^2) = 0 \tag{4-161}$$

The boundary conditions in terms of the function f are:

$$f = 0 \qquad \text{at } \eta = 0 \tag{4-162}$$

$$f' = 0 \qquad \text{at } \eta = 0 \tag{4-163}$$

$$f' = 1 \qquad \text{at } \eta = \infty \tag{4-164}$$

The energy equation is given as:

$$u\,\partial T/\partial x + v\,\partial T/\partial y = \alpha\,\partial^2 T/\partial y^2 + Q_v/\rho c_p \tag{4-165}$$

The bulk temperature is changing in the x direction due to the volumetric heat generation. An energy balance in the direction of the free stream may be written as:

$$\rho c_p U(x)\frac{dT_\infty}{dx} = Q_v \tag{4-166}$$

Substituting Eq. (4-157) into Eq. (4-166) and integrating, we obtain:

$$T(x,\infty) = T_{in} + \frac{Q_v x}{(1-m)\rho c_p U(x)} \tag{4-167}$$

The boundary conditions, in addition to Eq. (4-157), to be satisfied by Eq.

(4-165) are given as:

$$T(0,y) = T_{in} \tag{4-168}$$

$$T(x,0) = T_s \tag{4-169}$$

The solution to Eq. (4-165) is known for the condition of Q_v equal to zero.[66] An excess temperature, therefore, can be defined as:

$$T = T^0 + \phi \tag{4-170}$$

where T^0 is the solution for the homogenous part of the energy equation (Q_v = 0) and ϕ is the solution for the non-homogenous part of the equation. The excess temperature, ϕ, is governed by:

$$u\ \partial\phi/\partial x + v\ \partial\phi/\partial y = \alpha\ \partial^2\phi/\partial y^2 + Q_v/\rho c_p \tag{4-171}$$

The applicable boundary conditions are:

$$\phi(0,y) = 0 \tag{4-172}$$

$$\phi(x,0) = 0 \tag{4-173}$$

$$\phi(x,\infty) = \frac{Q_v x}{(1-m)\rho c_p U(x)} \tag{4-174}$$

Defining a new dimensionless and normalized temperature as:

$$\theta = \phi/\phi_\infty \tag{4-175}$$

and replacing u and v from Falkner-Skan analysis, Eqs. (4-159) and (4-160), the non-homogenous part of the energy equation becomes:

$$\theta''/Pr + f\theta' - 2(1-\beta)f'\theta + 2(1-\beta) = 0 \tag{4-176}$$

The applicable boundary conditions are:

$$\theta = 0 \qquad \text{at } \eta = 0 \tag{4-177}$$

$$\theta = 1 \qquad \text{at } \eta \to \infty \tag{4-178}$$

Equation (4-176) is solved numerically for different values of Pr and β.

A heat transfer coefficient is defined as:

$$-k \left(\frac{\partial T}{\partial y}\right)_{y=0} = h_x (T_s - T_{in}) \tag{4-179}$$

The local Nusselt number may be written as:

$$Nu_x = h_x x/k \tag{4-180}$$

Combining Eqs. (4-179) and (4-180), the equation obtained for the local Nusselt number is given by:

$$Nu_x = - \frac{x}{T_s - T_{in}} \left[\frac{\partial T}{\partial y}\right]_{y=0} \tag{4-181}$$

Using Eqs. (4-170) and (4-175) in Eq. (4-181), the resulting equation obtained for the local Nusselt number is given as:

$$Nu_x = - \frac{x}{T_s - T_{in}} \left[\frac{\partial T^0}{\partial y} + \phi_\infty \frac{\partial \theta}{\partial y}\right]_{y=0} \tag{4-182}$$

Denoting the Nusselt number under the condition of no heat generation as Nu_x^0, the local Nusselt number under the conditions of heat generation is then given by:

$$Nu_x = Nu_x^0 - \Delta Nu_x \tag{4-183}$$

Substituting for ϕ_∞ from Eq. (4-174) and transforming $\partial\theta/\partial y$ into new similarity variables, ΔNu_x may be written as:

$$\Delta Nu_x = \frac{\phi_\infty}{T_s - T_{in}} \left[\frac{m+1}{2}\right]^{1/2} Re_x^{1/2} \theta'(\eta=0) \tag{4-184}$$

For flow over wedge, using Eq. (4-157) for the free stream velocity, Eq. (4-

184) may be converted and rearranged to:

$$\Delta Nu_x = \frac{\lambda_x}{Re_x^{1/2} Pr} \frac{1}{(1-m)} \left[\frac{m+1}{2}\right]^{1/2} \theta'(0) \qquad (4\text{-}185)$$

where the local heat generation parameter $\lambda_x = Q_v x^2 / k(T_s - T_{in})$.

4.5.3 Limiting Cases of Pr → 0 and Pr → ∞

The limiting cases of low and high Prandtl numbers have special merit for consideration since they reveal the asymptotic thermal and hydrodynamic behavior of the problem. Prandtl number is a measure of how thick the momentum boundary layer is with respect to the thermal boundary layer. A very low Prandtl number indicates that the thermal boundary layer is much thicker than the momentum boundary layer, while a very large Prandtl number means that the thermal boundary layer is much thinner than the momentum boundary layer. Figure 4.5-2 shows these two cases and the corresponding velocity and temperature profiles.

For very small Prandtl numbers, the momentum boundary layer is much thinner than the thermal boundary layer. This means that most of the thermal boundary layer is outside of the velocity boundary layer and, as a result,

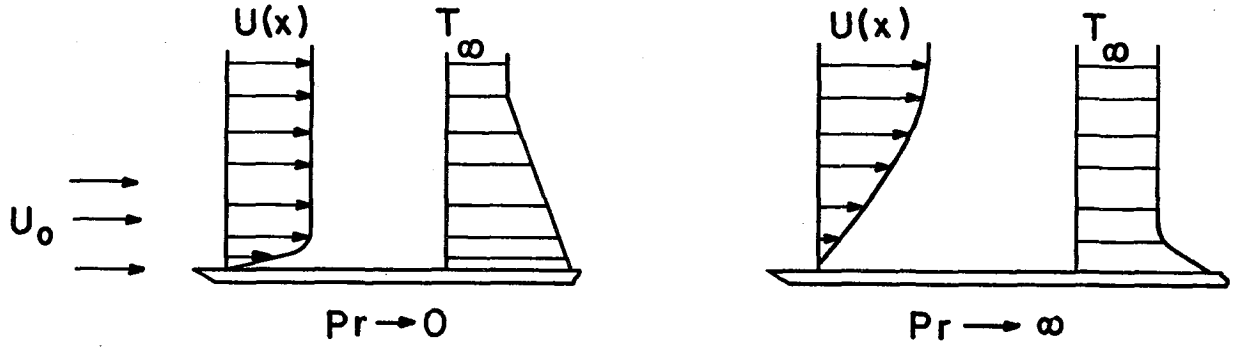


Figure 4.5-2 Comparison between the temperature and velocity fields in boundary layer for very small and very large Prandtl number fluids

potential flow velocity is applicable. Therefore, the following approximation is applicable:

$$u(X)/U(x) = f'(\eta) = 1 \tag{4-186}$$

Equation (4-186) may be integrated while using boundary condition in Eq. (4-162) to obtain:

$$f = \eta \tag{4-187}$$

The functions f and f' in the energy equation (4-176) may be replaced from Eqs. (4-186) and (4-187) to obtain a new energy equation for very small Prandtl numbers.

$$\theta''/Pr + \eta\theta' - 2(1-\beta)\theta + 2(1-\beta) = 0 \tag{4-188}$$

It is possible to scale out the Prandtl number in Eq. (4-188) by an appropriate new similarity variable as:

$$\hat{\eta} = Pr^{1/2}\eta \tag{4-189}$$

The new energy equation is written as:

$$\theta'' + \hat{\eta}\theta' - 2(1-\beta)\theta + 2(1-\beta) = 0 \tag{4-190}$$

The prime in θ' now means differentiation with respect to $\hat{\eta}$. The boundary conditions applied to Eq. (4-190) are similar to those in Eqs. (4-177) and (4-178). When compared with Eq. (4-188), it is seen that Eq. (4-190) does not contain the Prandtl number as a parameter. Equation (4-190) may be solved to obtain the temperature profile and subsequently the Nusselt number from Eq. (4-184).

For very large Prandtl numbers, the momentum boundary layer is much larger than the thermal boundary layer. This means that most of the thermal boundary layer is located deep into the momentum boundary layer and is mainly in a region near the wall. Therefore, in the thermal boundary layer, the velocity may be approximated to be linear.

$$f''(\eta) = f''(0) = \text{constant} \tag{4-191}$$

Equation (4-19) may be integrated twice while using boundary conditions in Eqs. (4-163) and (4-162) to obtain:

$$f'(\eta) = f''(0)\eta \tag{4-192}$$

$$f(\eta) = f''(0)\eta^2/2 \tag{4-193}$$

The functions f and f' in Eq. (4-176) may be replaced from Eqs. (4-193) and (4-192) to obtain:

$$\theta''/Pr + \frac{1}{2}\eta^2 f''(0)\theta' - 2(1-\beta)\eta f''(0)\theta + 2(1-\beta) = 0 \tag{4-194}$$

It is possible to scale out the Prandtl number in Eq. (4-194) by appropriate new similarity variables as:

$$\tilde{\eta} = Pr^{1/3}\eta \tag{4-195}$$

$$\tilde{\theta} = Pr^{-1/3}\theta \tag{4-196}$$

The governing Eq. (4-194) in new variables may be written as:

$$\tilde{\theta}''' + \frac{1}{2}\tilde{\eta}^2 f''(0)\tilde{\theta}' - 2(1-\beta)\tilde{\eta} f''(0)\tilde{\theta} + 2(1-\beta) = 0 \tag{4-197}$$

The boundary conditions applied to Eq. (4-197) are obtained by writing Eqs. (4-177) and (4-178) in terms of the new similarity variables.

$$\tilde{\theta} = 0 \qquad \text{at } \tilde{\eta} = 0 \tag{4-198}$$

$$\tilde{\theta} = 0 \qquad \text{at } \tilde{\eta} \to 0 \tag{4-199}$$

When compared with Eq. (4-194), it is observed that Eq. (4-197) does not contain the Prandtl number as a parameter. Equation (4-197), along with boundary conditions (4-198) and (4-199), may be solved to obtain the tempera-

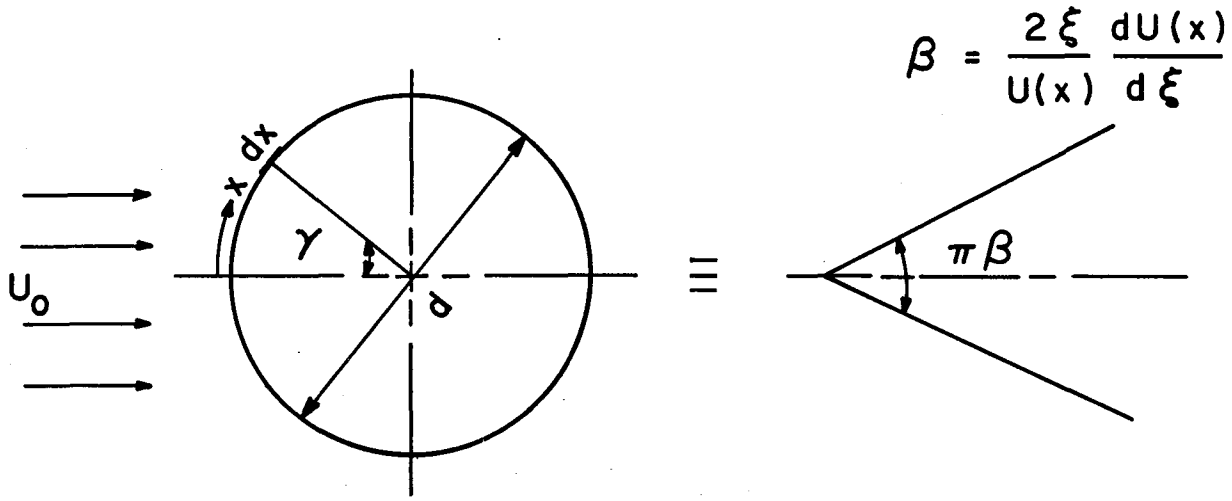
ture profile and subsequently the Nusselt number from Eq. (4-184).

4.5.4 Analysis for a Cylinder in Cross Flow

Up to this point, the analysis was performed for a wedge. The wedge analysis may be extended to a cylinder in cross flow by a technique called equivalent wedge. This technique is explained and employed by Merk.[67] The equivalent wedge method is used here for its simplicity and accuracy.

For each segment of a cylinder, an equivalent wedge is chosen such that the heat transfer characteristics of the flow over the cylinder are equivalent to those of the wedge. Figure 4.5-3 shows this transformation. A new modified coordinate in the direction of the x-coordinate is defined as:

$$\xi = \int_0^x [U(x)/U_o]dx/d \qquad (4\text{-}200)$$



$$[\theta'(\eta=0)]_{\text{cylinder segment } dx} \equiv [\theta'(\eta=0)]_{\text{wedge}}$$

Figure 4.5-3 Equivalent wedge for a segment dx on the cylinder

The wedge parameter for a given segment of the cylinder is given as:[67]

$$\beta = [2\xi/U(x)]\ [dU(x)/d\xi] \tag{4-201}$$

According to Eqs. (4-200) and (4-201), once the velocity variation U(x) is known, the equivalent wedge is calculated. This method, however, requires some knowledge about U(x). Two options are available and used here. First, we can use the potential flow velocity distribution.[66]

$$U(x)/U_o = [2(1-\cos 2\gamma)]^{1/2} \tag{4-202}$$

The second option is to use a well known experimentally obtained and verified velocity profile by Hiemenz.[68]

$$U(x)/U_o = u_1(x/d) - u_3(x/d)^3 - u_5(x/d)^5 \tag{4-203}$$

The experimental values for u's are:

$$u_1 = 3.631 \qquad u_3 = 2.171 \qquad u_5 = 1.514 \tag{4-204}$$

Once the equivalent wedge is obtained, the appropriate governing equations for the momentum and energy are solved to find the temperature profile as well as the temperature gradient at the wall, $\theta'(0)$. This gradient, according to the equivalent wedge analysis, is the same for the particular cylinder segment. Having the temperature gradient, the Nusselt number may then be calculated from Eq. (4-184). This would result in a relation for the local Nusselt number. An average Nusselt number based on the cylinder diameter may then be calculated by integrating the local Nusselt number around the cylinder. The relation for the average Nusselt number is given as:

$$\frac{\Delta\overline{Nu}_d Re_d^{1/2} Pr}{\lambda} = \int_0^{\gamma_s} \left[\frac{m+1}{2}\right]^{1/2} F_1(\gamma) F_2(\gamma)^{1/2} \theta'(0) \frac{d\gamma}{\gamma^{1/2}} \tag{4-205}$$

where γ is the angular position of the segment on the cylinder and F_1 and F_2 are defined as:

$$F_1(\gamma) = \int_0^{\gamma} \frac{U_o}{U(\gamma)}\, d\gamma \tag{4-206}$$

$$F_2(\gamma) = U(\gamma)/U_o \tag{4-207}$$

The parameter γ_s in Eq. (4-205) indicates the angle on the cylinder at which flow becomes separated. Since the flow in the separated area is highly irregular and may not be governed by the equations obtained in this study, the average heat transfer results presented in the present work are limited to the front of the cylinder where the flow is not separated. The parameter λ in Eq. (4-205) includes the volumetric heat generation and is defined as:

$$\lambda = [Q_v d^2]/[k(T_s - T_{in})] \tag{4-208}$$

An important observation may be made from Eq. (4-205). It is seen that in addition to the traditional dimensionless parameters, Reynolds number and Prandtl number, a third dimensionless parameter based on the volumetric heat generation, heat generation parameter λ, is present in the Nusselt number relation. It may be further noticed that, unlike most other cases, the Nusselt number here decreases with increasing Reynolds number.

4.5.5 Experimental Apparatus and Procedure

The theoretical results obtained in Section 4.5.2 were tested by conducting experiments in a liquid metal loop. In addition to the usual difficulties associated with liquid metal loops, e.g. high temperature and solidification, volumetric heat generation had to be introduced into the system. It was decided to use Joule heating. Due to the very low electrical resistance of liquid metals and very high volumetric heating rate necessary to simulate reactor conditions, a power supply with very high current and very low voltage was needed. The specifications of the liquid metal loop are described below.

4.5.5.1 Apparatus

A schematic drawing for the experimental setup is shown in Figure 4.5-4. The liquid metal loop consists of the following components:

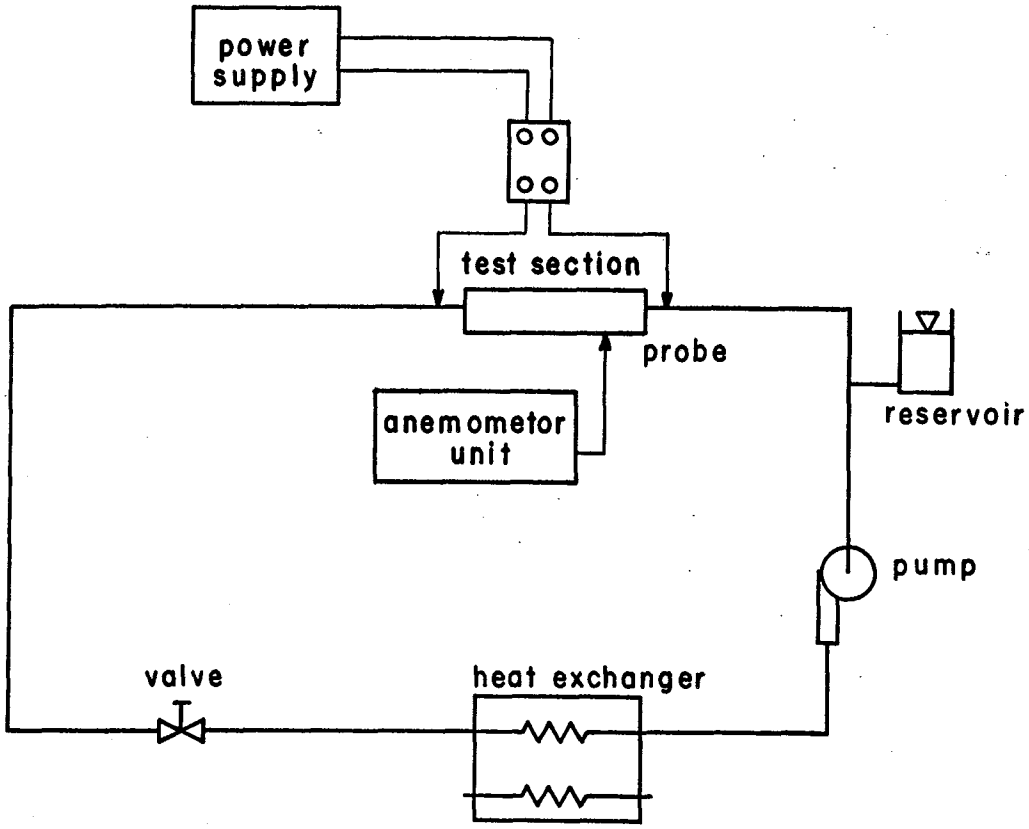


Figure 4.5-4 Schematic drawing of the experimental set-up

- liquid metal, a bismuth-based eutectic;
- hot film probe and anemometer control unit;
- pump;
- stainless steel tubing, 3/4" inside diameter;
- copper coil heat exchanger;
- DC power source;
- test section;
- liquid metal reservoir; and
- hot plate.

The liquid metal used here is a bismuth eutectic that melts at 70°C.

Table 4.5-1 lists the thermophysical properties as well as the composition of the metal. Being a eutectic, there is a sharply defined melting temperature and the alloy is very stable.

Tables 4.5-2 and 4.5-3 list the specification of the hot film probe and the anemometer control system.

A variable flow positive displacement pump with a capability of withstanding temperatures up to 150°C is used to pump the liquid metal through the

Table 4.5-1 Properties of the Liquid Metal

Density, ρ	9403 kg/m^3
Specific heat, c_p	167.47 J/kg K
Thermal conductivity, k	18.81 W/m k
Kinematic viscosity, ν	1.6×10^{-7} m^2/s
Prandtl number, Pr	0.0134
Melting temperature	70°C
Composition of the liquid metal by weight	
Bismuth	50%
Lead	26.7%
Tin	13.3%
Cadmium	10%

Table 4.5-2 Specifications of Hot Film Anemometer Probe

Diameter of the probe, d	152 μm
Probe resistance at 0°C	3.77 ohms
Probe resistance at 100°C	4.5 ohms
Internal probe resistance	0.20 ohms
Probe model	1210-60 NaCl
Probe manufacturer	TSI

Table 4.5-3 Specifications of the Anemometer Unit

Bridge ratio	1:20
Probe operating resistance range	0-61 ohms (selectable in steps of 0.01 ohms)
Probe temperature coefficient	Only positive temperature coefficients
Bridge accuracy	± 0.5% ± 0.01 ohms in absolute measurement of probe resistance, ± 0.25% ± 0.01 ohms in relative measurement
Bridge stability	Temperature coefficient of resistors is less than $\pm 20 \times 10^{-6}$ per deg. Celcius
Anemometer model	55D01
Anemometer manufacturer	DISA

loop. The loop is made of stainless steel tubing so as to avoid any chemical reactions between the liquid metal and the tubing material. Compression fittings made from brass join the tubing.

Due to heat generation in the liquid metal, a heat exchanger is necessary to keep the temperature of the liquid metal under control. A coil made from soft copper tubing is used as a heat exchanger. The copper coil is placed in a box containing water. The temperature of the water is controlled in order to achieve a desired temperature for the liquid metal leaving the copper coil.

In order to generate heat in the test section, direct current is passed through the test section. A Harnischfeger A.O. Smith model A12, 500-T4 DC

power source is used. To carry the current into the test section, copper electrodes made from 3/4" diameter rods are used. The ends of the electrodes are cut in the shape of a segment of a cylinder such that the liquid metal flow is not disturbed.

The test section is also made of stainless steel tubing. The inside diameter is 3/4", while the length of the test section is 15". The test section contains a hole of the same size as the anemometer shield. This serves as an entry port for the hot film anemometer probe.

The reservoir is made of stainless steel and is located at an elevation higher than the test section in order to facilitate the start-up of the pump. A two-piece leakproof divider is used inside the reservoir to separate the inlet and outlet flow of the liquid metal. The purpose of the lower part is to separate any dross formed in the flow before the liquid metal re-enters the loop. The height of the lower divider is chosen such that the top edge of the divider lies a few inches below the surface level of the liquid metal.

The upper divider serves the purpose of measuring the flow rate of the liquid metal. The height of the upper divider is chosen such that when placed over the lower part, the divider will completely separate the two halves of the liquid metal reservoir. Each half contains either the inlet or outlet flow of the liquid metal. As soon as the upper divider is installed, the height of the liquid metal in the section containing the outlet decreases while the height of the other section starts to increase. The rate of the recession of the liquid metal surface is directly proportional to the total flow rate of the liquid metal. The reservoir is placed on a hot plate so as to keep the metal molten during the experiment.

4.5.5.2 Procedure

The most involved part of the procedure is the start-up of the liquid metal loop. Since the liquid metal has a melting point of 70°C, it is in a solid form at room temperature. To avoid the difficult task of freezing and remelting, a dual coolant system is employed. At the beginning, before the liquid metal is introduced in the loop, the loop is filled up with water at room temperature. Then, the pump is turned on. While the water is in circulation, the hot plate is turned on, causing the water to warm up. As the water is circulated through the loop, it heats up all the components in the

loop. When the water temperature reaches a prescribed level, say 10°K above the melting temperature of the liquid metal, molten liquid metal is introduced in the loop by pouring it into the reservoir. Eventually, all the water is removed from the loop. Meanwhile, the hot plate is still on and, therefore, heats the liquid metal. The circulation temperature of the liquid metal is chosen to be 90°C. Once this temperature is attained, the temperature of the water in the copper coil heat exchanger is adjusted such that the temperature of the circulating liquid metal is maintained constant. This concludes the start-up phase of the liquid metal loop.

Once the start-up phase is concluded, the anemometer probe is placed in the centerline of the test tube and the output of the anemometer is registered. Then the DC power source is turned on. While changing the level of direct current through the test tube, the output of the anemometer is registered.

Table 4.5-4 lists the test section parameters and raw data obtained from the few experiments performed.

Table 4.5-4 Experimental Observations

Diameter of the test section	3/4"
Length of the test section	15"
Temperature of liquid metal in reservoir	93 °C
Flow rate of metal	3.87×10^{-5} m^3/s
Mean flow velocity	0.1358 m/s
Reynolds number of flow, Re_d	129
Reynolds number based on test section diameter	16167

Test No.	Current Through Test Section (amps)	Voltage Drop (volts)	Heat Generation (W/m^3)	Operating Resistance (ohms)	Reading of Probe (volts)
1	0	0	0	4.52	20.70
2	250	0.38	8.22×10^5	4.52	20.80
3	500	0.75	32.89×10^5	4.52	20.44

4.5.6 Results and Discussion

The ordinary differential equations governing the velocity and the temperature of the flow over a wedge, as given by Eqs. (4-161) and (4-176), are solved numerically by a shooting technique. A detailed explanation of the numerical procedure is given in Ref. [69]. The purpose of this work is not to report results for flow with no heat generation since these are readily available in the literature. Therefore, only parameters corresponding to the case with volumetric heat generation are presented. These include excess normalized temperature, θ, change in Nusselt number due to volumetric heat generation, ΔNu, etc.

Figure 4.5-5 shows the boundary layer temperature profile for flow over a flat plate. The characteristic temperature profile for flow over a wedge is expected to be similar to that for the flat plate. An unexpected behavior is

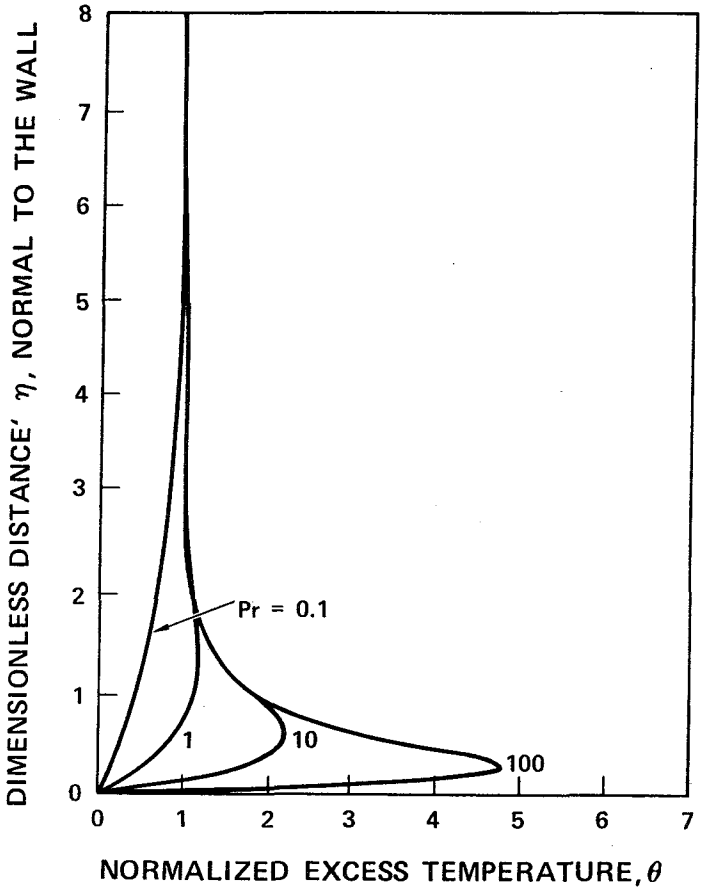


Figure 4.5-5 Boundary layer temperature profile for flow over a flat plate

observed in this figure. There is an overshoot in the temperature indicating that somewhere in the flow the temperature is greater than the wall and free stream temperatures. This overshoot might further limit the design of first wall channels in fusion reactors since the coolant often has maximum operating temperatures.

Figure 4.5-6 shows the amount of temperature overshoot and the position for this overshoot as a function of the Prandtl number. It is seen that the overshoot decreases as the Prandtl number decreases. For example, for the Prandtl number of unity, the overshoot is about 20%, $\theta_{max} = 1.2$. The location of the maximum temperature is closer to the wall as the Prandtl number increases.

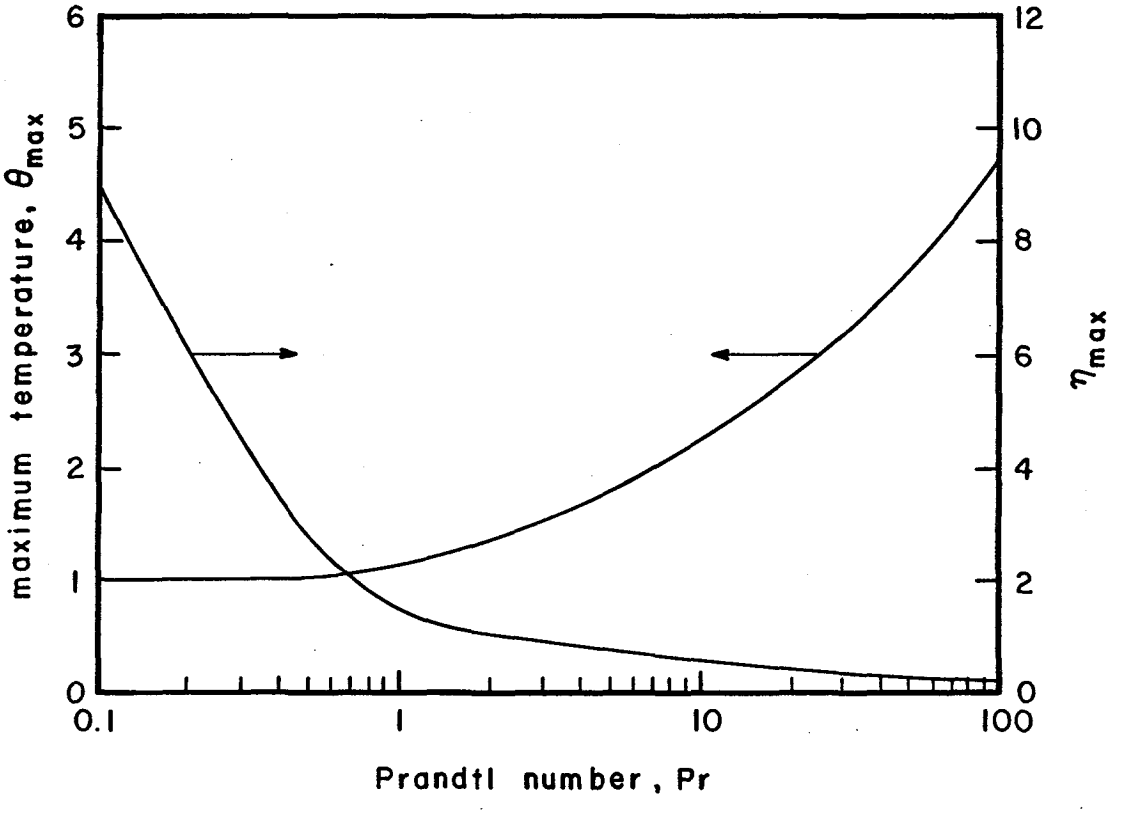


Figure 4.5-6 Variation and location of maximum temperature as a function of the Prandtl number

Next, the results for flow over a wedge are presented. Figure 4.5-7 shows the dependence of the temperature gradient at the wall as a function of the Prandtl number for various wedge angles. Once the gradient is known, the Nusselt number may be calculated from Eq. (4-185). The results are given for a flat plate, a right angle wedge, and for stagnation flow.

As mentioned in the analysis, limiting cases of very low and very high Prandtl number merit separate consideration. Figure 4.5-8 shows the temperature profile across the boundary layer for the limiting case of Pr = 0 for flow over a flat plate. The gradient at the wall is calculated to be $\hat{\theta}'(\hat{\eta}=0) = 1.596$, which upon substitution in Eq. (4-185) yields the following relation for the Nusselt number:

$$\Delta Nu_x = 1.128\, \lambda_x Re_x^{-1/2} Pr^{-1/2} \qquad Pr \to 0 \qquad (4\text{-}209)$$

Equation (4-209) is exact for Pr = 0 but is a good approximation for low Prandtl numbers. For example, for Pr = 0.01 (liquid metal in this study), Eq. (4-209) under-predicts the Nusselt number by 1.7%.

Figure 4.5-9 shows the temperature profile across the boundary layer for the limiting case of $Pr \to \infty$ for flow over a flat plate. The gradient at the wall is calculated to be $\tilde{\theta}'(\tilde{\eta}=0) = 1.905$, which upon substitution in Eq. (4-185) yields the following relation for the Nusselt number:

$$\Delta Nu_x = 1.347\, \lambda_x Re_x^{-1/2} Pr^{-1/3} \qquad Pr \to \infty \qquad (4\text{-}210)$$

Equation (4-210) is exact for $Pr \to \infty$ but is a good approximation for high Prandtl numbers. For example, for Pr = 10, Eq. (4-210) over-predicts the Nusselt number by 0.97%. The temperature overshoot and the location of the overshoot are calculated from Figure 4.5-9 to be:

$$\theta_{max} = 1.019\, Pr^{1/3} \qquad Pr \to \infty \qquad (4\text{-}211)$$

$$\eta_{max} = 1.3\, Pr^{-1/3} \qquad Pr \to \infty \qquad (4\text{-}212)$$

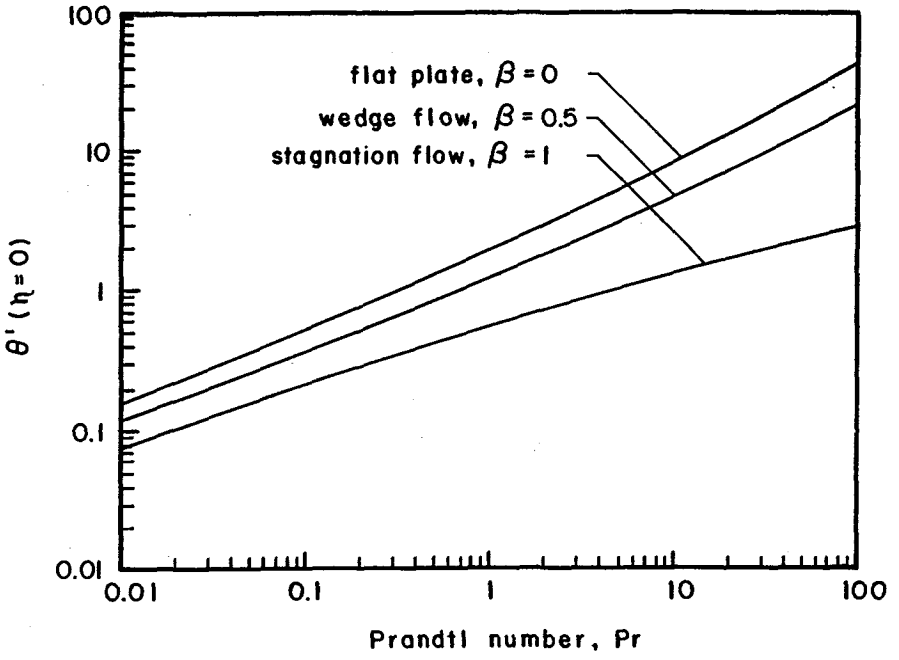


Figure 4.5-7 Temperature gradient at the wall for flow over a wedge as a function of the Prandtl number

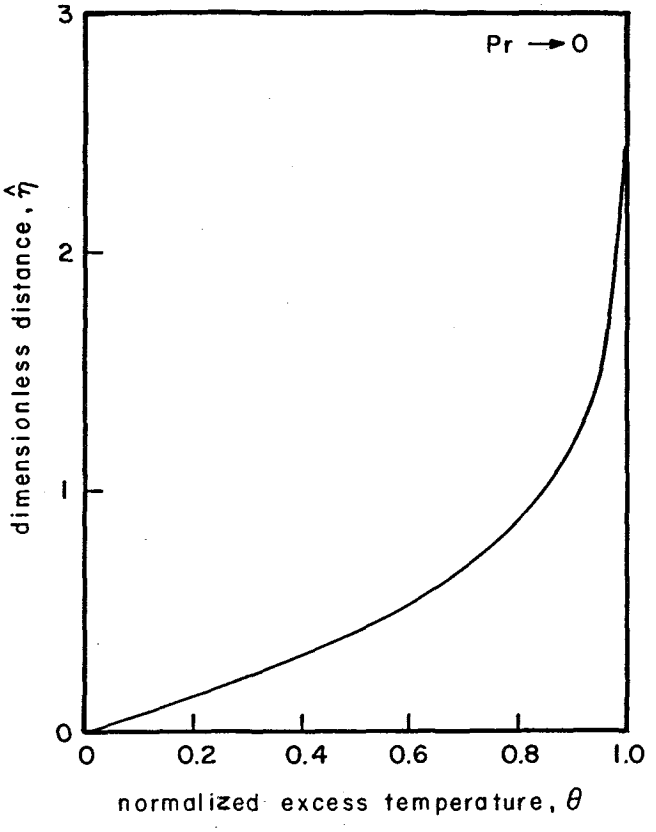


Figure 4.5-8 Boundary layer temperature profile in flow over a flat plate for the Prandtl number Pr=0.

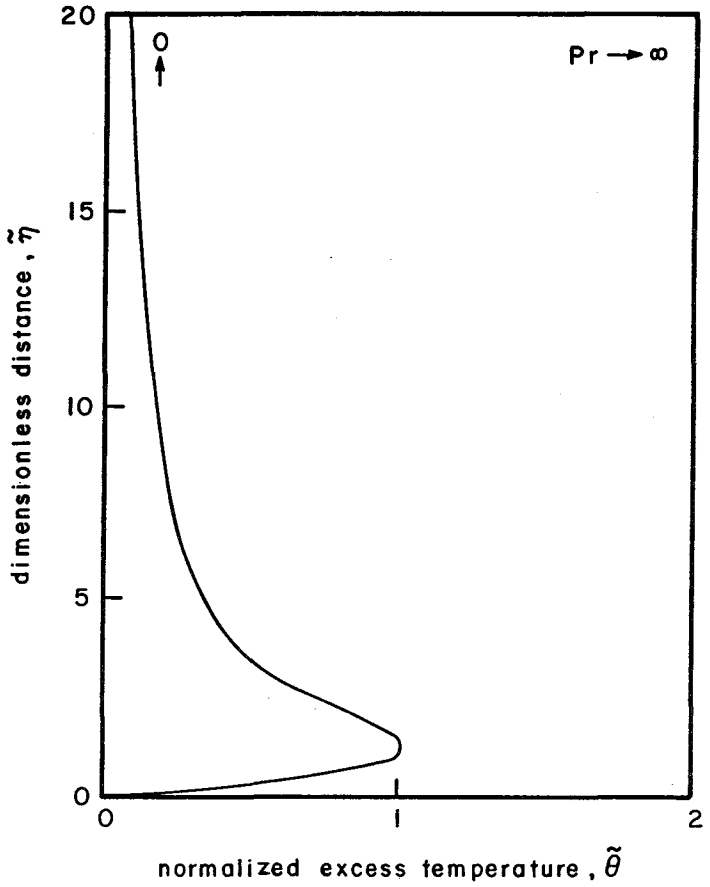


Figure 4.5-9 Boundary layer temperature profile for flow over a flat plate for the case of $Pr \to \infty$

The results obtained for wedge flow and presented so far may be used to predict heat transfer characteristics of a cylinder in a cross flow. A technique called equivalent wedge is employed and explained earlier. Figure 4.5-10 shows the local Nusselt number as a function of the angular position on the cylinder surface. Results are given only for Pr = 0.01 which applies to liquid metals. Results for both potential velocity field, Eq. (4-202), and velocity distribution obtained by Hiemenz,[68] Eq. (4-204), are given. The comparison between these two cases is rather satisfactory. It is seen that the correction to the Nusselt number at the stagnation point is zero. This may also be seen from equation (4-205). However, as the location is moved away from the stagnation point, the absolute value of the change in Nusselt number increases up to a certain angle and then decreases. No results are given for angles past 70° since the flow is separated in this region.

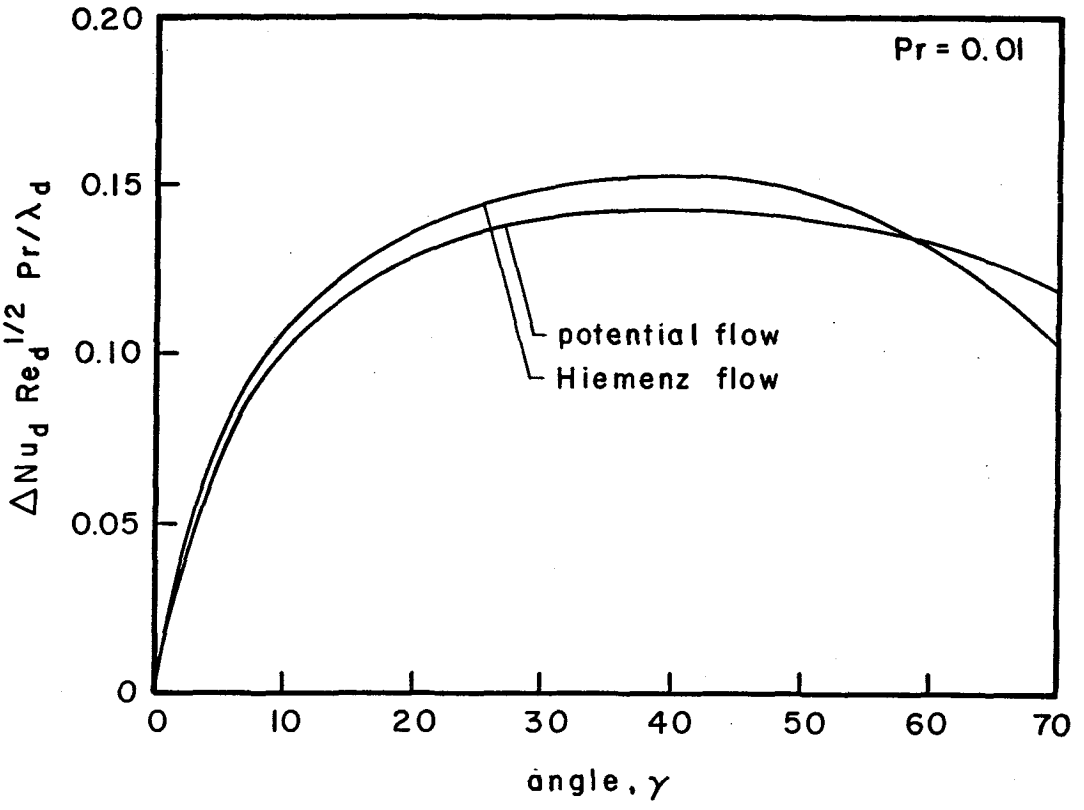


Figure 4.5-10 Change in local Nusselt number around the circular cylinder up to the point of separation for Pr = 0.01

It is desired to obtain the average change in Nusselt number around the cylinder. However, averaging is not possible in the present work since no results are available for the region where the flow is separated. Nevertheless, one might only average over the region that the flow is attached and present the result. This is shown in Figure 4.5-11. This figure shows the average change in the Nusselt number as a function of the Prandtl number.

Figures 4.5-10 and 4.5-11 show the absolute value of the change in the Nusselt number due to volumetric heat generation. To obtain the actual Nusselt number, first the Nusselt number for the no heat generation situation should be obtained from the existing literature. Then the change is obtained from the present figures. Finally, Eq. (4-183) is used to calculate the actual Nusselt number.

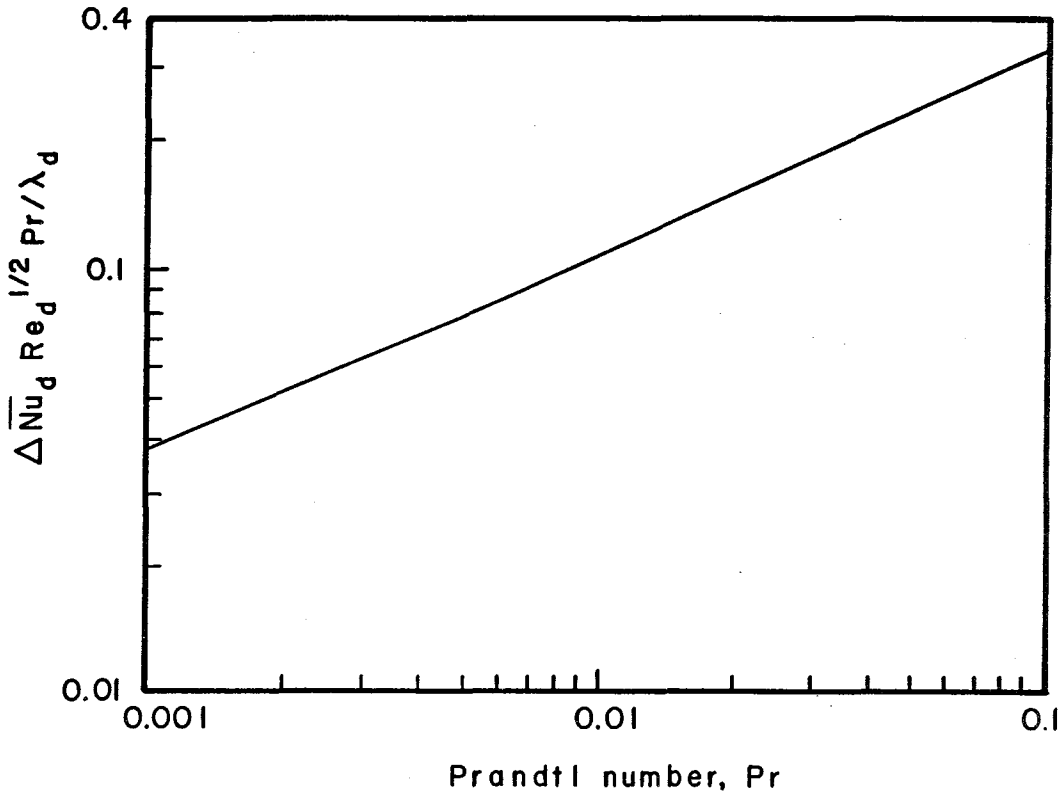


Figure 4.5-11 Change in average Nusselt number due to volumetric heat generation for flow over a cylinder

It would be useful to show the relative value of the change in the Nusselt number for a particular Prandtl number. Figure 4.5-12 shows this for Pr = 0.7. The results for the case with no heat generation are obtained from Ref. [67].

A figure similar to Figure 4.5-12, but for Pr = 0.01, would have been most useful for our liquid metal situation. However, no results for low Prandtl number and no heat generation are available in the literature, although the analysis is there.

As an approximate way of estimating the effect of heat generation on the heat transfer coefficient for flow over a hot film anemometer, one may calculate $\Delta Nu_x/Nu_x^0$ for a flat plate when $x = \pi d/4$. This value of x corresponds to the top location of the cylinder ($\gamma = 90^0$) if the cylinder is cut open and

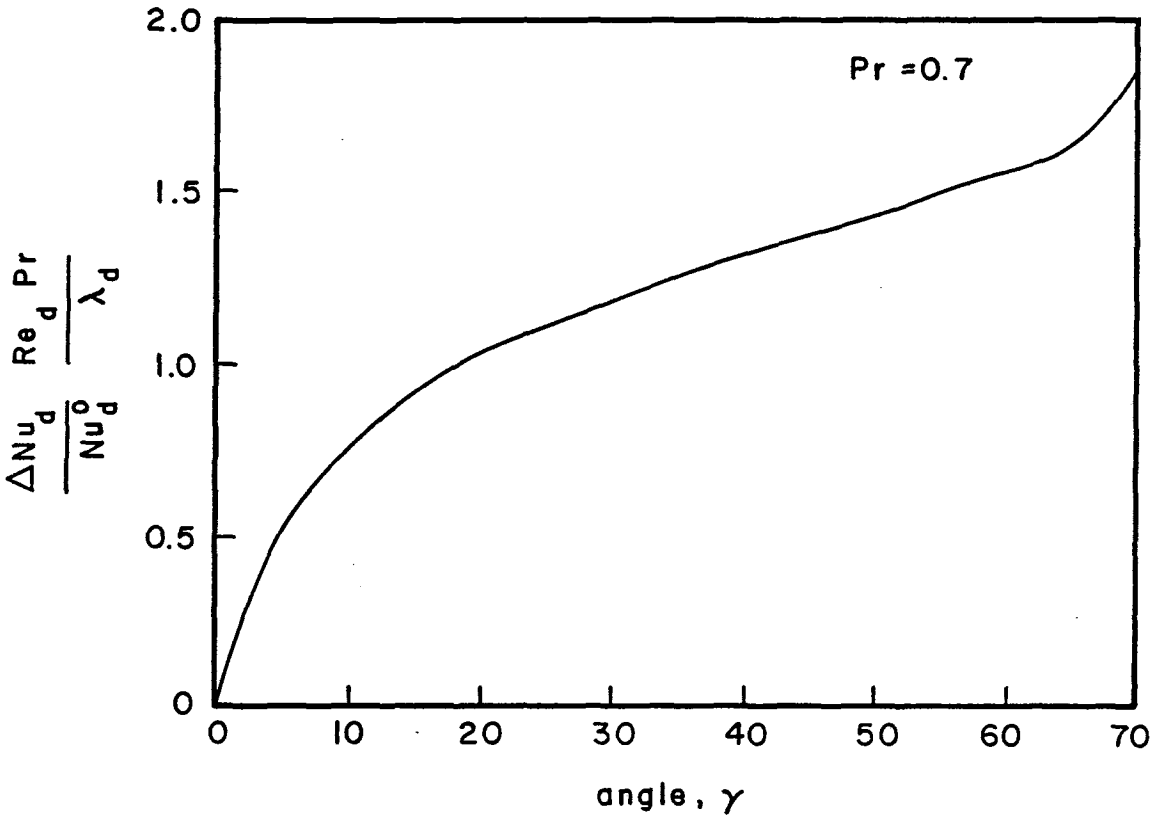


Figure 4.5-12 Ratio of local ΔNu_d to local $Nu_d^{0\,(67)}$ at different angles on the cylinder for Pr=0.7

transformed to a flat plate. The relation for Nusselt number for the case of no heat generation and Pr = 0 is obtained from Ref. [66] as:

$$Nu_x^0 = 0.564\ Re^{1/2} Pr^{1/2} \qquad Pr \to 0 \qquad (4\text{-}213)$$

Using Eq. (4-209) for the change in Nusselt number, $\Delta Nu_x/Nu_x^0$ may be written as:

$$\frac{\Delta Nu_x}{Nu_x^0} = \frac{2\lambda_x}{Re_x Pr} \qquad Pr \to 0 \qquad (4\text{-}214)$$

Equation (4-214) indicates that the change is proportional to the heat generation parameter, and inversely proportional to the Reynolds and Prandtl numbers. Therefore, the change is the largest for higher heat generation,

lower velocity, and low Prandtl number fluids. Table 4.5-5 shows the result of such comparison for various Reynolds numbers and the heat generation parameter, λ. As can be seen from this table, the change is negligible for our case of hot film anemometer in liquid metal flow.

The low change in Nusselt number is mostly due to small film diameter. This agrees with the experimental observation listed in Table 4.5-4. The first three cases in Table 4.5-5 are for the present experimental conditions except that the diameter of the cylinder is varying. It may be seen that for a cylinder of 5 cm diameter, the change in Nusselt number is about 13%, which is quite large. The second three cases are for actual fusion environment conditions, while again the diameter of the cylinder is changing. It is evident that the effect on a hot film is still negligible but that the effect is quite large for larger cylinders.

Table 4.5-5 Change in Nusselt Number Due to Heat Generation for a Pr = 0 Flow Over a Cylinder[a]

d (m)	Q_v (W/m^3)	V (m/s)	$\Delta Nu_x/Nu_x^0$ (%)
152×10^{-6}	33×10^5	0.14	0.04
10×10^{-3}	33×10^5	0.14	0.3
5×10^{-2}	33×10^5	0.14	13
152×10^{-6}	50×10^6	1	0.08
10×10^{-3}	50×10^6	1	0.5
5×10^{-2}	50×10^6	1	26

[a]The cylinder is approximated by a flat plate with the length of $x = \pi d/4$.

4.5.7 Summary and Conclusions

Heat transfer in flow over a wedge under the condition of volumetric heat generation is analyzed. The analytical results are given in terms of the change in Nusselt number due to the heat sources. It is observed that in addition to the customary dimensionless parameters, i.e., Reynolds number and Prandtl number, a third parameter, referred to here as the heat generation

parameter, is present in the Nusselt number relations. The heat generation parameter is defined as:

$$\lambda_x = Q_v x^2 / k\Delta T \tag{4-215}$$

The dependence of the Nusselt number on the Reynolds and Prandtl numbers is not conventional. This is seen by the following two relations for flow over a flat plate for the limiting cases of very low and very high Prandtl numbers.

$$\Delta Nu_x = 1.128\ \lambda_x Re_x^{-1/2}\ Pr^{-1/2} \qquad Pr \to 0 \tag{4-209}$$

$$\Delta Nu_x = 1.347\ \lambda_x Re_x^{-1/2}\ Pr^{-1/2} \qquad Pr \to \infty \tag{4-210}$$

Equation (4-209) should be a good approximation for $Pr < 0.1$ and Eq. (4-210) for $Pr > 1$. The negative signs in these equations indicate that the Nusselt number is decreased as a result of heat generation.

The relative change in Nusselt number is given below for a flat plate for the case of $Pr \to 1$.

$$\frac{\Delta Nu_x}{Nu_x^0} = \frac{2\lambda_x}{Re_x Pr} \tag{4-214}$$

According to this relation, the relative change in the Nusselt number increases with heat generation and distance from the leading edge and decreases with approach velocity and Prandtl number.

The analysis for wedge flow is applied to a cylinder in cross flow using an equivalent wedge technique. An average Nusselt number for the unseparated flow region of the cylinder was obtained for $Pr \to 0$ as:

$$\overline{\Delta Nu}_d = 1.23\ \lambda Re_d^{-1/2}\ Pr^{-1/2} \tag{4-216}$$

In one application of this work, results were obtained for a hot film anemometer placed in a liquid metal cross flow. No appreciable change in the Nusselt number is observed. The negligible change is attributed to the small film diameter. To check this experimentally, a liquid metal loop was built.

The results of the few experiments performed confirm the prediction that the change in Nusselt number is small.

Another application of this work relates to heat transfer in the entrance region of coolant channels where the velocity boundary layer is developing. In a case where the boundary layer is developing on a flat plate or a wedge, the analysis presented here may be used to estimate the heat transfer coefficient as well as the temperature profile in the fluid.

4.6 Liquid Metal/Structural Material Interactions Research

4.6.1 Introduction

The breeding of tritium for fuel self-sufficiency in fusion reactors requires lithium in some form to be integrated into the blanket design. Liquid metal designs with a liquid lithium breeder and a ferritic steel alloy (HT9 or 12Cr-1Mo) have been identified as an attractive design concept.[6] Mass transport and material interaction are major uncertainties in these designs.[59] Currently available data and models for the mass transport processes involved are insufficient to accurately set system parameter limits (maximum interface temperature, flow velocity, impurity concentrations, etc.) for most liquid breeder/structural alloy combinations. A better understanding of the physical processes of corrosion and mass transport must exist before technically feasible designs may progress. Understanding can be greatly increased through the cooperation between experimental and mechanistic modeling investigations. The first part of this section describes a generic mechanistic model of mass removal (corrosion), mass transport and deposition for a liquid metal system. The last part of this section describes an experimental program which is being performed in conjunction with an analytical effort to specifically model corrosion and deposition in lithium and HT9 systems. The experiments will provide data for input to and comparison with the model described along with providing much needed data for design. Cooperation between analysis and experiments will bring about a better understanding of the phenomena of mass transport and will ultimately lead to better, more feasible designs. The experiments and analysis are to be performed within the next year.

The mass transport model will include: one-dimensional solid state diffusion of structural material constituents, convection and bulk transport of corrosion products and reactants, chemical reactions in solution with lithium and at the solid/liquid interface, particle growth and dissolution, and particle and molecular deposition.

The experimental program consists of two thermal convection loops with removable tubular coupons which monitor the corrosion process. The loops will simultaneously collect data from 350 °C to 650 °C in chemically similar lithium for up to 3000 hours of integrated exposure. The experimental loops have

been designed such that some of the uncertainties associated with modeling mass transfer experiments in the past have been eliminated.

4.6.2 Analytical Approach to Mass Transport

Figure 4.6-1 shows a block diagram representing the chemical and transport processes for a general liquid metal system with both mass removal and deposition. Material constituents from the solid diffuse through a solid matrix to an interface where they undergo surface reactions. The species may be either in elemental or a corrosion product compound form and/or be released into the adjacent liquid or form an adherent corrosion product surface layer. Once in the liquid the species may react, diffuse or be transported in the

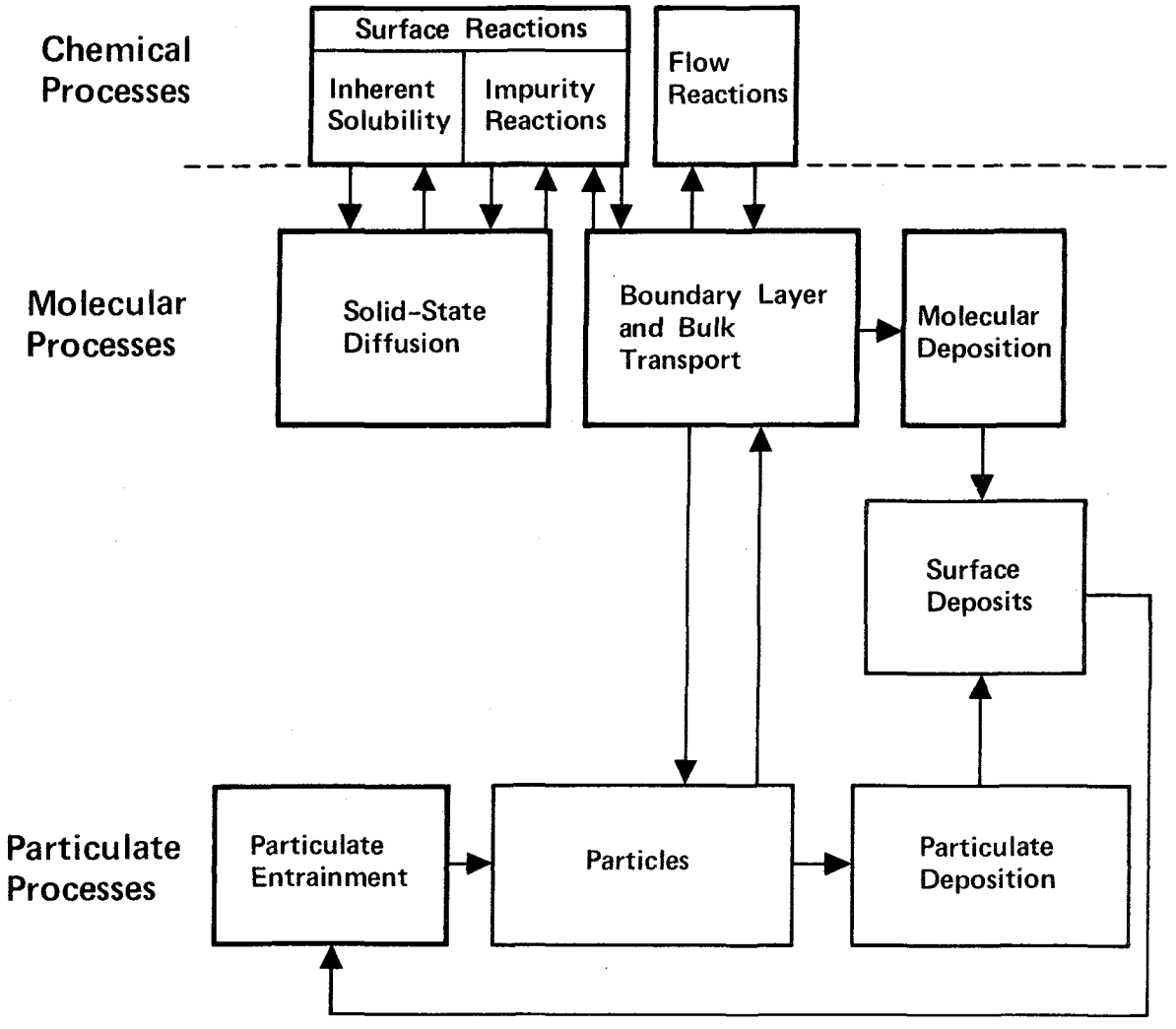


Figure 4.6-1 Block diagram of mass transport processes

liquid. The dissolved molecules or atoms may either remain in solution or agglomerate into particles. Deposition may be either by molecular diffusion or particle deposition.

Previous models have focused on the molecular diffusion portions of the processes outlined in Fig. 4.6-1 for various liquid metal/alloy combinations. Chemical and particle processes have been treated in separate analyses, but a comprehensive model has not been exercised to model corrosion and deposition in liquid metal experiments. No modeling effort specifically for a lithium/HT9 system has ever been attempted. Table 4.6-1 gives a summary of the modeling efforts and their level of complexity.

There are three distinct physical regions which must be modeled: the solid phase, the liquid phase, and the interface between the solid and liquid phases. We begin our modeling in the liquid phase.

4.6.3 Liquid Phase Transport Modeling

We begin by considering a control volume (cv) and control surface (cs) for a fluid element, as shown in Figure 4.6-2. The cv contains a mass of material species i, either in liquid solution with mass fraction y_i, or in solid particle form. The particles are assumed spherical and have a distribution $n_{i,B}(R,t)$ between radii, R^o and R^*. The particles are assumed small enough such that they are carried by the flow, and their number density is such that their presence does not affect the mean fluid density. The particles will grow or dissolve via the same surface reactions as the cs to help relieve super- or sub-saturation conditions in the loop as the fluid element traverses the loop. It is assumed that the number of particles is stationary (no nucleation or destruction) in time and that only their distribution changes with respect to size and position in the loop. Chemical reactions between species in the cv are allowed which either "produce" or "destroy" species i. We may write the following mass balance for the conservation of species i in the cv,

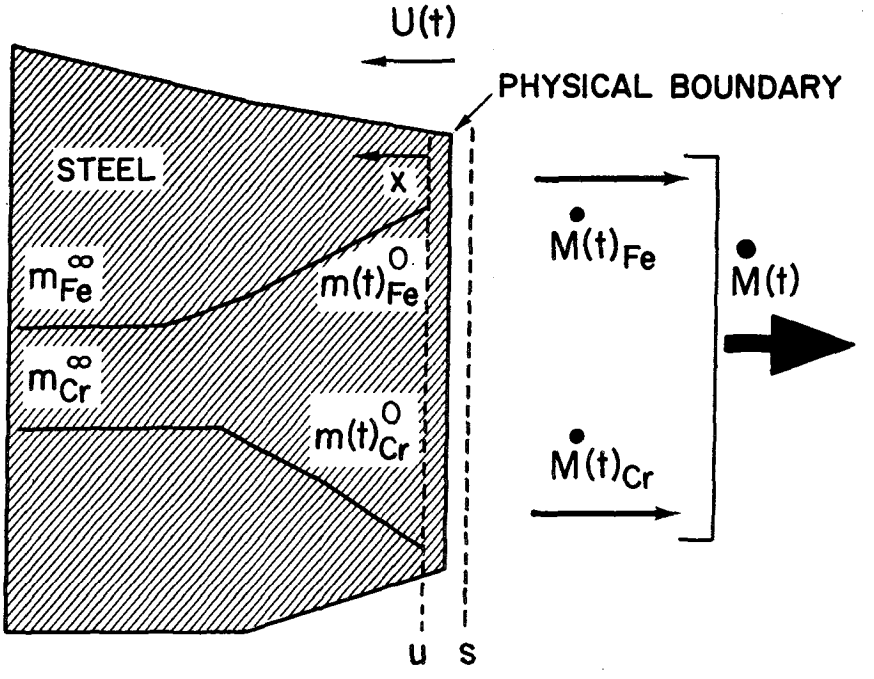
Table 4.6-1 Summary of Modeling in Liquid Metal Mass Transport Investigators

Investigator	Liquid Metal Alloy	Transient (T) or Steady-State (SS)	Single/Mult. Species	Geometry[a]	Solid Phase	Liquid Phase	Reactions[b]	Particle	Experiments[c]
Malang[70]	LiPb/HT9	SS	Single	C	No	Yes	No	Yes/No	Yes/No
Bjorndahl and Gordon[71]	LiPb/HT9	SS	Single	C,R	No	Yes	Y(N)	No	No
Klein and Vogelsang[72]	Various	T	Mult.	R	No	Yes	Y(N)	Yes/No	No
Bauer[73]	Li/316SS	SS	Single	L	No	Yes	No	No	Yes
Schad[74]	Na/31SS	T	Mult.	C,R,L	Yes	Yes	No	No	Yes
Polley and Skyrme[75]	Na/31SS	T	Mult.	L	Yes	Yes	Y(N)	Yes/No	Yes
Clement[76]	Generic	SS	Single	L	No	Yes	Y(CS)	Yes	No
Epstein[77]	Various	SS	Single	L	No	Yes	No	No	Yes/No

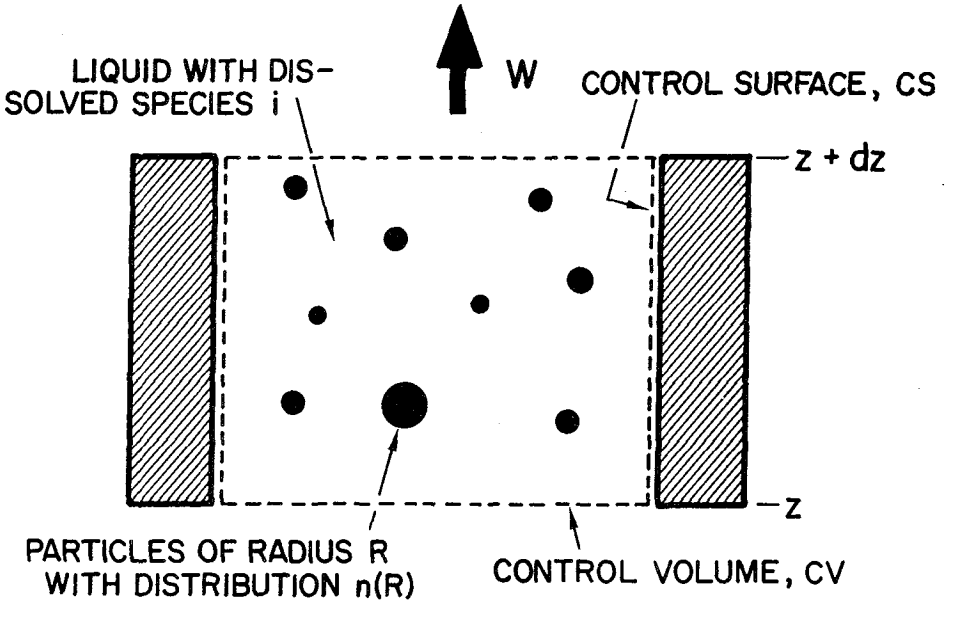
[a] C = channel, L = loop, R = reactor system

[b] N = nuclear, CS = chemical surface, CH = chemical homogeneous

[c] Yes = compared to own experiment, No = no comparison to any experiment, Yes/No = comparison to someone else's experiment



PHYSICAL MODEL OF SOLID PHASE TRANSPORT



PHYSICAL MODEL OF LIQUID PHASE TRANSPORT

Figure 4.6-2 Schematics for liquid- and solid-phase models

$$\begin{pmatrix}\text{The rate of accumulation of}\\ \text{mass of species i in the cv}\end{pmatrix} =$$

$$\begin{pmatrix}\text{Transport of i}\\ \text{into the cv}\end{pmatrix} - \begin{pmatrix}\text{Transport of i}\\ \text{out of the cv}\end{pmatrix}$$

+ (Sources or sinks for species i)

$$\frac{\partial}{\partial t}\left(\rho_L \bar{y}_i A_c dz\right) = \rho_L \frac{k_B^i \; k_D^i}{k_B^i + k_D^i}\left(y_i^E - \bar{y}_i\right) P dz$$

Accumulation in cv Boundary layer and surface reaction

$$+ \left(A_c \rho_L \bar{y}_i\right)\Big|_z \bar{w} - \left(A_c \rho_L \bar{y}_i\right)\Big|_{z+dz} \bar{w}$$

Net Axial Transport

$$+ \left(\sum K_{ij}^{+} \bar{y}_i \bar{y}_j\right) \rho_L A_c dz$$ Homogeneous reactions which produce i

$$- \left(\sum K_{i\ell}^{-} \bar{y}_i \bar{y}_\ell\right) \rho_L A_c dz$$ Homogeneous reactions which destroy i

$$+ \left[\int_{R^o}^{R^*} \rho_{i,p}\, 4\pi\, R^2\, \dot{R}\, n_{i,B}(R,z) dR\right] A_c dz \qquad (4\text{-}217)$$

Particle mass exchange term

where,

ρ_L = liquid density, [kg/m^3]

$\bar{y}_i$ = average or bulk mass fraction of species i in cv, [1]

A_c = cross-sectional area of duct, [m^2]

k_B^i = boundary layer mass transfer coefficient for i, [m/s]

k_D^i = surface deposition reaction constant for i, [m/s]

y_i^E = surface equilibrium concentration of species i, [1]

$\bar{w}$ = average axial velocity, [m/s]

K_{ij}^{+} = bulk reaction rate for production of i, [1/s]

$K^i_{i\ell}$ = bulk reaction rate for destruction of i, [1/s]

R^*, R^o = upper and lower radii of particle size distribution, [m]

$\rho_{i,p}$ = density of species i in particle form, [kg/m^3]

R = particle radii, [m]

$n_{i,B}$ = number of particles per unit volume with radii dR about R at time t, [#/m^3-m]

$\dot{R}$ = rate of change of radius of particle of radius R, [m/s]

P = Perimeter (m)

If we assume the change in liquid density is small around the loop (~ 1.4% for lithium; ΔT = 150 °C) and the duct has constant cross-sectional area, we may write,

$$\frac{\partial}{\partial t}\bar{y}_i + \bar{w}\frac{\partial}{\partial z}\bar{y}_i = \frac{k^i_B \; k^i_D}{k^i_B + k^i_D}(y^E_i - \bar{y}_i)\left(\frac{P}{A_c}\right) + \sum K^+_{ij}\,\bar{y}_i\,\bar{y}_j - \sum K^-_{i1}\,\bar{y}_i\,\bar{y}_\ell + \frac{4\pi\,\rho_{i,P}}{\rho_L}\int_{R^o}^{R^+} R^2\,\dot{R}\,n_{iB}(R,z)\,dR \qquad (4\text{-}218)$$

This equation describes the behavior and transport of the bulk mass fraction of species i in the fluid, which is related to the solid phase by the equilibrium mass fraction, to the particle behavior and to the chemical reactions both at the surface and in the bulk flow. An equation such as that found in Section 4.6-3 is written for each constituent species i. The reaction rates are defined such that conservation of mass is satisfied for the each reaction and the system as a whole. The model requires k_D, k_B, K^+, K^-, and y^E as inputs. k_B can be estimated from heat transfer analogies. k_D, K^+ and K^- are related to the chemical kinetics of the surface and homogeneous reactions. y^E is related to chemical equilibrium of the surface reaction. Characterization of the particulate terms is given in Section 4.6.4.

4.6.4 Particle Mass Transport Modeling

In this section, we will deal with particles of only one species. The

extension to multiple species is straightforward. Our basic assumptions about the particles are that:

1. The particles may be characterized as spheres with radius R and number distribution $n_B(R)$.
2. The ratio of the partial density of species i in solution to the particle solid density is small compared to 1 (typically 10^{-7}).
3. The particles are large enough such that surface tension effects on the equilibrium surface concentration are small. For micron-size iron particles at 650 °C, changes in concentration due to surface tension effects are on the order of parts per billion, while changes in concentration due to temperature changes of 100 °C or more are on the order of parts per million.
4. Particles which transfer mass to/from the containment surfaces may do so by either diffusing as molecules or via turbulent motion of the fluid. Particles which are sufficiently small (i.e., those whose radii are smaller than the turbulent microscale of the flow), cannot penetrate the velocity boundary layer because they remain trapped in turbulent eddies (i.e., they travel with the flow). These particles behave as molecules. Larger particles acquire momentum from the turbulent eddies and are able to penetrate the boundary layer. We assume that the particles are sufficiently small to be considered molecules, and their diffusivity is given by the Stokes-Einstein model of diffusivity:

$$D_p = \frac{k_B T}{6\pi \nu} \tag{4-219}$$

where,

D_p = particle diffusivity, [m^2/s]

k_B = Boltzmann's constant, [J/K]

T = absolute temperature, [K]

ν = kinematic viscosity, [m^2/s]

Particles in the loop can be involved in mass transfer in two manners. First, particles can move to the walls where they adhere or "stick." Hutchinson, et al.,[80] developed a statistical model for large particles

(> 30 microns). This model is quite complex and the radial dependence of n_B is necessary to describe the transport. For our purposes, we will consider this a diffusion process without considering Hutchinson's model. Secondly, particles can grow or dissolve and thus, change the concentration in the bulk fluid. This was seen earlier in the section on modeling mass transport in the fluid.

We describe transport for a surface due to particles similar to that for molecules in terms of a surface reaction. The net particle mass transfer rate to/from a surface via particles can be described as

$$R_p = R_{sp} - k_{Dp}\, n_s \tag{4-220}$$

or

$$R_p = k_{Bf}\, n_s - k_{Bt}\, n_B \tag{4-221}$$

where,

R_p = net particle transfer rate

R_{sp} = rate of particle solution

k_{Dp} = deposition constant for particles

n_s = concentration of particles near the surface

k_{Bt} = transfer coefficient of particles to surface

k_{Bf} = transfer coefficient of particles from surface

In our case, where diffusion of particles is dominant, k_{Bt} and k_{Bf} are equal to k_{Bp} and may be taken from heat transfer correlations with diffusivities from Stokes-Einstein model for D_p. We can eliminate n_s between these two equations to give:

$$R_p = \frac{k_{Bf} R_{sp} - k_{Dp} k_{Bt}\, n_B}{k_{Bf} + k_{Dp}} \tag{4-222}$$

The actual particle mass transfer rate is given by

$$R_{cp}(z) = \int \frac{u}{3}\, \pi\, R^3 \rho_p R_p(R,z) dR$$

It can be shown that the particle distribution must satisfy the following

continuity equation,

$$\frac{\partial n_B}{\partial t} + \frac{\partial}{\partial R}(\dot{R}\, n_B) = o \qquad (4\text{-}223)$$

We still require a model for R for both the particle transport and bulk liquid concentration equations. Clement[76] showed that for small particles in turbulent flow, the rate of change of radius may be described by

$$\dot{R} = \frac{-k_D \rho_L}{\rho_s} \frac{(y^E - \bar{y})}{1 + \delta}, \quad \delta = k_D\, R/D_L \qquad (4\text{-}224)$$

If we ignore the nucleation phase, as shown by Clement[76,78], such that n_B is stationary with respect to time, we may rewrite the continuity equation as,

$$\frac{\partial n_B}{\partial z} + \frac{k_o \rho_L (y^E - \bar{y}(z))}{\rho_s \bar{w}} \frac{\partial}{\partial R}\left(\frac{n_B}{1 + \delta}\right) = \left(\frac{4A_c}{P}\right) k_{Bp}\left(\frac{R_{sp} - k_{Dp}\, n_B}{k_{Bp} + k_{Dp}}\right) \qquad (4\text{-}225)$$

This equation requires relations for k_D, k_{Dp}, R_{sp} and k_{Bp}. Models for these quantities will have to be developed as part of the research.

We see from the equations that very small particles will enter the mean flow easily because of their large diffusivity ($D_p = 1/R$). These particles may subsequently grow until they reach the size where they no longer can remain trapped in the turbulent eddies and are removed to the containment surface.[76] Thus, we suspect that the most persistent particles will be those near the limit where they are carried with the flow.[78]

4.6.5 Solid Phase Mass Transport Modeling

Characteristic length scales for solid-state diffusion of chromium and iron in ferritic steel structures are on the order of 10-100 microns for operation at 700 °C for 10,000 hours. Typical wall thicknesses of the exposure and containment material are on the order of 1000-2000 microns. On this basis, we will model the solid phase as a one-dimensional, semi-infinite solid. We begin by assuming that the interface between the solid and liquid is receding or advancing as material is removed or deposited on the solid surface. The conservation of species i in the solid with a moving interface may be written as

$$\frac{\partial}{\partial t}(\rho_s m_i) \pm \bar{u}\frac{\partial}{\partial x}(\rho_s m_i) = \frac{\partial}{\partial x}\left(\rho_s D_{i_{Fe}}\frac{\partial m_i}{\partial x}\right) + \dot{S} \qquad (4\text{-}226)$$

ρ_s = density of local solid, [kg/m^3]

m_i = mass fraction of species in the solid phase, [1]

$D_{i_{Fe}}$ = diffusion coefficient of species i in iron, [m^2/s]

$\bar{u}$ = speed of interface, (±= corrosion/deposition), [m/s]

$\dot{S}$ = homogeneous source of species i = 0, [kg of i/m^3-s]

x = spatial coordinate, [m]

t = time, [s]

The total mass flux from the surface is the sum of the species mass fluxes,

$$\dot{M}_i^s(t) = \rho_s m_i \bar{u} + \rho_s D_{i_{Fe}}\frac{\partial}{\partial x} m_i(o,t) \qquad (4\text{-}227)$$

$$\dot{M}_T(t) = \sum_i \dot{M}_i^s(t) \qquad (4\text{-}228)$$

where

$\dot{M}_T$ = total mass flux at solid/liquid interface, [kg/m^2-s]

$\dot{M}_i^s$ = mass flux of species i at solid/liquid interface, [kg of i/m^2-s]

The boundary and initial conditions may be stated as,

$$x = 0 \quad m_i = m_i^o$$

$$x \to \infty \quad m_i \to m_i^\infty$$

$$t = 0 \quad m_i = m_i^\infty$$

The solid and liquid phases are linked by requiring that the total mass fluxes on either side of the moving interface be equal. The solid state diffusion model requires diffusivity information and a relation between the liquid-side equilibrium, y^E, and solid-phase surface concentration, m^o.

$$\sum_i \dot{M}_i^L(t) = \sum_i \dot{M}_i^s(t)$$

$$\bar{u} = \frac{\dot{M}_T}{\rho_s} \qquad (4\text{-}229)$$

Models such as these were used by Brush[79] along with surface composition data from his sodium and 316 stainless steel experiments to successfully model solid phase transport.

The possibility of an adherent insoluble surface corrosion product layer has been suggested.[81,82] In this case we will model the solid phase as a two region problem with a moving-boundary separating the two regions.

The coupled equations for n_{Bi}, y_i and m_i constitute a joint particle-molecule transport model with chemical reactions for a loop circuit. These models require inputs for the transport and chemical kinetic information as well as equilibrium data and models for surface reactions.

4.6.6 Chemical Reactions for Lithium/HT9

Until recently, the chemical reactions leading to the dissolution of iron/chromium alloy in contact with lithium had not been identified. It is generally accepted that lithium nitride (Li_3N) reactions between iron and chromium alloying elements lead to mass removal and deposition. Pulham[81] has proposed that the reactions are given by,

$$Fe_{(s)} \rightarrow Fe_{(\ell)}$$

$$Cr_{(s)} \rightarrow Cr_{(\ell)}$$

$$2\ Li_3N_{(\ell)} + Fe_{(s)} \rightarrow Li_3N_{2(s\ or\ \ell)} + 3\ Li$$

$$5\ Li_3N_{(\ell)} + Cr_{(s)} \rightarrow Li_9CrN_{5(s\ or\ \ell)} + 6\ Li$$

where the subscripts refer to the solid or liquid form of the reactant or product. The first two reactions are so-called inherent solubility reactions and the last two are impurity reactions with lithium nitride. The backward and forward kinetics of these reactions are described by rate coefficient,

k_{1b} or f, k_{2b} or f, k_{3b} or f and k_{4b} or f. Some data exist for these reaction coefficients, but models for the others or data from other sources will have to be found as part of the research.[81,82]

4.6.7 Experimental Investigations of Mass Transport in Lithium/HT9 Systems

4.6.7.1 Introduction

This section describes the design of two thermal convection loop (TCL) systems to investigate mass transfer (corrosion and deposition) in lithium/HT9 which are currently being fabricated at Oak Ridge National Laboratory (ORNL). The experimental program is being carried out as a cooperative effort between ORNL and UCLA and blends together experimental and analytical modeling work. These experiments have been designed with the purpose of providing data for both comparison with the analytical modeling work described in the previous sections and for generation of metallurgical data. For example, a TCL design was chosen as opposed to a forced convection loop design (which uses a pump to drive the flow) because it is difficult to assess the impact of such a pump on the behavior of ferromagnetic elements such as iron dissolved in the flow. Although these effects will eventually need to be assessed as part of the fusion research program, their presence in these experiments would tend to make interpretation of the data more difficult. These experiments are meant as an example of how analysis and modeling can interplay to give more meaningful results and experiments.

Corrosion phenomena can be, in general, quite complex and liquid metal systems are no exception. The principal processes which contribute to the corrosion of structural alloys by liquid metals are simple solution (or sometimes referred to as dissolution), thermal and concentrations gradient mass transport, liquid metal/structural material alloying, intergranular penetration, impurity reactions, and interstitial alloy element transport. Given the number and variety of processes occurring, the number of variables which affect the corrosion and deposition rates is correspondingly large. Corrosion in liquid metal systems for fusion (lithium and lithium-lead) is known to be a function of system absolute and differential temperature, chemical composition (alloy, liquid metal and impurities), microstructure of the alloy, flow velocity, geometry and configuration, and exposure time. In order to gather infor-

mation about the mechanisms it will be necessary to conduct experiments which vary only one parameter while all others are held constant. In the subject experiments, only absolute temperature will be varied.

The primary emphasis of the study of mass transport and corrosion in liquid metal systems has been generally metallurgical in scope: generation of data from thermal or forced convection apparatuses for a variety of microstructures and alloys. Few experiments have been performed with the expressed purpose of determining the mechanisms of mass transport. These metallurgical apparatuses are usually difficult to model because of complex geometries or dissimilar metals used in loop construction and samples exposed in the loop. Moreover, variations in experimental conditions, methods, geometry and mixtures of alloys used in loop construction and tested, make comparison between experiments difficult and highly speculative. Further, time scales for the mass transfer processes in which significant results can be attained are on the order of 1000's of hours and thus collection of data is slow and it is difficult to collect data from the same experiment in a short period of time. Also, there is no means by which the corrosion and mass transfer process can be continuously monitored in-situ. Experiments typically utilize coupons inserted and withdrawn in portions of the loop to monitor and indicate the corrosion phenomena.

The materials literature contains many investigations of the compatibility of liquid metals and various alloys. There is a plethora of information regarding material compatibility and corrosion of many structural alloys in sodium and other liquid metals from the liquid metal fast breeder reactor (LMFBR) and other nuclear/energy related programs. However, the direct applicability of these data to lithium is not clear. The release of material from the surface to the adjacent liquid is largely a chemical process. Changing the environment (liquid metal) or the alloy in the system can drastically alter the corrosion processes. For example, although lithium and sodium are adjacent elements in Group 1 of the Periodic Chart and chemically similar in some ways, lithium does show significant differences from sodium in its physical properties, chemical reactions with dissolved species in the liquid metal (notably lithium nitride, Li_3N), and in its corrosion behavior towards transition metals and steels. Sodium is quite sensitive to oxygen contamination, while lithium is almost completely insensitive to oxygen contamination due to

the thermodynamic stability of lithium oxide Li_2O. Indiscriminate application of sodium or other liquid metals to lithium is highly speculative, although some of the aspects of mechanistic modeling (e.g., preferential dissolution and associated effects) are helpful in understanding the corrosion process. Additionally, most of the data available for lithium and HT9 would be difficult to model due to test system complexities (geometry, cold or hot traps, etc.) already mentioned.

4.6.7.2 Thermal Convection Loop Program for Lithium/HT9

Overview

The proposed two-loop program will evaluate the effects of local temperature from 350 °C to 650 °C at constant loop temperature difference of 150 °C, moderate nitrogen content in liquid lithium (< 150 ppm) and exposure periods of up to 3000 hours. The samples will be removed and examined at integrated exposures of 100, 300, 500, 1000, 1500, 2000 and 3000 hours to determine the time-dependent kinetics of the mass transport processes. The two loops will be constructed entirely of HT9 alloy to minimize dissimilar metal mass transport. A more complete description of the apparatus, coupons and experiments is given below. Coupon analysis will consist of weight change data for all samples in both the hot and cold leg regions of the loop at the end of each exposure period. Compositional and microscopic analysis of selected samples will be performed at the end of the total experimental period. The experimental loops will be fabricated and operated at Oak Ridge National Laboratory (ORNL) in the Corrosion Laboratory of the Metals & Ceramics Division (M&C).

Details of the Experiments

The TCL experiments are similar in design to loops which have been operated at ORNL for more than 20 years. A schematic of the loop design is given in Figure 4.6-3. The differences in the design are in the surge tank and the removable coupon stringers. In the standard ORNL design, two surge tanks are provided, one above the hot leg and one above the cold leg of the loop. The purpose of these surge tanks is to provide a volume of liquid through which coupons may be inserted and removed and into which the liquid in the loop may expand as it is heated. In the new design, only one surge tank is provided

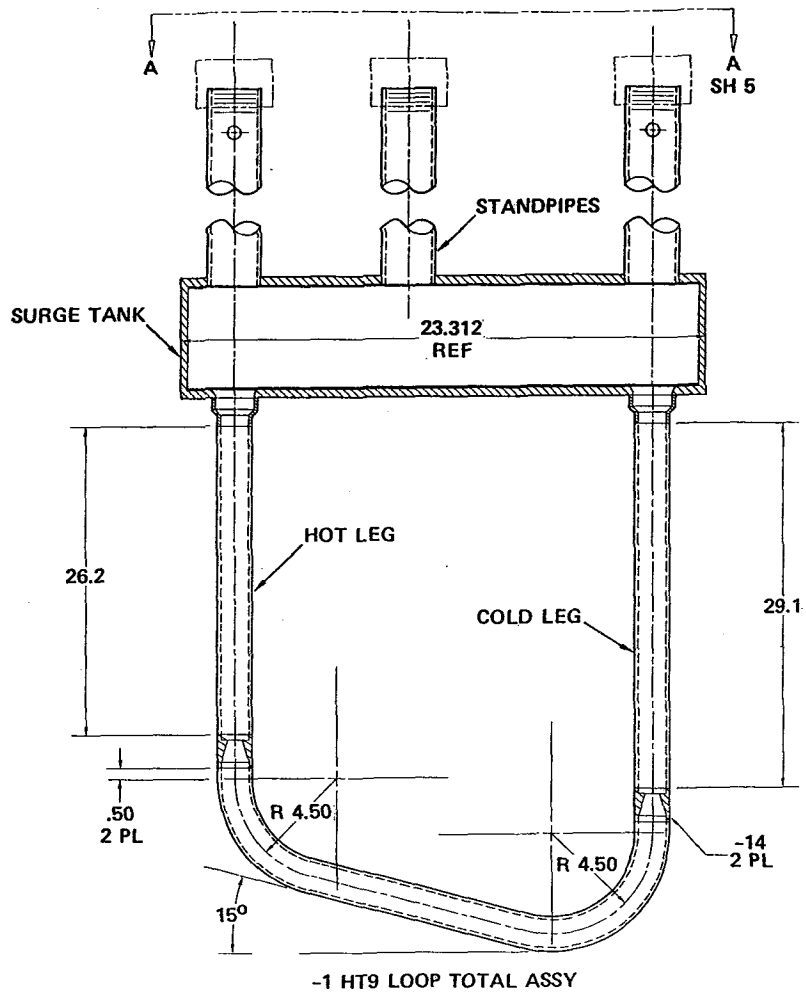
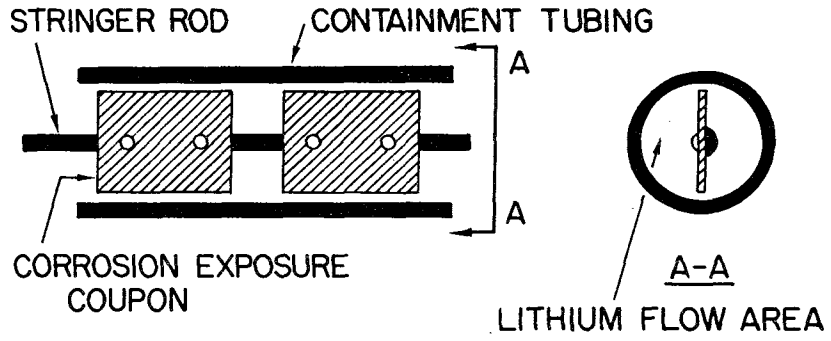


Figure 4.6-3 Schematic of thermal convection loop

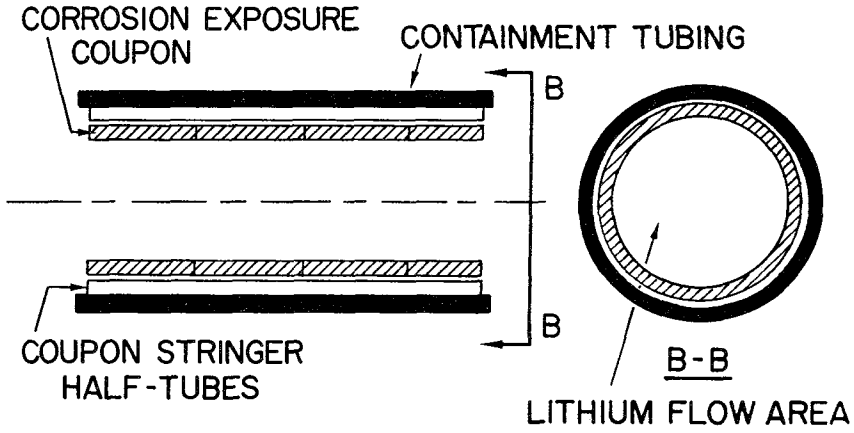
which reduces the amount of fabrication necessary for each loop and decreases distortion due to welding. Alignment of the hot and cold legs of the loop is critical due to the close tolerance for insertion and withdrawal of the coupon stringers. The primary difference between the standard design and the new design is the re-design of the removable coupon stringer which allows the coupons to be inserted and withdrawn from the loop without interrupting the liquid flow. The standard ORNL design uses a series of flat exposure coupons (3/4" x 1" x 0.030") which are mounted on a 1/4" rod at spacings of about 1" between coupons. The new design uses interlocking tubular coupons which form a smooth continuous path for the liquid to flow over the coupon. In the ORNL design, the flow path is disrupted by the discrete nature of the coupons and the mounting rod. A comparison between the standard ORNL and the new coupon design is shown in Figure 4.6-4. The new design presents a more uniform cross-section to the flow, and analytic modeling of these circular cross-

sections should be somewhat easier than the previous flat coupon design.

Flow in the loop is driven by the density difference between the vertical hot and cold leg sections of the loop. The hot leg is heated by clamshell heaters with a total thermal power input of 4 to 5 kilowatts. Trace heaters and thermal insulation are provided around the loop to maintain temperature control and to keep the lithium from freezing during operational and start-up transients. Flow rate is controlled by an adjustable flow restriction at the inlet to the surge tank from the hot leg. The heat is removed in the cold leg by the HVAC system for the surrounding lab space. Velocities in the hot and cold leg test sections are expected to be on the order of 3 to 5 cm/s.



ORNL STANDARD TCL COUPON GEOMETRY



NEW COUPON GEOMETRY

Figure 4.6-4 Comparison of flow geometries

This experiment is to be materially homogeneous. All loop components which are intimately in contact with lithium during normal operations of the loop will be made of the same material, HT9 (12Cr-1Mo), to minimize dissimilar metal (concentration gradient) mass transfer. Loop components such as standpipes, insertion/removal valves and tubes which are only in contact with small amounts of lithium for short periods of time during coupon stringer movement will be austenitic (304 or 316 stainless steel). This apparent inhomogeniety is necessary because HT9 is not a widely available commercial material, but should not lead to significant contamination of the system because of the short contact periods.

The main body of the loop will be constucted from 1-1/2" O.D.- 0.120" wall HT9 tubing which forms the primary containment for the flowing lithium. The surge tank is constructed from 3/8" and 1/4" thick HT9 plate stock. The surge tanks are operated with a high purity argon cover gas to prevent possible contamination of lithium from free-surface contact with the gas phase. The material for construction of the loops has been obtained from GA Technologies in San Diego and ORNL as part of the Alloy Development for Irradiation Performance (ADIP) program. The composition and properties of the material were also provided as part of the ADIP program.

Corrosion coupons are to be inserted in both the hot and cold leg sections of the loop, via stringer assemblies, so that corrosion and deposition can be monitored simultaneously. Each hot leg coupon stringer consists of 18 interlocking tubular coupons (3/4" O.D. - 0.030" wall x 1.5" long) and axially supporting stringer tube. The cold leg is slightly longer and has 20 interlocking coupons of similar dimensions. The coupons will be fabricated and fit to provide a smooth continuous surface for the lithium to flow over. After fabrication, each coupon will be numbered, normalized and tempered (0.5 hour at 1050 °C, 2.5 hours at 780 °C), oven-dried and weighed prior to initial insertion into the loop to provide identification, uniform microstructure and initial weight data for mass loss measurements. All materials used in construction of the loops will be normalized and tempered before assembly.

These loops have been designed and will be operated such that the primary difference between the two loops is absolute temperature. The Low Temperature Loop (LTL) will cover the temperature range between 350 and 500 °C and the High Temperature Loop (HTL) will cover the range between 500 and 650 °C. Due

to variations in properties with temperature there will be some differences in transport properties between loops. However, average flow velocity in the two loops will be adjusted such that the average Reynold's numbers, and thus the convective portion of the mass transfer process, are approximately equal in both loops.

Operation of the TCL Experiments

After fabrication and prior to coupon stringer insertion, the loops will be operated with a flush charge of lithium to remove any impurities which might have adhered to the walls of the containment during fabrication. This flush charge will then be drained into the dump tank. The loop will then be filled with a fresh charge of lithium, the temperature distribution and flow initiated by the heaters and insulation, and operation of the loop begun. Both the flush charge and the operational fill charge will be equilibriated at 815 °C in a titanium-lined, zirconium-foil-filled gettering pot to reduce the concentrations of nitrogen and oxygen to below 150 ppm and 30 ppm, respectively. The lithium flush and fill charges for both loops will be taken from the same batch-gettered lithium tank to increase chemical uniformity between the two loops. The loops will normally operate continuously. Thermal control and data acquisition will be exercised by the ORNL Metals & Ceramics Division Hewlett-Packard computer system, which controls the heater power input and system temperature distribution. Alarms and control systems are provided to discontinue loop operation, and procedures exist for notification of responsible personnel in the event of a flow stoppage or other system malfunction.

Experimental Data Collection and Utilization

The loops will continue to operate even during coupon removal and insertion. The stringer assemblies will be removed and dismantled at 100, 300, 500, 1000, 1500, 2000 and 3000 hours of integrated coupon exposure. The coupons will be cleaned with water or alcohol to remove the semi-adherent lithium, oven-dried to remove excess moisture and weighed to determine mass loss data as a function of exposure time. The purity of the lithium in the loop will be periodically determined, primarily for nitrogen content, during the course of the experiments. The stringers will be re-assembled and re-inserted into the loop for further exposure. At the end of the total exposure

period (i.e., at 3000 hours of integrated exposure) compositional and microscopic examination of a selected few coupons will be prepared for analysis of alloy end-of-life composition and morphology. Thus, the experiments will yield profiles of mass loss and deposition in space and in time, lithium purity as a function of time and end-of-life coupon composition and morphology for comparison with analytic models.

Unfortunately, the nature of the experimental analysis is such that the solid phase modeling will benefit most from the experiments. However, periodic analysis of the constituents of the lithium in the loop will aid in liquid phase modeling.

4.6.8 Summary and Future Experimental Work

There is a general need to investigate mass transfer for alloys relevant to fusion reactor designs. By cooperation between experiments and analytical modeling, greater understanding should be possible. The models and experiments outlined above are intended to be a first step in such an effort for lithium/HT9.

After establishing a baseline data set for lithium/HT9 in a homogeneous environment, bi-metallic studies could be undertaken. Since it is accepted that actual fusion systems will be materially heterogeneous, possibly combining refractory and ferrous alloys, coupons of different alloys could be inserted into the hot and cold legs to determine the effects of mixed alloys on the material interaction. Through modeling of such a multiple effect test (i.e., thermal gradient and dissimilar metal transport), the loops could provide valuable design data and lend insights into the more complex mass transport processes.

4.7 Tritium Transport in Solid Breeders

The importance of tritium modeling derives from the need, dictated by safety concerns, to account for all the tritium generated and to predict the tritium inventory in solid breeder blankets. Tritium modeling is also needed in conjunction with the on-going and proposed tritium experiments for solid breeders since modeling of physical laws and experimental verification are both necessary to determine tritium-related properties of the solid breeder materials. At the same time, in view of the discussions concerning whether the next fusion test facility should operate in pulsed mode or in steady state, the modeling of tritium transport in the transient state is necessary to predict the tritium behavior during pulsed operation and to provide the analytical results which could help in the choice of the operating mode.

In light of the above discussion, a tritium modeling effort was recently started as part of the FINESSE program. The initial model focuses on the different mechanisms transporting the tritium generated in the solid breeder grain to the purge flow, which will carry it out of the blanket or test module for subsequent removal and measurement. The transport mechanisms which bring the tritium from the grain to the purge flow are as follows:

(i) Intra-granular diffusion to the solid breeder grain boundary;

(ii) Diffusion along the grain boundary to pores in the solid breeder material;

(iii) Surface desorption to pores;

(iv) Diffusion along pores to the purge flow (assuming open, interconnected porosity);

(v) Mass transfer to the purge flow and convection in purge flow.

The solubility of tritium in the solid breeder material also enters in the process since it will affect the amount of tritium which diffuses through the grain.

It is proposed to concentrate initially on modeling the first four mechanisms and including the solubility effect. The results would then apply for the solid breeder at the purge flow inlet where the tritium concentration in the purge flow is not affected by any upstream tritium production. However, if the purge flow velocity is high enough that the time for the purge flow to go once through the blanket or test module is much shorter than the characteristic time for the rate limiting tritium transport step, then the

results apply for any breeder location along the purge flow path.

Since all the tritium transport mechanisms are very dependent on the temperature, a model for the transient temperature distribution over the solid breeder is required first. The transient 2-D heat conduction equation was solved using the alternating direction implicit (ADI) finite difference technique. This technique is advantageous since solving the equation by an explicit scheme would severely restrict the time step due to stability requirements and, thus, also restrict the maximum time period that can be considered due to computer storage and/or running time limitations. The ADI method[83] solves the 2-D equation by alternately using an implicit finite difference approximation in the x and y directions. The method is valid for all ratios of $\delta t/(\delta x)^2$ and $\delta t/(\delta y)^2$.

The tritium transport model assumes constant temperature within each control volume, as calculated above. The intra-granular diffusion to the grain boundary is calculated using the 1-D transient mass diffusion equation[84] and assuming a spherical grain. The tritium generation rate in the breeder grain is obtained from neutronics calculations, but the source term must also include the mass rate of change of dissolved tritium per unit volume of solid breeder. The concentration of tritium dissolved in the solid breeder is estimated from a Sievert-type equation, which includes the effect of the partial pressure of any added hydrogen to the purge flow on the amount of dissolved tritium. A time constant for dissolution is required for the transient calculation and it is assumed that it is similar to the time constant for intra-granular diffusion. Solubility tends to increase with temperature. Thus, an increase in temperature will tend to reduce the effective tritium generation rate, while a decrease in temperature will have the reverse effect.

Grain boundary diffusion to the pores, which is believed to be much faster than intra-granular diffusion, can be included by solving the transient diffusion equation for a simplified geometry. It is assumed that the process can be approximated by 1-D diffusion through a circular cylinder whose dimensions are calculated by equating the area and volume for grain boundary diffusion to the model cylindrical area and volume.

The tritium diffusion through the pores is also modeled using the 1-D transient diffusion equation. Pores are assumed to be interconnected and open

such that the tritium can diffuse from the grain boundary to the purge flow through a porous path. The model assumes a simplified 1-D cylindrical geometry whose dimensions are calculated by equating the pore volume to the model volume for a given pore length. The pore diffusion coefficient is modified to account for the pore tortuosity. The source term in the diffusion equation is estimated from any change in tritium surface adsorption inventory along the effective pore length and a time constant for adsorption (of the order of 3 hours from the TRIO results).[85]

A matrix set of equations results for the three diffusive processes in series and the linking elements between successive transport mechanism provided by given boundary conditions. The solution of this set of equations at each time step yields the tritium concentration distribution over the grain, grain boundary and pore for the next time step. The initial boundary conditions selected for the start and end of the transport chain are zero concentration gradient, by symmetry at the grain center for the former and zero concentration in the purge flow for the latter. The boundary condition at the interface between intra-granular diffusion and grain boundary diffusion is obtained by assuming that the concentration for both transport mechanisms is the same at the interface and by equating the mass flux out of the grain to the mass flux entering the grain boundary. The boundary condition at the interface between grain boundary diffusion and pore diffusion is also obtained by equating the mass flux coming to the grain boundary side to the mass transfer to the pore (dependent on a mass transfer coefficient) and to the mass flux on the pore side.

The proposed tritium model looks promising in that it tries to evaluate the combined time-dependent effect of the different transport mechanisms which have tended to be modeled separately and in steady state in the past. However, it does not consider the effect of different tritium species and a desirable future improvement would be to try to model the migration of each tritium species while keeping their concentration in chemical equilibrium. Another improvement would be to try to include the effect of porosity closure and of trapping due to radiation. The aim is to be able to extend the modeling so that it can be used, in conjunction with the increasing data which are starting to be available from the experimental program, to help understand, verify and predict the tritium-related behavior and properties of solid breeder materials.

4.8 Design Window for a Liquid Metal Cooled Limiter

4.8.1 Introduction

Liquid metals are strong candidates as breeders and coolants for fusion blankets.[86,6] A key feasibility condition defined recently for such blankets is to identify a viable non-water coolant for the in-vessel components such as limiters and divertor plates. The presence of water in close proximity to lithium is considered an unacceptable safety risk.[86,6,87] The purpose of this work is to investigate the feasibility and attractiveness of liquid metals as coolants for the in-vessel components. In detailed calculations, a pumped limiter in a commercial tokamak reactor was used as an example. A technique used extensively in this work is that of defining the possibility of a design using a design window. A design window can be explained as a permissible region of operation defined by various limits.

A key problem with the design of the pumped limiter, or other in-vessel components, is the simultaneous presence of high particle and heat fluxes. High particle fluxes dictate thick walls in order to withstand erosion. High heat fluxes require thinner walls to minimize temperature and stresses. Present designs,[88] e.g., INTOR, use water coolant at low temperature (< 100 °C), and hence, low pressure. Low temperature operation permits the use of high conductivity materials such as copper and the low pressure reduces stresses.

Liquid metal cooling of the limiter introduces new and difficult problems. The combination of high melting point and considerable film temperature drop in laminarized fluid flow under the effect of magnetic field results in operating temperatures of the structural material which are much greater than those acceptable for copper alloys. The much higher thermal stress induced in other structural materials sharply reduces the maximum allowable heat flux. Another problem is the MHD pressure drop in the liquid metal coolant. The resulting pressure stresses further reduce the allowable heat flux.

4.8.2 Design Approach

As the problem of cooling of a limiter with liquid metal was quite complicated, it was approached first by introducing various constraints which the design must observe; second, by choosing geometrical configuration and design

parameters in accordance with the constraints; third, by carrying out thermal and stress analysis of the limiter; and finally, by defining the design window for the limiter. While carrying out the thermal and stress analysis of the limiter, analyses were performed of the limiter, without coating first, and with coating later. Introduction of coating on the limiter reduces the maximum allowable surface temperature if low Z coatings are used. It also introduces a new constraint on the structure material, thus aggravating the thermal stress problem. Besides, the effect on overall design of the limiter due to coating depends upon the thickness of the coating material and its type. Thus, analysis of the limiter without coating has given an insight into the problems of the limiter design on a general basis.

4.8.3 Design Constraints

The constraints imposed on the limiter design were:

1) The limiter surface area should be large enough to provide lower particle and heat fluxes.
2) The space provided for the particles to be pumped must be sufficient to provide efficient impurity removal.
3) The materials used for surface coating must not excessively contaminate the plasma.
4) The structural materials must have good compatibility with the coolant.
5) As the corrosion due to liquid metals is temperature dependent, an upper limit on the interface temperature between the coolant and structure must be defined and observed.
6) The structural materials have a tendency to creep at higher temperatures. Thus, structural temperature during operation must remain below a limiting value.
7) In order to avoid the formation of cold spots in the system, the inlet temperature of the coolant must be ~ 50 °C above the melting point.
8) The sum of primary and secondary stresses arising in the material must remain below the 3 Sm value, as determined by the ASME code.
9) The primary stress in the material must remain below the Sm value, again as set by the ASME code.

4.8.4 Choice of Limiting Values and Material Properties

The choice of substrate material was made based on the criterion that material should have resistance to corrosion due to liquid metals and acceptable heat sink properties. Vanadium alloy V-15Cr-5Ti was considered appropriate in this respect. The mechanical and thermal properties were taken from Ref. [89]. Based upon previous studes,[86,6] a maximum value of 650 °C was selected for the interface temperature and a value of 670 °C for the structure temperature. The maximum temperature of coating was taken to be equal to the value below which vaporization or sputtering of the coating material does not become excessively high. A Nusselt number of 7 was chosen for heat transfer calculations, accounting for the fact that flow in the coolant channels on the face of the limiter is not fully developed.[1] However, reliable data for the type of heat transfer problem encountered in the limiter was not found, and we hope to investigate this issue in detail later.

4.8.5 Geometrical Configuration

In light of the above constraints, the geometrical configuration of the limiter was chosen and is shown in Figure 4.8-1. It is a curved, double-edged

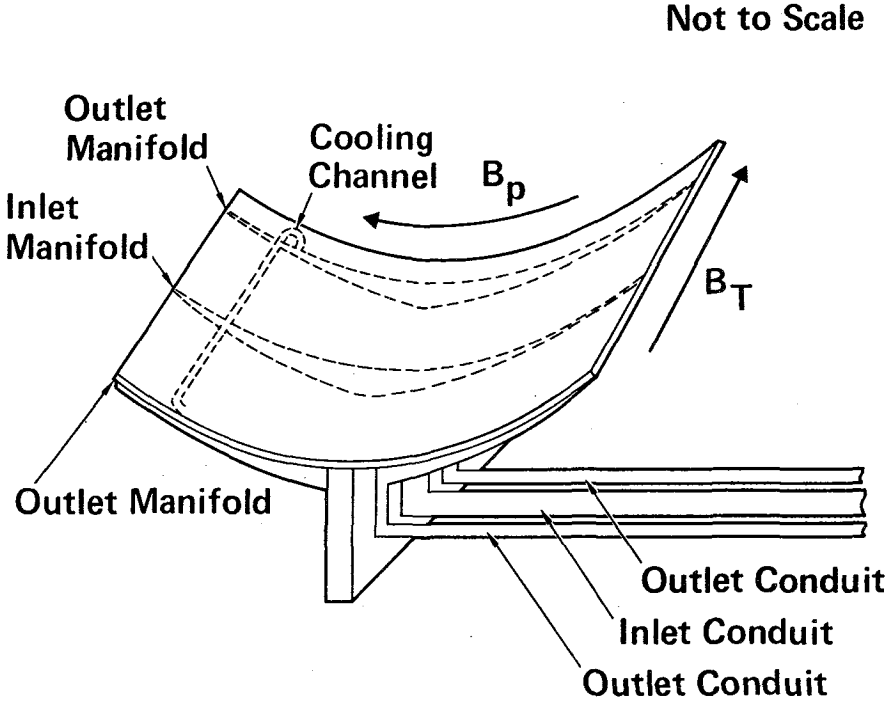


Figure 4.8-1 Geometrical configuration of the limiter

limiter with one inlet and two outlet feed pipes which we shall call conduits, one inlet and two outlet horn-shaped pipes which are called manifolds, and minute cooling channels running on the face of the limiter. The cooling channels rise from the inlet manifold, each separating into two parts and then terminating at the outlet manifold. The coolant flows on the face of the limiter in cooling channels parallel to the toroidal magnetic field, and flows perpendicular to the toroidal magnetic field in the conduits and in the manifolds. This flow pattern was primarily chosen because: 1) it provides shorter path lengths which are highly desirable to keep the rise in bulk temperature low because of the above-mentioned limits, and 2) the flow is parallel to the toroidal magnetic field where the flow speed is highest in order to reduce the MHD pressure drop. However, large MHD pressure drops are still expected to occur in the conduits and manifolds if conducting wall pipes are used.

4.8.6 Thermal and Stress Analysis

The first step towards obtaining a design window was to determine the dimensions of the coolant channels. The dimensions were picked after a thermal and stress analysis. The channel near the center of the flat face and the one at the leading edge were both chosen for analysis. Figure 4.8-2 shows the nomenclature and construction of the two channels. Each channel was analyzed

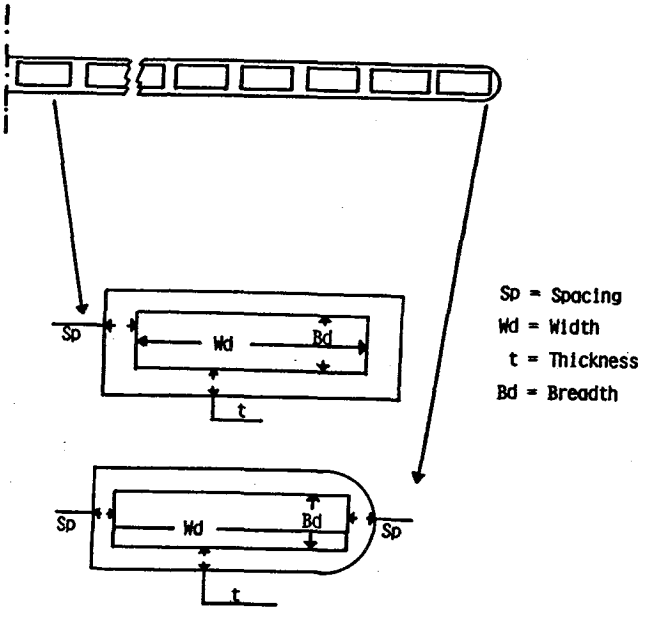


Figure 4.8-2 Details of the leading and center channel

in two parts; first, without coating, and then with coating. The procedure for analysis and the results are presented below.

4.8.6.1 Analysis of the Flat Face Channel Without Coating

For both thermal and stress analysis, the finite element code ANSYS[90] was used. The geometry and boundary conditions considered are shown in Figure 4.8-3. It shows the cross-section of a cooling channel which can for all practical reasons be considered symmetrical about the toroidal axis, as the limiter runs like a belt all along the torus. Figure 4.8-4 shows the number of elements and details of the nodes. Nodes (1), (9), (17), (25), (33), and (41) are restrained from moving in the x-direction and, except (1), are free to move in the y-direction. Node (1) is the fixed node. Nodes (8), (16), (24), (32), (40), and (48) are coupled and can move in both x and y directions. Uniform heat flux is assumed on the top and zero on all other faces. Uniform heat generation is assumed in the solid material. Bulk temperature and pressure of the fluid is specified. After specifying the geometry and boundary conditions all possible variables were considered and optimium configuration was sought. The variables considered were the front and back wall thickness (x), the side wall thickness (spacing) (sp), width of channel (wd), depth of channel (bd), wall heat flux, and bulk temperature of the fluid and its pressure. Effect of each on the allowable heat flux or total stress in the most critical element was observed.

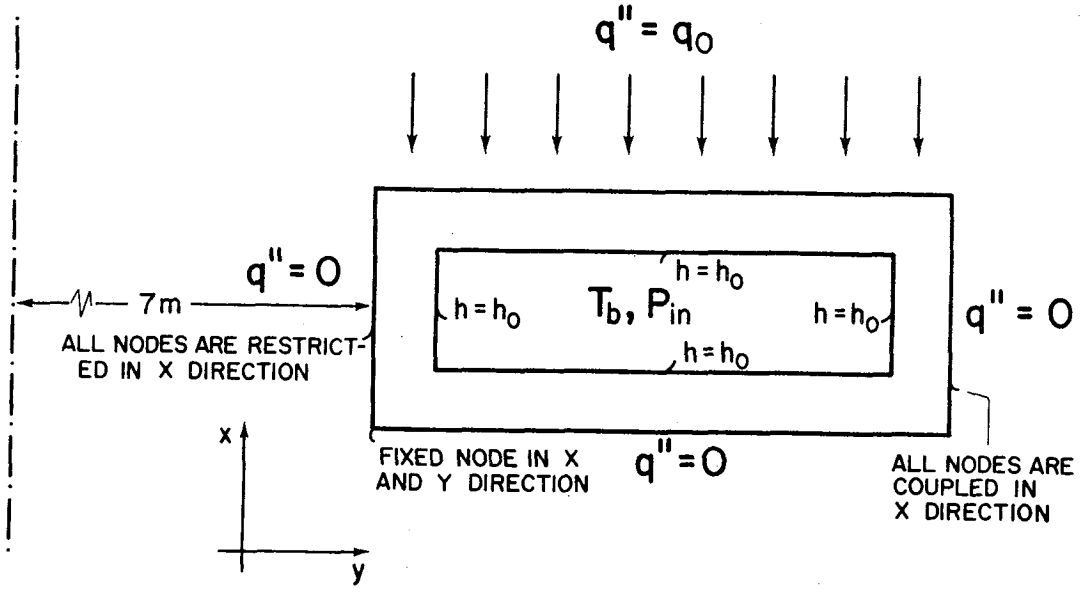


Figure 4.8-3 Thermal and stress boundary conditions for the limiter channel

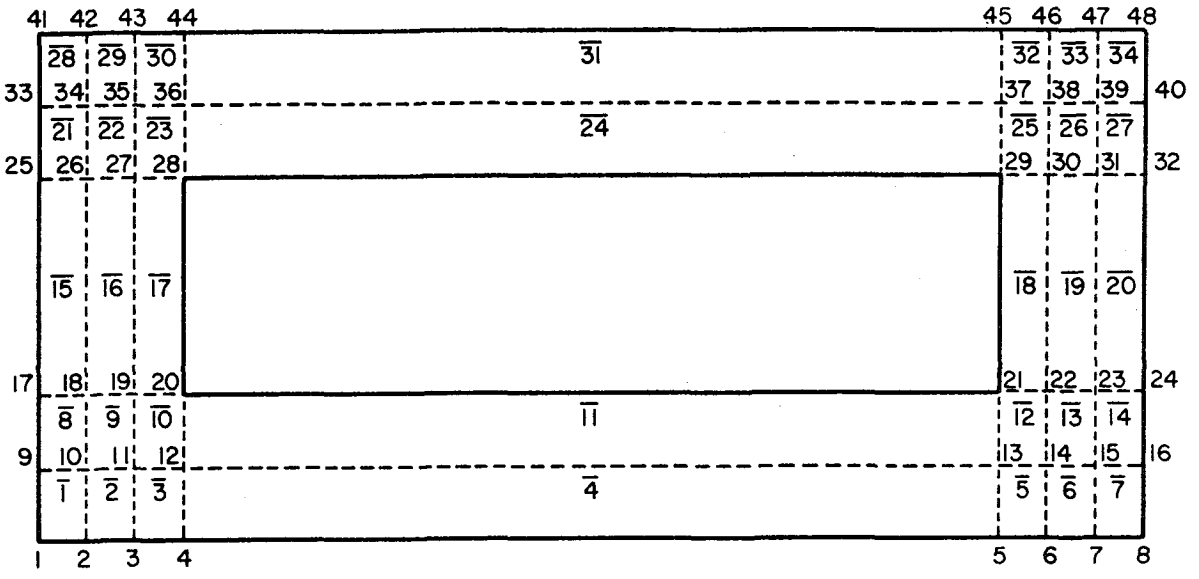


Figure 4.8-4 Description of elements for coolant channel without coating

Effect of Changing Wall Thickness on Maximum Allowable Heat Flux

Effect of changing the front and back wall thickness together on the total stress in the material was observed. Then, maximum allowable heat flux was determined based upon a 3 Sm limit. The results are shown in Figure 4.8-5. At different pressures the curves remain almost parallel to each other, but tend to converge once thickness is brought below 0.8 mm. The regular pattern of the stresses is disturbed when thickness goes below 0.5 mm.

Effect of Changing Side Wall Thickness on Maximum Permissible Heat Flux

Here we kept all other variables constant and varied just the thickness of the side walls (sp). The results are shown in Figure 4.8-6. The permissible heat flux increases as side wall thickness is decreased, and is higher at lower pressures. It was also observed that different pressure curves tend to converge when side wall thickness is decreased.

Effect of Changing Only Back Wall Thickness on Total Stress in the Critical Element

It was also important to observe the effect on total stress when back wall thickness was varied and front wall thickness was kept constant. The

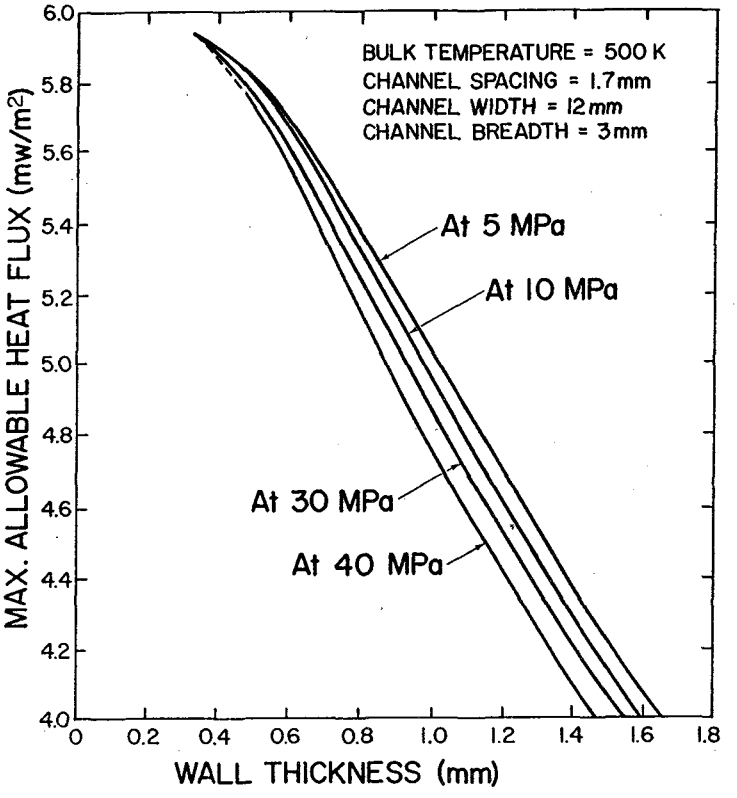


Figure 4.8-5 Maximum allowable heat flux vs. wall thickness of the channel

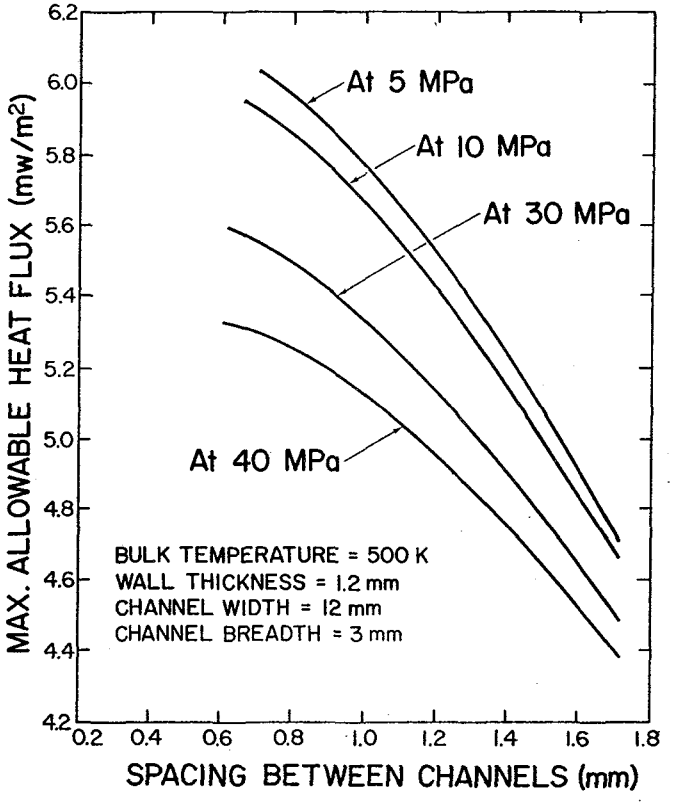


Figure 4.8-6 Allowable heat flux vs. spacing between channels

results are shown in Figure 4.8-7. It can be concluded from the figure that, for a limiter without coating, front and back walls should be kept at the same thickness.

Effect of Changing the Bulk Temperature of Fluid on Total Stress

It was observed that, irrespective of the geometry of the channel, an increase of 10 °K in the bulk temperature resulted in an increase of about 10 MPa in the critical element, and thus, a decrease of ~ 0.1 MW/m^2 in the allowable heat flux.

Effect of Changing Channel Width on Total Stress

The dependence of total stress on channel width (wd) was observed. The results are shown in Figure 4.8-8. It was observed that stress increases with an increase in width. However, this increase is marginal at lower pressures, but very steep at higher pressures. It was also observed that as the channel gets more and more rectangular in the x-directon the stress also increases. Thus, square channels appear to give better results as regards lower stresses. This, however, needs further investigation.

Effect of Changing Channel Depth on Total Stress

Observing the dependence of total stress on channel depth (bd) at different pressures was also considered important at this stage. Figure 4.8-9 shows the results. The stresses rise and fall and peak at about 6 mm, which is half of the width. However, as depth begins to increase tending towards square and then rectangular channels, in the y-direction the stress again begins to rise. This is very evident when the pressures are high. Thus, it can be safely concluded that square channels would be more appropriate from a pure stress point of view.

4.8.6.2 Identifying Maximum Permissible Heat Flux for Flat Face Channel Without Coating

Based on the above analysis, we conclude that higher allowable heat fluxes shall result for lower values of wall thickness and square cross-sections. However, in search of the most optimum combination, we set 1 mm as the manufacturing limit on wall thickness and varied the side wall thickness

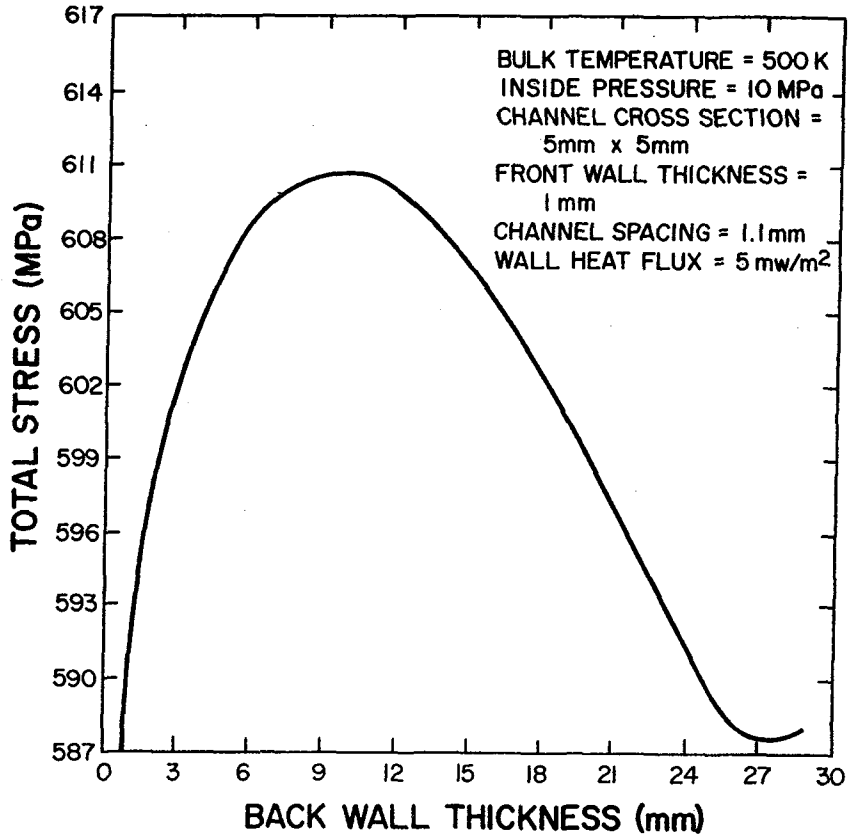


Figure 4.8-7 Variation of stresses with increasing back wall thickness

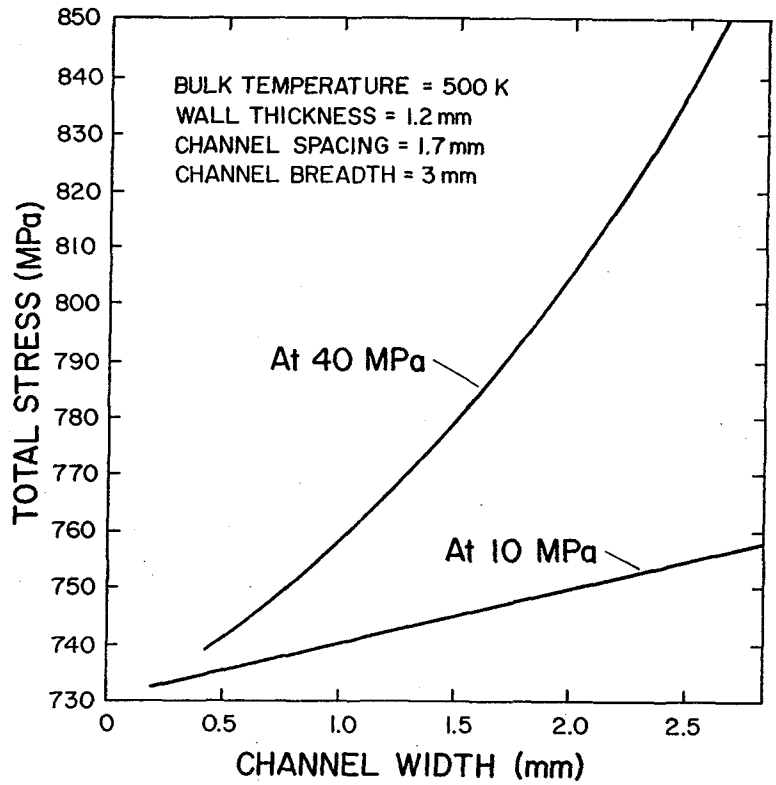


Figure 4.8-8 Dependence of total stress on the width of channel at different pressure

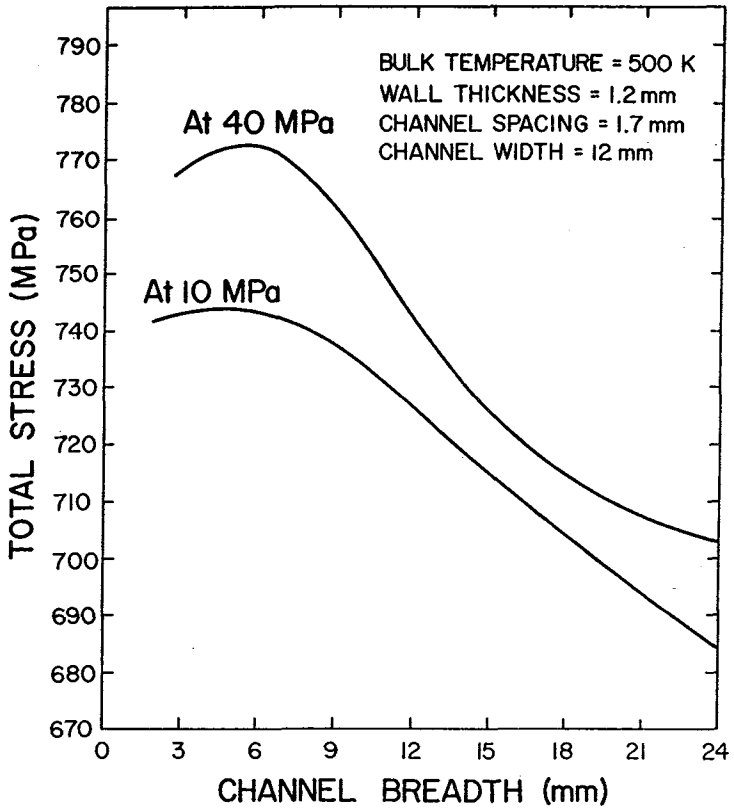


Figure 4.8-9 Dependence of total stress on channel breadth at different pressure

(sp) and cross-sections (wd x bd), and then obtained the results. The results are shown in Figure 4.8-10, for system pressure 10 MPa, and in Figure 4.8-11, for system pressure 40 MPa. As side wall thickness increases, the peak of the curves shift to the right. Also, allowable heat flux is lower at higher pressure and this difference increases at higher cross-sections.

4.8.6.3 Analysis of the Flat Face Channel with Coating

After analyzing the channel without coating, we analyzed the channel with coating. The effect of coating becomes pronounced when the coating is thick (i.e., about the thickness of the wall). Therefore, we considered low Z materials and chose beryllium coating. The properties of beryllium used were as reported in the INTOR report for pure beryllium.

For thermal and stress analysis, the configuration of the channel selected is shown in Figure 4.8-12. Nodes (1), (9), (17), (25), (33), (41), (49) and (57) were fixed in the x-direction, whereas only node (1) was fixed in the

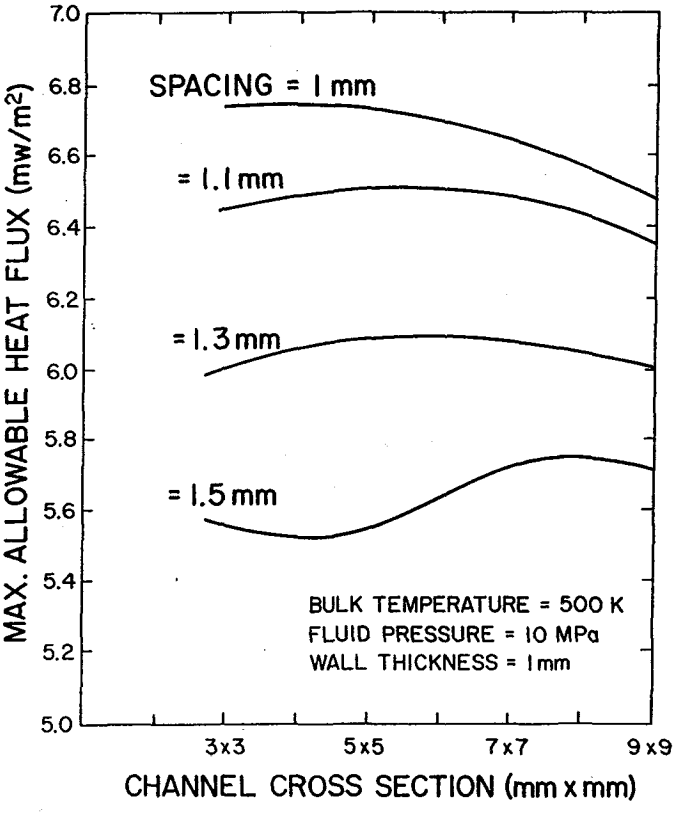


Figure 4.8-10 Maximum heat flux vs. channel cross-section for different channel spacing

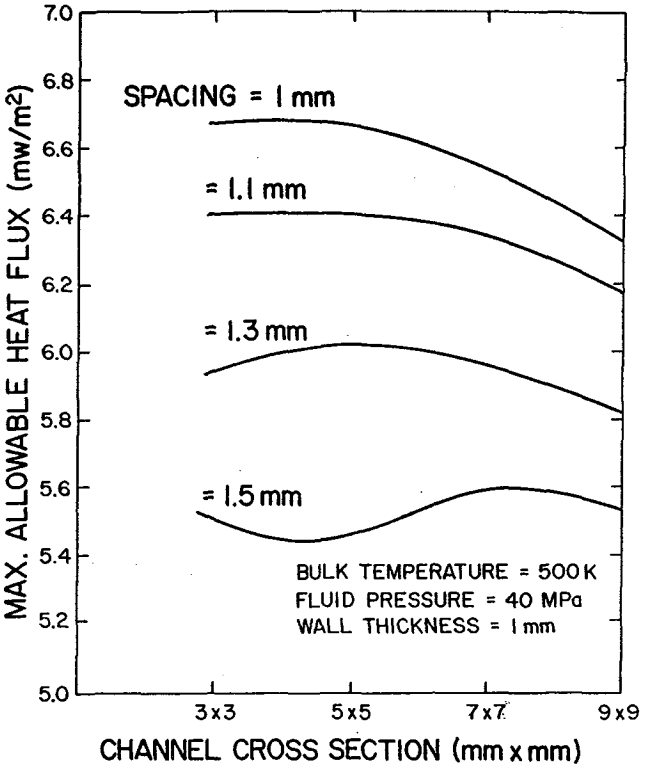


Figure 4.8-11 Maximum heat flux vs. channel cross-section for different channel spacing

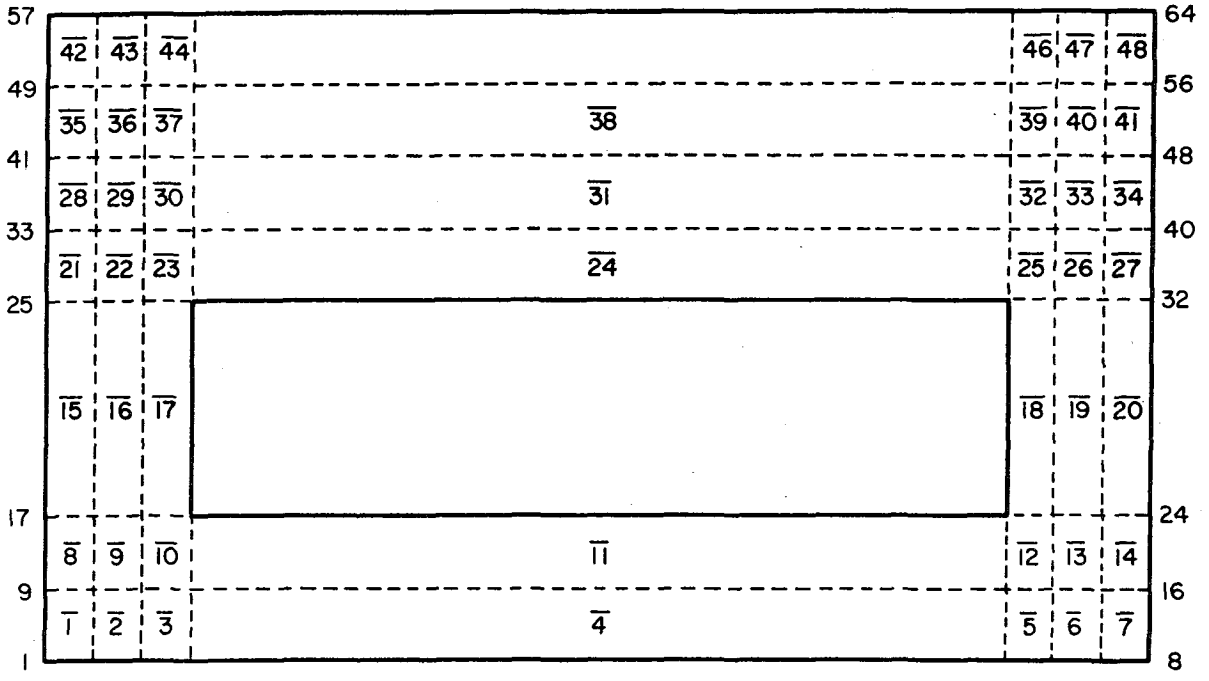


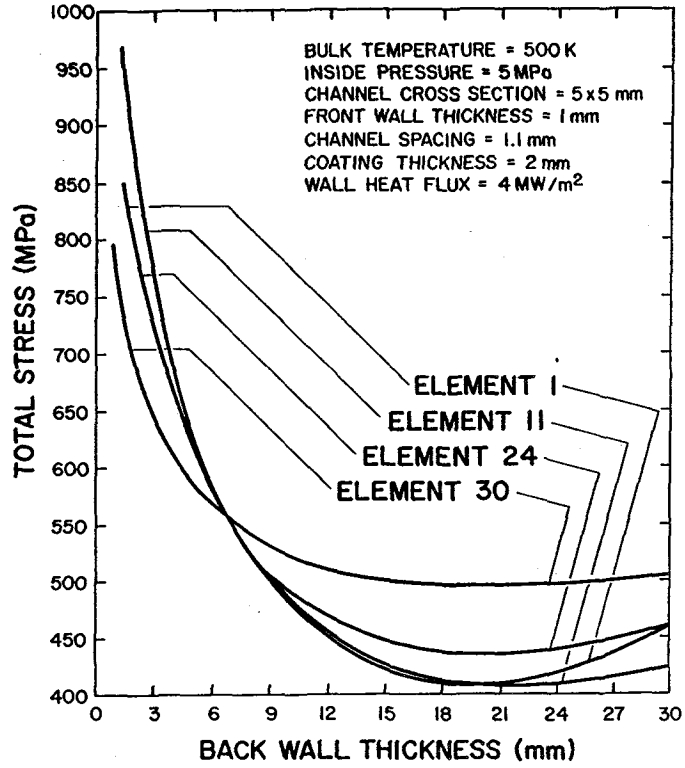
Figure 4.8-12 Description of elements for coolant channel with coating

y-direction. Nodes (8), (16), (24), (32), (40), (48), (56), and (64) are coupled. Detailed analyses are presented below.

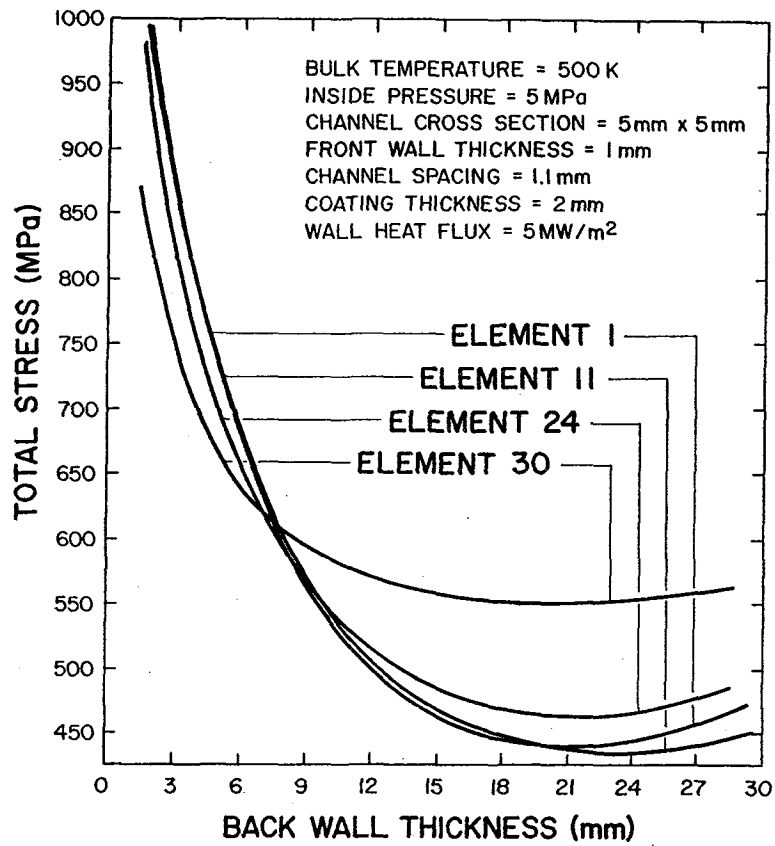
Effect of Increasing Back Wall Thickness

When coating was considered, it was observed that stresses increased drastically. However, the main concern was that extremely high stresses were observed in the back plate where previously they were not considerable. Thus, it became necessary to observe the effect of increasing back plate thickness. As in this case no one element could be considered as critical, stresses in most critical elements were considered and plotted. It was observed that for coating thickness (t_c) of 2 mm and front wall thickness (t_{fw}) of 1 mm the stresses became minimum for a back wall thickness (t_{bw}) of $t_{bw} \simeq 7(t_{fw} + t_c)$. This result remains valid inspite of increase in heat flux (q''), inside pressure (P_{in}), side wall thickness (sp), and higher cross-sectional area (wd x bd). This can be seen clearly in Figs. 4.8-13 through 4.8-18. However, when coating thickness was increased to 3 mm, 6 mm, and 10 mm, the following was observed:

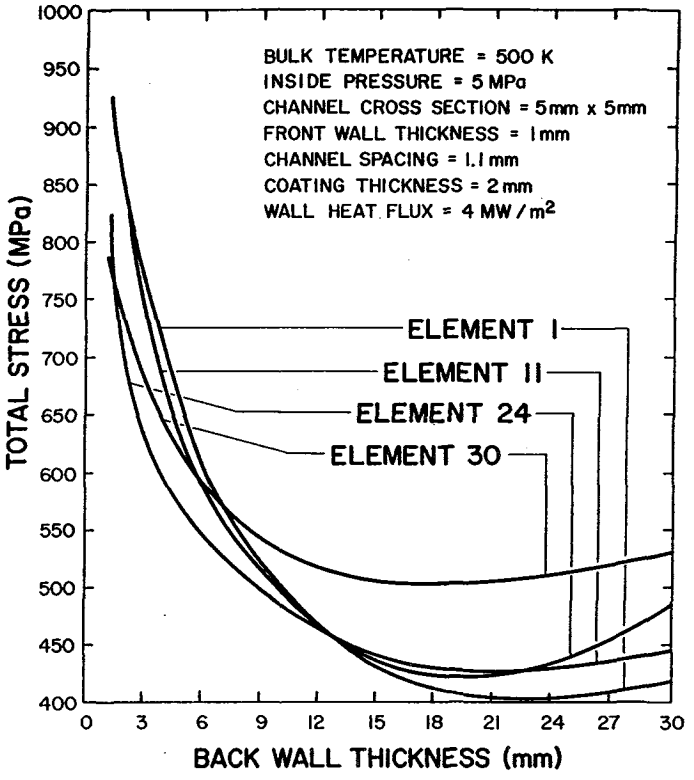
$$t_{fw} = 1 \text{ mm}; \; t_c = 2 \text{ mm} \quad \text{stress minimum at} \quad t_{bw} \simeq 7(t_{fw} + t_c)$$



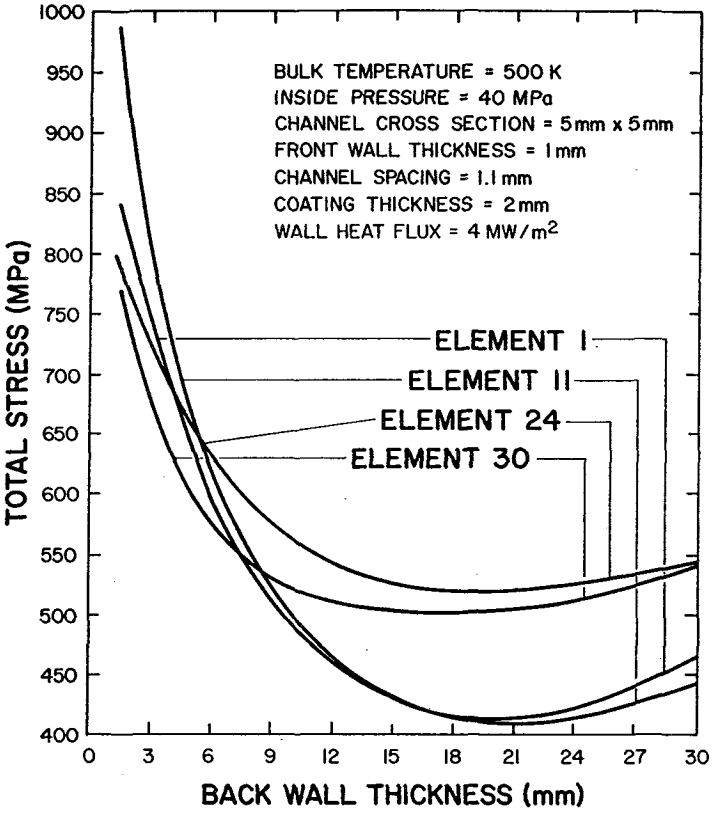
4.8-13 Variation of stresses with increasing back wall thickness



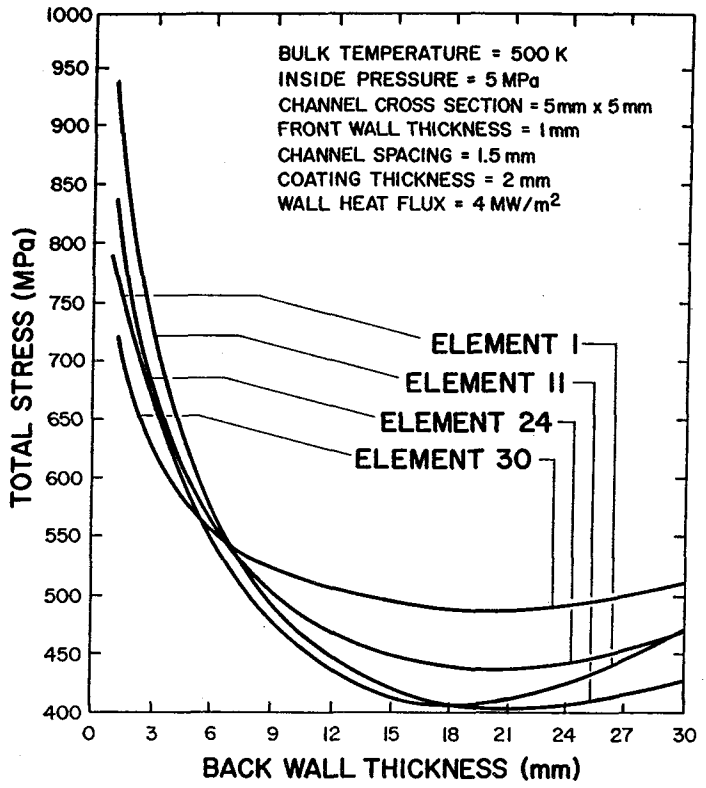
4.8-14 Variation of stresses with increasing back wall thickness



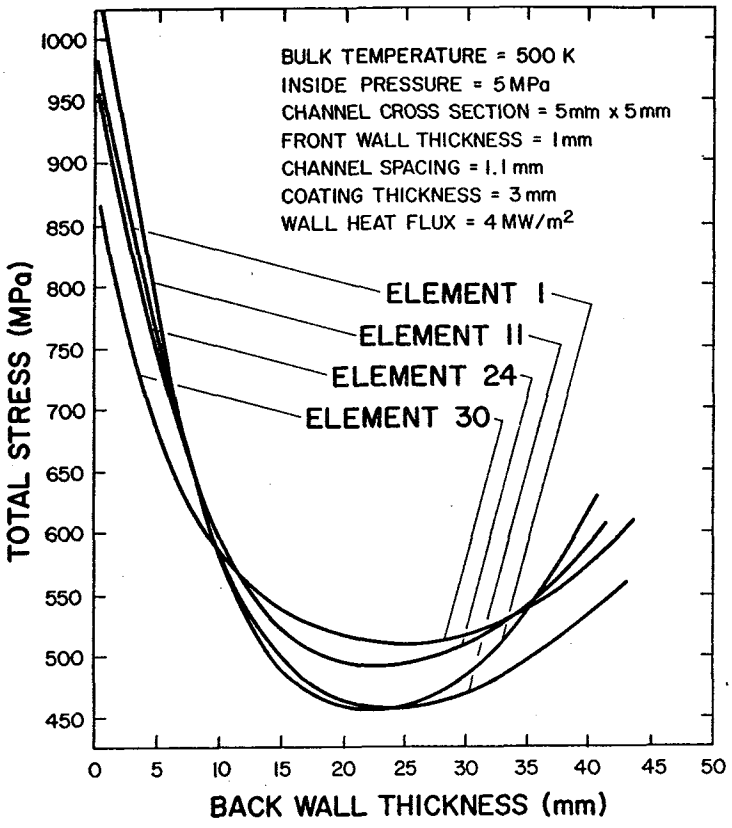
4.8-15 Variation of stresses with increasing back wall thickness



4.8-16 Variation of stresses with increasing back wall thickness



4.8-17 Variation of stresses with increasing back wall thickness



4.8-18 Variation of stresses with increasing back wall thickness

t_{fw} = 1 mm; t_c = 3 mm stress minimum at $t_{bw} \simeq 6\ (t_{fw} + t_c)$

t_{fw} = 1 mm; t_c = 6 mm stress minimum at $t_{bw} \simeq 5(t_{fw} + t_c)$

t_{fw} = 1 mm; t_c = 10 mm stress minimum at $t_{bw} \simeq 3(t_{fw} + t_c)$

After plotting this in Figure 4.8-19, we observed that for the following relationship

$$t_{bw} = m(t_{fw} + t_c)$$

'm' should observe

$$m = 8.5 - 1/2(t_{fw} + t_c)$$

This can be considered as a reasonable relationship to be observed in design calculations.

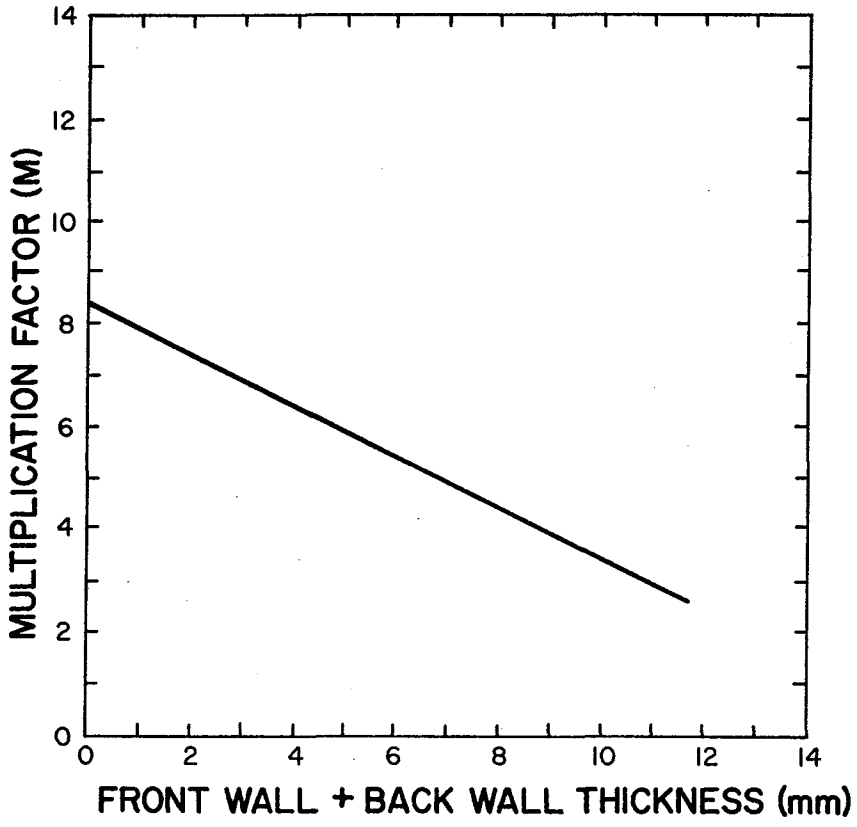


Figure 4.8-19 Multiplication factor vs. total front wall thickness

4.8.6.4 Defining Maximum Permissible Heat Flux for a Limiter Center Channel with Coating

Here we assumed that the square cross-sectional area we considered is still the most optimum choice and then calculated the maximum allowable heat flux. The coating was allowed to crack and a 3 Sm limit was observed only on the structure. Strong dependence on coating thickness and inside pressure was observed. Figures 4.8-20 and 4.8-21 show the details. Also, values of maximum allowable heat flux for closer spaced channels were higher.

4.8.6.5 Analysis of the Channel at the Leading Edge

Complete analyses of this channel have not been completed as yet, however, some preliminary calculations were done to obtain the design window for the limiter without coating. Thus, we shall not present any results for the leading channel in this report. However, we shall use the results of preliminary calculations to pick the channel dimensions.

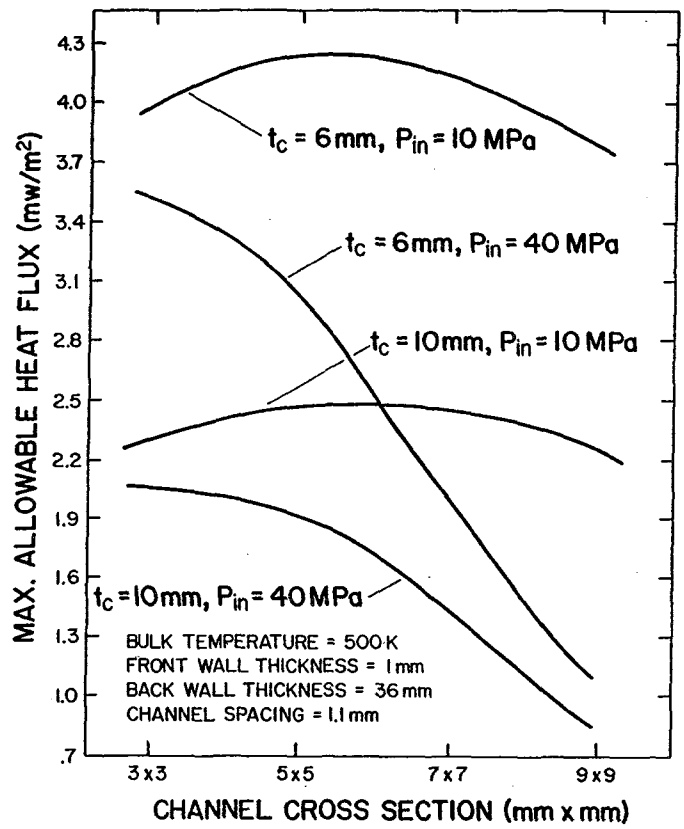


Figure 4.8-20 Maximum permissible heat flux for different cross-sectional areas

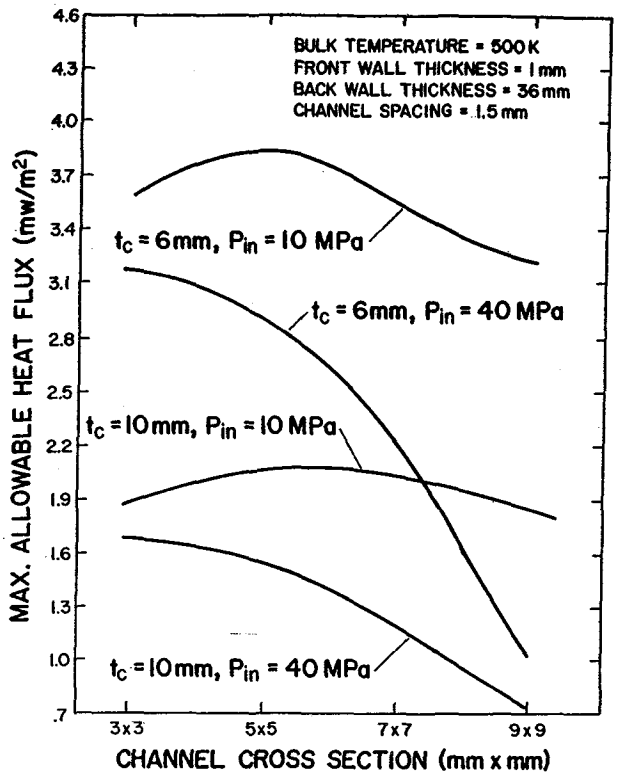


Figure 4.8-21 Maximum permissible heat flux for different cross-sectional areas

4.8.7 Design Window for Limiter Without Coating

Our work on the design window for a liquid metal cooled limiter is still in the development stages; therefore, we are presenting here the results which have been accomplished so far. To study the possibility of a design window for a limiter without coating, we chose the dimensions for the flat face channel and the leading channel as shown in Table 4.8-1. It has to be pointed out that the choice of dimensions has been made to comply with the other constraints, and these dimensions allow the flat face channel to take up to ~ 5 MW/m^2 and the leading channel to ~ 3 Mw/m^2. We would like to mention here that the channel dimensions can be changed to go towards better designs. However, the above choice necessarily fulfills our desire of understanding the limiter design on a general basis.

Choice of the dimension of the cooling channels essentially meant that once coolant velocity is chosen in the cooling channels, the total mass flow rate to the limiter can be determined. The determination of the mass flow rate would lead to a decision about wall thickness, cross-sectional area, and

Table 4.8-1 Dimensions of the Channels

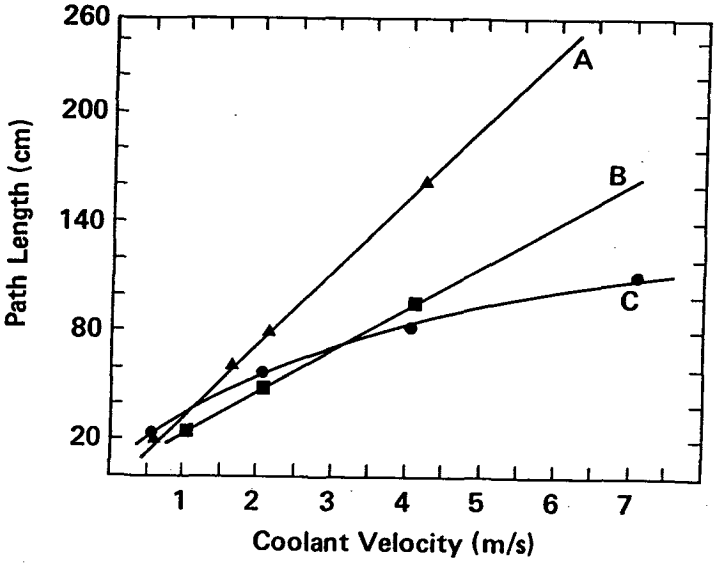
Center Channel	
PARAMETER	VALUE
Channel Width	12 mm
Channel Breadth	3 mm
Wall Thickness	1.2 mm
Channel Spacing	1.7 mm
Leading Channel	
PARAMETER	VALUE
Channel Width	12 mm
Channel Breadth	3 mm
Wall Thickness	1.2 mm
Channel Spacing	1 mm

coolant velocity in the manifolds and conduits once the hoop stress limit is applied. Here, because of the constraint of not excessively blocking the limiter slot (the space behind the limiter for pumping), an additional criterion was introduced to establish the viability of a particular design. This criterion is stated as:

The total length block by the feed pipes in the toroidal direction must be less than half the total toroidal length of the limiter.

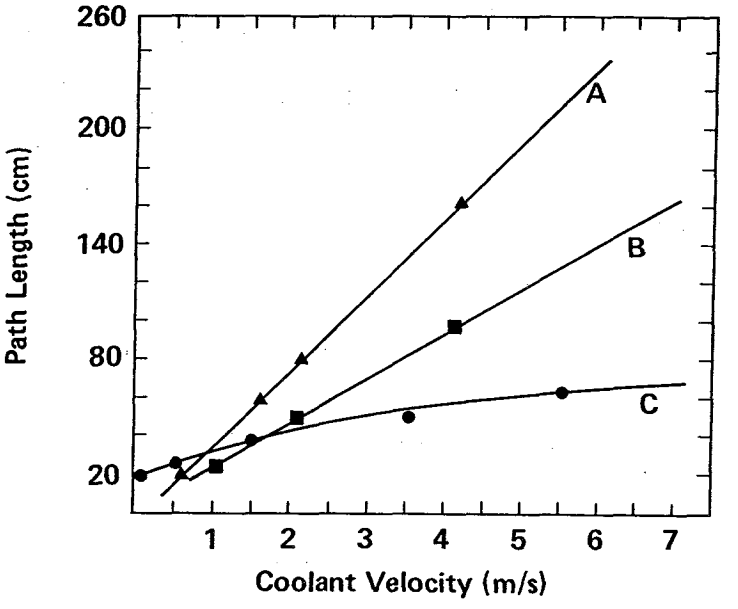
With this additional criterion in place there were three possibilities for the overall design, namely: 1) liquid metal cooled limiter using untapered, uninsulated conduits; 2) liquid metal cooled limiter using tapered conduits; 3) liquid metal cooled limiter using insulated conduits.

The effect of the above criterion on an uninsulated, untapered walled conduit design can be observed in Figure 4.8-22. It is a plot of path length versus coolant velocity in the cooling channels. As is obvious for a wall heat flux of 4 MW/m^2, it will be possible to satisfy the above criterion, although not for a wall heat flux of 5 MW/m^2. This can be seen from the plot, since, for coolant velocities up to 7-8 m/s, the maximum permissible path length does not exceed the minimum required path length. Above 7-8 m/s coolant velocity, the pipes get so thick that a design can be practically ruled out. This, however, does not occur for a design employing tapered conduits. For a coolant velocity of 5-6 m/s, the above mentioned criterion can be met for a wall heat flux of 5 MW/m^2. This can be observed in Figure 4.8-23.



A - Maximum permissible path length at 4 MW/m^2 heat flux
B - Maximum permissible path length at 5 MW/m^2 heat flux
C - Half of minimum required path length

Figure 4.8-22 Design margin with untapered conduits at 4 and 5 MW/m^2 heat flux



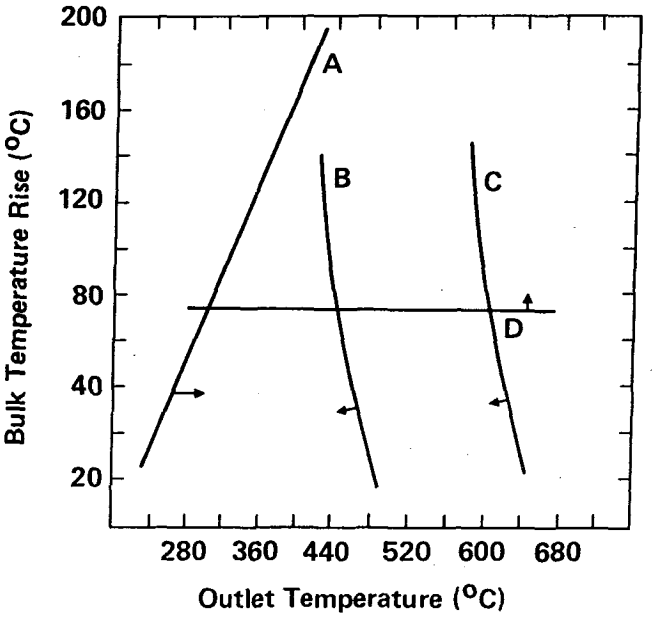
A - Maximum permissible path length at 4 MW/m^2 heat flux

B - Maximum permissible path length at 5 MW/m^2 heat flux

C - Half of minimum required path length

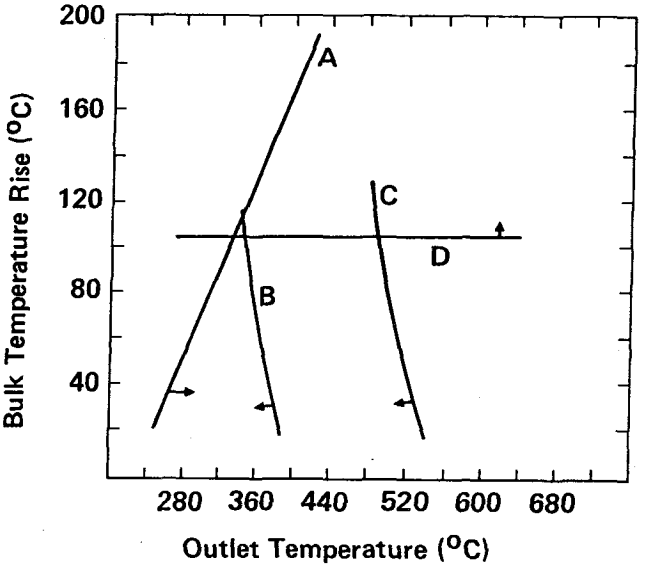
Figure 4.8-23 Design margin with tapered conduit at 4 and 5 MW/m^2 heat flux

The overall design, with all limits in place, was considered for the cases with tapered and insulated conduits. The design window obtained for these cases is shown in Figures 4.8-24 through 4.8-27. It exists for both the cases, however decreases considerably for a increase in wall heat flux from 4-5 MW/m^2. It is also observed that the design window for a design employing tapered conduits, at 5 MW/m^2 is very narrow, which essentially means that it will be possible to have a design, but without much flexibility in operation. Also noted is that a design employing insulated conduits appears to be the most attractive if insulators can be developed for the harsh radiation and corrosive environment.



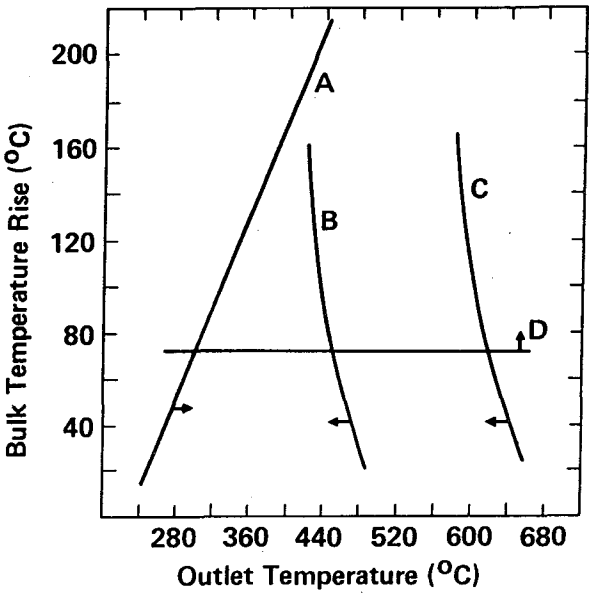
A - Minimum inlet temperature limit
B - Maximum structure temperature limit
C - Maximum interface temperature limit
D - Maximum primary stress limit

Figure 4.8-24 Design window with tapered conduit at 4 MW/m^2 heat flux



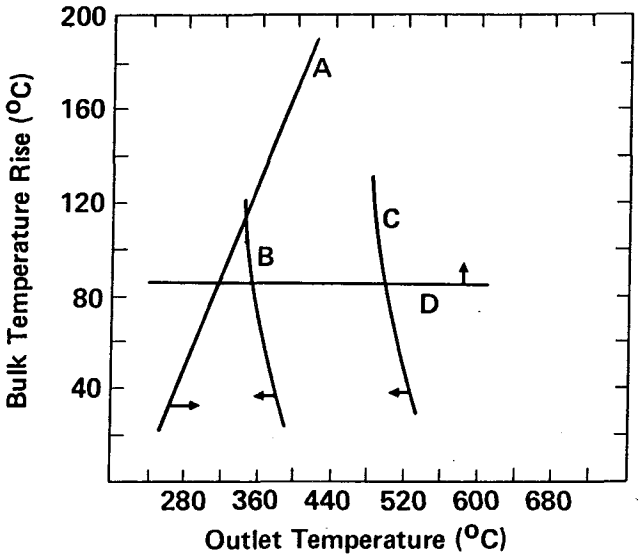
A - Minimum inlet temperature limit
B - Maximum structure temperature limit
C - Maximum interface temperature limit
D - Maximum primary stress limit

Figure 4.8-25 Design window with tapered conduit at 5 MW/m^2 heat flux



A - Minimum inlet temperature limit
B - Maximum structure temperature limit
C - Maximum interface temperature limit
D - Maximum primary stress limit

Figure 4.8-26 Design window with insulated conduit at 4 MW/m^2 heat flux



A - Minimum inlet temperature limit
B - Maximum structure temperature limit
C - Maximum interface temperature limit
D - Maximum primary stress limit

Figure 4.8-27 Design window with insulated conduit at 5 MW/m^2 heat flux

4.9 Thermal and Stress Analysis of Limiters

4.9.1 Introduction

Problems in the design of pump limiters arise from the presence of high particle and heat fluxes. Limiters are designed with optimum thickness to withstand erosion caused by the high particle flux and to minimize thermal and mechanical stresses caused by the high heat flux.

In the present section, thermal and stress analyses of the limiter are considered in detail. The thermal analysis considers the temperature distribution in an elemental section of the limiter for given wall heat fluxes. These temperatures are then used to calculate the stress distribution in the limiter section. Previous studies of the limiter, e.g., BCSS[6], calculated thermal and mechanical stresses using the finite element code, ANSYS. Two-dimensional stress calculations usually give lower stress predictions. Therefore, there is a need for three-dimensional stress calculations. A three-dimensional finite element code was developed to calculate thermal and mechanical stresses caused by temperature difference and coolant pressure. The limiter considered is similar to that of the INTOR[88] water cooled design. However, different limiters with different geometries can also be studied using this model.

4.9.2 Geometric Configuration

The geometric configuration of the limiter chosen for the present analysis is shown in Figure 4.9-1. It is curved and double-edged, with one inlet and two outlet feed pipes. The limiter is divided into many modules and extends toroidally around the entire plasma chamber. Coolant enters a limiter module through an inlet conduit at the center of the module and runs through narrow cooling channels along the face of the limiter in the toroidal direction, terminating at the outlet manifold.

The limiter is assumed to be made entirely of a single material. Copper and vanadium alloy were the two materials chosen. Water is assumed to be the coolant for the copper limiter, and lithium is the coolant for the vanadium limiter. The absence of coating in the present analysis gives conservative estimates for maximum surface temperature and stresses. However, different materials representing a protective tile on substrate can be included in the

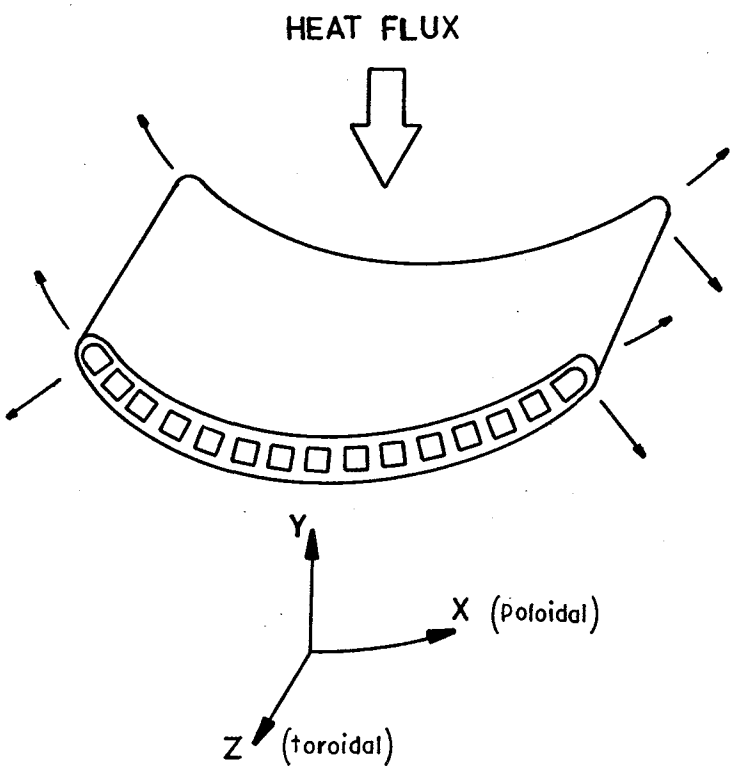


Figure 4.9-1 Geometric configuration of the limiter

present analysis.

Figure 4.9-2 shows a section of the limiter chosen for the analysis. Coolant flows along the z-direction through the duct cross-section, ABCD. The surface EFE'F' faces the plasma. The planes EE'H'H and FF'G'G are symmetrical planes in the x-direction.

4.9.3 Mathematical Formulation

The equations used to calculate the thermal and mechanical stresses are described, along with the method of solution.

4.9.3.1 Thermal Analysis

The critical area in the limiter is the top surface which is exposed to high surface heat fluxes. In order to perform thermal-hydraulic calculations, the heat flux distribution along the surface of the limiter must be provided (from plasma engineering calculations). For the curved double-edged limiter, the surface heat flux distribution is assumed to be constant (up to 10 MW/m^2)

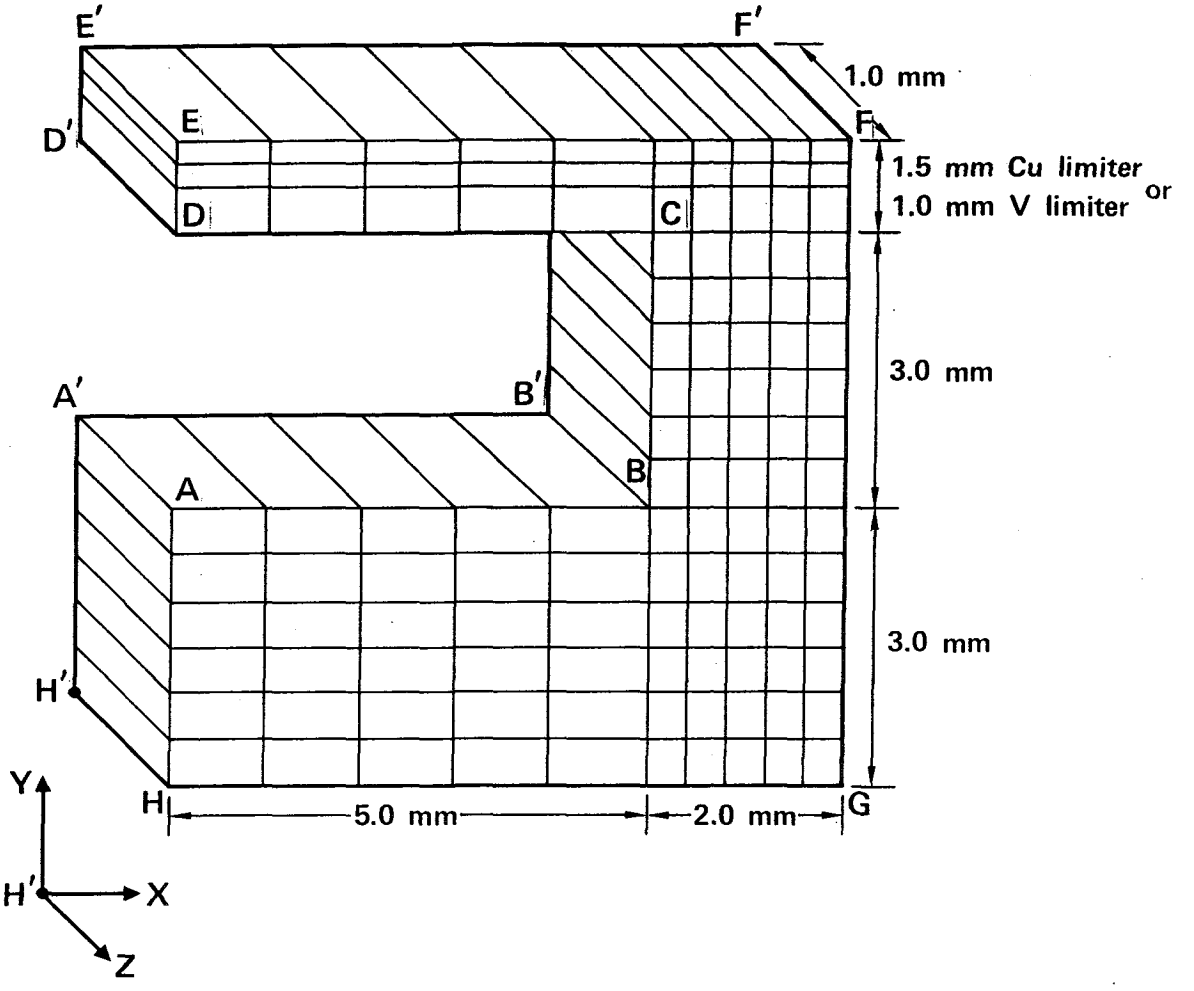


Figure 4.9-2 Three-dimensional mesh of a limiter specimen

along the top surface. Plasma engineering calculations indicate that the surface heat flux decreases gradually from the mid-plane to the beginning of the leading edge.

Thus, using a uniform surface heat flux along the top surface would provide conservative temperature distribution in the vertical direction where temperature gradients are much higher than those in the horizontal direction. As shown in Fig. 4.9-1, the elemental section of the limiter considered is at the mid-plane along the z-direction. Therefore, only two-dimensional (x-y) temperature distribution is required.

The basic equation to solve for the temperature distribution in the x-y plane is the energy equation:

$$K\left(\frac{\partial^2 T}{\partial x^2} + \frac{\partial^2 T}{\partial y^2}\right) + q = 0 \qquad (4\text{-}230)$$

where K = thermal conductivity,

T = temperature, and

q = volumetric heating rate.

Equation (4-230) was solved using the weighted residual method. The boundary conditions at the top surface are;

$$K \frac{\partial T}{\partial n} = q'',$$

where q'' is the wall heat flux, and n is the outward normal direction. The other boundary condition is at the structure-coolant interface;

$$K \frac{\partial T}{\partial n} = h\ (T-T_b)\ ,$$

where h is the heat transfer coefficient and T_b the coolant bulk temperature.

4.9.3.2 Stress Analysis

The relationships between stresses and strains are expressed in terms of constitutive equations. For an elastic solid, the strains can be defined as:

$$\text{direct strain:}\quad e_{xx} = \frac{\partial u}{\partial x},\ e_{yy} = \frac{\partial v}{\partial y} \text{ and } e_{zz} = \frac{\partial w}{\partial z} \tag{4-231}$$

$$\text{shear strain:}\quad e_{xy} = e_{yx} = \frac{\partial u}{\partial y} + \frac{\partial v}{\partial x} \tag{4-232}$$

$$e_{yz} = e_{zy} = \frac{\partial v}{\partial z} + \frac{\partial w}{\partial y} \tag{4-233}$$

$$e_{zx} = e_{xz} = \frac{\partial w}{\partial x} + \frac{\partial u}{\partial z} \tag{4-234}$$

where u, v and w are the components of displacement in x, y and z directions, respectively. In the present limiter stress analysis, the strains are produced both by the application of stress (coolant pressure) and by raising the temperature (surface heat flux).

The stress-strain relationship can be written as:

$$e_{xx} = \frac{1}{E}\left[\sigma_{xx} - \nu(\sigma_{yy} + \sigma_{zz})\right] + \alpha\Delta T \tag{4-235}$$

$$e_{yy} = \frac{1}{E}\left[\sigma_{yy} - \nu(\sigma_{zz} + \sigma_{xx})\right] + \alpha\Delta T \tag{4-236}$$

$$e_{zz} = \frac{1}{E}\left[\sigma_{zz} - \nu(\sigma_{xx} + \sigma_{yy})\right] + \alpha\Delta T \tag{4-237}$$

$$e_{xy} = \frac{2(1 + \nu)}{E}\sigma_{xy} \tag{4-238}$$

$$e_{yz} = \frac{2(1 + \nu)}{E}\sigma_{yz} \tag{4-239}$$

$$e_{zx} = \frac{2(1 + \nu)}{E}\sigma_{zx} \tag{4-240}$$

where σ_{xx}, σ_{yy} and σ_{zz} are direct stresses in x, y and z directions, respectively. σ_{xy}, σ_{yz} and σ_{zx} are shear stress components. E is the Young's modulus, ν is the Poisson ratio, α is the coefficient of thermal expansion and ΔT is the temperature rise.

Equations (235)-(240) can be rearranged in the following matrix form:

$$\begin{bmatrix} \sigma_{xx} \\ \sigma_{yy} \\ \sigma_{zz} \\ \sigma_{xy} \\ \sigma_{yz} \\ \sigma_{zx} \end{bmatrix} = \begin{bmatrix} d_1 & d_2 & d_2 & 0 & 0 & 0 \\ d_2 & d_1 & d_2 & 0 & 0 & 0 \\ d_2 & d_2 & d_1 & 0 & 0 & 0 \\ 0 & 0 & 0 & G & 0 & 0 \\ 0 & 0 & 0 & 0 & G & 0 \\ 0 & 0 & 0 & 0 & 0 & G \end{bmatrix} \begin{bmatrix} e_{xx} - \alpha\Delta T \\ e_{yy} - \alpha\Delta T \\ e_{zz} - \alpha\Delta T \\ e_{xy} \\ e_{yz} \\ e_{zx} \end{bmatrix} \tag{4-241}$$

$$\{\sigma\} = [D]\{e_t\}$$

where $d_1 = \frac{E(1 - \nu)}{(1 + \nu)(1 - 2\nu)}$, $d_2 = \frac{E\nu}{(1 + \nu)(1 - 2\nu)}$ and G = shear modulus = $\frac{E}{2(1 + \nu)}$.

Energy Principle

The strain energy potential U is given by:

$$U = \tfrac{1}{2}\iiint\left(e_{xx}\sigma_{xx} + e_{yy}\sigma_{yy} + e_{zz}\sigma_{zz} + e_{xy}\sigma_{xy} + e_{yz}\sigma_{yz} + e_{zx}\sigma_{zx}\right)dV \tag{4-242}$$

The potential energy of the external forces in the deformed configuration is defined as:

$$W = \iiint (ufx + vfy + wfz)\, dV \qquad (4\text{-}243)$$

where fx, fy, and fz are external forces in the x, y and z directions.

The total potential energy (ϕ) is defined as:

$$\phi = U - W \qquad (4\text{-}244)$$

Solutions are obtained by minimizing the total potential energy ϕ.

Finite Element Procedure

The finite element solution procedure can be summarized in the following steps:

1) The continuum is divided into three-dimensional finite elements, which are separated by straight lines.
2) The elements are assumed to be inter-connected at a discrete number of nodal points at element corners.
3) A shape function is chosen to represent any variations within each element. The following functions are used in the calculations:

$N_1 = (1 - \xi)(1 - \eta)(1 - \zeta)$

$N_2 = \xi(1 - \eta)(1 - \zeta)$

$N_3 = \xi\eta(1 - \zeta)$

$N_4 = (1 - \xi)\eta(1 - \zeta)$

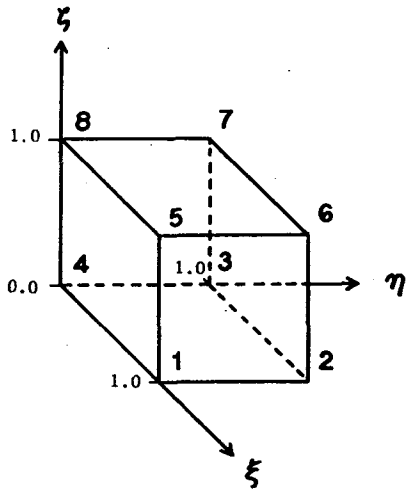
$N_5 = (1 - \xi)(1 - \eta)\zeta$

$N_6 = \xi(1 - \eta)\zeta$

$N_7 = \xi\eta\zeta$

$N_8 = (1 - \xi)\eta\zeta$

where ξ, η and ζ are variables of the local coordinate system shown below.



4) The x-displacement can be represented in each element by:

$$u = u_1 N_1 + u_2 N_2 + \ldots\ldots + u_8 N_8$$

where u_i is x-displacement at node i.

5) The strains are obtained by making appropriate differentiations of the displacement with respect to the relevant coordinate variable x, y and z.

$$\begin{bmatrix} e_{xx} \\ e_{yy} \\ e_{zz} \\ e_{xy} \\ e_{yz} \\ e_{zx} \end{bmatrix} = \begin{bmatrix} \frac{\partial N_1}{\partial x} & 0 & 0 & \cdots & \frac{\partial N_8}{\partial x} & 0 & 0 \\ 0 & \frac{\partial N_1}{\partial y} & 0 & \cdots & 0 & \frac{\partial N_8}{\partial y} & 0 \\ 0 & 0 & \frac{\partial N_1}{\partial z} & \cdots & 0 & 0 & \frac{\partial N_8}{\partial z} \\ \frac{\partial N_1}{\partial y} & \frac{\partial N_1}{\partial x} & 0 & \cdots & \frac{\partial N_8}{\partial y} & \frac{\partial N_8}{\partial x} & 0 \\ 0 & \frac{\partial N_1}{\partial z} & \frac{\partial N_1}{\partial y} & \cdots & 0 & \frac{\partial N_8}{\partial z} & \frac{\partial N_8}{\partial y} \\ \frac{\partial N_1}{\partial z} & 0 & \frac{\partial N_1}{\partial x} & \cdots & \frac{\partial N_8}{\partial z} & 0 & \frac{\partial N_8}{\partial x} \end{bmatrix} \begin{bmatrix} u_1 \\ v_1 \\ w_1 \\ u_2 \\ v_2 \\ w_2 \\ \vdots \\ u_8 \\ v_8 \\ w_8 \end{bmatrix}$$

$$\{e\} = [B]\{u\} \qquad (4\text{-}245)$$

where [B] is the strain matrix.

6) The stresses are related to the displacements by substituting into Eq. (4-241).

$$\{\sigma\} = [D][B]\{u\} \qquad (4\text{-}246)$$

7) The strain energy is given by:

$$u = \frac{1}{2}\iiint \{e\}^T\{\sigma\}\, dV$$

$$= \frac{1}{2}\iiint \{u\}^T[B]^T[D][B]\{u\}\, dV$$

$$= \frac{1}{2}\{u\}^T[K]\{u\}$$

in which the stiffness matrix [K] is given by:

$$[K] = \iiint [B]^T [D] [B] \, dV$$

8) The potential energy due to distributed loads $\{f\}$ can be written as:

$$W = \iiint \left(\sum_{i=1}^{8} u_i N_i \, fx + \sum_{i=1}^{8} vi \, N_i \, fy + \sum_{i=1}^{8} wi \, N_i \, fz \right) dV$$

$$= \sum_{i=1}^{8} u_i \iiint N_i \, fx \, dV + \sum_{i=1}^{8} vi \iiint N_i \, fy \, dV$$

$$+ \sum_{i=1}^{8} wi \iiint N_i \, fz \, dV$$

where

$$fx_i = \iiint N_i \, fx \, dV$$
$$fy_i = \iiint N_i \, fy \, dV$$
$$fz_i = \iiint N_i \, fz \, dV$$

$$\{f\} = \begin{bmatrix} fx_1 \\ fy_1 \\ \vdots \\ fz_8 \end{bmatrix}$$

then

$$W = \{u\}^T \{f\}$$

9) From Eq. (4-244) the total potential energy ϕ is given by:

$$\phi = u - W \qquad (4\text{-}247)$$
$$= \frac{1}{2} \{u\}^T [K] \{u\} - \{u\}^T \{f\}$$

10) The minimization procedure requires that

$$\left\{ \frac{\partial \phi}{\partial \{u\}} \right\} = 0$$

which yields the following equation:

$$[K] \{u\} = \{f\} \qquad (4\text{-}248)$$

Thermal Expansion

Thermal expansion in each element is given by equivalent nodal forces shown in Fig. 4.9-3 below. The temperature in the element is assumed uniform.

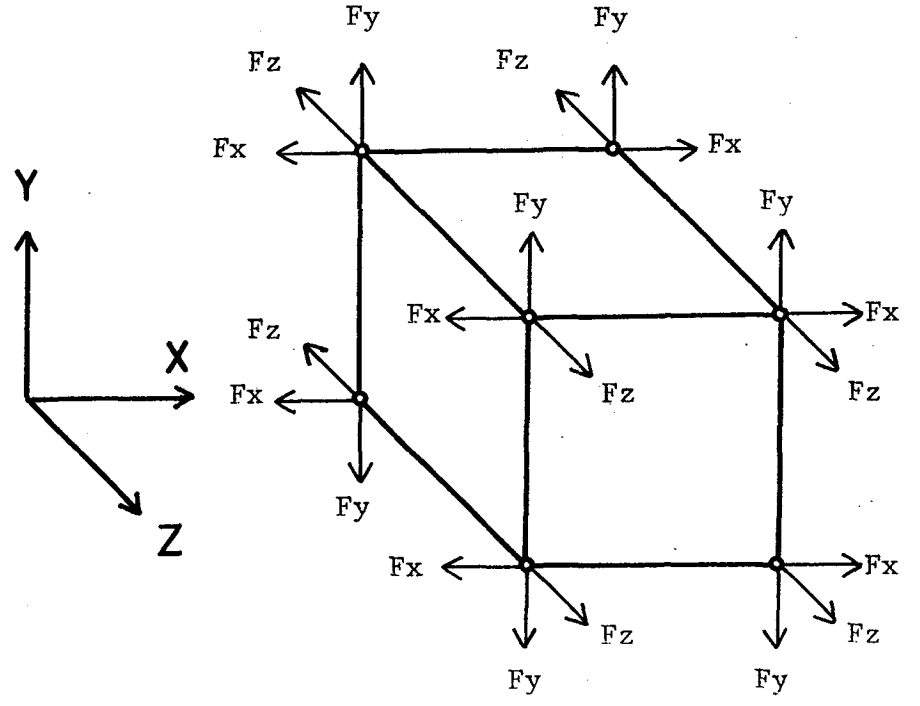


Figure 4.9-3 Equivalent nodal forces on an element

The strains produced by temperature rise are given by:

$$e_{xx} = \alpha\Delta T \qquad e_{yy} = \alpha\Delta T \qquad e_{zz} = \alpha\Delta T$$

The equivalent pressure, P, is given by:

$$-P = K(e_{xx} + e_{yy} + e_{zz}) = \frac{E}{3(1-2\nu)}\, 3\, \alpha\Delta T = \frac{E\alpha\Delta T}{1-2\nu}$$

where K = the bulk modulus $= \frac{E}{3(1-2\nu)}$

The equivalent nodal forces are then given by:

$$Fx = -P\ \Delta y\Delta z/4 = \frac{E\alpha\Delta T}{4(1-2\nu)}\ \Delta y\Delta z$$

$$Fy = -P\ \Delta z\Delta x/4 = \frac{E\alpha\Delta T}{4(1-2\nu)}\ \Delta z\Delta x$$

$$Fz = -P\ \Delta x\Delta y/4 = \frac{E\alpha\Delta T}{4(1-2\nu)}\ \Delta x\Delta y$$

4.9.3.3 Boundary Conditions

The following assumptions were used in the present analysis:

1) The boundary plane A`B`C`D`E`F`G`H` is fixed at Z = 0. The opposite boundary plane ABCDEFGH is constrained to be flat after deformation. This assumption is reasonable since temperature variations in the z-direction are negligible.
2) The specimen boundary plane FF'G'G is also constrained to be flat after deformation. This is reasonable since the heat flux does not vary sharply in the x-direction. If the heat flux in the x-direction does vary sharply, then a larger specimen region is needed for modeling.

Different kinds of possible deformation are shown in Figure 4.9-4. Case A represents uniform thermal expansion or translation in the x-direction with flat y-z planes. Case B represents a non-uniform thermal expansion in the x-

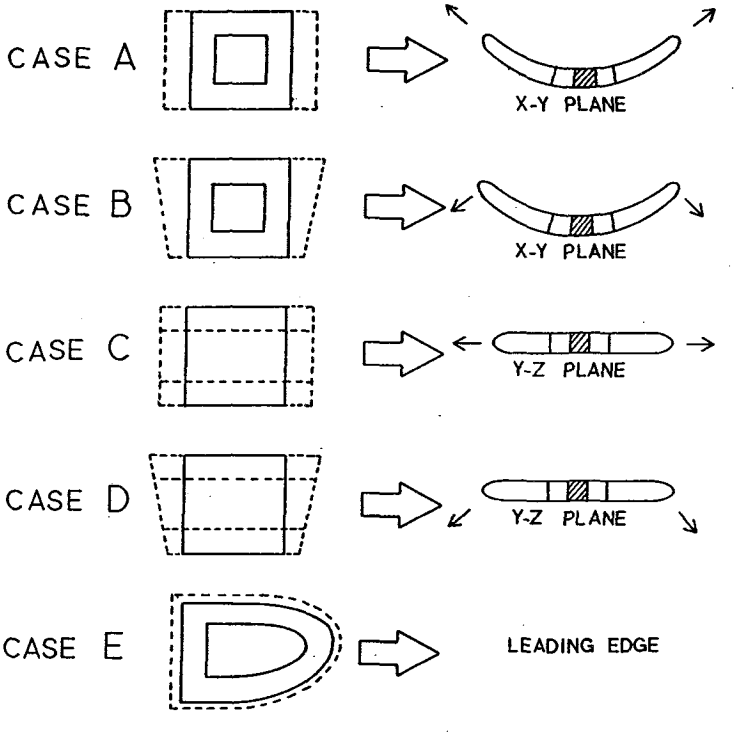


Figure 4.9-4 Different possible deformations of the limiter element

direction. Case C represents uniform thermal expansion in the z-direction. Case D represents non-uniform thermal expansion in the z-direction. Case E represents the leading edge free stress boundary.

Thermal stresses are usually affected by the constraints imposed on the limiter. Fewer constraints usually lead to lower thermal stresses. In the present analysis, Case A is considered because of the importance of curvature in the x-direction. Case D, which has less constraints in the z-direction than Case C, is also considered. Case E, representing the leading edge which has low thermal stresses due to free surface boundary was not considered in the present preliminary analysis. Further studies are being conducted to include the leading edge in the analysis.

Figure 4.9-5 shows a model of a section of the limiter blade. The limiter is assumed to be composed of a large number of identical sections. Boundary conditions arising from the contact with neighboring sections impose geometric constraints on the displacements. Referring to Fig. 4.9-5, each node is free to translate in the z-direction, but rotation about the x-axis is

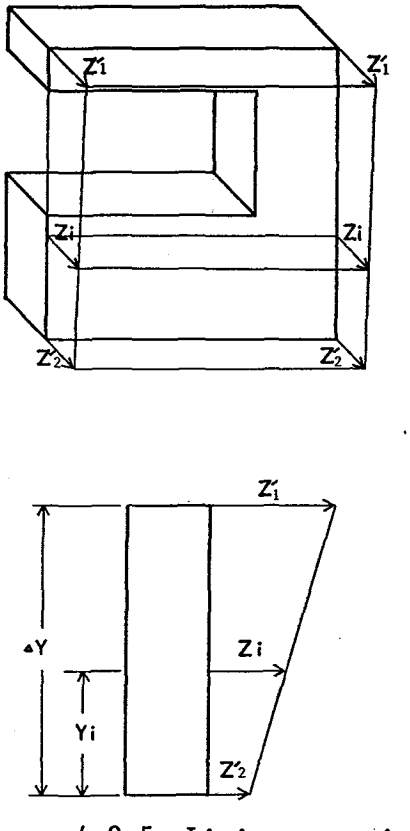


Figure 4.9-5 Limiter section

constrained to a constant value in any x-y plane. In other words, each point in a given x-y plane remains in a single plane after deformation.

The z-deflections for the nodes in any x-y plane can thus be determined from only two unknowns, z_1' and z_2', which represent the positions of the top and bottom points in the plane after deformation. The z position at any node in a given x-y plane is:

$$z_i = \frac{y_i}{\Delta y} z_1' + \frac{(\Delta y - y_i)}{\Delta y} z_2' \tag{4-249}$$

where y_i refers to the location of node i and Δy is the total height of the section. Equation (4-249) can be rewritten as:

$$z_i = \alpha_i z_1' + \beta_i z_2' \tag{4-250}$$

where $\alpha_i + \beta_i = 1$. Applying Eq. (4-250) to a single x-y plane gives a matrix equation for z, the displacement vector:

$$\{z\} = \begin{Bmatrix} z_1 \\ z_2 \\ \cdot \\ \cdot \\ \cdot \\ z_n \end{Bmatrix} = \begin{Bmatrix} \alpha_1 z_1' + \beta_1 z_2' \\ \alpha_2 z_1' + \beta_2 z_2' \\ \cdot \\ \cdot \\ \cdot \\ \alpha_n z_1' + \beta_n z'_2 \end{Bmatrix} = \begin{bmatrix} \alpha_1 & \beta_1 \\ \alpha_2 & \beta_2 \\ \cdot & \cdot \\ \cdot & \cdot \\ \alpha_n & \beta_n \end{bmatrix} \begin{Bmatrix} z_1' \\ z_2' \end{Bmatrix} = [\,[\alpha\,],\ [\beta\,]] \begin{Bmatrix} z_1' \\ z_2' \end{Bmatrix} \tag{4-251}$$

This system of constraints can be applied to the global system of equations to reduce the degrees of freedom in the z-direction to two. The global system is given by:

$$\frac{\partial \phi}{\partial \{u\}} = \begin{bmatrix} [ka] & [kb] \\ [kb]^T & [kc] \end{bmatrix} \begin{Bmatrix} x_1 \\ y_1 \\ z_1 \end{Bmatrix} + \begin{Bmatrix} fx_1 \\ fy_1 \\ fz_1 \end{Bmatrix} \tag{4-252}$$

where $\{u\} = \{x_1 \ldots, y_1 \ldots, z_1 \ldots\}$. Combining (4-251) and (4-252) yields the reduced system:

$$\frac{\partial\phi}{\partial\{u'\}} = \left\{\begin{array}{c|cc} [ka] & [kb] & [\alpha\beta] \\ \hline [\alpha\beta]^T\ [kb]^T & \begin{matrix}[\alpha]^T [kc] [\alpha] & [\alpha]^T [kc] [\beta] \\ [\beta]^T [kc] [\alpha] & [\beta]^T [kc] [\beta]\end{matrix} & \end{array}\right\} \left\{\begin{matrix} x_1 \\ y_1 \\ z'_1 \\ z'_2 \end{matrix}\right\} + \left\{\begin{matrix} fx_i \\ fy_i \\ [\alpha]^T \{fz_i\} \\ [\beta]^T \{fz_i\} \end{matrix}\right\} \tag{4-253}$$

where $\{u'\} = \{x_1 \ldots, y_1 \ldots, z'_1, z'_2\}$. The same boundary conditions are applied in the FF'G'G plane. A particular choice of boundary condition is $x'_1 = x'_2$, or equal x-displacements throughout a y-z plane. This condition can be applied to Eq. (4-253) without loss of symmetry in the matrix by adding the following 2x2 matrix to the lower right hand corner of the stiffness matrix in Eq. (4-253):

$$\begin{vmatrix} C & -C \\ -C & C \end{vmatrix}$$

where C is a large number. This procedure forces the condition $x'_1 = x'_2$.

4.9.4 Results

Given the coolant pressure and temperature, the values of heat transfer coefficients chosen for water coolant at 100 °C and 200 °C were 5.0×10^4 W/m^2 °K and 6.4×10^4 W/m^2 °K, respectively. For lithium coolant at 230 °C, the heat transfer coefficient used was 7.5×10^4 W/m^2 °K. The heat flux distribution on the first wall must be provided. Variable heat fluxes were considered up to 10 MW/m^2. Calculations then proceed by first calculating the temperature distribution in the x-y plane. Assuming a constant heat flux in the x-z plane, then a 2-D temperature distribution is required.

Figure 4.9-6 shows the maximum temperature obtained for different wall heat fluxes. The limiter is made of copper with water coolant at two different temperatures. The maximum temperature increases linearly with increasing wall heat flux. Figure 4.9-7 shows the maximum primary stress obtained due to coolant pressure alone (i.e., with no heat flux at the top surface). For water coolant under different driving pressures, the point of maximum stress intensity occurs at a mid-point between E and E'. The Sm limit (Sm = 2/3 yield stress) of about 40 MPa is obtained at a coolant pressure of about 3.7 MPa. Then, using coolant pressure below 3.7 MPa, both thermal and primary

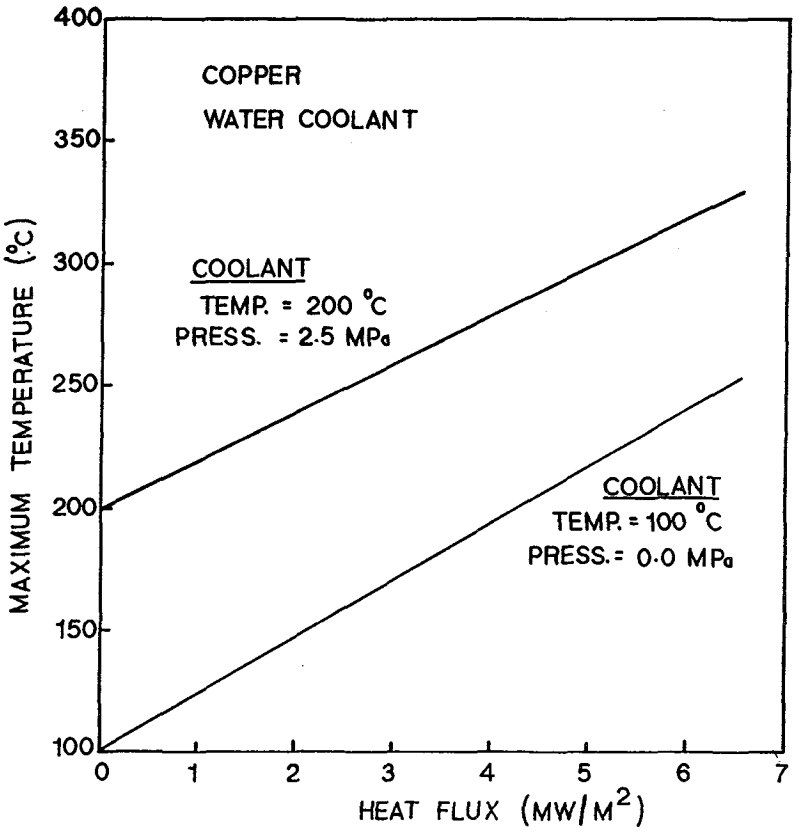


Figure 4.9-6 Maximum temperature at the limiter surface vs. wall heat flux

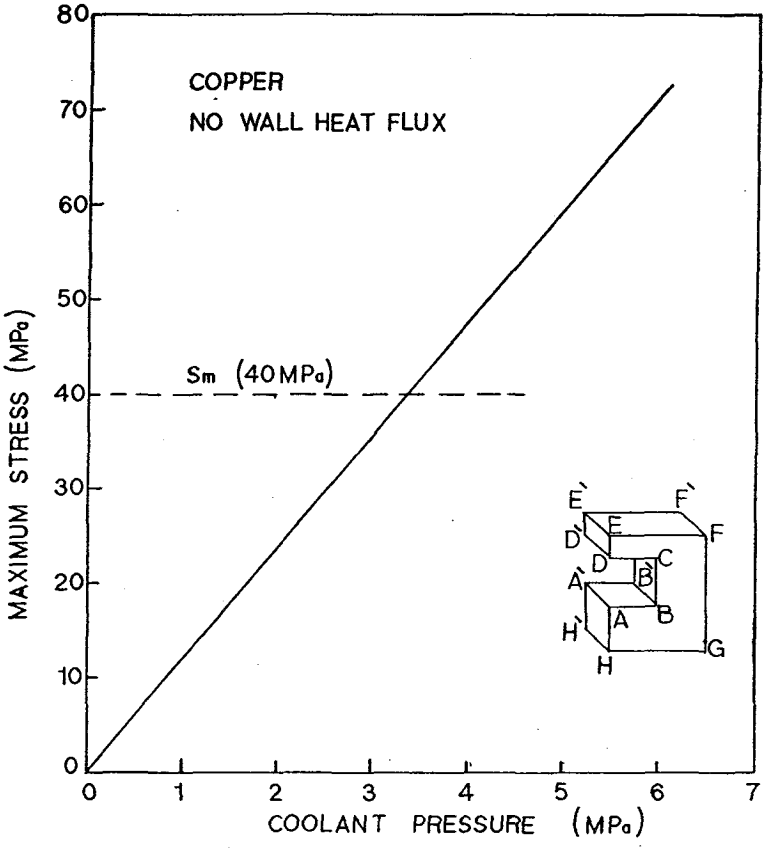


Figure 4.9-7 Maximum primary stresses vs. water coolant pressure

stresses are considered next. Figure 4.9-8 shows the maximum stress obtained for different wall heat fluxes and different coolant pressures. Maximum stress increases almost linearly with the wall heat flux. However, lower stresses are obtained with lower coolant pressures at low wall heat fluxes, since the primary stresses due to coolant pressure dominate. As the wall heat flux increases, thermal stresses become important and coolant pressure effects are reduced. The 3 Sm limit for copper, as shown in the figure, is obtained at a wall flux of about 5.2 MW/m^2.

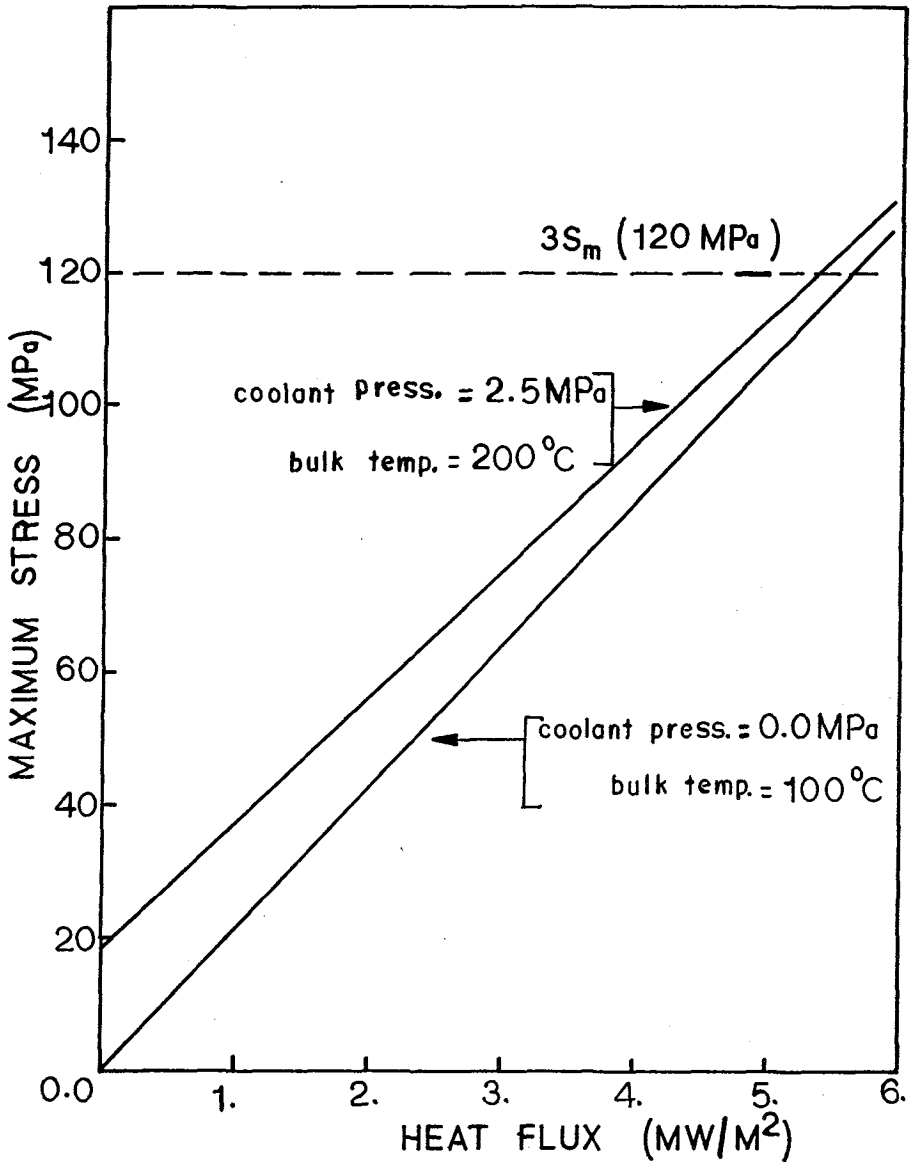


Figure 4.9-8 Maximum stress on the surface of a copper limiter vs. wall heat flux

Next, a vanadium alloy limiter is considered. Figure 4.9-9 shows the maximum temperature obtained for different wall heat fluxes. The coolant is liquid lithium at 230 °C and pressure of 5.5 MPa. The maximum temperature is obtained at point E. For vanadium alloys, the line of maximum allowable temperature is indicated (750 °C). The temperature requirement is easily satisfied, as long as the surface heat flux is below ~ 6.0 MW/m^2. Figure 4.9-10 shows the maximum primary stress obtained at zero wall heat flux for different coolant pressures. The maximum stress increases linearly with coolant pressure and the Sm limit (~ 187 MPa) is obtained at about 8.0 MPa coolant pressure. Figure 4.9-11 shows the maximum stress due to thermal and primary stresses. It can be seen that the 3 Sm stress requirement is satisfied easily, as long as the surface heat flux is below about 8 MW/m^2.

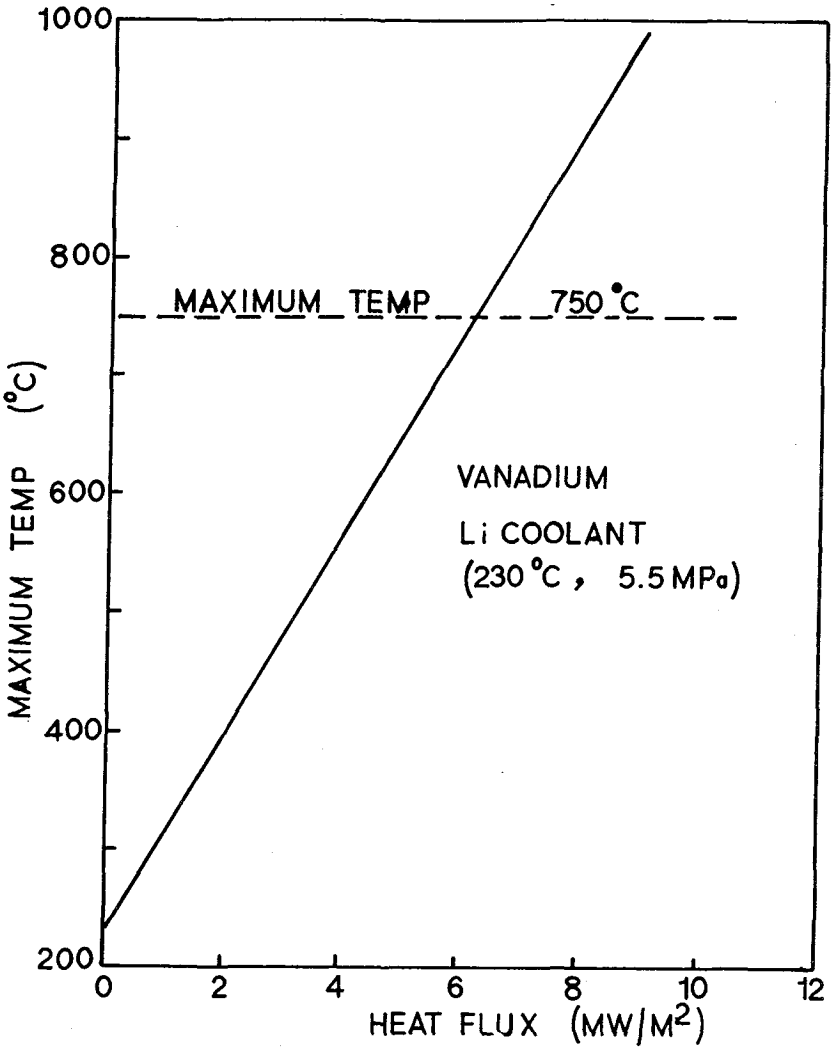


Figure 4.9-9 Maximum surface temperature vs. wall heat flux for a vanadium limiter

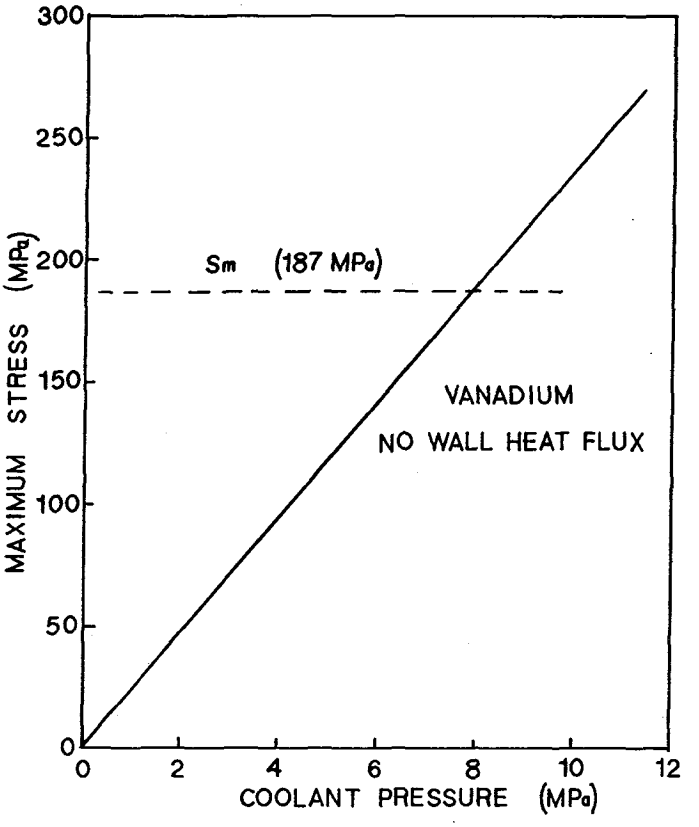


Figure 4.9-10 Maximum primary stress on the surface of vanadium limiter vs. Li coolant pressure

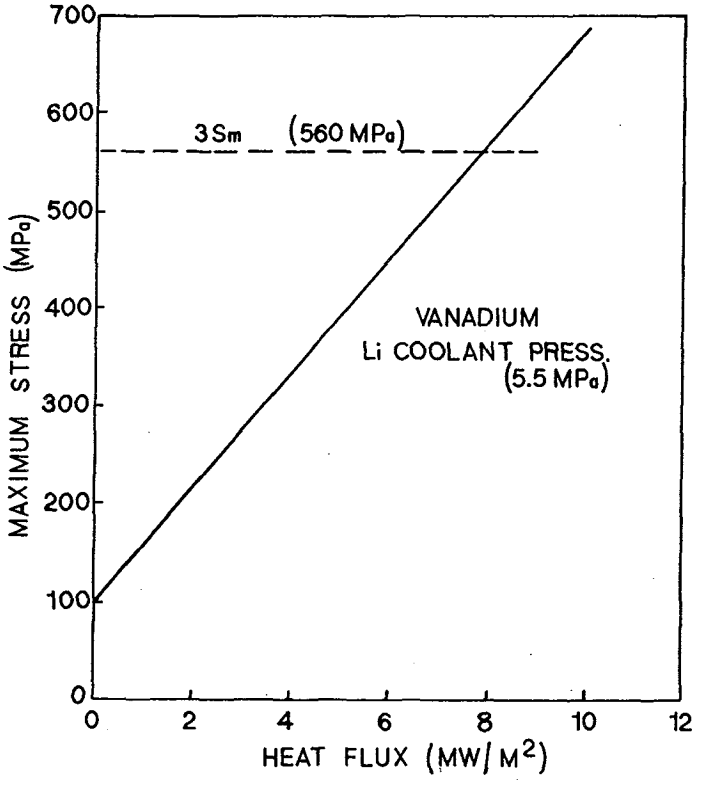


Figure 4.9-11 Maximum stress for a vanadium limiter vs. wall heat flux

Figure 4.9-12 shows the x-y temperature distribution in the vanadium alloy limiter for a wall heat flux of 6.0 MW/m^2. Figure 4.9-13 shows the stress intensity σ_{zz} in the x-y plane for a vanadium limiter with lithium coolant at a pressure of 5.5 MPa and wall heat flux of 6.0 MW/m^2. Also shown in Figure 4.9-13 is the stress intensity σ_{xx} along the y-direction of the face FF'G'G. Figure 4.9-14 shows the distribution of the von Mises stress, σ_t, where σ_t is defined as:

$$\sigma_t^2 = \frac{1}{2}\left[(\sigma_1 - \sigma_2)^2 + (\sigma_2 - \sigma_3)^2 + (\sigma_3 - \sigma_1)^2\right]$$

where σ_1, σ_2 and σ_3 are principal stresses. Three principal stresses are obtained by determining the roots of the following cubic equation:

$$\sigma^3 - (\sigma_{xx} + \sigma_{yy} + \sigma_{zz})\,\sigma^2 + (\sigma_{xx}\,\sigma_{yy} + \sigma_{zz} + \sigma_{zz}\,\sigma_{xx} - \sigma_{xy}^2 - \sigma_{yz}^2 - \sigma_{zx}^2)\,\sigma$$

$$- (\sigma_{xx}\,\sigma_{yy}\,\sigma_{zz} + 2\sigma_{xy}\,\sigma_{yz}\,\sigma_{zx} - \sigma_{xx}\,\sigma_{yz}^2 - \sigma_{yy}\,\sigma_{zx}^2 - \sigma_{zz}\,\sigma_{xy}^2) = 0$$

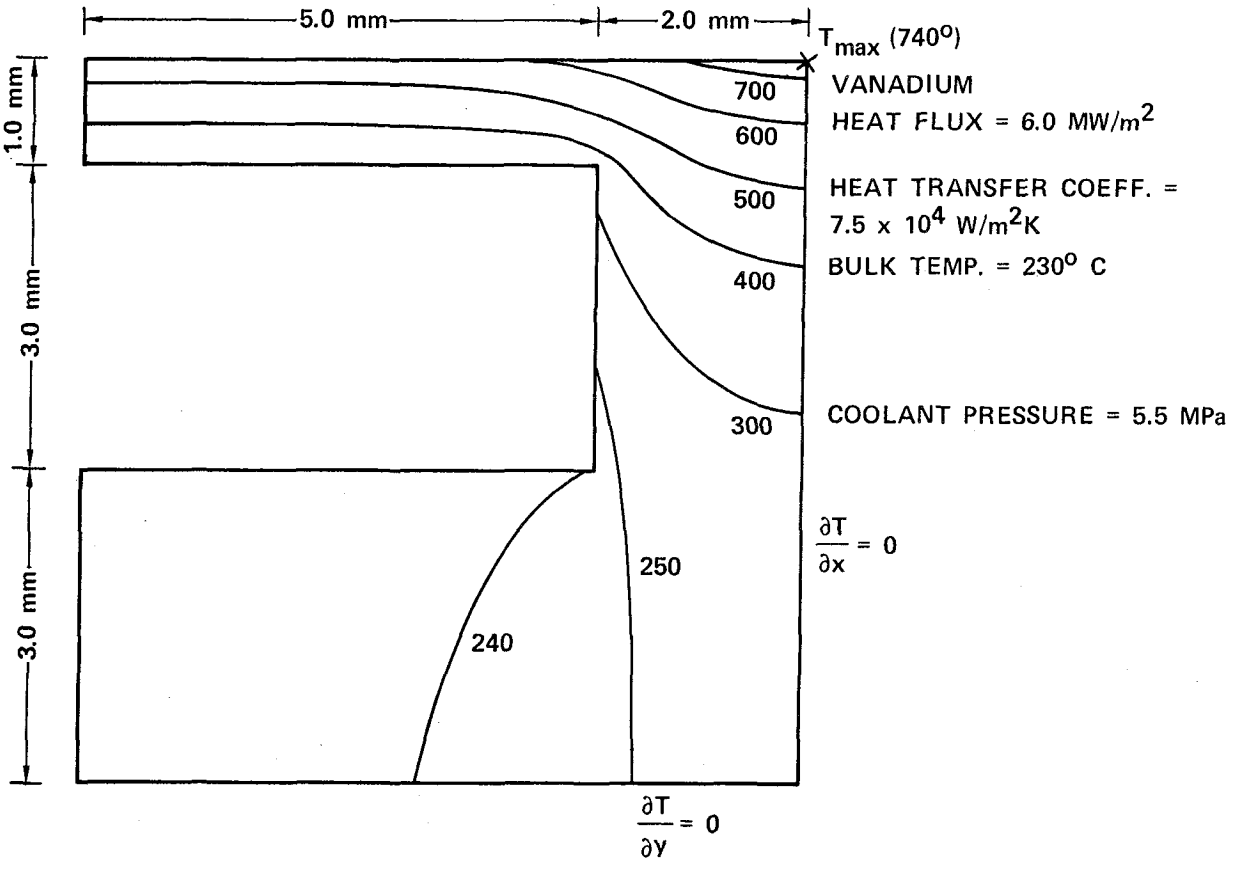


Figure 4.9-12 Temperature distribution

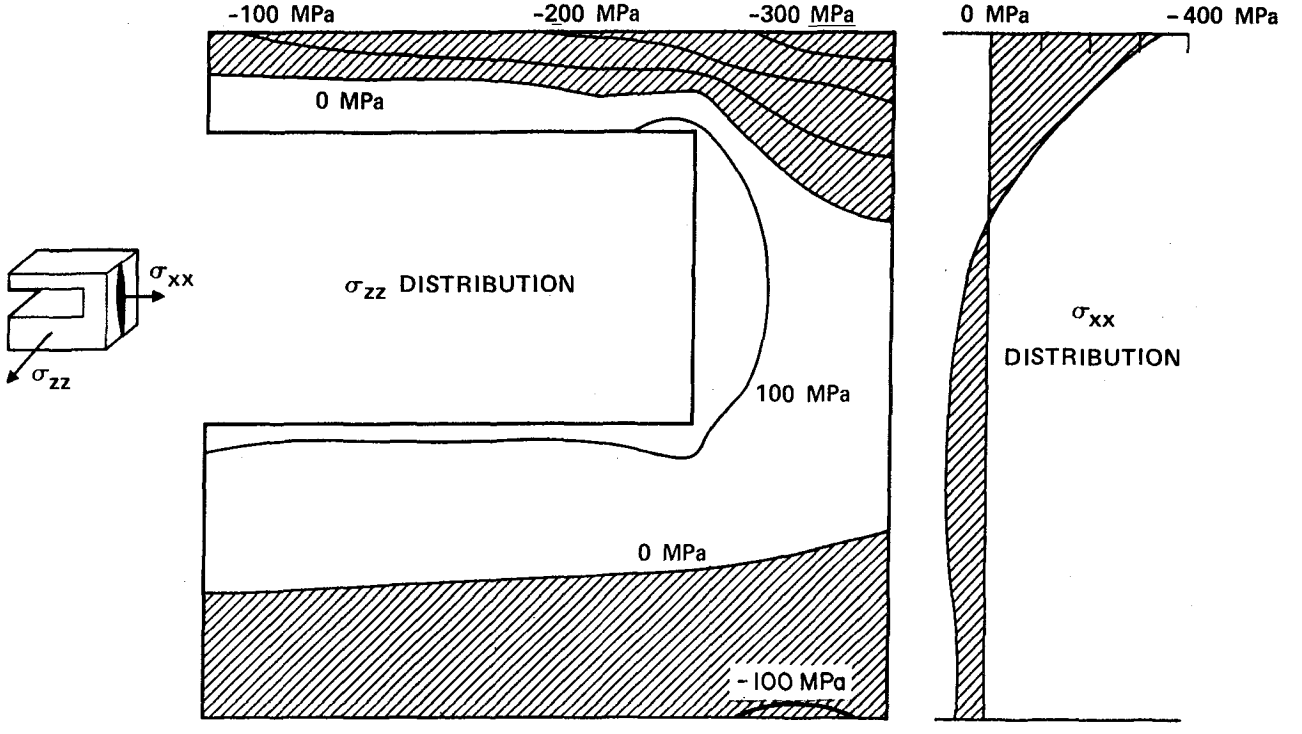


Figure 4.9-13 Stress distribution

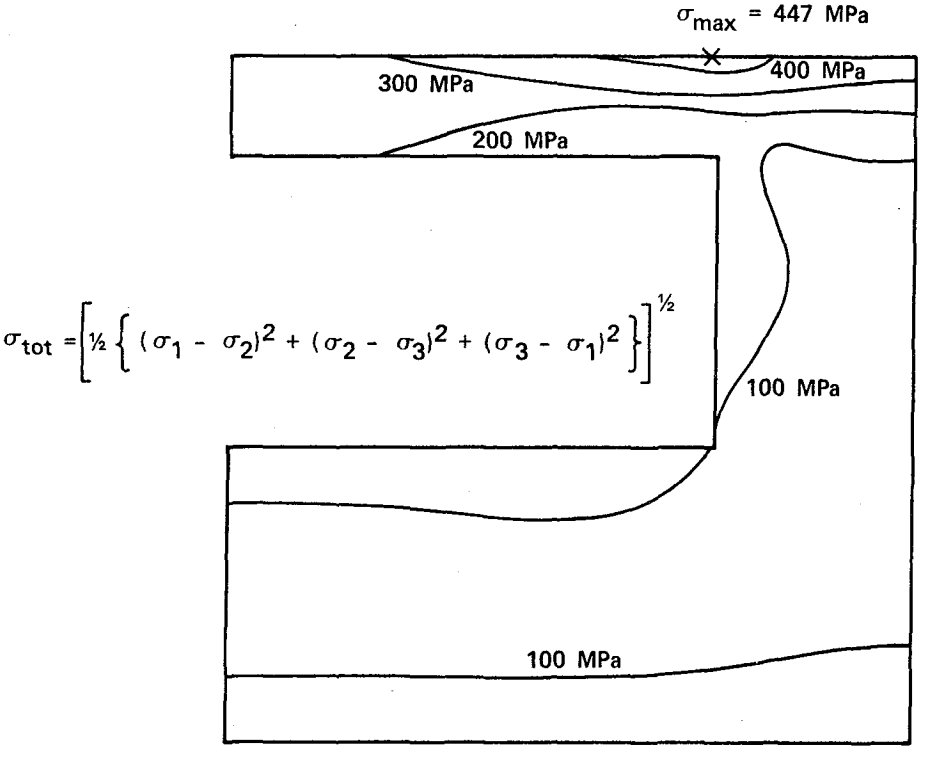


Figure 4.9-14 Von Mises stress distribution (σ_{ss})

4.9.5 Concluding Remarks

A three-dimensional stress analysis code was developed to analyze thermal and mechanical stresses of the limiter caused by surface heat flux and coolant pressure. The preliminary results obtained show that for copper limiters, a maximum stress limit (3 Sm) is obtained for a heat flux of about 5.2 MW/m^2 and a coolant pressure of about 3.3 MPa. Therefore, temperature and stress requirements can be satisfied for surface heat fluxes < 5.2 MW/m^2 and coolant pressures < 3.3 MPa for copper limiters. Vanadium alloy limiters, on the other hand, can operate at higher heat fluxes and coolant pressures. Stress limits for vanadium alloys are satisfied for surface heat fluxes < 6.0 MW/m^2 and coolant pressures < 8.0 MPa.

The results obtained in this section are for the central section of the limiter. Further work is being carried out for the edge part of the limiter and more results will be available in the near future.

References for Chapter 4

1. M.A. Abdou, et al., Technical Issues and Requirements of Experiments and Facilities for Fusion Nuclear Technology (FINESSE Phase I Report)," PPG-909, UCLA-ENG-85-39, University of California, Los Angeles (1985).

2. "Technical Planning Activity Final Report," ANL/FPP-87-1, Argonne National Laboratory (1987)

3. B.G. Logan, et al., "MARS: Mirror Advanced Reactor Study (Final Report)," UCRL-53480, Lawrence Livermore National Laboratory (1984).

4. C.C. Baker, et al., "Tokamak Power Systems Studies - FY 1985," ANL/FPP-85-2, Argonne National Laboratory (1985).

5. C. Copenhaver, R.A. Krakowski, N.M. Schnurr, et al., "Compact Reversed-Field-Pinch Reactors (CRFPR): Fusion-Power-Core Integration Study," LA-10500-MS, Los Alamos National Laboratory (1985).

6. "Blanket Comparison and Selection Study - Final Report," ANL/FPP-84-1, Argonne National Laboratory (1984).

7. R.J. Holroyd, "An Experimental Study of the Effects of Wall Conductivity, Non-Uniform Magnetic Fields and Variable-Area Ducts on Liquid Metal Flows at High Hartmann Number. Part 1. Ducts With Non-Conducting Walls," J. Fluid Mech., 93:4, 609-630 (1979).

8. V.P. Bocheninskii, G. Branover, A.V. Tananaev, and Y.P. Chernyaev, "Experimental Investigation of the Resistance to the Flow of a Conducting Fluid in Flat Insulated Ducts in the Presence of a Transverse Magnetic Field with Allowance for Fringe Effects and Wall Roughness," Fluid Dynamics, 6:4, 10-21 (1973).

9. C.B. Reed, B.F. Picologlou, and P.V. Dauzvardis, "Experimental Facility for Studying MHD Effects in Liquid Metal Cooled Blankets," Fusion Tech., 8:1, 257-263 (1985).

10. J.A. Dekeyser and J.L. Walnier, "Characteristics of Experimental Facilities for Research and Development in Lithium and Lithium-Lead Technology," FT/MOL/B4-7/T82-002, CEN/SCK (1985).

11. J.C.R. Hunt and R.J. Holroyd, "Applications of Laboratory and Theoretical MHD Duct Flow Studies in Fusion Reactor Technology," CLM-R 169, Culham Laboratory (1977).

12. H. Branover, E.S. Pierson, and J.S. Walker, "Magnetohydrodynamic Flows and Turbulence: A Report on the Fourth Beer-Sheva Seminar," J. Fluid Mech., 148, 461-476 (1984).

13. G.S.S. Ludford and J.S. Walker, "Current Status of MHD Duct Flow," Proceedings of the Second Bat-Sheva International Seminar, Beersheva, March 28-31, 1978.

14. O. LieLausis, "Liquid-Metal Magnetohydrodynamics," Atomic Energy Review, 13, 527-581 (1975).

15. H. Branover, Magnetohydrodynamic Flow in Ducts, Halsted Press, New York (1978).

16. H. Schlichting, Boundary-Layer Theory, McGraw-Hill Book Company, San Francisco (1979).

17. J.C. Hunt, "Magnetohydrodynamic Flow in Rectangular Ducts," J. Fluid Mech., 21, 577-590 (1965).

18. J.S. Walker, G.S. Ludford and J.C. Hunt, "Three-Dimensional MHD Duct Flows with Strong Transverse Magnetic Fields. Part 2. Variable-Area Rectangular Ducts with Conducting Sides," J. Fluid Mech., 46, 657-684 (1971).

19. J.S. Walker and G.S. Ludford, "Three-Dimensional MHD Duct Flows with Strong Transverse Magnetic Fields. Part 4. Fully Insulted, Variable-Area Rectangular Ducts with Small Divergences," J. Fluid Mech., 56, 481-496 (1972).

20. J.C. Petrykowski and J.S. Walker, "Liquid-Metal Flow in a Rectangular Duct with a Strong, Non-Uniform Magnetic Field," J. Fluid Mech., 139, 309-324 (1984).

21. F.H. Harlow and J.E. Welch, "Numerical Calculation of Time-dependent Viscous Incompressible Flow," Phys. Fluids, 8, 2182 (1965).

22. S.V. Patankar, Numerical Heat Transfer and Fluid Flow, McGraw-Hill, New York (1980).

23. J.I. Ramos and N.S. Winowich, "Magnetohydrodynamic Channel Flow Study," Physics of Fluids, 29, 992-997 (1986).

24. S.P. Vanka and R.K. Ahluwalia, "Three-Dimensional Flow and Heat Transfer Development in MHD Channels," AIAA Aerospace Sciences Meeting, St. Louis, Missouri (1981).

25. G.P. D'Arcy and P.S. Schmidt, "Entry Region Effects on Lithium Flow and Pressure Drop in Fusion-Reactor Blankets," Proc. Symp. Technology of Controlled Thermonuclear Fusion Experiments and the Engineering Aspects of Fusion Reactors, Univ. of Texas, Austin (1972).

26. E.R. Eckert and R.M. Drake, Analysis of Heat and Mass Transfer, McGraw-Hill, New York (1972).

27. Chia-Jung, Hsu and G.C. Lindauer, "The Influence of Axial Conduction on the Thermal Entry Region Heat Transfer in MHD Channel Flow," Nucl. Sci. and Eng., 32, 16-29 (1968).

28. R.K. Shah and A.L. London, "Laminar Flow Forced Convection in Ducts," Advances in Heat Transfer, Academic Press (1978).

29. E.O. Macagno and T.K. Hung, "Computational and Experimental Study of a Captive Annular Eddy," J. Fluid Mech., 28, 43-64 (1967).

30. J.M. McMichael and S. Deutsch, "Magnetohydrodynamics of Laminar Flow in Slowly Varying Tubes in an Axial Magnetic Field," Phys. Fluids, 27, 110-118 (1984).

31. T.N. Aitov, A.I.Kalutik and A.V. Tananaev, "Numerical Investigation of Three-Dimensional MHD Flow in a Curved Channel of Rectangular Cross Section," Magnetohydrodynamics, 4, 458-462 (1978).

32. J.J. Conner and C.A. Brebbia, Finite Element Techniques for Fluid Flow, Newnes-Butterworths (1976).

33. D.K. Gartling and E.B. Becker, "Finite Element Analysis of Viscous Incompressible Flow , Part 1: Basic Methodology," Comput. Meth. Appl. Mech. Eng., 8, 51-60 (1976).

34. D.K. Gartling and E.B. Becker, "Finite Element Analysis of Viscous Incompressible Flow , Part 2: Applications," Comput. Meth. Appl. Mech. Eng., 8, 127-138 (1976).

35. B. Singh and J. Lal, "Effect of Magnetic Field Orientation and Wall Conductivity on MHD Channel Flows Using Finite Element Method", Comput. Meth. Appl. Mech. Eng., 40, 159 (1983).

36. B. Singh and J. Lal, "Finite Element Method in Magnetohydrodynamic Channel Flow Problems," International Journal for Numerical Methods in Engineering, 18, 1104 (1982).

37. N.S. Winowich and W.F. Hughes, "A Finite-Element Analysis of Two-Dimensional MHD Flow," Liquid Metal Flows and Magnetohydrodynamics, ed. H. Branover, P.S. Lykoudis, and A. Yakhot, American Institute of Aeronautics and Astronautics, Inc. (1983).

38. G. Yagawa, M. Masuda, and Y. Ando, "Finite Element Analysis of Magnetohydrodynamics and its Application to Lithium Blanket Design of a Fusion Reactor", Nuclear Eng. and Design, 71, 121-136 (1982).

39. J.S. Walker and G.S.S. Ludford, "MHD Flow in Insulating Circular Expansions with Strong Transverse Magnetic Fields," Int. J. Eng. Sci., 12, 1045-1061 (1974).

40. H.H. Branover, "Suppression of Turbulence in Pipes with Transverse and Longitudinal Magnetic Fields," Magnetohydrodynamics, 47, 107 (1967).

41. M.A. Hoffman, "Magnetic Field Effects on the Heat Transfer of Potential Fusion Reactor Coolants", UCRL-73993 (1972).

42. R.A. Gardner and P.S. Lykoudis, "Magneto-fluid-mechanic Pipe Flow in a Transverse Magnetic Field. Part 1. Isothermal Flow," J. Fluid Mech., 47, 737 (1971).

43. H. Branover and P. Gershon, "Experimental Investigation of the Origin of Residual Disturbances in Turbulent MHD Flows After Laminarization," J. Fluid Mech., 94, 629 (1979).

44. H. Branover, et al., "Turbulence and the Feasibility of Self-Cooled Liquid Metal Blankets for Fusion Reactors," Fusion Tech., 10, 822-829 (1986).

45. S. Sukuriansky, I. Zilberman, and H. Branover, "Experimental Studies of Turbulence in Mercury Flows with Transverse Magnetic Fields," Experiments in Fluids 4, 11-16 (1986).

46. E.B. Becker, G.F. Carey, and J.T. Oden, Finite Elements, An Introduction, Vol. 1, Prentice Hall, Inc. (1981).

47. J.J. Conner and C.A. Brebbia, Finite Element Techniques for Fluid Flow, Newnes-Butterworths (1976).

48. V.A. Barker, ed., "Sparse Matrix Techniques," Lecture Notes in Computer Science, Springer-Verlag, Berlin, August 1976.

49. T.Z. Mai and D.M. Young, "ITPACK 3B User's Guide (Preliminary Version)," CNA-201, Center for Numerical Analysis, University of Texas at Austin (1986).

50. W.R. Dean, "Notes on the Motion of Fluid in a Curved Pipe," Phil. Mag. 14, 208 (1927).

51. D.J. McConalogue and S.R. Srivastava, "Motion of a Fluid in a Curved Tube," Proc. Roy. Soc., A, 307, 37-53 (1968).

52. S.V. Patankar, V.S. Pratap and D.B. Spalding, "Prediction of Laminar Flow and Heat Transfer in Hellically Coiled Pipes," J. Fluid Mech., 62, 539 (1974).

53. R.J. Holroyd, "An Experimental Study of the Effects of Wall Conductivity, Non-Uniform Magnetic Fields and Variable Area Ducts on Liquid Metal Flows at High Hartmann Number, Part 2. Ducts with Conducting Walls," J. Fluid Mech., 96, 355-374 (1980).

54. J.S. Walker, "Liquid Metal Flow Through a Thin Walled Elbow in a Plane Perpendicular to a Uniform Magnetic Field," ANL/FPP/TM-204, Argonne National Laboratory (1986).

55. J.A. Shercliff, The Theory of Electromagnetic Flow Measurement, University Press, Cambridge (1962).

56. R.J. Holroyd and J.S. Walker, "A Theoretical Study of the Effects of Wall Conductivity, Non-Uniform Magnetic Fields and Variable Area Ducts on Liquid Metal Flows at High Hartmann Number," J. Fluid Mech., 84, 471-495 (1978).

57. W.M. Wells, "Experiments and Calculations on the Feasibility of Pumping Liquid Lithium in a Thermonuclear Reaction Blanket," UCRL-50544 (1969).

58. K. Taghavi, M.S. Tillack, H. Madarame, "Special Features of First Wall Heat Transfer in Liquid Metal Fusion Reactor Blankets," to be published in Fusion Technology.

59. M.A. Abdou, et al., "FINESSE, A Study of the Issues, Experiments and Facilities for Fusion Nuclear Technology Research and Development (Interim Report)," University of California, Los Angeles, PPG-821, UCLA-ENG-84-30 (1984).

60. P.S. Lykoudis and P.F. Dunn, "Magneto-Fluid-Mechanic Heat Transfer from Hot Film Probes," Int. J. Heat Mass Transfer, 16, 1439-1452 (1973).

61. S. Ostrach, "Laminar Natural Convection Flow and Heat Transfer of Fluids With and Without Heat Sources in Channels With Constant Wall Temperatures," NACA TN2863 (1962).

62. T.M. Hallman, "Combined Forced and Free Laminar Heat Transfer in Vertical Tubes with Uniform Internal Heat Generation," Trans. ASME, 78, 1831-1841 (1956).

63. H.F. Poppendick, "Forced Convection Heat Transfer in Pipes with Volume Heat Sources Within the Fluid," Chemical Engineering Progress Symposium, Series No. 50, 239-254 (1954).

64. E.M. Sparrow and R. Siegal, "Laminar Tube Flow With Arbitrary Internal Heat Sources and Wall Heat Transfer," Nucl. Sci. and Eng., 4, 239-254 (1958).

65. P.L. Chambre, "The Laminar Boundary Layer with Distributed Heat Sources or Sinks," Applied Scientific Research, Section A, 6, 393-401 (1957).

66. H. Schlichting, Boundary Layer Theory, Sixth Edition, McGraw-Hill, New York (1968).

67. H.J. Merk, "Rapid Calculations for Boundary Layer Transfer Using Wedge Solutions and Asymptotic Expansions," J. Fluid Mech., 5, 460-480 (1959).

68. K. Hiemenz, "Die Grenzschict an einem in den gleichformigen Flussigkeltsstrom eingetauchten geraden Kreiszylinder," Thesis Gottingen (1911).

69. S. Tewani, "Heat Transfer of a Flow with Volumetric Heat Generation Over a Wedge or Across a Cylinder," M.S. Thesis, University of Kentucky (1987).

70. S. Malang, "On fluence of a Magnetic Field on Liquid Metal Corrosion," Proceedings of the 13th Symposium on Fusion Technology, Varese, Italy (1984).

71. W. Bjorndahl and J.D. Gordon, "MHD Effects on Liquid Metal Corrosion Product Transport," Proceedings of the American Nuclear Society Annual Meeting, New Orleans (1983).

72. A.C. Klein and W.F. Vogelsang, "Activation Product Transport in Fusion Reactors," J. Nucl. Mat., 122 & 123, 1236-1240 (1984).

73. D.G. Bauer, Kinetics of the Degradation of 316 Stainless Steel by Lithium, PhD Thesis, University of Wisconsin, Madison (1980).

74. M. Schad, " Application of a Sodium Austenitic Corrosion Model to a Fuel Rod," Nucl. Tech., 50, 267-288 (1980).

75. M.V. Polley and G. Skyrme, "An Analysis of Radioactive Corrosion Product Transfer in Sodium Loop Systems," J. Nucl. Mat., 75, 226-237 (1978).

76. C.F. Clement, "Theory of Mass Transport in Liquid Circuits," AERE-TP-606, Atomic Energy Research Establishment, Harwell (1975).

77. L.F. Epstein, "Static and Dynamic Corrosion and Mass Transfer in Liquid Metal Systems," Liquid Metal Technology--Chemical Engineering Progress Symposium Series, no. 20, 53 (1959).

78. C.F. Clement, "Models for the Growth and Dissolution of Small Particles in Liquids," AERE-TP-605, Atomic Energy Research Establishment, Harwell (1975).

79. E.G. Brush, "Sodium Mass Transfer XVI: The Selective Corrosion Component of Steel Exposed to Flowing Sodium," GEAP-4832, General Electric Company (1965).

80. P. Hutchinson and G.F. Hewitt, "Deposition of Liquid or Solid Dispersions from Turbulent Gas Streams: A Stochastic Model," Chemical Science and Engineering, 26, 419-439 (1971).

81. R.J. Pulham and P. Hubberstey, "Comparison of Chemical Reactions in Liquid Lithium with Those in Liquid Sodium," J. Nucl. Mat., 115, 239-250 (1983).

82. P. Hubberstey, "Dissolved Nitrogen in Liquid-Lithium--A Problem in Fusion Reactor Chemistry," Liquid Metal Eng. and Tech., 2, British Nuclear Eng. Society, London (1985).

83. G.D. Smith, Numerical Solution of Partial Differential Emphasis, Oxford University Press, London (1975).

84. R.B. Bird, et al., Transport Phenomena, John Wiley & Sons, New York, New York, 554 (1960).

85. M.C. Billone, "The Influence of Surface Desorption on Tritium Recovery and Inventory in Fusion Solid Breeders," J. Nucl. Mat., 141-143, 316-320 (1986).

86. "A Blanket Comparison and Selection Study - Interim Report," ANL/FPP-84-1, Argonne National Laboratory (1983).

87. S.J. Piet, "Common Views of Potentially Attractive Fusion Concepts," Fusion Tech., 10, 896-901 (1986).

88. M.A. Abdou, "INTOR Impurity Control and First Wall Systems," Fusion Technology 1982, Proc. 12th Symposium on Fusion Technology, Julich, West Germany, I:39 (1983).

89. W.M. Stacey, Jr., Fusion, John Wiley and Sons, Inc., New York (1984).

90. J.A. Swanson, et al., "ANSYS Engineering Analysis Systems Users Manual," Swanson Analysis Systems, Inc., Huston, PA (1983).